NASA RP–1190

INFRARED ASTRONOMICAL SATELLITE (IRAS)

CATALOGS AND ATLASES

VOLUME 1

EXPLANATORY SUPPLEMENT

Edited by
C. A. Beichman, G. Neugebauer, H. J. Habing, P. E. Clegg, and T. J. Chester

Prepared under the auspices of
The Joint IRAS Science Working Group

NASA Scientific and Technical Information Division 1988
National Aeronautics and Space Administration
Washington, DC

The Joint IRAS Science Working Group was composed of:

G. Neugebauer	1977-1984	Co-chairman	1977-1984
R. J. van Duinen	1977-1982	Co-chairman	1977-1982
H. J. Habing	1977-1984	Co-chairman	1982-1984

H. H. Aumann	1977-1984	T. de Jong	1977-1984	P. R. Wesselius	1982-1984
D. A. Beintema	1977-1984	F. J. Low	1977-1984	B. Baud	1982-1984
N. Boggess	1977-1984	P. L. Marsden	1977-1984	C. A. Beichman	1982-1984
J. Borgman	1977-1981	S. R. Pottasch	1977-1983	T. N. Gautier	1982-1984
P. E. Clegg	1977-1984	B. T. Soifer	1977-1984	S. Harris	1982-1984
F. C. Gillett	1977-1984	R. G. Walker	1977-1984	G. K. Miley	1982-1984
M. G. Hauser	1977-1984	J. P. Emerson	1979-1984	F. M. Olnon	1982-1984
J. R. Houck	1977-1984	E. Raimond	1979-1984	E. Young	1982-1984
R. E. Jennings	1977-1984	M. Rowan-Robinson	1979-1984		

Library of Congress Cataloging-in-Publication Data

Infrared Astronomical Satellite (IRAS) catalogs and atlases / prepared under the supervision of the Joint IRAS Science Working Group.
p. cm.— (NASA reference publication : 1190)
Contents: v. 1. Explanatory supplement / C.A. Beichman ... [et al.] — v. 2. The Point source catalog declination range 90° [greater than delta greater than] 30° — v. 3. The Point source catalog declination range 30° [greater than delta greater than] 0° —v. 4. The Point source catalog declination range 0° [greater than delta greater than] −30° — v. 5. The Point source catalog declination range −30° [greater than delta greater than] −50° — v. 6. The Point source catalog declination range −50° [greater than delta greater than] −90° — v. 7. The Small scale structure catalog /George Helou and D. W. Walker.
1. Infrared astronomy—Observations—Catalogs. 2. Infrared astronomy—Atlases. 3. Infrared source—Observations—Catalogs. 4. Infrared sources—Atlases. 5. Infrared Astronomical Satellite—Catalogs. 6. Infrared Astronomical Satellite—Atlases. I. Joint IRAS Science Working Group. II. Series.
QB470.I54 1988
523.8 9—dc19

For sale by the Superintendent of Documents, U.S. Government Printing Office
Washington, D.C. 20402

PREFACE TO THE SECOND EDITION

The *Explanatory Supplement* was first released in November 1984 as a preprint (Jet Propulsion Laboratory D-1855) to accompany the initial distribution of the IRAS Catalogs and Atlasses. Since that time a small number of errors have been found in both the data products themselves and in their description in the *Supplement*. Rather than completely rewrite the *Supplement* to remedy its shortcomings, we have chosen to fix only a few glaring errors in the main body of the text and to insert as Chapter XII a discussion of differences between the initial and present versions of the data. As a result of this choice, some inconsistencies in references to Chapters XII, XIII and XIV may be found in the text.

This version of the *Supplement* describes the data available as of March 1987 at the National Space Science Data Center (NSSDC) at the Goddard Space Flight Center; the interested reader is referred to the NSSDC for access to the IRAS data.

C. Beichman
Pasadena
March 1987

PREFACE TO 1985 EDITION

The attached Explanatory Supplement is being released in a preliminary version with the various catalogs and atlases because the information contained in this Supplement is essential for using the IRAS data. Many sections, but especially Chapters VII, VIII and XI, could not be written before the production of the catalogs was completed. As a result, the analysis is neither as complete nor as detailed as might be desired. Undoubtedly, the Supplement and catalogs contain errors. We have chosen to release the Explanatory Supplement in preprint form at this time. A hard-bound version of the Supplement and the Catalog will be issued shortly after February 1, 1985.

Any reader who finds errors in the text or the Catalog before February 1, 1985, is requested to communicate such errors to:

C. Beichman or G. Neugebauer
c/o IRAS Project Office
California Institute of Technology
Mail Stop 100-22
Pasadena, California 91125

TABLE OF CONTENTS

VIII. SKY COVERAGE, CONFUSION, COMPLETENESS AND RELIABILITY

IX. THE LOW RESOLUTION SPECTRA

X. THE FORMATS OF THE IRAS CATALOGS AND ATLASES

XI. KNOWN PROCESSING ANOMALIES

INDEX OF TABLES

INDEX OF TABLES - Continued

INDEX OF TABLES - Continued

INDEX OF FIGURES

INDEX OF FIGURES - Continued

INDEX OF FIGURES - Continued

INDEX OF FIGURES - Continued

I. INTRODUCTION

A. General Overview

A.1 The IRAS Mission

The primary mission of the Infrared Astronomical Satellite (IRAS) was to conduct a sensitive and unbiased survey of the sky in four wavelength bands centered at 12, 25, 60, and 100 μm. The project was initiated in 1975 as a joint program of the United States, the Netherlands, and the United Kingdom. Launched in January 1983, IRAS ceased operations in November 1983 after having successfully surveyed more than 96% of the sky.

The results of several portions of the IRAS mission are given in a catalog of infrared point sources, in a catalog of extended sources smaller than 8′, in a catalog of low-resolution spectra, and in an atlas of absolute surface brightness images of the entire infrared sky. These catalogs give the characteristics of some 250,000 point sources and 20,000 small extended sources down to a limiting flux density, away from confused regions of the sky, of about 0.5 Jy at 12, 25 and 60 μm and about 1.5 Jy at 100 μm for point sources, and about a factor of three brighter than this for small extended sources. The angular resolution of the instrument varied between about 0.5′ at 12 μm to about 2′ at 100 μm. The positional accuracy of sources detected by IRAS depends on their size, brightness and spectral energy distribution but is usually better than 20″. Approximately 5000 8-22 μm spectra of survey sources brighter than 10 Jy at 12 and 25 μm are available.

A.2 The Explanatory Supplement

This Explanatory Supplement is intended to be a complete and self-contained description of the IRAS mission in relation to the products of the survey. In Chapter II, the IRAS satellite, telescope and focal plane instrumentation are reviewed. The elements of the mission profile--the constraints, the design features, and the in-flight modifications to that design--are described in Chapter III and are accompanied by a chronology of the events of the mission. In-flight tests of those aspects of the performance of the instrument directly associated with the survey are presented in Chapter IV. Chapters V and VI describe the processing performed on the data; the summaries that precede the detailed discussions should be sufficient to acquaint the user with the contents of the catalogs. Since the flux reconstruction and calibration of the instrument probably hold intrinsic interest for many readers, these are described separately in Chapter VI.

A preliminary analysis of some of the statistical properties of the catalogs is given in Chapter VII. Emphasis is placed on general statistics, such as positional and photometric accuracy and on easily derived number counts. A preliminary analysis of the sky coverage and of the completeness and reliability of the catalog is given in Chapter VIII. The low-resolution spectrometer and the analysis of its measurements are described in Chapter IX. Chapter X explains the format and meaning of each of the entries in the catalogs. Each printed volume of the catalogs repeats the description of the formats of that catalog.

In order to produce the catalogs in a timely fashion, some processing errors and anomalies could not be fixed; those which were discovered before the release of the data in November 1984 are described in Chapter XI. A compilation of the names of people who worked on the IRAS project comprises

Chapter XII. The last chapter provides a series of plots giving the details of the coverage of the sky by the IRAS survey.

Each chapter of the Supplement was written by those members of the IRAS team whose names are appended to that chapter. The work described was obviously the result of efforts by many individuals and should not be ascribed to the authors alone.

A.3 Cautionary Notes

While it is unlikely that all aspects of the instrumental performance or the data processing will be of interest to all readers, even casual users should familiarize themselves with the various *caveats* described in the chapters appropriate to the type of data in question. All users of IRAS data should be cognizant of the following crucial facts:

a) The sky at 100 μm is dominated by filaments termed "*infrared cirrus*" which, although concentrated near the Galactic plane, can be found almost all the way up to the Galactic poles (Fig. I.C.4). The primary, deleterious effects of the cirrus are that it can generate well-confirmed point and small extended sources that are actually pieces of degree-sized structures rather than isolated, discrete objects and that it can corrupt 100 μm, and occasionally 60 μm, measurements of true point sources (Sections V.H.4, VIII.D.2).

b) The spectral bandwidths of the detectors were sufficiently wide that the quoted flux densities depend on the assumed energy distribution of the source. For the catalogs, the energy distribution was taken to be constant in the flux per logarithmic frequency interval. If the source has a different energy distribution than this, a *color correction*, as large as 50% in extreme cases, must be applied to the quoted flux densities (Section VI.C.3).

c) The survey is clearly *confusion limited* within about 10° of the Galactic plane and in several areas of the sky such as the Ophiuchus and Orion-Taurus regions. Considerable effort has been made to select only highly reliable sources in such areas, at the expense of completeness. The flags associated with sources with possible confusion-related problems should be examined very carefully (Sections V.D.8, V.H.6, VIII.C, VIII.D. and X.B).

d) The algorithm used to estimate the detector noise suffered from a significant lag. This caused an under-estimate of the true noise when approaching regions of rapidly changing noise and an over-estimate of the noise when leaving such areas. Regions with large and rapidly varying numbers of sources, such as the Galactic plane, also produced this effect. Since the source detection algorithm (Section V.C) thresholded on signal to noise ratio, the overestimated noise level resulted in a dearth of sources, or a *shadow*, in the areas observed just after passage across the Galactic plane. At 60 and 100 μm, where the effect is worst, a "coverage hole" can extend as far as 2° from the plane. The density of detected sources can differ, totally artificially, by as much as a factor of ten from one side of the plane to the other due to this shadowing (Section VIII.D).

e) While great pains were taken to confirm the reality of sources in the point and small extended source catalogs, no such attempt was made for the sky brightness images. Instead, separate images of the sky taken at times differing from weeks to months are given. It is the responsibility of the user to ensure that sources seen in the images are not due to transient sources such as asteroids.

B. Summary Description of Catalogs and Atlases

The IRAS data are presented in different ways depending on the angular sizes of the structures involved:

B.1 Point Sources

Sources that appeared as point-like are presented in three different ways depending on their reliability and on the detail of information given for the sources.

a) A catalog of some 250,000 well-confirmed point sources is available in both printed and machine readable forms. Positions, flux densities, uncertainties, associations with known astronomical objects and various cautionary flags are given for each object. The information available in this catalog should satisfy almost all users.

b) A file known as the Working Survey Data Base, available only on magnetic tape, is intended for researchers requiring specialized information about the observational and processing history of a source in the catalog.

c) A file of rejected sources, available only on magnetic tape, includes any sources that did not meet the reliability criteria of the catalog. Some of these sources will be wholly spurious and due, for example, to detector noise, space debris, radiation hits or processing errors; others will be solar system objects such as asteroids and comets; and some will be true extra-solar system objects that failed to meet the confirmation criteria due to their faintness or variability, or to confusion effects. Sources in that small portion of the sky which received only limited survey coverage will also be found here.

B.2 Small Extended Sources

Sources larger than point-like, but smaller than $8'$ in angular extent are to be found in the catalog of small extended sources which is available in both printed and machine readable versions.

B.3 Sky Brightness Images

The overall view of the sky, and the repository of IRAS data for structures larger than $8'$, is found in the images of 212 fields that cover the entire celestial sphere. The fields are 16.5° on a side and have been imaged in each of the four wavelength bands with $2'$ pixels and 4-$6'$ resolution. As many as four images based on observations separated by a few weeks to a few months are presented. These data give absolute surface brightness and are available in both digital and photographic representations.

These image data are also available in a galactic coordinate projection for galactic latitudes within 10° of the plane, and, at degraded resolution, in an Aitoff projection over the entire sky. A file giving the time history of the total sky brightness measured by IRAS is available at 0.5° resolution.

B.4 Low-Resolution Spectra

Point sources which are bright in the 8-22 μm range may have been detected by the low resolution spectrometer (Chapter IX). Spectra are available in both printed (*Astronomy and Astrophyics Supplement Series* 1985) and machine readable forms.

B.5 The Extragalactic Sub-Catalog

A catalog of well-confirmed sources that are positionally associated with previously identified extragalactic objects is available in printed and magnetic tape versions. All the sources in this catalog are contained in either the catalogs of point or small extended sources, but additional information about the associated galaxies and quasars, obtained from a variety of astronomical catalogs, is presented here.

C. Overview of Infrared Sky

The various depths of coverage by the IRAS survey are displayed in Fig. I.C.1. The clear areas in the middle plot were covered with at least two sets of confirming scans, while the clear areas in the bottom plot were covered with confirming scans three or more times. Because the basic requirement for inclusion in the IRAS catalogs was that an object had to be observed with at least two sets of confirming scans, the clear portion of the middle plot represents the basic area covered by the IRAS survey. The shaded areas in the top plot show the areas of sky that were missed entirely.

The general distribution of well-confirmed point sources observed by IRAS is shown in Galactic coordinates in Fig. I.C.2 to I.C.4. Three classes of source covering almost all objects in the point source catalog can be defined according to spectral energy distribution: most of 130,000 sources that are brighter at 12 μm than at 25 μm are stars (Figure I.C.2); most of the 50,000 objects that are brighter at 60 μm than at 25 μm and which are located more than 20° from the Galactic plane are external galaxies (Fig. I.C.3); most of the 35,000 sources detected only at 100 μm are cold, dense clumps within the interstellar cirrus (Fig.I.C.4).

Authors:

G. Neugebauer and C. A. Beichman.

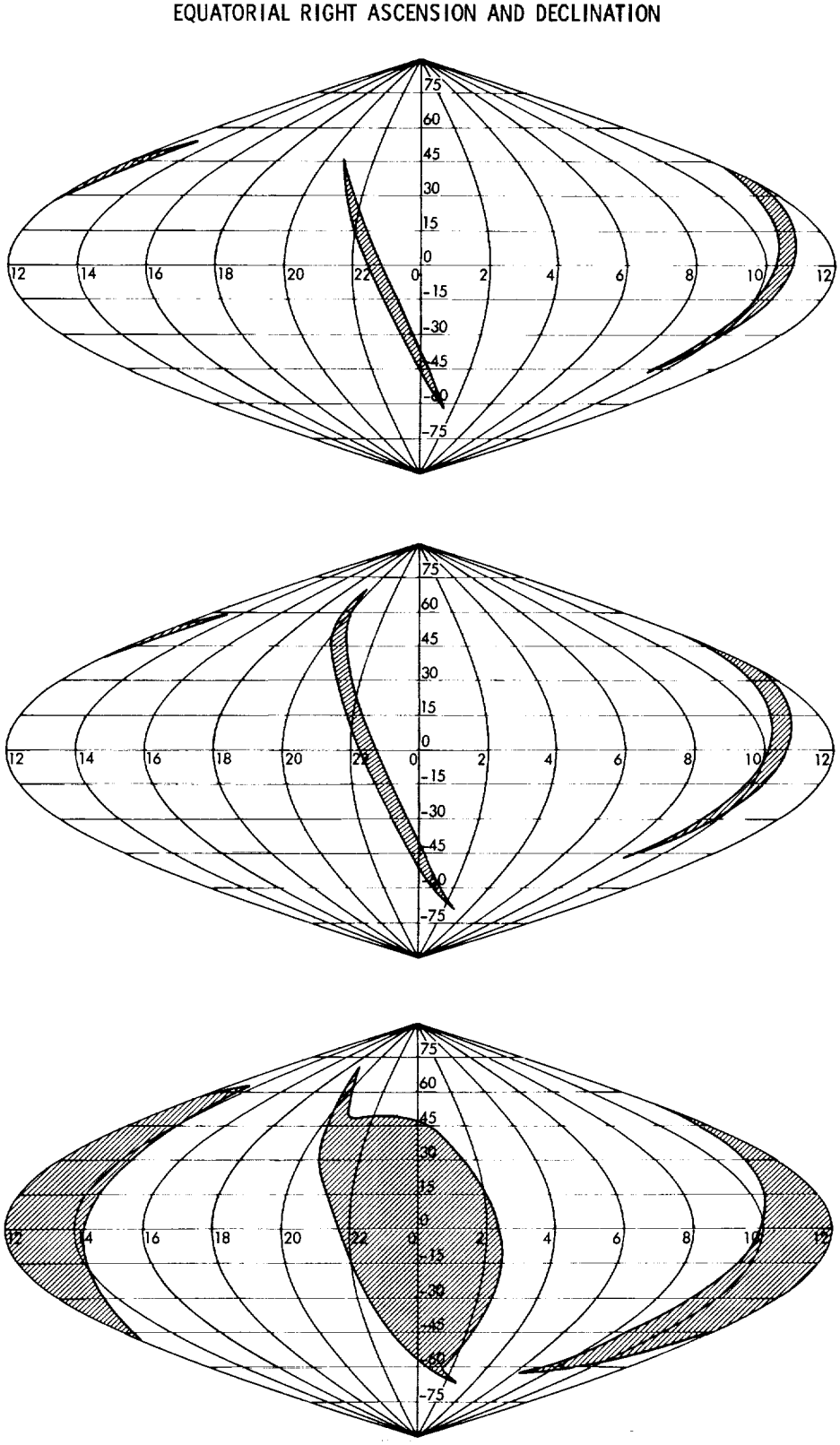

Figure I.C.1 Sky coverage of the IRAS survey. Three plots of the entire sky are shown with an equal area projection in equatorial coordinates (see text).

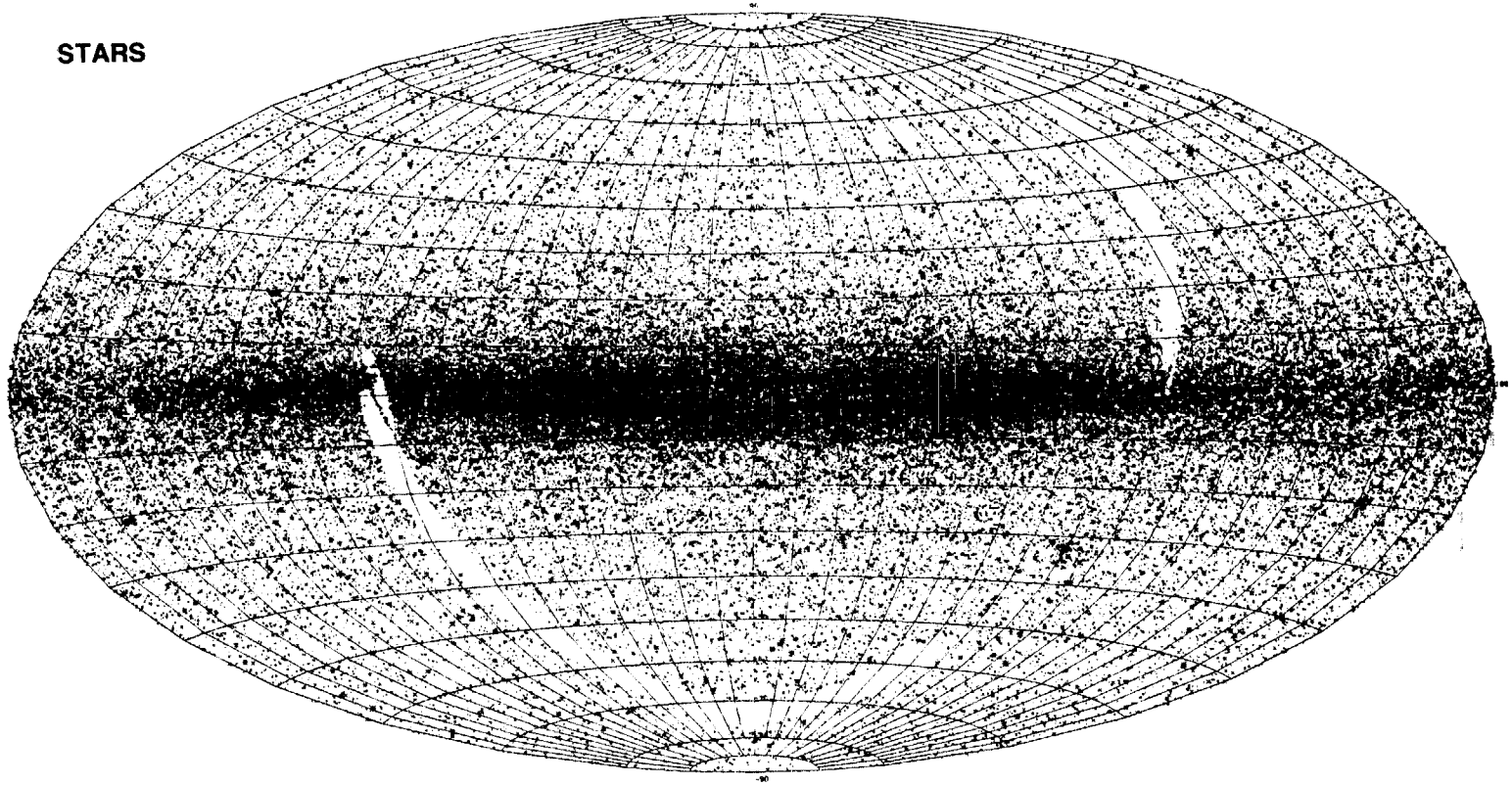

Figure I.C.2 The distribution of IRAS sources with stellar characteristics is shown in Galactic coordinates using an equal area Aitoff projection. (Galactic center at center, North at top, longitude increasing to left.)

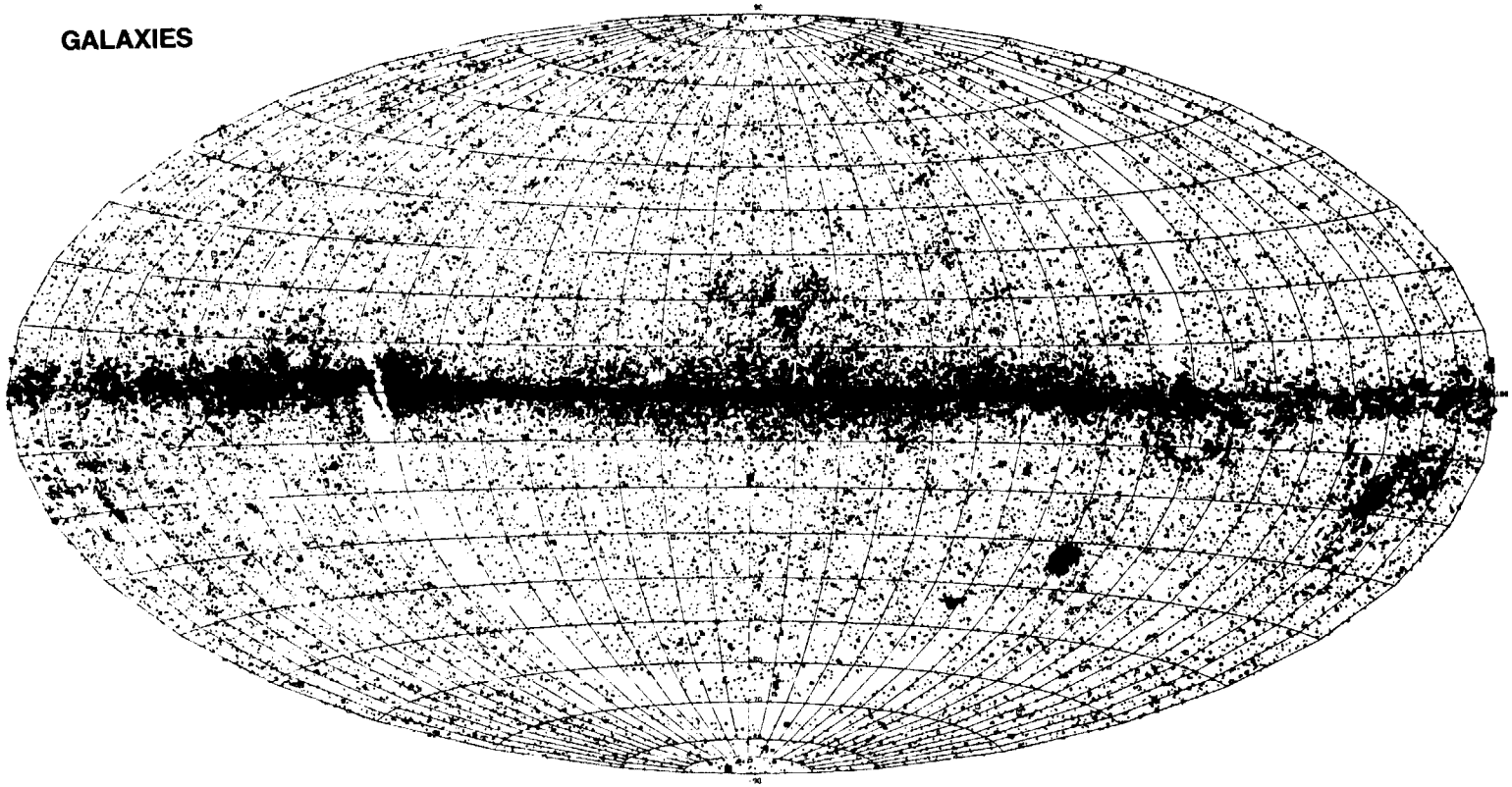

Figure I.C.3 The distribution of IRAS sources selected to isolate external galaxies is shown in Galactic coordinates in an equal area Aitoff projection. Areas near the Galactic plane and in the Ophiuchus and Orion-Taurus regions are heavily contaminated by Galactic objects. Galaxies detected only at 100 μm are discriminated against because of confusion with the infrared "cirrus" shown in Figure I.C.4

Figure I.C.4 The distribution of IRAS sources detected only at 100 μm is shown in Galactic coordinates using an equal area Aitoff projection. These sources are predominantly due to emission from compact pieces of extended filamentary interstellar dust structures, called infrared "cirrus".

II. SATELLITE DESCRIPTION

A. Introduction

The satellite consisted of two main parts, the spacecraft and the telescope system as shown in Fig. II.A.1. The overall dimensions of the satellite, with deployed solar panels, were: height 3.60 m, width 3.24 m, depth 2.05 m. The spacecraft and telescope system are described here with sufficient detail to allow the user of the catalog to understand how observations were made and the various limitations to the accuracy of these measurements. A fuller description of the spacecraft is given by Pouw (1983).

B. The Spacecraft

The features of the spacecraft of most relevance to the acquisition of the astronomical data were the control of the satellite, the method of executing the observational program, and the storage and transmission of data. To understand these, it is necessary to discuss the onboard computers and their associated software, the attitude control system, data recording and the communications links.

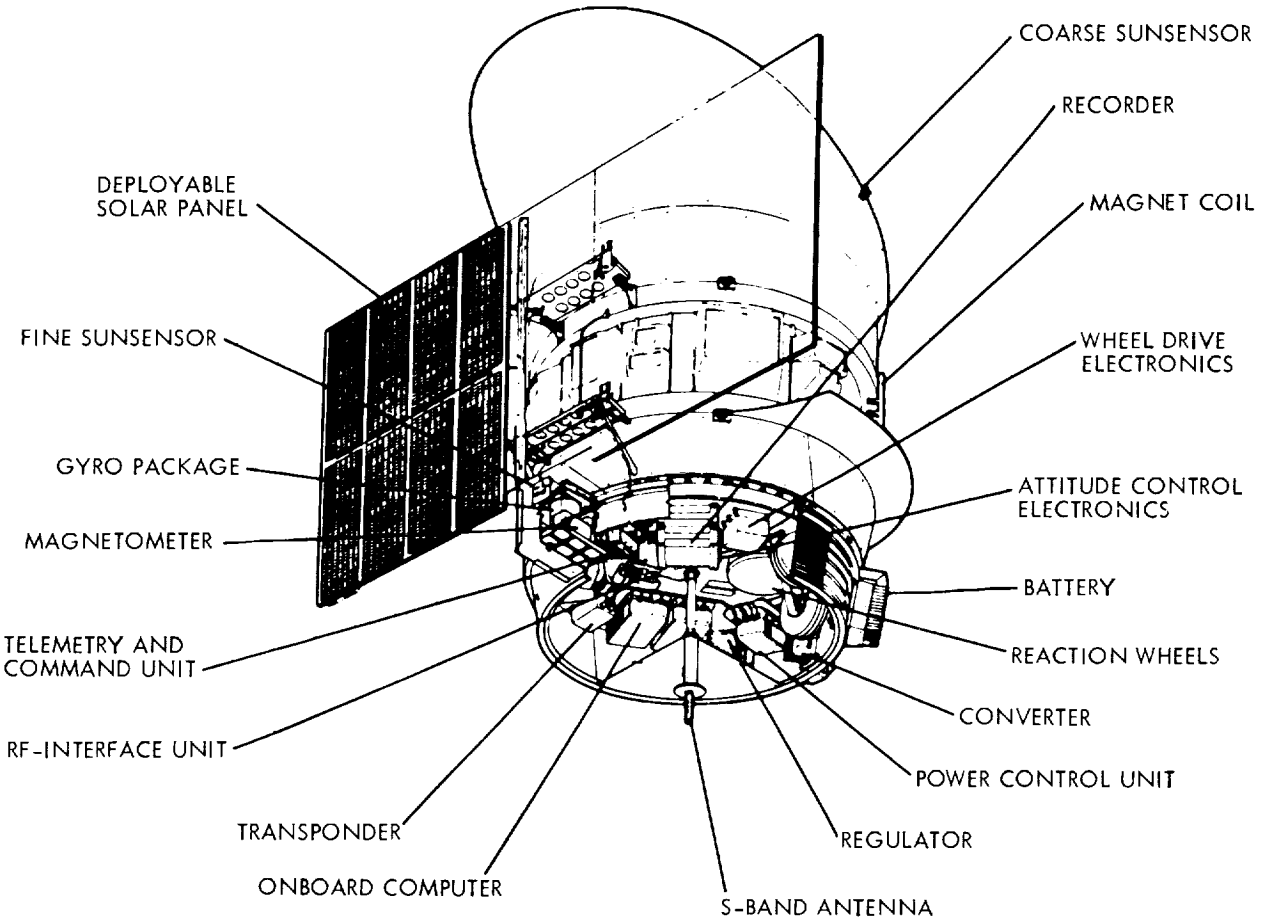

Figure II.A.1 Spacecraft configuration.

B.1 Onboard Computers and Software

Two identical computers provided redundancy. Each computer had a central processing unit with 32,000 16-bit words of random access memory, which could be accessed by either central processor, and 3000 words of read only memory. Each read only memory contained the routines essential for the safety of the satellite, for command handling and for the generation and downlink of housekeeping data. In particular, transition to read only memory control of the satellite could be, and indeed was, triggered by anomalous software or hardware behavior.

The random access memory contained the routines for executing a complete Satellite Operations Plan (hereafter denoted an SOP) for the ten to fourteen hour period between passes over the ground station and for generating the scientific data stream. Although 64,000 words of memory were available, this capacity was sometimes insufficient to store as large a program of observations as could be carried out during the observation period; this was a result of the high efficiency of the ground system at filling the observation time and applied particularly to the third coverage of the sky during the last four months of the mission (Section III.C.2).

B.2 Attitude Control

The satellite attitude was controlled by three orthogonal reaction wheels; excess momentum was dumped via magnetic coils to the Earth's magnetic field as necessary. The attitude, and changes in attitude, were sensed by a combination of an horizon sensor, a sun-sensor and three orthogonal gyros. The z-axis gyro was used in all modes of control and was duplicated to provide a redundant backup.

The spacecraft control axes are shown in Fig. II.B.1. In observational modes, the y-axis was always kept perpendicular to the satellite-Sun vector while the x-axis corresponded closely to the telescope boresight. Only two of the many possible control modes are described here. During normal operations, the signals to control rotations about the x- and y-axes were obtained from a two-axis Sun-sensor with $3.5'' \times 7''$ resolution. Signals from the z-gyro were used to control the rotation about the z-axis at the rate necessary to achieve the desired rate of scan, $d\psi/dt$, across the sky (see Section III.C.3). Towards the end of the mission, the Sun was eclipsed by the Earth for a time during each orbit and the Sun-sensor could not be used. At such times, all three gyros were used to control the satellite, although with a marked loss of control accuracy. No scientific data were taken during eclipses (see Section III.B.9).

Onboard attitude updates and ground attitude reconstruction were made using a two-axis star-sensor of the V-slit type in the focal plane of the telescope. Section V.B describes in detail the attitude reconstruction process. The absolute pointing accuracy for control purposes of the system was approximately $30''$. The accuracy of reconstructed positions is discussed in Sections V.B and VII.C.

B.3 Communication

The data for successive SOPs were recorded alternately on two tape recorders. In record mode, earlier data were erased. During a ground-station pass, the data recorded during the previous SOP were transmitted to the ground from one recorder while the other was commanded into its record mode ready for the data from the next SOP. This procedure protected data from being immediately over-written on the occasions when it proved impossible to transmit all the data to the ground during the prime station pass.

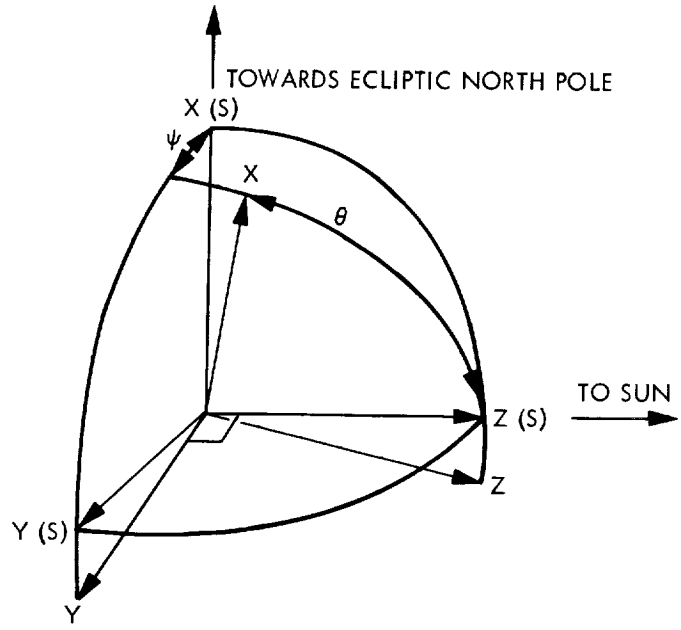

Figure II.B.1 Spacecraft control axes labeled x, y and z. The axes x(s), y(s) and z(s) are fixed with respect to the Sun and the north ecliptic pole.

C. Telescope System Overview

The IRAS telescope system configuration is shown in Fig. II.C.1. The telescope system comprised the upper part of the satellite and was composed of a two mirror, Ritchey-Chretien telescope mounted within a toroidal superfluid helium tank, which in turn was mounted within the evacuated main shell. The optical system was protected from contamination before launch and during the first week of the mission by an aperture cover cooled with supercritical helium. After the cover was ejected, the sunshade limited heat flow to the aperture by blocking direct solar radiation and reflecting away terrestrial infrared radiation. The telescope orientation was constrained to prevent sunlight from striking the inner surface of the sunshade and radiation from the Earth from illuminating the radiators around the telescope aperture. The telescope was cooled by contact with the superfluid helium tank to temperatures ranging from 2 to 5 K. The surfaces of the sunshade which could be viewed by the telescope aperture were cooled by a three-stage radiator to about 95 K.

The telescope system consisted of the cryogenics (Section II.C.1), the thermal control system (Section II.C.2), the optics (Section II.C.3), the focal plane assembly (Section II.C.4) and the electronics (Section II.C.5). The telescope system also provided interfaces at and behind the image plane for the low resolution spectrometer (Chapter IX) and the chopped photometric channel; the latter was not used for the survey. Key physical characteristics of the telescope system are listed in Table II.C.1.

C.1 Cryogenics

The telescope cryogenic system provided a 1.8 K thermal sink for controlling the temperatures of the optics and detectors. As shown in Fig. II.C.2, the main cryogen tank was toroidal in shape and

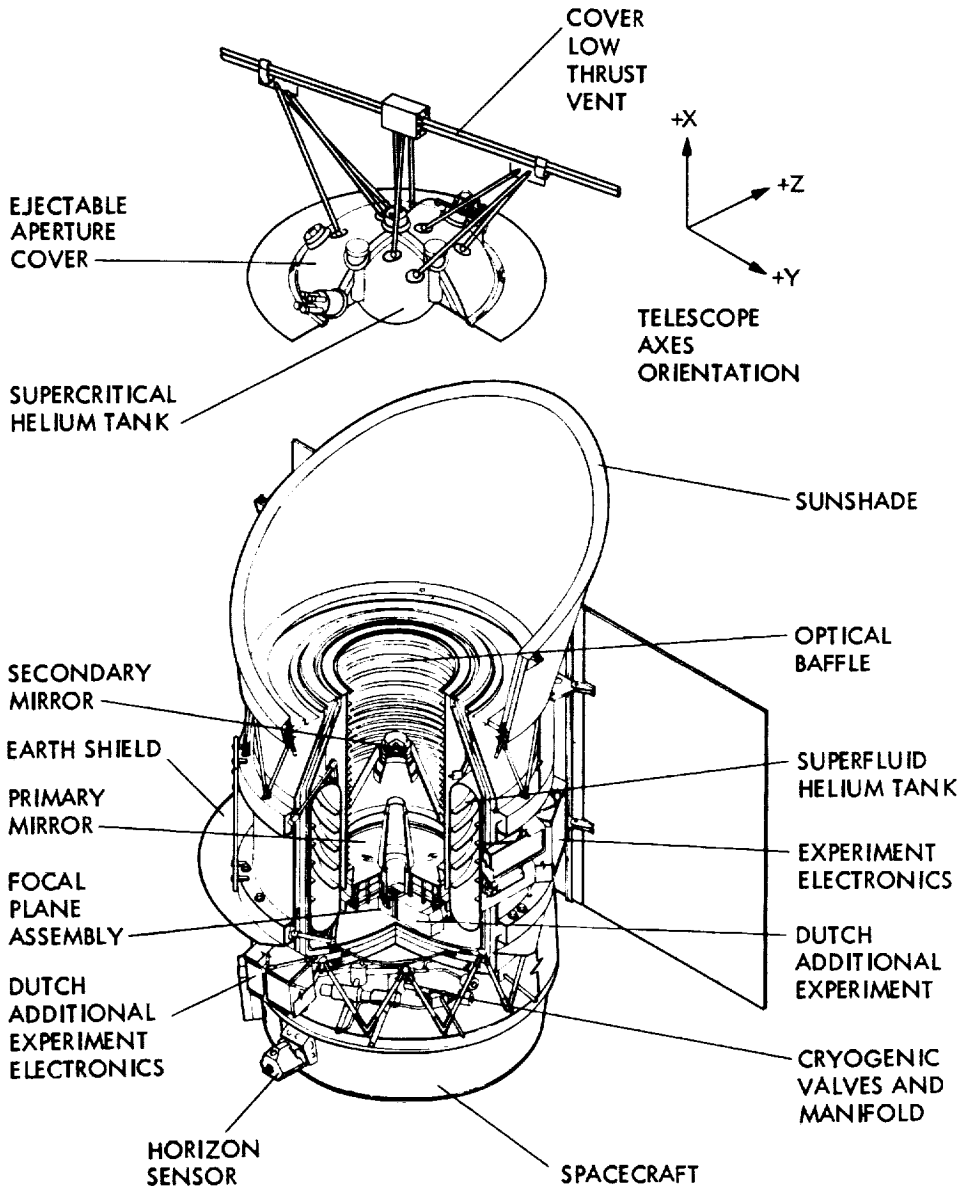

Figure II.C.1 Telescope system configuration.

surrounded the optics and focal plane. Because maximum mission lifetime required isolating the cryogen from external heat loads, the tank was suspended from nine fiberglass straps to isolate it thermally from the exterior main shell. Three shields cooled by venting gaseous helium and 57 layers of multilayer insulation provided additional isolation between the cryogen tank and the main shell. The helium gas left the main cryogen tank through a porous plug made from densely packed sintered stainless steel. The plug allowed vapor to vent while retaining the superfluid liquid. The telescope and focal plane instruments were cooled through the attachment of the optics subsystem to the main cryogen tank near the primary

Table II.C.1 Telescope System Physical Characteristics

CRYOGENICS	
Outer shell temperature	195 K
Main dewar capacity	78 kg superfluid helium
Cryogen temperature	1.8 K
Aperture cover dewar capacity	6 kg supercritical helium
THERMAL CONTROL	
Optics, Focal Plane	Cryogenic
Aperture cover	Cryogenic
Sunshade	Passive radiator, heater
Electronics	Surface coatings, blankets
Main Dewar	Multilayer insulation,shading, passive radiator
OPTICS	
Type	Two mirror, Ritchey-Chretien
Mirror material	Beryllium
Baffle material	Aluminum
Entrance pupil diameter	57 cm
Obscuration diameter	24 cm
Operating temperature	2 to 5 K
FOCAL PLANE ASSEMBLY	
Detector, feedback resistor operating temperature	2.6 K
JFET operating temperature	70 to 80 K
MOSFET operating temperature	2.6 K
Number of detectors	62 infrared, 8 visible
power dissipation	14 mW
Construction	Modular: 8 infrared subarrays 2 visible subarrays
ELECTRONICS	
Preamplifier type	trans-impedance amplifier, one per detector
Number of subassemblies	15
Power consumption	48.3 W
Operating temperature	0 to 15 C
A/D sensitivity	125 μV/data number
Data rates	
Engineering	128 bits per second (bps)
Infrared data	5888 bps
Visible data	128 bps
MASS	
External thermal control	73 kg
Main Liquid helium dewar	432 kg
Liquid helium at launch	73 kg
Optics	72 kg
Focal plane instruments	11 kg
Electronics and cables	90 kg
Structure and Miscellaneous	58 kg
Total	809 kg

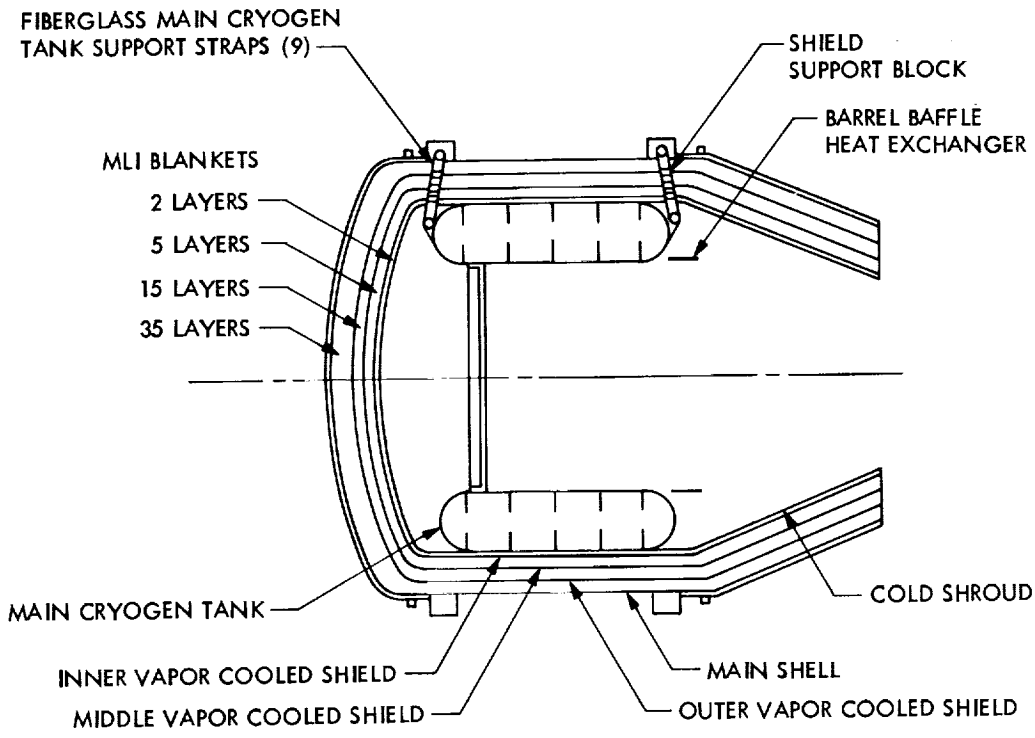

Figure II.C.2 Cross-sectional view of main cryogen dewar emphasizing components of insulation system.

mirror. Heat loads from the aperture were coupled to the venting helium gas by a strap connecting the baffle assembly to a heat exchanger. The gas finally exited to space through two vent nozzles located symmetrically on the dewar exterior.

Typical operating temperatures of the cryogen tank and exterior shell during flight were 1.8 K and 195 K, respectively. The 73 kg of superfluid helium in the tank at launch gave approximately a 300-day lifetime.

The aperture cover was an independent cryogenic system which included a cryogen tank, multilayer insulation blankets, a vapor-cooled shield, and a balanced vent system. The cover contained supercritical helium and operated between 6 and 15 K. A back-pressure regulator maintained the tank pressure to 37 ± 2 psia. After one week in orbit, the entire cover assembly was ejected from the telescope in preparation for survey observations.

C.2 Thermal Control

The external surfaces of the telescope system were designed to minimize the main shell temperature and, therefore, heat loads to the cryogen. The sunshade protected the telescope aperture from solar radiation when the telescope was pointed more than 60° from the telescope-Sun line. The specular inner surface of the sunshade minimized heat loads into the dewar by presenting a cold surface (95 K) to the aperture and by reflecting away radiation from the Earth. The dewar's location behind the solar panel

assembly also reduced the solar heat load. The Earth shield, located on the lower side of the telescope and facing away from the Sun, partially blocked terresterial radiation, while the dewar wall opposite the solar panels radiated unwanted heat to deep space. A large multilayer insulation blanket between the spacecraft and the lower dewar-shell minimized heat flow in that area. The signal processing electronics boxes were mounted on low conduction composite trusses and surrounded by blankets to reduce heat input into the dewar. The cables connecting the focal plane outputs on the main shell to the exterior electronics boxes were fabricated of low thermal conductivity stainless steel coaxial cables. For further discussion of the thermal performance, see Urbach (1984).

C.3 Optics

The optical subsystem (Fig. II.C.3) imaged the infrared and visible light onto the focal plane. The two-mirror Ritchey-Chretien telescope was made of beryllium to reduce mass and minimize thermal distortion upon cooling to cryogenic temperatures. The secondary mirror was coated with aluminum to enhance its reflection at visual wavelengths.

The telescope optical parameters and performance are given in Table II.C.2. The design goal for the image quality was that it be diffraction limited in all infrared bands. This goal was met except at 12 μm. Since the telescope was intended to be a survey instrument rather than a high resolution imaging instrument, the poor image quality at 12 μm did not interfere with the mission. For further discussion of the optical system, see Harned, Harned and Melugin (1981).

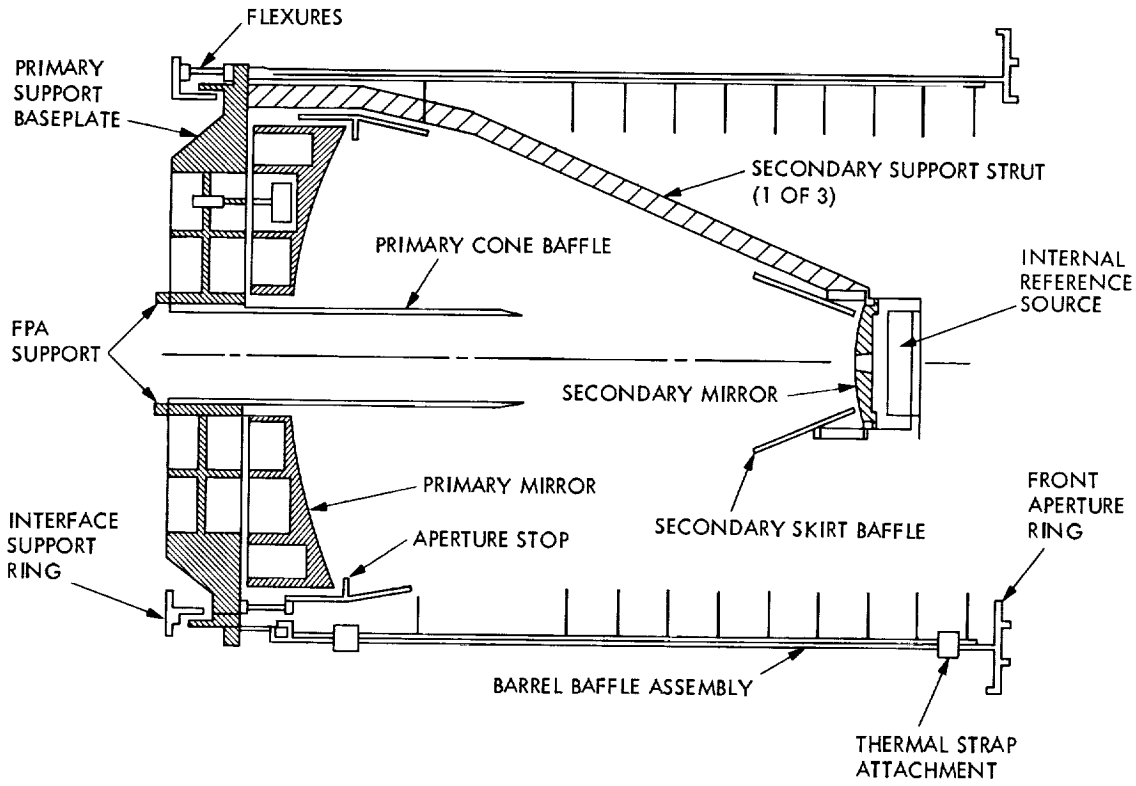

Figure II.C.3 Cross-sectional view of optical subsystem.

Table II.C.2 Telescope Optical Characteristics

DESIGN PARAMETERS	
Primary mirror diameter	60 cm
Unvignetted field of view	63.6′ dia.
System focal length(design)	550 cm
Back focal length	18.35 cm
TELESCOPE PRESCRIPTION	
Primary mirror vertex radius	-180.0 cm
Secondary mirror vertex radius	-36.48 cm
Primary eccentricity	1.00569
Secondary eccentricity	1.43206
Primary-secondary spacing	74.74 cm
TELESCOPE PERFORMANCE	
Entrance pupil diameter	57 cm
Central obscuration diameter	24 cm
Effective collecting area	2019 cm^2
System focal length (measured)	545 cm
System F/number	9.56
Plate scale at focal plane (measured)	1.585 mm/′
Diameter of 80% encircled energy	
12 μm	25″
25 μm	25″ *
60 μm	60″ *
100 μm	100″ *
Infrared surface reflectivity (all bands)	96%

* diffraction limited

An assembly mounted behind the secondary mirror contained ten thermal calibration sources, hereafter called "internal reference sources", several of which were used to provide stable pulses of infrared radiation for use as a reference during the mission and for ground testing prior to launch. Figure II.C.4 shows the location of the internal reference source assembly, the way in which a source illuminates the focal plane through a small hole in the center of the secondary mirror, and a cutaway view of an individual thermal source. The thermal source consisted of a 1 mm square diamond substrate coated with nichrome film and suspended by 0.051 mm diameter brass wires. During the mission an applied voltage ohmically heated the substrate to ~200 K in 13/16 sec. Two optical sources were included in the calibration assembly and used for ground testing of the star sensors.

Out-of-field radiation was absorbed by aluminum baffle structures which were coated with Martin Optical Black. Figure II.C.5 shows the calculated out-of-field performance in the four wavelength bands. The survey strategy (Section III.C) limited the angle between the boresight and the Moon, Earth, Sun and Jupiter to greater than 24°, 88°, 60° and 5°, respectively. At these angles the out-of-field radiation from

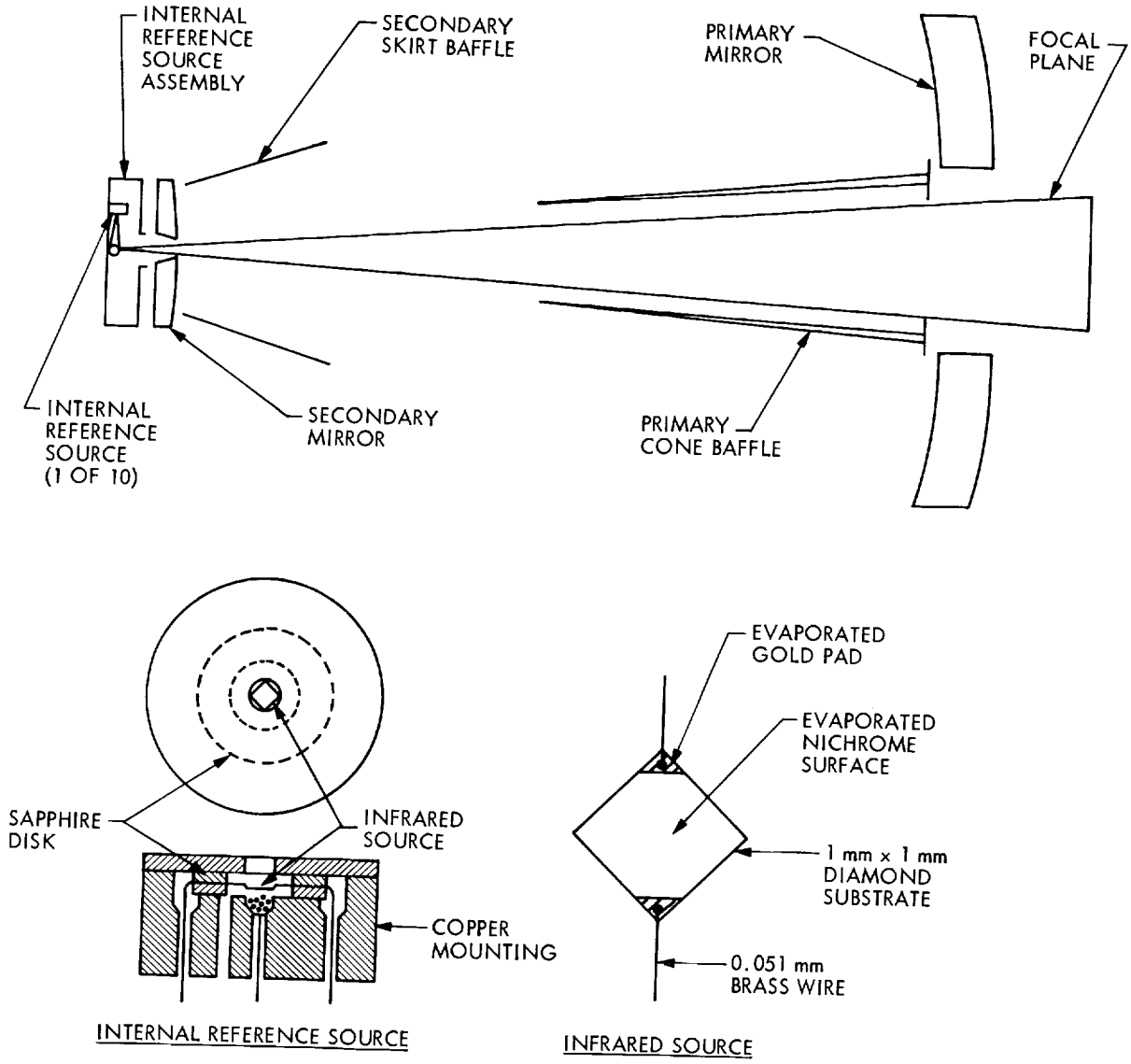

Figure II.C.4 Internal reference source assembly showing radiation path from source to focal plane and details of thermal source design

these sources is thought to be negligible (see, however, Section III.B.5 and IV.C for a discussion of lunar "glints"). Further discussion of the out-of-field performance is included in Harned, Breault, and Melugin (1980).

C.4 Focal Plane Assembly

The focal plane assembly contained the infrared and visible detectors, cold electronics, and associated masks, filters and field optics. It consisted of 62 infrared channels and eight visible channels. The infrared channels were divided into eight modules, two for each color band with each module containing either seven or eight detectors. Figure II.C.6 shows the layout of the focal plane and the numbers

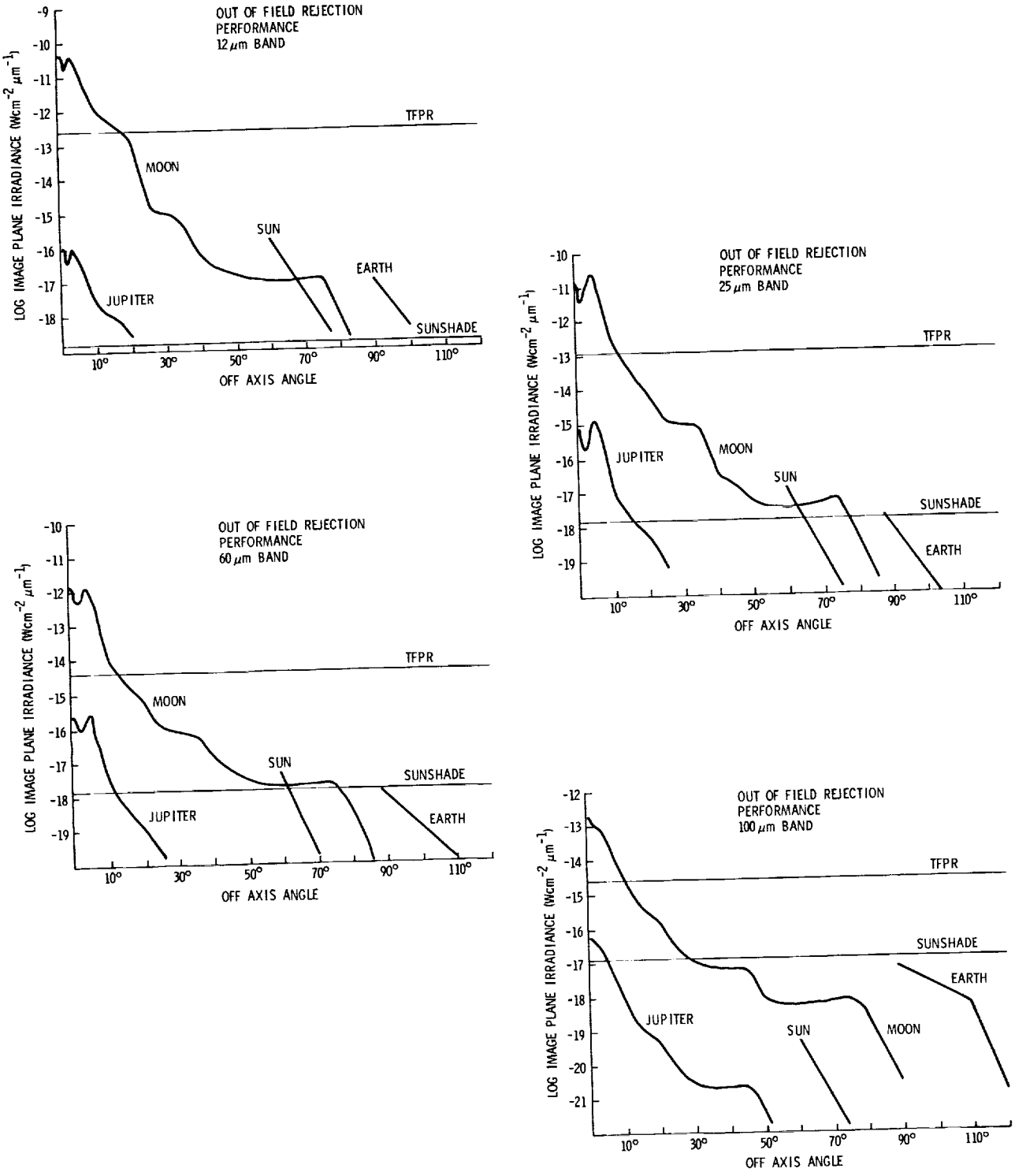

Figure II.C.5 Calculated out-of-field rejection performance of telescope system compared to the total flux photometric reference, or TFPR (Section VI.B), for 12, 25, 60 and 100 μm bands. The sunshade temperature was taken to be 95 K; the Earth was assumed to radiate as a 280 K blackbody; the moon, Sun and Jupiter were taken as 370, 5000 and 133 K blackbodies with angular diameters of 31, 31 and 0.75′, respectively.

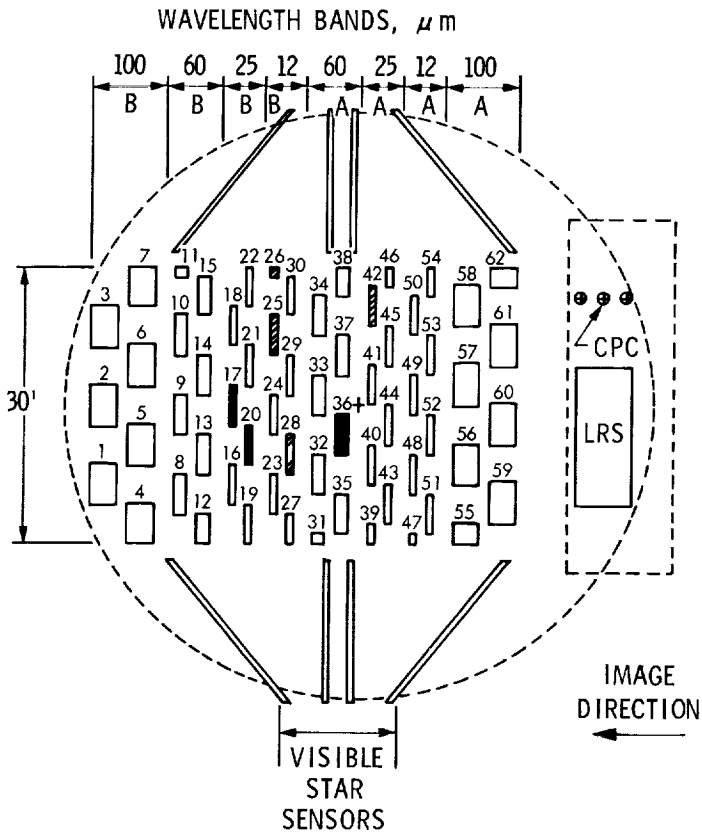

Figure II.C.6 A schematic drawing of the IRAS focal plane. The numbered rectangles in the central portion each represent the field of view of a detector, filter and field lens combination. The image of a source crossed the focal plane in the Y direction as indicated. The filled-in detectors were inoperative while the cross-hatched detectors showed degraded performance during the mission.

assigned to individual infrared detectors. Table II.C.3 lists the positions of the center of each detector mask relative to the boresight and the size of each mask projected through the optical system onto the sky. The detector masks were rectangular in aspect and infrared sources scanned across the focal plane parallel to the narrow dimension of the detectors in all observational modes.

Figure II.C.7 shows an exploded view of the focal plane. Infrared radiation passed through the field mask and spectral filters and was focused by the field lens onto the aperture defining the detector cavity entrance. The detector cavities were constructed of Au:Pt alloy to provide local high-Z shielding to absorb γ-rays with energies less than about 100 keV. In addition, for the 60 and 100 μm detectors, the cavities were designed as reflecting integrating cavities to increase photon absorption in the Ge:Ga material.

The visible wavelength channels were similar to the infrared wavelength channels in construction, except that they used visible light filters, no field lens, and silicon diode detectors. The visible wavelength detectors were placed in a double "V" arrangement in order to provide two-axis spacecraft attitude information during star crossings.

Table II.C.3 Characteristics of Survey Array

Det. No.	Offset Step (0-7)	Nominal Gain[1]	Mask Location arc min Y[4]	Z[5]	Size arc min ΔZ	ΔY
			--100 μm Band, Module B--			
1	3	26.6	27.87	8.71	5.05	3.03
2	3	24.6	27.80	0.04	5.05	3.03
3	3	25.4	27.86	-8.62	5.05	3.03
4	4	24.1	23.83	12.86	4.68	3.03
5	3[2]	26.2	24.04	4.37	5.05	3.03
6	4	25.9	23.65	-4.29	5.05	3.03
7	3	24.7	23.78	-12.77	5.05	3.03
			--60 μm Band, Module B--			
8	3	21.2	19.64	9.80	4.75	1.51
9	3	20.2	19.72	1.14	4.75	1.51
10	4	21.3	19.74	-7.53	4.75	1.51
11	3	21.1	19.70	-14.46	1.30	1.51
12	3	21.3	17.20	13.49	3.45	1.51
13	3	23.1	17.19	5.47	4.75	1.51
14	3	21.0	17.20	-3.20	4.75	1.51
15	4	21.3	17.20	-11.86	4.75	1.51
			--25 μm Band, Module B--			
16	4	12.3	14.01	8.71	4.65	0.76
17[3]	3	11.8	14.04	0.04	4.65	0.76
18	4	11.3	14.04	-8.62	4.65	0.76
19	4	13.1	12.24	12.96	4.48	0.76
20[3]	4	11.7	12.27	4.37	4.65	0.76
21	4	11.8	12.26	-4.29	4.65	0.76
22	4	11.9	12.27	-12.88	4.48	0.76
			--12 μm Band, Module B--			
23	4	14.2	9.47	9.81	4.45	0.76
24	4	14.8	9.46	1.14	4.45	0.76
25	4	15.5	9.47	-7.52	4.45	0.76
26	3	14.3	9.48	-14.50	1.20	0.76
27	4	14.2	7.71	13.55	3.33	0.76
28	3	15.3	7.71	5.47	4.55	0.76
29	4	13.9	7.70	-3.19	4.55	0.76
30	4	14.5	7.71	-11.86	4.55	0.76

Table II.C.3 Characteristics of Survey Array (Cont.)

Det. No.	Offset Step (0-7)	Nominal Gain[1]	Mask Location arc min Y[4]	Mask Location arc min Z[5]	Size arc min ΔZ	Size arc min ΔY
			--60 μm Band, Module A--			
31	3	20.8	4.56	14.55	1.28	1.51
32	3	20.8	4.59	7.61	4.75	1.51
33	3	22.6	4.58	-1.06	4.75	1.51
34	3	20.8	4.59	-9.73	4.75	1.51
35	3	21.0	2.06	11.94	4.75	1.51
36[3]	3	20.7	2.06	3.27	4.75	1.51
37	4	20.8	2.11	-5.40	4.75	1.51
38	3	18.9	2.10	-13.41	3.47	1.51
			--25 μm Band, Module A--			
39	4	15.2	-1.16	14.05	2.33	0.76
40	4	15.7	-1.16	6.55	4.65	0.76
41	3	14.7	-1.16	-2.12	4.65	0.76
42	4	16.1	-1.14	-10.78	4.65	0.76
43	3	13.9	-2.92	10.88	4.65	0.76
44	4	14.8	-2.92	2.22	4.65	0.76
45	3	15.3	-2.93	-6.45	4.65	0.76
46	3	15.4	-2.92	-13.95	2.33	0.76
			--12 μm Band, Module A--			
47	4	14.5	-5.67	14.64	1.18	0.76
48	3	14.0	-5.67	7.65	4.55	0.76
49	4	14.4	-5.67	-1.02	4.55	0.76
50	2	14.1	-5.66	-9.68	4.55	0.76
51	3	14.2	-7.42	11.98	4.55	0.76
52	3	14.3	-7.43	3.32	4.55	0.76
53	4	14.4	-7.43	-5.35	4.55	0.76
54	4	13.8	-7.42	-13.41	3.36	0.76
			--100 μm Band, Module A--			
55	4	22.9	-11.33	13.95	2.52	3.03
56	4	27.3	-11.42	6.55	5.05	3.03
57	3	26.2	-11.51	-2.12	5.05	3.03
58	4	27.6	-11.41	-10.79	5.05	3.03
59	3	26.8	-15.34	10.88	5.05	3.03
60	3	26.9	-15.49	2.21	5.05	3.03
61	4	26.8	-15.40	-6.46	5.05	3.03
62	4	26.5	-15.38	-13.85	2.53	3.03

[1] The ratios of nominal to low gain and nominal to high gain are 7.18, 0.107; 5.98, 0.109; 10.8, 0.102; and 13.4, 0.100 for the 12, 25, 60, and 100μm channels.

[2] Offset step changed after launch to 2

[3] Channel inoperative during mission

[4] During survey scans sources move from -Y to +Y

[5] Negative Z corresponds to larger angle to the Sun (θ)

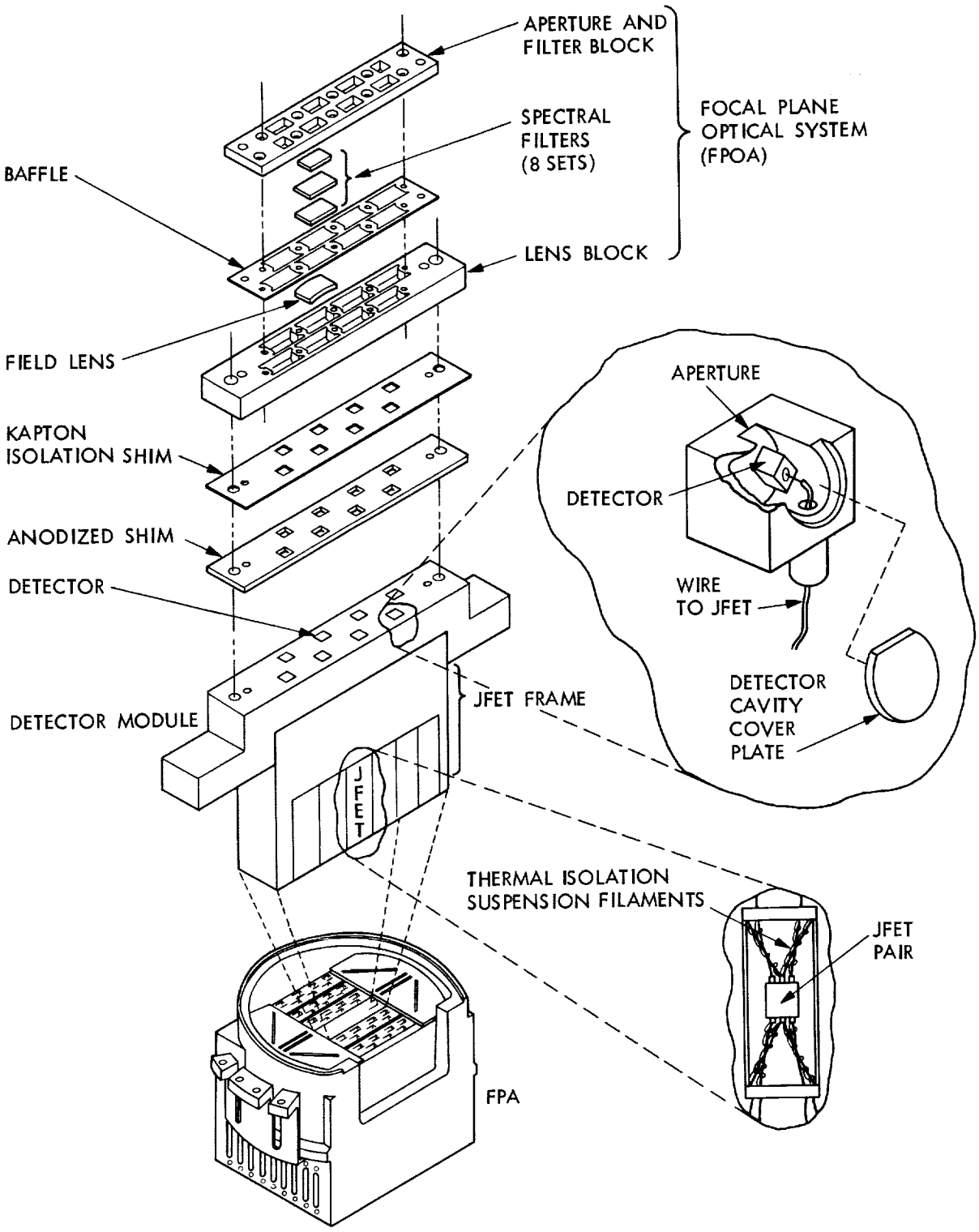

Figure II.C.7 Infrared subarray module exploded view showing module components.

Figure II.C.8 shows the focal plane filter/lens combinations and configurations for each color band and Table II.C.4 summarizes the optical characteristics of the survey array. The detailed optical system transmission, detector spectral response and overall relative spectral response for the four infrared bands are shown in Figs. II.C.9.a,b and are listed in Table II.C.5. These parameters were determined from pre-flight measurements of sample filters, field lens material and, with the exception of the 100 μm detectors, spare flight detectors. The response of the Ge:Ga detectors used at 100 μm was assumed to be the same as that of the 60 μm detectors even though the material came from a different source. Additional details of the focal plane optics can be found in Bamberg and Zuan (1984) and Darnell (1984).

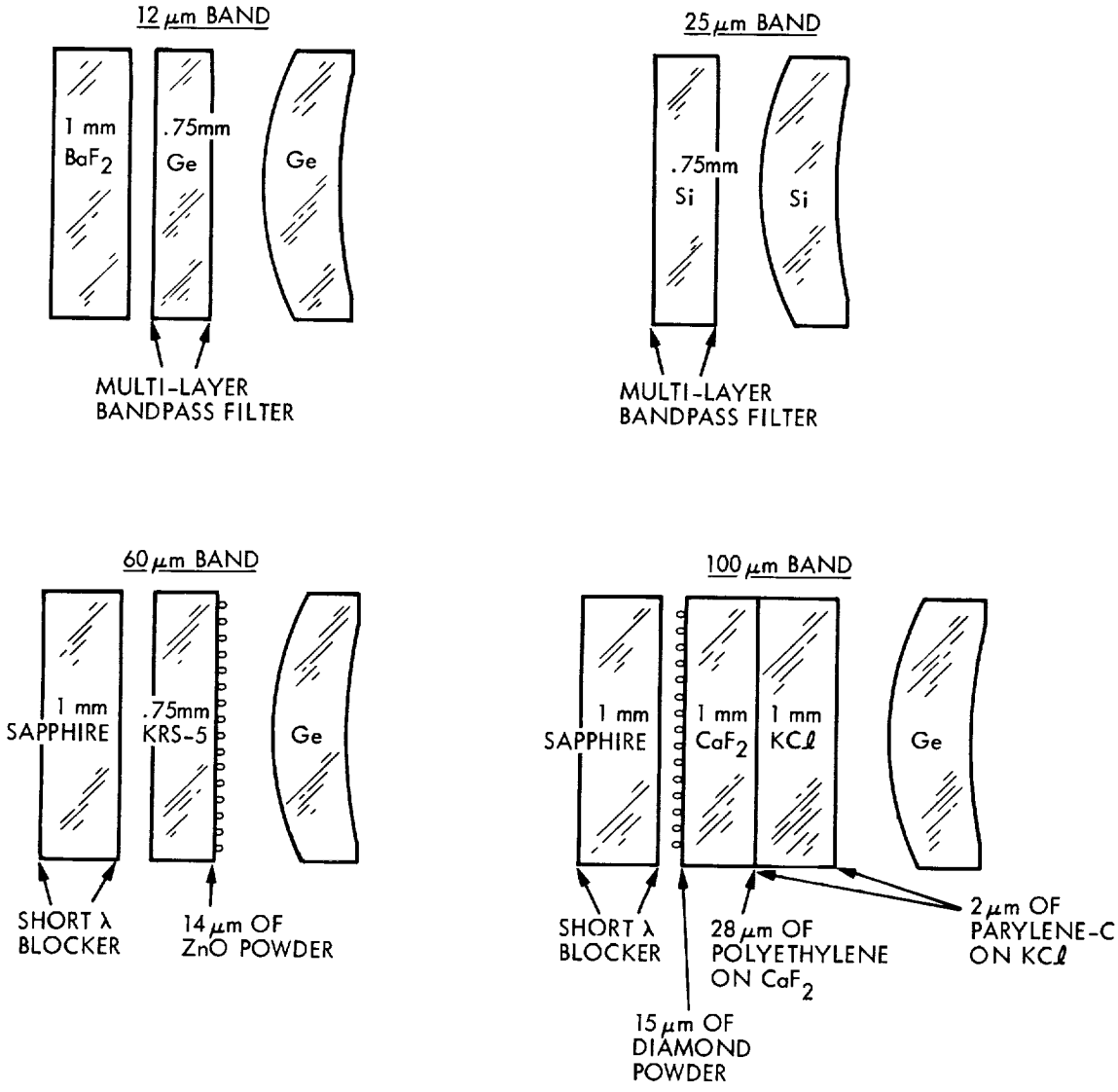

Figure II.C.8 Focal plane array filter and lens components and configuration.

Table II.C.4 Survey Array Optical Characteristics

BAND	12 μm	25 μm	60 μm	100 μm
FILTER FUNCTIONS				
Short Wavelength Blocking	MLIF*	MLIF	MLIF + Sapphire + ZnO powder	MLIF + Sapphire + CaF_2+ KCL + Diamond Powder
Short Wavelength Cuton	MLIF	MLIF	Sapphire + MLIF	KCL
Long Wavelength Cutoff	MLIF	Si:Sb	KRS-5	Ge:Ga
Long Wavelength Blocking	BaF_2+ MLIF + Si:As	Si:Sb	KRS-5	Ge:Ga
FIELD LENS				
Materials	Ge	Si	Ge	Ge
Anti-reflection coating	MLIF	MLIF	λ/4 parylene-C	λ/4 parylene-C
Focal length	6.53 mm	6.59 mm	6.98 mm	8.34 mm
Exit pupil diameter	1.0 mm	1.0 mm	1.0 mm	1.16 mm
DETECTORS				
Materials	Si:As	Si:Sb	Ge:Ga	Ge:Ga
size (L×W), mm	1.0×1.78	1.0×1.78	1.5×1.5	1.25×1.25
Electrode Spacing (mm)	0.64	0.71	1.0	1.25
OPTICAL PERFORMANCE				
Bandwidth (FWHM)	7.0 μm	11.15 μm	32.5 μm	31.5 μm
Average Inband Transmission	0.54	0.50	0.29	0.34
OUT-OF-BAND LEAKS				
Short Wavelength	$<2 \times 10^{-5}$	$<5 \times 10^{-5}$	$<2\times 10^{-4}$ **	$< 9 \times 10^{-2}$ **
Long Wavelength	$<3 \times 10^{-6}$	$<2 \times 10^{-4}$	$<2 \times 10^{-4}$	$<5\times 10^{-2}$

*MLIF = multi-layer interference filter
**See Section II.C.4

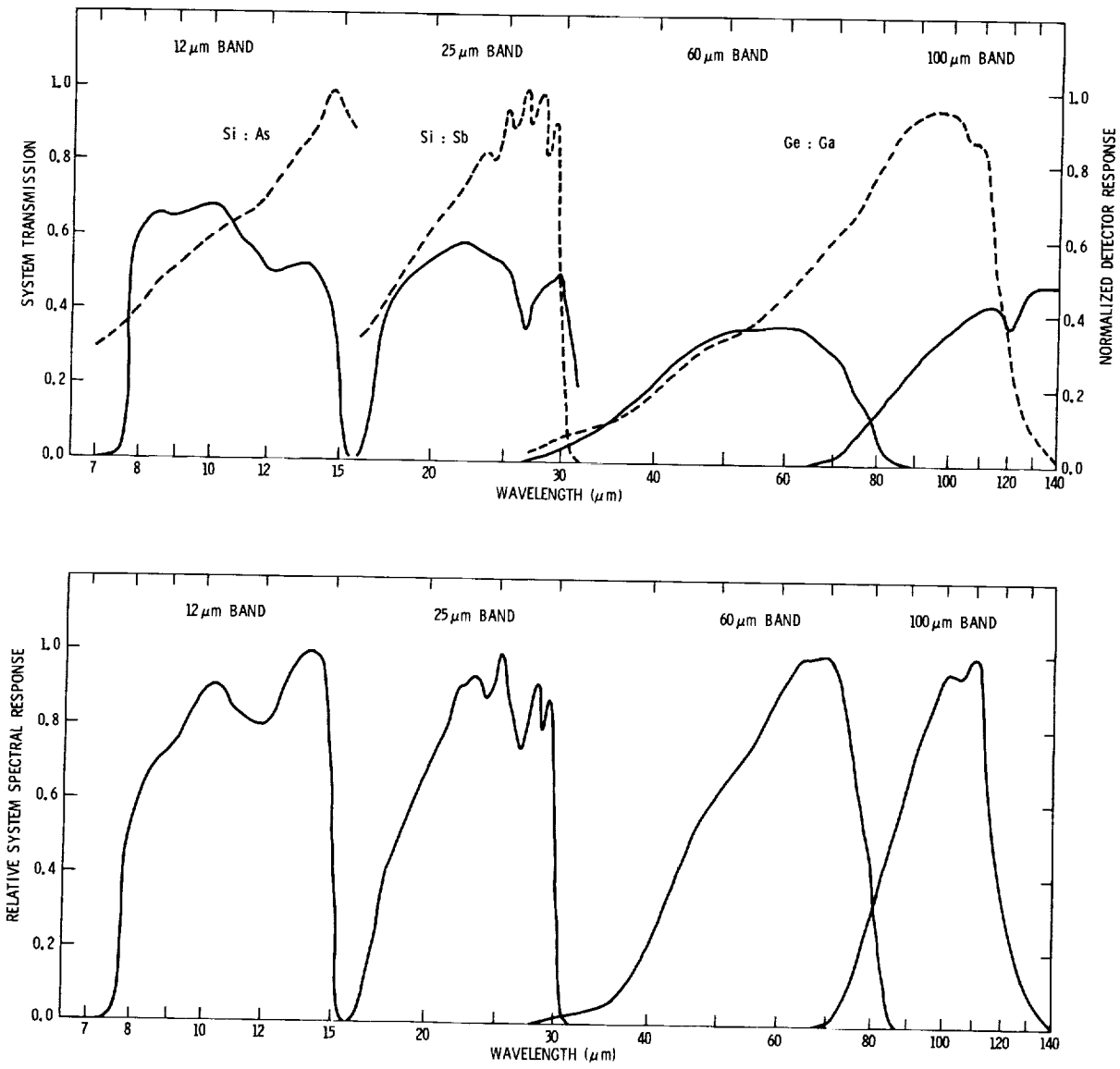

Figure II.C.9 a) Response vs. wavelength of optical components. Solid lines show the transmission of filters and lenses. Dashed lines show relative detector response to constant energy input; b) Relative system spectral response.

Out-of-band leaks listed in Table II.C.4 are defined as the ratio of the integrated energy longward or shortward of the 2% relative response wavelength to the integrated inband energy. The calculations were based on illumination from a 2000 K blackbody for short wavelength leaks and a 200 K blackbody for long wavelength leaks. The tabulated limits come from tests of the final flight focal plane except for the 100 μm detectors which were changed shortly before launch. These measured limits differ from an earlier set of measurements of the individual components. At 100 μm these latter tests give an out-of-band rejection less than 1.5×10^{-3} for a 2000 K source, significantly lower than the upper limit in the table. At 60 μm these component tests indicated the presence of a spectral leak between 1.6 and 7 μm that

Table II.C.5 Spectral Response

λ (μm)	Trans.	Relative Det. resp.	Relative System resp.
	12 μm Band		
7.0	0.00	0.30	0.000
7.5	0.01	0.35	0.008
8.0	0.60	0.41	0.535
8.5	0.66	0.48	0.689
9.0	0.65	0.52	0.735
9.5	0.67	0.56	0.815
10.0	0.69	0.60	0.900
10.5	0.66	0.63	0.904
11.0	0.59	0.65	0.834
11.5	0.56	0.67	0.816
12.0	0.50	0.73	0.793
12.5	0.51	0.77	0.854
13.0	0.52	0.83	0.938
13.5	0.53	0.86	0.991
14.0	0.50	0.92	1.000
14.5	0.43	1.00	0.934
15.0	0.19	0.94	0.388
15.5	0.00	0.90	0.000
	60 μm Band		
27.0	0.00	0.02	0.000
30.0	0.03	0.06	0.01
33.0	0.075	0.09	0.036
36.0	0.115	0.11	0.068
39.0	0.19	0.17	0.174
42.0	0.255	0.23	0.315
45.0	0.31	0.29	0.483
48.0	0.34	0.32	0.585
51.0	0.36	0.34	0.658
54.0	0.36	0.37	0.716
57.0	0.365	0.42	0.824
60.0	0.37	0.46	0.915
63.0	0.36	0.51	0.987
66.0	0.335	0.55	0.990
69.0	0.305	0.61	1.000
72.0	0.275	0.64	0.946
75.0	0.195	0.68	0.713
78.0	0.13	0.76	0.531
81.0	0.04	0.81	0.174
84.0	0.01	0.88	0.047
87.0	0.00	0.91	0.000

λ (μm)	Trans.	Relative Det. resp.	Relative System resp.
	25 μm Band		
16.0	0.01	0.33	0.007
16.5	0.14	0.36	0.101
17.0	0.35	0.41	0.288
17.5	0.42	0.46	0.388
18.0	0.46	0.49	0.452
18.5	0.49	0.53	0.521
19.0	0.50	0.56	0.562
19.5	0.52	0.60	0.626
20.0	0.54	0.63	0.683
20.5	0.55	0.66	0.729
21.0	0.57	0.68	0.778
21.5	0.58	0.715	0.832
22.0	0.59	0.75	0.912
22.5	0.58	0.785	0.914
23.0	0.57	0.82	0.938
23.5	0.56	0.83	0.933
24.0	0.545	0.80	0.875
24.5	0.54	0.84	0.910
25.0	0.53	0.94	1.000
25.5	0.51	0.89	0.911
26.0	0.46	0.91	0.840
26.5	0.38	1.00	0.763
27.0	0.41	0.91	0.749
27.5	0.43	0.96	0.829
28.0	0.46	0.99	0.914
28.5	0.48	0.82	0.790
29.0	0.48	0.91	0.877
29.5	0.51	0.545	0.558
30.0	0.47	0.29	0.274
30.5	0.38	0.09	0.069
31.0	0.31	0.02	0.012
31.5	0.20	0.00	0.000
	100 μm Band		
65.0	0.00	0.54	0.000
70.0	0.005	0.62	0.01
75.0	0.06	0.68	0.113
80.0	0.14	0.79	0.306
85.0	0.205	0.89	0.505
90.0	0.27	0.93	0.695
95.0	0.31	0.96	0.824
100.0	0.36	0.95	0.947
105.0	0.39	0.87	0.939
110.0	0.42	0.86	1.000
115.0	0.43	0.53	0.631
120.0	0.36	0.32	0.319
125.0	0.44	0.16	0.195
130.0	0.48	0.08	0.106
135.0	0.48	0.04	0.053
140.0	0.48	0.01	0.01

could be as large as 0.02 for a 2000 K source and 0.08 for a 10,000 K source, significantly larger than the tabulated limit. The origin of this discrepancy is not understood. A discussion of the in-flight tests of the spectral response is given in Section IV.B.2, and of the possible impact of leaks on the calibration in VI.C.

C.5 Electronics

The photoconductive detector elements responded to infrared radiation by altering their electrical resistance. Figure II.C.10.a shows schematically the nominal preamplifier and bias voltage design. A matched pair of junction field effect transistors (JFETs) for each detector acted as a unity-gain source-follower amplifier, converting the high impedance output of the photodetectors to low impedance for transmission to the warm electronics outside the dewar (Low 1981). The JFET pairs were each suspended by Dacron threads inside a small 2 K light-tight box such that electrical dissipation in the JFETs themselves (about 200 microwatts) maintained the JFETs at temperatures of 60 to 70 K. A 3 MΩ metal-film resistor cemented to the JFET acted as a heater for cold starting the amplifier during ground testing and several hours after launch. The JFETs formed a differential input stage of the trans-impedance amplifier. At low frequencies the output voltage of the trans-impedance amplifier was equal to the voltage difference between the gates of the JFET pair plus any offset voltage at the input of the operational amplifier plus the voltage drop across the feedback resistor due to the photocurrent from the detector.

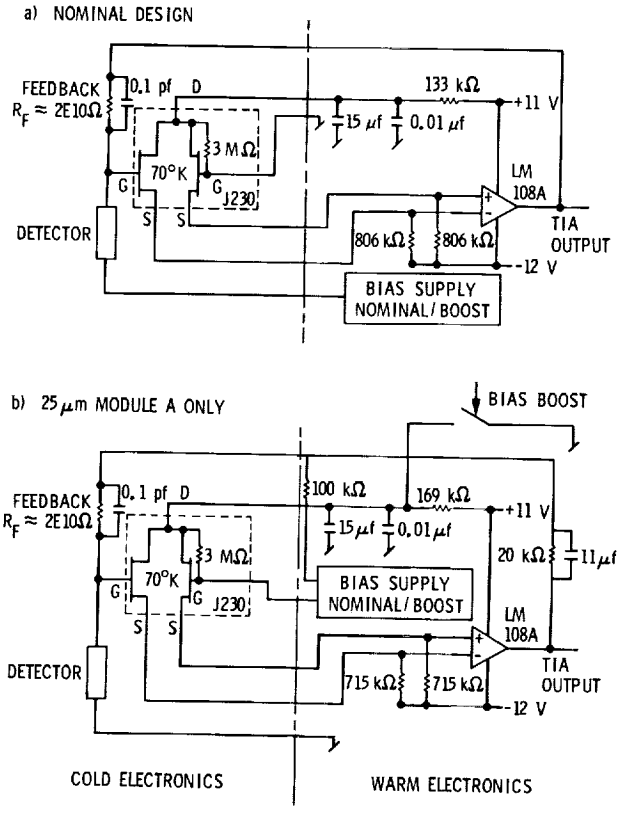

Figure II.C.10 Preamp and bias supply schematic. The JFET module is indicated by the dashed line, the dewar boundary by the dash-dot line.

The detector bias was applied to one detector contact and the trans-impedance amplifier maintained the other contact at a constant DC voltage very near signal ground independent of photocurrent until the trans-impedance amplifier output saturated at about 11 volts. All detectors in a module had a common bias voltage, applied through the module frame, which are listed in Table II.C.6. An exception to this biasing scheme was module A in the 25 μm band. During testing, the frame of this module became shorted to signal ground rendering the entire module inoperative. The alternative biasing approach used for this module only (suggested by Dr. J. Houck) is shown in Fig. II.C.10.b. The bias voltage, with reversed polarity, was applied to the gate of the reference JFET. This voltage also appeared at the operational amplifier input so the output of the trans-impedance amplifier was compensated by the same amount. The net effect of this modification was to increase the gain of the trans-impedance amplifier by a factor of 1.2.

Table II.C.6 Electrical Characteristics of Survey Array

Effective Wavelength (μm)	12	25	60	100
Nominal bias (volts)	3.27(A) 2.50(B)	1.50	0.160	0.185
Boosted bias (volts)	2.50(A) 2.00(B)	11.00(A) 7.00(B)	1.00	1.00
Nominal/Low Gain	7.18	5.98	10.8	13.4
Nominal/High Gain	0.107	0.109	0.102	0.100

During laboratory testing the responsivity and noise of the detectors were found to depend on their history of exposure to energetic radiation, such as γ-rays, and energetic electrons and protons. The observed responsivity change resulting from an exposure of 0.6 Rads of Co^{60}, roughly equivalent in dosage to a passage through a deep portion of the South Atlantic Anomaly (SAA), was about a factor of 1.2, 2, 6 and 10 for the 12, 25, 60 and 100 μm detectors. Biasing the detectors into a "breakdown" condition resulted in a large current flowing through the detector that annealed the radiation effects. The hardware provided a second bias voltage level, called the "bias boost" voltage, which effected this annealing process after exposure to SAA protons during the mission. The bias boost voltages are listed in Table II.C.6 and the effects of the bias boost are discussed in Section IV.A.7. Because the 12 μm detectors did not require annealing, the second bias voltage provided an alternative operating bias.

The rolloff frequency of the trans-impedance amplifier was set to approximately 80 Hz by a 0.1 pf shunt capacitor across the feedback resistor. The feedback resistors, Eltec model 102 metal film resistors, were selected from $1 \times 10^{10}\ \Omega$ room temperature elements. At 2 K their impedance was $2.05 \pm 0.1 \times 10^{10}\ \Omega$ and varied slightly with voltage. Figure II.C.11 shows a sample resistance vs. voltage curve as measured at 2 K. A combination of three straight lines fitted to the measured points defined the shape of the non-linear resistance versus voltage relationship used for data reduction (see Section VI.A.5).

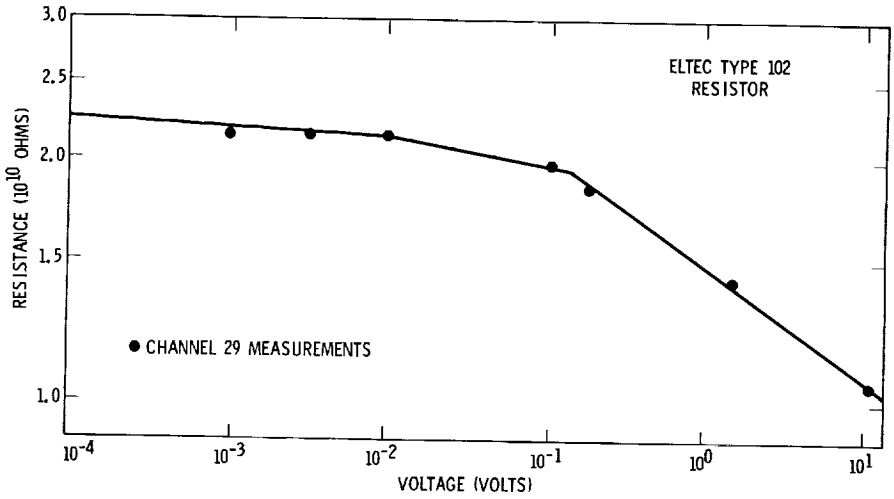

Figure II.C.11 Resistance vs. voltage characteristics of feedback resistor for detector 29. Measurements were made at 2 K. Solid line shows the shape of resistance vs. voltage relation adopted for processing.

The rest of the telescope electronics processed the signals from the visible and infrared preamplifiers, transferred data to the spacecraft onboard computer for storage and subsequent transmission to the ground station, and received commands from the spacecraft and distributed them to the telescope systems. This data-processing was split into two major elements: the analog electronics and the digital electronics. More details are contained in Langford *et al.* (1983) and Long and Langford (1983).

The analog signal path for the infrared detectors was entirely DC-coupled. Figure II.C.12 shows a functional diagram of the components of the analog electronics for one infrared detector channel. In order to maintain a negative voltage at the output of the analog electronics, the DC offset voltage at the output of the trans-impedance amplifier could be changed by 17.8 mV steps using an 8 level commandable offset with level 4 corresponding to no change. The commandable offset levels utilized during the mission are listed in Table II.C.3.

Nuclear pulse circumvention circuitry prevented sharp pulses from cosmic rays and charged particle hits on the detectors in the SAA and in the polar horns from contaminating the infrared data stream. The output of the trans-impedance amplifier was fed to an integrator and to a pole-zero amplifier which flattened the frequency response to 450 Hz to improve the operation of the circumvention circuit. The output of the pole-zero amplifier went to a differentiator and to a Bessel filter which delayed the signal by about 150 μs. The differentiated and integrated signals led to a comparator which opened a switch to prevent the unwanted, fast rise-time pulses from passing through the system. The integrator raised the minimum threshold to blank the unwanted spike as the DC voltage from the trans-impedance amplifier increased. The track/hold capacitor clamped the input to the gain amplifier to a fixed level while the switch was open. Further details of the design and performance of the pulse circumvention circuitry can be found in Emming *et al.* (1983) and Long and Langford (1983).

The Bessel filter boosted the trans-impedance amplifier output by a factor of two. An additional amplifier could increase the system gain by software commandable factors of unity (low gain), of 5 to 12

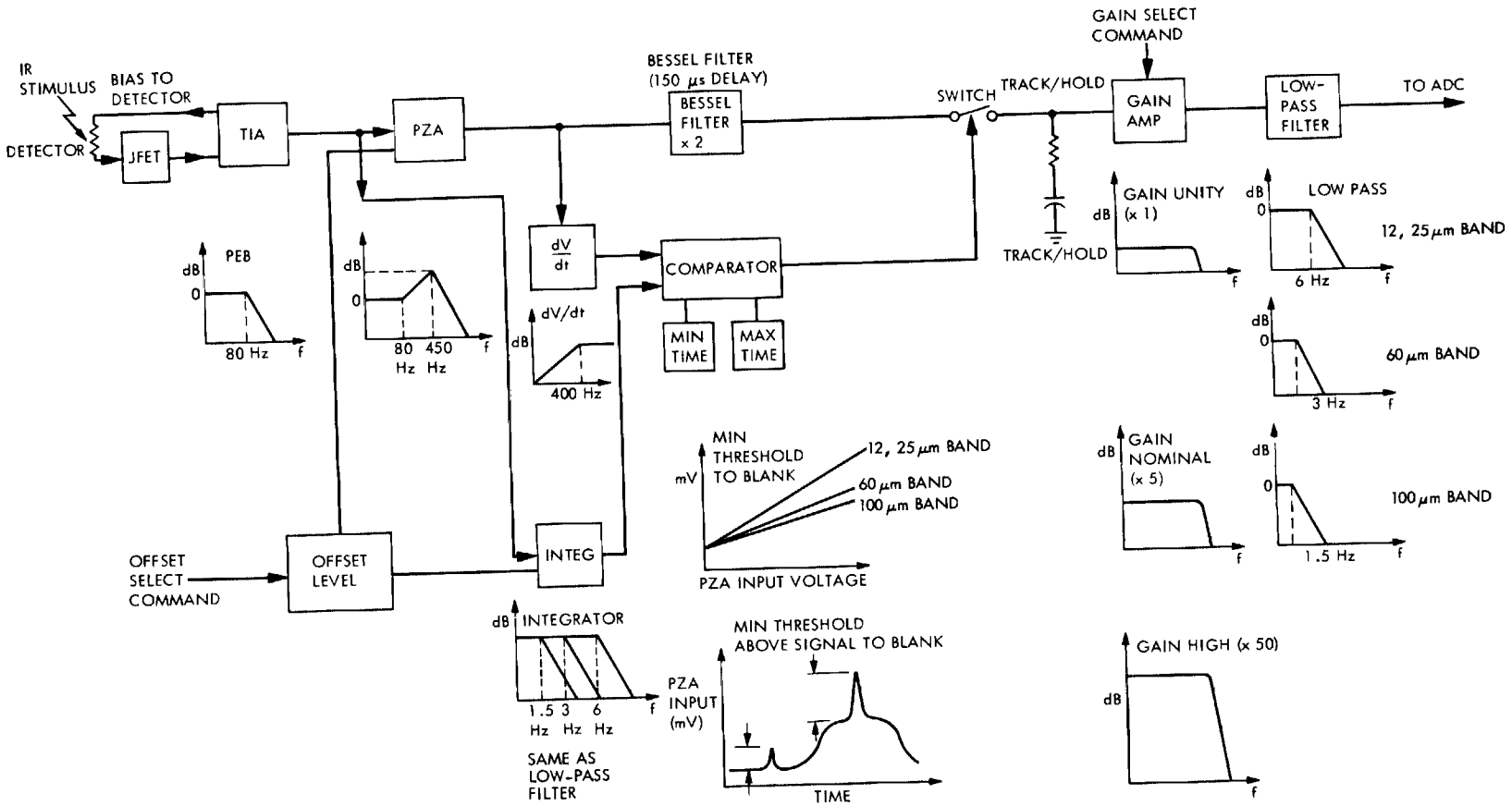

Figure II.C.12 Focal plane array infrared channel data flow.

depending on the wavelength band (nominal gain), and of ten times nominal gain (high gain). All survey scans were made using the nominal gain except for some of the brightest regions in the Galactic plane. Some of these areas were rescanned using low gain (Section III.D). The overall nominal gain for each infrared channel and the ratios of the nominal to low and high gains for the different detector modules are listed in Table II.C.3. Finally, 12 dB/octave low-pass filters with cutoff frequencies of 6, 6, 3, 1.5 Hz for the 12, 25, 60 and 100 μm bands, respectively, limited the frequency response and reduced high frequency noise. The outputs of the low-pass filters were fed into multiplexers and then to a 16-bit analog-to-digital converter operating at 125 μV per data number for subsequent processing by the digital electronics.

The visible detector data flow was similar to the infrared data flow, except that the trans-impedance amplifier was AC-coupled to a MOSFET preamplifier. For both infrared and visible channels, the pole zero amplifier, integrator, differentiator, comparator, track/hold capacitor, switch, gain amplifier and low-pass filter were contained in a single miniature hybrid circuit.

Under low background conditions the limiting noise in the analog electronics chain was the Johnson noise of the $2 \times 10^{10}\Omega$ feedback resistor. At a temperature of 2 K this noise level was roughly 1.6 $\mu V\ Hz^{-1/2}$.

The digital electronics processed the digitized infrared and visible detector data, collected telemetry information from various sensors located on the telescope, received and executed commands issued from the onboard computer and transmitted the formatted telemetry, infrared and visible detector data to the onboard computer. The infrared detectors were sampled at 16, 16, 8 and 4 Hz at 12, 25, 60 and 100 μm, respectively. To minimize spacecraft data storage requirements, the digital electronics compressed each 16-bit infrared detector value to an 8-bit value representing the difference between the successive 16-bit numbers. For details of compression scheme, see Appendix II.1.

During star crossings, two of the eight visual detectors were sampled at a 500 Hz rate. The onboard digital electronics determined the visual magnitude of the star and its crossing time, passed this information to the spacecraft attitude control software to update the satellite pointing and recorded the data for subsequent use in the attitude reconstruction. The digital electronics also measured 108 temperatures, voltages and pressures to monitor the health of the telescope. These and other housekeeping data were multiplexed, digitized and formatted for transferral to the onboard computer.

Authors:

F. C. Gillett, P. Clegg, D. Rosing, G. Neugebauer, D. Langford, A. Pouw, W. Irace, and J. Houck.

References

Bamberg, J.P., and Zaun, N.H. 1984, *S.P.I.E. Proceedings*, **509**, in press.

Darnell, R.J. 1984, *S.P.I.E. Proceedings*, **509**, in press.

Emming, J.G., Arenz, R.F., Downey, C.H., Long, E.C., Smeins, L.G. 1983, *S.P.I.E. Proceedings*, **445**, 254.

Harned, N., Harned, R., and Melugin, R. 1981, *Optical Engineering*, **20**, 195.

Harned, R., Breault, R., Melugin, R. 1980, *S.P.I.E. Proceedings*, **257**, 119.

Langford, D., Simmons, J., Ozawa, T., Long, E.C., Paris, R. 1983, *S.P.I.E. Proceedings*, **445**, 244.

Low, F.J., 1981, *S.P.I.E. Proceedings*, **280**, 56.

Pouw, A. 1983, *Journal British Interplanetary Soc.*, **36**, 17.

Urbach, A.R. 1984, *S.P.I.E. Proceedings*, **509**, in press.

APPENDIX II.1 - DATA COMPRESSION

In order to conserve space on the spacecraft digital tape recorder, the 16-bit output of the analog to digital converter was compressed to an an 8-bit value. The current 8-bit data output represented the absolute difference between the current 16-bit analog to digital value for a detector and the same detector's reconstructed 16-bit value. The reconstructed value was derived from the previous 8-bit compressed difference value taken during the preceding data iteration.

The compressed 8-bit value represented only the 4 to 5 most significant bits of the difference between the current analog to digital converter reading and the reconstructed value. The 8-bit compressed value consisted of the sign of the difference (positive or negative), three significant bits of the difference called the significand, and a shift code indicating the most significant bit of the difference as indicated in Fig. II.Ap.1.a.

Figure II.Ap.1.b shows the correlation between the shift code, the positions of the 3-bit significand, and the most significant bits of the difference. The right column indicates the total number of significant bits of the difference that could be stored in the 8-bit compressed form.

Every 4 seconds the 16-bit value, called the key value, for a detector was inserted as the first word of a data line. The key value was provided as a means to monitor and synchronize the data compression with the ground reconstruction software.

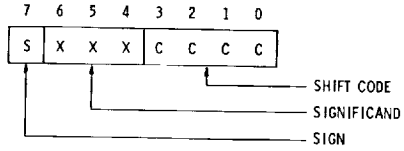

MSB 0 1 2 3 4 5 6 7 8 9 10 11 12 13 14 15	SHIFT CODE	SIGNIFICANT BITS
1 X X X 0 0 0 0 0 0 0 0 0 0 0 0	0 0 0 0	4
0 1 X X X 0 0 0 0 0 0 0 0 0 0 0 0	0 0 0 1	5
0 0 1 X X X 0 0 0 0 0 0 0 0 0 0 0	0 0 1 0	6
0 0 0 1 X X X 0 0 0 0 0 0 0 0 0 0	0 0 1 1	7
0 0 0 0 1 X X X 0 0 0 0 0 0 0 0 0	0 1 0 0	8
0 0 0 0 0 1 X X X 0 0 0 0 0 0 0 0	0 1 0 1	9
0 0 0 0 0 0 1 X X X 0 0 0 0 0 0 0	0 1 1 0	10
0 0 0 0 0 0 0 1 X X X 0 0 0 0 0 0	0 1 1 1	11
0 0 0 0 0 0 0 0 1 X X X 0 0 0 0 0	1 0 0 0	12
0 0 0 0 0 0 0 0 0 1 X X X 0 0 0 0	1 0 0 1	13
0 0 0 0 0 0 0 0 0 0 1 1 X X X 0	1 0 1 0	15
0 0 0 0 0 0 0 0 0 0 1 0 X X X 0	1 0 1 1	15
0 0 0 0 0 0 0 0 0 0 0 1 1 X X X	1 1 0 0	16
0 0 0 0 0 0 0 0 0 0 0 1 0 X X X	1 1 0 1	16
0 0 0 0 0 0 0 0 0 0 0 0 1 X X X	1 1 1 0	16
0 0 0 0 0 0 0 0 0 0 0 0 0 X X X	1 1 1 1	16

X X X - THREE BITS OF SIGNIFICAND

Figure II.Ap.1 a) The format of the compressed 8-bit data word (top); and b) the meaning of portions of the code used for data compression (bottom).

III. THE IRAS MISSION

A. Requirements

The IRAS mission was designed to observe the entire sky in the infrared and to insure that the resultant survey was reliable and complete down to a specifiable flux level. This requirement was specified numerically as a catalog of point sources over 95% of the sky, that was 98% complete in unconfused regions and 99.8% reliable. To create accurate maps of the total sky brightness, observations of diffuse emission also needed to be free of significant background variations due to local effects such as Sun and Earth shine. It was desirable to observe the same distant sky through different regions of the solar system so that the effects of solar system backgrounds could be separated from Galactic and other backgrounds.

Many non-astronomical sources of infrared radiation were detected by IRAS, including contaminants released by IRAS itself, Earth orbiting dust particles, Earth orbiting satellites and other space debris. Asteroids and comets were also detected. The difficulties caused by dust particles and debris can be highlighted by noting that a dust particle of diameter 100 μm radiating as a blackbody at a temperature of 200 K could be seen by the 12, 25 and 60 μm detectors with a signal to noise ratio of >3 for distances closer than about 18 km. The infrared detectors were also sensitive to impacts by cosmic rays and charged particles from the Earth's trapped radiation belts. The residual effects of these impacts could not be entirely removed by the on-board nuclear pulse circumvention electronics (Section II.C.5) and so were a potential source of difficulty.

The requirement for a reliable survey, along with the above considerations, necessitated multiple observations of the sky to discriminate between the fixed (distant) astronomical objects and the moving (nearby) objects in the solar system, and against noise sources such as particle radiation effects on the detectors. By reobserving the sky on a time scale of seconds the residual effects of the radiation hits and the fastest moving local material were recognized and rejected (seconds-confirmation); by reobserving on a time scale of hours slower moving but still relatively local sources were recognized (hours-confirmation); and by reobserving on a time scale of weeks and months, slowly moving solar system objects such as asteroids were recognized (weeks-confirmation).

It should be borne in mind that the purpose of multiple coverage was to enhance the reliability of the point source detections, not to coadd data to enhance sensitivity.

The demand that a source should be seen twice within seconds was fulfilled by the design of the focal plane. A mission design plan (McLaughlin 1984) and a survey strategy plan (Lundy 1984) to achieve the required, homogeneous, multiply-confirmed coverage of the whole sky were evolved subject to the instrumental and observational constraints. It is necessary to explain the observational constraints that had to be met as these are important for understanding the strategy and the reasons that, in practice, the sky coverage was neither completely uniform nor homogeneous.

B. Constraints

B.1 Introduction

IRAS was successfully launched into its planned 900 km altitude, 99° inclination Sun-synchronous polar orbit with a period of 103 minutes. This orbital altitude was low enough to be below most particles in the Earth's trapped particle belts yet high enough that only a negligible amount of residual atmospheric gasses would build up on the cold mirror surfaces during the mission. With the telescope pointing radially outwards from the Earth and perpendicular to the Sun vector, no Earth or sunlight could enter the telescope and all ecliptic latitudes would be swept out during one orbit while, as the line of nodes precessed at a rate of about 1° per day to remain perpendicular to the Sun vector, all ecliptic longitudes would be covered in a period of six months (Fig. III.B.1). Such a simple solution would, however, have allowed no flexibility. The attitude control system and telescope were designed to allow pointing away from the local vertical within certain constraints which are described below.

B.2 Attitude Control

The first constraint was designed into the spacecraft attitude control system and required the telescope to point no further away from the Sun than 120°. At greater angles the fine Sun sensor could no longer see the Sun well enough to function.

B.3 Solar Radiation

The second constraint was that the sunshield design did not allow the telescope to point closer than 60° towards the Sun without solar radiation falling onto the inside of the sunshade. These first two constraints limited the celestial sphere available to IRAS at any one epoch as shown schematically in Fig.III.B.2.

B.4 Earth Radiation

The third constraint arose from prohibiting any infrared radiation from the Earth from falling upon the inside of the sunshield or the top of the telescope baffle system. This constraint is shown in telescope coordinates in Fig. III.B.3 and the corresponding area of the sky available on any one orbit is shown in Fig. III.B.4. The Earth radiation constraint together with the spacecraft orbital rate determined the maximum time of 15.6 min. during which the satellite could point at a given fixed celestial position, if no other constraints interfered. Because of the varying solar declination during the mission, the joint effect of these constraints changed during the mission; Fig. III.B.5 shows schematically the combined constraints at two epochs six months apart.

B.5 Moon and Planets

Infrared radiation from the Moon and the planet Jupiter was sufficiently strong to affect the performance of the detectors for a significant time after passage over the focal plane. Of the other planets, only Venus was bright enough to have this effect but it was always too close to the Sun to be observed. An avoidance radius of 1° from Jupiter was set within which the telescope did not point. For the moon, an avoidance radius of 25° was used during the first two months of the survey but was lowered to 20° after April 3 except between August 26 and September 9 where it was lowered to 13°; at 25° significant "moon glints" were introduced into the data-stream (see Section IV.C).

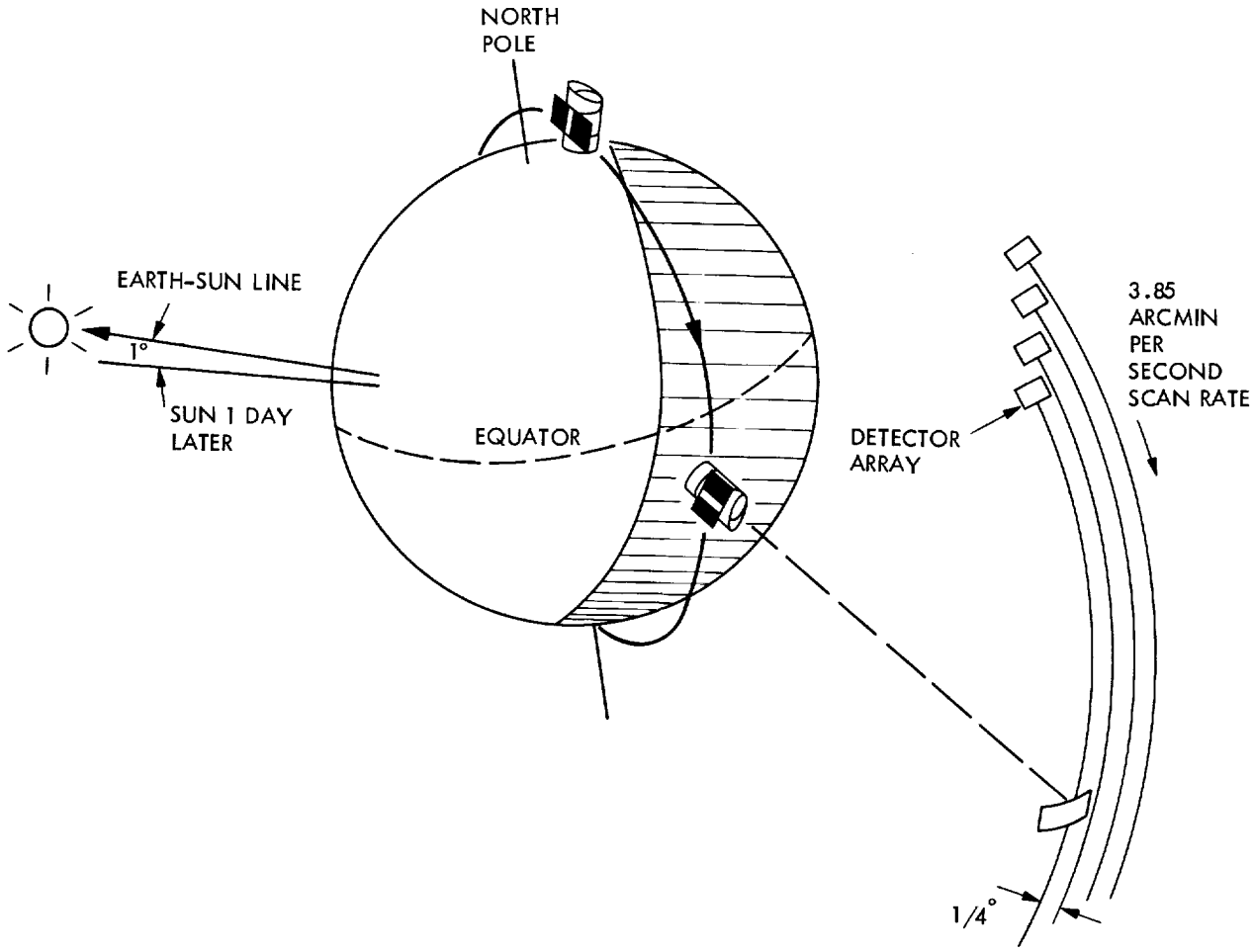

Figure III.B.1 A schematic drawing of the orbital geometry. The orbital altitude, 900 km, and inclination, 99°, combined with the Earth's equatorial bulge lead to a precession of the plane of the orbit about 1° per day. As a result, the orbit normal always pointed towards the Sun as the satellite orbited above the Earth's terminator. By pointing the satellite radially away from the Earth, the cold telescope was shielded from the heat loads from the Sun and Earth while providing natural scanning motion across the entire sky in about six months. A sequence of hours-confirming scans on the celestial sphere is also shown.

B.6 South Atlantic Anomaly

Another constraint was the depression in the Van Allen belts known as the South Atlantic Anomaly (SAA). Proton hits in the detectors when passing through the SAA increased the noise to such an extent that it was impossible to continue observations. Data were not taken whenever the satellite entered a geographically fixed flux/energy contour. As a result of analysis of the effects of radiation on the detectors, the contour shown in Fig. III.B.6 was adopted. In May, it was slightly reduced in an attempt to minimize the adverse effects on the survey scans. Both contours are shown in Fig. III.B.6.

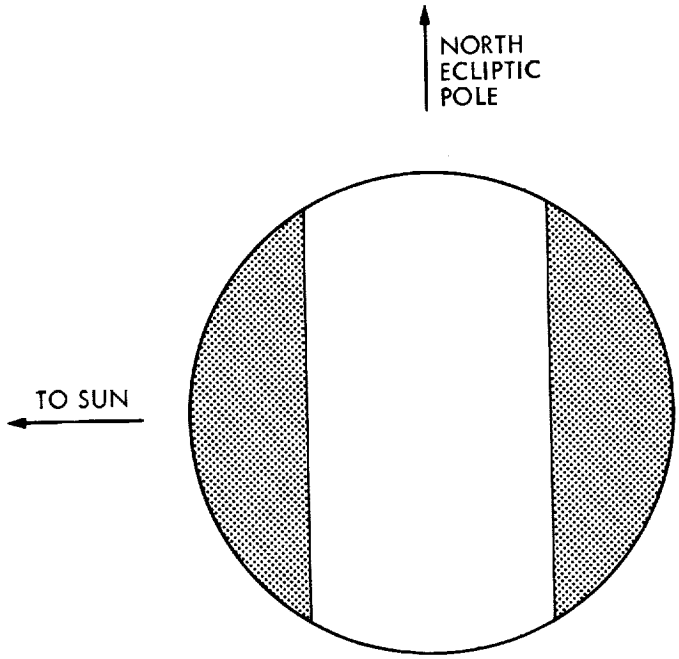

Figure III.B.2 With IRAS at the center of the celestial sphere, the solar constraint on solar radiation and visibility to fine Sun sensors prohibited viewing closer than 60° from the Sun and farther than 120°, the area shown shaded in the figure.

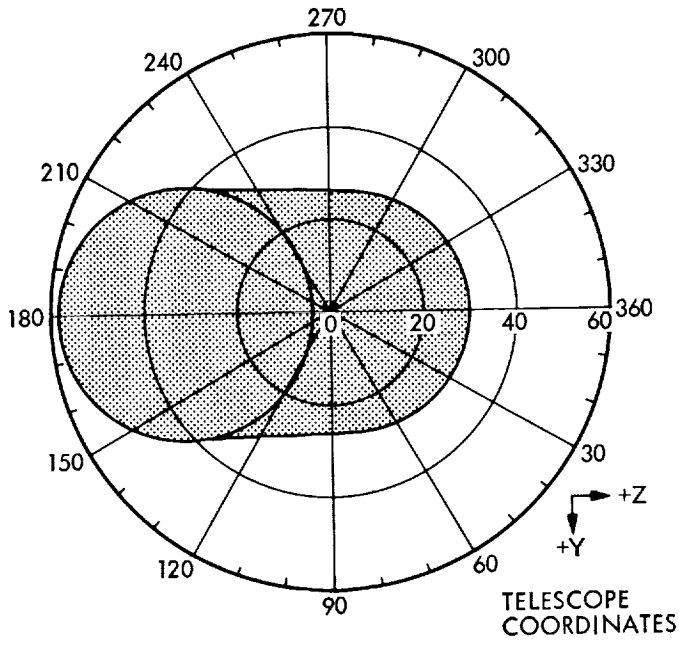

Figure III.B.3 The Earth infrared radiation constraint is shown in telescope coordinates. The telescope boresight is at the origin with the +X axis out of the page. The scanning direction is toward -Y. The satellite position vector had to remain within the shaded region at all times.

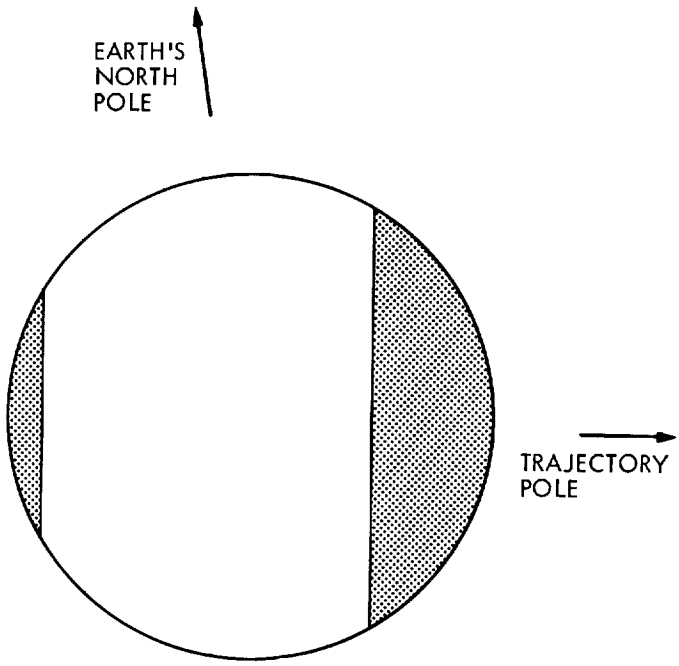

Figure III.B.4 The shaded region depicts the portion of the celestial sphere not available for viewing during any given orbit due to the Earth infrared constraint. The normal to the plane of the IRAS orbit is indicated "Trajectory Pole".

A second effect of a passage through the SAA was a long term enhancement, by as much as factors of ten, in the responsivity and noise caused by the large radiation dosage. As described in Section II.C.5, these large changes could be erased by increasing the bias voltage on the detectors, a technique referred to as "bias boosting".

B.7 Station Passes

No observations could be carried out during the prime pass over the ground station (Bevan *et al.* 1983), as during this time (typically 10 minutes every 10-14 hours) data from the preceding 10-14 hour observation period were being transmitted from the on-board tape recorders to the ground and the commands for the next 10-14 hours of observations were being sent to the satellite (Mount 1983; MacDougall *et al.* 1984).

B.8 Constant Sun Angle

Figure III.B.7 shows the attitude-control coordinate system of the spacecraft. Although the spacecraft had gyros for 3-axis control, it normally used only one, the z-axis gyro (see Fig. II.B.1). Control of the other two axes was maintained by the fine Sun sensor which ensured that the y-axis was always perpendicular to the satellite-Sun vector (see Section II.B.2). The satellite scanned with a fixed cone-angle θ between the telescope boresight and the Sun vector.

A consequence of the constant Sun cone angle constraint, together with the fact that the ecliptic longitude of the Sun constantly increases, is that it was never possible to repeat exactly the coverage obtained by any scan, except at the ecliptic plane, or after an interval of six months. For example, a

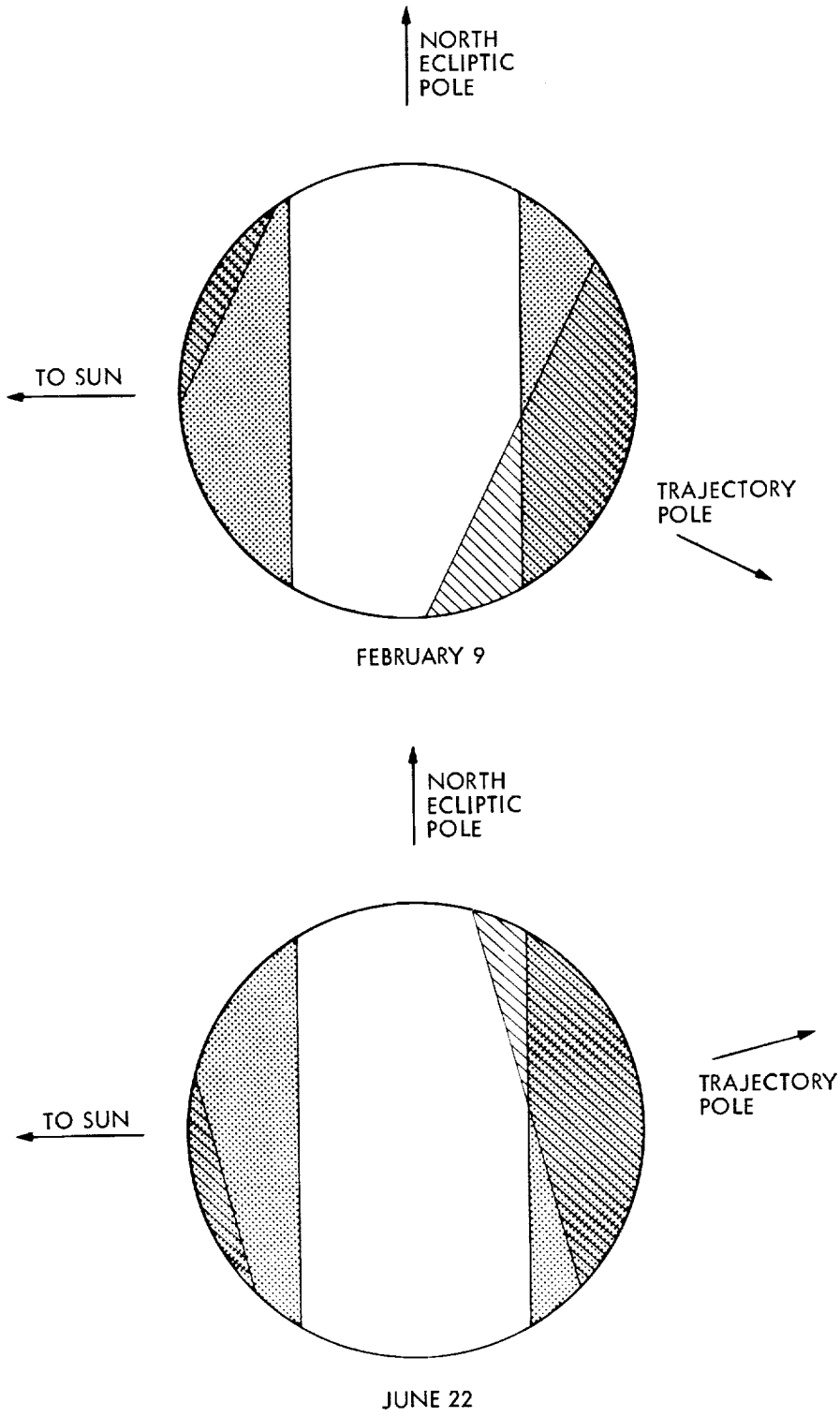

Figure III.B.5 Basic viewing window (unshaded) on the celestial sphere for two different dates during the survey.

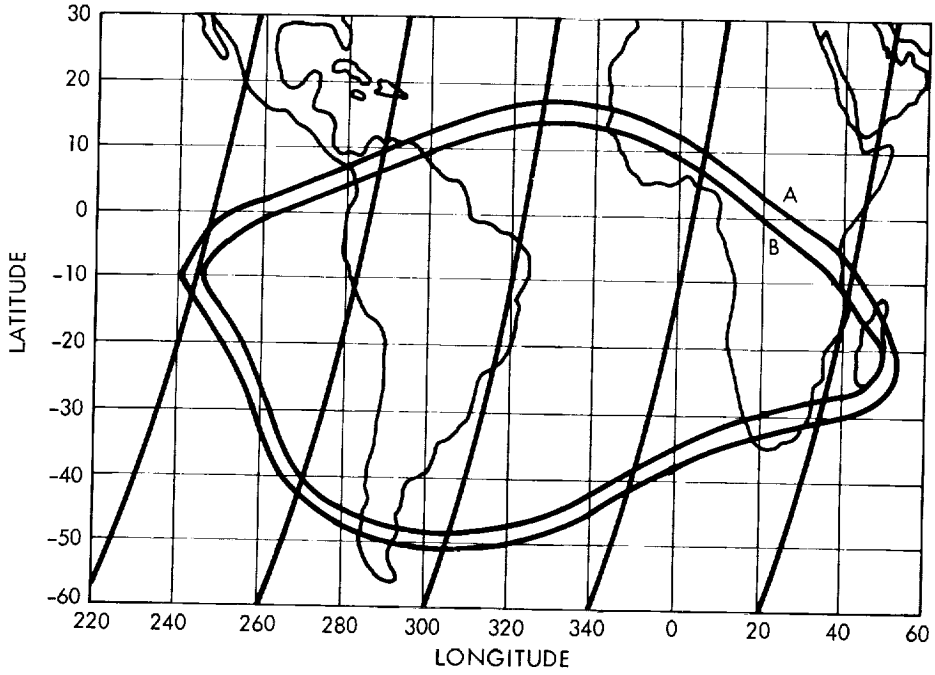

Figure III.B.6 Sample orbital tracks through the South Atlantic Anomaly (SAA) at 900 km and the contours used for SAA avoidance are given. The contour (A) was determined during in orbit checkout; the less conservative contour (B) was used after May 9 to help reduce the SAA affects on the survey scans.

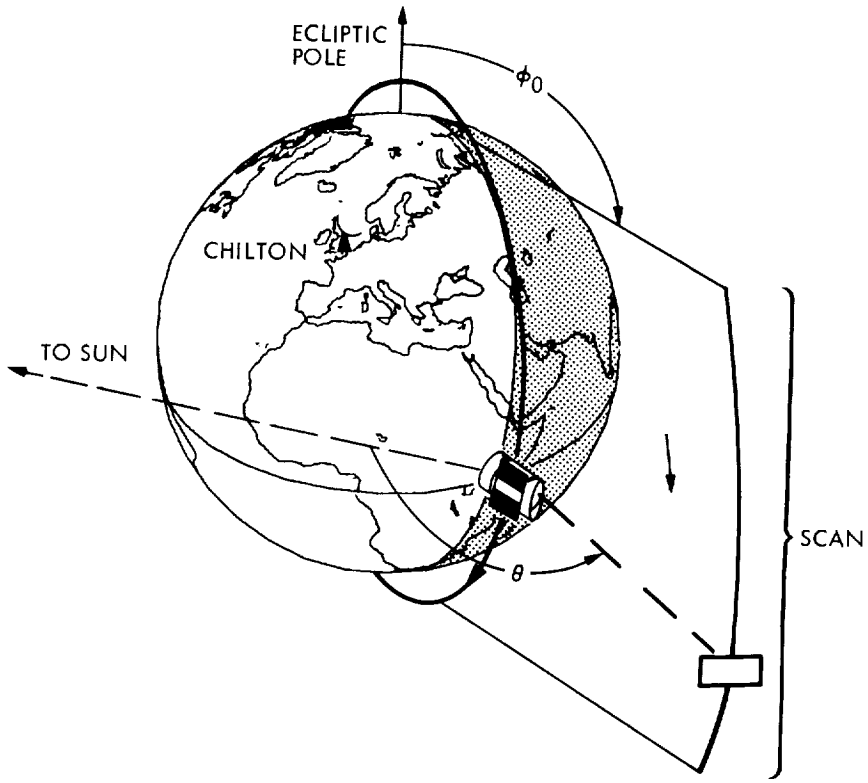

Figure III.B.7 The cone and clock system were used to define the scan geometry. The cone angle (θ) is the angle between the satellite-Sunline and the boresight. The clock angle (φ_0) is measured in the plane perpendicular to the Sun-line, clockwise as viewed from the Sun. Sometimes $\psi = 360°-\varphi$ is also used.

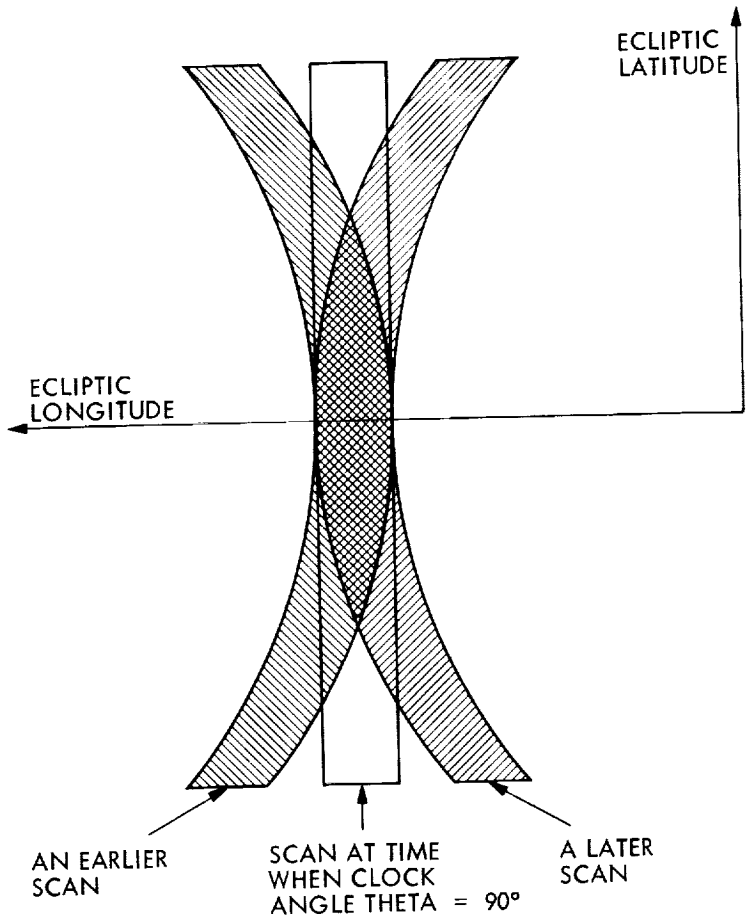

Figure III.B.8 The curvature of scans taken at $\theta \neq 90°$ is called the "banana effect". See Section III.B.8.

pole-to-pole scan executed at cone angle $\theta = 90°$ and passing through a specified longitude in the ecliptic plane would be rectangular in the ecliptic coordinate system. A pole-to-pole scan through the same specified longitude in the ecliptic plane at a later or earlier time ($\theta \neq 90°$) would be an arc whose curvature increased with $|90-\theta|$ (Fig. III.B.8). This "banana effect" meant that overlapping scans had to be made at almost the same time with only small θ differences.

B.9 Eclipse Operations

Towards the end of the mission, the solar declination became such that the Sun was eclipsed by the Earth during part of the orbit. Because the satellite could not use its Sun sensor, gyros were used to control all three axes during this period. This resulted in a considerable loss of control accuracy and, in particular, meant that slewing maneuvers ended in unpredictable positions. Consequently, it was decided not to continue survey scans or other normal observations during eclipses.

C. Design

C.1 Basic Strategy

The basic time interval of the operations and data acquisition was the time between station passes, varying between seven or eight orbits or 10 to 14 hours. During each such period, the survey strategy discussed below was implemented in a series of commands sent to the satellite called a Satellite Observation Plan, hereafter denoted as SOP. There were two SOPs per day and 600 SOPs in the entire mission.

The strategy developed to achieve the goals of multiple survey coverage on various timescales divided the celestial sphere into units of half overlapping "lunes" in the ecliptic coordinate system (Lundy 1984). Lunes were defined as the area between two ecliptic meridians 30° apart (Fig. III.C.1). The lunes were "painted" by survey scans, one after the other, as they passed through the viewing window of the telescope. Figure III.C.2 illustrates the shape of a lune sketched onto a plane and, with a very exaggerated focal plane width, how it was covered by different survey scans each at a fixed cone angle from the Sun. The first scan in a lune was placed so that it crossed the ecliptic at the lower longitude boundary of the lune. Successive scans were laid down at increasing ecliptic longitudes, each one shifted over by 14.23′, that is by half the width of the focal plane minus a safety margin to account for the pointing limit cycle of the telescope. The overlap ensured that measurements of the same area of sky were repeated within a few orbits (for hours-confirmation) and that the "banana effect" (Section III.B.8) was not too severe. The criterion for hours-confirmation was that the hours-confirming scans had to be made within three SOPs (34-38 hours) of each other.

Two lunes in opposite hemispheres were observed simultaneously, one on the ascending side of the orbit and one on the descending side. Figure III.C.3 shows a typical day's survey coverage and the regions forbidden by the constraints. After a lune was filled, a second lune in the same hemisphere was started; it overlapped half of the first lune, ensuring that another hour's-confirming set of scans was repeated after about one to two weeks, thus providing the required repetition on the time scale of weeks (Fig. III.C.4).

The observing conditions were considerably worse during some orbits than during others. Orbits that crossed the SAA or contained a station prime pass were interrupted for significant amounts of time. When a long interruption occurred, the continuation of a survey scan was sometimes impossible and a small hole in the coverage resulted. To minimize such events only the nine (out of 14) orbits per day least affected by the SAA were used for the survey scans.

The survey strategy aimed for four coverages (two sets of hours-confirming coverages) in the first six months and two coverages (a third set of hours-confirming coverages) in the second six months. Any time left over was used to recover survey observations lost because of the various constraints, to make the necessary calibration observations and to carry out additional, non-survey, pointed observations to attain higher sensitivity or spatial resolution. For the first two weeks of observations (February 10-23, 1983, SOPs 31-57) half circle scans, which give redundant coverage in the ecliptic polar areas (Fig. III.C.5), were used for increased initial coverage as insurance against an early failure of the satellite. Subsequently, the more efficient lune method was used for the rest of the first six months of the survey.

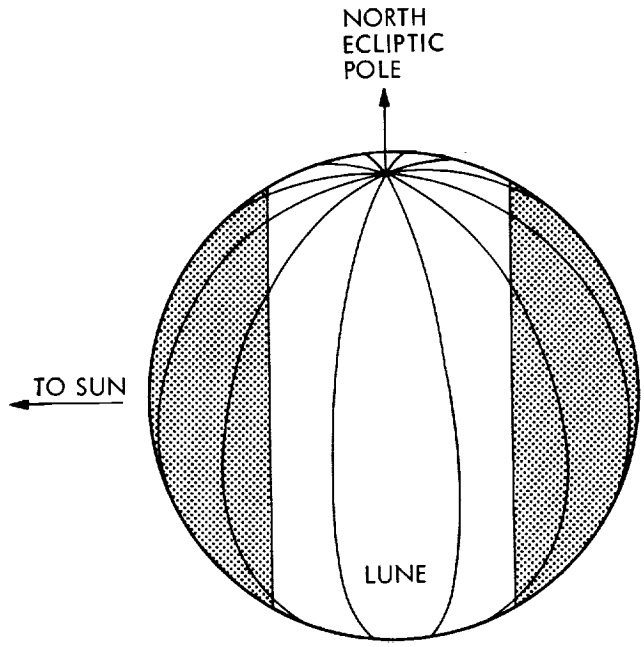

Figure III.C.1 Lunes are sketched on the celestial sphere. Shaded zone is not allowed by Sun constraint.

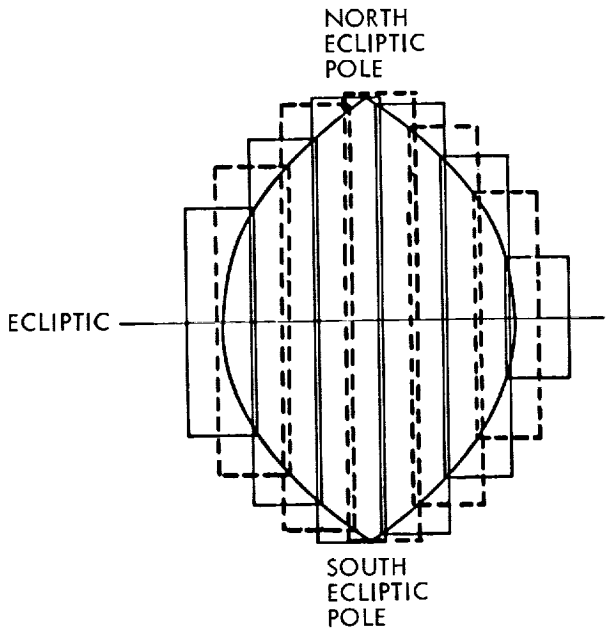

Figure III.C.2 Half-overlapping scan swaths (highly exaggerated) fill a lune with one hours-confirming layer

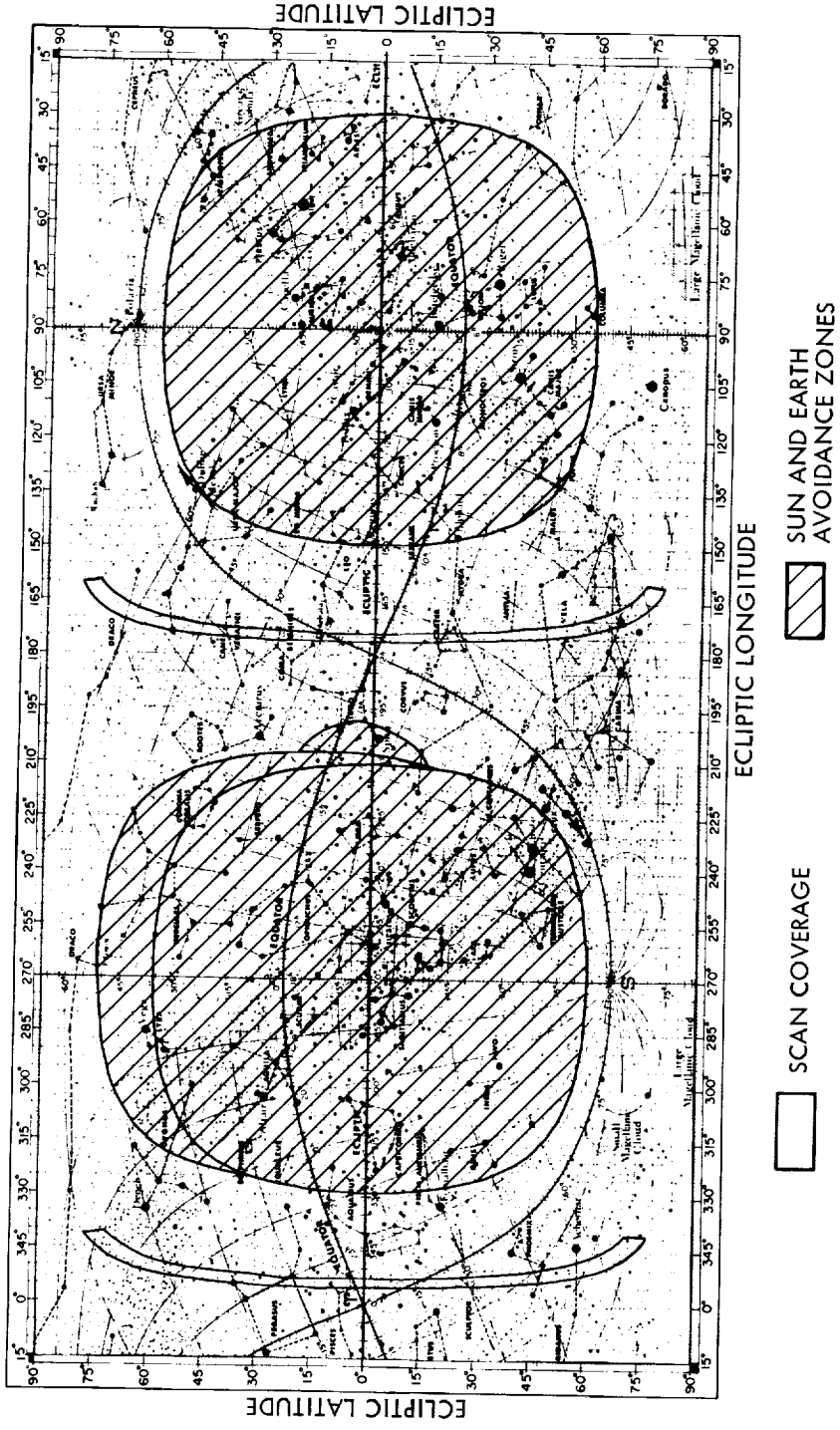

Figure III.C.3 A typical days survey coverage (clear regions at approximate ecliptic longitudes 167° and 347°) is plotted on a map of the sky in ecliptic coordinates. The two shaded regions centered on ecliptic longitudes 90° and 270° are forbidden by the Sun and Earth constraints.

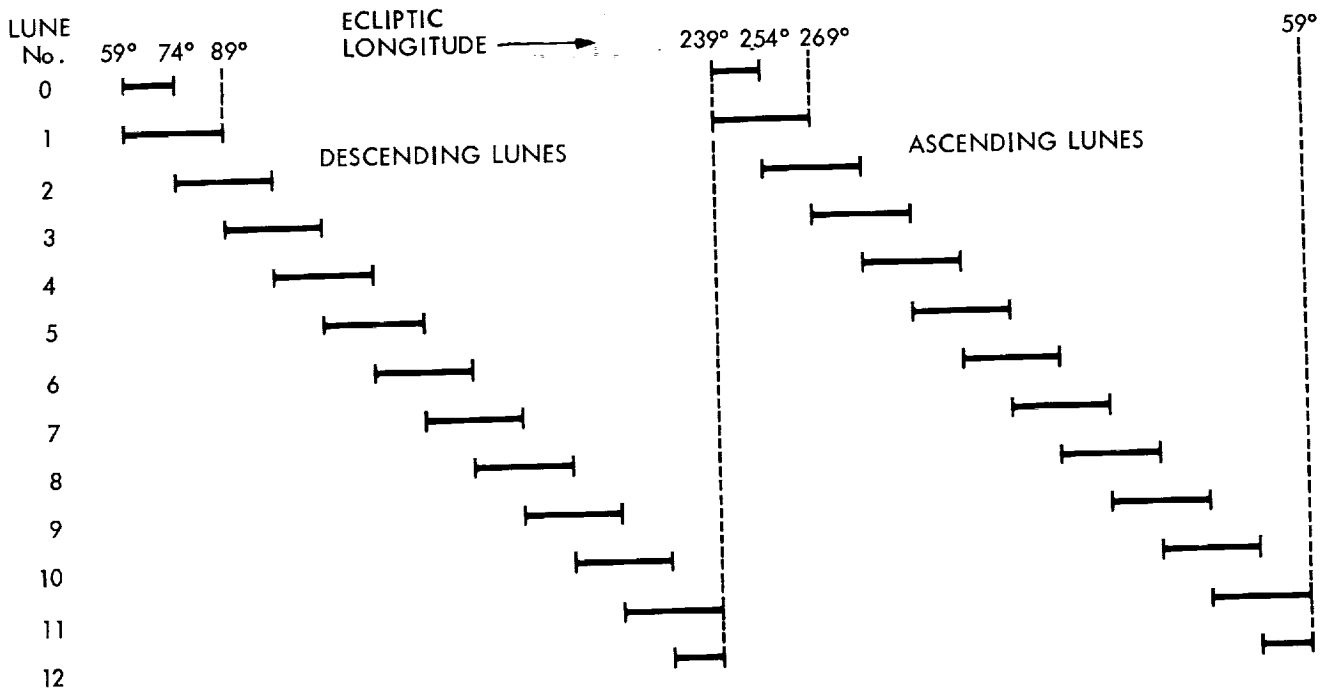

Figure III.C.4 The lune coverage scheme is shown for the first two sets of hours-confirming scans. Each line represents a single hours-confirming coverage of an entire 30° lune (except short lines at beginning and end which represent half-lune coverage).

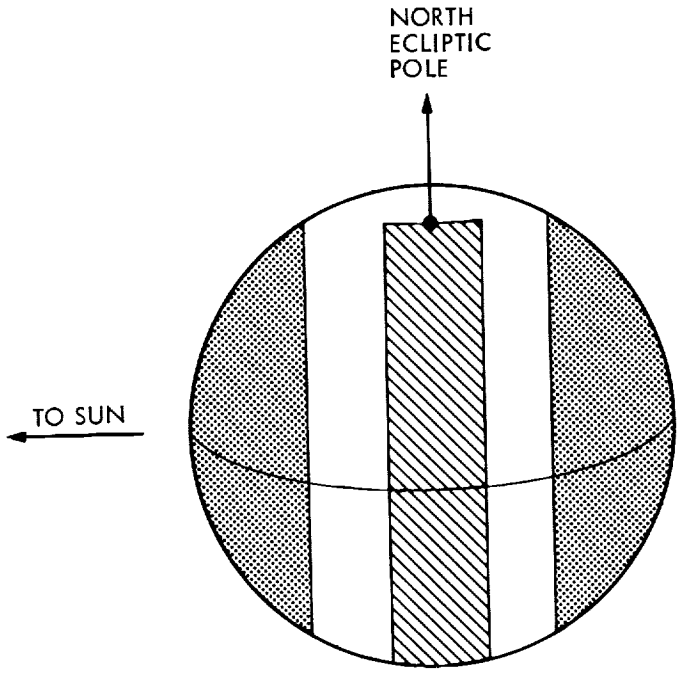

Figure III.C.5 A zone of half-circle scans is drawn on the celestial sphere.

C.2 The Second Six Months

The first sky survey was completed on August 26, 1983, with nearly a full second six months of operations expected. The survey was continued, but aimed at a coverage by only one set of hours-confirmed scans and using seven orbits per day. This plan covered many of the large number of small regions that the survey had missed for reasons explained elsewhere in this chapter, without the time consuming necessity of covering each hole separately, and also improved the survey's completeness for weaker sources (signal-to-noise ratio 5-10). Another important goal was the coverage of a 5° gap left in the first six months' survey (Section III.D.5). This latter goal was never achieved because the helium supply was exhausted earlier than expected. Half circles rather than lunes were used in the second six months because the additional coverage in the ecliptic polar regions in August and September filled in regions that would be inaccessible later due to eclipses and a severe Earth infrared radiation constraint in December and January.

C.3 Scan Rate

Using two gyros, the spacecraft clock-angle φ_0 (Fig. III.B.7) was decreased at a rate of $(3.85/\cos(90-\theta))'$ per second (which resulted in scanning the sky at a rate of $3.85'$ per second independent of θ), i.e. 10% faster than the orbital rate of the satellite of $3.5'$ per second. This increased rate gave increased pointing flexibility with respect to the constraints and, in particular, helped to reduce the effects of the SAA.

C.4 Strategy during South Atlantic Anomaly Passage

Survey observations were interrupted for up to 14 minutes during SAA passages even after selection of the least affected orbits. When the telescope entered the SAA during a survey scan its scanning motion was halted and it remained pointing at the same point on the celestial sphere until it emerged from the SAA when the scan was restarted with an overlap. During the SAA passage, "bias boost" was applied to the 60 and 100 μm detectors until about three minutes before exit. The internal reference sources were flashed just before entry and just after exit at the end and beginning of survey scans (Section III.B.3). Some SAA passages required so much time that the telescope would have violated the Earth infrared constraint (Section III.B.4) after SAA passage. In such cases it was necessary to leave a hole in the sky coverage and try to recover it with specially prepared short scans in the preceding or succeeding pair of SOPs. The failure to recover all of these holes contributed to the variable depth of sky coverage.

C.5 Moon and Jupiter Avoidance Strategy

Jupiter was avoided by stopping a scan when it reached within 1° of the planet and side stepping by 1° for 2° of scan before coming back to resume the original scan; hence the Jupiter avoidance procedure left a 2° square hole on the sky which needed to be recovered later in the survey. Figure III.C.6.1-3 clearly show the three square holes on the ecliptic at longitude approximately 250° (RA about 17 hrs). Each was left by one of the three sets of hours-confirming coverages. There is no residual Jupiter hole when the effect of all the coverage is added.

To avoid the moon in the same way as Jupiter would have left extremely large holes which would have been difficult to fill. The policy adopted, therefore, was to stop the survey on the moon's side of the orbit for the approximately three days needed for the moon to pass through this approximately 40° avoidance region.

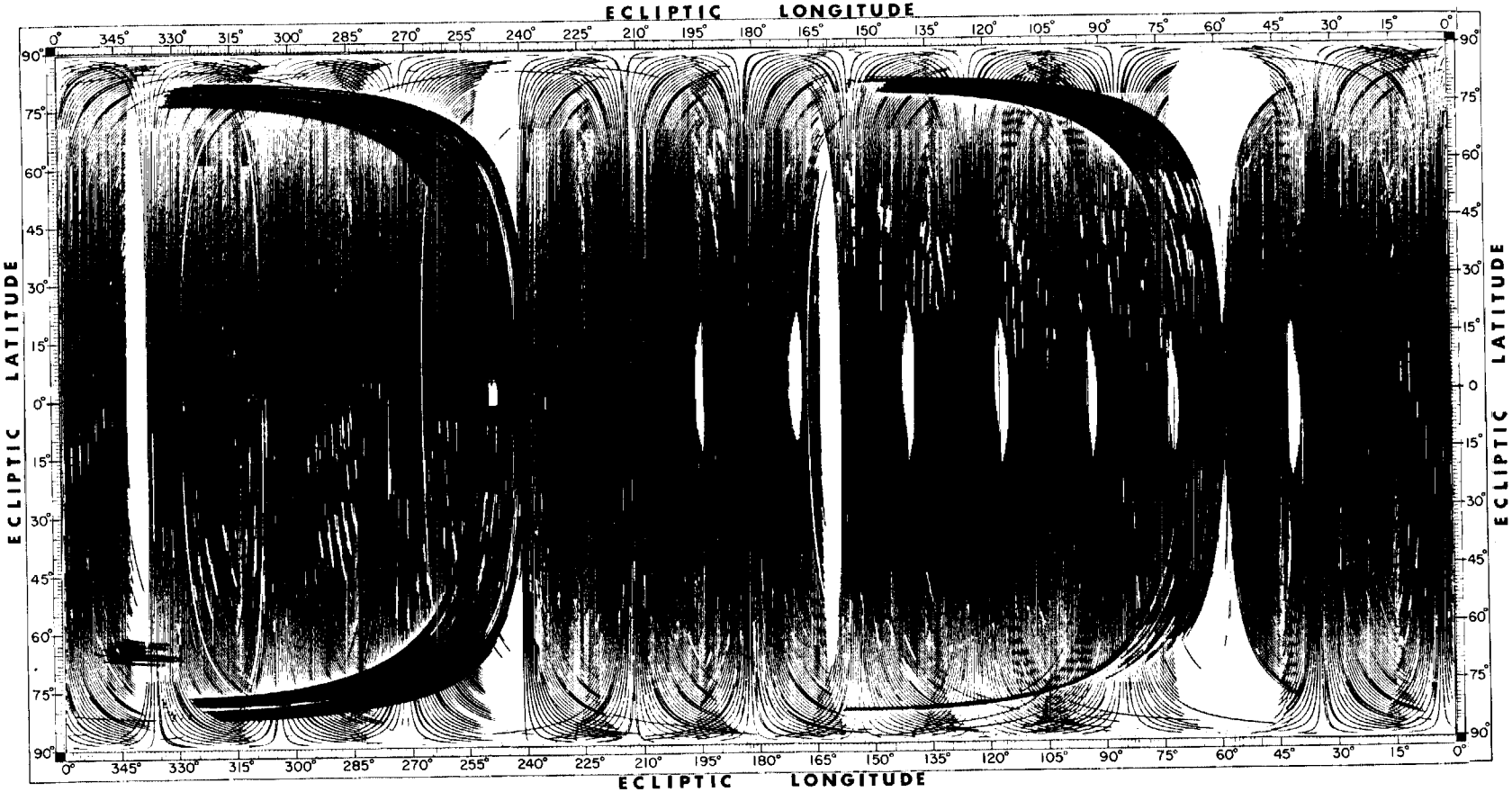

Figure III.C.6.1 The first hours-confirmed coverage is overlaid on a map of the sky in ecliptic coordinates. The scans converge at the ecliptic poles. Small, equally spaced holes in the ecliptic plane are due to the lunar avoidance stragegy and represent gaps in the sky coverage used to generate the extended emission images. The point source survey was not affected by these gaps.

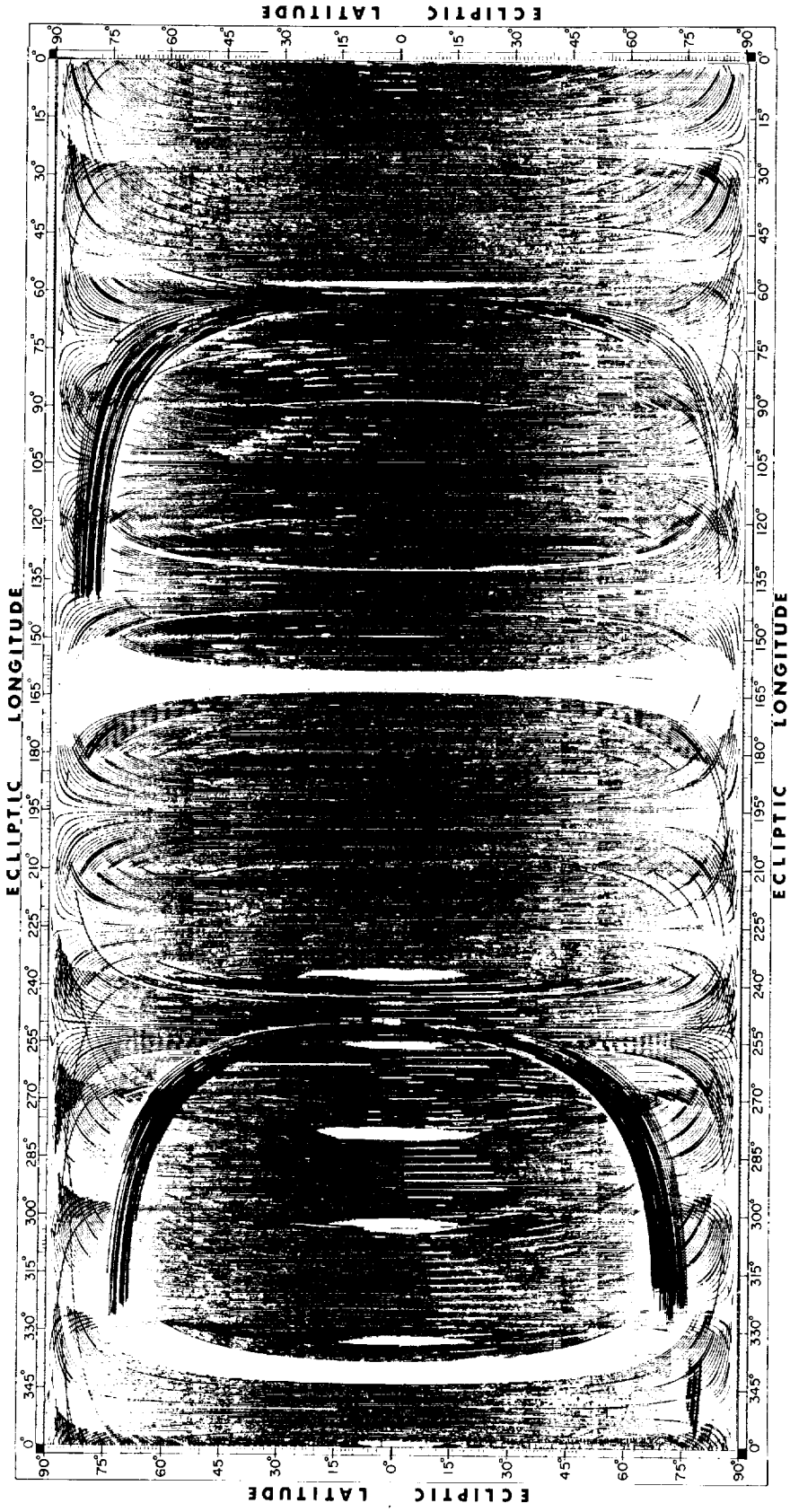

Figure III.C.6.2 Same as Fig. III.C.6.1, except for the second hours-confirming coverage.

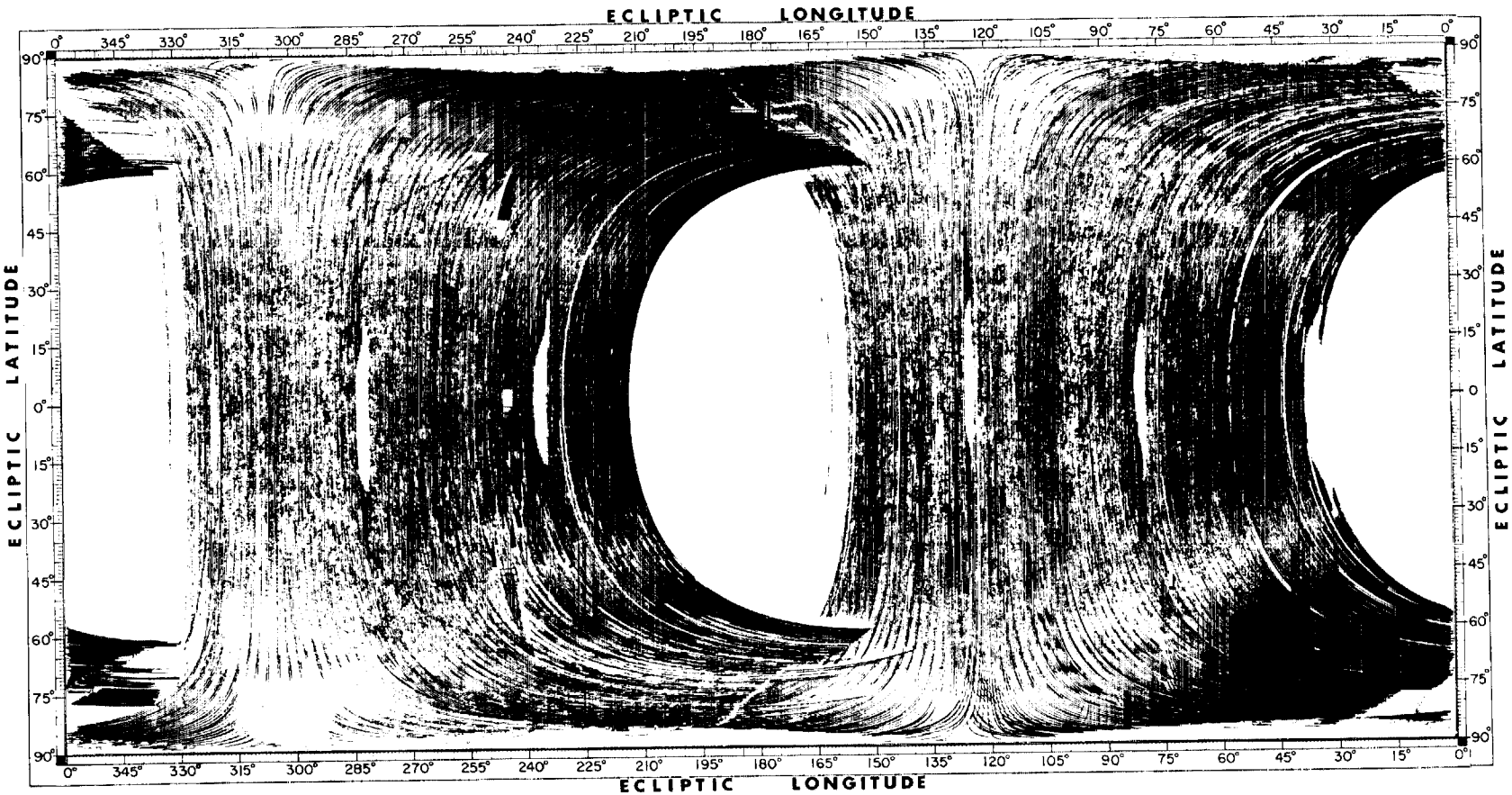

Figure III.C.6.3 Same as Fig. III.C.6.1, except for the third hours-confirmed coverage.

C.6 Strategy of Attitude and Photometric Calibration

To refine the pointing after the slew to the beginning point of a scan, attitude calibrations were made using visual stars at the beginning and end of each scan. Star sightings near the middle of the scan, if possible, allowed any pointing drifts to be detected and corrected (Section V.B). Long scans proved most suitable as they offered the greatest probability of finding these calibration stars.

To check the photometric calibration the internal reference sources were flashed at the beginning and end of every scan, including scans broken by the SAA. The internal reference sources were themselves regularly checked against an astronomical reference source (Section VI.A).

C.7 Realization of Survey Strategy

The survey scans resulting from this strategy and the constraints were generated by a computerized scheduling program (Oord *et al.* 1981). As well as generating the survey scans, the program reported which pieces of sky were not covered due to a combination of constraints, so that scans could be generated separately for inclusion elsewhere in the same or other SOPs (MacDougall 1984). It was not always possible to generate these scans within the constraints and so holes were left.

C.8 Half-Orbit Constraint

The scheduling program constrained survey scans to stop at the end of a half-orbit at one of the ecliptic poles. A side effect of this half-orbit design was that on occasions when the satellite had looked back in its orbit to cover a region of sky whose observation had been interrupted by a long SAA passage (Section III.C.4), the scan was cut short by reaching the end of its half-orbit, even though no other constraints had been violated.

C.9 Lune Constraint

Full coverage with the lune method required that while a lune was being painted it had to contain the meridian at 90° from the Sun. Otherwise the ecliptic poles could not be reached and holes would result. The scheduling program used to generate the survey scans also required that $\theta = 90°$ lie within the lune. This geometry became a hard constraint on the lune strategy, and became relevant to the decision that led to the 5° gap (III.D.5).

C.10 Hole Recovery Strategy

A record was maintained of those regions of the sky that were not covered by the automatically generated scans due to constraint violations and as suitable opportunities arose, attempts were made to fill the holes (Lau and Wolff 1984; Lundy 1984).

C.11 Pre-Survey Observations

Before commencing survey operations numerous checks were required to verify the health and safety of the satellite and to determine the best modes of operation. The cooled aperture cover was kept on the telescope for the first six days to allow sufficient time for contaminants carried up with the satellite to outgas and disperse so that they would not freeze on the cold optics when the cover was ejected. The eight days after cover ejection were used to test those aspects of the instrument that could not be tested with the cover on. This period was followed by a period of repeated surveying on a limited region of sky to verify the survey strategy and the data processing facilities (Section VIII.D; Rowan-Robinson *et al.*,

Table III.C.1 Mission Chronology

(All dates are 1983 and given in GMT)

Date	SOP	Event
26 Jan	1	Launch 02h 17m
26-31 Jan	1-12	In Orbit Checkout (Cover on) Outgassing of satellite
31 Jan	12	Cover ejection 19h 37m
31 Jan-8 Feb	12-28	In Orbit Checkout (Cover off)
9 Feb	29	SAA contour A (Fig. III.B.6) usage begins
9-10 Feb	29-30	Minisurvey layer 1 Hand made scans
10 Feb	31	Start first two hours-confirming coverages using half circles.
11-12 Feb	33-34	Minisurvey layer 2 Hand made scans
13-14 Feb	37-38	Minisurvey layer 3 Hand made scans
15 Feb	41	Minisurvey layer 4a Hand made scans
16 Feb	43	Minisurvey layer 4b Hand made scans
23 Feb	57	Half circle method ended
23 Feb	58	Lune method started
3 Apr	135	Moon avoidance radius lowered from 25 to 20°
9 May	207	SAA contour B (Fig. III.B.6) usage begins
26 Aug	425	End of first two hours-confirming coverages
26 Aug	426	Start third hours-confirming coverage
26 Aug	426	Moon avoidance radius lowered from 20 to 13°
9 Sep	454	Moon avoidance radius raised from 13 to 20°
18 Nov	593	First eclipse. Fallback to safety mode
21 Nov	600	Survey operations resumed 19h 40m
22 Nov	600	Liquid helium ran out 00h 16m
22 Nov	600	Last survey scan started 03h 34m
23 Nov	603	12 μm detector baselines saturated 09h 30m

1984). The scans of this "minisurvey" were hand-tailored for maximum efficiency in coverage. After all these tests had been completed and the problems they revealed had been resolved (MacDougall *et al.* 1984), the all-sky survey was started. The dates of these and other important events are given in Table III.C.1.

D. In-Flight Modifications

D.1 Introduction

Although the implementation of the survey strategy was remarkably effective, there daily arose regions of sky that should have been covered but for one reason or another (to be discussed below) were not. Attempts made to recover these scans were not always successful with a resultant loss in depth of sky coverage and data quality. The checks that were made at the ground station, including a search for moving objects such as asteroids and comets (Davies *et al.* 1984) are described elsewhere (Thomas 1983, MacDougall *et al.* 1984). These coverage gaps were not predictable and so recovery scans had to be generated rapidly to allow the uplink of commands during the next prime pass some 12 hours after the downlink of the data that revealed the difficulty. Given the time needed to process the data to reveal the problem, generate the recovery observation and regenerate the SOP, this was a tight schedule to maintain. The occasional failures are reflected in some of the remaining coverage holes.

The coverage obtained in each of the first two hour-confirming layers is summarized in Fig. III.C.6.1,.2.

D.2 Polar Horns

An unexpected source of noise was particle hits in the horns of the Van Allen belts (Fig. III.D.2). The effects of the horns were variable and often negligible. However, observations affected by increased noise were rescanned. The criterion used to require recovery scans for trapped particle radiation (usually in the polar horns) was that the on-board nuclear particle circumvention electronics (Section II.C.5) be activated during more than an average of about 0.7% of the time in 48 sec. This duration was determined empirically to correspond to roughly a doubling of the noise at 60 and 100 μm. In fact, because of the high degree of redundancy inherent in the data processing, the point source results were not noticeably affected by the level of radiation hits in the polar horns. The point source processing used both the data suffering from high radiation hit rates and the rescans. The extended emission maps (Section V.G) do not use data affected by radiation hits. In many cases the recovery scans were themselves affected by high radiation as the location of the satellite relative to the horns was often similar to that in the original scan. Losses due to the horns were greatest at the start of the mission because of a period of intense solar activity, which reduced considerably later on. The radiation recovery is discussed in greater detail by Wolff (1984).

D.3 Operations Problems

Scans lost because of occasional problems with the satellite or ground station (see e.g. Holdaway 1984, and MacDougall *et al.* 1984) were recovered as soon as possible after the events. Occasionally the outage was so great that it would have been impractical, within the geometrical constraints and operational timescales, to recover the gaps with individual recovery scans and it became necessary to reset the survey parameters in the scheduling program (Section III.C.7) and restart the survey from where it had left off.

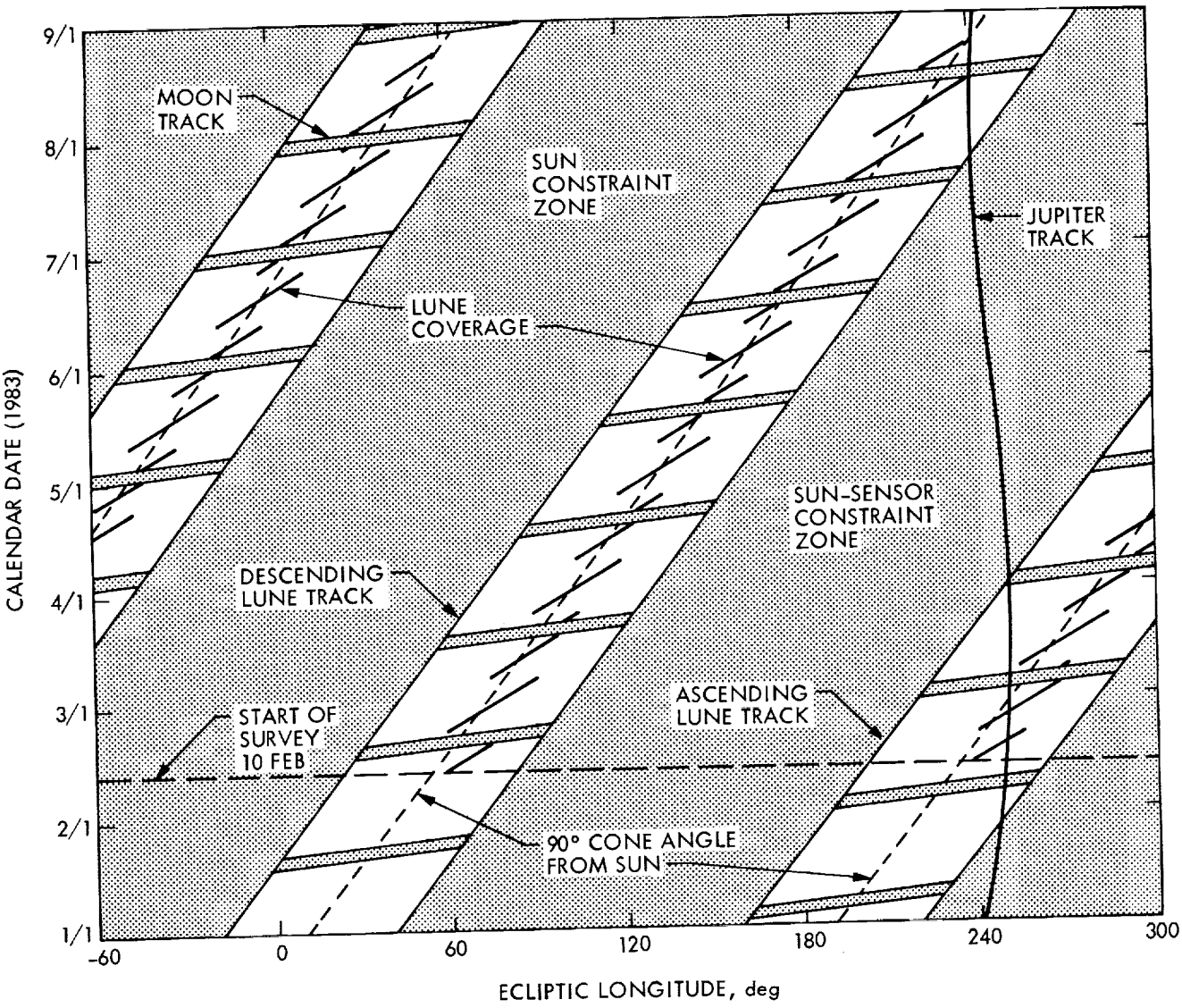

Figure III.D.1 Lune coverage is given as a function of date. The grey shaded regions are forbidden by the constraints indicated on the diagram.The dashed lines running at about 45° through the clear constraint free zones is the 90° cone angle line. The survey lune coverages are indicted by the solid black lines.

D.4 Saturation

Some saturation of the electronics by bright sources occurred as had been expected. Recovery on low gain was initially attempted in a systematic way and was successful for regions including the Galactic Center, the Orion Nebula, M17, W43, NGC6334, NGC6357, and IRC+10216. It was later decided that tracking and recovering saturated portions of scans was too time consuming and that it would be more fruitful to concentrate on filling missing sky coverage due to other causes. Recovery of saturated scans was commanded only if the bright object was not one that was, from prior knowledge, expected to be very bright. Most of these sources were well known HII regions which are so bright that the saturated parts can be measured from ground or airborne telescopes.

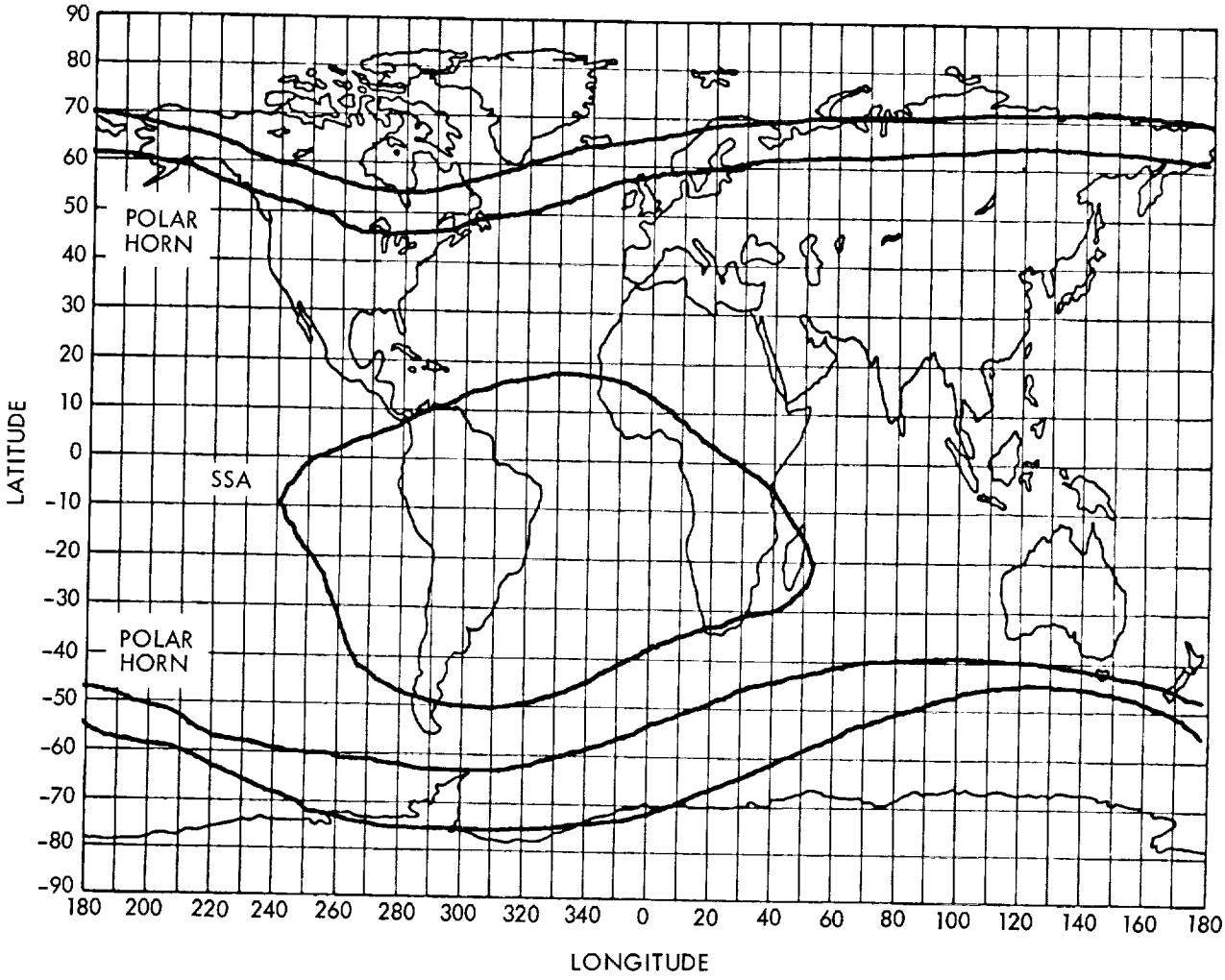

Figure III.D.2 The SAA (> 10 protons cm^{-2} sec^{-1} with E > 50 MeV and Polar Horns (> 10^5 electrons cm^{-2} sec^{-1}) with E > 0.5 MeV at an altitude of 900 km (Stassinopoulos 1978).

D.5 The 5° Gap

The scan generation software required that each of the two lunes under observation should contain an ecliptic meridian 90° away from the Sun. Otherwise the coverage of the ecliptic polar caps could not be part of the regular survey planning. Progress in completing the survey was slow enough that these 90° meridians slowly drifted toward the edge of the lunes. By mid May 1983 only 1° of slack was left and, once the lune boundary was reached, either a gap in the coverage would be required or the more efficient lune method would have to be replaced with the half circle method. A related problem was that it was becoming necessary to make survey scans at large solar offset angles (90°–θ). Such scans were particularly vulnerable to interruptions due to the SAA, station passage, Earth infrared constraint, etc. Consequently, a large number of small holes occurred in the sky coverage. As an important part of the sky, the North Galactic Pole, was approaching the observation window it was decided to avoid falling off the θ = 90° line in an uncontrolled way determined by the accumulation of the inevitable, small losses of

coverage. A topologically simple gap was chosen that would be accessible in the second six months of the mission (in early December). The survey was therefore advanced by 5°, giving a 6° pad. This decision was based on the prediction that the liquid helium supply would last until January 1984. Unfortunately, the last of the liquid helium boiled away in late November, leaving the 5° gap almost completely unobserved except for a few scans around its periphery.

D.6 Early Eclipse and Warm Up

The first eclipse of the satellite occurred 4 days earlier than expected due to an incorrect modeling of the effects of atmospheric refraction. The satellite fell into its safety mode during which no observations were made and the pattern of the third set of hours-confirming scans was interrupted. The coverage obtained before this event is shown in Figure III.C.6.3. A correction to the eclipse prediction program was derived and survey operations resumed after three days. Unfortunately, on the day that the survey was resumed the liquid helium boil-off rate dropped to zero as the last of the cryogen was expended. The telescope and focal plane began to warm up. By 09h 30m on November 23, 1983, 300 days after launch, the baselines of the 12 μm detectors saturated and the flight part of the mission was officially terminated.

The final depth of coverage by hours-confirming pairs of survey scans that was obtained is shown approximately in Fig. III.D.3 and, in more detail, in Chapter XIII.

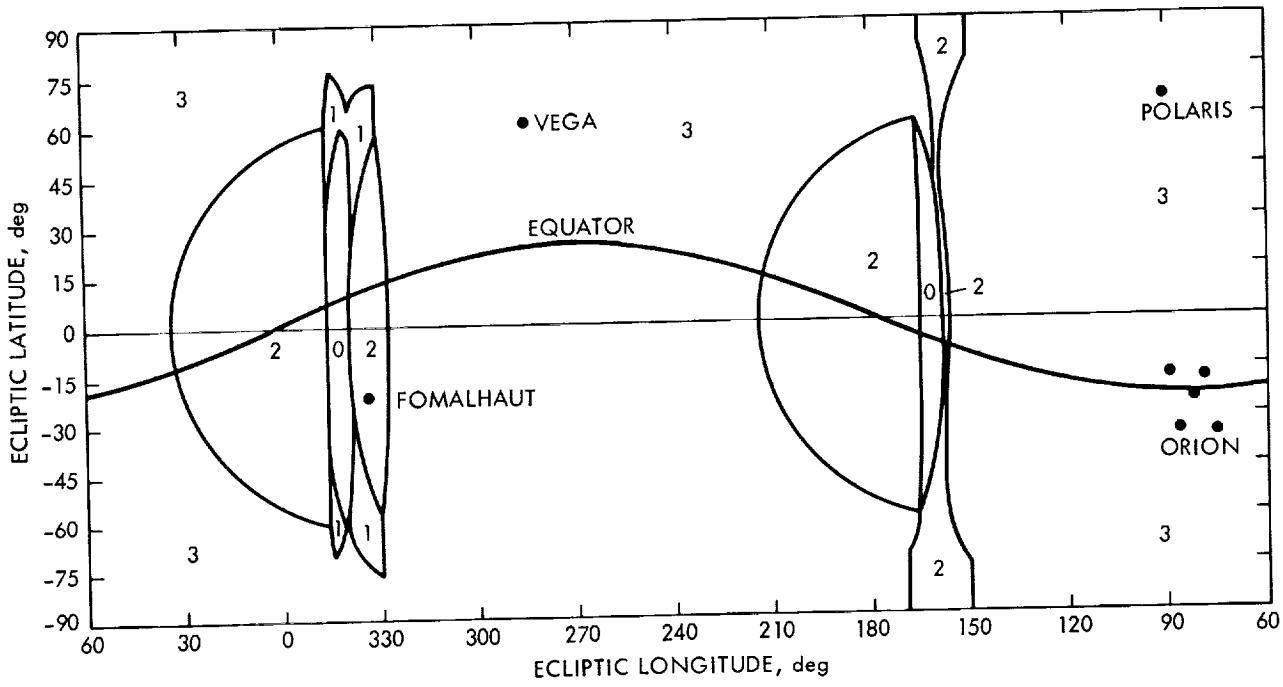

Figure III.D.3 A diagram of the survey coverage indicates approximately the number of hours-confirming coverages over the entire sky.

Authors:

J.P. Emerson, H.J. Habing, P.E. Clegg, S. Lundy

References

Bevan, H.C., McPherson, P.H., Champion, R.J.R. and Reid, M.F., 1983, *Journal British Interplanetary Soc.* **36**, 10.

Davies, J.K., Green, S.F., Stewart, B.C., Meadows, A.J. and Aumann, H.H., 1984, *Nature* **309**, 31.

Holdaway, R., 1984, *American Institute of Aeronautics and Astronautics 22nd Aerospace Meeting*, AIAA-84-0151.

Lau, C.O. and Wolff, D.M., 1984, *American Institute of Aeronautics and Astronautics Astrodynamics Conference*, AIAA-84-2012.

Lundy, S.A., 1984, *American Institute of Aeronautics and Astronautics 22nd Aerospace Meeting*, AIAA-84-0149.

MacDougall, J.R., 1984, *American Institute of Aeronautics and Astronautics 22nd Aerospace Meeting*, AIAA-84-0148.

MacDougall, J.R., McPherson, P.H., Mount, K.E., and Thomas, G.R., 1984, *Journal British Interplanetary Soc.*, **37**, 337.

McLaughlin, W.I., 1984, *American Institute of Aeronautics and Astronautics 22nd Aerospace Meeting*, AIAA-84-0147.

Mount, K.E., 1983, *Journal British Interplanetary Soc.*, **36**, 34.

Oord, E., de Pagter, P.J., van Holtz, R.C. and MacDougall, J.R., 1981, *Proc. Int. Symp. Spacecraft Flight Dynamics*, ESA SP-160.

Rowan-Robinson, M., *et al.*, 1984, *Ap. J. (Lett.)*, **278**, L7.

Stassinopoulos, E.G., 1978, NASA Technical Report X-601-79-7.

Thomas, G.R., 1983, *Journal British Interplanetary Soc.*, **36**, 38.

van Holtz, R.C., 1983, *Journal British Interplanetary Soc.* **36**, 6.

Wolff, D.M., 1984, *American Institute of Aeronautics and Astronautics 22nd Aerospace Meeting*, AIAA-84-0150.

IV. IN-FLIGHT TESTS

During the mission, a number of in-flight tests were conducted to verify or understand those aspects of the performance of the instrument which could not be estimated with sufficient accuracy before the flight. These tests are described in this chapter.

A. Detector/Focal Plane Performance

A.1 Detector Sensitivity and Responsivity

Although the performance of the individual detectors was quite uniform during the course of the mission, there was a range of sensitivities within each wavelength band. The noise equivalent flux density (NEFD) was calculated for each operating detector to quantify this spread. Five-minute long segments of data taken at high galactic latitude away from regions of obvious infrared cirrus were used to calculate the NEFD of each detector. After a baseline was subtracted from the data, a Gaussian noise estimator that discriminated against point sources was used to estimate the 1 σ rms noise in a single data sample. NEFD's from six representative SOPs were averaged together to give a single estimate of the noise in each detector. The NEFD for a given detector varied by less than 25 % for the data examined.

The results of this analysis are shown in the histograms of Fig. IV.A.1a-d which give the NEFD's of each detector. A mean noise for the band was calculated by leaving out those few detectors that were significantly noisier than their siblings. It should be pointed out that since a point source contributes

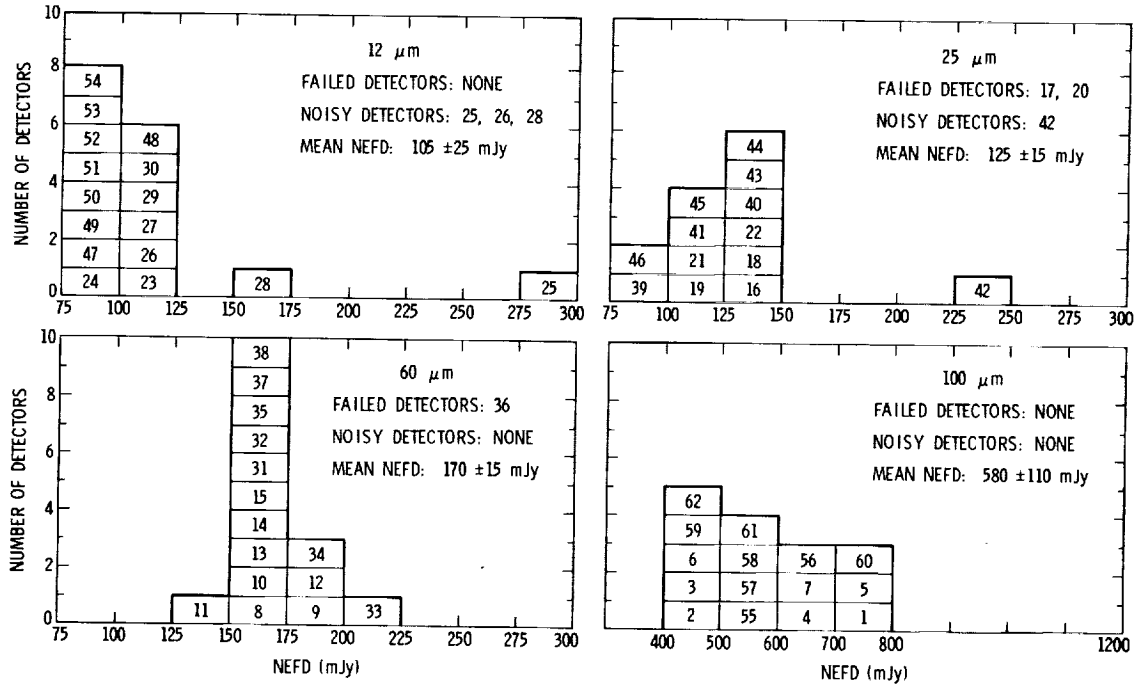

Figure IV.A.1 A histogram of noise equivalent flux densities under quiescent conditions. The detector number is indicated in each box. The absolute calibration is discussed in Chapter VI. The "noisy" detectors were excluded from the means.

to three data samples, two of which have weights of 0.5, the noise in the bandwidth appropriate to a point source is approximately $\sqrt{1.5}$ smaller than the values quoted in the figure. As discussed in Chapter V.A.3.c, however, the signal-to-noise ratio quoted throughout the data processing is based on the single sample noise.

The absolute calibration procedure used to derive these numbers is described in Chapter VI. Degradations of the sensitivity due to high photon backgrounds, to electron hits on the detectors in the polar horns of the Van Allen belts, to cosmic rays and to proton hits in the South Atlantic Anomaly (the SAA) are discussed below.

The detector responsivity and sensitivity depend on the background photon and particle environment. The responsivity as a function of time was determined by comparison with flashes from the internal reference source which was shown to be stable to better than 2% (Section IV.D). Figure IV.A.2 shows histograms of the distribution of the responsivity of each detector, normalized to the mean of the entire mission, as measured throughout the flight. The small intrinsic dispersion of the responsivities in

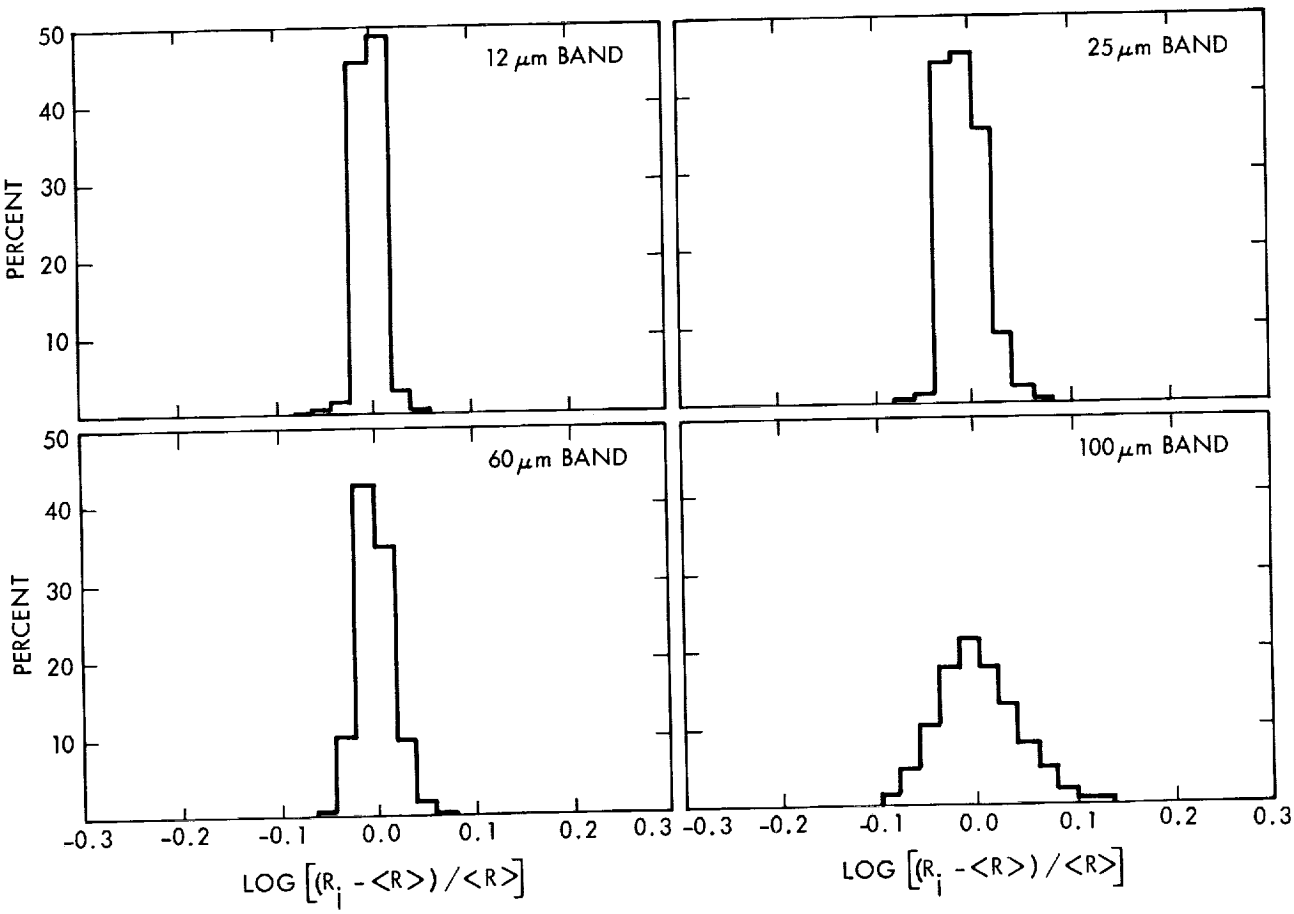

Figure IV.A.2 Histogram of the distribution of the uncorrected responsivities of the individual detectors for each wavelength band. The responsivities were found from the amplitudes of the response relative to flashes from the internal reference source obtained at the start and end of each survey scan. Responses to the latter under stable conditions had a dispersion of less than 2%; see Section IV.D.

the shorter wavelength bands is evidence that the changes in the uncorrected sensitivity from scan to scan were not extreme.

A.2 Detector Reliability/Anomalies

Throughout the mission the performance of the infrared detectors was very stable. Most detectors exhibited their pre-launch behavior. Detectors 17, 20 and 36 remained dead. Power spectra of detector data streams revealed that many of the detectors, especially the 12 μm and 25 μm detectors, were subject to low level 1 Hz electronic cross talk from the temperature sensors in the focal plane. Only for detectors 19 and 43 did the cross talk exceed the rms noise. In addition, detector 5 (100 μm) was subject to 0.25 Hz cross talk from an engineering data multiplexer. These three detectors had shown no excess noise before launch. As described in Section VI.A.4 it proved possible to either remove (in the case of detector 5), or to greatly reduce (detectors 19 and 43) the detrimental effects with the ground software.

Detector 26 exhibited a factor of three more noise than normal in the periods 1983 February 2-10 (SOPs 17-33) and 1983 March 16-June 6 (SOPs 101-265) for unknown reasons. Detectors 25 and 42 were generally a factor of two to three times noisier than other detectors in their bands. Detector 28 showed an abnormal cross-scan response as discussed below. These detectors were sufficiently noisy to be declared "failed" in the processing as discussed in Section V.D.2.d.

A.3 Cross-scan Response

The variations in individual detector responsivity with position across the detector were measured by scanning a celestial point source over closely spaced tracks across the focal plane. Four or five different cuts across a full width detector could be measured in this way. The results from the scans of the planetary nebula NGC6543 are shown in Fig. IV.A.3.1-3.4. The individual data points have been normalized to the peak response for each detector and a certain amount of artistic license was used to draw the solid curve representing the cross-scan response. Table IV.A.1 gives the effective solid angle of each detector based on the measured cross-scan and in-scan response.

Detector 28 had abnormal cross-scan response and was declared failed for seconds-confirmation purposes (Section VII.D).

A.4 Verification of Linearity

The responsivity of infrared detectors can depend on their frequency response and on the total amount of infrared radiation falling on them. In-flight tests were conducted to investigate the importance of these effects Necessarily, the two types of tests were often coupled and the results were not always unambiguous.

The effect of the total photon flux on the responsivity was measured by repeatedly observing asteroids as they approached the lunar limb to within 3°, making use of the out-of-field stray radiation from the moon. The highest background levels reached by this technique were 5, 4, 9 and 34 times the zodiacal background in the ecliptic plane. The test was thus overly severe in the 12 and 25 μm bands where the flux in the zodiacal bands represented the maximum background. The tests were adequate at the longer wavelengths where the background flux in the Galactic plane exceeds that in the ecliptic. The internal reference source was flashed immediately before and after each observation at the same background level.

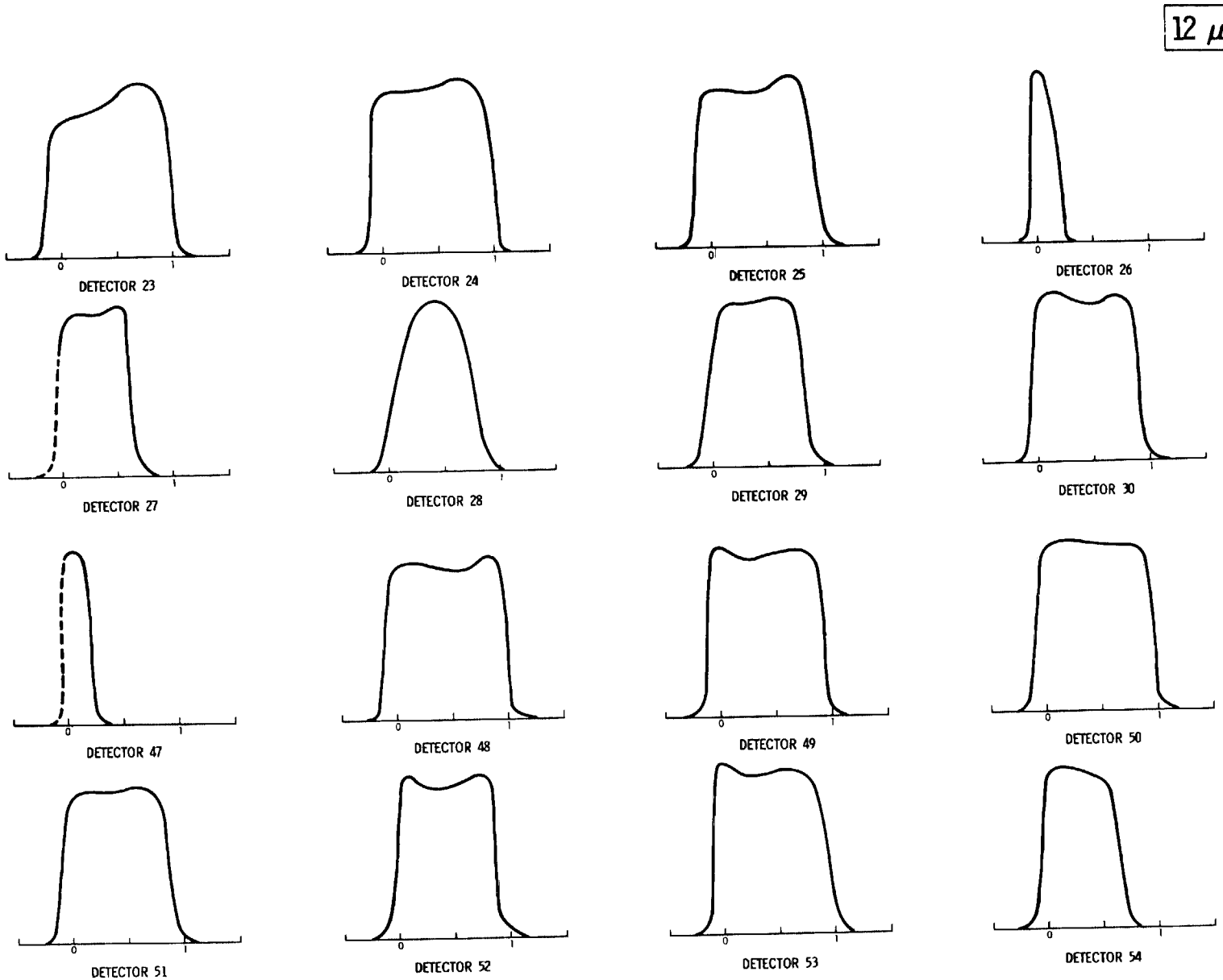

Figure IV.A.3.1 Cross-scan profiles of each 12 μm detector deduced from scans across NGC6543. The measurements were made in the pointed mode where cross scan position is well known. Each scan has been normalized to unity at its peak value.

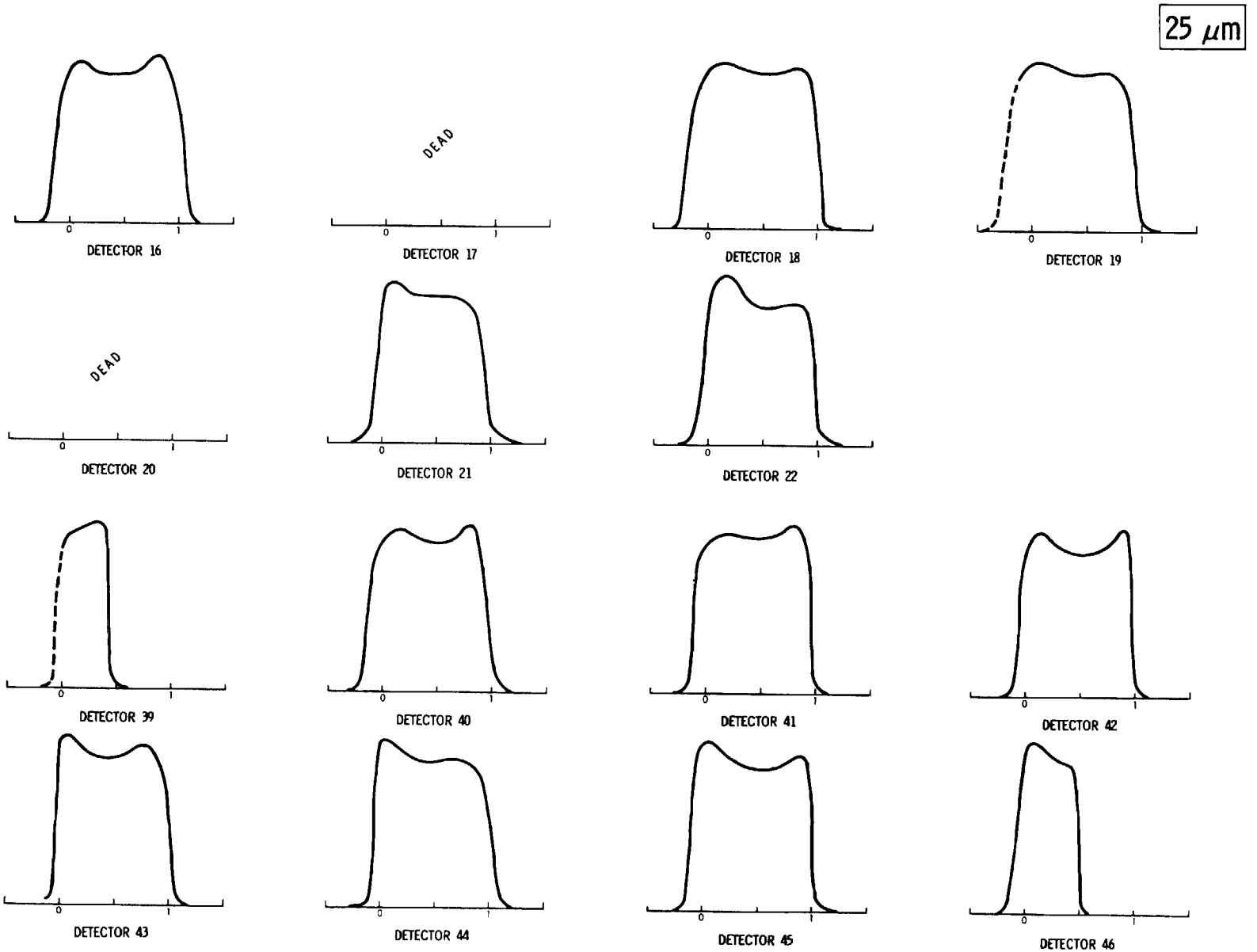

Figure IV.A.3.2 Same as Figure IV.A.3.1, except for 25 μm.

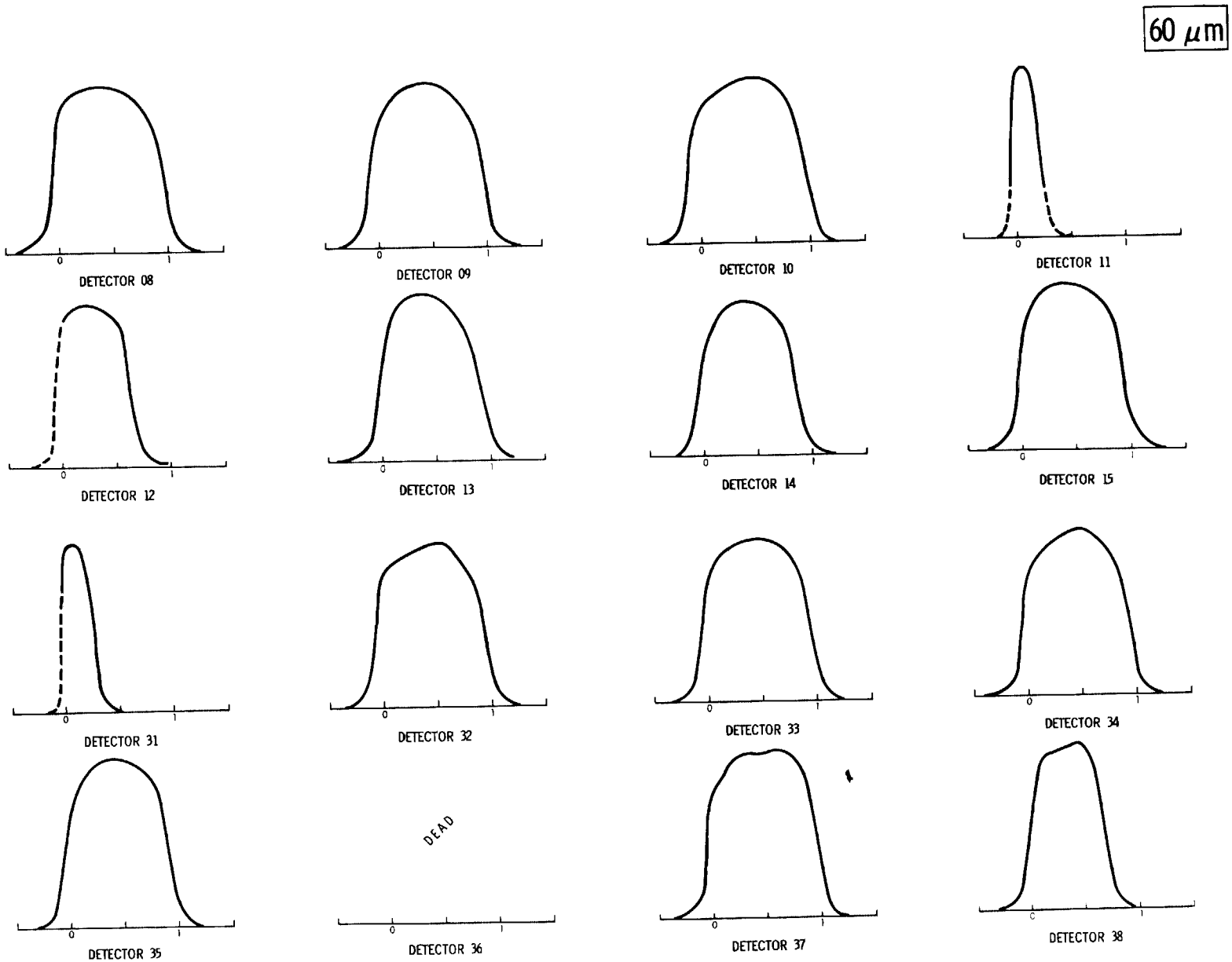

Figure IV.A.3.3 Same as Figure IV.A.3.1, except for 60 μm.

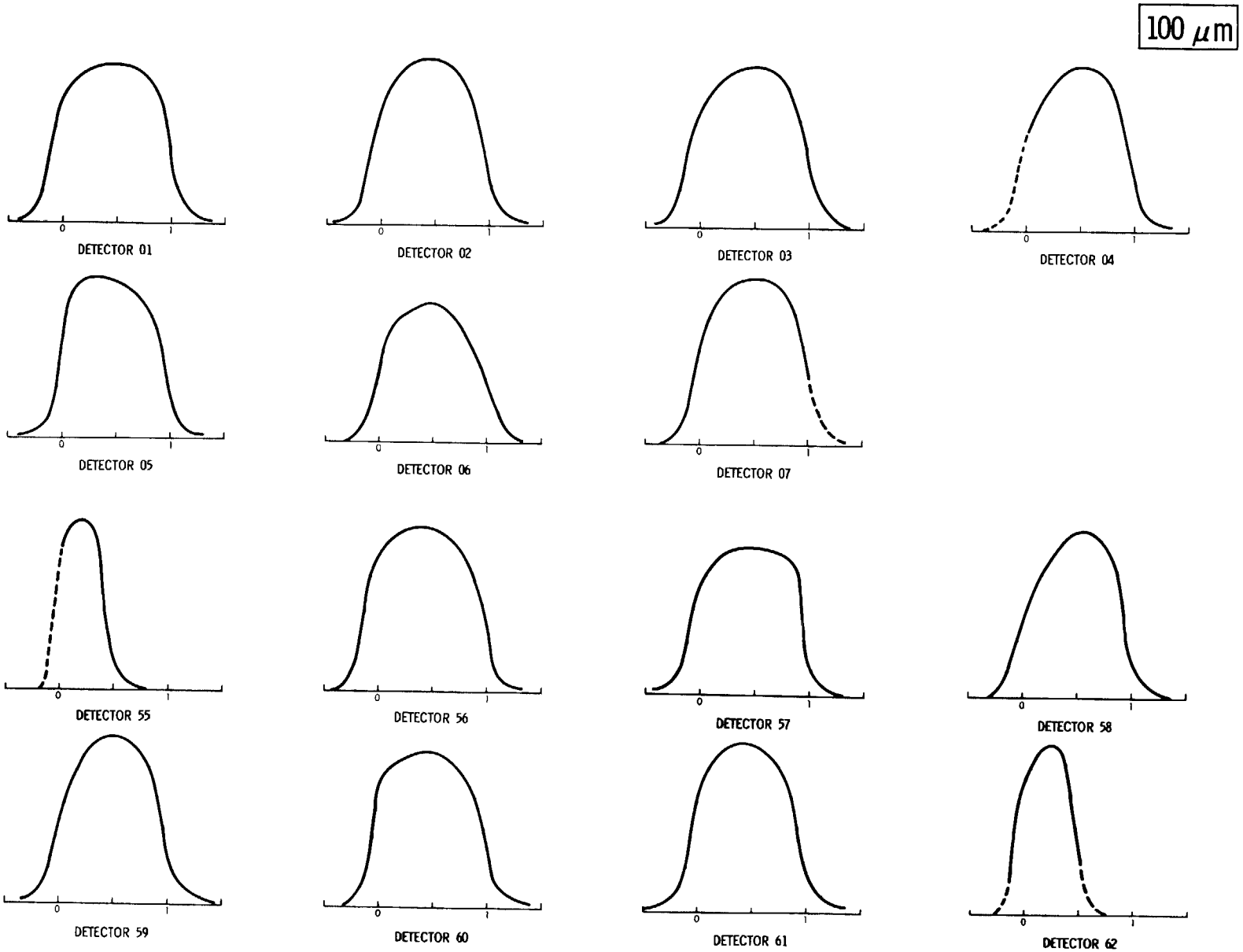

Figure IV.A.3.4 Same as Figure IV.A.3.1, except for 100 μm.

Table IV.A.1 Detector Data Based on NGC6543 Scans

Band	Det #	Solid Angle* [10^{-7} sr]	Cross-Scan** Dispersion %	Solid Angle Det #	Cross-Scan [10^{-7} sr]	Dispersion %
100 μm	1	14.5	9	55	7.1	11
	2	12.7	9	56	14.0	9
	3	13.0	10	57	13.2	8
	4	11.53	13	58	11.2	15
	5	12.0	11	59	11.7	14
	6	12.4	12	60	13.3	11
	7	12.6	10	61	13.5	11
				62	10.6	10
60μm	8	7.2	9	31	2.1	9
	9	6.7	9	32	6.4	9
	10	6.6	10	33	5.9	9
	11	2.8	9	34	6.5	12
	12	4.3	9	35	6.3	13
	13	6.6	14	36	---	--
	14	6.1	12	37	6.6	11
	15	6.2	10	38	3.9	14
25μm	16	3.5	4	39	1.4	7
	17	---	--	40	3.1	7
	18	3.6	7	41	3.1	6
	19	2.8	4	42	3.4	6
	20	---	--	43	3.2	6
	21	2.8	12	44	3.2	6
	22	3.1	9	45	3.2	7
				46	2.4	7
12μm	23	2.9	7	47	0.77	4
	24	3.0	4	48	3.1	6
	25	3.2	4	49	2.9	6
	26	1.2	9	50	3.0	7
	27	2.0	8	51	2.7	6
	28	3.1	37	52	2.5	7
	29	2.5	22	53	2.8	7
	30	2.8	10	54	2.0	8

* Solid angle based on the measured detector cross-scan response. In-scan response based on average point source detector template.

** Cross-scan dispersion is the uncertainty in the flux assigned to a single detection due to the fact that the detector cross-scan response is not uniform, but the source crosses the detector with uniform probability in the non-overlap region.

The frequency response was measured by scanning a given source at rates varying from the nominal scan rate (3.85 ′ s $^{-1}$) to 1/16 the nominal scan rate. In addition, the internal reference source was observed for varying lengths of time up to 120 seconds. Finally, selected sources were observed in the "stare" mode with one detector being positioned on the source for up to 120 seconds; this procedure was never successfully executed using a 25 μm detector.

In Fig. IV.A.4.1,.2 the results of the tests to measure the dependence of the responsivity with frequency are given for the four IRAS bands. The ratio of the responsivity at nominal survey scan speed to that at "DC" was adopted as 0.78, 0.82, 0.92 and 1.0 at 12, 25, 60 and 100 μm; these ratios are indicated in the figures.

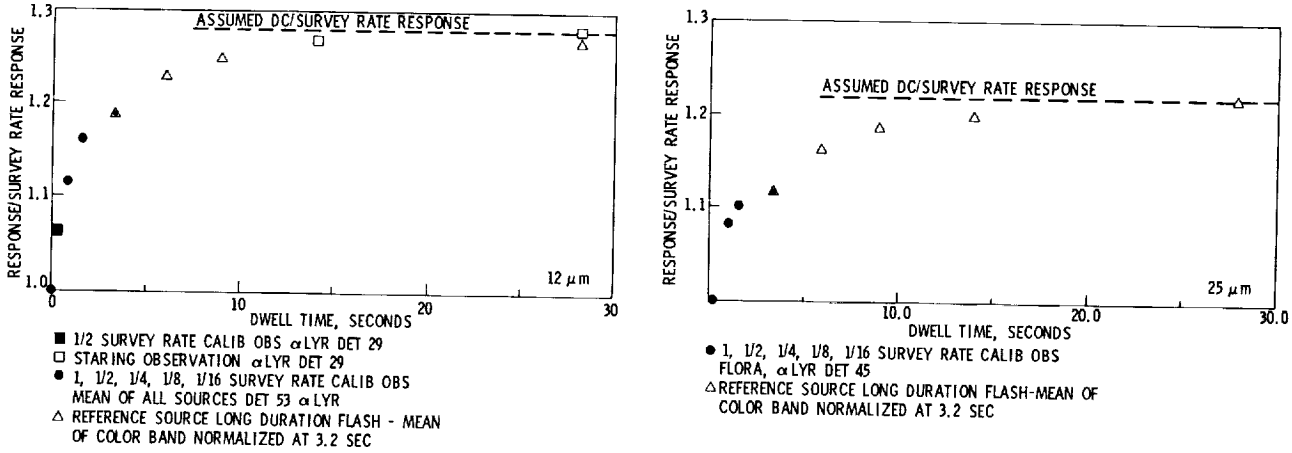

Figure IV.A.4.1 Measurements of the response vs. dwell time to measure frequency dependence of the detectors at 12 (left panel) and 25 (right panel) μm. The measurements were made either by crossing a source at scan rates less than the survey rates or by viewing long flashes of the internal reference source.

The tests also show that, at the 5% level, there was, at 12 and 25 μm, no effect of the source strength on the dependence of the responsivity with frequency. The "mean" observations in the figures represent stars whose amplitudes span more than a factor of 100 in brightness and which show no significant departure from the curves shown. At 60 and 100 μm the situation is clearly different. Tests of sources up to 10 times brighter than α Lyr show the same behavior as does α Lyr. Stronger sources show a variety of behaviors as indicated in the figures.

Of particular interest is the frequency dependence between observations at the survey rate and observations taken at half survey rate since the latter rate was used in pointed observations, some of which were crucial in the absolute calibration procedure. In Fig. IV.A.5 the magnitude differences between the observations at the survey rate and at 1/2 survey rate are given for sources of varying strengths.

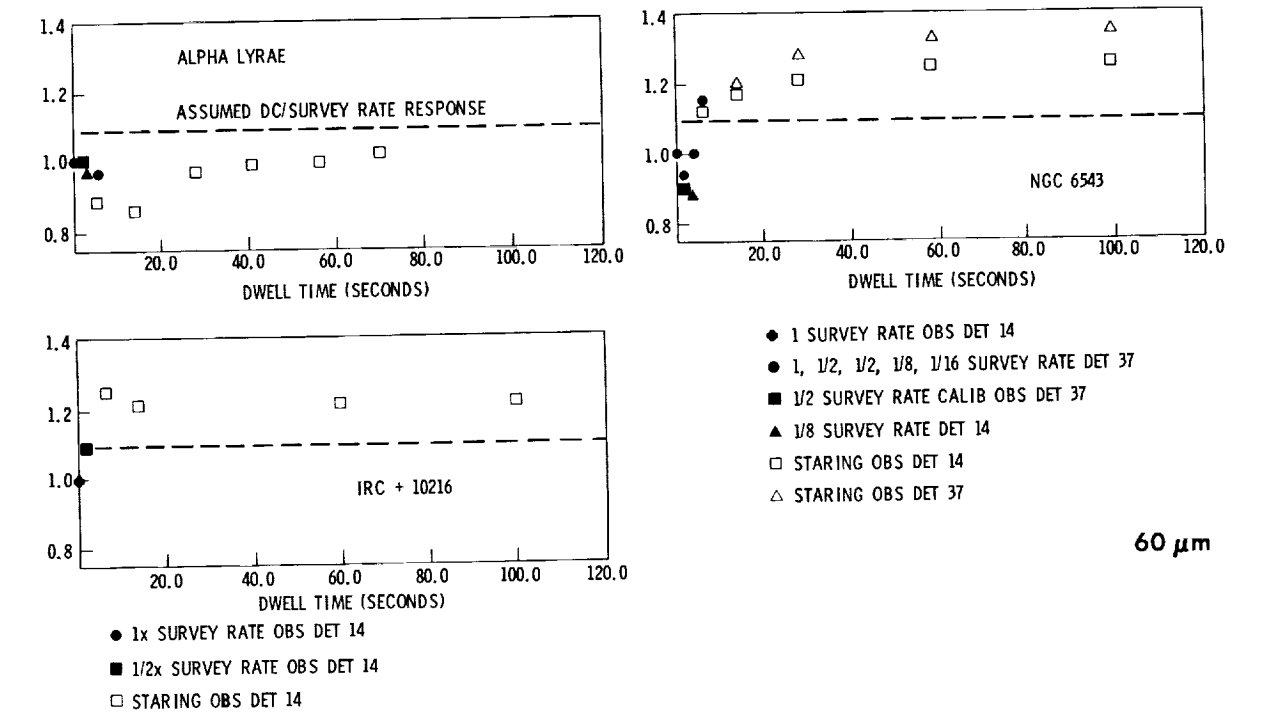

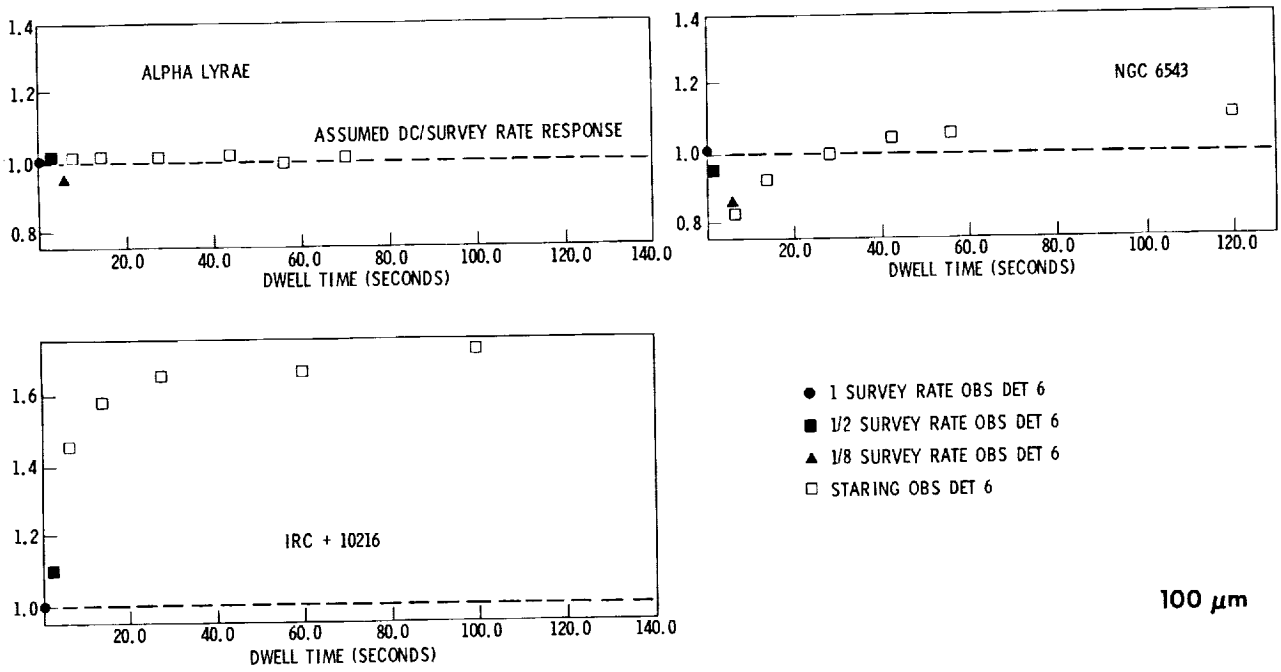

Figure IV.A.4.2 Measurements of the response vs. dwell time to measure frequency dependence of the detectors at 60 (top panels) and 100 (bottom)μm. The measurements were made either by crossing a source at scan rates less than the survey rates or by viewing long flashes of the internal reference source.

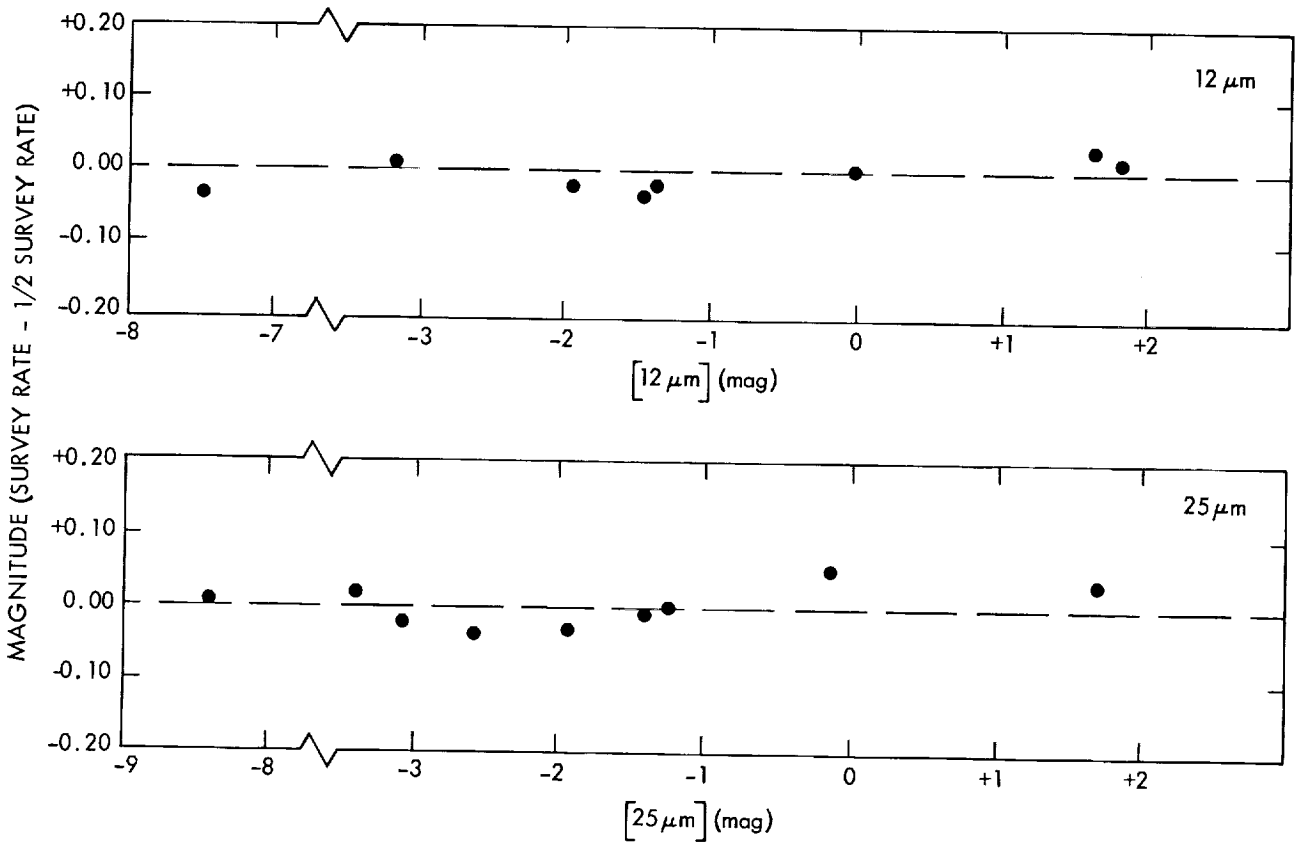

Figure IV.A.5 Measurements at survey and 1/2 survey scan speeds. The magnitude scale is defined in Section VI.C.2.a. The source IRC+10216 is at the extreme left in both panels.

A.5 Baseline Stability

The electronic baseline stability proved to be quite good on a time scale of a day, with drifts typically less than 5% of the sky brightness toward the north ecliptic pole over this period at 12 and 25 μm and less than 20% at 60 and 100 μm. Throughout the mission, baseline drifts over periods longer than about one day were monitored by daily observations of a region of sky near the north ecliptic pole which was called the Total Flux Photometric Reference (TFPR). A detailed discussion of the determination of the brightness of this region and its time variation is given in Section VI.B.3. Additional differential effects between detectors which were important in the extended emission maps were removed in the destriping processor described in Section V.G.6.

A.6 Particle Radiation Effects

In order to minimize the expected degradation of the data quality due to energetic particle radiation, the IRAS hardware incorporated a number of features including nuclear shielding, radiation hit deglitchers, radiation hit deadtime counters and bias boost circuits; see Section II.C. In addition, operational procedures were developed during the in-orbit checkout phase to minimize radiation effects. These procedures were incorporated into the routine mission procedures (see Section III.B.6 and III.C.4).

A.6.a Detector Responsivity and Noise

The radiation effects from the horns of the van Allen belts were basically limited to an increase, typically by a factor of two or less, in noise due to many small pulses not eliminated by the deglitcher circuitry. Passage through the SAA caused large changes to the detector responsivity particularly in the 60 and 100 μm bands. These were monitored by comparisons with flashes from the internal reference source after passage through the SAA. Cosmic ray hits at the rate of about one per twenty seconds on each detector were handled adequately by the nuclear spike deglitchers and caused little degradation to the data (Section VII.D).

A.6.b Radiation Effects on Detector Baselines

Ionizing radiation in the IRAS environment affected the baseline stability in two ways. Residual noise spikes from polar horn passage and entry into the edges of the SAA were not removed from the data, and when added into the extended emission maps resulted in elevation of the baseline and increased noise. The radiation level was monitored by using the activation of the nuclear particle circumvention circuit as described in Section III.D.2, and data taken during times of high radiation levels (blanking time greater than 10%) were excluded from the extended emission data base.

A.7 Effects of Bias Boost

The bias boost (Sections II.C.5 and III.B.6) applied to the 60 and 100 μm detectors to minimize radiation exposure effects during deep SAA passages reduced the responsivity and noise as expected from the pre-flight measurements. The change in the responsivity of the 25 μm detectors was sufficiently small that no bias boost in that band was regularly applied. Figure IV.A.6 shows the mean response to the internal reference source from the detectors of each of the four IRAS bands as function of time before and after two consecutive SAA crossings of more than average radiation dosage using the bias boost procedures developed during in-orbit checkout. It can be seen that the responsivity was stable to within 5%-10% in the 12 and 100 μm bands, about 15% in the 25 μm band and better than 5% in the 60 μm band.

The bias boost also resulted in a baseline shift significantly larger than described in Section IV.A.5 which decayed exponentially with time. The details of this behavior were measured by special observations and analysis; a complete description is given in Section VI.A.3. There were times when the track of the satellite went near the boundary of the SAA, but when no bias boost was applied. If the internal reference source was activated near the SAA in these cases, errors in the responsivity as large as 8%, which resemble baseline errors, affected all detectors in the band. These produced increased apparent brightness at 12, 25 and 60 μm and decreased apparent brightness at 100 μm.

A.8 Photon Induced Responsivity Enhancement

After the mission was completed, a comparison of scans which crossed the Galactic plane in an ascending manner with those crossing it in a descending manner showed an enhancement in the responsivity in the 100 μm detectors due to passage through the Galactic plane.

Subsequent analysis of special calibration scans over Saturn confirmed that this effect was due to responsivity enhancement caused by infrared photons. During these special observations, Saturn was scanned across the focal plane ten times with an integrated photon dose on the 100 μm detectors ranging up to 12×10^{-10} Joules μm^{-2}. The enhancement associated with this photon dose was defined as the ratio

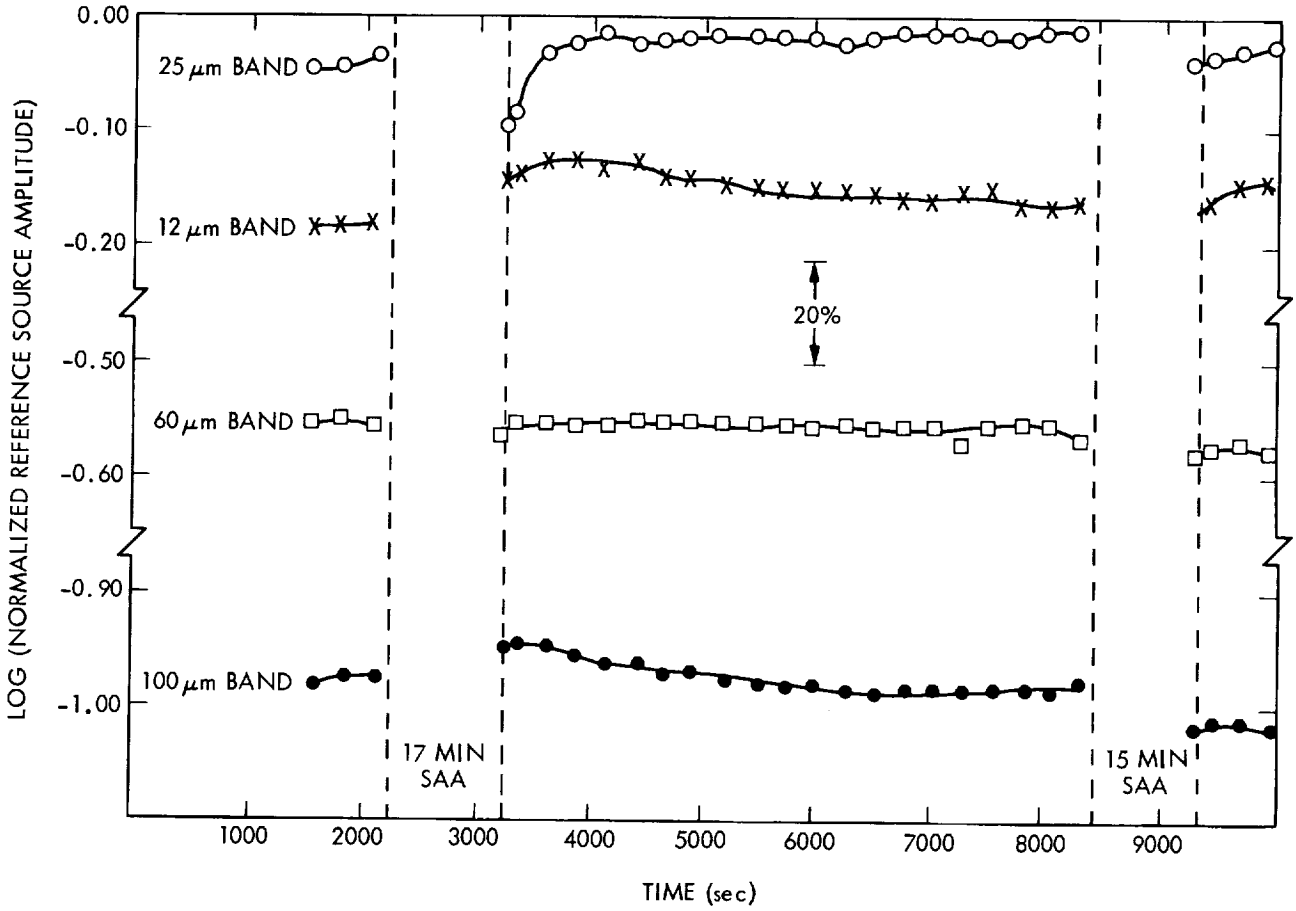

Figure IV.A.6 Effect of bias boost on responsivity after passage through SAA. The responsivity was measured by comparison with repeated flashes of the internal reference source. For clarity, the 25, 60 and 100 μm observations have been shifted by arbitrary amounts.

of the amplitude of the internal reference source after the observation to the amplitude of the flash prior to the observation. The results are shown in Fig. IV.A.7. The 100 μm detectors 3, 6, and 7 show little enhancement while the rest of the 100 μm detectors show an enhancement increasing with increasing dose to about 13% enhancement at about 9×10^{-10} Joules m^{-2}.

Figure IV.A.8 illustrates how the response to the internal reference source decayed with time after a Saturn exposure. Each amplitude of the flash from the internal reference source has been normalized to the amplitude from the source flash that preceded the Saturn exposure. This was done for three observations following a Saturn observation. Care was taken to ensure no bias boost occurred between these observations. Of course, there is no guarantee that the response of the detectors to the internal reference source was not affected by photon exposure within these post-Saturn observations.

Figure IV.A.9 shows the integrated 100 μm photon dose due to the Galactic plane emission as a function of ecliptic longitude for a nominal scan inclination of 45° with respect to the Galactic plane. The integrated photon dose is generally in the range of dosages encountered in the Saturn observations with peak dosage near the Galactic center being approximately twice the peak Saturn dosage. No significant enhancement was observed for the 12, 25 or 60 μm detectors in the Saturn observations.

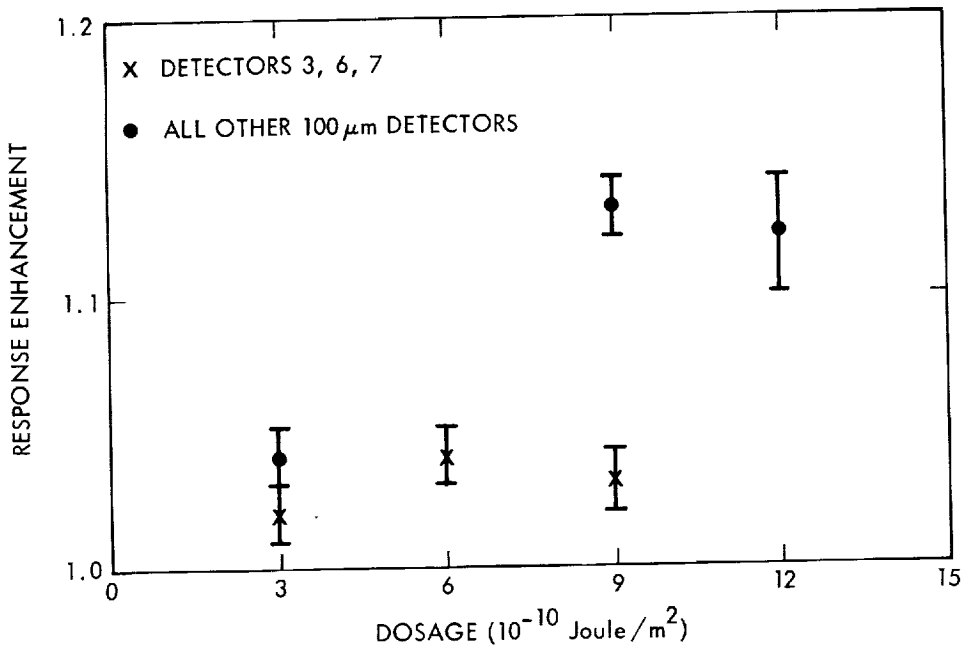

Figure IV.A.7 Observations of photon induced responsivity enhancement in the 100 μm detectors after scans of Saturn. The response for the three detectors #3, 6 and 7 are plotted separately; the responses of the other 100 μm detectors are averaged.

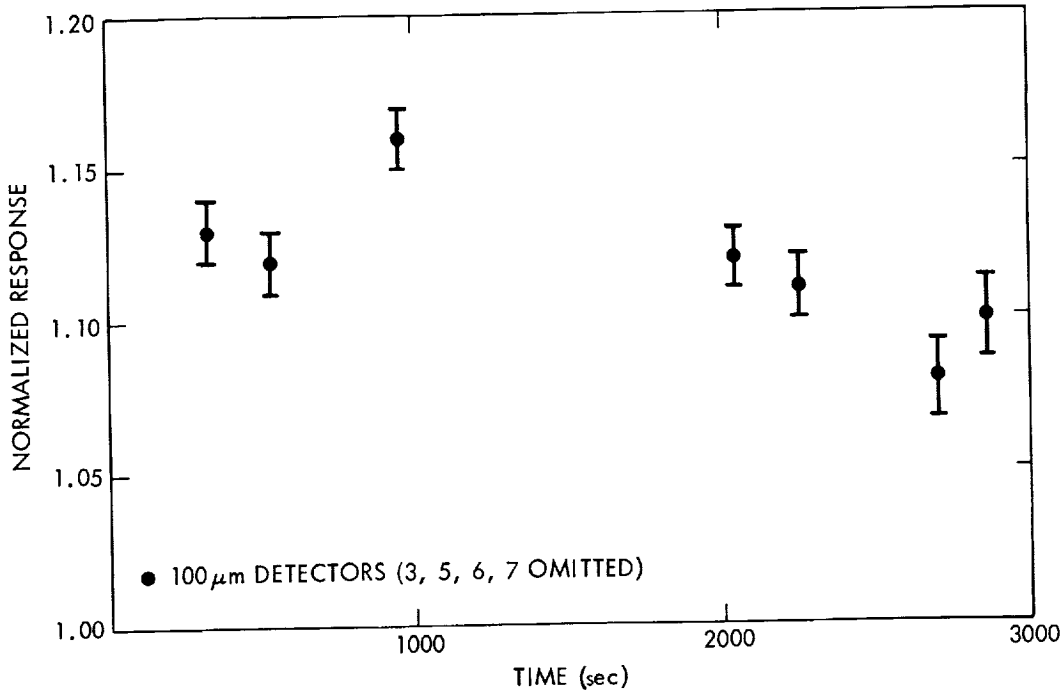

Figure IV.A.8 Observations of the decay of photon induced responsivity enhancement after scans over Saturn. The response was measured using flashes of the internal reference source and is normalized to the flash amplitude which just preceded the scan over Saturn. The Saturn crossing occurred between 0 and 300 seconds.

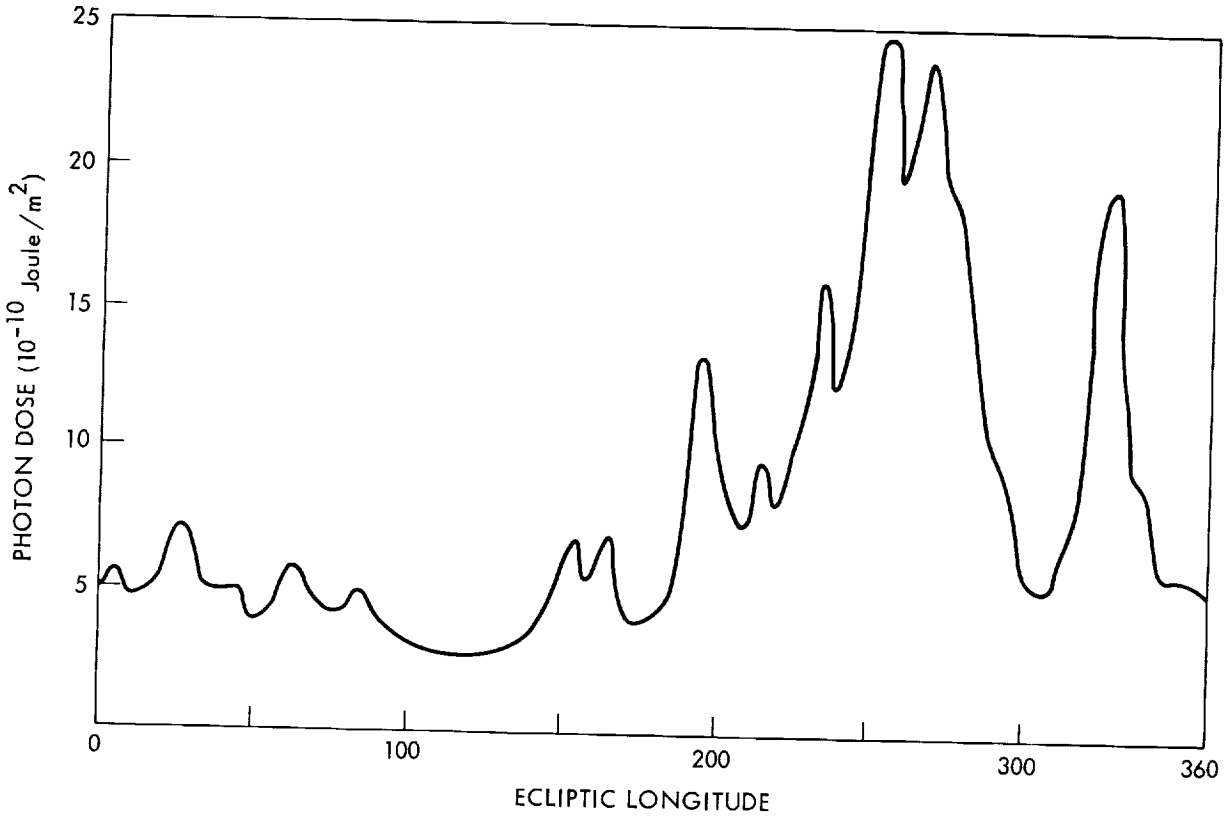

Figure IV.A.9 Typical photon dosages in the 100 μm detectors for 45° crossings of the Galactic plane. The dosages were calculated from the mean surface brightness within 20° of the Galactic plane in 0.5° intervals.

The statistical analysis of the effect of photon induced responsivity enhancement cause by passage over the Galactic plane is discussed in Section VI.B.4.c.

A.9 Feedback Resistor Nonlinearity Analysis

The impedance of the detector feedback resistors, nominally $2 \times 10^{10}\Omega$, decreases with increasing voltage as shown in Fig. II.C.2. The shape of the resistance versus voltage relation for the feedback resistors was verified by (a) comparing fluxes for stars measured at 12 and 25 μm with ground-based observations (Tokunaga, 1984; Rieke et al., 1984) and (b) special low gain calibration observations of IRC+10216. Since IRC +10216 is known to be variable, the latter were compared with nearly simultaneous 10 μm ground-based observations (Joyce, 1984). The results for the 12 and 25 μm bands are shown in Fig. IV.A.10. In this test the 25 μm comparison value for IRC+10216 was estimated from the published spectral distribution (Campbell *et al.*, 1976) normalized to the 12 μm measurement. Detector-to-detector differences in the R_f shape were assessed by comparison of detector response ratios. There appears to be no significant deviation from the adopted R_f vs. voltage curve over the range examined. Furthermore, there appears to be no source strength dependent term larger than a few percent in the 12 and 25 μm bands.

Similar tests for the 60 and 100 μm bands were not carried out due to uncertainty in the 60 and 100 μm flux from IRC+10216 at the time of the IRAS observation and the lack of bright, pointlike iso-

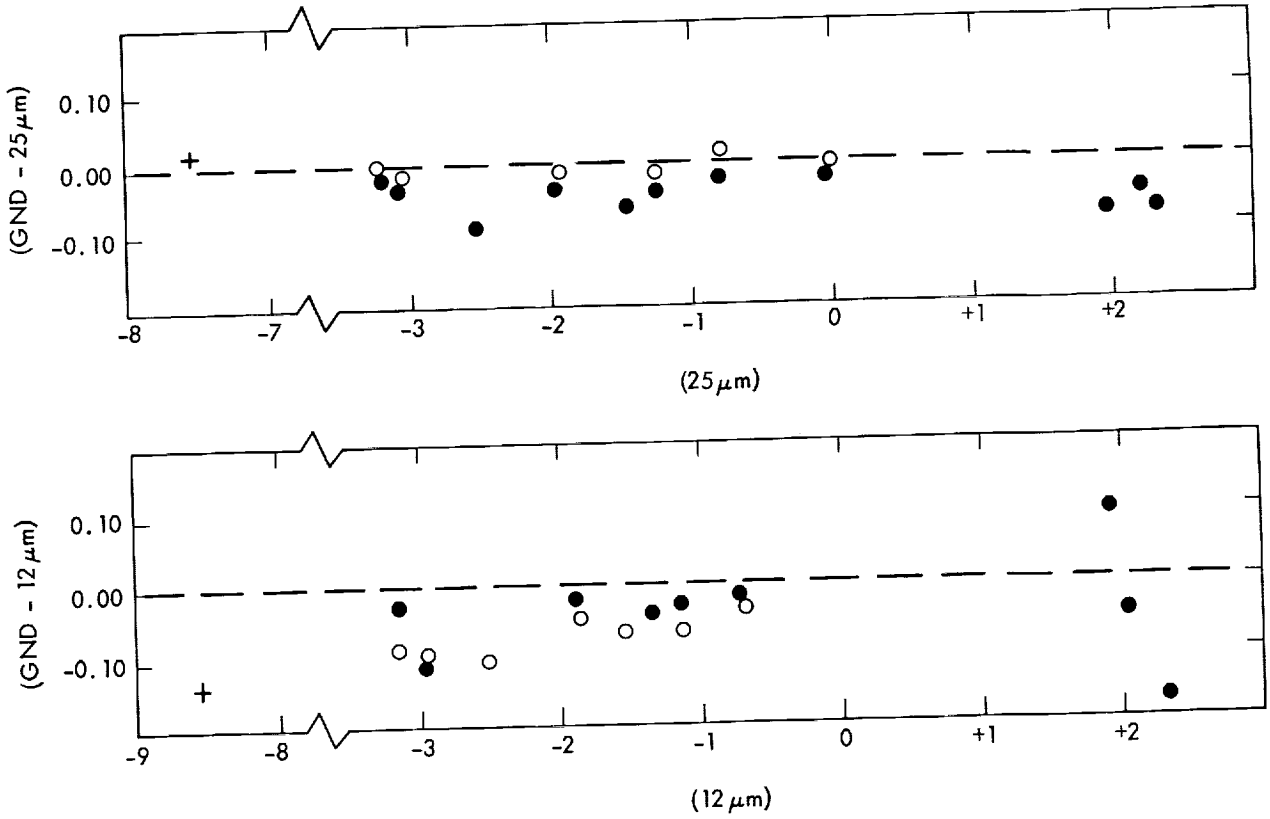

Figure IV.A.10 Comparisons of 12 and 25 μm IRAS pointed observations with ground based observations over a wide range of magnitudes (Section VI.C.2.a) to check nonlinearity of the feedback resistor. The ground based observations of standard stars are from Rieke *et al.* (1984) (open circles) and from Tokunaga (1984) (closed circles). The offsets reflect a zero point difference of 0.02 mag used by Tokunaga and the fact that both ground based systems adopt zero color difference between 10 μm and 20 μm, whereas a color difference of 0.03 mag has been adopted for the IRAS calibration. See Section VI.C. The ground observations of IRC +10216 are by Joyce (1984; see Section IV.A.9).

lated sources well observed with other telescopes which were also observed with IRAS calibration observations.

B. Spectral Passband Verification

The product of the transmission efficiency of the optical filter stack and the detector efficiency defines the effective wavelength passbands and the nominal out-of-band rejection performance of the detectors. This is described in Section II.C.5 and Tables II.C.4 and II.C.5. The detector passbands were verified before launch at the component level, but not at the system level. In-flight tests were performed to test the consistency of the passbands and out-of-band rejection within each band and to verify the nominal passbands. There was no direct in-orbit verification of the effective transmission characteristics of the detector/filter combination.

B.1. Verification of the Relative Consistency

The consistency of the transmission characteristics within each band was checked by a two step procedure. First, all detectors were carefully calibrated relative to NGC 6543, which, for the purposes of this test, may be considered as a 150 K blackbody with spectral lines. The second step was to measure with each detector a number of sources with much hotter or colder spectral flux density distributions than NGC6543.

Numerically, the approach was to measure, in each wavelength band, the flux $S_{i,j}$ from test source i on detector j. The average of $S_{i,j}$ over the detectors in the wavelength band, $\langle S_i \rangle$, then gives the best estimate of the flux from the source in that wavelength band. The statistical distribution of the ratio

$$R_{i,j} = S_{i,j}/\langle S_i \rangle \qquad \text{(IV.B.1)}$$

has, by definition, a mean of one if all detectors respond equally to the test source and NGC6543. The test sources (Table IV.B.1) were four stars and two cold sources, Neptune and the galaxy UGC11348.

The stars probe the short wavelength rejection and the short wavelength transmission cuton of the detectors in all bands. The two 50 K sources probe the longwave cutoff and longwave rejection in the 12 and 25 μm bands and the inband transmission of the 60 and 100 μm bands. Significant changes in the band pass characteristics of an individual detector relative to the band average transmission would be detectable as a statistically abnormal member of the $R_{i,j}$ data set.

The results of this test indicate that deviations in the flux estimates from the mean are typically less than 10%, with a worst case value of 16%. Table IV.B.2 gives the typical and worst case value of the absolute deviation of $R_{i,j}$ from unity in each band for the stars and the cold sources. In spite of their wide temperature range, there was no difference between the hottest and the coolest star.

B.2. Verification of the Nominal Inband/Out-of-band Transmission

The nominal response of the filter/detector combination and results of preflight tests at the component level are summarized in Section II.C.4. In-flight verification was required for two reasons. First, it was not possible to test fully the detector/filter combinations before the flight even at the component level. This applies in particular to the spectral response of the 100 μm detectors. Furthermore, a number of problems could have resulted in a degradation during system integration or during the flight.

Potential problems with the spectral response can be divided into two categories, those that represent systematic deviations from the nominal characteristics of all detectors in a band and those that result in a random scattering in one or several detectors in a band from the band average. Problems likely to result in random scattering are cracking or delamination of the filters, photon leaks around filter mounts etc. Extensive in-flight tests, described in the previous section, indicate that the detectors had rather similar pass-bands, thus eliminating random, but not necessarily systematic, effects.

An attempt was made to address the problem of systematic deviations of the nominal inband and out-of-band transmission of the four bands in a semi-quantitative way, by using observations of stars with widely different temperatures, asteroids and the planet Uranus to probe different portions of the passband.

Table IV.B.1 Out-of-Band Rejection Test Sources

Hot test source			Cold test source	
α Vir,	B1 IV	Te=24000 K	Neptune	Te=55 K
α CMa,	A1 V	Te=10000 K		
α Car,	F2 II	Te=6900 K	UGC11348	Te=50 K
β Peg,	M2.5	Te=2800 K		

Table IV.B.2 Out-of-Band Rejection Test Results

$|(R_{i,j} - 1)|$

Band	Stars		Planet/Galaxy	
μm	Typical	Worst Case	Typical	Worst Case
12	0.02	0.09	*	*
25	0.02	0.07	0.05	0.14
60	0.03	0.09	0.06	0.12
100	0.10 #	0.13 #	0.06	0.16

* not detected # low signal-to-noise ratio

The following hardware related issues affect the various bands:

a. 12 μm band: Rejection of 15-23 μm depends on an interference filter. A weak upper limit on the mean transmission in this region is based on the non-detection of Uranus in the 12 μm band.

b. 60 μm band: Rejection shortward of 27 μm depends on a combination of blocking filters and the Ge:Ga detector response. Very high short wave blocking is required in the case of stars. Based on the semi-quantitative analysis of observations of hot stars, cool stars and asteroids, the shortwave blocking is consistent with the design specifications given in Section II.C.4.

c. 100 μm band: Rejection shortward of 50 μm depends on a combination of blocking filters and the Ge:Ga detector response. The comments in b above apply. The longwave cutoff is determined by the

detector cutoff at approximately 120 μm. The detector response, including this cutoff, was not measured on the actual flight detectors and the cutoff may vary a few microns from one detector to another.

C. Optical Performance

Diffraction and scattering of the infrared radiation from bright sources from optical surfaces or telescope structures result in potential artifacts in the IRAS data. Early in the mission an effort was made to assess the magnitude of such effects using specially designed observations of Jupiter and Saturn. Observational procedures (discussed in Chapter III) and software (Section V.D.2.c) were used to eliminate most of the artifacts from routine observations.

C.1. Optical Cross Talk due to Bright Sources Crossing the Focal Plane

Optical cross talk is here defined to mean the detection of the flux from a source on a detector that is inconsistent with the reconstructed position of the image of that detector and the position of the source on the sky. This is distinct from electronic cross talk in that the detected signal is in fact due to infrared radiation incident on the detector.

The fact that the secondary mirror is supported by three spider arms resulted in a diffraction pattern consisting of an Airy disk and six diffraction spikes equally spaced on a circle. Two of the diffraction spikes are aligned with the scan direction. The diffraction spikes constitute a minor component of the point source diffraction pattern, but the point source detection algorithm (see Section V.C) is quite sensitive to the diffraction spikes.

C.2. Optical Cross Talk from Sources not directly on the Focal Plane

Bright sources not directly imaged onto the focal plane could produce apparent infrared signals which, if care were not taken, could be confused with real infrared sources. The attenuation of such signals as a function of angular distance from the telescope boresight is defined as the out-of-field rejection ratio, with the nominal specifications given in Section II.C.3. A number of tests were carried out to verify the nominal out-of-field performance and to check for unexpected glints. These tests confirmed the anticipated need for operational procedures not to make routine observations closer than 1° from Jupiter, 20° from the moon, 60° from the Sun and 88° from the Earth horizon. Estimates of the in-orbit out-of-field rejection are included in the discussion in Section II.C.3.

Cross talk from Jupiter appeared to be associated with diffraction from the secondary mirror support structure. The amplitude of the spikes and associated diffuse cross talk components was generally less than that predicted from simple telescope models by about a factor of three.

The moon tests revealed significant "glints", in addition to the anticipated amount of diffuse out-of-field radiation. Glints are well defined regions of about 1/2° extent, where the telescope out-of-field performance is significantly reduced. The glints are of two types, one of which propagates across the focal plane in the survey scan direction affecting all detectors along the scan and the other which affects only specific detectors around the edge of the array. Figure IV.C.1 shows a map of all presently known moon glints out to 30° from the moon. It should be noted that routine observations were carried out as close as 20° from the moon.

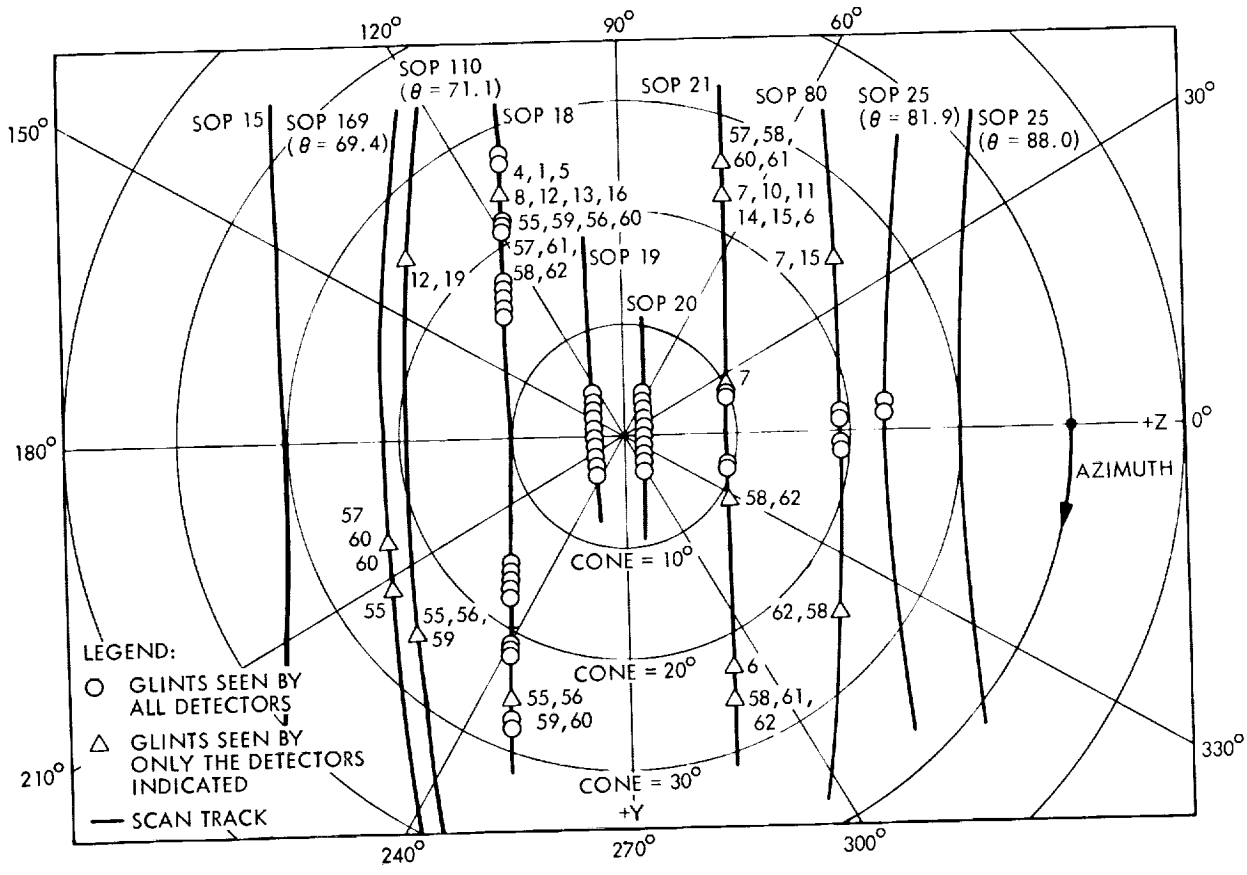

Figure IV.C.1 A polar plot showing where glints from the moon were detected by the numbered detectors. The boresight of the telescope is at the center. The moon is at the cone and azimuth angle plotted with the tracks. The angle θ gives the angle to the sun.

C.3. Out of Field Rejection Monitoring:

Due to concern about possible slow degradation of the out-of- field performance during the mission, the out-of-field performance was monitored throughout the mission using two observational procedures.

The first was a test using the moon as a bright source. Approximately once per month, with the moon about 90° from the Sun, the spacecraft made 60° long scans which passed within 20° of the moon. These scans were compared with reference scans over (roughly) the same strip of the sky preceding (or following) the lunar scan by one day, such that the moon was roughly 32° from the boresight at the closest approach. The difference in the flux for the same point on the sky measured in the two scans was taken to be due to out-of-field radiation from the moon. The results of this monitoring program are shown in Fig. IV.C.2. No significant changes in the out-of-field performance were observed during the course of the mission and the deduced mean value of the out-of-field radiation from the moon at 20° from the boresight is in good agreement with expected performance.

The second approach was to attempt to monitor and/or detect out-of-field radiation from the Earth, due to radiation from the Earth scattered off the inner surface of the sunshade, followed by diffraction and/or scattering through the baffle structures. The technique employed was to observe several regions of

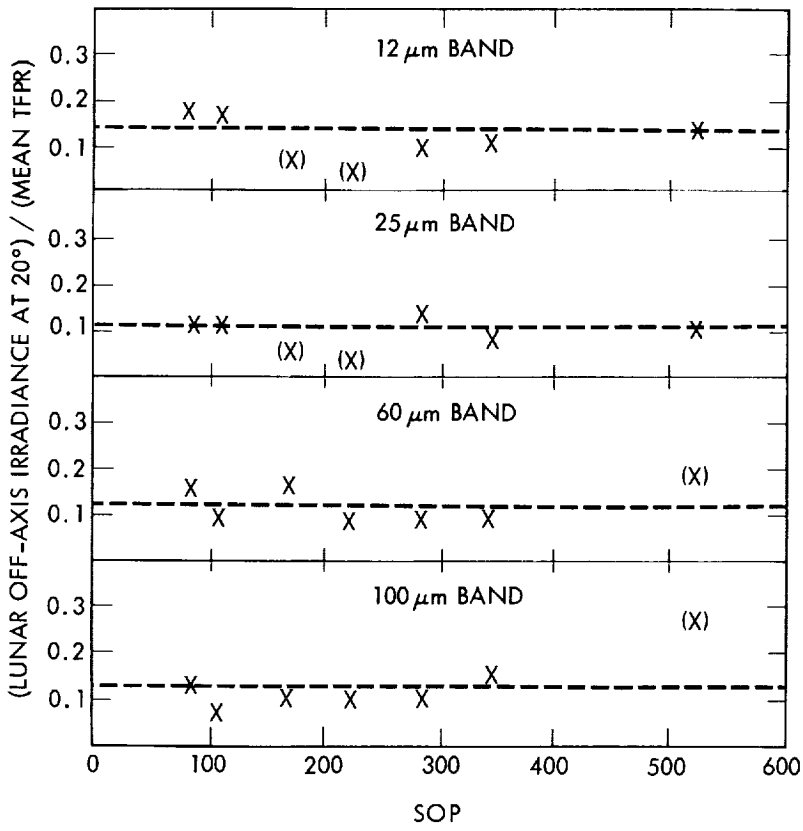

Figure IV.C.2 Monitoring of the out-of-field rejection by observations of the moon 20° off axis. The observations are normalized to values of the TFPR as are the calculations in Fig. II.C.5. The dashed lines show the mean values which are consistent with the pre-launch calculations shown in Fig. II.C.5. The bracketed points are of low weight. The observations in SOPs 170 and 225 required large corrections for responsivity changes in the 25 μm band.

the sky, generally twice, when the orientation of the sky was such that the region could be observed while no Earth radiation was incident on the inner surface of the sunshade. The observation of the same region was then repeated, typically about a month later, when the orientation of the sky was such that the inner surface of the sunshade was as nearly fully illuminated as possible without violating the Earth limit pointing constraint. The difference in observed flux, after correcting for zodiacal emission differences and changes in the baseline attributable to electronics drift is presumably due to out-of-field radiation from the Earth. The analysis is limited by the accuracy of the zodiacal emission model and baseline uncertainties. The upper limits from the tests represented a background less than 0.1 the flux from the TFPR (see Section IV.A.5), but the tests were not sensitive enough to confirm pre-launch calculations of the out-of-field rejection (see Fig. II.C.5).

The extended emission data reduction subsystem further controlled the effects of out-of-field radiation by rejecting data taken with larger avoidance cones around bright objects. Tests early in the mission indicated that the moon was the only object bright enough to warrant further avoidance and any data taken within 30° of the moon was ignored. A more detailed discussion of avoidance angles is given in Section III.C.5.

D. Internal Reference Source Stability

During the course of the entire mission, the stability of the internal reference source was monitored at least daily relative to the planetary nebula NGC6543. The results of this monitoring program at 25 μm for a large fraction of the mission are shown in Fig. IV.D.1. Let $R_{i,t}$ be, for detector i and time t, the ratio of the amplitudes from a flash of the internal reference source and from a scan over NGC6543. If $\langle R_{i,t} \rangle$ is the mean ratio averaged over the duration of the mission, the quantity

$$Y_{i,t} = (R_{i,t}/\langle R_{i,t} \rangle - 1) \qquad \text{(IV.D.1)}$$

is a direct measure of the stability of the internal reference source since the infrared output from NGC6543 can be presumed to be stable. The quantity $Y_{i,t}$ is shown as the ordinate in Fig. IV.D.1 for all full-size detectors in the 25 μm band as a function of time from the start to the end of the mission. This wavelength band was selected for presentation since the signal-to-noise ratios for both the stimulator flashes and NGC6543 were the highest in this band. The dispersion in the measurements at 25 μm is 1.6%, consistent with the dispersion due to the measurement uncertainties. The measurements in the 12, 60 and 100 μm bands give dispersions of 2.6, 1.7 and 2.7% respectively. The stability of the internal reference source is thus better than 2% throughout the mission.

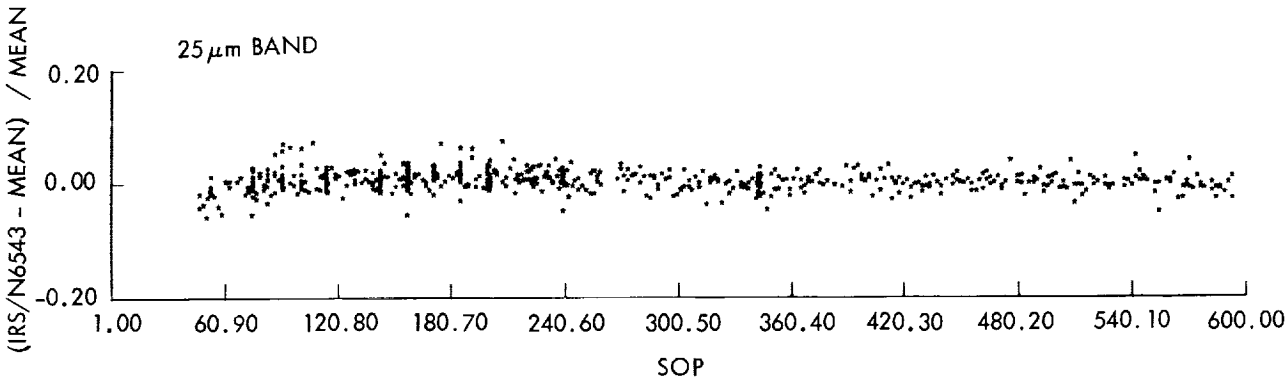

Figure IV.D.1 The response of the individual detectors to the internal reference source compared to that from the planetary nebula NGC6543 at 25 μm. The results from all the 25 μm detectors were combined after normalization to the mean response over the duration of the mission.

Authors:

H. H. Aumann, T. N. Gautier, F. C. Gillett, P. Hacking, G. Neugebauer, F. Olnon, S. Wheelock

References

Campbell, M. F., Elias, J. H., Gezari, D. Y., Harvey, P. M., Hoffmann, W. F., Hudson, H. S., Neugebauer, G., Soifer, B. T., Werner, M. W., and Westbrook, W. E. 1976, *Ap. J.* **208**, 396.

Joyce, R. 1984, private communication.

Rieke, G. H., Lebofsky, M. and Low, F. J. 1984, preprint.

Tokunaga, A. 1984, *A.J.* **89**, 172.

C-2

V. DATA REDUCTION

This chapter describes the transformation of the raw data into its final forms. Section V.A provides a general overview of the data reduction, while subsequent sections provide a more detailed description. The relative and absolute calibration of the data is discussed separately in Chapter VI. The results of the analysis of the data processing are given in Chapter VII. An overall description of the survey, including sky coverage, completeness and reliability, is given in Chapter VIII.

A. Overview

A.1 General

The Science Data Analysis System (SDAS) at JPL received the scientific and housekeeping data taken by the satellite from the ground operations facility at Rutherford Appleton Laboratory in Chilton, England. The data were obtained and processed in units of a Satellite Operations Plan (SOP) containing 10-14 hours of data (Section III.C.1). A single SOP was further divided into 10-60 observations or scans, each of 3-50 minutes duration. Survey observations obtained the data for the all-sky survey, while calibration observations were made to determine, monitor and verify the survey photometry.

The survey strategy and observation constraints produced scans that were generally along meridians of ecliptic longitude. At the ecliptic plane, the scans followed meridians exactly, while at higher latitudes, deviations from meridians could become pronounced. The rectangular aspect of the infrared detectors (Section II.C.4.) combined with the survey strategy means that there are important differences between quantities, such as source size and positional uncertainties, measured in the in-scan direction (roughly ecliptic latitude) and those in the cross-scan direction (roughly ecliptic longitude). In extreme cases, whether a source is found in the point or small extended source catalogs could depend on whether it was extended in the in-scan direction.

A.2 IRAS Catalogs and Atlases

The results of the survey are to be found in either the catalogs of point sources or small extended sources, or in the catalog of low-resolution spectra or in the atlas of sky brightness images. Where the data for a given astronomical object are located depends primarily on its angular size. Sources with angular extents less than approximately 0.5, 0.5, 1.0, 2.0′ (in the in-scan direction) at 12, 25, 60 and 100 μm, respectively, are listed in the point source catalog. As discussed in Chapter IX, low-resolution spectra in the 8-22 μm region are available for objects brighter than about 10 Jy at 12 or 25 μm. Sources with angular extents larger than the above values but less than about 8′ may be found in the catalog of small extended sources. Information about sources larger than about 8′ in-scan will be found only in the atlas of sky brightness images. The images have a pixel size of 2′ and an angular resolution of 4-6′.

A.3 Processing Summary

The following processing steps were applied to the data:

1. Data reconstruction (Section V.A),
2. Pointing reconstruction (Section V.B),
3. Calibration (Chapter VI),

4. Source detection (Section V.C),
5. Point source confirmation (Section V.D),
6. Low-resolution spectra extraction (Chapter IX),
7. Small extended source confirmation (Section V.E),
8. Identification of possible asteroids and comets (Section V.F),
9. Data compression for extended source images (Section V.G).

The point source catalog was generated after all of the data had been processed to create the intermediate Working Survey Data Base (WSDB) which contained all sources that were hours- or weeks-confirmed. The following steps were then applied to sources in the WSDB (Section V.H):

1. Final calibration,
2. Source clean-up and neighbor tagging,
3. Average flux computation, calculation of flux uncertainty and source variability analysis,
4. High source density region clean-up,
5. Source selection,
6. Association and classification of low-resolution spectra (Chapter IX).
7. Positional associations with other astronomical catalogs,
8. Cirrus flagging,
9. Transformation of coordinates, assignment of source names and calculation of positional uncertainty ellipses.

To generate the small extended source catalog, the following steps were applied to a file containing hours-confirmed small extended sources (Section V.E):

1. Cluster analysis processing,
2. Weeks- and months-confirmation,
3. Band-merging,
4. Final calibration,
5. Positional associations with other astronomical catalogs.

To generate the atlas of all-sky images, the following steps were applied to the compressed data (Section V.G):

1. Quality checking and data selection,
2. Regridding into images in equatorial coordinates,
3. Final calibration.

The remainder of this overview briefly describes these basic processing steps, except for calibration which is discussed in Chapter VI. A much more detailed discussion of each topic is given in the subsequent sections of this chapter.

A.3.a Data Reconstruction

The detector data were reconstructed from the telemetry data as discussed in Appendix II.1. Any one-second frame of detector data containing more than one parity error, indicative of a transmission error from the satellite station to the ground, or from Chilton to JPL, was discarded. Frames next to a data outage with even one parity error were also discarded. The frequency of such errors was quite low, with typically fewer than five seconds of data being rejected from each SOP. Each second of data was tagged with its time of observation in seconds since 1981, January 1.0 UT.

A.3.b Pointing Reconstruction

Data from Sun sensors, gyros, and observations of bright, $m_v < 7$, visual stars were combined to determine a continuous record of the position in the sky that a reference point in the focal plane was observing. Infrared observations of stars were not used in the reconstruction process, but were used to verify the accuracy of the pointing. Most survey observations contained two or more visual star observations, so that in-scan pointing errors were typically less than 5″ and cross-scan pointing errors less than 10″. However, a few survey observations had none or only one visual star observation with resultant in-scan errors as large as 1-2′.

A.3.c Source Detection

For point sources, a zero-sum square-wave filter was used to search the calibrated data stream from each detector for peaks larger than roughly 2.5 times the rms noise. The noise at a given time was approximated by a filtered running average of the values of all preceding square-wave peaks. The noise estimator was a one-sided estimate of the noise which was in error when the noise changed rapidly. For each candidate peak, an 11-point template was fitted to the data, giving the amplitude and crossing time of the peak and a correlation coefficient. Those peaks with an amplitude above 3.0 times the noise and a correlation coefficient greater than 0.87 were passed to the confirmation processor as valid detections. Since the noise refers to a single data point and a point source contributes to three successive data points (with weights 0.5, 1.0 and 0.5), the true signal-to-noise threshold of the detection process was roughly 3.7, which is significantly below the local signal-to-noise cutoff of about 5.7, implied by a correlation coefficient cutoff of 0.87. The noise on a single data point was quoted throughout the processing.

For small extended sources a simpler algorithm was used to detect potential sources. Zero-sum square-wave filters of various angular extents were applied to the data from each detector. The filter sizes were 1, 2, 4, 8, and 16′ at 12 and 25 μm, 2, 4, 8 and 16′ at 60 μm, and 4, 8 and 16′ at 100 μm. The data streams filtered with the smallest (1′ at 12 and 25 μm, 2′ at 60 μm and 4′ at 100 μm) and largest (16′) spatial filters were used to discriminate against point sources and extended sources larger than 8′. Detections with a larger flux in one of the extended source filters than in the point source filter were considered as possible extended sources and passed to the corresponding confirmation processor, independently of whether a point source detection occurred.

A.3.d Point Source Confirmation

The aim of point source confirmation was to glean from the hundreds of thousands of detections per day the properties of those sources, and of only those sources, which appeared as inertially fixed on the sky. Detections of dust, space debris and asteroids had to be rigorously excluded, yet not at the

expense of celestial objects, if the complementary goals of completeness and reliability were to be satisfied. The existence of a point source had to be confirmed on timescales of seconds, hours and weeks for the object to be included in the catalog.

The layout of the focal plane ensured that any stationary source of infrared radiation would cross at least two detectors in each wavelength band as the satellite scanned the sky (Fig. II.C.6). The seconds-confirmation processor, which treated each wavelength band independently, examined each detection in turn in an attempt to find a detection on one of the other detectors in the focal plane. The other detection had to occur on one of the two detectors that could be hit by a true source traversing the focal plane, at the correct displacement in time, and agree in flux with the first detection to within roughly a factor of two. Detections satisfying these criteria were merged to become *seconds-confirmed detections*. A successful seconds-confirmation resulted in a refinement of both the flux and position of the object.

After all of the detections in the four bands for a given survey scan were examined, an attempt was made to combine observations in the different bands to produce a *seconds-confirmed band-merged* source. Detections in the different bands had to satisfy tests based on in-scan timing and cross-scan position. The order in which bands were taken in the search for merger candidates proved to be important because of the effects of the 100 μm "cirrus". As discussed in Section V.D.3.b, a priority was chosen to minimize these deleterious effects. Bands that were not filled by successful mergers were given upper limits by determining which detectors in those bands were crossed by the source and then taking three times the noise on the detector with the lowest noise. The source position was refined during band-merging.

A file containing roughly 32000 previously known sources including SAO stars, asteroids with well determined orbits, and objects from the Two Micron and AFGL Surveys (Neugebauer and Leighton 1969; Price and Walker 1976) was used to predict positions and fluxes for routine monitoring of the processing. The seconds-confirmed band-merged sources were compared to the predictions, and identification numbers were assigned to successful matches.

The next level of confirmation, hours-confirmation, was run on groups of three successive SOPs in at least one band. Every source in the first SOP received its turn to find candidates from successive scans in any of the three SOPs. Candidates had to pass a position and flux test (again, roughly a factor of two) in at least one band to become an hours-confirmed source. An hours-confirmed source had to have either two seconds-confirmed detections, one seconds-confirmed sighting plus one non-seconds-confirmed sighting or two non-seconds-confirmed sightings, each with the alibi of a failed detector. A successful hours-confirmation resulted in a refined position and a refined flux for each band where possible. If each candidate source had only upper limits in a given band, the lowest upper limit was adopted.

Finally, the third level of confirmation, weeks-confirmation, was attempted for each hours-confirmed source prior to its entry into the WSDB by examining the WSDB for any other hours or previously weeks-confirmed sources that could pass a position test. Successful matches resulted in a refined position for the source, but not a refined flux; *individual hours-confirmed fluxes were retained for each source.* It is important to note that weeks-confirmation represents the first and only time interval for which at least rough flux constancy was not required. Thus, the catalog is weakly biased against celestial sources more variable than a factor of two on time scales shorter than a few days.

A.3.e Small Extended Source Confirmation

The objective of the processing of small extended sources was to detect stationary sources which were resolved by the telescope, up to 8′ in extent. Because of the simple detection algorithm described above, it was not intended that the processing produce intensity or flux measurements more accurate than about 50%. Nor were stringent goals of either completeness or reliability set.

Potential small extended source detections were identified in the raw data stream by their response to square-wave filters (Section V.A.3.c). Each detection was tested to discriminate against point sources and sources larger than 8′. After individual source detections were identified, they were tested for seconds-confirmation; those that failed were discarded. Detections which were seconds-confirmed, which were from the same hours-confirming survey coverage, and which were sufficiently close together on the sky, were combined to produce a single source. These small extended sources became the input for all subsequent processing. No attempt was made to combine observations at different wavelengths until the last stages of the processing.

Structure on the scales of 2′ to 10′ within much larger extended sources gave rise to clusters of small extended sources. Such clusters were eliminated so that only those sources whose sizes were compatible with the square-wave filter used for detection were accepted. Sources were then tested for repeatability in position and flux on time scales of weeks and months. Any source which was not weeks-confirmed was discarded. The final stage of the processing was to combine those weeks-confirmed sources observed at different wavelengths which were sufficiently close together on the sky, and to merge them into a multi-band source.

A.3.f Asteroids and Comets

Asteroids are a population of bright infrared sources, particularly at 12 and 25 μm. The hours- and weeks-confirmation strategy was developed to discriminate against these moving sources. Positions of known asteroids were calculated and associated with those of hours-confirmed point sources. In this manner the known asteroids were identified and used as tracers to evaluate the effectiveness of the confirmation filters. No known asteroids satisfied the stringent position coincidence requirements to become final catalog sources. As discussed in Section VII.F, confusion with asteroids (known and previously unknown) was the cause of about 100 unreliable sources and fluxes within 25° of the ecliptic plane.

To provide data for the study of the properties of known and newly discovered asteroids, all sources with infrared colors typical of solar system objects were written to auxiliary files at both seconds- and hours-confirmation. The emphasis was on completeness. The results of analyzing these data are not included in any of the IRAS catalogs released in 1984.

A.3.g Extended Emission Processing

The goal of the extended emission processing was to produce moderate resolution maps of the total infrared emission over the whole sky at 12, 25, 60 and 100 μm. Special procedures discussed in Chapter VI were used to calibrate the absolute DC level of the data from each detector. These data were smoothed and resampled (compressed) in the time domain to produce two samples per second. At the nominal scan rate of 3.85′ s^{-1} this sampling closely matched the 2′ spacing of detectors across the focal plane. The focal plane geometry and the reconstructed pointing information were used to locate the

position on the sky of each data sample for projection into the 212 images, each 16.5 × 16.5°, that cover the whole sky with 2′ × 2′ pixels.

Data suspected of being either noisy due to particle radiation events or contaminated by scattered light from bright celestial sources were automatically discarded. Human inspection of each image removed obviously bad data that occurred, for example, because of the presence of near field objects which flooded the focal plane with radiation. Otherwise, nothing was done to remove data which were inconsistent from one measurement to the next. Thus, many non-confirming sources appear in the maps. Each of the three sky coverages of the survey was made into a separate set of images so that spurious, moving or variable sources could be detected by comparison or "blinking" of the coverages. A fourth set of images was made of the limited region of sky known as the mini-survey (Section III.C).

Differences in the path length of the line of sight through the interplanetary dust cloud caused significant variability of the zodiacal emission background from one survey coverage to the next. The Zodiacal History File consists of time ordered 0.5 × 0.5° averages of the intensity data at each wavelength and associated pointing information. This information was designed to simplify modeling and removal of the zodiacal component.

A set of maps with 2′ pixels of the Galactic plane for latitudes within 10° of the plane and two maps of the full sky with 0.5° resolution, one centered on the Galactic center and one centered on the Galactic anti-center, were also produced.

A.3.h Final Processing Steps

After the data from the entire mission had been processed, several programs operated on the WSDB to produce the final entries for the point source catalog. For example, these programs applied final calibration corrections, deleted unreliable sources in regions of high source density, and searched for associations in other astronomical catalogs.

All of the objects found in the point source catalog were selected from the WSDB according to criteria that depended on the density of sources in a 1 sq. deg area containing the source (see V.H.6 for a detailed discussion). Outside of high-density areas sources were required to have at least one band that was hours-confirmed at least twice and at least one of those sightings had to have a valid seconds-confirmed detection without the alibi of a failed detector. For objects detected in two or more bands, this rule was relaxed somewhat. Inside high-density areas, sources had to satisfy much more stringent criteria: they had to be perfectly hours-confirmed in one band at least twice, have no brighter or confusing close neighbors, have no fluxes more discrepant than a factor of three and have satisfied a detection correlation coefficient threshold greater than 0.97.

B. Pointing Reconstruction

The term "pointing reconstruction" as used here refers to the process of reconstructing the pointing direction of a fiducial point in the focal plane, as well as the twist angle of the telescope about the reference point, referred to as the boresight. Since the accuracy with which the pointing could be reconstructed varied as a function of time, uncertainty histories were also specified. Use was made of all available fine attitude sensor data to maximize the accuracy of the reconstructed pointing during the various

attitude modes. A smoothed estimate of the pointing was obtained using a recursive form of an extended Kalman filter. A more detailed discussion of the pointing reconstruction than is given here is provided by McCallon and Kopan (1985).

The pointing reconstruction was based on the output of the fine attitude sensors which include eight slit-type visible star sensors, a three-degree-of-freedom gyro package and a dual-axis fine Sun sensor. The star sensors were mounted on the periphery of the focal plane, four slits being normal to the scan direction, and the remaining four slits skewed at angles of approximately $\pm 40°$ (see Fig. II.C.6). The slits were used in pairs, one normal and one skewed, to provide two axes of boresight information at each visual star sighting, hereafter called a fine attitude calibration, or FAC. The gyros and fine Sun sensors were mounted together on the outside of the spacecraft. There were, of course, misalignments between the gyros and fine Sun sensors due to limits on the accuracy with which they could be positioned. Unfortunately, the misalignments between the gyro-Sun sensor package and the telescope were found to vary with time (mainly in cross-scan) due to bending of the telescope mount with respect to the spacecraft due to temperature gradients.

Pointing reconstruction was accomplished by integrating the gyro outputs to provide an initial estimate of the attitude history. Concurrent processing of frequent Sun sensor measurements and relatively infrequent FACs was performed with an extended Kalman filter to estimate model parameter errors and refine the attitude history. The model parameters estimated include initial-attitude errors, spacecraft-telescope misalignment errors, gyro drift, gyro scale factor errors, and gyro alignment errors. Gyro drift was modelled as a constant rate plus a random Gauss-Markov process. Process noise was added to all model parameters with the exception of the initial attitude parameters to allow for modelling errors and slow changes with time.

The recursive Kalman filter was run first forward in time and then backward over a scan and then the two estimates were combined to provide a smoothed estimate sampled every second. The Kalman filter was reinitialized with the updated model parameters, and the process was repeated for the next scan using any available boundary conditions. The scan was chosen as the basic processing block because it normally contained at least two FACs and was of manageable length. A special file of boundary conditions was maintained for each SOP, and processing of observations with fewer than two FACs was deferred until the multi-FAC observations were finished in order to pick up final boundary conditions for the others.

This approach to the pointing reconstruction worked quite well as shown by the statistics on known star position matches (see Section VII.C). One danger which was carefully guarded against was giving bad data to the filter. Considerable effort was put into algorithms to perform automated consistency checking and to provide measurement rejection capability. There were problems associated with each type of attitude sensor.

The fine Sun sensor hardware had severe spiking problems from the beginning of the mission. This had the greatest effect on spacecraft control, causing several fallbacks to the safe attitude control mode. The spikes were thrown out in the pointing reconstruction algorithm by consistency checks. Spikes occasionally caused a brief cross-scan excursion in the actual pointing.

Another problem associated with the fine Sun sensors was less dramatic but potentially of greater consequence for the pointing reconstruction. The y-axis fine Sun sensor characteristics varied with time over the mission. Thus the transfer function used to convert from the integer output of that Sun sensor to the desired cross-scan angle should have been varied slowly over the course of the mission. This problem was only partially alleviated by the fact that the spacecraft-telescope misalignment angle about the y-axis was being continually re-estimated. The pointing reconstruction used only two transfer functions for the y-axis fine sun sensor over the course of the mission. Ideally, a separate transfer function would have been used for every 75 to 100 SOPs.

The gyros also had their difficulties. Early in the mission it was apparent that the gyros (especially one of the z-axis gyros, denoted Gyro ZA) were noisier than expected, and that their characteristics, especially those of the x-axis gyro, varied with time. Gyro ZA was used by the on-board control system for in-scan control. Unfortunately the control system was not designed for a gyro as noisy as ZA, and this resulted in the occasional occurrence of a phenomenon referred to as the limit-cycle-burst problem. During a burst, the limit cycle amplitude and frequency increased by a factor of three or four; amplitudes of 13″ were observed. This problem occurred much more frequently after the start of the third hours-confirming coverage and was finally solved by switching to Gyro ZB for control. The limit cycle bursts were, however, reconstructed without apparent difficulty. The long-term changes in gyro characteristics were tracked by the Kalman filter, but process noise had to be increased to give the filter enough freedom to follow the changes. There was also some indication of even faster changes suggestive of thermally induced misalignments between the gyros and the fine Sun sensors. These problems worsened as the mission progressed. The x-axis gyro was dropped from use in reconstruction beginning with SOP 187 and the y-axis gyro was dropped beginning with SOP 316.

The gyros were far more susceptible to the Earth's magnetic field than expected. This problem was discovered early in the mission, and a software compensation algorithm was developed for pointing reconstruction.

Very early in the processing it was noted that errors in the reconstructed position of known infrared sources were sometimes larger near certain FACs rather than smaller as expected. It appeared that the FAC was degrading the solution. These cases became generally known as "biased FACs". Most biased FACs had errors on the order of 5″ to 10″, but some were much worse, up to 6′. It was determined that the worst biased FACs were the result of having selected stars for FACs which had other bright stars close enough to interfere with the star sensor observations. Occasionally, biased FACs were the result of catalog errors. An algorithm was developed to identify the FACs with disturbing stars, and in reprocessing SOPs 29 through 446 these FACs were either given larger uncertainties or deleted. The worst biased FACs (errors greater than 30″) in the 446 to 600 SOP range were corrected in the same manner.

Another problem was the thermal misalignment about the y-axis (cross-scan) between the gyro/Sun sensor package and the telescope. This caused particular difficulties during the third sky coverage because of large and frequent changes in solar aspect angle.

Lack of a time-variant y-axis fine Sun sensor transfer function had the greatest effect on cross-scan reconstruction for observations with slews between the FAC and the survey scan. In this situation the

Kalman filter was unable to compensate for the y-axis fine Sun sensor errors by adjusting the telescope misalignment about the y-axis as it would normally do. In the worst-case, cross-scan slews on the order of one to two degrees resulted in reconstruction errors as large as 25″. The actual magnitude of the error varied greatly depending on the exact start and end points of the slew and was not necessarily greater for longer slews. The only survey scans affected by this problem were those with out-of-scan FACs.

Lack of the improved y-axis thermal misalignment model was significant only for observations which were both without a FAC and without a boundary condition on the same end. In the worst-case situation, cross-scan reconstruction errors as large as 30″ were possible for a one-FAC observation; this could happen on full length observation following a maximum cross-scan slew with the worst possible placement of the FAC. Such large slews were executed only after the start of the third survey coverage (SOPs 426 to 600). For SOPs 29 to 425, peak errors due to this problem were less than half as large.

C. Source Detection

The calibrated raw data for each of the 59 operating detectors were examined for point sources and small extended sources. The detection of the latter is described in Section V.E.1. For each observation the accepted point source detections were passed, with detector number, time of detection (and uncertainty), flux (and uncertainty), signal-to-noise ratio (SNR), and the correlation coefficient with the point source template (CC, see below), to the seconds-confirmation processor (Section V.D.2). A noise history was also created for each detector. If a detection occurred in a one-second period in which the analog-to-digital converter was saturated, then the detection was flagged.

C.1 Square Wave Filter

The first step in the detection process was to search for potential sources by applying a narrow bandpass digital filter to the detector data streams. This filter consisted of an eight-point zero-sum square-wave function. The effect of the filter was to subtract the first two and last two points from the sum of the middle four points; more formally, for a sequence of data points x_i (Fig. V.C.1a), the amplitude of the square-wave of x at the point i is defined as:

$$E(x,i) = -x_i - x_{i+1} + x_{i+2} + x_{i+3} + x_{i+4} + x_{i+5} - x_{i+6} - x_{i+7} \qquad \text{(V.C.1)}$$

This square-wave filter was applied at each point in the data stream, and a search was made for positive square-wave excursions between zero crossings, defined as a pair of data points (i,j) such that (see Fig. V.C.1b)

$E(x,i) > 0$;
$E(x,k) \geqslant 0$ for $i \leqslant k \leqslant j$;
$E(x,j+1) < 0$;
and for some n, $E(x,n) < 0$
and $E(x,n)$,....., $E(x,i-1) < 0$.

That is, find the values n, i, j such that: n with $E(x,n) < 0$; the first $i > n$ with $E(x,i) > 0$; and the first $j > i$ with $E(x,j+1) < 0$. The positive excursion (i,j) has a peak at the first p with $i \leqslant p \leqslant j$, such that $E(x,p)$ is maximal among $E(x,i)$,..., $E(x,j)$. Peaks with square-wave amplitudes, $E(n,p)$, greater than 2.5 times the noise N_x were passed on as candidates for point sources.

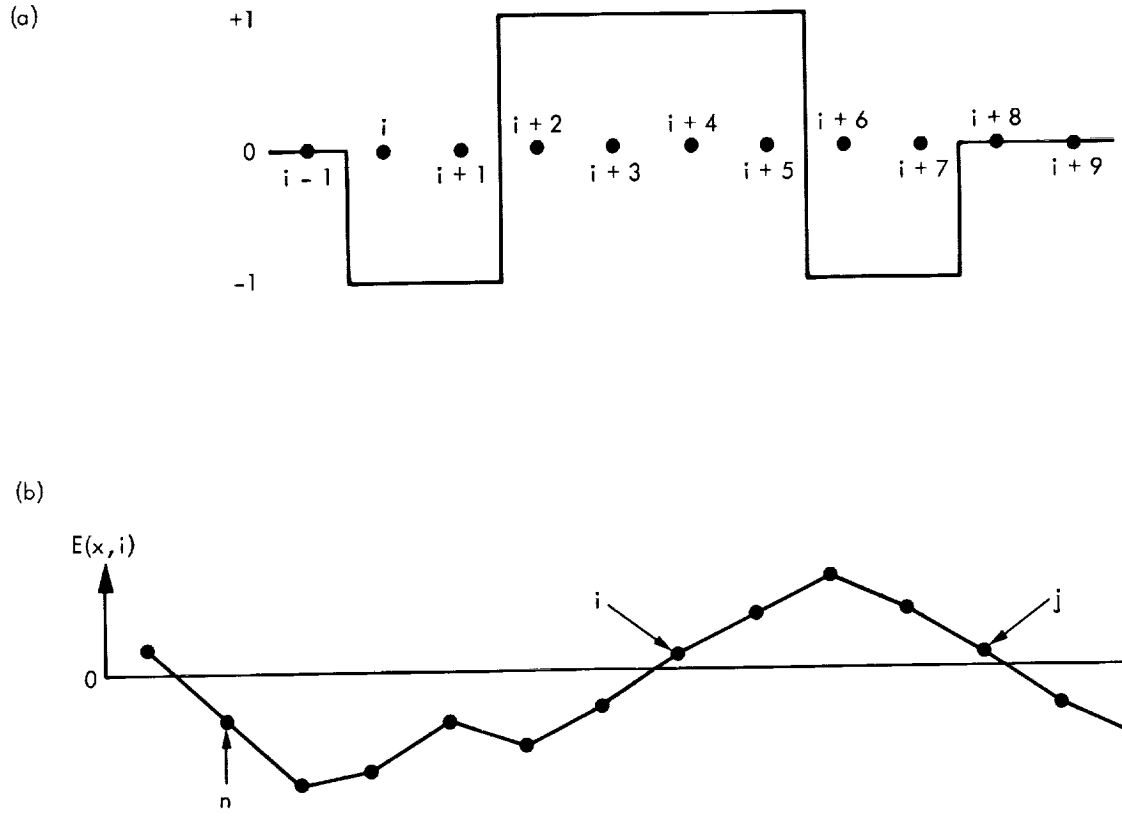

Figure V.C.1 a) An eight-point zero-sum, square-wave filter was applied to the data streams (top panel); b) The detection processor looked for positive square wave peaks between zero crossings in the filtered data stream (bottom panel).

C.2 Noise Estimator

The noise N_x for a data stream was defined as the median of all $E(x,p)$ for square-wave peaks p. Such positive square-wave excursions occurred about once every 6 samples. It was found from prelaunch simulations and from analysis of in-flight data that this median noise estimator gave a reasonable representation of the rms noise, in the sense that

$$\sigma_{rms} \approx 1.2\, N_x \qquad \text{(V.C.2)}$$

The enormous volume of data meant that determination of a running estimate of the rms noise would have involved a prohibitive computational run time.

The initial value of N_x was the median of the first 50 square-wave peaks. N_x was then updated at every square-wave peak $E(x,p)$ as follows:

if $E(x,p) < N_x$ then reduce N_x by the factor λ (<1); otherwise, increase N_x by the factor $1/\lambda$.

The parameter λ controlled the stability of the noise estimator. As λ approached 1, the noise estimator became very stable, but it also lagged behind any change in the noise by about $5/(1 - \lambda)$ samples. In tuning the value of λ, great importance was attached to achieving a stable noise estimate at high Galactic latitudes, where the noise was mainly due to detector noise, and a value $\lambda = 0.95$ was set at 12, 25 and 60 μm, and 0.90 at 100 μm. This meant that the noise estimate lagged by about 25′, 25′, 50′, 50′ at 12, 25, 60 and 100 μm. Regions with steep gradients in the density of point sources, such as the Galactic plane, had large gradients in the noise amplitude. Hence the noise was underestimated as the plane was approached and overestimated after it was passed (Sections V.C.7, VIII.D.6). This error was very large, and since sources were thresholded partly on signal-to-noise ratio (Section V.C.4, below), the effective threshold was raised to very large values after passing the Galactic plane, resulting in a shadow zone in which few sources were accepted. To keep the extent of the 100 μm shadow zone no larger than that at 60 μm, λ was set to 0.90 at 100 μm compared with 0.95 at 60 μm. However, this adversely affected the stability of the 100 μm noise estimate in the presence of cirrus at higher Galactic latitudes, resulting in the rejection of some detections that should have been accepted and hence a reduction in completeness of the catalog at 100 μm (Section VIII.D).

The noise estimate was maintained in a noise history file for each detector after multiplication by the factor to convert it to an estimate of the rms noise on a single sample. To compress the size of this file, an entry was made only if linear extrapolation of the previous two entries would lead to an error greater than 35%.

C.3 Timing Estimate

The time of the square-wave peak at $E(x,p)$ was estimated from the maximum of the parabola passing through the three points $(p - 1,E(x,p - 1))$, $(p,E(x,p))$, $(p + 1,E(x,p + 1))$. The delay between a source in the unfiltered data and its peak in the square-wave function was subtracted from the estimate to give the detection time. A small offset to account for electronic delay and the sampling time of the detector was included. The timing uncertainty was taken from a look-up table as a function of the values of signal-to-noise ratio and correlation coefficient for the source.

C.4 Correlation with Point Source Template

The heart of the point source detection processor was the comparison of the data for candidate sources selected by the square-wave filter with the profile, or template, expected for an ideal point source. For this purpose the 11 samples centered on the candidate detection time, y_i, $i = 0...10$, were compared with the appropriately shifted template R_i superimposed on a linear baseline. The amplitude A of the detection was determined from fitting the 11 data values y_i to the function

$$AR_i + iM + B \ , \ \ i = 0...10 \ , \qquad \text{(V.C.3)}$$

where B is the baseline height and M is its slope. A, M, and B were determined by the method of least squares, i.e., by minimizing

$$U = \Sigma \, (AR_i + iM + B - y_i)^2$$

where Σ stands for $[\Sigma \sum_{i=0}^{10}]$

Thus,

$$B = \frac{I}{V}\begin{vmatrix} \Sigma R_i R_i & \Sigma y_i R_i & \Sigma i R_i \\ \Sigma R_i & \Sigma y_i & 55 \\ \Sigma i R_i & \Sigma i y_i & 385 \end{vmatrix}$$

$$M = \frac{I}{V}\begin{vmatrix} \Sigma R_i R_i & \Sigma R_i & \Sigma y_i R_i \\ \Sigma R_i & 11 & \Sigma y_i \\ \Sigma i R_i & 55 & \Sigma i y_i \end{vmatrix}$$

$$A = \frac{I}{V}\begin{vmatrix} \Sigma y_i R_i & \Sigma R_i & \Sigma i R_i \\ \Sigma y_i & 11 & 55 \\ \Sigma i y_i & 55 & 385 \end{vmatrix}$$

$$\text{where } V = \begin{vmatrix} \Sigma R_i R_i & \Sigma R_i & \Sigma i R_i \\ \Sigma R_i & 11 & 55 \\ \Sigma i R_i & 55 & 385 \end{vmatrix} \qquad \text{(V.C.4)}$$

The correlation coefficient of y_i with R_i is given by

$$CC = \Sigma Z_i R_i / (\Sigma Z_i^2 \times \Sigma R_i^2)^{1/2} \qquad \text{(V.C.5)}$$

where $Z_i = y_i - (iM + B)$.

A candidate detection was accepted only if

(i) $CC \geqslant 0.87$

and (V.C.6)

(ii) $SNR = A/1.2N_x \geqslant 3$,

where the factor 1.2 converts the median noise estimate to an rms noise estimate (see Section V.C.2).

The total rms uncertainty in amplitude, A, over the 11 data samples can be shown to be

$$\frac{A}{\sigma_A} = \sqrt{2}\, CC(1 - CC^2)^{-1/2} \qquad \text{(V.C.7)}$$

Thus the correlation coefficient is a measure of the local signal-to-noise ratio and a threshold of 0.87 corresponds to a signal-to-noise ratio of about 2.5. In regions where the noise was roughly independent of time, the main thresholding was therefore provided by the signal-to-noise ratio. The square-wave filter threshold (Section V.C.1 above) was set low so that as few acceptable detections as possible were rejected, within the constraints of the available computer time. It should be noted that a low correlation coefficient for a bright point-source is probably an indication that the source is slightly extended. In regions of high source density (see Section V.H.6), where extended structure is a considerable problem, the correlation coefficient threshold was increased to 0.97.

C.5 Determination of Templates

The templates for each wavelength band were stored with a sampling frequency 64 times that of the survey data. The candidate detection time in sampling was determined, rounded off to the nearest 1/64th of a sample and the appropriate 11-point template selected by taking every 64th point from the template array.

Immediately after launch, predicted detector responses to an ideal point source were used. Composite templates were constructed for each detector using sources detected with high correlation coefficient and signal-to-noise ratio. The *a priori* templates were replaced with the composite templates and the analysis repeated, using 12 hours worth of data. Convergence was achieved after only a few iterations. Figure V.C.2 shows representative point source templates for one detector in each wavelength band. Since no evidence for detector-to-detector variation within a band was found, the results for all the detectors in each band were averaged together to produce the final composite templates.

C.6 Low Signal-to-Noise Detections

A secondary class of detections called low signal-to-noise detections was defined as those with signal-to-noise ratios between 3 and the threshold required for a valid detection. Because the threshold for valid detections was itself set at 3, no low signal-to-noise detections should have been generated. However, due to the round-off errors in the computation of the signal-to-noise ratio, a few were created. These were only used to provide upper limits for sources confirmed in other bands.

C.7 Source Shadowing

When two sources crossed the same detector within 6 samples of each other, i.e., within 1.4′, 1.4′, 2.9′, 5.9′ of each other in the scan direction at 12, 25, 60 and 100 μm, respectively, the detection of one or both of the sources may have been inhibited. Generally, the brighter source was detected without mishap, but the fainter source may have had its baseline so modified by the brighter source that it failed to be detected at all. This is the phenomenon of source "shadowing". A source may have been shadowed in a longer wavelength band but detected perfectly at shorter wavelengths. To warn of the possibility of this effect, sources were tagged at a later stage in the processing (see Section V.H.3) if they had near neighbors. The fluxes of such flagged sources should be regarded with caution. No significance should be attached to the absence of a detected flux in a shadowed band. The completeness figures given in Chapter VIII do not apply to the shadow zone around a source.

D. Point Source Confirmation

D.1 Processing Overview

The arrangement of the detectors in the focal plane of the telescope and the survey strategy permitted reobservation of inertially fixed point sources after time intervals of several seconds, several hours, and several weeks. The confirmation process consisted of examining those multiple observations and identifying which plausibly belonged to the same object. Once this identification was made for a given source, refinement of the parameters describing that source was performed by combining the observations into a single improved description.

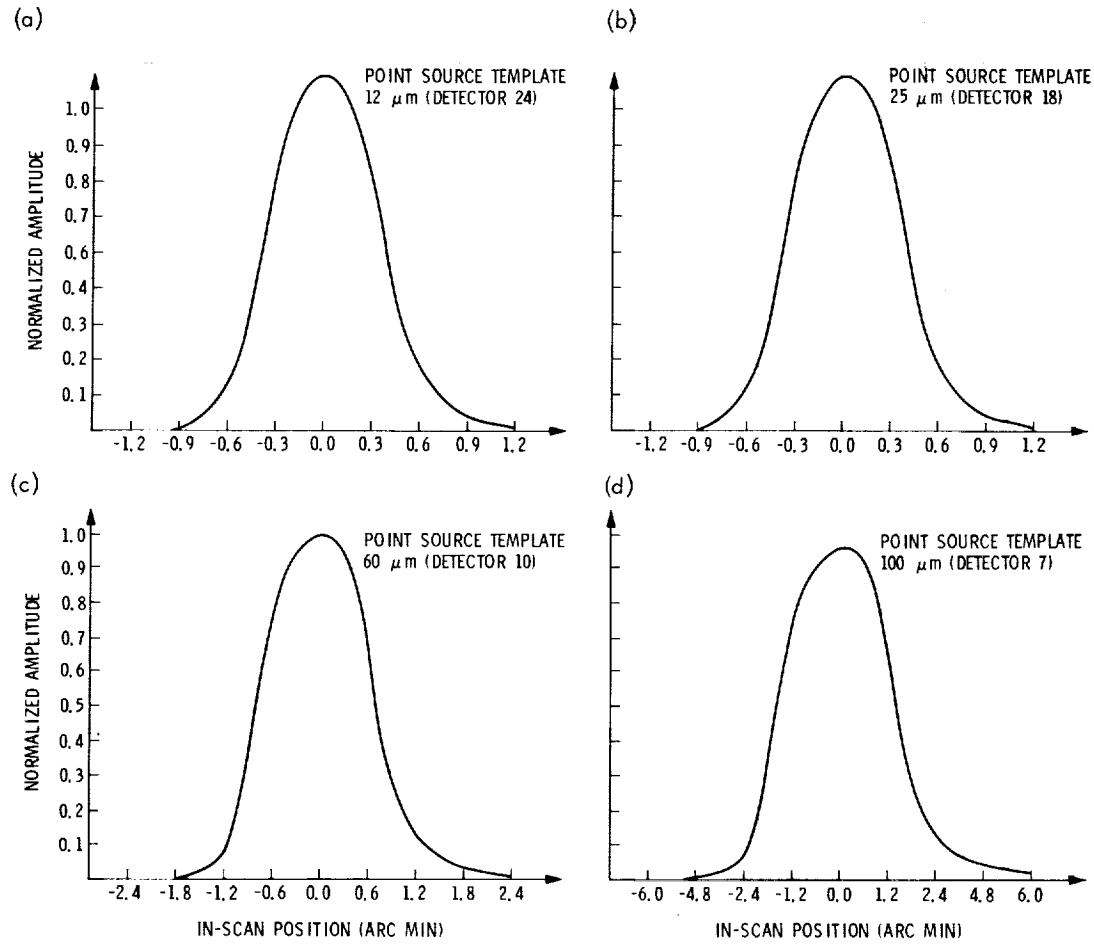

Figure V.C.2.a-d Detections found by the square-wave filter were compared with the response of the telescope-detector-electronics combination to a true point source. Representative point source templates are shown for one detector in each wavelength band.

When comparing two sightings, positional agreement was always a part of the decision whether to accept them as the same object. Over the seconds and hours intervals, photometric agreement was required as well. Because the cross-scan position was tested only by requiring that a real object be sighted by a compatible pair (or triplet) of detectors, the decision problem at the seconds-confirmation level involved only in-scan position agreement, and the tests could be based on Gaussian error models. At the hours and weeks level, the position error had to be modeled as a non-Gaussian random variable because of the uniform uncertainty due to the cross-scan extents of the detector slots.

The hours-and weeks-confirmation decision was based on the correlation of the probability density functions which describe the two-dimensional position information. The parameter which was required to be above a certain threshold to confirm two sightings was the cross-covariance of these density functions, evaluated at the separation of the nominal positions. The formalism is discussed and derived by Fowler and Rolfe (1982). There were several virtues in this approach, among which the most important was its freedom from the Gaussian approximation. The position error due to the detector slots was uni-

formly distributed, making any Gaussian algorithm unacceptable. Another aspect of the decision algorithm was that the fraction of true cases accepted increased as the size of the position uncertainties decreased. Because the threshold could not easily be set to accept a specific fraction of all cases, it was set during simulation tests by opening up the the threshold until just before the acceptance of false events became significant.

Figure V.D.1a depicts two position probability density functions in a typical case. Each density function has a broad, flat ridge which shows the uniform contribution of the net intersection of the seconds-confirmed detector slots' cross-scan domains. The orthogonal direction is that of the scanning motion, and the corresponding position errors were found to be well modeled as Gaussian. In the figure, the agreement between the two position estimates is about as good as it could be. The large difference shown between the scan directions occurred only at the weeks-confirmation level. At hours-confirmation, the major axes of the density functions were approximately parallel. Refinement of position leads to a new probability density function which is more centrally concentrated, as shown in Fig. V.D.1b for the current example.

The confirmation decisions are summarized in Table V.D.1 which gives, for each step in the confirmation process, the type of position test (Gaussian or two-dimensional), the threshold used, the flux agreement required and the net effect of these criteria on real sources.

Although the confirmation decision and parameter refinement lay at the core of the point source confirmation processing, many peripheral issues also had to handled. These aspects are discussed at a level of detail which attempts to be concise while not leaving an inordinate number of questions unanswered.

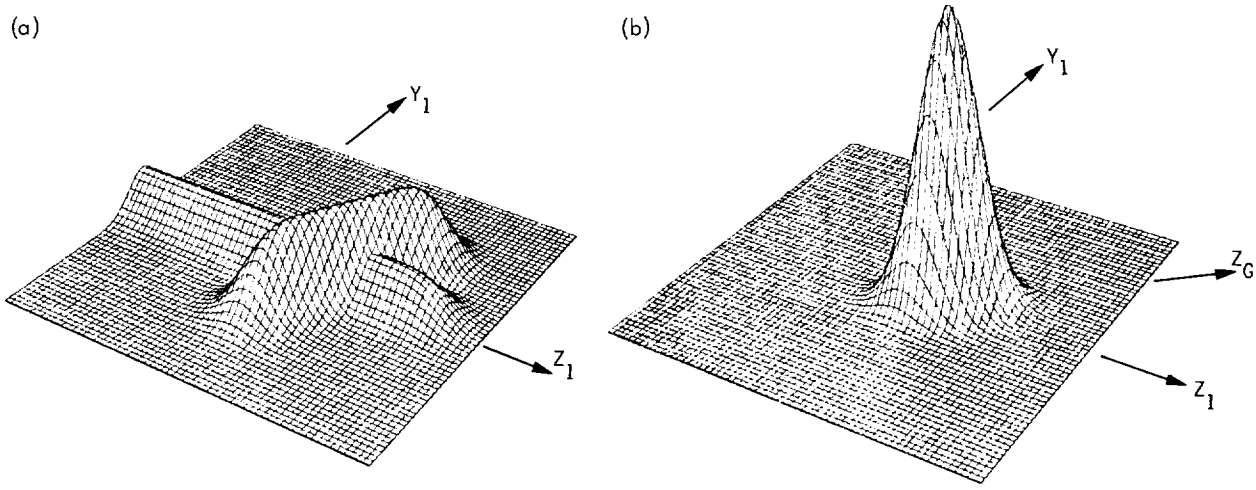

Figure V.D.1 a) As described in the text, the position and associated uncertainty of each source is represented by a probability distribution function consisting of Gaussian and uniform components. Shown here (left) are the distribution functions for two sightings of a single source. b) The position of the source resulting from the merging of the two sightings shown in V.D.1.a is described by the new probability distribution function shown here (right).

Table V.D.1 Confirmation Summary

Confirmation Level	In-Scan Limit	X-Scan Limit	2-D Limit	Flux Ratio Limit	Comment
Seconds	4.4 Sigma	Compat. Det.	-	2	1 Real Match per 50,000 Rejected
Band Merge	4.2 Sigma	Compat. Det.	-	-	1 Real Match per 40,000 Rejected
Hours	-	-	1×10^{-4} sr^{-1}	2	1 Real Match per 20,000 Rejected
Months	-	-	1×10^{-4} sr^{-1}	-	1 Real Match per 20,000 Rejected

D.2 Overview of Seconds-Confirmation

Point sources were required to be observed more than once within a few seconds by redundant detectors in the focal plane to eliminate false alarms caused by various noise processes. Exceptions to this rule were granted only on the basis of known problems in a redundant detector, either an outright failure or a significantly degraded sensitivity compared to other detectors in the same band. Because of measurement errors in the photometry and timing, it was not always trivial to identify which detections were in fact observations of the same inertially fixed point source. Noise, radiation hits and confusion by more than one source aggravated the problem.

The input data to the seconds-confirmation processor are described in Table V.D.2. When several detections in a band were accepted as applicable to a single point source, the information contained in the multiple observations was combined to obtain a single refined description of the object.

The seconds-confirmation process first dealt with detections in each band separately and later tried to combine observations from all bands. Comparisons of IRAS observations with known infrared sources were then made. Along the way, considerable statistical analysis was performed to calibrate the focal plane geometry as mapped onto the sky through the optics and to verify the quality of the position reconstruction.

D.2.a Band Seconds-Confirmation

In-band seconds-confirmation was done in the position domain rather than the time domain to account for variations in the scan rate. The design of the focal plane permitted legitimate sources to produce pairs or triplets of detections, and these modes were handled separately. When neither mode appeared correct, confusion processing was required. Although this salvaged useful detections, it could also let false alarms leak through. The confirmation process, however, may be considered a serial filter

arrangement, and so a few false alarms slipping through one stage are very unlikely to penetrate the entire obstacle course.

After accepting a confirmed point source, the flux and position estimates were refined. The multiple observations were used in statistical computations aimed at gathering information about the instrument and the *a priori* statistics.

D.2.b Position Reconstruction

Detections in a single band were processed in time order. Each detection had its position in the Sun-referenced coordinate system computed. At the same time the photometric uncertainties, modeled as a white-noise Gaussian random variable in the logarithm of the flux and a constant but unknown calibration scale factor error in the flux, were obtained from lookup tables as functions of signal-to-noise ratio and correlation coefficient.

The position reconstruction was performed by searching the pointing history for records with time tags bracketing that of the detection. The matrices for transforming from the focal plane coordinates to the Sun-referenced system and to the 1950.0 mean ecliptic system were obtained by cubic spline interpolation. Each detector was characterized by a unique unit vector in the focal plane coordinate system. The transformation matrices yielded the polar, azimuthal, and twist angles defining the position of the detector slot on the sky in the Sun-referenced and 1950.0 mean ecliptic systems. The cross-scan half-width of the slot defined the uniform error component, denoted L_Z, in that direction. The cross-scan limit cycle reconstruction uncertainty was modeled as a Gaussian random error, σ_Z. These and the in-scan errors discussed below were the only significant uncertainties involved in the confirmation decision process. After all confirmation and refinement processing was completed, the absolute position angle errors, which were estimated by the pointing reconstruction program but which cancel out of the confirmation decision, were taken into account.

The uncertainties in the scan direction which affected the confirmation decision were a time-interpolation error and the detection timing uncertainty. The latter yielded an angular uncertainty when

Table V.D.2 Input Data for In-Band Seconds Confirmation

Detections:	Flux and uncertainty, time and uncertainty, signal-to-noise ratio, detection correlation coefficient, and detector number.
Pointing:	Telescope boresight angles in the Sun-referenced system and uncertainties, scan rate, time tag, sines and cosines of the angles in both the Sun-referenced and 1950.0 mean ecliptic systems, and rates of these angles, all sampled at one-second intervals.
Detectors:	Status (on/off) and geometrical models in image space.
Optics:	Point-spread function model.
Error Tables:	Model of pointing reconstruction error due to time interpolations; photometric error as a function of signal-to-noise ratio and correlation coefficient for each band.
Thresholds:	Confirmation acceptance, search windows, etc.

multiplied by the scan rate. These were taken to be independent Gaussian errors with a combined effect of a zero-mean Gaussian random error, denoted σ_Y, with a variance equal to to the sum of the two error variances.

D.2.c Optical Crosstalk Removal

Each detection was checked to see whether it was bright enough to cause spurious sources due to optical crosstalk on adjacent detectors (see Section VII.E.5). This decision was made on the basis of the bright source's signal-to-noise ratio, since the detection process triggered on that parameter, not flux level. For example, a source which might elicit optical crosstalk detections in quiet sky might not do so in the Galactic plane, where the higher noise level could mask the crosstalk.

A lookup table for each band was used to determine the cross-scan distance over which a source might cause optical crosstalk detections. This was a function of the signal-to-noise ratio of the source, and was based on the prelaunch evaluation of the optical point-spread function. The signal-to-noise ratio thresholds for closer examination were 5000, 1200, 300, and 200 in the 12, 25, 60, and 100 μm bands, respectively. When a detection was above this threshold, the cross-scan distance to search for other detections caused by crosstalk was obtained from the lookup table. The in-scan search distance was constant, with values of 14″, 14″, 29″, and 58″ in the 12, 25, 60, and 100 μm bands, respectively. Any detections in the window which were fainter than the one being processed were deleted from further consideration. The deletions were performed only for the module containing the detector which yielded the bright source, in order not to eliminate its confirmation partner.

No attempt was made to identify crosstalk caused by the secondary mirror support spider. The characteristics of the bright source and those deleted were subsequently used in the small extended source processing. An analysis of the effects of bright sources is given in Section VII.E.5.

D.2.d In-Band Seconds-Confirmation Decision

The oldest detection being considered at any time was processed for seconds-confirmation by searching the rest of the buffer for detections which had not yet been used and which occurred on compatible detectors. This oldest detection was called the *drop-dead* detection, because it had to confirm with another detection in the buffer or be rejected. This terminology runs through band merging, hours-confirmation, and weeks-confirmation, as well as the similar phases of small extended source processing. Coarse windows in time and in-scan position were used to isolate possible candidates. When such were found, the fine position test was applied. This consisted of an $n\sigma$ test on the absolute in-scan position discrepancy between the drop-dead and the candidate, in units of the standard deviation of the discrepancy random variable. Assuming independent errors, this is the square root of the sum of the in-scan error variances of the two detections. This test was used primarily for its computational speed and for the fact that it permitted one to set the threshold by selecting the fraction of all true events which one was willing to sacrifice in order to deter false events (Table V.D.1).

When the coarse in-scan window was exhausted, the search for candidates was terminated. At that point, the number of candidates which passed the fine position test with the drop-dead determined the next step. If only one was found, the double-detection mode was processed. If two were found, the triple-detection mode was examined. If more than two candidates satisfied the position agreement requirement, then confusion processing was invoked. Each of these three cases is discussed below.

If no acceptable candidates were found, or if none remained after the additional testing discussed below, then the drop-dead detection was rejected. This means that it was considered either *non-seconds-confirmed (NSC)* if all of the compatible redundant detectors were operational, or *non-seconds-confirmed due to a failed detector (NSCF)* if the alibi of a dead or degraded detector was applicable.

D.2.e Double-Detection Mode

The double-detection mode was the most common mode of seconds-confirmation. A combined test on flux and position was applied which consisted of a two-degree-of-freedom χ^2 test. The $n\sigma$ position discrepancy contributed one of the degrees of freedom, and the discrepancy in the log of the two fluxes in units of the log-flux standard deviation provided the other. A threshold value corresponding to sacrificing one real event out of every hundred thousand was used for this test for unconfused cases, and one corresponding to sacrificing one real source in a million was used for cases which had been processed for confusion before arriving at this point. If this test failed, the drop-dead fell back to rejection processing as described above; otherwise parameter refinement was performed for the flux and position (see below), and the next detection was processed.

D.2.f Triple-Detection Mode (Edge Detections)

Some scan paths available to inertially fixed point source images traversed three detector slots in the same wavelength band, as portrayed in Fig. V.D.2a. Only some combinations of detector slots were consistent with this possibility. When three detections were found to be confirmable on the basis of position, the slots involved were tested for compatibility with this triple-detection mode. If they were consistent, then the source position could be localized to within the small region of cross-scan overlap, and a small uniform uncertainty in the cross-scan position of the source resulted. Many sources in the catalog have at least one edge detection, resulting in correspondingly small cross-scan uncertainties.

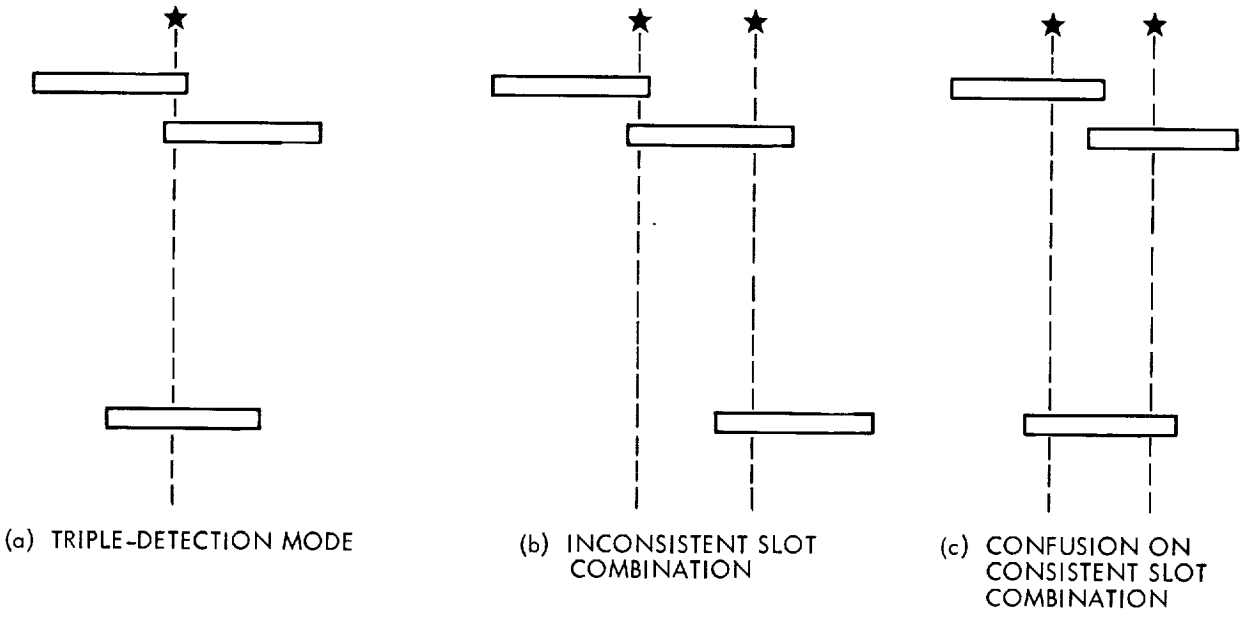

Figure V.D.2a-c The confusion processing described in the text attempted to deal with the various combinations of possibly multiple sources seen on more than one detector.

If the slots were not consistent with an edge detection, then the situation was diagnosed as confused (see below). An example of three detections which were not consistent with the triple-detection mode is shown in Fig. V.D.2b. Whenever a legitimate triple-detection pattern occurred, the possibility that two or more point source images were confused on the central detector had to be considered. Figure V.D.2c shows two point-source image paths which are close together in the scan direction but separated in the cross-scan direction, so that the central detection is a confused response to the two. The additional cross-scan coverage of the triple-detection mode increased the probability that such confusion would occur. The only thing that could be done to avoid accepting this case as a single point source was to require the edge-overlap detections to be of roughly comparable brightness, so that if they were actually two different sources, one would expect the central detector to see about twice as much flux. This would tend to cause the flux test to be failed, so that the triple-detection mode would be rejected, and confusion processing would be invoked. A faint confused source might not upset the flux test, and so relative faintness on an edge-overlap detector itself was made to be a reason for disqualification of the triple-detection mode. On the other hand, if only one source were involved but it barely grazed one of the edge-overlap slots, there would be no great loss in disallowing it, as it contained little information anyway, although the detection could cause confusion again at hours-confirmation.

These considerations led to requiring the ratio of fainter to brighter edge-overlap detection to be greater than 0.01 in order to continue to entertain the possibility of a triple detection mode. Failure to pass this test caused the situation to be processed for confusion processing.

Next a flux test was applied to the brighter of the two edge-overlap detections and the full-hit detection. This was an $n\sigma$ test on the log-flux discrepancy and had a threshold of 4.4 σ (i.e., reject one real source per hundred thousand). If this test failed, confusion processing was applied; otherwise parameter refinement was performed for position and flux. The fainter edge-overlap detection was not used for flux refinement, and the brighter was used only if the ratio of the fainter flux to the full-hit flux was less than 0.1, as this indicated that the brighter edge-overlap detection's slot should have intercepted essentially all of the flux. To reduce the effects of spurious weak detections, the fainter edge-overlap detection could contribute to the position refinement only by having a signal-to-noise ratio above 5 and a detection correlation coefficient above 0.96. If it qualified, then the pairwise position refinement described below was performed first for pair consisting of it and the full-hit detection, so that the slot-extension logic (see below) could be activated for this pair. The brighter edge-overlap detection contributed position and flux information according to the same rules as the double-detection mode; these are discussed in the parameter refinement sections below.

D.2.g In-Band Seconds-Confirmation Confusion Processing

The drop-dead detection and all candidates which had passed the fine position test were immediately marked as confused upon initiation of confusion processing. Status bits set here and in corresponding subsequent analyses were carried in a status word, hereafter denoted CSTAT, throughout all remaining processing stages (see Table V.D.3a,b).

Several attempts were made to unravel confused situations. The first stage involved discarding any detections with signal-to-noise ratios below 5 or detection correlation coefficients below 0.92. Such detections were never used in any future confirmation processing. If this dropped the number of candidates to

zero or one, then the drop-dead was processed for rejection or for the double-detection mode, respectively. Otherwise confusion processing continued by attempting to identify pairs of candidates which would confirm each other without the help of the drop-dead detection and without confusion from other detections in the buffer. Any such detection pairs were set aside from the current situation and left for the time when one of them would become a drop-dead. Finding such pairs reduced the number of candidates involved in the confused situation being processed, and after all such possible reduction had been achieved, the number of remaining candidates was checked as described above.

If the situation remained confused, then processing continued by casting aside the detections whose slots had an edge-overlap relationship with the drop-dead's slot, if any, unless the detector status information indicated that these were allowable for pairwise confirmation with the drop-dead. Again the branching possibilities were checked. In this case, and in all remaining cases in this section, discarded candidates remained eligible for future confirmations on subsequent processing.

Table V.D.3a Confusion Status (CSTAT) Bit Assignments

Bit No.	Meaning (Applies if Bit = 1)
0	Either triple-detection mode or possible confusion in seconds-confirmation
1	Triple-detection mode accepted
2	Confusion diagnosed and cleanup attempted in seconds-confirmation
3	Confusion diagnosed in band-merging, only best match retained
4	Confusion diagnosed in hours-confirmation, only best match retained
5	In 12 μm Band Byte: Not Used In 25 μm Band Byte: Not Used In 60 μm Band Byte: Detector number arrays (all bands) are out of time order In 100 μm Band Byte: More then 3 sightings were hours-confirmed
6	ADC saturation occurred for at least one detection in this band
7	Not used

Table V.D.3b. Common CSTAT Values (Decimal)

CSTAT	Meaning
3	Triple-detection mode
5	Possibly confused
7	Triple-detection mode after confusion cleanup; usually not reliable
8	Possibly confused in band-merging
13	Possibly confused in both seconds-confirmation and band-merging
16	Possibly confused in hours-confirmation

If further candidate reduction was needed, the candidates were required to pass a stricter position test, similar to the one discussed above, but with a threshold value such that one real detection pair out of one hundred would be expected to fail this test. Again the branches considered above were checked, except this time the case of two remaining candidates was included, with a branch to the triple-detection mode processing if applicable, provided that a branch from that mode to confusion processing had not already been executed.

If more than two candidates remained at this point (or two which had been found unacceptable for the triple-detection mode), then that combination whose summed fluxes came closest to those of the drop-dead were retained, and the others were discarded. If this left no candidates, the drop-dead was rejected; if only one candidate remained, the double-detection mode processing was performed. Otherwise, a flux test between the summed candidate fluxes and the drop-dead flux was performed which was similar to the triple-detection mode flux test, except that the threshold value used was chosen so that one real case out of a million would be rejected. If this test was passed, then all remaining candidates were confirmed with the drop-dead, which was considered to be a simultaneous confused observation of all of them. This type of salvaging was possible only when the drop-dead was the confused sighting (rather than one of the candidates). In this case, no flux refinement was performed; the individual candidate fluxes were retained, but position refinement was performed as described below.

D.2.h In-Band Seconds-Confirmation Position Refinement

Position refinement was performed for detection pairs as follows. The in-scan position angle and its uncertainty were obtained from those of the two detections by applying Gaussian estimation. The cross-scan position angle and its uncertainty were obtained by computing the nominal intersection of the slot extents as mapped onto the sky (i.e., including spacecraft limit cycle motion), and then including a "slot extension" safety term if the ratio of the fainter detection to the brighter was below 0.8 in the 12, 25, and 60 μm bands, and in all cases for the 100 μm band. This slot extension was obtained from a lookup table for each band which gave the amount of extension as a function of the flux ratio. The edge of the fainter-detection slot defining the net cross-scan range is the edge which was extended. For flux ratios greater than about 0.6, this extension was negligible. For a flux ratio of 0.4, the extensions in the 12, 25, 60, and 100 μm bands were 13″, 13″, 28″, and 34″, respectively. For a flux ratio of 0.2, the extensions are 20″, 20″, 43″, and 65″, respectively. In cases involving only detectors at the cross-scan boundary of the entire survey array, a slot extension to allow for the possible passage of the image outside of the detector area was added; the values used for this were 45″, 89″, 138″, and 206″ in the 12, 25, 60, and 100 μm bands, respectively.

The error due to the net remaining slot overlap was modeled as a uniformly distributed random variable from this point on. This completed the computation of the position angles and their uncertainties in the uncorrelated-error frame of reference. The correlated errors (i.e., the relatively slowly varying absolute pointing errors) were taken to be those associated with the drop-dead source. These were modeled as Gaussian random variables, but were not yet convolved with the other uncertainties because they did not enter the band-merging problem (see below). Instead they were merely carried along so that they could be included after the band-merging was completed.

The twist angle for the refined position was simply interpolated linearly in time from those of the two detections being processed. No uncertainty was carried for the twist angle because the reconstruction error could have been an order of magnitude larger than the requirement without significantly affecting the position information; the reconstruction appears to have been well within its requirements.

D.2.i In-Band Seconds-Confirmation Photometric Refinement

Photometric refinement was performed for pairs of detections which passed several qualification rules. When performed, Gaussian estimation was used, where the Gaussian error was assumed to be in the logarithm of the flux. The estimates for the *a priori* errors were derived from analysis of *a posteriori* discrepancy dispersions as functions of signal-to-noise ratio in each band, and the combination of the Gaussian assumption with well-modeled variances was found to be quite good in subsequent χ^2.

To be eligible for flux refinement processing, the ratio of the fainter detection to the brighter one had to be greater than 0.67; otherwise the brighter detection alone was used. In cases of confusion (except detections discarded in a previously processed case), only candidate fluxes were used, because confusion was detected only when it was the drop-dead detection that was composed of more than one source image. When the detections were unconfused and met the flux ratio requirement, they were still required not to show saturation of the analog-to-digital converter; if both detections were saturated, then the brighter flux was used. If one and only one was saturated, then the unsaturated detection alone was used. Finally, if the detections were on edge-overlap slots opposite a dead redundant detector (or a significantly noisy one which produced no detection confirmable with the pair being processed), then only the brighter detection was used for flux information, unless it was saturated, in which case the fainter detection alone was used.

The drop-dead detection always provided the source name (time tag and detector number). The numbers of all detectors involved were always recorded in the arrays set up for this purpose (see Table X.B.6). When only one detection was used for flux information, it also supplied the signal-to-noise ratio, detection correlation coefficient, and baseline value. When refinement was done, the maximum signal-to-noise ratio and detection correlation coefficient were retained, and the unweighted average of the two baselines was kept.

The order of the detector numbers in the array was determined as follows. In the double-detection mode, the first number is the candidate, and the second one is the drop-dead, unless one and only one detection was saturated, in which case the first number is that of the saturated detector. There is no way to tell the difference between both detections being saturated and only the candidate being saturated without recourse to additional data. In the triple-detection mode, the detector numbers are in decreasing detection time order if there was no analog-to-digital converter saturation involved. Otherwise the first number is the fainter edge-overlap detector, and the other two follow the rules for double-detection mode number order.

D.2.j In-Band Seconds-Confirmation Statistical Processing

When detections were found to be confirmable in the absence of confusion, saturation, effects due to failed or noisy detectors, fluxes which did not qualify for refinement, or occurrence of the detections exclusively at the boundary of the survey detector array area in the focal plane, then the discrepancies in

the in-scan position angle and the flux were computed for statistical analysis. The values and significances of these were used to adjust and then verify the *a priori* error variance models.

In each band, the relative flux discrepancy standard deviation as a function of signal-to-noise ratio was computed. The mean discrepancy was not significantly different from zero, and typical standard deviations ran from 20% for weak sources to about 10% in the 12 μm band, 15% in the 25 μm band, and 20% in the 60 and 100 μm bands for bright sources. These standard deviations were used to examine the behavior of the photometric error at the sampling intervals involved. After about 30 days of data had been accumulated, the variances obtained in this way were used to supply new *a priori* flux error variances for the rest of the mission. It was not necessary to cycle subsequent results through this process again, i.e., the statistical properties of the photometric discrepancies sampled at intervals of a few seconds and a few hours (from similar analysis at hours-confirmation) were stable over the lifetime of the spacecraft.

D.3 Band-Merging

D.3.a Overview of Band-Merging

Band-merging was performed in a manner very similar to in-band seconds-confirmation, except that detection buffers were maintained for all bands simultaneously, and detections in different bands were combined. Again a "drop-dead" source was selected as a nucleus to which detections in other bands were attached if they could be associated with it. Up to four attempts were made to obtain some type of flux measure to put in all three other bands for each drop-dead. In the first round, a detection from the primary source buffer in each band was sought. These buffers contained sources which were either seconds-confirmed (SC) or were on detectors opposite a failed or noisy redundant detector (NSCF). The drop-dead source was selected as the SC or NSCF source with the earliest time tag. The drop-dead's band determined the order in which the other bands were searched, according to Table V.D.4.

Coarse windows in time and in-scan position angle were used to limit the search for merging candidates. When found, such candidates were subjected to a fine position test such as that of in-band seconds-confirmation, an $n\sigma$ test on the in-scan position angle (Table V.D.1). In the cross-scan direction, the nominal slot extents of the drop-dead and the candidate were required to overlap.

If more than one candidate was acceptable in a given band, the priority was given to SC candidates over NSCF candidates, and otherwise the best in-scan match was taken. A bit was set in the confusion status word for the source.

Table V.D.4 Order of Band-Merging

Drop-Dead Band (μm)	Order in which Other Bands Were Searched (μm)		
12	25,	60,	100
25	10,	60,	100
60	25,	100,	12
100	60,	25,	10

When a candidate was merged with a drop-dead, the position parameters were refined immediately with the same algorithm as that used for in-band seconds-confirmation. This was done before resuming the merging search in the next band, so that subsequent candidates would have to be compatible with the position information of all detections merged up to that point.

D.3.b Band Filling

After the attempt to merge sources from the SC/NSCF buffers, if any bands remained empty, the non-seconds-confirmed (NSC) detections were searched for band-filling candidates. These were the detections which failed seconds-confirmation without the alibi of a dead or noisy redundant detector. The tests were identical to those for SC/NSCF sources, except that the threshold used was just under 4.1 σ, which should reject one true case out of every 20,000. The NSC detections were used for flux estimates only; their position information was considered too risky to use for parameter refinement. If more than one NSC detection was acceptable for filling a given band, the confusion status bit for that band was set, and the best in-scan position match was kept. After the NSC buffers were searched, unused NSC detections were passed on to the input file for use at hours-confirmation.

Any bands which remained empty were filled with low signal-to-noise detections (Section V.C.8) or with upper limits based on the noise histories of the detectors which the source image crossed. If any detectors were certain to have been crossed, then the upper limit was based on the lowest noise of any such detector; otherwise the highest noise on any detector which might have been crossed was used.

D.3.c Special Considerations Regarding Band-Merging

Three special considerations entered the band-merging problem. These were deferred in the discussion above in order to minimize the complexity of the description. The first of these was concerned with the selection of the drop-dead detection from one of the SC/NSCF buffers. Rather than selecting the oldest detection in any of the four bands, a time offset of seven seconds was applied against detections in the 100 μm band in order to reduce the amount of cirrus contamination. This compensated for the fact that the 100 μm band was the first to register observable point source detections, because of its location at the entrance to the focal plane. Without the time offset, cirrus detections had been able to claim nearby point source detections before they could be associated with their proper partners. Implementing the seven-second delay forced all multi-band sources to begin band-merging with drop-dead detections at shorter wavelengths, where cirrus was much less of a problem.

The second special consideration related to the handling of SC and NSCF detections of the same source in the same band. It was not unusual for edge-overlap detectors opposite a noisy detector to participate in a triple-detection with the noisy detector. Usually this triple-detection mode was processed without any problem, but occasionally the three detections would fail the tests required for acceptance of the triple-detection mode. These tests attempted to prevent confusion of close sources, as described above under in-band seconds-confirmation. When these tests failed, it was possible for the source to be carried forward in both the SC form and the NSCF form. Experience showed that the SC form was practically always a better representation of the source than the NSCF form, but half of the time the NSCF had the earlier time tag and hence had first choice of band-merging candidates. In order to correct this, a test was added after selection of a drop-dead to see whether it was NSCF and was followed closely by any

SC source in the same band. In such cases, the SC and NSCF sources were swapped in the buffer, so that the SC source would be processed for band-merging first. The time windows used were one second in the 12, 25, and 60 μm bands, and 1.5 seconds in the 100 μm band.

The third special consideration involved the use of position information of NSCF sources in parameter refinement. With three dead detectors and several more with degraded noise properties, NSCF sources were too numerous to permit completely ignoring their position information. On the other hand, false alarms on detectors opposite dead or noisy redundant detectors had to be accepted as NSCF. The only partially distinguishing characteristic of false alarms was their tendency toward low detection correlation coefficients. A compromise was therefore developed which permitted the use of NSCF position information in parameter refinement provided that the detection had a signal-to-noise ratio of at least ten with a correlation coefficient of at least 0.98. The only exception to this rule was when no SC or qualifying NSCF sources were present, in which case all NSCF position information was used in parameter refinement.

D.3.d Focal Plane Geometry Analysis

The mean in-scan position angle discrepancies for each pair of redundant detectors in a band were interpreted as errors in the focal-plane geometry as mapped through the optics onto the sky. These errors could not not be distinguished from timing errors, because all data were taken at the survey scan rate, but separation into components was not necessary for survey analysis purposes. Whenever detections in different bands were merged and qualified for position refinement, the in-scan position discrepancies were computed for all possible band combinations. After sufficient data were obtained, these mean discrepancies were forced toward zero by modifying the model of the focal plane geometry.

D.4 Known Source Correlation

A measure of processing quality was obtained by tracking the progress of certain known sources of infrared emission through the various stages of the data reduction. These included most of the IRC and AFGL objects, along with about 25,000 K Stars and 2500 numbered asteroids. A dozen comets and the major planets within the viewing constraints were also included, as well as about 200 objects which were selected on the basis of potential interest to users of the low-resolution spectrometer.

D.4.a Known Source Prediction

The *a priori* fluxes in the IRAS bands for the IRC, AFGL, and K stars were estimated by blackbody curves run through measured flux points. The K star estimates were adjusted by global rescaling after a month's accumulation of data. The fluxes for the solar system objects were obtained via standard thermal models. The low-resolution spectrometer objects had no flux estimates.

For each survey scan, the known objects which were to be covered were predicted. The predictions involved the detectors which would be crossed by each source image, the times of these crossings, the flux that should be observed, and a measure of the probability that a detection would result. The scan parameters and the known positions of the sources were used with the detailed boresight pointing history to calculate the geometrical predictions, and once the detectors were identified, their sensitivities and the intersections of their slots with the image blur were used to obtain the expected flux values. The probability of detection was based on the expected signal-to-noise ratio and photometric error, along with the uncer-

tainty in the reconstructed solar aspect angle, the clearance in the slot of the image center, and the width of the image blur. The probability increased with higher signal-to-noise ratio, as photometric error became less likely to thwart the detection process, and it decreased with smaller slot clearance, as cross-scan limit cycling and image blur width became more likely to prevent the necessary amount of flux from arriving at the detector. For the solar system objects, orbital position calculations were necessary. These were computed in heliocentric ecliptic coordinates at the time corresponding to the middle of the observation period and transformed to spacecraft-centered position angles. The remainder of the task was the same as for inertially fixed sources.

After each anticipated known source image had been mapped through the focal plane, the number of detections predicted for it was checked to determine whether the source could reasonably be expected to be detected. The flux predicted for each detector was required to be above a certain level corresponding to the detection threshold on that detector. At least one SC or NSCF prediction was required before any prediction at all was generated. If any prediction was issued, then the estimated fluxes in all bands, even those below threshold, were passed on to the correlation analysis, although no detectors were associated with any band for which the fluxes were expected to be below the detection threshold.

D.4.b Correlation of Observations With Predictions

Association of an observed source with a predicted known source was done strictly on the basis of position agreement using the non-Gaussian statistics described at the beginning of Section V.D.1 (Fowler and Rolfe 1982). After an identification was made, a subsequent identification of the same prediction with another observation could still occur and have a chance to replace the earlier association if appropriate. In such a case, the two associations were compared, and only the better match was kept. Similarly, if one observed source was found to pass the tests for association with more than one prediction, only the best match was kept.

If a predicted source was never matched to an observation, then the predicted probabilities of detection were checked to see whether any were above 0.99 and, if so, a warning message issued. A given prediction was considered unable to acquire further matches if the latest observation processed was more than $41'$ past it in the scan direction, or if another prediction at least five positions further downstream was matched.

D.4.c Known Source Flux and Position Discrepancy Analysis

When final match decisions had been made for each predicted known source, those which were identified with observations were investigated for discrepancies in the flux and position. The various types of known sources mentioned above were all kept separated in the statistical analysis of the discrepancies.

In-scan position discrepancies were used to compute the mean, variance, and statistical significance of this error. The information was used in the focal plane geometrical calibration. Only very small mean errors were found, and the variances indicated that the *a priori* errors were slightly conservative. In addition, data were grouped in cross-scan cells in order to determine whether the mean in-scan error was a function of the cross-scan location of the detectors involved. This would reveal any significant rotational

misalignment of the focal plane about the optical axis; an upper limit of less than half a second of arc was found for the impact of this effect on source position reconstruction.

Cross-scan position discrepancies were studied in three groups: sources observed only in one band, sources observed in more than one band, and sources containing any triple detections. These groups have distinctive ranges of cross-scan errors, and are listed above in order of decreasing uncertainty. For each group, the mean and variance of the cross-scan position discrepancies were computed. General agreement with *a priori* values was found.

D.5 Overview of Hours-Confirmation

The next level of source confirmation involved observations with time separations from 100 minutes up to 36 hours. Most objects were observed on consecutive orbits, but the upper limit was chosen to accommodate recovery scans for areas of sky not covered satisfactorily on the first attempt for a variety of reasons (see Section III.D). Generally, hours-confirmation was run on goups of three successive SOPs, although this rule was violated during the minisurvey (SOPs 29-44) and in two cases of survey restarts (SOPs 57-61, 256-257, and 265).

The "drop-dead" approach was used again to select a source for processing. When the oldest source became 36 hours older than the most recently acquired source, then the oldest source became eligible for hours-confirmation processing. A maximum of four scans were allowed to participate in one hours-confirmation of one source. Match candidates were selected by taking all subsequent unconfirmed observations within a coarse window centered on the drop-dead source. This window was 27.5′ across in ecliptic longitude and 10.3′ high in latitude. When the drop-dead source was within 30′ of an ecliptic pole, all unconfirmed sources within 30′ of that pole were included in the candidate set.

Both seconds-confirmed/band-merged and non-seconds-confirmed (NSC) sources were included in the processing, but drop-dead sources were taken only from the seconds-confirmed set until all eligible ones had been processed, after which all eligible NSC sources were used in time order as drop-deads.

D.5.a Hours-Confirmation Decision

The candidates were required to come from orbits other than that of the drop-dead source, or else they were discarded from the processing of the drop-dead. They were also required to have detected fluxes (i.e., not band-filled fluxes) in at least one band in common with the drop-dead. Those remaining were then tested pairwise with the drop-dead for position agreement, and any which were not acceptable on this basis were discarded. Those that passed were grouped into sets belonging to individual orbits and checked for confusion. If no two remaining candidates were from the same orbit, then processing proceeded to flux tests and combined flux/position tests. If two or more candidates from the same orbit had detected fluxes in at least one common band, then confusion was diagnosed, and status bits were set which would identify this condition to all downstream processing (Section V.D.8). If more than one candidate remained from a given orbit, but no common bands were found, then the situation was not labeled as confusion, but only one candidate was retained; this was the one which passed the combined flux/position test with the highest score.

If no candidates were found to be acceptable, the drop-dead source was rejected. Otherwise parameter refinement was performed for the flux and position information. Tracking of known sources was performed, and various statistical computations were carried out. Candidates which were not confirmed

with the drop-dead source remained for subsequent use, but confirmed candidates were not available for further hours-confirmation.

D.5.b Position Agreement

Each pairing of the drop-dead source with a candidate was tested for position agreement with the method mentioned at the beginning of this section. The position of the candidate was transformed to the local in-scan/cross-scan coordinates of the drop-dead, and the two-dimensional cross-covariance of the two position probability density functions was evaluated for the separation observed. If the result was below the threshold (Table V.D.1), the candidate was not considered further for confirmation with the drop-dead. Otherwise the result was stored for use later, and the candidate remained viable.

The threshold was set during simulation tests, and it was verified as acceptable during the processing of early survey data. As in the known source correlation processing, it was easier to arrive at a threshold experimentally than to attempt to accept a specific fraction of all true cases. This follows from the fact that the algorithm's acceptance fraction of true cases increases as the position uncertainties decrease.

D.5.c Photometric Agreement

Each candidate which survived the position test was examined for photometric agreement with the drop-dead in all bands in which both sources had detected fluxes. A χ^2 test was used which was based on the logarithmic discrepancies of the fluxes and the corresponding variances. The number of degrees of freedom was the number of common bands. The parameter tested was the complement of the cumulative probability; this was required to be above 1×10^{-4}, or else the candidate was discarded. No more than one true case out of every ten thousand should be rejected by this test. If the requirement was met, then a combined flux/position test was performed which required the product of the flux test score and the position test score to be above ten. Again the candidate was discarded or retained based on the outcome of this test, which also served as the tie breaker when more than one candidate from the same orbit passed all the tests.

D.5.d Hours-Confirmation Confusion Processing

When more than one candidate was confirmed with the drop-dead source, a series of pairings of each candidate with each other was performed, and the requirements placed on each pairing were to have at least one band with detected fluxes in common, to pass the position test, the flux test, and the combined flux/position test. When one of these requirements was not met, the candidate with the higher combined flux/position test score with respect to the drop-dead source was retained, and the other was discarded.

D.5.e Hours-Confirmation Position and Photometric Refinement

Position refinement was performed for the drop-dead source and all confirmed candidates by applying the technique discussed by Fowler and Rolfe (1982) in pairwise fashion to the drop-dead source and the first candidate, then to the result of this process and the next candidate, and so on until all source observations involved had been processed. The method essentially computes the renormalized product of all of the position probability density functions and calculates the parameters which describe this product in terms an approximation to the original form of the density function. In this way, the near-optimal treatment of the non-Gaussian errors was maintained.

Pairwise photometric refinement was performed in a manner analogous to the position refinement. Bands in which the paired observations had equal flux status were refined, otherwise the flux with the higher status was retained alone. Fluxes obtained by detection with the point-source template were taken as having the highest status; seconds-confirmed and non-seconds-confirmed both qualified. These were refined with Gaussian estimation applied to the logarithms of the fluxes, and so seconds-confirmed fluxes were usually weighted more heavily because of their smaller uncertainties. Low signal-to-noise ratio fluxes were refined by simple weighted averaging of the fluxes, with the signal-to-noise ratio values used as the weights. Upper limits based on noise were refined by retaining the *lower* value. All detector numbers involved were stored in arrays (see Section V.D.1) and kept with the confirmed source with the following exceptions. Detectors supplying noise fills which were not used were discarded. When four source observations were confirmed, only the first, second, and last set of detector number arrays were kept; this was done for purposes of space conservation, and a flag was set to indicate this condition.

D.5.f Hours-Confirmation Statistical Processing

Confirmed source positions were written to an output file for downstream tracking of confirmation frequency as a function of sky position, and histogram data were maintained to display confirmation frequency as a function of signal-to-noise ratio. A histogram counter corresponding to the highest signal-to-noise ratio in any rejected source was also maintained.

Flux discrepancies in each band were processed to obtain the mean and the standard deviation as functions of signal-to-noise ratio; this was done in a format similar to that of seconds-confirmation, and was used in the photometric uncertainty analysis to feed back *a posteriori* dispersions for use as subsequent *a priori* errors. χ^2 tests on the fidelity of the photometric error modeling showed that this process was working as expected. Only confirmed sources devoid of confusion, outer-slot confinement, and other questionable symptoms were used to generate the photometric dispersion data. The standard deviations were similar to those of seconds-confirmation but slightly larger, indicating more power in the photometric error spectrum at orbital frequencies.

Position discrepancies were examined for in-scan mean error, variance, and statistical significance, and the cross-scan discrepancies were studied as functions of latitude. The solar motion caused the scan overlap from one orbit to the next to be a function of latitude, and the overlap was designed to minimize the total cross-scan error of single-band sources. This anticipated effect was confirmed, and this strengthened confidence in the fidelity of the error modeling. Slightly larger discrepancies were found very near the ecliptic, and these were probably due to the confirmation of asteroids which moved slightly between observations but not enough to preclude confirmation. This effect was not included in the prelaunch estimation of position errors at hours-confirmation. The primary effect, larger cross-scan errors for single-band sources at latitudes between 40° and 50° from the ecliptic, was clearly present.

Histograms of the threshold parameters were generated to show their distributions. The main concern was for the cutoffs to lie in regions where variations in value did not cause significant variations in the number of confirmations and rejections. This would be possible if the noise processes were not saturating the decision process, and if the cutoffs were placed well above the values produced by most correct matches and well below the values produced by most false matches. This appeared to be the case.

Confirmation and rejection of numbered asteroids were tracked and printed in the summary. The fraction of these which survived hours-confirmation was about half, as predicted before launch.

D.5.g Special Considerations Regarding Hours-Confirmation

Some complications to the hours-confirmation processing were omitted from the discussion above in order to limit its intricacy. These provisos will be described briefly in this section.

As mentioned in the discussion of seconds-confirmation, sometimes a source was observed only on detectors which lay at the cross-scan boundary of the survey array. It was not possible on a single pass to determine whether the source actually missed the detector slots, so that both its flux and position information would be incorrect. The position uncertainties were expanded as described above, as this could be done in a way which virtually guaranteed bracketing the true position; there could be no such guarantee for the flux. As a result, the flux test was not performed when at least one of the sightings involved only outer-slot detectors in all bands containing detected fluxes. Flux refinement was also bypassed in these cases unless both sightings being processed were exclusively on outer slots; when this happened, the refined flux kept the status of being outer-slot only. If a subsequent pairing involved a sighting with detections inside the survey array cross-scan boundaries, its fluxes were retained without any averaging, and the outer-slot status was removed.

When any source was processed which was detected but not seconds-confirmed in the 25 μm band next to the gap left by the demise of detectors 17 and 20, special checking was performed. If detections in other bands were present, the detector geometry was examined to determine whether actual image center passage between the cross-scan limits of the 25 μm band detector could be verified; if so, no further special action was taken. Otherwise the flux in the 25 μm band was treated as an outer-slot flux, since the image center may actually have missed the slot involved in the detection. This disqualified the source's 25 μm flux from testing, inclusion in the photometric dispersion analysis, and contributing to refinement unless no better data were available.

Particle radiation posed a significant threat to the photometric accuracy, and sources observed in all four bands were more likely to be affected by it. The error caused by this source of noise produced a broad non-Gaussian component to the photometric dispersion which highlighted the fact that it did not conform to the assumptions underlying the χ^2 tests used for flux agreement. A rule was implemented, therefore, which was applied when the sources tested had at least three bands in common and failed the flux test. In such a case, the single most discrepant band was removed from consideration, and the χ^2 test with one fewer degree of freedom was used. This exemption could be invoked only once per source pair.

D.6 Overview of Weeks-Confirmation

The last stage in the confirmation chain searched for observations of the same sources with time separations on the order of a week to six months. All hours-confirmed sources became input to the weeks-confirmation processor. Sources which were not confirmed were placed in the WSDB along with those which were, and no rejections were enforced until final catalog preparation. As each new regionof sky was processed, the new sources were put unconfirmed into the WSDB, where they remained until that region was covered again, at which time the sources from the earlier coverage served as candidates to confirm the newer ones.

As each hours-confirmed source arrived for processing, a coarse window on the sky was used to select candidates from the WSDB. These may or may not have been weeks-confirmed already. The window was 10.3′ square, and the candidates were required to be separated in time by at least 36 hours from the source being processed. No flux tests were performed. Only a position test was used, and if more than one candidate passed this test, only the candidate with the highest score was kept as a match. Because of the sequential testing, valid multiple sightings should have been confirmed pairwise as each new sighting entered the processing, removing the need to identify more than one correct candidate from the WSDB. When a choice had to be made, a counter was incremented for possible confusion. Typically only about 3% of the confirmed sources were diagnosed as potentially confused at weeks-confirmation.

If there were no acceptable candidates, the new source was placed in the WSDB. Otherwise position refinement and discrepancy statistical computations were performed.

D.6.a Weeks-Confirmation Decision

The confirmation decision algorithm was a position test applied to each pairing of the new hours-confirmed source with the candidates. The candidate position probability density function was mapped into the in-scan/cross-scan coordinate system of the new source. The test was based on the two-dimensional cross-covariance of the position probability density functions, evaluated at the observed nominal separation. The underlying principle was identical to the position test used at hours confirmation, and for relative twist angles of less than 4.6°, the same algorithm was employed. Otherwise, a generalized implementation was used which was extensively complicated by the need to handle arbitrary relative twist angles between the axes of symmetry of the density functions. The details of this generalized version are discussed by Rolfe, Otake, and Fowler (1984). When the value of the cross-covariance fell below the threshold, the candidate was released from consideration.

D.6.b Weeks-Confirmation Position Refinement

Confirmed source sightings were processed for refinement of the position parameters by renormalizing the product of the probability density functions. This procedure was similar in concept to that of hours-confirmation, but was complicated by the generalization to arbitrary relative twist angles. When the relative twist angle was less than 4.6°, the hours- confirmation algorithm was used. For larger angles, the refined density function was sufficiently Gaussian that it was satisfactory merely to assign a value of one second of arc to the uniform-error component.

D.6.c Weeks-Confirmation Statistical Processing

As at hours-confirmation, histograms of the value of the threshold parameter for confirmed and non-confirmed sources were separately accumulated, position data for both types were output for downstream analysis of the sky distribution of these events, and known source tracking was performed.

Statistical summations for computing the means and variances of position discrepancies were maintained over the SOP period and over periods of approximately 50 days. This was done for the observed sightings relative to each other, and separately for known sources relative to refined position parameters, where applicable. Good agreement between *a priori* error modeling and the observed dispersions was found.

D.7 Auxiliary Processing for Low Resolution Spectra

All observations associated with known sources were processed for extraction of low-resolution spectrometer data (Chapter IX). This was also done for any observations above a signal-to-noise ratio of 25 in the 12 or 25 μm band, even if they were not associated with a known source. The path of the source image through the focal plane was checked for passage over the spectrometer aperture, and if this was found, then the crossing time and scan rate were inserted into the output source record so that extraction requests for sources which survived hours-confirmation could be issued.

Weeks-confirmed source sightings for which spectrometer extraction requests had been issued were processed for index association. This involved generating a record which associated the name of the later sighting with that of the earlier one, and which provided some housekeeping information about the extraction requests.

D.8 Flux and Confusion Status Words

Two status words were used to track the progress of a source through all levels of the confirmation processing. Each wavelength band of each hours-confirmed sighting has associated with it a flux status (FSTAT) and a confusion status (CSTAT) word which describe the quality of the quoted flux and whether the processor detected any possibly confusing neighbor sources nearby. Both of these status words were used in deciding which sources were to be included in the final catalog (see Section V.H). FSTAT (Table V.D.5) tells whether in a given band the quoted flux is an upper limit, an unconfirmed detection(s) or a well-confirmed measurement. CSTAT tells whether a sighting was potentially confused by other detections at the times of seconds- or hours-confirmation or during band-merging. Tables V.D.3a,b lists values of CSTAT.

Table V.D.5 Flux Status (FSTAT) Values

Status	Meaning
7	Hours-confirmed; detector number array reveals number of detections.
6	One seconds-confirmed detection that was never hours-confirmed but was associated with at least one low-signal-to-noise detection.
5	One seconds-confirmed detection that was never hours-confirmed or associated with any other detection.
4	Two or more NSCF detections hours-confirmed and possibly including NSC detections.
3	At least one NSC detection associated with no more than one NSCF detection.
2	One NSC or NSCF detection and possibly any number of low-signal-to-noise detections (S/N > 2.9) or at least one low-signal-to-noise detection (S/N < 3)
1	Lowest three-sigma noise value found

D.9 Conversion of Position Uncertainties to Gaussian Approximation

Throughout the processing, the position error model was based on the non-Gaussian formalism mentioned in Section V.D.1. Because most of the point source position probability density functions evolve toward Gaussian shapes at each stage of refinement, the catalog description was designed to approximate the more familiar error ellipses of two-dimensional Gaussians, while retaining most of the accuracy of the non-Gaussian model. This involved bracketing the nominal positions on each coordinate axis with a single number to be interpreted as a confidence interval on that axis. This is a simplification of the optimal cross-scan description, which requires two numbers to define the distribution about the mean.

For sources with strongly non-Gaussian position uncertainties, there is no way to escape the fact that some aspects of the error behavior will not generally be Gaussian. An important specific example is the relation between error in sigma units and the fraction of all cases exceeding that error. Because of the decision to quote the axes of the two-dimensional contour enclosing 95% of the probability mass, the error bars given were selected to match the corresponding deviations on the axes of the random variables used in the error model. Thus the expected frequency at which the true source position lies outside of the quoted contour is 5%. The contour is not generally elliptical, however, as this is a Gaussian feature not necessarily shared by the actual distributions. The error incurred by assuming that the contours are all elliptical, on the other hand, should not be extreme, and in fact this approximation played a role in mapping the two-dimensional 95% confidence into one-dimensional confidences on each axis.

The error bars were obtained as follows. For Gaussian errors, the two- dimensional 95% confidence would correspond to a χ^2 probability of 0.95 with two degrees of freedom. This implies a value of 5.99 for the χ^2 random variable, so that the ellipse crosses each axis at 2.45 sigma, corresponding to a confidence of 98.6%. This was used for the confidence level for both axes. On the Gaussian axis of the error model, the interval used was $2.45\sigma_y$. On the non-Gaussian axis, a lookup table was used to obtain the 98.6% confidence deviation as a function of the ratio of the uniform half-width, L_z, to the Gaussian σ_z. This table was computed by numerical quadrature for a grid of these ratios ranging from 0.1 to 30. Below 0.1, the probability density was considered Gaussian, and above 30 it was taken as purely uniform.

E. Overview of Small Extended Source Data Processing

The small extended source processor used detections at scales larger than that of point sources to locate and measure stationary, unconfused sources resolved by the detectors but smaller than 8′. The identification of candidates was similar to that of point sources, in that the data stream of each detector was examined using zero-sum square-wave filters. The detections were checked for seconds-confirmation, then all the detections in the hours-confirming coverage were assembled to construct a model of the source from which estimates were made of the source parameters. Before weeks-confirmation, an effort was made to discard sources that were either confused, larger than 8′ or fragments of larger structures. Sources were then weeks-confirmed and, when possible, band-merged. A set of criteria described in the introduction to the Small Extended Source Catalog was used to select sources for inclusion in that catalog.

E.1 Potential Detections

To locate potential small extended sources the data stream of each detector was first successively compressed by adding consecutive pairs of data samples. Designating the original data stream of each detector to be of level 0, new data streams of higher levels were generated according to the rule that the jth data sample in the kth level data stream was given by,

$$X(j,k) = X(j,k-1) + X(j+1,k-1) \qquad \text{(V.E.1)}$$

Potential detections in any data stream were found by applying a narrow-bandpass, digital filter at each point in the data stream. This filter consisted of an eight-point, zero-sum, square-wave which subtracted the first and last two data points from the middle four (Eq. (V.C.1)). When the filter passed over a source it gave rise to a characteristic peak, and thus picked out structures whose width spanned approximately four sample points. If we denote the spatial sampling frequency of the level 0 data stream by S (i.e. S is the number of data samples per arc min in the data stream of level 0), then the approximate width of an object (in arcmin) detected by the square-wave filtering the kth level data stream is given by,

$$W(k) = (4/S) \times (2^k) \qquad \text{(V.E.2)}$$

The spatial sampling frequency, S, was approximately 4 in the 12 μm and 25 μm wavelength bands, 2 in the 60 μm wavelength band, and 1 in the 100 μm wavelength band. Since it was not intended to detect structures greater than 8′ in extent, the 12 μm and 25 μm detections were retained from levels 1, 2 and 3, corresponding to characteristic square-widths of 2′, 4′, and 8′. At 60 μm the level 1 and 2 data streams were searched for sources 4′ and 8′ in size while at 100 μm only level 1 detections were kept for small extended sources.

A peak in the kth level data stream which was picked out by the square-wave filter was accepted as a potential detection if its amplitude was greater than 3 times the local noise appropriate for that data stream. The amplitude of a square-wave peak was defined as

$$A(k) = E/(2^k) \qquad \text{(V.E.3)}$$

where E is the maximum value attained above zero in the square-wave filtered data stream. The noise was estimated for each data stream as described for point sources.

Since a source typically produced detections in more than just a single data stream for a given detector, each candidate detection from a level k data stream was compared with all candidates from the level $(k + 1)$ data stream of the same detector that were within a distance of five level k samples. In such a comparison the detection with the largest square-wave peak was chosen as the best representation of the source, and other detections were rejected. To reject sources larger than 8′, a comparison was also made with the amplitude on a scale of 16′. If, as a result of this comparison, the accepted detection had a characteristic size of 16′ (corresponding to a level 4 detection at 12 μm and 25 μm, a level 3 detection at 60 μm, and a level 2 detection at 100 μm), then this source was rejected. Similarly, since point sources were also to be excluded, a comparison of each extended source detection was made with any level 0 detections (point source) in the neighborhood. If the level 1 detection was found to have a square-wave

amplitude less than 0.75 times the level 0 amplitude, then the level 1 detection was discarded. The value 0.75 proved to be optimal for the discrimination between point-like and extended sources and was evaluated after processing data from the Large Magellanic Cloud, where many small extended sources could be clearly seen.

E.2 Seconds-Confirmation

The focal plane array was designed so that the scan track of each stationary source crossed at least two detectors in each wavelength band each time the focal plane array passed over the source. All potential detections which passed the comparisons described in Section E.2 above were checked for seconds-confirmation, and those which did not seconds-confirm were rejected unless the detector with which they would have confirmed had been declared failed. The latter condition arose most frequently at 25 μm.

E.3 Source Construction and Hours-Confirmation

In *point source* processing each pair of seconds-confirming detections was merged into a single detection. This was not the case for extended sources, nor was there any explicit check analogous to the *point source* hours-confirmation processing. Each individual seconds-confirmed detection was passed to a processor which attempted to piece together detections from the same band and the same hours-confirming coverage into a single source. Detections were considered to be from the same hours-confirming coverage if they were observed within 36 hours of each other. In most cases this process resulted in an hours-confirmed source in the *point source* processing sense, i.e., the resultant source was made up of two or more pairs of seconds-confirming detections whose detection times differed by a few hours. However, it was also possible for two or more seconds-confirming detections without a subsequent hours-confirming sighting to result in an acceptable source.

The piecing together of sources involved several stages. First, seconds-confirmed detections which lay sufficiently close to one another on the sky and which had detection times within 36 hours were linked together. If a detection failed to link with any other detection, it was rejected and not used in subsequent processing. Each group of linked detections was mapped onto a rectangular grid, representing their distribution on the sky. Each pixel in the grid was a 1′ square. The size of each detection was just the detector size in the cross-scan direction, and W(k) in the in-scan direction (Eq. (V.E.2)). This grid consisted of a number of cells which may be referred to by the coordinates (K,L). The number of detections, N(K,L), which overlapped each grid cell was found, and each cell was assigned a weight, W(K,L), which was proportional to the sum of the intensities in each of the detections overlapping the cell. The intensity in a detection was taken to be the amplitude of the square-wave peak divided by the detector aperture area. The flux from the source seen by each of the detectors was calculated. This flux was then distributed among the grid cells overlapped by the detector according to the weights W(K,L). The total intensity associated with each grid cell was then the sum of the contributions from each overlapping detector, divided by the number of such detectors.

Having assigned an intensity to each grid cell, the cells which were regarded as contributing to the source were identified. The cell with the maximum intensity was located. If this lay close to the boundary of the grid then no source was identified. Otherwise all the cells near to the maximum intensity cell which had an intensity above 1% of the maximum were linked into a single source; if the intensity distri-

bution had a minimum boundary and then a rise beyond the minimum, the linking process was stopped at this minimum.

After all the cells within the source were identified, a check was made to see if most of the source lay on the grid. This was done by requiring the intensity on all four boundaries of the grid to be less than 10% of the maximum intensity on the grid. If this was not the case then "source run off" was said to have occurred. If, in addition to source run-off, the maximum intensities on either pair of opposite grid boundaries were sufficiently different, indicating the presence of a strong flux gradient, then the source was likely to be a relatively small bump on the side of a larger source, and no source was returned. If source run-off occurred, but there was no evidence of a strong flux gradient across the grid, then the source was accepted, but a flag was set to indicate that it was possibly a fragment of a larger source.

The flux of the source was taken to be the sum of the intensities of all the grid cells which were linked into the source, multiplied by the grid cell area. The intensity-weighted sum of the number of detections contributing to each grid cell in the source was found. This was called the confirmation level of the source, and gives an indication of how well the various detections contributing to the source were put together to form a single source. Only those sources whose confirmation level was above a threshold of 2 were passed on for further processing.

Sources which passed the confirmation level and signal-to-noise thresholds became the input for subsequent confirmation processing; they were referred to as intermediate small extended sources, and were treated as hours-confirmed sources. The centroid and extent of each of those sources was computed, the extent being characterized by the matrix of the second moments of the flux distribution. This matrix was diagonalized to yield the semi-major and semi-minor axes of the source, together with the angle between the semi-major axis and the ecliptic meridian. The number of detections in the source was also carried. A detection was counted if it contributed more than half its own flux to the source.

E.4 Cluster Analysis Processing

Before weeks-confirmation was attempted, it proved necessary to verify that the candidates were well-defined and relatively isolated.

When the focal plane passed over an object more extended than $10'$, structures within the object often gave rise to many detections whose properties depended on the scan direction. The simple detection algorithm grossly misrepresented such large sources, since only the flux at the spatial frequencies of the square-wave filters was detected. This value could be far less than the true total flux. Large extended objects were characterized by strings and clusters of sources. This behavior was found particularly pronounced at 100 μm.

A somewhat similar situation arose in regions with a high density of sources, or equivalently, because of complex backgrounds, such as the Galactic plane. The results from such regions were particularly sensitive to scan direction. Fluxes quoted in regions of complex structure should NEVER be taken at face value.

Before weeks-confirmation was attempted, the sources were first analyzed by the cluster analysis processor, which looked for clusters of detections at the same wavelength and from the same hours-

confirming coverage. If the cluster was below a certain critical size then its constituent detections were merged into a single source which was then ready for weeks-confirmation. If, however, the cluster was larger than the threshold size, then it was deemed part of a large extended object, and the sources contributing to the cluster were rejected from any further processing. All detections which were not found to be members of large clusters were kept for subsequent processing.

Clusters were identified by finding sources observed within 36 hours and which could be linked together spatially. A detection was considered to be linked to a cluster if it was a close neighbor to at least one other source in the cluster. Two detections were considered to be close neighbors if their link parameter, L, was less than a certain threshold. The link parameter, L, is given by,

$$L = D/(r_1 + r_2) \tag{V.E.4}$$

where D is the distance between the centroids of the two sources and r_1 and r_2 are the radii of their equivalent-area circles, i.e. if a and b are the semi-major and semi-minor axes of the source, then the equivalent-area circle has a radius given by

$$r = \sqrt{a \times b} \tag{V.E.5}$$

The value of the threshold on the link parameter was taken to be 3.5 for reasons discussed in Section V.E.7.a.

When the detections in a cluster were merged, the flux of the merged object was taken to be the sum of the fluxes of the constituent sources. The position was the flux-weighted centroid from all the constituent detections in the cluster. The extent of the source was obtained by combining the covariance matrices about the new centroid; the new matrix was then diagonalized to yield new estimates of the semi-major and semi-minor axes and twist angle. Relatively bright sources were not greatly altered when merged with fainter detections.

The maximum semi-major axis that a merged cluster could have before being rejected was set at $5'$, since extended source processing was not intended for larger sources and could not accurately estimate fluxes on size scales greater than about $8'$.

E.5 Weeks-Confirmation

After cluster analysis processing, the remaining small extended sources were tested for repeatability on the weeks/months timescales of weeks to months. Only those detections found on at least two hours-confirming coverages were accepted as reliable sources. Two sources were regarded as being weeks-confirmed if,

(a) they were in the same wavelength band;

(b) they had detection times which differed by at least 36 hours;

(c) they satisfied a position confirmation criterion detailed below; and

(d) the ratio of the flux of the brighter detection to that of the fainter was less than 3.

The link parameter for weeks-confirmation was taken to be the χ^2 statistic of the two-dimensional position-match confidence of the two detections; in computing χ^2, each detection was modelled as a two-

dimensional Gaussian distribution characterized by the extent matrix. Two detections positionally confirmed if their link parameter was less than 1.4 (see Section V.E.7.b).

When a group of two or more weeks-confirming sources was identified, it was merged into a single weeks-confirmed source. The flux was taken to be the average of the fluxes of the two sources. The centroid and extent matrix of the weeks-confirmed source were calculated, and the extent matrix was diagonalized to yield semi-major and semi-minor axes and the twist angle between the semi-major axis and the ecliptic meridian.

If all the hours-confirmed sources contributing to a weeks-confirmed source positionally confirmed each other, then the source was said to be mutually confirmed. If an hours-confirmed source (denoted by A) weeks-confirmed with two or more other sources (denoted by B1, B2, etc.) which did not mutually confirm, the following was done to extract the best weeks-confirmed source. First, a decision function, D, was evaluated for each of sources B1, B2, etc., where

$$D = (\chi^2) \times (1 + \chi^2) + (R - 1) \times R \qquad \text{(V.E.6)}$$

and χ^2 is the link parameter between sources A and B and R is the ratio of the brighter flux to that of the fainter.

The source for which D was the smallest was found, and the ratio $D/D_{\min}$ was found for each of the sources B1, B2, etc. All sources for which $D/D_{\min}$ was above a threshold of 2 were discarded. If only one source remained, then this was chosen as the weeks-confirming partner of source A. Otherwise, the source was considered confused and the candidates were rejected.

E.6 Band-Merging

The weeks-confirmed, single-band sources were analyzed to see if they could merge with weeks-confirmed sources in other bands to become multi-band sources. Those sources in the four wavelength bands which positionally confirmed were linked together. The sources were tested for positional confirmation in the same way as in the cluster analysis processor, i.e. two sources positionally confirmed if their link parameter, χ^2 as in Section V.E.5, was less than a certain threshold. If all the single-band sources contributing to a band-merged source confirmed with one another, then the source was said to be a mutually confirmed merger.

The information describing each band-merged source became the basis for the small extended source catalog. Where two weeks-confirmed sources from one band competed to merge with a single source in another band, the band-merging attempt was abandoned and the various single band components were listed separately in the catalog. A flag was set to indicate that the sources could not be successfully band-merged.

As an additional check on previous processing steps, the band-merging processor was allowed to look for possible band-mergers between weeks-confirmed sources from the same band. A total of 166 cases were found. Upon inspection, they were all found to occur in areas with at least four hours-confirming coverages, each of which had yielded an hours-confirmed detection. These four detections formed a pattern that generated two weeks-confirmed sources; the failure of all four to link together could

be due to scanning structures in different directions, flux estimation errors, pointing errors, or to artifacts of the processing. The two weeks-confirmed sources obtained were naturally larger than the individual hours-confirmed sources by a sufficient amount that the band-merging processor managed to link them.

All these cases of weeks-confirming candidated discovered too late were treated just like cases where several sources from the same band competed to band-merge with a single candidate from another band; the "band-merging" attempt was abandoned, and the various single band components were kept and subjected to clean-up processing individually (see catalog introduction).

E.7 Optimizing the Processor

The intermediate file of hours-confirmed sources (in the restricted sense of Section V.E.3 above) accumulated as the satellite data were processed. Cluster analysis, weeks-confirmation, and band-merging were run repeatedly on this intermediate file to optimize the the thresholds in these processors. This section describes how the thresholds were arrived at and discusses the implications of the choices.

It was determined from preliminary analysis that the threshold on the link parameter used in the cluster analysis processor would have to be larger than 2, and that the weeks-confirmation threshold would have to be in the vicinity of 1. It also became clear that in the range of interest, the clustering threshold had the greatest influence on the output. This threshold was therefore optimized with the weeks-confirmation threshold held at 0.8; then the weeks-confirmation threshold was chosen. The final changes in confirmation did not affect the clustering enough to require more tuning.

The goal in optimizing the processor was enhanced reliability; completeness was only a secondary concern. Reliability included the requirement that the source be free of potentially confusing neighbors. Regions of low source density (such as high Galactic latitudes) were the prime areas where the processor was expected to perform well.

E.7.a Choosing the Clustering Threshold

As stated earlier (Section V.E.4), cluster analysis was meant to filter out fragments of sources that were larger than $8'$ and sources that were confused.

Neither problem was common at high Galactic latitudes, and while it was necessary to apply cluster processing in these areas, it was not possible to select an optimal threshold by studying these areas alone. Figure V.E.1 illustrates this point clearly by showing that the number of weeks-confirmed sources at high Galactic latitudes was essentially independent of the clustering threshold at 12 μm and 25 μm; at 60 μm and 100 μm the number of sources dropped as the clustering threshold increased, indicating the presence of complex structure at these wavelengths. Figure V.E.1 displays the results of processing in a region (henceforth Region A) at high Galactic latitudes, defined in ecliptic coordinates by $0° < \beta < 90°$ and $135° < \lambda < 205°$; its total area was about 4010 sq. deg, about 10% of the sky. The source density was on the order of 0.02 to 0.05 per sq. deg, too low for confusion to be a problem.

Figure V.E.2 displays the number of weeks-confirmed sources as a function of clustering threshold for Region B, which includes a crowded portion of the Galactic plane. It was defined in ecliptic coordinates by $25° < \beta < 45°$, and $280° < \lambda < 300°$; its total area was about 326 sq. deg, which implies a

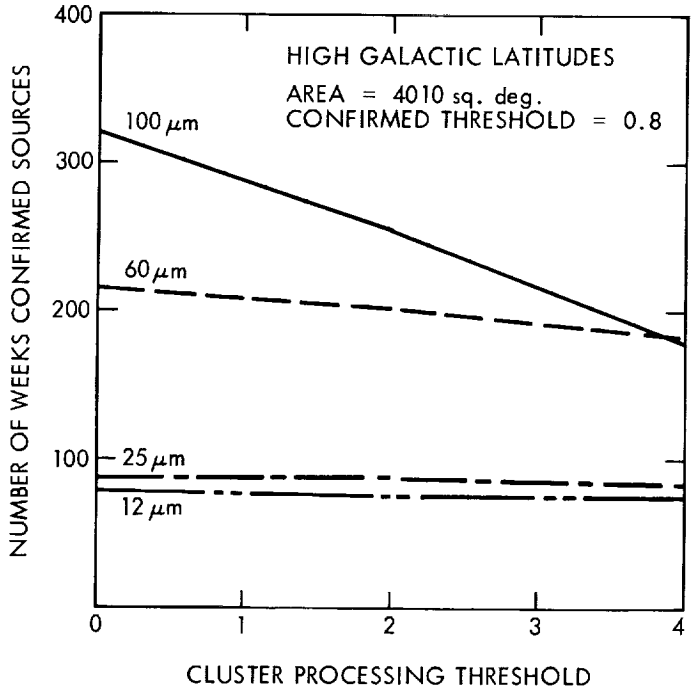

Figure V.E.1 This shows that cluster analysis processing does not greatly affect the number of small extended sources that are weeks-confirmed at high galactic latitudes. Only at 100 μm is there a substantial dependence, because of the cirrus.

source density of about 0.3 to 6.0 per sq. deg. Both figures V.E.1 and V.E.2 were obtained with a weeks-confirmation threshold of 0.8.

The shape of the curves in Figure V.E.2 suggested that a natural choice of clustering threshold could be based on keeping the final source density near the confusion limit. The confusion limit was obtained by requiring a minimum number of 25 beams per source (as in Section V.H.6), which corresponds to a probability less than 0.1% that two sources will be found in the same beam, and a probability of about 1% that two adjacent beams will both have sources in them, assuming Poisson statistics. To use this criterion, an estimate was needed for beam size. A close upper limit was simply the in-scan width of the largest detector template (about 10′) times twice the cross-scan width of a detector (about 10′), leading to an effective "beam size" of 1/36 sq. deg.

In practice, however, and especially at 12 and 25 μm, detections on smaller templates were common, and the effective beam size was found to be smaller than the upper limit by a factor two or more. To estimate the effective beam size, the average density of small extended source detections per survey coverage per band was found in the five most crowded bins on the sky. Each bin was approximately a sq. deg in size. This density was the same at 12 and 25 μm, namely 77 sources per sq. deg, with a population dispersion of 4; at 100 μm, the density was 40 ± 5 per sq. deg At 60 μm, the average density in the five most crowded bins was 78 ± 20; if the highest-density bin was thrown out, the average in the next five was 68 ± 10. The result at 100 μm was quite close to the upper limit estimate above, as expected, since only the largest template was available at 100 μm.

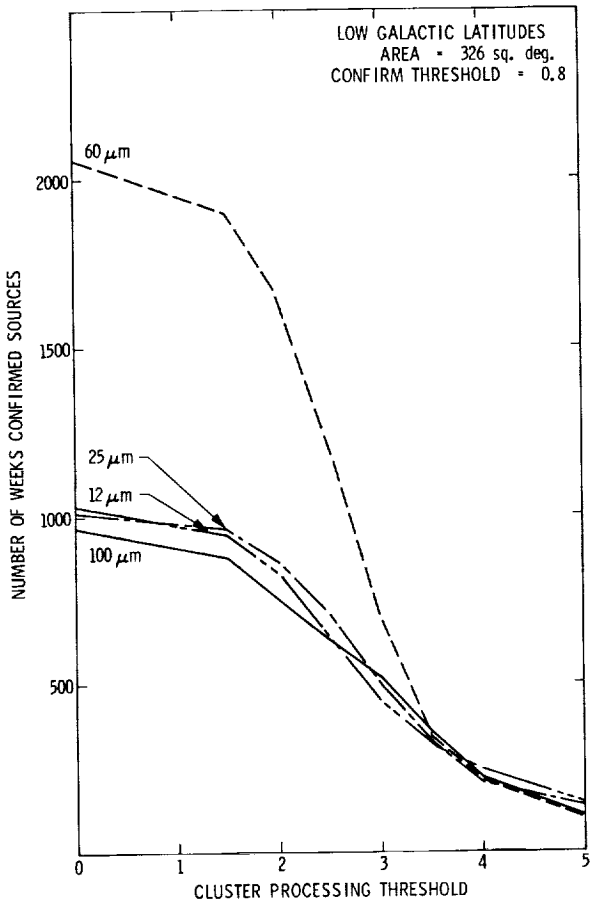

Figure V.E.2 In contrast with Figure V.E.1, regions of high source density are heavily affected by cluster analysis.

Adopting as effective beam sizes 1/40, 1/68, 1/77 and 1/77 sq. deg, respectively in the 100 μm, 60 μm, 25 μm and 12 μm, the critical densities are 1.6, 2.7, 3.1 and 3.1 sources per sq. deg. To find the corresponding critical clustering threshold, three small heavily populated windows within Region B, with a total area of 9.8 sq. deg were used. The average density of weeks-confirmed sources dropped quickly as the clustering threshold increased from 2 to 3, and then leveled off, in a way similar to, but steeper than, what was seen in Fig. V.E.2. The critical source density was reached in all bands for thresholds between 3 and 4. A value of 3.5 was chosen for all four bands.

E.7.b Choosing the Weeks-Confirmation Threshold

Figure V.E.3 shows the number of weeks-confirmed sources as a function of the weeks-confirmation threshold for Region A. Clearly, almost all confirmations were acquired by a threshold of 2; the slow rise beyond that point was roughly linear, as expected for false confirmations. The linear rise with threshold was expected because the search area (rather than the search radius) scales linearly with the confirmation threshold. Reliability dictated minimizing these false confirmations, while completeness demanded keeping as many of the better positional matches as possible. A value of 1.4 for weeks-confirmation threshold

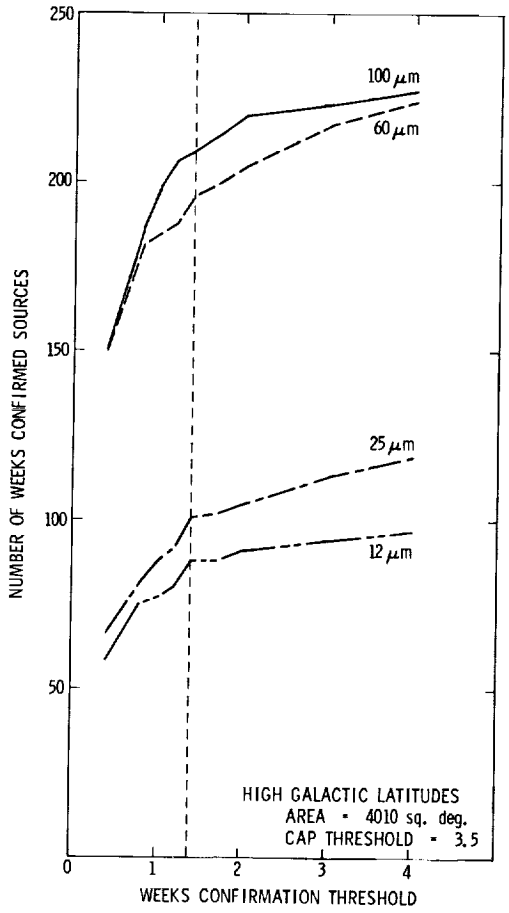

Figure V.E.3 Effect of weeks-confirmation threshold on the number of sources. The chosen threshold is indicated by the vertical broken line.

was selected because it marked the boundary between the steep climb due to true confirmations and the gradual climb due to the false confirmations.

E.7.c Choosing the Band-Merging Threshold

Because both spatial resolution and source properties changed with wavelength, an astronomical object could appear extended in one band and point-like in others. In view of that, band-merging was carried out after confirmation, in contrast to point source processing.

Figure V.E.4 shows the output of the band-merge processor as a function of the band-merging link parameter threshold in Region B (low Galactic latitudes). As anticipated, most sources turned out to be single-band sources. Past a threshold of 1.4 very little new band-merging took place. A threshold of 1.4, the same as for weeks-confirmation, was adopted.

E.7.d Summary and Discussion

It was evident that the performance of the small extended source processor at high Galactic latitudes varied slowly as a function of the cluster processing threshold. In contrast, crowded regions pro-

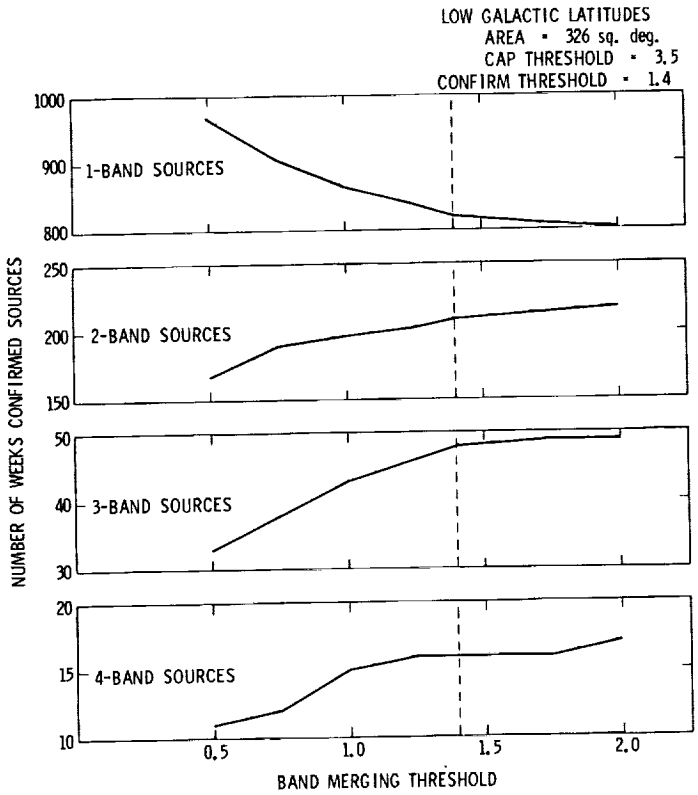

Figure V.E.4 The optimal threshold for band-merging is indicated by the vertical broken line. It is the same as for weeks-confirmation.

vided the testing ground for selecting an optimal clustering threshold. With a first determination of 3.5 as the clustering threshold, high Galactic latitudes provided the optimal choice of 1.4 as the weeks-confirmation threshold (Fig. V.E.2). A value of 1.4 was also chosen as the optimal threshold for band-merging.

The final iteration was to repeat clustering optimization using the final choice for confirmation threshold. This was done using Fig. V.E.5, where the density of weeks-confirmed sources is shown as a function of the clustering threshold in the three crowded regions mentioned in Section V.E.7.a. The confusion limits were 3.1, 3.1, 2.7, and 1.6 sources per sq. deg in the 12, 25, 60, and 100 μm bands, respectively. This critical density was reached for all bands between clustering thresholds of 3 and 4; as expected, a value of 3.5 was still the optimal common choice for all bands.

To assess the significance of this choice, one can estimate the size of the area searched for close neighbors by the cluster analysis processor both in relative and absolute terms.

If an extended source is thought of as a square-wave in one dimension with total width W, then its corresponding rms size is $W/(2 \times 3^{0.5})$. The template used for detecting this source would have been itself square-wave shaped with a width W, and baseline segments W/2 on each side. A clustering threshold of 3.5 implies that 2 sources are considered close neighbors as soon as the baseline segments of their

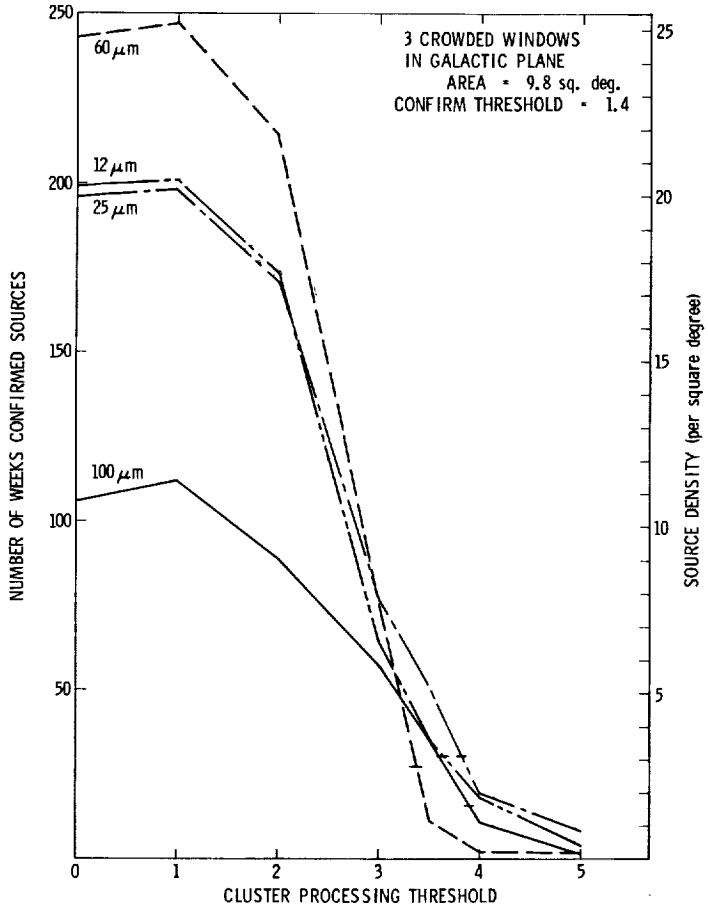

Figure V.E.5 A final check on the optimal thresholds: the weeks-confirmation threshold used here is the final one (1.4); the effects of cluster analysis are quite drastic, as expected. The tick mark on each curve indicates the critical source density; in all cases this density is obtained at thresholds greater than the optimal choice of 3.5.

respective detection templates start to overlap. This was clearly a reasonable, though somewhat conservative, way of guarding against confusion.

To estimate the angular distances involved in cluster analysis, the mean size of a sample of 111 sources in each band was calculated after clustering and weeks-confirmation; these mean sizes (always close to the medians as well) were 1.5′, 1.5′, 1.8′, and 2.2′ at 12, 25, 60, and 100 μm. The largest size in any band was 3′. On average, therefore, cluster analysis treated as "close neighbors" two sources within 10′ of each other at 12 and 25 μm, 12′ at 60 μm, and 15′ at 100 μm.

Cluster analysis fulfilled its objective in recognizing and setting aside large structures that were fragmented into small extended sources; this was the reason for the decrease in 100 μm and 60 μm source counts with increasing clustering threshold in Region A (Fig. V.E.1): cirrus was integrated into larger structures and dropped from further processing. It should be stressed, however, that cirrus is not absent from the small extended source catalog.

Cluster processing also fulfilled its objective as a confusion processor, as shown by the reduction by an order of magnitude of the source density in crowded areas (Fig. V.E.4) as the clustering threshold was varied from 1 to greater than 3.5. The sources that survived in densely populated areas were either very isolated or locally dominant. Isolated sources had no neighbors within the search window. Dominant sources were so much brighter than their neighbors that when the latter were combined with them the source parameters were barely altered, so that the size in particular did not grow beyond the maximum cutoff value. In confused areas most sources were dropped because they combined with a neighbor within the search radius, but far enough away that the combined structure exceeded the size limit. Such occurrences were recognized by the rejected source having an axial ratio much larger than unity.

It should, therefore, be stressed that the absence of a small extended source where one was expected, in crowded or uncrowded regions, may be due to the presence of a neighbor; the two sources may have combined into too large a source.

Table V.E.1 traces the number of small extended sources that were processed through clustering analysis and weeks-confirmation with the final choice for the thresholds in Regions A and B. The fraction of sources that survived cluster analysis and went on to weeks-confirm was much higher in Region A (high latitude) than in Region B (low latitude). At 12 and 25 μm, about 90% of the sources surviving cluster analysis did not pass weeks- confirmation and were therefore discarded; this percentage decreased at longer wavelengths but remained substantial. The main reason for this high failure rate was the lack of a rigorous requirement for hours-confirmation, such as was required for point sources. Detector noise or other transients could trigger detections which seconds-confirmed, and then were used to construct a source that was discarded only at weeks-confirmation.

The excess of 25 μm detections in Region A was a direct result of the lack of hours-confirmation: the dead detectors in this band relaxed the seconds-confirmation filter, and therefore allowed many more. stray detections than in other bands. The problem was hardly noticeable in Region B because most detections there were triggered by real but complex structure on the sky. That difference just reflects the contrasting definitions of Regions A and B: A has a low surface density of sources at the survey sensitivity, and the noise was dominated by the detector noise; B was dominated by confusion noise, in the sense that it was densely packed with detectable sources. The result was that most detections were discarded by cluster processing in Region B, and by weeks-confirmation in Region A. When all bands were combined it turned out that in both regions about one out of every seven detections ended up contributing to a weeks-confirmed source; this fraction was remarkable similar for Regions A and B.

E.8 The Small Extended Source Catalog

Sources included in the small extended source catalog were obtained from the pool of weeks-confirmed sources and had to survive additional filtering to reject spurious or unreliable sources due to crosstalk, or to weak point sources combining with radiation hits and noise (see the catalog introducton).

Associations were made between small extended sources and objects in other astronomical catalogs, following the procedure used for the point source catalog (Section V.H.9). The only difference was that the minimum search radius for all associations was 120″.

Table V.E.1a Processing Results in Region A (High Galactic Latitude)

Band	Number of Seconds/ Hours Confirmed	Number Surviving Cluster Processing	Number of Weeks-Confirmations	NCOVR(2)	NCOVR(3)	NCOVR(>3)*
12 μm	2593	2507	88	74	13	1
25 μm	3339	3249	101	70	31	0
60 μm	2170	1989	196	147	45	4
100 μm	1753	1249	209	174	30	5

Table V.E.1b Processing Results in Region B (Galactic Plane)

Band	Number of Seconds/ Hours Confirmed	Number Surviving Cluster Processing	Number of Weeks-Confirmations	NCOVR(2)	NCOVR(3)	NCOVR(>3)*
12 μm	5095	2212	350	274	70	6
25 μm	4988	2206	364	261	95	8
60 μm	8706	2104	364	296	65	3
100 μm	4036	1687	369	273	86	10

* NCOVR(n) is the number of weeks-confirmed sources that were detected on n hours-confirming survey coverages.

F. Asteroids and Comets

To achieve the objective of high reliability in the measurement of inertially fixed sources, the survey required that a source be repeatedly detected on several time scales (see discussion in Section V.D.1). This multiple confirmation process provided the means of detecting and rejecting objects moving at a variety of angular rates with respect to the inertial sky and the orbiting satellite. Detections which failed seconds-confirmation were due to radiation hits and infrared sources near the spacecraft, such as material emitted by IRAS itself, space debris, and Earth orbiting satellites. Failures at hours- and weeks-confirmation were used to detect comets and asteroids, effectively rejecting them from the catalog.

Solar system objects moving across the sky more rapidly than about 1′ per hour failed the hours-confirmation test. This test was used during the mission to search for fast-moving objects and resulted in the discovery of six comets, an extensive cometary debris trail, and two Apollo asteroids, one of which may be an extinct cometary nucleus. The details of the search for fast moving objects are given in Section III.D.1.

Asteroids and comets moving more slowly than 1′ per hour would hours-confirm, and thus reside in the WSDB. To assess the efficiency of the weeks-confirmation filter, the coordinates of all hours-confirmed sources were positionally associated with the coordinates predicted from the orbital elements of asteroids numbered 1 through 2736, 12 periodic comets, and the 6 outer planets. The tagged sources enabled one to trace known solar system objects through the confirmation process. An analysis of these sources is given in Section VII.F.

G. Extended Source Products

G.1 Processing Overview

The basic approach to the compilation of the two-dimensional images and related time-ordered files was to select high-quality data meeting criteria based on observing conditions and the performance of individual detectors. Since extensive automatic confirmation tests were not applied as in the case of the discrete sources, internal consistency between different detectors within each survey observation was imposed by adjusting individual baselines and responsivities to produce the same mean brightness as the band average for that observation (the "destriping" operation). Weighted averages of the data were used to mosaic data from multiple survey scans of the same region into single digital images. Consistency between the scans forming an hours-confirming coverage was checked by human scanning of difference images; significantly discrepant data were deleted from the images. Finally, since the zodiacal emission toward any given direction on the celestial sphere depended upon the Earth's orbital position and Sun-referenced observation angles at the time of the observation, data obtained in the three hours-confirming coverages of the sky were processed and presented separately. A file needed to reconstruct the observing geometry for each observation of a given region of the sky, the Zodiacal Observation History File, was produced.

G.2 Quality Checking, Selection, and Weights

Calibrated time-ordered detector data were used for the extended emission files if they had been obtained under acceptable observing conditions with respect to nuclear radiation event rate, adequate off-axis distance from strong potential sources of stray light, and satellite scanning rate. Data were deleted near the beginning and end of scans when the scan rate deviated from the nominal survey value, or if the detector signal saturated the analog-to-digital converter.

The radiation blanking time introduced by triggering of the spike "deglitcher" in two detectors of each band was averaged over 2.5 sec intervals. Data were deleted from any band during any interval in which the dead time introduced by the deglitcher exceeded 10% in that band.

The processing was designed to allow definition of a cone of avoidance for closest approach to the Earth, Moon, Mars, Jupiter, and Saturn. Stray light performance of the instrument was examined early

in the mission, and it was concluded that the nominal scan constraints on closest approach to the Earth and Jupiter produced data of acceptable quality for extended source processing, and that no constraint on data near Saturn or Mars would be imposed. No data within 30° of the Moon were included in the extended source products. This resulted in a series of lune shaped gaps spread across the ecliptic plane in each of the three sky coverages (Fig. III.C.6).

A weight factor was assigned to each sample from each detector as a quality indicator for that sample. The weights followed the samples through all subsequent averaging, image creation, and image mosaic processes, yielding a weight map corresponding to each intensity map produced. A general weight was assigned to data from each detector based on the nominal sensitivity and noise of that detector observed early in the mission. Inoperative detectors were assigned zero weight. The weight was proportional to the variance of the data sample, so that it could be used as a statistical weight in an averaging process.

The extended source images were not intended to give high-quality photometric information for point or small extended sources. However, to maintain consistency for small sources, data from the two edge detectors in each band which were substantially smaller than nominal detectors in that band (detectors 26, 47, 39, 42, 11, 31, 4, and 55) were deleted.

G.3 Phasing, Sorting, and Gaps

In preparation for smoothing and binning the data for the various extended source products, the time-ordered calibrated data were adjusted on a detector-by-detector basis to align samples obtained at the same sky position of the telescope boresight. This phasing took account of both the scan rate of the telescope and of electronic phase shifts in the sampling of individual detectors. Detector data were also sorted into cross-scan order in each band according to their centroid positions. Because of the phasing operation, some data were lost at the beginning of each scan and whenever a gap in the telemetry stream occurred. The start-up time for the phasing was 11 seconds, or about 3/4° on the sky.

G.4 Conversion to Surface Brightness

Detector data were converted from calibrated in-band fluxes (W m^{-2}) to surface brightness, (W $m^{-2}sr^{-1}$), using an effective instantaneous field of view for each detector obtained from slow scans of point sources across the array (Table IV.A.1).

G.5 Compression and the Time-Ordered Files

The detector data were compressed in the in-scan direction prior to projection into the image domain. Compression was accomplished by filtering and then decimating in order to prevent aliasing. A symmetric filter was desired to provide zero phase shifts, and a Lanczos single smoothed filter ($(\sin x/x)^2$ weighting in the window) was selected. The filter width was chosen for each band to provide two output samples per second, corresponding to a nominal 2′ sample spacing. No compression or interpolation was applied in the cross-scan direction because the construction of the telescope's focal plane array produced samples with 2′ spacing. These compressed data formed the time-ordered input for the sky plates and Galactic plane maps.

A lower resolution time-ordered file of intensity data was also created. The Zodiacal Observation History File (ZOHF) contains the data samples obtained by averaging data from all detectors in each

band (according to their weights) over an interval of 8 seconds of time. This provides data samples at approximately 30′ intervals in both the in-scan and cross-scan directions. The file also retains, in addition to celestial coordinates, the Sun-referenced observation angles and time, and information necessary to evaluate the zodiacal emission contribution to the intensity in each sample (see discussion below). Data from this file were used to create the low-resolution all-sky maps.

G.6 Destriping

In the course of reducing the scan data into images, it was found that, in spite of the efforts to calibrate the gain and offset for each detector individually, small inconsistencies remained between detectors in a given band within a single scan. Such systematic inconsistencies showed up clearly as "stripes", i.e., persistent streaks in the in-scan direction in the images on the cross-scan scale of a detector length. A "destriping" procedure was developed to remove these high spatial-frequency inconsistencies while preserving the best available photometric information for the band as a whole. The procedure consisted of determining a responsivity and baseline correction for the data from each detector for each survey scan, and then applying that correction to the time-ordered data file prior to projection into images. The corrections were determined by requiring that the intensity from each detector follow the weighted band-average intensity during that observation. This procedure depended on the scan passing over areas of both low and high average background so that responsivity effects could be separated from baseline effects. Prominent small sources (high curvature regions) in the data were excluded in computing the averages. If insufficient data were available in a given observation, or if the correlation of the output of a detector with the band average was poor, the corrections determined in the previous observation were used.

This process reduced the striping on a scale of a few arc minutes introduced by variations among the detectors in the focal plane. It did nothing to remove the 1/2° wide stripes caused by variations in calibration or sky brightness between different scans of the same piece of sky. The treatment of these wider stripes is discussed below under the topic of consistency checking in Section G.8.

G.7 Projection into Sky Maps

After phasing, smoothing, and resampling to produce the compressed data, the time-ordered detector data formed the equivalent of a two-dimensional array 15 or 16 samples wide (depending on the band) and several thousand samples long. Exact positional information was carried for every other sample of the two detectors at the edges of the array in each band, the "tie points". The map projection was accomplished by projecting the exact positions of the tie points into the line and sample space of the map images with the mapping transformation, and doing a bi-linear interpolation in line and sample space to get the projections of the other samples. All projections were done so that the sky coordinate associated with a pixel refers to the position at the center of the pixel. The map projections used are discussed in Section X.D. Once assigned a position in image space, a particular data sample was binned by dividing the weight of the sample among the nearest four bins with an inverse bi-linear interpolation, multiplying the sample value by the divided weights and accumulating the weighted samples into the four bins of the intensity image and the weights into the four bins of the weight image. Maintaining these separate weighted intensity and weight images facilitated combining data from multiple scans into a single image. The final average intensity image was produced by dividing the weighted intensity image, pixel-by-pixel,

by the weight image. These procedures applied to the processing of the low-resolution all-sky map data as well as the sky plate data.

G.8 Consistency Checking and Removal of Bad Data

After the data had been assembled into maps, the images were examined to check for anomalies. One coverage of the sky consisted of 1/2°-wide survey scans spaced every 1/4°. By selecting alternate scans, a coverage could be split into two sets of non-overlapping scans, each of which essentially covered the whole sky. The check consisted of examining the difference image between these two halves of a sky coverage. Anomalies discovered in this way were then classified and, if necessary, examined further in the two direct intensity images. If the anomaly was severe, the offending data were removed from the map. Three classes of anomalies were removed:

1) Obvious flooding of the focal plane by near-field objects.

2) Scans or sections of scans which were substantially noisier than their neighbors. The random noise level needed to be about two times larger than normal before this effect was noticeable, so relatively few data were removed for this reason. More frequently, the destriping strategy would fail and noise in the form of objectionable 2′-wide stripes would appear. Scans causing such stripes were rejected.

3) The brightness of the scan differed substantially from the generally smooth background level of its neighbors. The criterion used for removal was a difference of more than 10% of the baseline value from neighboring scans on adjacent orbits. A substantial amount of data was removed for this reason. Particularly offensive in this respect were 25 μm scans made near edges of the South Atlantic Anomaly (SAA) where bias-boost (Section III.C.4) procedures were not used.

Data removal was accomplished by adding the offending scan or section of a scan back into the map with the negative of its original weight.

Several known residual anomalies remain from this cleaning process. No attempt was made to remove or even find small scale discrepancies between different scans of the same piece of sky, and many small, generally point-like, sources remain in the maps which DO NOT appear in the same place in two different scans. This point cannot be overemphasized; when using the sky maps to look at small sources, even bright ones, at least two separate coverages MUST BE COMPARED or THE USER WILL BE FOOLED. Many, maybe most, of the non-confirming sources are due to asteroids; however, they do occur in all parts of the sky, and caution must be exercised in all cases.

Noticeable 1/2°-wide stripes run across many of the sky plates. Regularly spaced patterns of these stripes were due to the effects of non-boosted SAA crossings, as mentioned above. Isolated stripes were due to some undetermined calibration anomaly. Almost none of the stripes exceed the 10% difference criterion; however, an occasional stripe which differs by more that this has been left in to prevent creation of a hole in the map.

It is not known at this time whether the scans deleted due to non-boosted SAA crossings, or their neighboring scans, were correct. The maps have been made flatter by the deletions of data, but the possibility of small, systematic DC calibration errors in the middle of scans, deemed unlikely, cannot be excluded.

No attempt has been made to exclude the effects of photon-induced responsivity enhancement in the data (see Section IV.A.8). For instance, passage across bright regions in the Galactic plane increased the responsivities of the 60 and 100 μm detectors for some time after passage. Similar effects near bright discrete sources are evident as well. Again, comparison among the three sky coverages should be made to avoid unrecognized problems due to these effects. All three coverages should be compared for this purpose, since the first two coverages generally passed over a given piece of sky in nearly the same direction, while the third coverage, where present, generally passed in a different direction.

G.9 Final Map Image Generation

The final steps in production of sky plate maps were the reduction to average intensity, conversion from in-band average intensity to brightness density (Jy sr^{-1}) and application of final calibration data. Reduction to average in-band intensity was accomplished by division of the weighted intensity image by the corresponding weight image. The conversion to brightness density was based on the knowledge of the shapes of the filter passbands of the instrument and the assumption of a radiation source with an energy distribution flat in flux per octave. Small corrections modified the baseline and rescaled the resulting brightness on a pixel-by-pixel basis to reflect the final calibration.

Maps of the sky within 10° of the Galactic plane were made by remapping the pixels from the sky plates into Galactic coordinates using the cylindrical projection described in Section X.D. The remapping was done by the tie point technique described above, where the full map transformation was applied only to a subset of the pixels and linear interpolation is applied to the rest. Binning of a data sample into the nearest four pixels was also done as described in Section V.G.7.

The low-resolution all-sky maps and the Zodiacal Observation History File were subject to the same modifications as the sky plates for final generation processing.

H. The Point Source Catalog

H.1 Processing Overview

After the Working Survey Data Base (WSDB) was completed by the sequential processing of every SOP, several programs processed that data base to create the catalog.

The major steps were as follows:

1. Final calibration corrections,
2. Clean-up processing, which forced sources closer than 30" (in-scan) and 90" (cross-scan) to weeks-confirm,
3. Point source and small extended source neighbor tagging,
4. Cirrus (highly structured 100 μm emission) flagging,
5. High source density processing,
6. Variability tagging and average flux computation,
7. Association and classification of low-resolution spectra,
8. Associations with previously known astronomical sources,

9. Catalog source selections,
10. Transformation of coordinates, assignment of position uncertainties and assignment of source names.

Each of these steps is discussed separately below except for step 1. Step 1, incorporating the final calibration, is discussed in Section VI.B.

H.2 Clean-Up Processing

An analysis of sources in the WSDB that were within several arc minutes of each other showed that roughly 5% of all sources did not have every possible hours-confirmed detection combined into one source. There were three reasons for this. First, sources scanned more than five times within one hours-confirming coverage were separated into two distinct hours-confirming detections due to an upper limit of four scans per hours-confirming detection imposed by the processing. Only one of these two detections was allowed to weeks-confirm with other hours-confirmed detections already present in the WSDB. Second, sources that suffered band merging difficulties occasionally produced two hours-confirmed detections out of one hours-confirming coverage. Only one piece was allowed to weeks-confirm. Finally, due to the way the minisurvey scans were scheduled, the first survey coverage was not allowed to weeks-confirm with some of the minisurvey sources. Each of these cases was sufficiently well defined to allow a clean-up processor to give these pieces a chance to weeks-confirm with each other. Additional problems were caused by radiation hits, source confusion and by multiple scans inadvertently spaced too close together in time to allow weeks-confirmation. These sources were cleaned up in a two-step process. First, all weeks-confirmed sources were given the opportunity to confirm using the standard threshold with any hours- or weeks-confirmed neighbors located within 30" in-scan and 90" cross-scan. Most sources that confirmed at this stage were ones that had earlier been denied the opportunity for purely technical reasons. A single source with a refined position resulted.

The second stage of clean-up was to force all weeks-confirmed sources to merge with any neighbors located within 30" in-scan and 90" cross-scan, whether or not the sources were confirmable according to the weeks-confirmation decision process. No position refinement attempt was made. This step proved necessary because analysis of near neighbors showed that most were caused by the incorrect splitting of single sources in confused regions by the various confirmation processors.

A separate processing problem was partially solved by the clean-up processor as well. Two normal survey scans were placed within one layer of the minisurvey (Section III.C.11, Table III.1). These scans were inadvertently processed twice; once as part of the minisurvey and once as part of the regular survey. Thus some sources (those missed by that layer of the minisurvey) had identical hours-confirming detections present as two separate entries within the source. One of these was deleted by the clean-up processor, although nothing could be done to remove the double weight given to that sighting in the position refinement process.

H.3 Neighbor Tagging

The relative isolation of a source provides the user with an indication of its quality. Associated with each source are the numbers of hours- and weeks-confirmed point sources and small extended sources. The search area used was a box 6′ (half-width) in-scan, which was the largest detection shadow-

ing distance (Section V.C.7), and 4.5′ (half-width) cross-scan, which was a detector length. Neighbors were tagged before the clean-up processor was applied. However, neighbors that were confirmed with the source during clean-up were not counted, nor, due to an error, were any sources within a box that had been successfully cleaned up.

If no neighbors were found, it is unlikely that processing or confusion problems exist. The presence of neighbors should make the user check those neighbors to investigate the possibility that the source was extended, was in a confused patch of sky, or suffered some other problem.

H.4 Cirrus Flagging

At 100 μm the infrared sky is characterized by emission from interstellar dust on all spatial scales, known affectionately as "infrared cirrus". A significant chance exists that ANY catalog source has been affected by components of this long-wavelength emission on the point source scale. Four separate quantities were derived for each source to assess the importance of contamination by cirrus. While these are imperfect flags (a source may be affected by cirrus without any of these flags being set, or may not be affected at all even at high values of the flags) they work for the majority of sources and provide a simple description of the sky at 100 μm in the vicinity of each catalog object.

Flag 1 (CIRR1) is the density of WSDB sources (hours and/or weeks-confirmed) detected only at 100 μm within a ±1/2° ecliptic coordinate box of the source position. Cirrus typically produces strings of such sources, giving rise to a high density. Weak cirrus, producing only a few 100 μm sources, may still affect the quality of catalog sources.

Flags 2 (CIRR2) and 3 (CIRR3) come from the 100 μm extended source data at a resolution of 1/2° (see Section V.G.5). Although the angular resolution is a serious limitation for these flags, since the angular scale of point sources is 10-30 times smaller, cirrus on the point source scale usually shows structure on the 1/2° scale as well.

CIRR2 was derived from a spatially filtered version of the 1/2° averaged 100 μm emission. The value of the filtered sky brightness at a point, J_i, is given by

$$J_i = -0.5 \times I_{i-1} + I_i - 0.5 \times I_{i+1} \qquad \text{(V.H.1)}$$

where adjacent measurements, I_i, of the total intensity were separated by 1/2° in the in-scan direction. This filtered surface brightness was converted into a "cirrus flux", F_c, by multiplying J_i by the solid angle of a typical 3′×5′ 100 μm detector. The cirrus flux was then compared with the 100 μm flux (or upper limit) of each catalog source, F_s. The value of CIRR2 was scaled logarithmically to fit in the range 1 to 9 according to

$$CIRR2 = (8/3) \times \log (F_c/F_s) + (19/3) \qquad \text{(V.H.2)}$$

A value of CIRR2=1 corresponds to the cirrus flux being less than or equal to 0.01 of the source flux while CIRR2=9 corresponds to the cirrus flux being equal to the source flux. As described in Section VII.H, CIRR2 less than about 4 is indicative of little or no cirrus contamination, while larger values probably indicate significant contamination. A value of CIRR2=0 indicates that no 100 μm extended emission data were available.

Flag 3 (CIRR3) is the total intensity of the 100 μm extended emission in a 1/2° beam (MJy sr^{-1}). High values are indicative of a large column density of interstellar dust.

A fourth cirrus indicator is the presence of nearby small extended sources at 100 μm. Since the small extended sources have sizes much closer to point sources than the 1/2° data, this flag (SES1), which gives the number of hours-confirmed small extended sources, will normally be an accurate cirrus indicator. However, because of the higher thresholds used for this processing, weak cirrus may not be detected.

As discussed in more detail in Section VII.H, if any of these flags takes on a large value, one should be cautious. Cirrus can affect the point source flux in any band by causing band-merging difficulties and can certainly affect the quality of a quoted 100 μm flux.

H.5 Average Flux Computation and Variability Analysis

In the computation of an average flux for each source, three levels of flux quality were recognized:

1) *High quality* fluxes had no confirmation problems other than missing detections due to failed detectors, with at least one hours-confirming detection with *no* problems. For *aficionados*, at least two hours-confirming sightings with flux status, FSTAT =4 or 7, with at least one 7, were required (see Section V.D.8).

2) *Moderate quality* fluxes were believed to be reliable, but were missing some detections, usually because the source was at the detection threshold. Two hours-confirming sightings with FSTAT=3-7 were required.

3) *Upper limits* were given for bands lacking high or moderate quality fluxes. Measurements in these bands had no more than one measurement with FSTAT=3-7. The upper limits were derived from all of the measurements. An analysis showed that measurements in a given band with only a single detection (FSTAT=2) within an hours-confirming coverage were severely contaminated by radiation hits and were unreliable. These single "detections" were used only as upper limits. Quoted upper limits are nominally 3σ values.

High and moderate quality fluxes were obtained by log-flux averaging of individual acceptable hours-confirmed fluxes weighted by the inverse of the log-flux variances. If the flux discrepancy flag was set (see below) and the source had more than two hours-confirmed fluxes, then one flux was removed from the averaging process. The rejected flux was the one farthest from the median flux in units of the error. The median flux was arbitrarily picked to be the larger of the middle two fluxes when there was an even number of fluxes present. The rationale behind this was that discrepant fluxes occasionally occurred because of radiation hits, a passing asteroid, a failed detector, or processing problems. With more than two measurements it was possible to weed out the discrepant flux. For quoted fluxes, a χ^2 test was applied to each band. If the value of the reduced χ^2 was greater than 9, the flux discrepancy flag was set in that band.

Uncertainties quoted for high and moderate quality fluxes were the maximum of: a) the uncertainty of the mean derived from the accepted fluxes; or b) the uncertainty of the mean derived by propagating the quoted uncertainties of the individual, accepted flux measurements.

Fluxes quoted as upper limits were obtained from the the largest flux (or limit) for sources with only two hours-confirmed sightings and from the median flux for sources with more than two

detections. The median was taken as the largest of the two middle fluxes for sources with an even number of observations. The flux discrepancy flag was set if the largest and smallest flux from all the limits for low quality detections differed by more than a factor of 3.

Sources with high or moderate quality fluxes at both 12 and 25 μm were examined for variability. A percentage probability of being variable was quoted for sources whose fluxes at BOTH 12 and 25 μm either increased or decreased significantly from one hours-confirmed sighting to another. In other words, the changes in flux at 12 and 25 μm had to be correlated. Although variability could have been detected in other ways, this method led to a simple and reliable determination of variability of a large number of sources. For sources with more than one pair of sightings, the value determined for the pair of sightings with the greatest likelihood of variability was given.

The probability that a source brightness varied was calculated by comparing the number of sources with *correlated* flux excursions exceeding m σ at 12 and 25 μm, $N_{corr}(\geq m)$, with those sources showing *anti-correlated* flux excursions exceeding m σ in both bands, $N_{anti}(\geq m)$. The probability that a source is variable is given by

$$p(m) = \frac{\frac{N_{corr}(\geq m)}{N_{corr}(\geq o)} - \frac{N_{anti}(\geq m)}{N_{anti}(\geq o)}}{\frac{N_{corr}(\geq m)}{N_{corr}(\geq o)} + \frac{N_{anti}(\geq m)}{N_{anti}(\geq o)}} \qquad \text{(V.H.3)}$$

This approach was adopted because there are many ways in addition to true variability that a discrepant flux could be obtained, including radiation hits, processing problems caused by failed detectors and confusion with transient spurious sources which would increase the flux in one band at one sighting. Thus, while Eq. (V.H.3) is not rigorous, it gives a good measure of the significance of any flux excursion. As discussed in Section VII.D.3, the sources deemed likely to be variable ($p>0.9$) represent approximately 20% of the 12 and 25 μm objects in the catalog.

H.6 High Source Density Regions

The density of sources in the WSDB exceeds the resolving capability of the instrument over some parts of the sky. The nature of both the sky and the instrument make this a wavelength-dependent effect; at 12 μm the instrumental resolution was less than 1′ and the sky was dominated by point sources, while at 100 μm the resolution was about 4′ and much of the sky was dominated by highly structured diffuse emission.

The overriding concern in developing a strategy for regions of high source density was to insure the reliability of the information presented in the point source catalog. Reliability, in this context, has three meanings: 1) a point source must be an inertially fixed, celestial source (the basic meaning of reliability throughout the catalog); 2) a source must represent a very compact structure that, to the extent possible, is not merely a fragment of a complex background; and 3) the intensity measurements reported in the catalog must repeatably represent the brightness of a source above the local background.

The first step in processing high source density regions was to determine whether the number of sources in a given wavelength band in a 1 sq. deg bin exceeded a "confusion limit". Sources in bins with more than the threshold number of sources were subject to additional criteria for inclusion in the catalog. The decision to apply the criteria was made independently on a band-by-band basis. Thus, a multi-band source might have high source density rules applied to its 100 μm measurements, but not to its 12 μm measurements. Once the high source density rules were invoked in a band, each source in that band in that bin was examined for the quality and repeatability of its individual measurements and for its isolation from other potentially confusing sources. The high source density processor determined whether the measurement of the source in that band was of high, medium or low (upper limit) quality, where these definitions differ from those in lower density areas, and calculated an average flux for the source in that band. Many sources were found wanting and were excluded from the catalog.

The high source density selection criteria used only information contained within the WSDB to judge the relative merits of a source. The confusion processing algorithms were developed and tuned in two confused regions, one in the Large Magellanic Cloud (LMC) and one near the Galactic Center. Detector strip charts were examined for many of the sources to verify the validity of the selection criteria.

H.6.a Location of High Source Density Regions

The confusion-limited source density is determined by the instrumental angular resolution and how many detector beam areas are, on average, required per source for a reliable measurement. A conservative limit of 25 beams per source leads to maximum source densities of 50, 50, 25 and 12 sources per sq. deg at 12, 25, 60 and 100 μm (assuming a detector area of the nominal in-scan detector size times the detector cross-scan width). Aitoff projection maps in Galactic coordinates showing the density of sources with moderate or high quality fluxes (according to the basic rules described in V.H.5) in a given wavelength band are shown in Figs. V.H.1a-d. At 12, 25 and 60 μm the region within 3-5° of the Galactic plane and within ±100° of longitude of the Galactic center plus small regions in Orion, Ophiuchus and the LMC present the major problem areas. The 100 μm sky presents a more complicated picture because the regions of high source density cover large parts of the sky due to the infrared cirrus.

To set the thresholds for high source density processing, the numbers of sources in 1 sq. deg and 0.25 sq. deg bins were examined in the WSDB. It was determined that processing all 1 sq. deg bins containing at least 45, 45, 16, and 6 sources (at 12, 25, 60 and 100 μm) would clean up 90% of all 0.25 sq. deg areas with confusion-limited source densities. Thus, any 1 sq. deg bin (defined in ecliptic coordinates, cf. Appendix X.1) containing at least the threshold number of sources in a particular band was processed according to high source density rules in that band. No attempt was made to join together high source density regions into a few simply connected areas. A list of the high source density bins in each band is available with the machine readable version of the catalog.

High source density rules were occasionally invoked for wavelength bands with fewer than the threshold number of sources in a bin if failure to include that band would have resulted in a non-adjacent set of bands being processed, i.e., a "spectral hole". Thus, for example, if the number of sources at 25 and 100 μm, but not at 60 μm, exceeded the thresholds, the decision was made to process 60 μm sources as well.

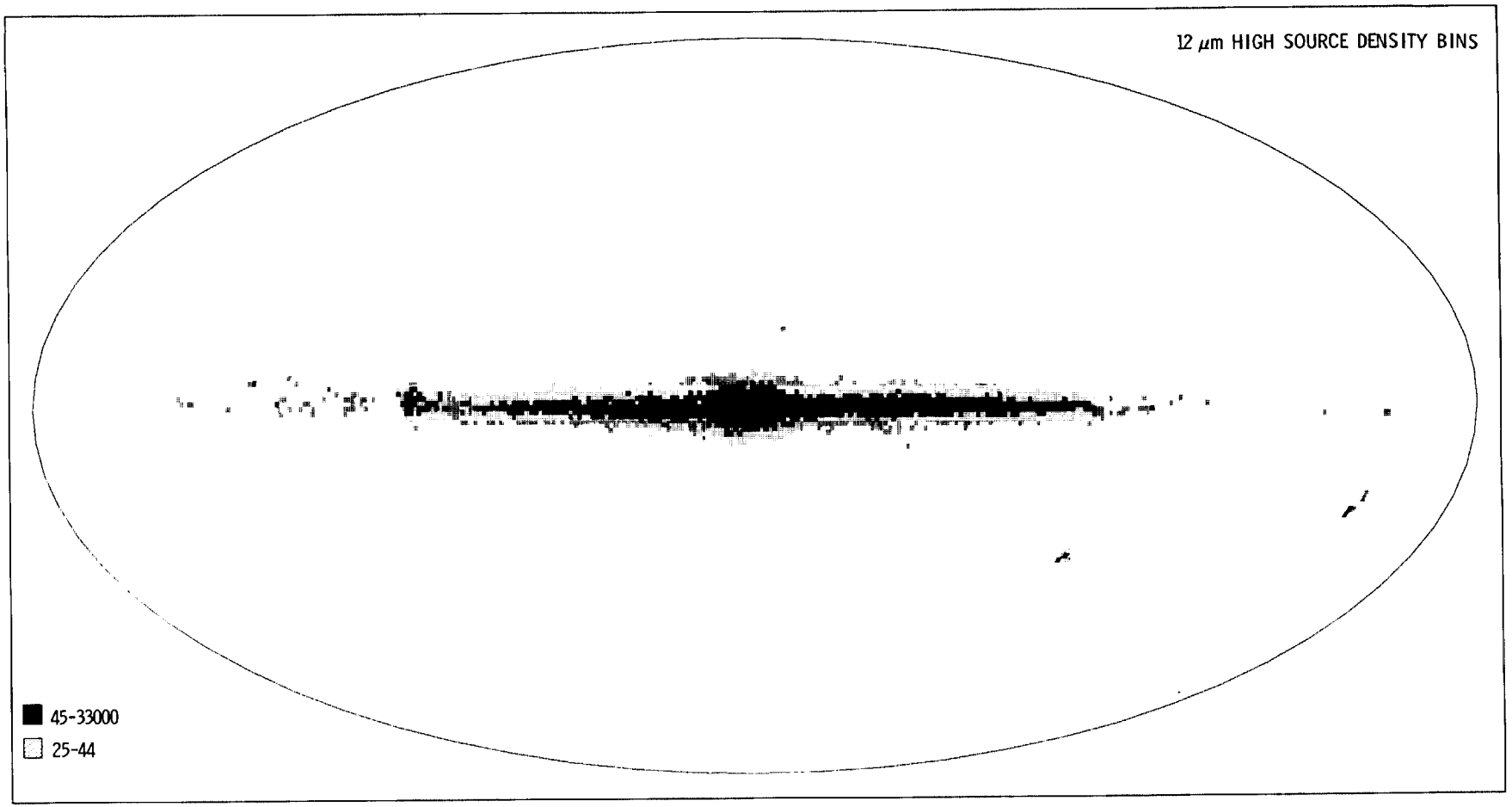

Figure V.H.1.1 The parts of the 12 μm sky processed according to high source density rules are shown in an Aitoff projection in Galactic coordinates. The black regions contain more than 45 sources per sq. deg, the threshold for high source density processing; the grey areas contain more than 25 sources per sq. deg, one-half the confusion limit.

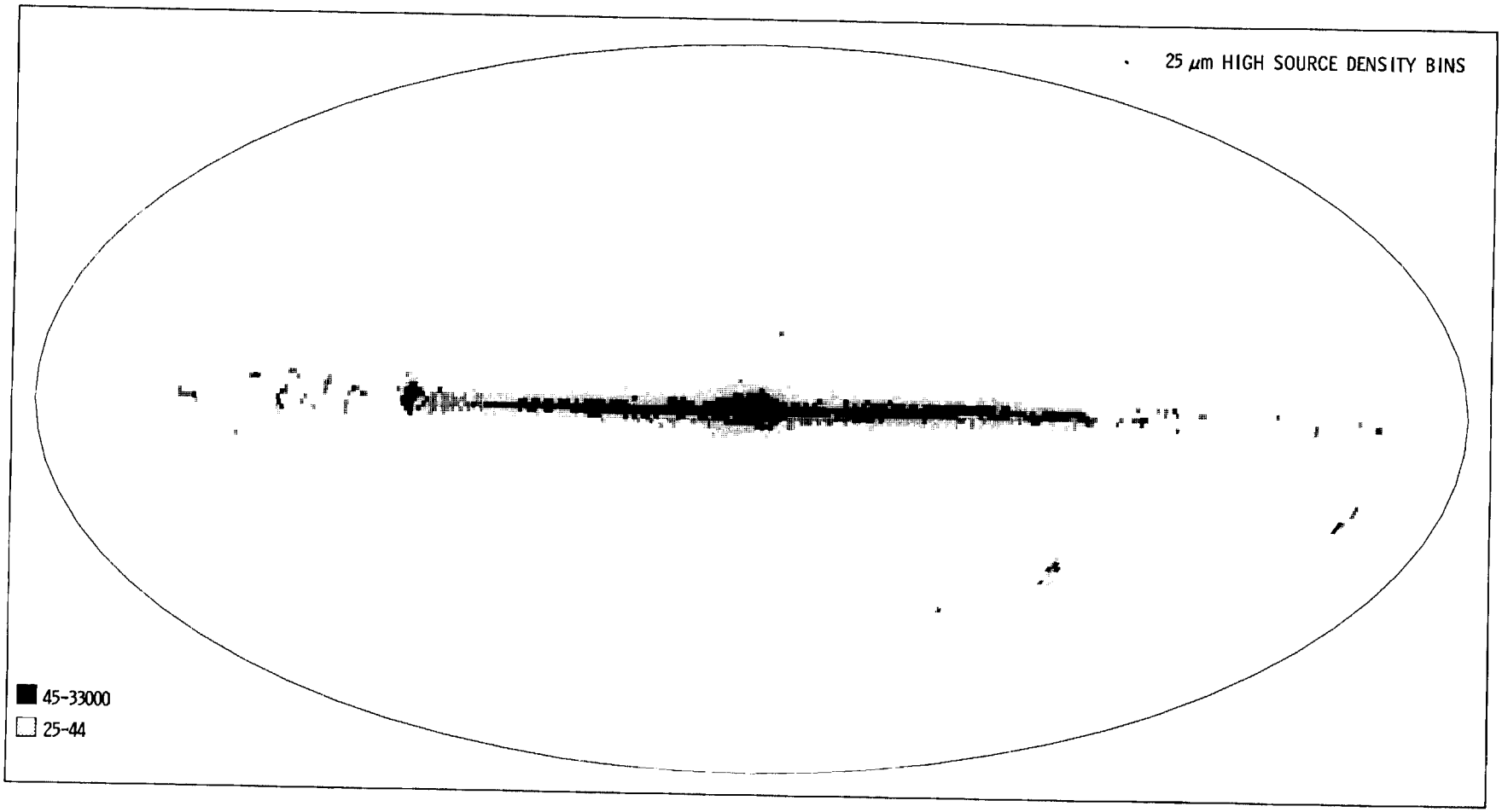

Figure V.H.1.2 The parts of the 25 μm sky processed according to high source density rules are shown in an Aitoff projection in Galactic coordinates. The black regions contain more than 45 sources per sq. deg, the threshold for high source density processing; the grey areas contain more than 25 sources per sq. deg, one-half the confusion limit.

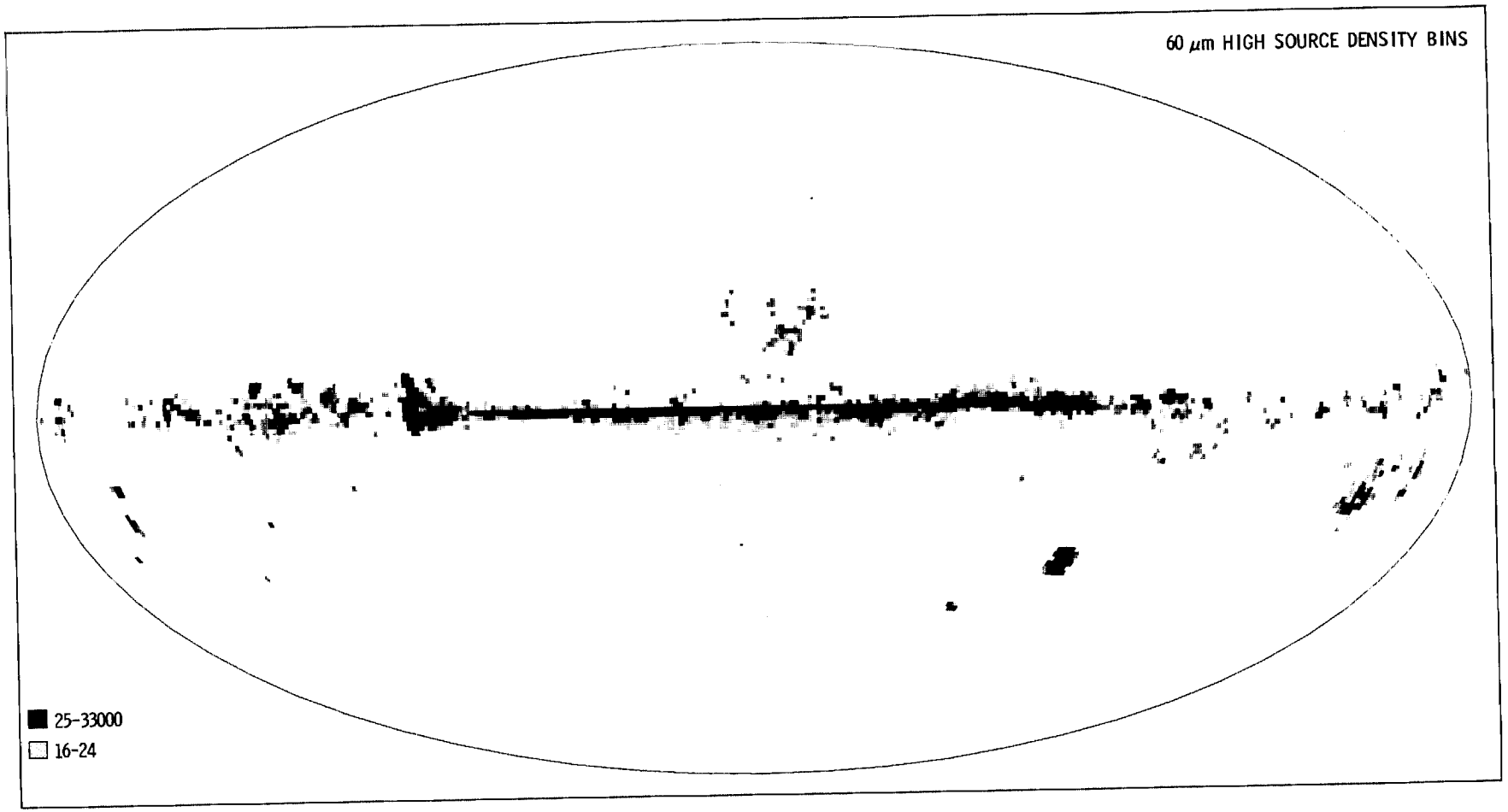

Figure V.H.1.3 The parts of the 60 μm sky processed according to high source density rules are shown in an Aitoff projection in Galactic coordinates. The black regions contain more than 16 sources per sq. deg, the threshold for high source density processing; the grey areas contain more than 12 sources per sq. deg, one-half the confusion limit.

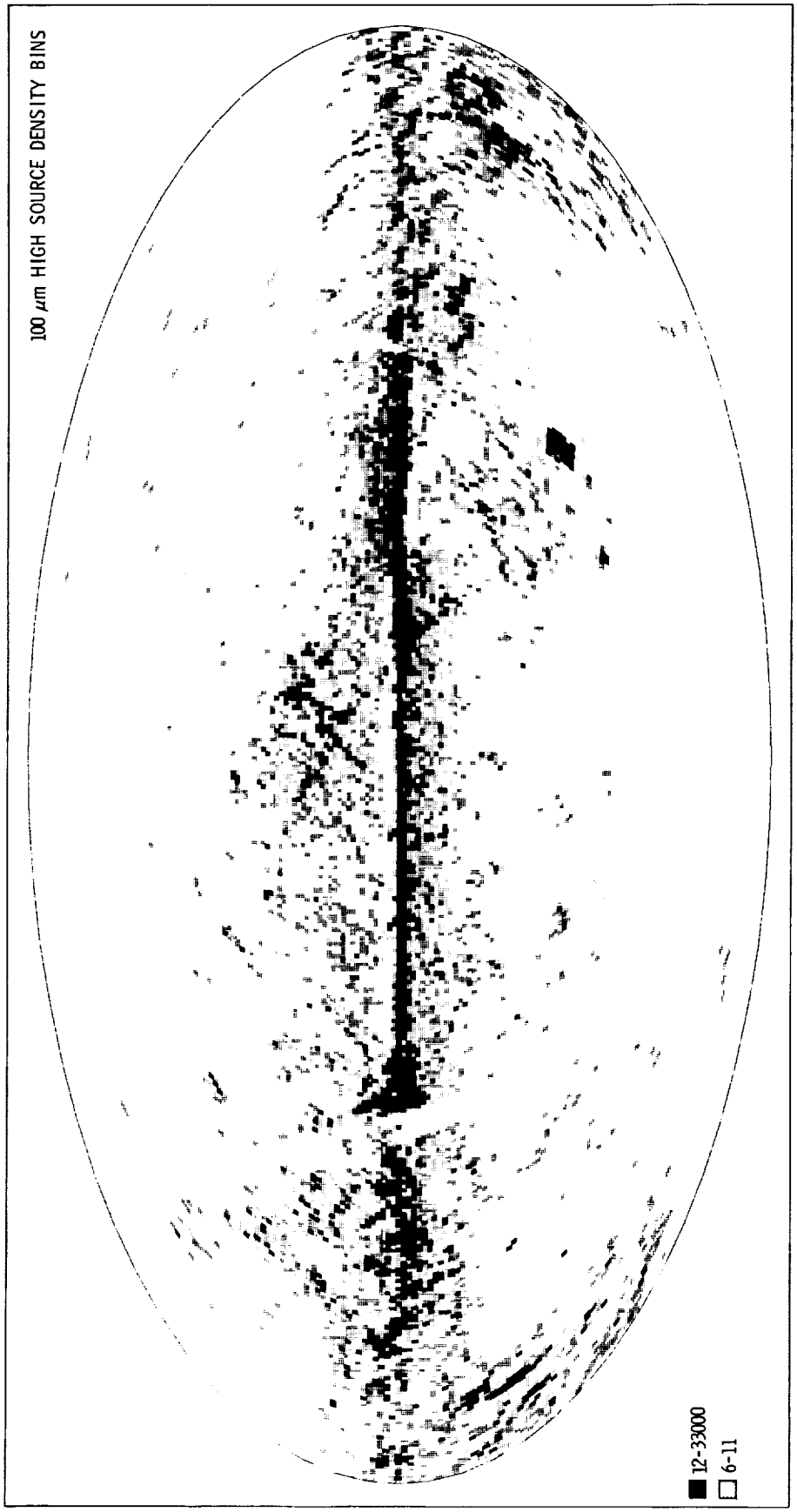

Figure V.H.1.4 The parts of the 100 μm sky processed according to high source density rules are shown in an Aitoff projection in Galactic coordinates. The black regions contain more than 12 sources per sq. deg, the confusion limit; the grey areas contain more than 6 sources per sq. deg, the threshold used for high source density processing.

H.6.b Catalog Selection Criteria in High Source Density Regions

In unconfused regions where the reliability of a single hours-confirmed source is high, the criteria for including sources in the catalog emphasized completeness. In high source density regions, however, the criteria emphasized reliability. Thus, the first step toward weeding out unreliable point sources was to stiffen the requirements for accepted detections and valid weeks-confirmed sources in a given band.

The concept of high, medium and low quality fluxes is crucial to understanding how sources were included in the catalog. High quality measurements were those which passed through the entire data processing chain without blemishes such as more than one missing detection (per hours-confirmed sighting), even those missing due to failed detectors. Medium quality fluxes could suffer from a variety of problems due either to the faintness of the source, the presence of failed detectors, the complexity of the background or peculiarities of the data processing. Low quality fluxes were upper limits based on an estimate of the local noise. The definition of the relative quality of fluxes and the way that sources were selected for inclusion in the catalog on the basis of their quality differ depending on whether a source was found in a region of high or low source density.

In regions of high source density, tests were applied successively to the measurements of a source to determine its quality. If all of the criteria described below were satisfied, the source was deemed to have a high quality measurement in that band. If only a subset of the criteria were satisfied, then the source was considered to have a medium quality measurement in that band. If none, or only a few, of the criteria were satisfied, then an upper limit was given for the flux of that source. *To be included in the catalog a source had to have a high quality measurement in at least one band.*

For high source density regions the requirements for a high quality flux were stiffened by demanding that at least two hours-confirmed sightings in one band each meet all of the following criteria: 1) seconds-confirmed detections on at least two orbits; 2) a minimum correlation coefficient of 0.97, corresponding to a local signal-to-noise ratio of about 6; and 3) fewer than four detections within the seconds-confirmation window on a given scan. Simple edge detections (3 detections) were permitted.

A high quality measurement had to be repeatable. The ratio of brightest to faintest high quality flux measurements in a band had to differ by less than a factor of 3.0. If this repeatability requirement was not satisfied, then the brightest measurement was taken as a medium quality measurement. Although this requirement in principle biases the catalog against variable sources in high source density regions, in practice, relatively few sources were rejected for this reason.

H.6.c Weaker Neighbors

The above rules all pertain to a single source, independent of its environment. The weaker neighbor algorithm was designed to remove sources adversely affected by brighter, neighboring sources. The "neighbor" of a source with a high quality flux in some band must itself have at least two hours-confirmed measurements in that same band and lie within a wavelength dependent position window. If the brightest flux of one source was a factor of 1.2 weaker than the faintest flux of the other object in the same band, then the fainter object was marked as a "weaker neighbor" in that band. The flux status of the weaker neighbor was demoted to low quality and the upper limit assigned was that of the flux of the brighter object. The half-widths of the weaker neighbor window at (12, 25, 60 and 100 μm) were (90″, 90″,180″ and 360″) and the half-lengths were (270″, 272″,286″, 300″--a detector length).

H.6.d Confused Neighbors

A good indicator that a source was part of a more extended structure was to have two or more sources located very close together. A source with a high quality measurement in one band was examined for neighbors in the same window as described for weaker neighbors. If another source were located sufficiently close to the first and if any confusion status flags other than edge detection flags (Section V.D.2) were set in either source, then the fluxes of both were marked low quality and the brightest of the two fluxes was assigned as an upper limit to each source. If no confusion status flags were set, neither source was changed. The definition of a neighbor and the size of the confused neighbor window were as described above for the weaker neighbor test.

H.6.e Very Near Neighbors

One of the original selection rules was to exclude from the catalog all sources, in all bands, with a neighbor closer than 30″ in-scan and 90″ cross-scan. Because the clean-up processor described in Section V.H.2 forced the weeks-confirmation of all sources within such a box, there should have been no such sources remaining to delete. Due, however, to slight differences in the way in which the neighbor boxes were calculated by the two programs, about twenty sources at the periphery of the neighbor box were deleted by the high source density processor.

H.6.f Moderate Quality Fluxes

Measurements that failed one or another of the above rules could still carry useful information about the strength of a source in a given band. Moderate quality fluxes had to have at least two hours-confirmed measurements with flux status, FSTAT=3,4,5 or 7, and correlation coefficient $\geqslant 0.95$. Fluxes of otherwise moderate quality could be demoted to low quality by either the weaker or confused neighbor rules.

H.6.g Low Quality Fluxes (Upper limits)

Measurements in a given band that failed to meet either the high or moderate quality criteria become upper limits for the source. If multiple detections were available, the brightest one was given. As mentioned above, confused or weaker neighbors were given the brightest flux of either of the two sources as an upper limit. Sources of low quality were examined for brighter neighbors and were assigned the brightest neighboring flux (see above for neighbor rules). Sources with no detections on any sighting (i.e., with only noise fills present) and no neighbors were given an upper limit based on 12 times the 1 σ value reported by the noise estimator. This value was chosen since the correlation coefficient requirement of $\geqslant 0.97$ corresponds to roughly a local signal-to-noise ratio of 12.

H.6.h Flux Averaging and Uncertainties

In all cases, averages and uncertainties were computed using the logarithms of the fluxes, not the fluxes themselves. However, the technique used to obtain the average values for both high and moderate quality fluxes in high source density regions was different from the one used outside of dense regions. Rather than computing *inverse-variance weighted averages* in regions where the noise estimator was suspect, simple averages of the logarithms of the valid high (or moderate) quality fluxes were computed. The uncertainty associated with the measurement was the greater of: 1) the average of the N uncertainties quoted for the N valid hours-confirmed measurements, divided by $N^{1/2}$; or 2) the standard deviation of the mean of the N values averaged together to obtain the flux average.

H.7 Catalog Source Selection

Outside of regions of high source density, two rules were used to select weeks-confirmed WSDB sources for inclusion in the catalog: sources had to have either a high quality flux in at least one band or two or more moderate quality fluxes in adjacent bands (Section V.H.5). The minimum time separation of 123,000 sec. required for two hours-confirmed sightings to "weeks-confirm" was found to be long enough to reject even slow moving asteroids.

Within high source density regions, as described in V.H.6, sources had to have at least one high quality flux in one band and be relatively isolated from other sources to be included in the catalog.

H.8 Low-Resolution Spectral Associations

For each source in the WSDB, a check was made to see whether a low-resolution spectrum was available. See Chapter IX for more details.

H.9 Associations

Positional associations of IRAS sources are made with objects in other astronomical catalogs. The associations in the IRAS catalog were based purely on positional agreement, with no attempt made to distinguish between multiple sources associated with a particular IRAS source. Any number of sources from a variety of catalogs could be associated with a specific IRAS object as long as the position test was met. No attempt was made to "identify" an IRAS source with a source from another catalog, by requiring the IRAS source to have a "reasonable" energy distribution for the identification. The only attempt to preclude spurious associations was to forbid a source with only a 100 μm flux (i.e., a source having a significant likelihood of being Galactic "cirrus") from being associated with stars.

Because the catalogs used for associations had a wide range of positional accuracies, and the IRAS positions were intermediate between the very high positional accuracy catalogs and the lower accuracy catalogs, the following procedures were adopted to make the associations. For the high-positional-accuracy catalogs, a window of half width 8″ in-scan and 45″ cross-scan was used. If the position of the IRAS source lay within this distance of the cataloged source, then an association was made. For those catalogs where the positional uncertainty was greater than that of the IRAS source, an association was made if the source position and the IRAS position agreed to within a fixed radius or to within the radius (see below) of the cataloged source, if available.

In addition to the other catalogs, associations with IRAS small extended sources have been included, so that the user will know if a small extended source is close to the point source.

Table V.H.1 identifies the catalogs used and gives the search radius for the association and an indication of whether a source size was used for the association radius. The information carried with the association is described in detail in Section X.B and includes such information as visible magnitude, size, spectral type, and morphological type. In addition, the distance and position angle from the IRAS position to the location of the cataloged source are given.

Table V.H.1 Catalogs Used for Associations with IRAS Sources

Catalog No.	Catalog Type*	Catalog Name	Search Radius	Source Size Used in Association
01	2	General Catalogue of Variable Stars Kukarkin, *et al.*	90″	
02	2	Dearborn Observatory Catalogue of Faint Red Stars, Lee, *et al.*	90″	
03	3	Air Force Geophysical Laboratory Four-Color Survey, Price & Walker	90″	
04	2	Two Micron Sky Survey Neugebauer and Leighton	90″	
05	3	Globule List Wesselius	90″	X
06	1	Second Reference Catalogue of Bright Galaxies, de Vaucouleurs, *et al.*	90″	
07	2	Early Type Stars with Emission Lines Wackerling	90″	
08	3	Equatorial Infrared Catalogue	90″	
09	1	Uppsala General Catalogue of Galaxies Nilson	90″	
10	1	Morphological Catalog of Galaxies Vorontsov-Velyaminov, *et al.*	180″	

* Catalog types include (1) extragalactic, (2) stellar or (3) other, e.g. dark clouds, HII regions, etc.

Table V.H.1 Catalogs Used for Associations with IRAS Sources (Cont.)

Catalog No.	Catalog Type*	Catalog Name	Search Radius	Source Size Used in Association
11	3	Strasbourg Planetary Nebulae	90″	
12	1	Catalogue of Galaxies and Clusters of Galaxies, Zwicky, *et al.*	90″	
13	1	Smithsonian Astrophysical Observatory Star Catalog	45″(x-scan) ×8″(in-scan)	
14	3	ESO/Uppsala Survey of the ESO (B) Atlas, Lauberts	90″	
15	2	Bright Star Catalogue - 4th Edition Hoffleit	45″×8″	
16	2	New Catalog of Suspected Variable Stars Kukarkin, *et al.*	90″	
17	2	General Catalogue of Cool Carbon Stars	90″	
18	2	Catalog of Nearby Stars Gliese	45″×30″	
19	2	General Catalog of S Stars Stephenson	90″	
20	3	Parkes HII Region Survey Haynes, *et al.*	120″	X

* Catalog types include (1) extragalactic, (2) stellar or (3) other, e.g. dark clouds, HII regions, etc.

Table V.H.1 Catalogs Used for Associations with IRAS Sources (Cont.)

Catalog No.	Catalog Type*	Catalog Name	Search Radius	Source Size Used in Association
21	3	Bonn HII Region Survey Altenhoff, *et al.*	80″	
22	3	Catalog of CO Radial Velocities Toward Galactic HII Regions, Blitz *et al.*	80″	X
23	3	Catalogue of Dark Nebulae Lynds Comparison Catalog of HII Regions Marsalkova Catalog of Star Clusters and Associations Alter, *et al.* Catalogue of Bright Diffuse Galactic Nebulae, Cederblad Untersuchungen Über Reflexionsnebel am Palomar Sky Survey, Dorschner and Gürtler A Study of Reflection Nebulae van den Bergh Catalog of Southern Stars Embedded in Nebulosity, van den Bergh and Herbst		X
24	2	Two Micron Sky Survey with Improved Positions, Kleinmann and Joyce	45″×8″	

* Catalog types include (1) extragalactic, (2) stellar or (3) other, e.g. dark clouds, HII regions, etc.

Table V.H.1 Catalogs Used for Associations with IRAS Sources (Cont.)

Catalog No.	Catalog Type*	Catalog Name	Search Radius	Source Size Used in Association
25	1	Catalog of Dwarf Galaxies van den Bergh	90″	
26	1	Atlas of Peculiar Galaxies Arp	120″	
27	1	Galaxies with an Ultraviolet Continuum, Markarian, *et al.*	90″	
28	1	Catalog of Extragalactic Radio Sources Having Flux Densities Greater than 1 Jy at 5 GHz, Kuhr, *et al.*	60″	
29	1	Catalogue of Quasars and Active Nuclei, Veron-Cetty and Veron	90″	
30	1	Lists of Galaxies Zwicky	90″	
31	1	Atlas and Catalog of Interacting Galaxies, Vorontsov-Velyaminov	120″	
32	3	IRAS Small Scale Structure Catalog	min(120″, diameter/2)	diameter/2
39†	3	Ohio State University Radio Catalog	120″	
40	2	University of Michigan Spectral Atlas	60″ 45″ × 8″	(Vol. 1) (Vols. 2,3)
41	3	IRAS Serendipitous Survey Catalog	60″	

*Catalog types include (1) extragalactic, (2) stellar or (3) other, e.g. dark clouds, HII regions, etc.

†Catalog numbers 33-38 reserved for internal use.

Authors:

T. Chester, B. T. Soifer, C. Beichman, J. Fowler, T.N. Gautier, G. Helou, H. McCallon, M. Rowan-Robinson, T. Conrow, M. Hauser, D. Walker, R. Walker.

References:

Acker, A., Marcout, J., and Ochsenbein, F., 1981, *Astron. Astrophys.* [Supp.] **43**, 265.

Altenhoff, W.J., Downes, D., Pauls, T., and Schraml, J., 1979, *Astron. Astrophys.* [Suppl.] **35**, 23.

Alter, G., Balasz, B., and Ruprecht, J., 1970, *Catalogue of Star Clusters and Associations.* Budapest: Akademiai Kiado.

Arp, H., 1966, *Ap.J.* [Suppl.] **14**, 1.

Blitz, L., Fich, M. and Stark, A.A., 1982, *Ap.J.* [Supp.] **49**, 183.

Cederblad, S., 1946, *Lund Annals*, Ser. 2, No. 119.

de Vaucouleurs, G., de Vaucouleurs, A., and Corwin, Jr., H.G., 1976, *Second Reference Catalogue of Bright Galaxies.* Austin: University of Texas Press.

Dorschner, V.J., and Gurtler, J., 1964, *Ast. Nachr.* **287**, 257.

Fisher, J.R., and Tully, R.B., 1975, *Astron. Astrophys.* **44**, 151.

Foltz, C.B., Peterson, B.M., and Boronson, T.A., 1980, *A. J.* **85**, 1328.

Fowler, J.W., and Rolfe, E.G., 1982, *Journal of the Astronautical Sciences*, Vol. XXX, No. 4, 385

Gliese, W., 1969, *Veroffentl. Astron. Rechen-Instituts Heidelberg*, No. 22.

Haynes, R.F., Caswell, J.L., and Simons, L.W.J., 1979, *Aust. J. Phys. Astrophys.* [Supp.], No. 48.

Hoffleit, D., and Jascheck, C., 1982, *The Bright Star Catalogue, Fourth Revised Edition.* New Haven: Yale University Observatory.

Kleinmann, S.G., and Joyce, R.R., 1984, private communication.

Kojoian, G., Chute, P.A., and Aumann, C.E., 1984, *A. J.* **89**, 332.

Kojoian, G., Elliott, R., and Bicay, M.D., 1981, *A. J.* **86**, 816.

Kojoian, G., Elliott, R., and Bicay, M.D., 1982, *A. J.* **87**, 1364.

Kojoian, G., Elliott, R., and Tovmassian, H.M., 1978, *A. J.* **83**, 1545.

Kojoian, G., Elliott, R., and Tovmassian, H.M., 1981, *A. J.* **86**, 811.

Kuhr, H., Witzel, A., Pauliny-Toth, I.I.K., and Nauber, U., 1981, *Astron. Astrophys.* [Supp.] **45**, 367.

Kukarkin, B.V., Kholopov, P.N., Artirukhina, N.M., Fedorich, V.P., Frolov, M.S., Goranskij, V.P., Gorynya, N.A., Karitskaya, E.A., Kireeva, N.N., Kukarkina, N.P., Kurochkin, N.E., Medvedevna, G.I., Perova, N.B., Ponomareva, J.A., Samus', N.N., and Shugarov, S. Yu., 1981, *New Catalog of Suspected Variable Stars* (on magnetic tape), Moscow.

Kukarkin, B.V., Kholopov, P.N., Efremov, Yu. N., Kukarkina, N.P., Kurochkin, N.E., Medvedeva, G.I., Perova, N.B., Fedorovich, V.P., and Frolov, M.S., 1970, *General Catalog of Variable Stars, Vol II.* Sternberg Inst., Moscow State University.

Kukarkin, B.V., Kholopov, P.N., Pskovsky, Yu.P., Efremov, Yu.N., Kukarkina, N.P., Kurochkin, N.E., Medvedeva, G.I., Perova, N.B., Fedorovich, V.P., and Frolov, M.S., 1971, *General Catalogue of Variable Stars, Vol. III.* Sternberg Inst., Moscow State University.

Lauberts, A., 1982, *The ESO/Uppsala Survey of the ESO(B) Atlas.* Mucnich: European Southern Observatory.

Lee, O.J., Baldwin, R.J., and Hamlin, D.W., 1943, *Annals of the Dearborn Observatory V, Part 1A.*

Lee, O.J., and Bartlett, T.J., 1944, *Annals of the Dearborn Observatory V, Part 1B.*

Lee, O.J., Gore, G.D., and Bartlett, T.J., 1947, *Annals of the Dearborn Observatory V, Part 1C.*

Lynds, B.T., 1962, *Ap. J.* [Suppl.] **7**, 1.

Markarian, B.E., 1967, *Astrofizika 3*, **55**.

Markarian, B.E., 1969a, *Astrofizika 5*, **443**.

Markarian, B.E., 1969b, *Astrofizika 5*, **581**.

Markarian, B.E., and Lipovetskii, V.A., 1971, *Astrofizika 7*, **511**.

Markarian, B.E., and Lipovetskii, V.A., 1972, *Astrofizika 8*, **155**.

Markarian, B.E., and Lipovetskii, V.A., 1973, *Astrofizika 9*, **487**.

Markarian, B.E., and Lipovetskii, V.A., 1974, *Astrofizika 10*, **307**.

Markarian, B.E., and Lipovetskii, V.A., 1976a, *Astrofizika 12*, **389**.

Markarian, B.E., and Lipovetskii, V.A., 1976b, *Astrofizika 12*, **657**.

Markarian, B.E., Lipovetskii, V.A., and Stepanyan, D.A., 1977a, *Astrofizika 13*, **225**.

Markarian, B.E., Lipovetskii, V.A., and Stepanyan, D.A., 1977b, *Astrofizika 13*, **397**.

Markarian, B.E., Lipovetskii, V.A., and Stepanyan, D.A., 1979a, *Astofizika 15*, **201**.

Markarian, B.E., Lipovetskii, V.A., and Stepanyan, D.A., 1979b, *Astrofizika 15*, **363**.

Markarian, B.E., Lipovetskii, V.A., and Stepanyan, D.A., 1979c, *Astrofizika 15*, **549**.

Markarian, B.E., Lipovetskii, V.A. and Stepanyan, D.A., 1981, *Astrofizika 17*, **619**.

Marsalkova, P. 1974, *Astrophys. Sp. Sci.* **27**, 3.

McCallon, H.L. and Kopan, E.L., *IRAS Telescope Pointing Reconstruction,* JPL Publication No. 85-1, to be published.

Neugebauer, G., and Leighton, R.B., 1969, *Two-Micron Sky Survey, NASA SP-3047.* Washington, D.C.: National Aeronautics and Space Administration.

Nilson, P., 1973, *Uppsala General Catalogue of Galaxies.* Act Universitatis Upsaliensis, Nova Regiae Societatis Upsaliensis, Series V:A, Vol. 1.

Peterson, D.S., 1973, *A. J.* **78**, 811.

Price, S.D., and Murdock, T.L., 1983, *The Revised Air Force Geophysics Laboratory Infrared Sky Survey, AFGL-TR-83-0161.* Hanscom Air Force Base, Massachusetts: Air Force Geophysics Laboratory.

Rolfe, E.G., Otake, H., and Fowler, J.W., 1984 (in preparation for submission to the *Journal of the Astronautical Sciences*).

Smithsonian Astrophysical Observatory Star Catalog (4 vols.) 1966. Washington, D.C.: Smithsonian Institution.

Stephenson, C.B., 1973, *Publications of the Warner and Swasey Observatory, Case Western Reserve University*, **1**, No. 4.

Stephenson, C.B., 1976, *Publications of the Warner and Swasey Observatory, Case Western Reserve University*, **2**, No. 2.

Sweeney, L.H., Heinsheimer, T.F., Yates, F.F., Maran, S.P., Lesh, J.R., and Nagy, T.A., 1978, *Interim Equatorial Infrared Catalogue, TR-0078(3409-20)-1.* Los Angeles: The Aerospace Corporation.

van den Bergh, S., 1966a, *A. J.* **71**, 922.

van den Bergh, S., 1966b, *A. J.* **71**, 990.

van den Bergh, S., and Herbst, W., 1975, *A. J.* **80**, 208.

Veron-Cetty, M.P., and Veron, P., 1984, *A Catalogue of Quasars and Active Nuclei.* Munich: European Southern Observatory.

Vorontsov-Velyaminov, B.A., 1959, *Atlas and Catalog of Interacting Galaxies.* Sternberg Inst., Moscow State University.

Vorontsov-Velyaminov, B.A., and Arhipova, V.P., 1963, *Morphological Catalog of Galaxies, Part III.* Moscow State University.

Vorontsov-Velyaminov, B.A., and Arhipova, V.P., 1964, *Morphological Catalog of Galaxies, Part II.* Moscow State University.

Vorontsov-Velyaminov, B.A., and Arhipova, V.P., 1968, *Morphological Catalog of Galaxies, Part IV.* Moscow State University.

Vorontsov-Velyaminov, B.A., and Arhipova, V.P., 1974, *Morphological Catalog of Galaxies, Part V.* Moscow State University.

Vorontsov-Velyaminov, B.A., and Krasnogorskaja, A.A., 1962, *Morphological Catalog of Galaxies, Part I.* Moscow State University.

Wackerling, L.R., 1970, *Mem. R.A.S.* **73**, 153.

Wesselius, P.R., 1979, unpublished.

Zwicky, F., and Herzog, E., 1963, *Catalogue of Galaxies and of Clusters of Galaxies, Vol II.* Pasadena: California Institute of Technology.

Zwicky, F., and Herzog, E., 1966, *Catalogue of Galaxies and of Clusters of Galaxies, Vol III.* Pasadena: California Institute of Technology.

Zwicky, F., and Herzog, E., 1968, *Catalogue of Galaxies and of Clusters of Galaxies, Vol IV.* Pasadena: California Institute of Technology.

Zwicky, F., Herzog, E., and Wild, P., 1961, *Catalogue of Galaxies and of Clusters of Galaxies, Vol I.* Pasadena: California Institute of Technology.

Zwicky, F., Karpowicz, M., and Kowal, C.T., 1965, *Catalogue of Galaxies and of Clusters of Galaxies, Vol. V.* Pasadena: California Institute of Technology.

Zwicky, F. and Kowal, C.T., 1968, *Catalogue of Galaxies and of Clusters of Galaxies, Vol. VI.* Pasadena: California Institute of Technology.

Zwicky, F., Sargent, W.L.W., and Kowal, C.T., 1975, *A. J.* **80**, 545.

Zwicky, F., and Zwicky, M.A., 1971, *Catalogue of Selected Compact Galaxies and of Post-eruptive Galaxies.* Zurich: Offsetdruk L. Speich.

VI. FLUX RECONSTRUCTION AND CALIBRATION

Three quite separate functions must be performed in order to reconstruct the flux of a source from the telescope data stream. First, the effects of the telescope transfer function must be removed from the data. Second, the results must be transferred to relative photometric units. In the case of IRAS, this amounted to establishing the relationship between source amplitudes observed during the survey scans and outputs of flashes of the internal reference source. Third, the relative photometry must be put on an absolute scale, i.e., the flashes of the internal reference source must be calibrated in an absolute sense.

In the following discussion, the processing by which the signal received at the ground station was converted to the effective detector current is described, followed by the description of the process by which the relative and, finally, the absolute photometry was achieved.

A. Processing - Removal of Telescope Transfer Function

The electronic chain by which the current caused by photons incident onto the detector is transferred to the signal received at the ground station is described in Section II.C.5. Briefly, the detector acted as a current source as a result of the incident photons. This current was input to a trans-impedance amplifier which transformed the signal into a voltage equaling the total current times the feedback resistor plus a small offset voltage due primarily to the imbalance in the cold JFETs at the inputs to the operational amplifiers. The output voltage from the trans-impedance amplifier was amplified and shaped by analog electronics, fast rise time nuclear particle spikes were removed and the analog voltage was converted into a digital signal for transmission in a compressed format to the Earth. In the processing, the route was reversed. As described below, the received signal, in data numbers, was retraced to the current at the detector.

A.1 Digital Electronics

Pre-launch ground tests determined that there were no significant errors or non-linearities introduced by the digital electronics or by the analog to digital conversion. Any errors introduced by the compression of digital data on board the telescope and reconstruction at the processing center were assumed to be random and to be in the least significant bit and were ignored. The raw input was therefore assumed to correspond exactly to the output of the analog to digital converter. Since a linear analog to digital converter was assumed, the voltage into the analog to digital converter, i.e., the voltage at the output of the analog chain was given by:

$$V_{anlg} = C_0 + C_1 \times DN \qquad \text{(VI.A.1)}$$

where

V_{anlg} = voltage at output of the analog amplifier = voltage at the analog digital converter

C_0 = inherent voltage offset of the analog digital converter

DN = observed signal in data numbers.

C_1 = data number voltage conversion factor (volts/DN)

Preflight measurements showed that any adverse effect on the data due to the multiplexer should be negligible and it was therefore assumed to be linear.

A.2 Analog Electronics Amplifiers

The analog electronics contained the commandable gains and offsets. The input voltage to this part of the electronics can be recovered by

$$V_{tia} = \frac{V_{anlg}}{G_i} - S_j \qquad \text{(VI.A.2)}$$

where,

V_{tia} = voltage at trans–impedance amplifier output

G_i = commandable gain, $i = 1, 2, 3$.

S_j = commandable offset, $j = 1, 2,..., 8$.

The effects on the flux calibration due to the pole zero amplifier and the pulse circumvention circuit (deglitcher), which also lie in the analog electronics board between the output of the preamplifier electronics and the commandable offset electronics, were ignored. The analog electronics also contained a filter to remove high frequencies in the signal. Adverse effects due to the filter were considered to be small at the frequencies of interest and were therefore ignored.

A.3 Trans-impedance Amplifier

In order to recover the extended component of the incident flux, it was necessary to determine, and remove, any electronic baseline offset. The voltage at the output of the trans-impedance amplifier was taken to be of the form:

$$V_{tia}[observed] = I_d \times R_f + V_{tia}[off] \qquad \text{(VI.A.3)}$$

where I_d is the current through the detector and R_f is the feedback resistor.

The offset voltage, $V_{tia}[off]$ represents a sum of terms due to (a) offsets in the trans-impedance amplifier, including the cold JFETs, and (b) offsets in the analog electronic boards. Since the effects are indistinguishable at the output, both have been lumped into one equivalent offset voltage at the output of the trans-impedance amplifier. Although these offsets were in principle temperature dependent, it was concluded from pre-flight tests of the relevant temperature coefficients, and the relative stability of the electronics boxes in flight, that this effect was small enough that it was not necessary to model the temperature dependent aspects of $V_{tia}[off]$. A single fixed value for the electronic baseline was therefore used for each SOP. The details of the determination of $V_{tia}[off]$ are given in Section VI.B.3.

After launch, the electronic baselines at 60 and 100 μm were found to be affected by the bias boosts induced during crossings of the South Atlantic Anomaly (SAA). The effect is thought to be due to the differential heating of the JFETs because of the large current passing through the JFET connected to the

detector. This effect was modeled by adding a time dependent exponential function to $V_{tia}[off]$

$$Corr = (a + b \times T) \times \exp(-\Delta/\tau) \qquad \text{(VI.A.4)}$$

where:

T = duration of the most recent bias boost

a,b = constants

Δ = time interval between time of interest and end of most recent bias boost

τ = characteristic decay time of the baseline shift

This correction was added to the electronic baseline value before removing the electronic baseline from the data. For a typical passage through the SAA, the magnitude of this baseline shift was about 20% and 80% of the signal from the TFPR at 60 μm and 100 μm. The time constant τ was typically 52 minutes at 60 μm and 42 minutes at 100 μm.

A.4 Removal of Coherent Detector Noise

Detector 5 (100 μm) exhibited a stable, coherent 0.25 Hz waveform. By adding successive 4-second intervals of data coherently, it was possible to determine the shape of the waveform to better than 1% of the remaining rms noise. This wave form was then subtracted from the detector 5 data stream. This resulted in an order of magnitude improvement in the rms noise and greatly reduced the number of spurious point source detections for detector 5. After removal of the wave form, the character of the resulting detector 5 data stream was typical of 100 μm detectors.

Detector 19 (25 μm) exhibited a spike, of randomly varying amplitude, every second at sample #9 of the 16 Hz sampled data stream. The typical amplitude was approximately 6-8 times the cleaned rms noise for detector 19. The amplitude was measured by subtracting the average of the neighboring samples, which showed no evidence of electronic cross-talk, from the value of the spike sample. If the spike amplitude was less than a maximum allowable amplitude (approximately 10 times the rms noise of the cleaned detector 19 data), then the spiked sample was replaced by the average of its neighboring samples. If the spike amplitude was greater than the maximum allowable amplitude, then the maximum allowable amplitude was subtracted from the spike sample. The latter case can occur in the 6% of detector 19 detections for which the spike appears on top of a point source. If the signal to noise ratio of such a point source after the spike was removed is less than 20, the result will be a "topped" source. This process can lower the correlation coefficient below threshold for some of the weaker sources. Sources brighter than signal to noise ratio $\sim$ 20 will have progressively higher correlation coefficients. After removing the spikes, the overall rms noise for detector 19 was reduced by a factor $\sim$ 3.

Detector 43 exhibited a 1 Hz waveform that consisted of a positive spike with signal to noise ratio $\sim$ 2 at sample #9 of the 16 Hz sampled output, followed by a small negative spike, with signal to noise ratio $\sim$ 0.5, at sample #10. The amplitude varied randomly, but remained small, with a signal to noise ratio $<$ 3. In this case a constant waveform of the above shape was subtracted, resulting in a reduction of the detector 43 rms noise by a factor of $\sim$ 1.3. All subtractions were effectively done at the output of the trans-impedance amplifier.

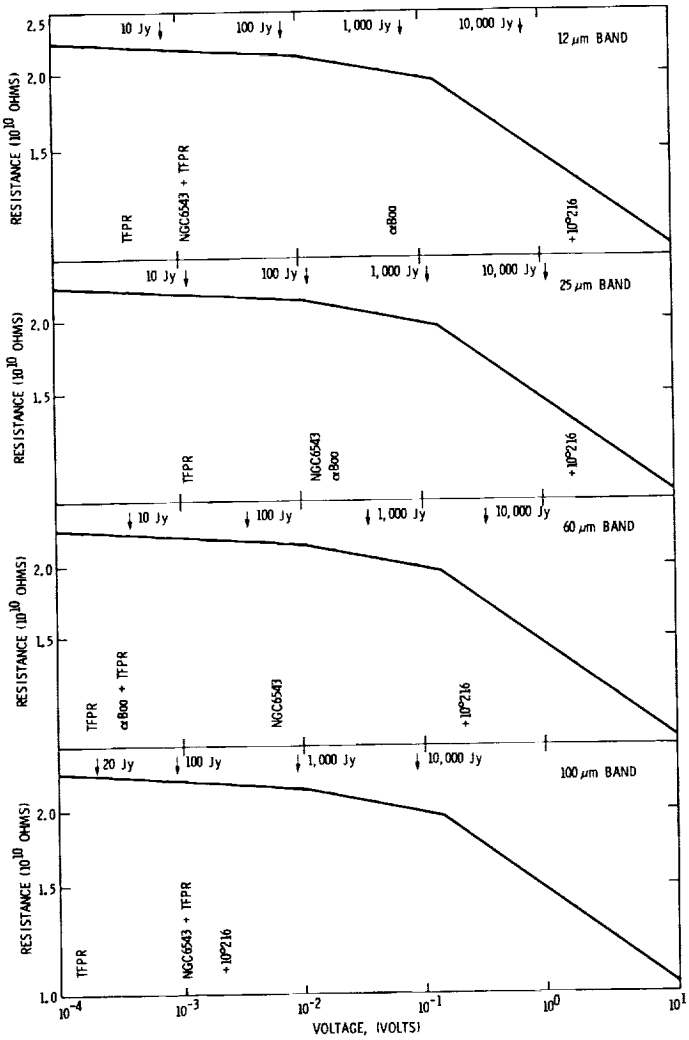

Figure VI.A.1 The fit used to represent the feedback resistor is shown in the four wavelength bands. The flux densities corresponding to the appropriate voltages across the resistor are shown. The same fit, that shown in Fig. II.C.12, was used for all the detectors.

A.5 Feedback Resistor

The feedback resistors had a nominal resistance of 2×10^{10} Ω, but in fact the resistance of the feedback resistor was dependent on the voltage across the resistor. The fit to the feedback resistor used in the data reduction is a three-piece curve shown in Fig. VI.A.1.a-d. It is the same fit as shown in Fig. II.C.12. This was the only nonlinearity assumed in the processing.

A.6 Summary

The processing to remove the instrumental transfer functions can be summarized by the following equation for the current in the detector:

$$I_d = \left(\frac{C_0 + C_1 \times DN}{G_i} - S_j - V_{tia}[off] \right) / R_f \ . \qquad \text{(VI.A.5)}$$

B. Determination of Relative Flux

The processing outlined above resulted in a current which was assumed to be proportional to the flux incident on the detector except for small effects due to the dwell time on a source. The conversion of the current to relative flux was effected by a comparison of source amplitudes with amplitudes resulting from flashes from the internal reference source (see Section II.C.3) which provided a secondary relative calibration source. The internal reference source was in turn absolutely calibrated with respect to celestial sources using NGC 6543 as a secondary transfer standard; see Section VI.C below. The processing to obtain the relative photometry of the IRAS sources is discussed in this section.

B.1 Overall Procedure to Determine Relative Photometry

Each survey scan was initiated and terminated with a pair of flashes of the internal reference source to monitor the responsivity of the system. Because it was assumed that responsivity changes were slow, responsivity values between internal reference source flashes were determined by linear interpolation between these flashes. In principle, therefore, the responsivity was determined separately for each scan. If, as discussed below, both of the flashes at one end of a scan were unusable, the extrapolation was continued to the closest accepted flashes on adjoining scans. There was, however, never an interpolation across a bias boost (see Sections II.C.5, III.B.6, III.C.4 and IV.A.7) since the bias boost largely erased the detector's memory. In this case, the detector's responsivity was assumed to equal that calculated from the most recent flash accepted.

The responsivity relative to the flashes of the internal reference source, as determined from the flashes at the ends of the scans, was used to scale both point sources and extended emission. As seen in Fig. IV.A.2, the actual variations in the responsivity as measured by the flashes of the internal reference source are typically $< 10\%$ in the 12, 25 and 60 μm bands and $< 15\%$ in the 100 μm band.

As discussed in Section IV.A.4, the responsivity is a function of the spatial frequencies present in observing a source. Multiplicative factors appropriate for either the point source responsivity or the extended emission ("DC") were applied in the source detection processing (Sections V.C, V.G). No attempt has been made to adjust the calibration of the small extended sources to account for the appropriate spatial frequencies encountered (Section V.E). Additionally, the observations were reduced assuming a responsivity independent of the total flux falling on the detector; as indicated by the observations of Fig. IV.A.4, this assumption was clearly wrong in the 60 and 100 μm bands.

The design of the entire detector and electronics system used in IRAS was DC coupled, thus allowing, in principle, a measurement of the absolute brightness of the sky from a measurement of the total photo-current. There was, however, no absolute radiometric reference included in the experiment in order to evaluate $V_{tia}[off]$ directly, an essential quantity in determining the true sky brightness. The reconstruction of the offset $V_{tia}[off]$ for each of the detector channels was the most difficult part of the effort to produce properly calibrated absolute sky brightness data for all parts of the sky. For example, in order to determine the total incident flux on each detector to an accuracy of one percent, it would be necessary to determine the absolute value of the DC voltage level at the input of each amplifier to about 1 microvolt. Despite this handicap, the extraordinary DC stability of the system, when coupled with the calibration procedures described below, provided an accurate and sensitive measurement of the sky brightness in all four wavelength bands.

B.2 Photometry of Point Sources and Small Extended Sources

The point source responsivity obtained from the measurements of the internal reference source as described above were applied directly to the output of the point source recognizer. No attempt was made in the reconstruction to correct for the cross-scan response profile other than in a statistical sense. However, as part of the calibration procedure using the flashes of the internal reference source and the celestial source NGC 6543, the shape of the cross-scan response of each individual detector (Section IV.A.3) was combined with the knowledge of the cross-scan position of the standard calibration track to produce a single correction factor for the standard calibration response. This correction factor would result in zero average error for point sources passing over uniformly distributed cross-scan positions. In the 25 μm band the difference between the measured amplitude and the average amplitude never exceeded 10%, while in the other bands the difference did not exceed 5%. The variations in the amplitudes caused by the cross scan response implies that a minimum uncertainty of 5% must be assigned to all fluxes determined in the survey.

The small extended sources were treated like the point sources except that a 10% and 8% increase in responsivity was assumed at 12 and 25 μm to approximate sources typically 4 times the nominal point source template in spatial extent. Except for this small correction, no attempt was made to take the variation of the responsivity with size of the source into account; see Section IV.A.4. Although this procedure incurred large uncertainties, the uncertainties introduced because of a lack of knowledge of the true spatial distribution of the sources dominated the basic photometric uncertainties.

B.3 Photometry of Extended Emission

Since there were neither on-board calibration techniques to establish the electronic offset voltage directly for each detector under zero photon flux conditions nor celestial sources of known total sky brightness, it was necessary to follow a special procedure to determine $V_{tia}[off]$. The procedures can be summarized as follows:

a) An area of the sky with a smoothly varying sky brightness, free from point sources and near the north ecliptic pole and NGC6543, was selected to serve as a secondary calibration source for the diffuse emission. The area was called the total flux photometric reference or TFPR. Since the viewing geometry of the TFPR through the zodiacal dust cloud varied throughout the duration of the mission, the signal from this area of the sky varied with time.

b) On several occasions during the mission direct measurements of V_{tia} [off] were obtained while pointing at the TFPR. These yielded direct comparisons of the flux from the TFPR, F[TFPR], with flashes from the internal reference source (see Section B.3.a below). Hence values for the total sky brightness, B[TFPR], were obtained using measured values for the solid angles in each band. More accurate and more frequent measures of the annual variation of B[TFPR] were obtained by differencing the fluxes from the north and south ecliptic poles obtained on individual scans which passed over both poles (see Section B.3.b below). These data are shown in Fig. VI.B.1 along with the best fit models for the annual variation. Table VI.B.1 gives the parameters for the model in each band and summarizes the errors of measurement.

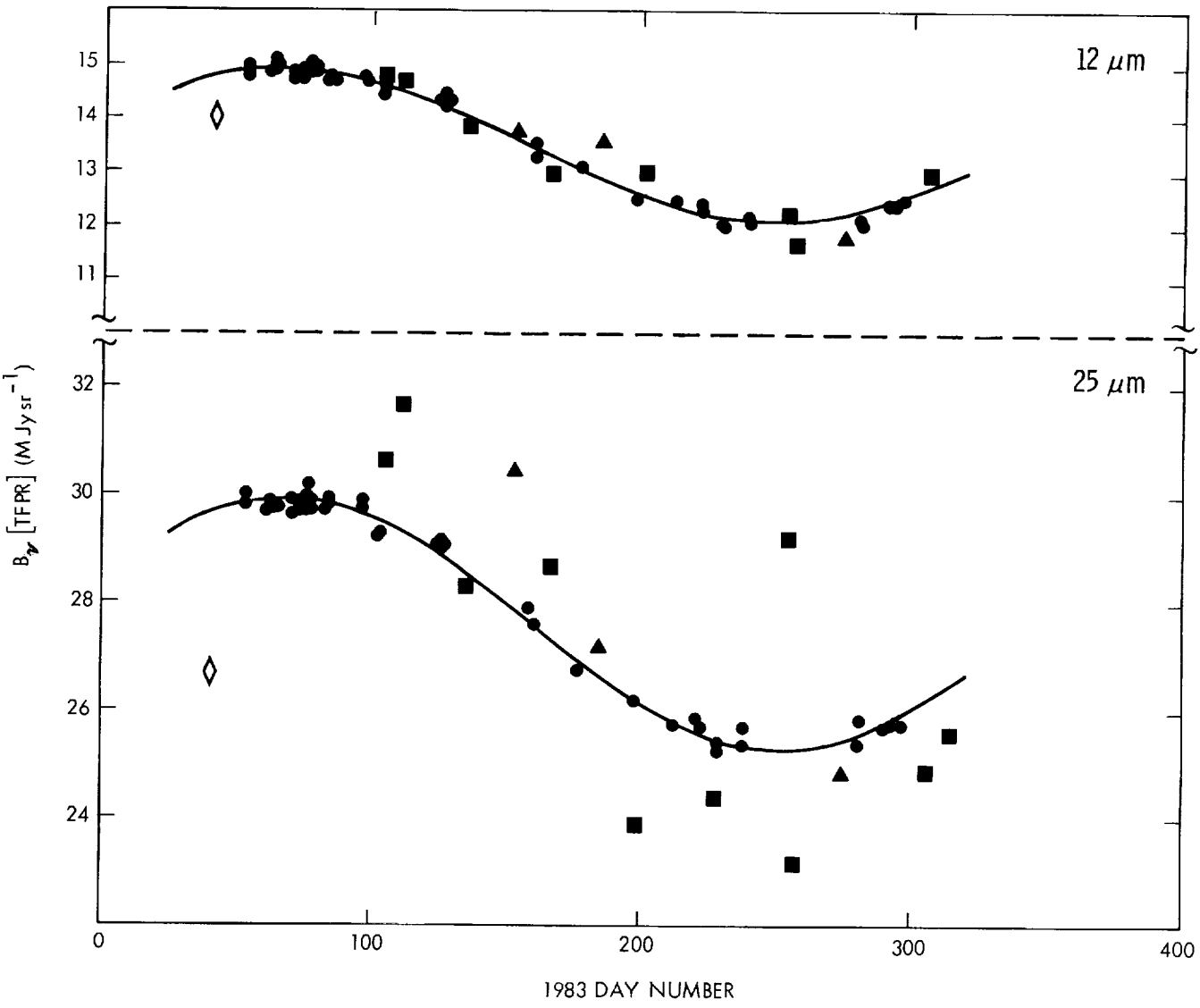

Figure VI.B.1.1 The variation of total sky brightness at 12 and 25 μm at the north ecliptic pole is shown as a function of day number of the year (1983, January 1 (UT) is day 1). See Section VI.B.3.b for explanation of symbols.

c) In order to update the values of V_{tia} [off] as needed for regular processing of the survey data, observations of the TFPR were made twice daily and the signals for each detector derived from the models of B[TFPR] versus day number were subtracted.

B.3.a Determination of F[TFPR]

The determination of F[TFPR] was based on the possibility of changing the detector responsivity, and hence the total photocurrent, while leaving the offset voltage V_{tia} [off] unchanged. In the case of the 12 μm detectors, the responsivity change was easily achieved since two bias voltage levels were available within the operating range of the detectors; see Section II.C.5. In the other wavelength bands, where the second bias levels resulted in channel saturation, the required change in responsivity was obtained as a result of passage through a dense portion of the SAA *uncorrected by bias boosting* (see Section IV.A.7),

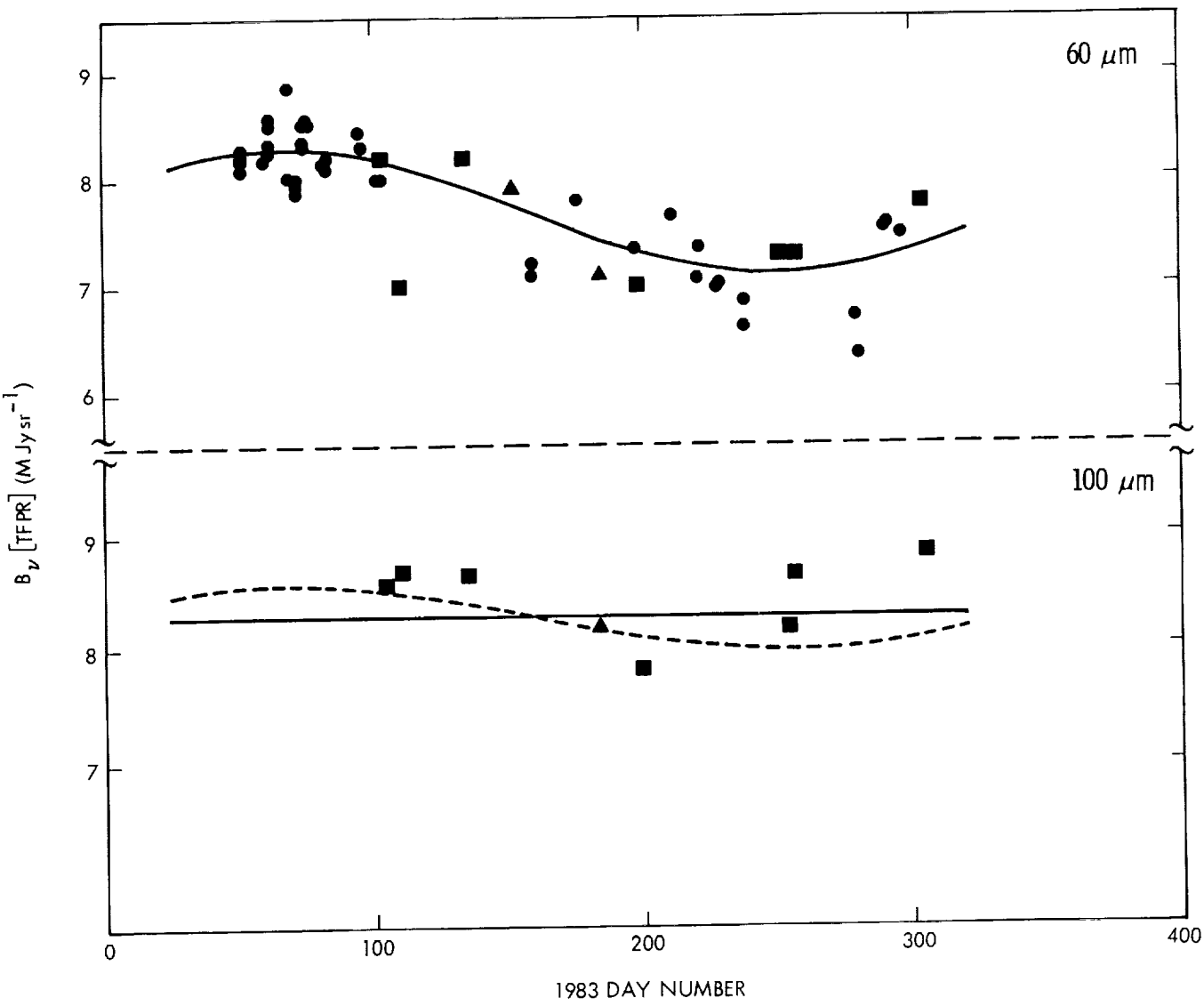

Figure VI.B.1.2 The variation of total sky brightness at 60 and 100 μm at the north ecliptic pole is shown as a function of day number of the year (1983, January 1 (UT) is day 1). See Section VI.B.3.b for explanation of symbols.

and the change in responsivity was achieved by applying bias boost while the TFPR was still observable. The special sequences to do this were started and ended by 13/16 second and 15 second multiple flashes of the internal reference source.

The reduction of the special calibration observations is illustrated with the equations representing the voltage at the trans-impedance amplifier as:

$$V_{tia}[TFPR,1] = R[1] \times F[TFPR] + V_{tia}[off]$$

and (VI.B.1)

$$V_{tia}[TFPR,2] = R[2] \times F[TFPR] + V_{tia}[off]$$

where the symbols [1] and [2] indicate high responsivity and low responsivity conditions of the detector. $F[TFPR]$ and $V_{tia}[off]$ are assumed constant during the observation.

$R[1]$ and $R[2]$, the responsivities in the two states, can be determined from the differential responses to the internal reference source:

$$\Delta(V_{tia}[IRS,1]) = R[1] \times F[IRS] \qquad \text{(VI.B.2)}$$

and

$$\Delta(V_{tia}[IRS,2]) = R[2] \times F[IRS]$$

where $F[IRS]$ is the source strength of the internal reference source. The effects of the backgrounds and offsets cancel out since the measurements are differential. In practice, the flashes used for these special measurements were 15 seconds long; they therefore had to be calibrated relative to the 13/16 seconds flashes normally used.

The relative source strength of the TFPR can now be found from:

$$F[TFPR] = \frac{V_{tia}[TFPR,1] - V_{tia}[TFPR,2]}{\Delta(V_{tia}[IRS,1]) - \Delta(V_{tia}[IRS,2])} \times F[IRS] \qquad \text{(VI.B.3)}$$

The quality of these special calibration observations varied with the wavelength band; see Fig. VI.B.1. At 12 μm the observations yielded a smooth sine wave which agreed in phase and amplitude with measurements of the ecliptic polar differences seen in pole-to-pole scans; see below. At 25μm it was necessary to use only one of the two detector modules (module 2A) since bias boosting altered the electronic offset appreciably compared to the relatively small change in responsivity produced by a 2 to 3 minute bias boost. Module 2A had been modified to overcome pre-flight wiring failures inside the dewar and, fortunately, these modifications greatly reduced the effects of bias boosting on V_{tia} [off].

Some independent information concerning the zero point for each detector was available during the first week of the mission when the cryogenically cooled cover was still in place. This afforded essentially zero background conditions for the 12 and 25 μm detectors and allowed their electronic offsets to be measured directly. These measurements agreed with the results of the special calibration measurements described above within 6% and 10% at 12 and 25 μm respectively. Unfortunately the internal dewar background was not low enough with the cover in place at 60 and 100 μm to give useful results.

At 60 and 100 μm the change in responsivity of the detectors as a result of the SAA dose and a short bias boost application was substantial and it was possible to obtain useful data on a number of occasions by delaying the bias boost until the telescope was pointed at the TFPR. All detectors responded well to this procedure and repeatable results were obtained even though the data are not as well behaved as those obtained in the 12 μm band (see Fig. VI.B.1); in part this is due to the fact that the sky brightness at 60 and 100 μm is considerably lower than at shorter wavelengths.

Studies of the variation of V_{tia} [off] throughout the mission in each of the bands show similar behavior; the relatively smooth long term drift appears to be well correlated with measured changes in the temperatures of the warm electronics boxes.

Table VI.B.1 TFPR Model Parameters[1]

Effective wavelength (μm)	12	25	60	100
Parameter:[2]				
B_0 (MJy/sr)[3]	13.5	27.6	7.7	8.3
statistical uncertainty[5]	0.1	0.8	0.2	0.2
total uncertainty[6]	1.6	3.6	1.0	1.6
B_1 (MJy/sr)[3]	1.40	2.3	0.58	0
statistical uncertainty[5]	0.03	0.1	0.07	0.7[7]
total uncertainty[6]	.17	0.3	0.10	
φ (day)[4]	-23.8	-22.3	-26	-
statistical uncertainty[5]	1.2	1.3	9	-
total uncertainty[6]	3	3	10	-

[1] The parameters have been converted to sky brightness (MJy sr^{-1}) in order to illustrate the relative magnitudes of the parameters. The parameters were originally derived relative to the flashes of the internal reference source.

[2] At a time t in days the model assumes B[TFPR] to be:

$$B[TFPR] = B_0 + B_1 \times \sin[(2\pi/365.25) \times (t - \varphi)]$$

[3] The usual convention of using a flat spectral distribution for the sources was followed in deriving the flux densities.

[4] 1983 January 1 (UT) is day 1.

[5] The statistical uncertainty corresponds to a 1 standard deviation in the fit to the observations.

[6] The total uncertainty incorporates the estimated systematic uncertainties: 5, 6, 7 and 10% in the absolute calibration at 12, 25, 60, and 100 μm respectively; 5% for the frequency response and 10% for the solid angle. Note that these uncertainties are estimated to apply at the TFPR; they are clearly exceeded in other places in the sky.

[7] 3 σ upper limit.

It must be kept in mind that no tests were available to validate the design goal that the instrumental background would be negligible at 60 and 100 μm. The tests carried out to measure the out of field radiation, however, indicate that stray radiation from the Sun and Earth were negligible (see Section IV.C.3). It is assumed that no significant radiation from within the instrument was able to reach the detectors.

B.3.b Determination of the TFPR Annual Variation

As discussed by Hauser *et al.* (1984) the component of the sky brightness produced by the zodiacal dust emission varies as the Earth makes its way through the interplanetary dust cloud. It was possible to measure this variation without knowledge of the electronic offset voltage by assuming that $V_{tia}[off]$ changes negligibly on the time scale of half an IRAS orbit. The observed difference between the brightness of the north and south ecliptic poles on a single scan is therefore a measure of the true difference in the sky brightness. This difference was found to vary seasonally and to be well represented in all wavelength bands except at 100 μm by a sinusoidal modulation of half amplitude B_1 [TFPR], where the phase angle does not vary with wavelength.

The pole-to-pole differences determined the time dependence of the TFPR brightness much more accurately than the special calibration measurements. The polar difference data were used to determine the phase angle and modulation amplitude of the TFPR variation, while the special calibrations provided the average DC brightness B_o [TFPR]. The best fit sinusoidal models in each band are presented in Fig. VI.B.1, along with the half values of the ecliptic polar differences. B_o was determined by a least squares fit of the special calibration data to the independently determined sinusoidal model for the annual variation.

In Fig. VI.B.1 the solid dots represent half of the observed difference between the north and south ecliptic poles measured on single pole-to-pole scans. The total sky brightness measured with the special calibration observations is shown by solid squares for the north calibration polar region (TFPR) and by solid triangles for the south polar region. The polar difference data were positioned vertically by fitting them to the north polar special calibration observations. The model of sky brightness variation derived from these data and given in Table VI.B.1 is shown as the solid curves. The special calibration observation data for the south polar region was inverted in phase before plotting in the figure. The dotted curve at 100 μm shows the best fit sine function. The open diamonds show the TFPR brightness after the cover was ejected, assuming the telescope background with the cover on was zero at 12 and 25 μm.

At 100 μm the annual variation was so small that the polar differences were dominated by small variations resulting from small differences in scan tracks passing over "cirrus" clouds near the poles (see Low *et al.* 1984). As a result, the value of B_1 [TFPR] at 100 μm was taken to be zero. An upper limit to the value of B_1 [TFPR] at 100 μm was found by fitting a sinusoid of the same phase found at shorter wavelengths to the special calibration data. As can be seen in Fig. VI.B.1, the result is a poor fit to the data and the 3 σ upper limit is listed in Table VI.B.1.

Over half of the observations of the survey went through two passes of processing. The first pass of the data reduction was used to determine parameters of the model for the time dependent behavior of the TFPR. Once the values for B_1 and B_o listed in Table VI.B.1 were derived as described above, they were used during the second pass to recompute the twice daily determinations of V_{tia} [TFPR] which were then used to correct all of the survey observations for small variations in the electronic offsets. No attempt was made to include higher order terms in the model for the annual variation.

Systematic uncertainties in the value of B(TFPR) remain due to the limitations of the total flux calibration procedure in fixing the average value of the TFPR brightness, the assumption of sinusoidal time variation of the TFPR, the methods used to determine the amplitude of the variation, the ratio of point

source to DC responsivity (Section IV.A.4) and the effective detector solid angles (Section IV.A.3). The statistical uncertainties listed in Table VI.B.1 are derived from the fits to the observations. The total uncertainties listed in Table VI.B.1 include the uncertainties in the absolute calibration (Section VI.C.2.c), an estimated 5% uncertainty in the frequency response for sources as bright as the TFPR, and a 10% uncertainty in the determination of the solid angles. The uncertainty in determining the average value of the TFPR brightness using the responsivity-switching procedures is difficult to estimate, but the comparison with the cover on/cover off test suggests this may be on the order of 10% at 12 and 25 μm. No independent corroboration is available at 60 and 100 μm. Refer to Section V.G for a discussion of additional effects in directions other than the ecliptic poles, such as the fixed pattern noise and corrections for the variations caused by motion through the zodiacal cloud.

B.4 Problems

B.4.a Rejected Internal Reference Source Flashes

The ability to extract an accurate measure of the amplitude of the internal reference source flash was complicated because of the structure of the sky over which the internal reference source was flashed. In particular, a good measure of the baseline accompanying the flash was required. The difficulty in extracting this information increased as the complexity of the sky emission increased. Several checks were implemented in the software to assure that an unreliable internal reference source measurement was rejected.

Errors could arise if extrapolations had to be made over a rejected flash to the next available one and also if an internal reference source flash was accepted but should have been rejected. This usually occurred when the majority of internal reference source measurements in a band were rejected due to complex sky background, but one or two slipped past the threshold checks in the software. Reference flashes were rejected in fewer than 7% of survey scans and this usually occurred at 60 or 100 μm. The photometric error associated with the extrapolation to the next available reference outside the current scan is estimated to be less than 5% in the 12, 25, and 60 μm bands. In the 100 μm band possible photon induced responsivity enhancement (Section IV.A.8 and VI.B.4.c) may result in photometric errors up to 15%. The error associated with the use of reference flashes which should have been rejected is estimated to be less than 10% at 12 and 25 μm and less than 20% at 60 and 100 μm.

B.4.b Radiation

The flux reconstruction took into account the effects of the bias boost by making sure that no detector's responsivity was interpolated across a bias boost event and by implementing a model to account for the time dependent exponential baseline decay after the bias boost event. Any linear change in the responsivity after a bias boost was corrected by the interpolation between reference flashes, but residual nonlinear responsivity variations and changes associated with low level radiation exposure, such as at the polar horns, were ignored in the flux reconstruction process. It is estimated that not accounting for radiation exposure should introduce an uncertainty of less than a few percent in the data.

B.4.c Photon Induced Responsivity Enhancement

Point Sources

As discussed in Section IV.A.8, analysis after the mission showed that passage over a bright infrared source such as Saturn or, more typically, the Galactic plane increased the responsivity of the 100 μm detectors by as much as 15%. The enhancement decayed with a long but unknown time constant, thus invalidating the basic assumption of a linear change in the responsivity in the time between flashes of the internal reference source.

The sign and magnitude of the effects of photon induced responsivity enhancement on the photometry depends crucially on the relative location of the detected source, on the location of the bright source of infrared radiation, i.e., of the Galactic plane, and on the time of the flashes of the internal reference source relative to the bright source exposure. This is illustrated in Fig. VI.B.2. As an example, if the flashes occurred far from the Galactic plane, (flashes (3) and (1) in Fig. VI.B.2.a), the flux of sources located on the trailing side of the plane would be overestimated and sources on the leading side of the plane would be underestimated. On the other hand, if the flash occurred near the Galactic plane, (e.g., as shown in Fig. VI.B.2.a with flashes (2) and (1)) the linear interpolation of the responsivity would lead to an underestimate of the flux of the same source.

The enhancement had not been measured or modeled before flight. In principle, this effect could be accounted for on a scan by scan basis by calculating a nonlinear time history for the responsivity between flashes of the internal reference source. In practice, however, because the effect was discovered only after a significant amount of processing was completed, it was not possible to make a proper correction for this effect, and a statistical approach was taken. The basis of the approach is to assume that a series of scans were laid down with sufficient regularity that on the average a given area of the sky relative to the Galactic plane was affected uniformly. For example, if the flashes were all taken sufficiently far from the plane that the effects of the enhancement had decayed, the observed fluxes would resemble those in Fig. VI.B.2.c. The ratio of fluxes observed on descending scans to those seen on ascending scans would then be as indicated in Fig. VI.B.2.d. Such a signature was in fact observed at a number of ecliptic longitudes; see Fig. VI.B.3.1.

Unfortunately, a significant area of the sky was not covered with overlapping descending and ascending scans. The areas which were covered with scans in both directions and for which $\geqslant$ 50 sources were found in bins 20 × 5° in ecliptic longitude and latitude are indicated in Fig. VI.B.4. On the basis of this figure, a correction factor was assigned at the locations where at least 50 overlapping values of F_D and F_A, the fluxes measured on descending and ascending scans were measured. The asymmetry about the Galactic plane seen in the figure is a result of the manner in which the survey scans were made. For example, at ecliptic longitudes 60° to 160°, some of the descending scans ended prior to crossing the Galactic plane giving virtually no responsivity enhancement while other descending scans crossed the plane resulting in significant responsivity enhancement. Likewise the same affect occurs for the ascending scans between ecliptic longitudes of 240° to 340°, giving lower corrections for the negative Galactic latitudes. The correction was quantized into four non-zero values, ± 2.5% and ± 7.5% on the basis of the value of log (F_D/F_A), shown in Fig. VI.B.4. An arbitrary extrapolation of these correction factors was

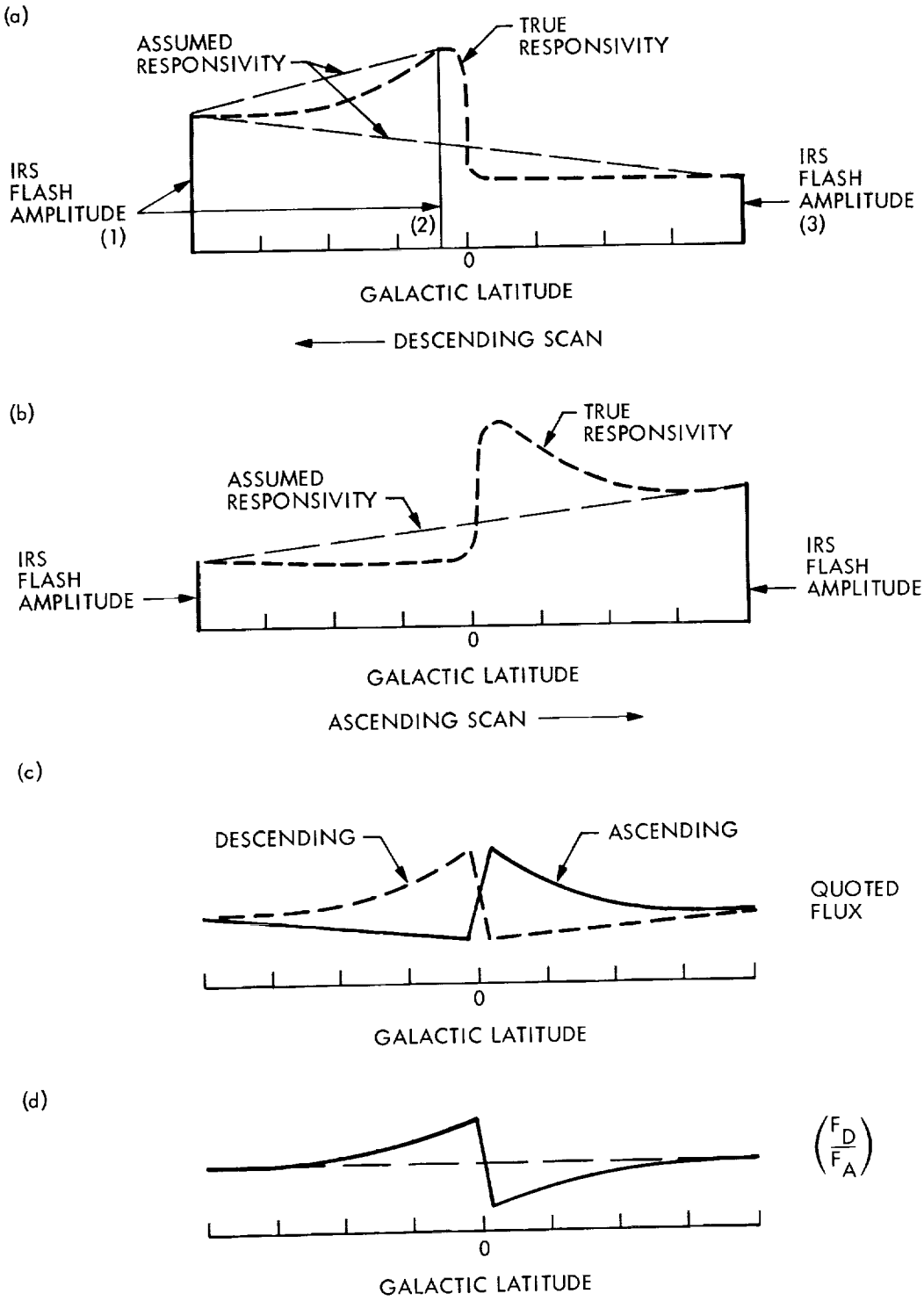

Figure VI.B.2 A schematic representation of the effects of photon induced responsivity enhancement. Sketches (a) and (b) show the true and assumed responsivity for ascending and descending scans. It is seen that if the first flash of the internal reference source occurs before the plane crossing, the sign of the effect is reversed from the case when it occurs after the plane crossing. Sketches (c) and (d) show the effect on the quoted fluxes and on the ratio of fluxes obtained on descending and ascending scans.

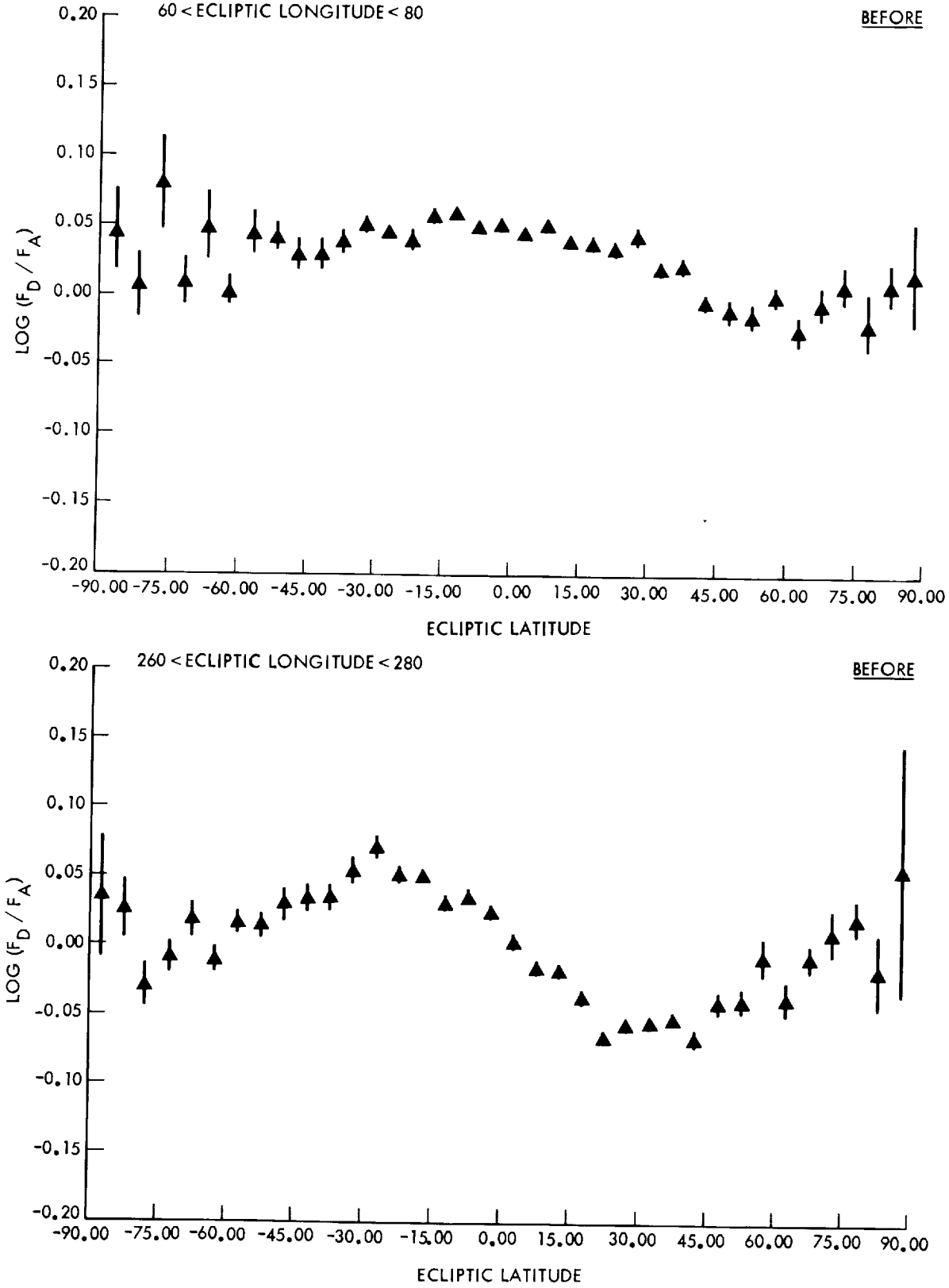

Figure VI.B.3 Results of comparisons of fluxes at 100 μm of sources observed on descending and ascending scans for sources within the ecliptic longitudes indicated. The ordinate is $\log(F_D/F_A)$ where F_A is the flux found on ascending scans and F_D is the flux found on descending scans.

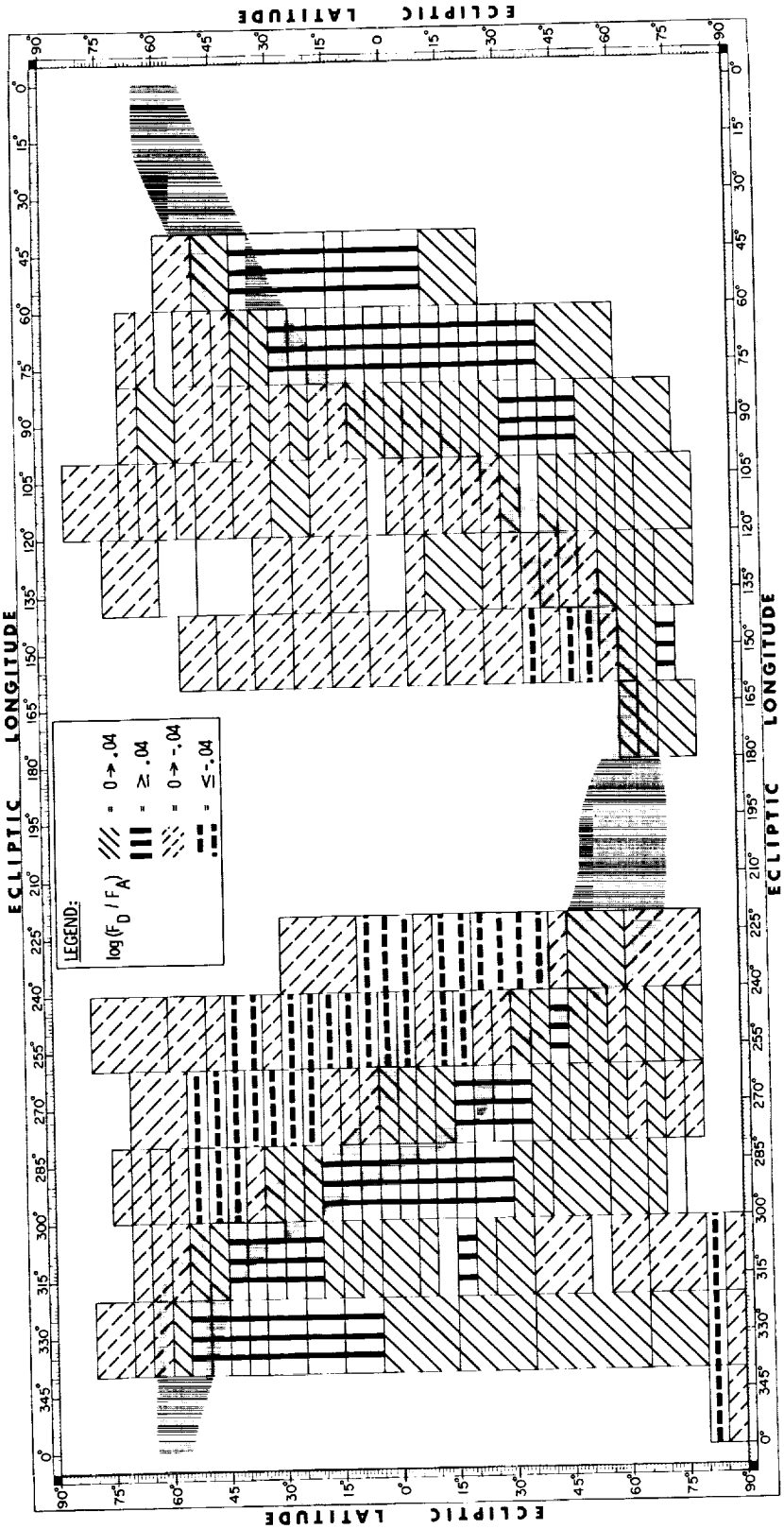

Figure VI.B.4 Areas of sky in ecliptic coordinates which have more than 50 sources observed at 100 μm in both descending and ascending scans. The measure of the photon induced responsivity enhancement, $\log(F_D/F_A)$ is indicated by the cross hatches.

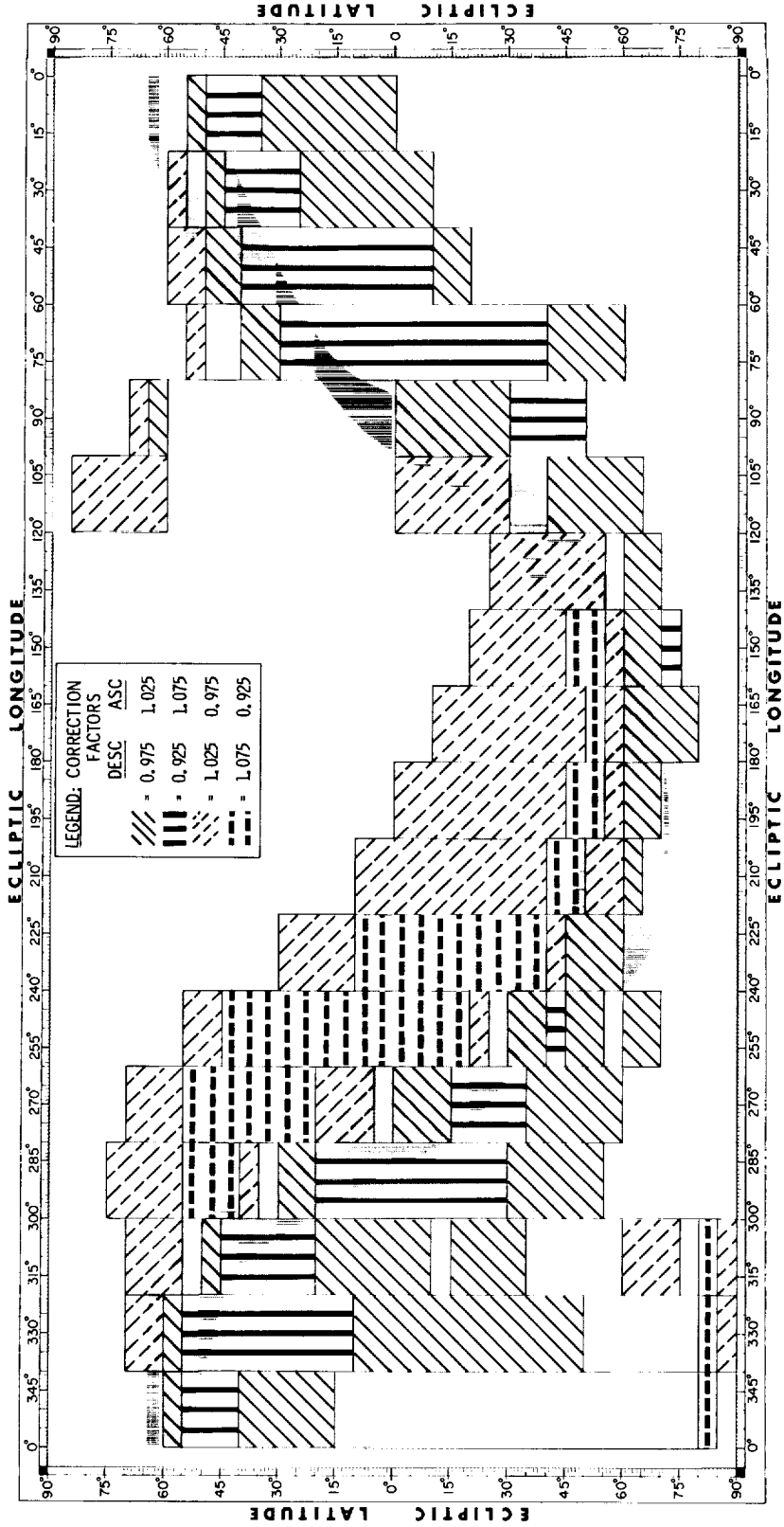

Figure VI.B.5 The correction factors, assigned on the basis of Fig.VI.B.4, used to correct for the photon-induced responsivity enhancement at 100 μm. See text.

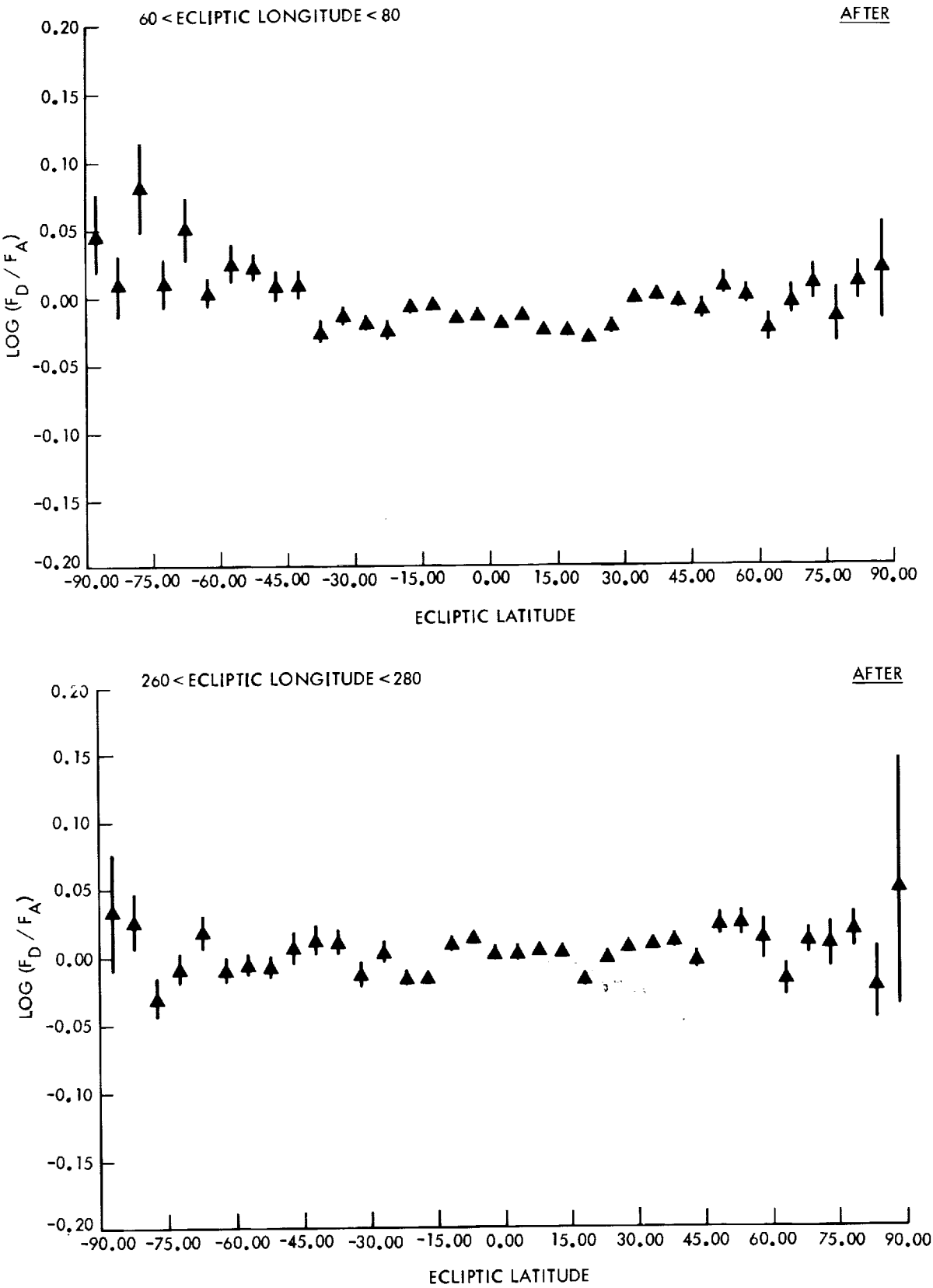

Figure VI.B.6 The same observations as in Figure VI.B.3, but with the fluxes corrected using the correction factors of Figure VI.B.5.

assumed for areas where sufficient coverage by both ascending and descending scans was missing; the resulting corrections are shown in Fig. VI.B.5. Subsequently, the correction was applied to each source found at 100 μm on a descending scan and its negative was applied to the sources found at 100 μm on ascending scans whether or not it was in a region of overlapping ascending and descending scans. Clearly this procedure is very approximate. Figure VI.B.6 shows the results of applying these corrections to the same observations presented in Fig. VI.B.3.

Extended Emission

The effects of photon induced responsivity enhancement on the extended emission data were observed by comparing, pixel by pixel, low resolution (0.5° square pixels) maps of the first sky coverage to the last sky coverage. Photon induced responsivity enhancement from bright portions of the Galactic plane appears to affect the extended emission in both the 60 and 100 μm bands to a larger extent than it does the point sources.

This problem has not been well enough understood at the release of this catalog (November 1984) to properly remove the effect. No correction has been applied to the quoted surface brightnesses, but separate data sets for the three sky coverages have been produced. When all of these data sets are released, the user will be able to determine if photon induced responsivity enhancement effects are important in a particular area of interest. The zodiacal history file (Section X.D.6) should be consulted to determine if the different sky coverages did indeed cover the area in different directions.

B.4.d Variation of Frequency Response with Total Flux

The observations shown in Fig. IV.A.4 indicate that in the 60 and 100 μm bands, at least, the frequency response depends on the brightness of the source. The observations have not been analyzed in detail, but sources up to ten times brighter than α Lyr apparently follow the pattern shown by α Lyr. It is not clear whether the change for brighter sources comes in the point source response at survey rate or in the low frequency responsivity. Thus the photometry of all sources brighter than about 100 Jy at 60 or 100 μm has uncertainties ranging to 30% at 60 μm and 70% at 100 μm that are not understood. This caution must apply equally to the extended emission atlases and to the small extended sources where the variations in the responsivity with frequency apparently change sign in going from weak to bright sources and from point sources to regions of large scale emission.

C. Absolute Calibration

C.1 General Philosophy

The absolute calibration of the IRAS point source observations is tied directly to the absolute calibration by Rieke *et al.* (1984) of the ground based photometric system at 10 μm. Specifically, the 12 μm IRAS band is calibrated via measurements of α Tau, with the assumption that its absolute flux density is as given in Rieke *et al.* Extrapolation to the 25 and 60 μm bands is achieved using models of stars, normalized to observations of the Sun. In this latter respect, the IRAS calibration differs in principle from the ground based calibrations of Rieke *et al.* and of Tokunaga (1984) who assumed that the flux density of α Lyr between 10 and 20 μm varied as that of a 10,000 K blackbody. The extrapolation of the absolute calibration from 60 to 100 μm is based on observations and model calculations of asteroids whose absolute flux at 60 μm was obtained using the stellar calibration.

The spectral response of the bands is sufficiently broad (Section II.C.2) that it is necessary to specify the continuum energy distribution of the source being observed when defining flux densities at a given wavelength. The approach used for IRAS was to assign effective wavelengths of 12, 25, 60 and 100 μm for the four bands. The effective bandwidth of each band was then calculated such that the quoted flux densities are correct if the source has an energy distribution with a flux per logarithmic frequency interval $\nu \times f_\nu = \lambda \times f_\lambda$ which is constant with frequency ν. Any other continuum distribution, and in particular that of hot stars, requires a color correction. This color correction, which ranges up to 50% for astronomically interesting continua, is discussed in detail in Section VI.C.3 below.

C.2 Point Source Calibration

The point source amplitudes used to determine the absolute calibration of the IRAS bands were all measured using the pointed observation mode, rather than using the results of the survey *per se*. These pointed mode measurements have less intrinsic scatter than measurements obtained during the survey since the cross-scan position of a source with respect to individual detectors is well defined and flashes of the internal reference source were taken at the same time as the calibration source measurement. Each source was crossed at least five times on at least two separate occasions. In addition the reductions of the pointed observations were available before the survey processing was completed. Table VI.C.1 shows, however, that statistically the results of the survey reductions and pointed observations agree. The three piece fit to the feedback resistor curve shown in Figure VI.A.1 was assumed throughout. Except for this the system was assumed to be linear.

C.2.a Stellar Calibration

The absolute calibration at 12 μm was set so that the color corrected flux density of α Tau at that wavelength was 448 Jy, in agreement with ground based measurements by Rieke *et al.* (1984) at 10 μm. Alpha Tau was chosen on the basis that it was the primary stellar source in the absolute calibration of Rieke *et al.* and that it was well measured, with high signal to noise ratio, by IRAS. Although the absolute scale was set using observations of this one star, the IRAS measurements of a significant subset of the stars used by Rieke *et al.* are in excellent agreement with the ground based observations. In Table VI.C.2 the flux densities at 12 μm of stars measured using the pointed mode of IRAS are compared with the results of Rieke *et al.* at 10.6 μm. In this table, and in the following discussion, the flux densities obtained from IRAS have been color corrected assuming the energy distribution follows that of a hot blackbody. The flux densities obtained from the ground based observations have been extrapolated from 10.6 μm to 12 μm again assuming the energy distribution of the star follows that of a hot blackbody. The average ratio of the ground based flux densities to those obtained by IRAS is 1.01 ± 0.01.

In order to extrapolate the absolute calibration which was established for the 12 μm band to the longer IRAS wavelengths, it is convenient to define a magnitude system for inter-comparisons of the photometry in different wavelength bands which normalizes out the energy continuum of hot stars. Because the energy distributions of the stars are very nearly black bodies, the magnitude system has been defined such that zero magnitude corresponds to a flux density in Janskys:

$$f_\nu(0.0\ mag) = 1.57 \times 10^{-16} \times B_\nu(10{,}000\ K) \qquad \text{(VI.C.1)}$$

Table VI.C.1 Difference Between Survey and Pointed Observations

Band	12μm		25μm		60μm		100μm	
Star	mag[1]	dif[2]	mag	dif	mag	dif	mag	dif
α Tau	-3.08	-0.08	-3.02	-0.05	-3.03	-0.08	-2.81	-0.02
α Aur	-1.90	+0.01	-1.95	-0.03	-1.85	+0.01	-1.85	-0.06
α CMa	-1.36	-0.00	-1.38	-0.06	-1.23	+0.04	-	-
α CMi	-0.71	+0.03	-0.72	+0.00	-0.72	-0.02	-	-
β Gem	-1.21	-0.01	-1.19	-0.02	-1.22	-0.05	-1.19	+0.19
α Leo	+1.58	-0.08	+1.63	-0.09	-	-	-	-
γ UMa	+2.39	+0.01	+2.33	+0.03	-	-	-	-
ζ UMa	+1.99	-0.00	+1.93	-0.09	-	-	-	-
α Boo	-3.22	-0.07	-3.09	+0.01	-3.02	+0.09	-3.02	+0.21
γ Dra	-1.44	-0.01	-1.50	-0.03	-1.42	+0.06	-1.48	+0.07
α Lyr	-0.02	-0.03	-0.17	+0.01	-1.94	+0.01	-3.00	+0.12
β Gru	-3.40	+0.02	-3.50	-0.05	-3.52	-0.02	-3.48	+0.19
Avg		-0.019		-0.030		+0.005		+0.10
Sigma[3]		0.036		0.040		0.053		0.11

[1] mag = the magnitude derived from survey observations.

[2] dif = the difference between the magnitude derived from the survey and pointed observations.

[3] sigma = the population standard deviation.

---

where B_ν is the Planck function in Jy sr^{-1}. For the IRAS effective wavelengths $f_\nu[0.00\ mag]$ is 28.3, 6.73, 1.19 and 0.43 Jy at 12, 25, 60 and 100 μm. On this system α Lyr has a 12 μm magnitude of [12 μm](α Lyr) = 0.02 mag if it behaves as a 10,000 K blackbody beyond 2.2 μm and [12 μm](α Tau) = -3.00 mag.

The extrapolation of the stellar model to 25 μm was based on the compilation of solar photometry presented by Vernazza, Avrett, and Loeser (1976). A comparison of several stellar model calculations (Gustafsson, *et al.* 1975; Kurucz, 1979; Bell, 1984) with the data in Vernazza *et al.* predicted a smaller color difference, by about 2%, in the models than observed for the Sun. The models did show, however, that stars with a wide range of effective temperatures and surface gravities have the same [12 μm] - [25 μm] and [25 μm] - [60 μm] colors. The following colors, obtained from the observations of the solar fluxes, were thus adopted for the average of a set of calibration stars:

Table VI.C.2 Comparison with Ground-Based Observations

Star	$\frac{f_\nu \text{ (Rieke } et\ al.\text{)*}}{f_\nu \text{ (IRAS, 12 } \mu\text{m)}}$
α Tau	1.01
α Aur	1.01
α CMi	0.98
β Gem	1.01
α Boo	1.00
γ Dra	1.05
α Lyr	1.00

*extrapolated to 12μm using hot black body energy distribution

$$[12\mu m] - [25\mu m] = -0.03\ mag \qquad \text{(VI.C.2)}$$

$$[25\mu m] - [60\mu m] = -0.03\ mag$$

In Table VI.C.3 the stars used to develop the calibration are listed along with the resultant magnitudes from IRAS pointed observations. The stars were selected because reliable models were available for these stars and because there was no obvious excess at 60 μm relative to α Tau.

C.2.b Asteroid Calibration

The fluxes from the asteroids Hygiea, Europa and Bamberga were observed on eight occasions using the pointed mode of IRAS. Ten individual crossing of the focal plane were measured for Hygiea and Europa while 20 crossings were recorded for Bamberga. Color temperatures were derived for each observation using the stellar calibration at 25 and 60 μm, and the assumption was then made that these color temperatures would remain unchanged between 60 and 100 μm. The flux at 100 μm was then calculated for each observation from the appropriate blackbody function and the stellar calibration at 60 μm. The average of the predicted 100 μm fluxes for the three asteroids was then adopted as the basis of the 100 μm absolute calibration. The average color temperatures and the ratio of the predicted 100 μm flux to that adopted are given in Table VI.C.4.

Table VI.C.3 IRAS Magnitudes of Calibration Stars in Pointed Mode[1]

Star	[12 μm] (mag)	[25 μm] (mag)	[60 μm] (mag)
α Tau	-3.00	-2.97	-2.95
α Aur	-1.91	-1.91	-1.86
α Car	-1.40	-1.38	-1.33
α CMa	-1.36	-1.32	-1.27
α CMi	-0.74	-0.72	-0.70
β Gem	-1.20	-1.18	-1.17
α Leo	1.66	1.72	---
α Boo	-3.15	-3.10	-3.11

[1]See Section VI.C.2.a for definition of magnitude scale.

The asteroids Hygiea, Europa and Bamberga were selected for the basis of the 100 μm calibration because the analysis of ground based observations (Lebofsky, 1984) indicated that the standard asteroid model was a good fit out to 20 μm and could thus reasonably be expected to fit the longer IRAS wavelengths as well. This expectation was in fact borne out by the IRAS observations.

Several other asteroids were observed with IRAS. These are included in Table VI.C.4 in order to show the dispersion in the method. It should be emphasized that those selected as the basis of the 100 μm calibration were those which *a priori* fit the "standard asteroid model" described below between 12 and 60 μm.

As a check on the above procedure and the simple assumptions concerning asteroid colors, the observed flux densities for all the asteroids measured already, including the three used in the 60 to 100 μm extrapolation, were compared to calculations based on the "standard asteroid model" of Morrison (1973) and Jones and Morrison (1974). The infrared emissivity of the surface was taken to be 0.9 independent of wavelength and the thermal modeling constant β was 0.9; the albedo was taken from the TRIAD file (Zellner, 1979). The temperature distribution on the surface was assumed to follow:

$$T = T_{ss} \cos^{0.25} z \qquad \text{(VI.C.3)}$$

Table VI.C.4 Color Temperatures of Asteroids between 25 and 60 μm

Asteroid	Color Temp.[1,3] K	Obs./Pred. Flux[2,3]
Europa	228±15	0.97±0.12
Bamberga	243±10	1.01±0.15
Hygeia	232±16	1.01±0.13
Eukrate	292±29	1.19±0.12
Egeria	259±19	0.95±0.13
Ceres	234±12	1.13±0.12
Flora	297±40	1.43±0.25
Berberic	301±32	1.52±0.26
Pallas	232±7	1.05±0.08

1 The color temperature is based on the 25 and 60 μm fluxes

2 The predicted 100 μm flux is extrapolated from the 60 μm flux density obtained from the stellar calibration and the color temperature.

3 The uncertainties are the population standard deviations

---

where T_{ss} is the subsolar point temperature and z is the zenith angle of the Sun. The temperature of the dark side was taken to be 0 K; this assumption does not lead to a significant error since mainly the sunlit sides of the asteroids were observed by IRAS.

The asteroid diameters were adjusted for each observation to match the 60 μm stellar calibration exactly, i.e. all ratios of observed/model fluxes at 60 μm are identical to unity. The 100 μm calibration was adjusted such that for the asteroids the mean of the ratio of the observed flux to the model flux was equal to unity. The resultant ratios of observed fluxes to those derived from the model are given in Table VI.C.5.

C.2.c Estimated Accuracy

The estimated absolute accuracy of the stellar plus asteroid calibration relative to the 10 μm ground based calibration is 2%, 5% and 5% at 12, 25 and 60 μm, based on the uncertainty in the stellar models and the scatter in the standard stars, and 10% at 100 μm based on the uncertainty of the asteroid model extrapolation. The stated accuracy of the 10 μm absolute calibration is 3% (Rieke *et al.* 1984). The

Table VI.C.5 Ratio of Observed to Model Fluxes of Asteroids

Asteroid	Observed/Model Fluxes[1]		
	25 μm	60 μm[2]	100 μm
Europa	1.026	1.000	1.000
	1.026	1.000	0.965
Hygiea	1.052	1.000	1.005
	1.062	1.000	1.015
Bamberga	1.000	1.000	0.980
	1.000	1.000	1.035
	1.082	1.000	1.015
	1.066	1.000	1.025
Average Asteroid	1.039	1.000	1.000[3]
Population Dispersion	±0.031		±0.029

(1) Observed 25 and 60 μm fluxes are based on stellar calibration. The model fluxes are based on the standard asteroid model (Morrison, 1973; Jones and Morrison, 1974) with the beaming factor $\beta = 0.9$, emissivity $\varepsilon = 0.9$, and albedo from the TRIAD file (Zellner, 1979).

(2) The asteroid diameter is used to normalize the model flux to the observed flux at 60 μm, i.e. observed/model = 1.000 for each asteroid.

(3) By definition of the calibration procedure, the mean ratio of observed/model = 1.000.

---

error introduced into the absolute calibration due to uncertainties in the spectral pass-bands is estimated to be less than 4% for objects as warm, or hotter than asteroids.

The ratios listed in Table VI.C.5 indicate that, for the three asteroids used in the calibration, the flux at 25 μm is higher than expected on the basis of the stellar calibration and the asteroid models by 4 ± 1% once the fluxes have been normalized at 60 μm. This is well within the expected accuracy of the stellar and asteroid models. The dispersion of the ratio of observed to model fluxes at 100 μm is only 3%, the mean being identical to unity by definition of the asteroid calibration procedure. The good fit at 25 μm and the small dispersion at 100 μm gives confidence that the extrapolation of these asteroids is a valid procedure.

C-3

TABLE Suppl.VI.C.6 Color Correction Factors, K[1]

INTRINSIC POWER LAW[2]	RATIO OF FLUX DENSITIES BEFORE COLOR-CORRECTION			CORRECTION FACTOR			
α	$\frac{f_\nu(12\ \mu m)}{f_\nu(25\ \mu m)}$	$\frac{f_\nu(25\ \mu m)}{f_\nu(60\ \mu m)}$	$\frac{f_\nu(60\ \mu m)}{f_\nu(100 \mu m)}$	K(12 μm)	K(25 μm)	K(60 μm)	K(100 μm)
-3.0	0.113	0.063	0.21	0.91	0.89	1.02	1.02
-2.5	0.162	0.102	0.275	0.92	0.91	1.00	1.01
-2.0	0.232	0.164	0.355	0.94	0.93	0.99	1.00
-1.5	0.333	0.262	0.460	0.97	0.96	0.99	1.00
-1.0	0.480	0.417	0.600	1.00	1.00	1.00	1.00
-0.5	0.694	0.662	0.786	1.04	1.04	1.02	1.00
0.0	1.005	1.045	1.037	1.10	1.10	1.05	1.01
0.5	1.459	1.642	1.378	1.17	1.16	1.09	1.02
1.0	2.123	2.567	1.843	1.25	1.23	1.15	1.04
1.5	3.094	3.992	2.484	1.35	1.32	1.23	1.06
2.0	4.519	6.170	3.373	1.47	1.41	1.32	1.09
2.5	6.610	9.480	4.617	1.61	1.53	1.44	1.12
3.0	9.681	14.475	6.370	1.78	1.67	1.59	1.16

INTRINSIC TEMP (K)	RATIO OF FLUX DENSITIES BEFORE COLOR-CORRECTION			CORRECTION FACTOR			
	$\frac{f_\nu(12\ \mu m)}{f_\nu(25\ \mu m)}$	$\frac{f_\nu(25\ \mu m)}{f_\nu(60\ \mu m)}$	$\frac{f_\nu(60\ \mu m)}{f_\nu(100\ \mu m)}$	K(12 μm)	K(25 μm)	K(60 μm)	K(100 μm)
10000	4.345	6.050	3.350	1.45	1.41	1.32	1.09
5000	4.172	5.931	3.327	1.43	1.40	1.32	1.09
4000	4.086	5.872	3.316	1.42	1.40	1.31	1.09
3000	3.944	5.773	3.297	1.41	1.39	1.31	1.09
2000	3.666	5.578	3.259	1.38	1.38	1.31	1.09
1000	2.891	5.005	3.145	1.27	1.34	1.29	1.08
800	2.545	4.730	3.088	1.22	1.32	1.28	1.08
600	2.036	4.287	2.995	1.15	1.29	1.27	1.08
500	1.692	3.950	2.920	1.09	1.26	1.26	1.08
400	1.272	3.478	2.810	1.01	1.22	1.24	1.08
300	0.785	2.780	2.630	0.92	1.15	1.21	1.07
290	0.734	2.693	2.606	0.91	1.15	1.21	1.07
280	0.684	2.602	2.580	0.90	1.14	1.20	1.07
270	0.633	2.506	2.553	0.89	1.13	1.20	1.07
260	0.583	2.407	2.523	0.88	1.12	1.19	1.07
250	0.534	2.304	2.491	0.87	1.11	1.19	1.07
240	0.486	2.196	2.457	0.86	1.09	1.18	1.07
230	0.438	2.084	2.420	0.85	1.08	1.18	1.07
220	0.392	1.967	2.381	0.85	1.07	1.17	1.07
210	0.347	1.845	2.338	0.84	1.06	1.16	1.06
200	0.304	1.719	2.291	0.83	1.04	1.16	1.06
190	0.263	1.589	2.240	0.83	1.02	1.15	1.06
180	0.224	1.455	2.184	0.83	1.01	1.14	1.06
170	0.188	1.317	2.124	0.83	0.99	1.13	1.06
160	0.154	1.176	2.057	0.84	0.97	1.12	1.06
150	0.124	1.034	1.983	0.85	0.95	1.11	1.05
140	0.097	0.892	1.901	0.87	0.93	1.09	1.05
130	0.073	0.751	1.810	0.90	0.91	1.08	1.05
120	0.053	0.614	1.709	0.94	0.89	1.06	1.04
110	0.036	0.484	1.595	1.01	0.86	1.04	1.04
100	0.023	0.363	1.468	1.12	0.84	1.02	1.04
95	0.018	0.307	1.400	1.19	0.83	1.01	1.03
90	0.014	0.256	1.326	1.28	0.83	1.00	1.03
85	0.010	0.208	1.249	1.39	0.82	0.99	1.03
80	0.007	0.165	1.168	1.54	0.81	0.97	1.02
75	0.005	0.127	1.082	1.74	0.81	0.96	1.02
70	0.003	0.095	0.993	2.01	0.81	0.95	1.01
65	0.002	0.067	0.898	2.40	0.82	0.94	1.01
60	0.001	0.045	0.801	2.97	0.83	0.93	1.00
55	—	0.028	0.700	3.86	0.86	0.92	1.00
50	—	0.016	0.597	5.35	0.90	0.91	0.99
45	—	0.008	0.493	8.09	0.97	0.92	0.98
40	—	0.003	0.391	13.79	1.08	0.93	0.98

[1] f_ν[actual] = f_ν[quoted]/K spectral response given in Table Suppl.II.C.5.

[2] $f_\nu = \nu^\alpha$

An alternative explanation of the results in Table VI.C.5 is that the difference between the observed and predicted 60 to 25 μm flux ratio could be a manifestation of a short wavelength leak in the 60 μm spectral response such as reported from the preflight component tests (Section II.C.4). An examination of the 60 μm to 12 and 25 μm colors of the calibration stars (Table VI.C.3), however, shows no change in color larger than 0.02 mag for different effective stellar temperatures; whereas the colors should change by 0.04 mag for effective temperatures varying from 4000 to 10,000 K, if the short wavelength leak were real.

C.3 Color Corrections

In the catalog, the flux densities have been quoted for the effective wavelengths and an input energy distribution which is constant in the flux per logarithmic frequency interval (essentially the flux per octave); i.e., the flux density with frequency ν goes as $f_\nu \propto \nu^{-1}$ while the flux density with wavelength λ goes as $f_\lambda \propto \lambda^{-1}$. No loss in generality in incurred by such a procedure, nor does it prejudice subsequent correction for the correct source distribution.

If the input energy distribution is not constant in flux per octave a correction, the "color correction", must be applied to the quoted flux densities. This correction depends on the shape of the intrinsic energy distribution and on the details of the wavelength response of the system. The color corrections for a number of input energy distributions are given in Table VI.C.6.

The flux F measured by a detector is given by:

$$F = f_{\nu_0}\,[\text{actual}] \int (f_\nu/f_{\nu_0})\,[\text{actual}]\, R_\nu d\nu \qquad \text{(VI.C.4)}$$

$$= f_{\nu_0}\,[\text{quoted}] \int (f_\nu/f_{\nu_0})\,[\text{quoted}] R_\nu d\nu \qquad \text{(VI.C.5)}$$

$$= \frac{f_{\nu_0}\,[\text{quoted}]}{K} \int (f_\nu/f_{\nu_0})\,[\text{actual}]\, R_\nu d\nu \qquad \text{(VI.C.6)}$$

In these equations, ν_0 is the effective frequency of 25, 12. 5, and 3×10^{12} Hz corresponding to the effective wavelengths of 12, 25, 60 and 100 μm, f_ν is either the actual or quoted flux density of the source, (f_ν/f_{ν_0}) is the flux density normalized to the effective frequency of the band and R_ν is the relative system response listed in the last column of Table II.C.5. Equations VI.C.4 and VI.C.6 show that the true flux density at ν_0 is given by:

$$f_{\nu_0}\,[\text{actual}] = f_{\nu_0}\,[\text{quoted}]/K \qquad \text{(VI.C.7)}$$

where, from Eq. VI.C.4 and VI.C.5,

$$K = \left[\int (f_\nu/f_{\nu_0})\,[\text{actual}]\, R_\nu d\nu \right] \Big/ \left[\int (f_\nu/f_{\nu_0})\,[\text{quoted}]\, R_\nu d\nu \right] \qquad \text{(VI.C.8)}$$

It should be emphasized that there is no prejudice in the procedure or assumptions. The uncertainty in the quoted flux densities results directly from the lack of knowledge of the spectral response of the system. Deriving the true flux densities requires a knowledge of the intrinsic energy distribution of the astronomical sources.

The sensitivity of the color corrections to uncertainties in the spectral band passes was checked by numerical simulations. For many sources of interest in the catalog, the 60 μm band flux densities are especially sensitive to errors caused by lack of knowledge of the spectral pass bands. Specifically, in this band, uncertainties in the short wavelength parameters of the transmission of the optics, and in the detector efficiency, affect the response for extremely cold objects ($T \sim 60\ K$) in a significantly different way than for the stellar energy distribution of the calibrating sources. The numerical tests show that the sensitivity of the color corrections to wavelength shifts of the entire response is approximately 7%/μm; prelaunch measurements of the spectral shape should be accurate to $\sim$ 0.3 μm. On the other hand, if the effective responsivity of the system increases by an additive 1% over the entire bandwidth, starting at 24 μm, the calibration for 60 K sources changes by 16% relative to the stellar calibration. Uncertainties of this magnitude in the effective response are the maximum expected from pre-flight measurements. Errors in the long wave cutoff of the 100 μm band could also result in significant errors in the flux densities of objects colder than 30 K.

C.4 Absolute Calibration of Extended Emission

The absolute calibration of the extended emission observed by IRAS was based directly on the absolute calibration of the point sources. Thus the value of the equivalent absolute flux density assigned to the flashes of the internal reference source was carried directly to the calibration of the extended emission with the additional corrections for the frequency response and effective detector areas; see Sections IV.A.3 and IV.A.4.

D. Comparison of IRAS Observations with Ground Based Observations

In Table VI.D.1 a comparison is given between the IRAS measurements of selected stars made in the pointed mode and the results of ground based measurements by Tokunaga (1984) and Rieke *et al.* (1984). At 12 μm, the IRAS measurements agree with the ground based magnitudes within 1%. The difference is largely due to γ Dra.

If α Lyr is omitted, the average difference (and the uncertainty in the mean) between the IRAS magnitudes and those of Tokunaga (1984) at 25 μm is -0.01 ± 0.02 while the difference between the IRAS magnitudes and those of Rieke *et al.* (1984) is 0.04 ± 0.01. The 0.02 mag difference in zero point between the IRAS magnitudes and those of Tokunaga has been incorporated in these differences as well as the difference of 0.03 mag assumed in the 12 to 25 μm color. A corollary of this good agreement is that the excess in α Lyr does not start until longward of the long wavelength cutoff of the filters used in the ground based observations.

The most accurately calibrated measurements to compare with the IRAS 60 and 100 μm observations are those of the planets Uranus and Neptune by Hildebrand *et al.* (1984) using NASA's Kuiper Airborne Observatory (KAO). Hildebrand *et al.*'s measurements of Uranus are compared to observations taken early in the IRAS mission in Figure VI.D.1. It is seen that the flux densities obtained by IRAS are $\sim$ 20% lower than those obtained by Hildebrand *et al.* The cause of the discrepancy is not understood at this time.

It should be noted that the temperature of Uranus is $\sim$ 60 K. The planet thus has an energy distribution quite different from that used in the calibration procedure. Although a short wavelength leak in

the 60 μm filters as large or larger than 20% would account for this discrepancy, the good fit of the asteroid and stellar models at 25 and 60 μm and the near constant stellar colors with effective temperature appear to rule out a short wavelength leak of this magnitude. It should be noted, however, that all the measurements from the KAO derive their absolute calibration from observations of Mars and a single model thereof. Thus the internal agreement of the KAO observations at different wavelengths does not reflect independent calibrations. An analysis of the final IRAS survey flux densities, as contrasted to those obtained from the pointed observations, is given in Chapter VII.

Table VI.D.1 Comparison with Ground-Based Observations

	[12 μm]			[25μm]		
Star	IRAS (mag)	Δ_T (mag)	Δ_R (mag)	IRAS (mag)	Δ_T (mag)	Δ_R (mag)
α Tau	-3.00	-0.01	-0.01	-2.97	+0.07	+0.07
α Aur	-1.91	-0.01	-0.01	-1.91	-0.03	-0.02
α CMa	-1.36	-0.04	--	-1.32	-0.01	--
α CMi	-0.74	-0.00	-0.02	-0.72	-0.04	-0.01
β Gem	-1.20	-0.02	-0.01	-1.18	-0.02	-0.04
α Boo	-3.15	-0.00	-0.00	-3.10	-0.02	+0.06
γ Dra	-1.43	--	-0.05	-1.47	--	+0.04
α Lyr	0.02	0.00	+0.00	-0.18	+0.23	+0.23

Δ_T and Δ_R are the differences between the IRAS [12 μm] and [25 μm] magnitudes and the corresponding values from Tokunaga (Δ_T) and Rieke *et al.* (Δ_R). Differences are in the sense Δ = [IRAS] - [ground-based]. In displaying these differences, the 10.1 μm magnitudes of Tokunaga have been adjusted by 0.02 mag to account for a different zero point convention, and the 20.1 and 21 μm magnitudes of Tokunaga and Rieke *et al.* have been similarly adjusted by 0.05 and 0.03 mag to agree with Eq. (VI.C.2).

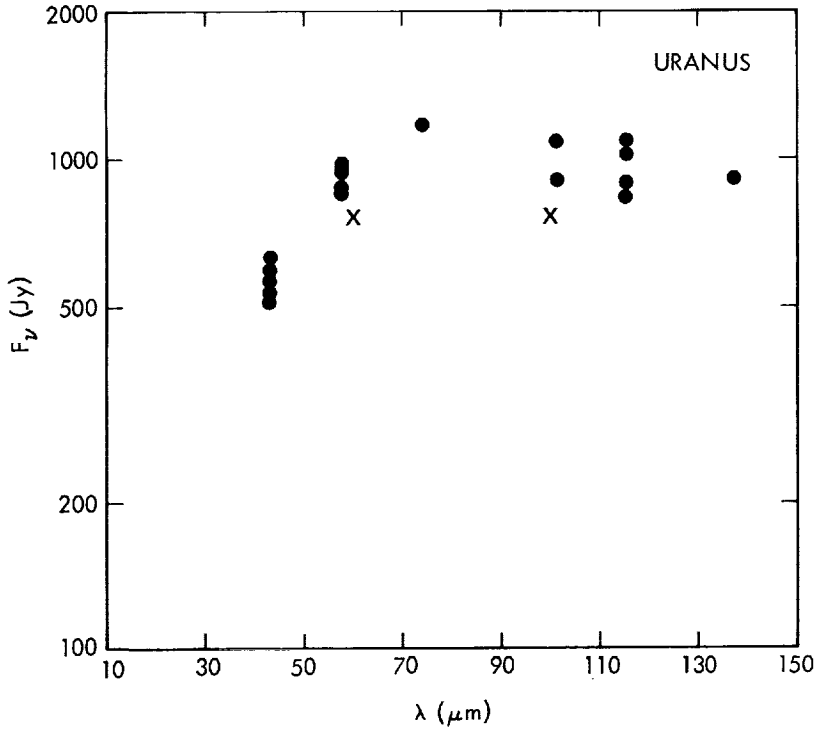

Figure VI.D.1 Comparison of measurements of Uranus at infrared wavelengths with those of IRAS. The observations have been normalized to a distance of 17.75 A.U.

Authors:

G. Neugebauer, S. Wheelock, F. Gillett, H. H. Aumann, T. N. Gautier, F. J. Low, P. Hacking, M. Hauser, S. Harris, P. Clegg.

References

Allen, D.A. 1970, *Nature,* **227**, 158.

Allen, D.A. 1971, in *Physical Studies of Minor Planets*, editor T. Gehrels, Univ. Ariz. Press, p. 41.

Bell, R. 1984 private communication.

Gustafsson, Bell, Ericksson, Nordlund, 1975, *Astr. Ap.*, **42**, 407.

Hauser, M. *et al.* 1984, *Ap. J. (Lett.),* **278**, L15.

Hildebrand, R.H., Lowenstein, R.F., Harper, D.F., Orton, G.S., Keene, J., and Whitcomb, S. 1984, pre-print

Jones, T.J., and Morrison, D. 1974, *A. J.,* **79**, 892.

Kurucz 1979, *Ap. J. (Suppl.),* **40**, 1.

Lebofsky 1984, personal communication.

Low, F.J., *et al.* 1984, *Ap. J. (Lett.),* **278**, L19

Morrison, D. 1973, *A. J.,* **194**, 203.

Rieke, G.H., Lebofsky, M. and Low, F.J. 1984, preprint.

Tokunaga, A. 1984, *A. J.,* **89**, 172.

Vernazza, J.E., Avrett, E.H., and Loeser, R. 1976, *Ap. J. (Suppl.),* **30**, 1.

Zellner, B. 1979 in *Asteroids*, editor T. Gehrels, Univ. Ariz. Press, p. 1011.

VII. ANALYSIS OF PROCESSING

A. Overview

The purpose of this chapter is to describe the general characteristics of the catalogs of point and small extended sources and of the sky brightness images. The distribution on the sky of different types of infrared sources is presented not for scientific purposes, but to provide a context within which to interpret the characteristics of specific objects (Section VII.B). Detailed discussions are presented of the positional and photometric accuracy of the point sources (Sections VII.C,D). Although the important questions of the completeness and reliability of the catalogs are deferred until the next chapter, some of the results of the processing relevant to these topics are discussed in Sections VII.E and VII.F. An overview of the results of associating IRAS sources with objects appearing in other catalogs is given in Section VII.G. Because it is crucial that the user gain an understanding of the various flags that accompany the observations of a source, the properties of these flags, in particular the threshold values that indicate that the measurement of a source may be suspect, are described in Section VII.H. The properties of the catalog of small extended sources are presented in Section VII.I. The extended emission images are discussed in Section VII.J.

B. General Statistics of the Point Source Processing and Catalog

B.1 The Generation of Reliable Point Sources

The complementary aims of completeness and reliability resulted in the design of detection and confirmation programs that acted as a series of filters to weed out spurious sources at each level of the data processing. Because the detection thresholds were set low to improve completeness, subsequent stages of confirmation were used to establish the reliability of the IRAS sources.

Approximately 500,000 events per day triggered the square-wave filter detection algorithm (Section V.C.2). Approximately 20 to 40% of these detections passed the signal-to-noise and correlation coefficient thresholds. The largest fraction of the detections that were accepted, about one-third of the total, came at 25 μm. Detections at 12 μm and 100 μm, each contributed one-quarter of the total number, while the remainder, about one-sixth of the total number, came at 60 μm. About two-thirds of the accepted detections were sightings at different wavelengths of approximately 25,000 seconds-confirmed band-merged sources produced daily. About one-third of the seconds-confirmed sources were used in the roughly 4,000 hours-confirmed sources (hereafter denoted as HCONs) generated per day of surveying.

Hours-confirmed sources were placed into a Working Survey Data Base (WSDB) to await possible weeks-confirmation. At the completion of the initial data processing the WSDB contained about 1.2 million hours-confirmed sources spread over the entire sky. Of these, some 317,000 failed to be matched with a weeks-confirming partner during the initial processing. The remaining 885,000 HCONs were combined by the weeks-confirmation processor during the normal processing into 319,000 distinct sources each consisting of two or more HCONs. The clean-up processing discussed in Section V.H.2 forced close neighboring sources into single weeks-confirmed sources, decreasing the number of distinct objects while increasing the average number of HCONs per source. After clean-up there were about

304,000 single HCONs and 314,000 weeks-confirmed sources, each consisting of two or more HCONs. The breakdown of the catalog by numbers of HCONs is given in Table VII.B.1.

There were three reasons why even a weeks-confirmed source could be excluded from the catalog. First, the source could fail to satisfy the criteria of having at least one high quality flux in one band or two or more moderate quality fluxes in adjacent bands (Section V.H.5); some 12,000 sources were rejected for this reason. Second, the high source density processing could eliminate a source due to the strict selection rules imposed in such areas (Section V.H.6 and VII.E.1.b); about 57,000 sources which had all survived the first test were rejected by these criteria. Third, a source could be deleted because it was a spurious object produced near a bright source (Section VII.E.4); there were 22 such sources outside of the Galactic plane. Of the 314,000 weeks-confirmed sources in the WSDB, 245,839 survived all these criteria to appear in the catalog.

B.2 Distribution of Sources in the Catalog

As mentioned in Section I.C, there is a meaningful astrophysical classification for almost all of the IRAS sources. Objects detected at 12 μm and having $f_\nu(12\ \mu m) > f_\nu(25\ \mu m)$ are typically stars (Fig. I.C.2, type S in Table VII.B.2). Objects detected at 60 μm and having $f_\nu(60\ \mu m) > f_\nu(25\ \mu m)$ are either galaxies if they are located away from the Galactic plane or warm Galactic objects if located near the plane (type G, Fig. I.C.3). Objects detected only at 100 μm are predominantly cirrus sources, although some at very high Galactic latitudes may be external galaxies (type C, Fig. I.C.4). Sources meeting none of these criteria are classified "other" and lie mostly in the Galactic plane. Figure VII.B.1 shows histograms of the distribution of the four types of sources as a function of Galactic latitude.

All cataloged sources can also be classified into 15 different spectral groups depending on which bands have measurements of either moderate or high quality. The numbers in each category are given in Table VII.B.2, where a code has been used to specify which bands were reliably detected. If the presence or absence of a measured flux density at 12, 25, 60 and 100 μm is considered in that order to correspond to a "1" or "0" in a four digit number, then a source measured only at 12 μm is denoted by "1000", while one measured at 12 μm and 60 μm is denoted by "1010", etc. The distribution on the sky of each of these color combinations is shown in a series of equal area projections in Galactic coordinates. These figures are shown in an appendix at the end of the chapter (Figs. VII.Ap.1-15).

C. Positional Accuracy

C.1 Positional Accuracy of Catalog Sources

Stars from the Star Catalog of the Smithsonian Astrophysical Observatory (1966, henceforth the SAO Catalog) and UGC galaxies with accurately determined positions (Dressel and Condon 1976, henceforth the Dressel and Condon Catalog) were used to investigate the accuracy of the positions quoted in the IRAS point source catalog.

Small areas of half-width 20″ in-scan by 75 ″ cross-scan around sources brighter at 12 μm than at 25 μm and located more than 20° from the Galactic plane, were searched for SAO stars. Stars with spectral class O, B, and A, and those with no spectral classification were specifically excluded. Inadvertently, stars of spectral types MA, MB, NA and NB were also excluded. This reduced the size of the sample of stars used, but, as a subsequent examination revealed, had no effect on the statistics reported below.

Table VII.B.1 Number of HCONs in WSDB and Final Catalog

Number of HCONs	Number of WSDB Sources	Number of Sources after Clean-up	Number of Catalog sources
1	317,764	304,334	0
2	129,336	122,705	76,724
3	150,545	151,039	132,974
4	27,233	28,028	24,902
5	6,906	7,289	6,479
6	2,731	2,958	2,617
7	1,565	1,730	1,586
8	406	456	433
9-23	100	124	124
Total weeks-confirmed ($\geqslant$ 2 HCONs)	318,822	314,329	245,839

Table VII.B.2 Spectral Classification of Catalog Sources

Combination	Number	Type S	Type G	Type C	Type O
1000	67,332	57,315			10,017
1100	67,015	61,776			5,239
1110	13,233	9,387*	4,114*		1,454
1111	6,343	2,287*	4,583*		290
0100	3,936				3,936
0110	3,642		3,470		172
0111	3,873		3,860		13
0010	19,264		18,494		770
0011	22,702		22,197		505
0001	33,146			33,146	
1101	2,025	1,478			547
1010	1,100	647*	1,062*		33
1011	520	297*	515*		3
1001	1,207	905			302
0101	501				501
Total	245,839	134,092*	58,295*	33,146	23,782

*3,476 sources are both Type S and G categories.

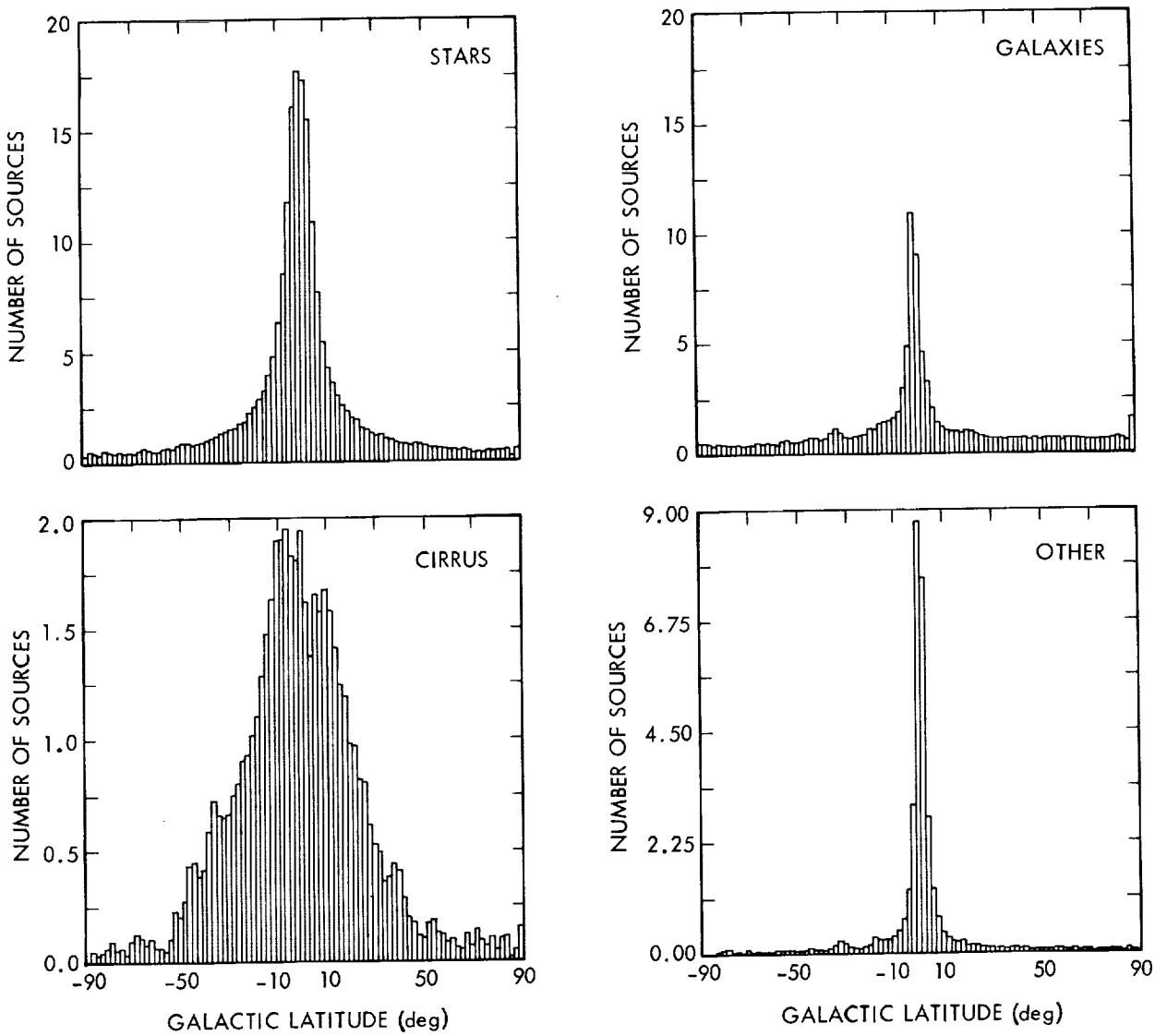

Figure VII.B.1 The number density (per sq. deg) of four kinds of IRAS source (see text) is shown as a function of Galactic latitude, averaged over all Galactic longitudes.

Areas of the same size around sources detected at 60 μm, which were brighter at 60 μm than at 25 μm, and located more than 30° from the Galactic plane, were searched for a galaxy in the Dressel and Condon catalog. If there was more than one cataloged star or galaxy within the search box of the IRAS source, the source was not used. Matches with position differences greater than seven times the *a priori* uncertainty on either axis were also discarded. No galaxies and fewer than 0.1% of the stars were rejected for this reason.

The analysis was done separately for bright sources (flux densities greater than 1.2 and 1.9 Jy at 12 and 60 μm respectively) and faint sources (flux densities lower than the above limits). The number of such sources in each sample are given in Table VII.C.1.

Table VII.C.1 Absolute Position Difference Statistics

	Number N	In-Scan Mean difference (″)	In-Scan Population σ (″)	In-Scan χ^2/N	Cross-Scan Mean difference (″)	Cross-Scan Population σ (″)	Cross-Scan χ^2/N
SAO Stars							
Bright	4757	0.0	1.9	0.42	0.1	8.4	0.55
Faint	10558	0.0	2.8	0.65	0.2	15.6	0.87
Galaxies							
Bright	340	-1.2	5.3 (3.5*)	1.04	1.0	12.8 (12.2*)	1.30
Faint	814	-1.2	5.7 (4.1*)	0.91	0.4	15.2 (14.7*)	1.00

*4″ uncertainty removed.

C.1.a Accuracy of the Absolute Positions

The absolute positional differences between the 12 μm sources and the associated stars are shown in Figs. VII.C.1 and VII.C.2 for the in-scan and cross-scan directions. The same information is given for 60 μm sources and the associated galaxies in Figs. VII.C.3 and VII.C.4. In the top panel of each figure a histogram of the number of bright sources is plotted as a function of the absolute position difference. The bottom panel repeats this plot for the fainter sources. In each case an equal-area Gaussian distribution with the mean and standard deviation of the sample is plotted for comparison. From these figures it is apparent that the in-scan errors are reasonably well represented by Gaussian distributions. The cross-scan errors are less Gaussian, showing a more concentrated center and more extended tails.

The mean and population standard deviation of the positional differences for all sources in the samples described above are given in Table VII.C.1. Because the SAO positions are more accurate than the IRAS positions, the listed discrepancies should be representative of the IRAS position errors for sources detected at the short wavelengths. Since the rms position errors in the Dressel and Condon catalog are 4″ in each direction, i.e., approximately the same as the IRAS in-scan errors, it is necessary to correct the statistics for this additional uncertainty. The estimates obtained by subtracting the 4″ errors in quadrature from the calculated standard deviations in both directions are given in parentheses in the table. No account has been made for any offset of the IRAS source from the optical nucleus of the galaxy. Any such effect would cause an overestimate of the IRAS position errors.

The mean positions of the IRAS stars do not deviate significantly from the SAO positions. This is not surprising since the in-flight calibration of the IRAS focal plane geometry used SAO stars detected at 12 μm to determine the geometric position of the infrared focal plane with respect to the visible star sensors (Section V.D.3). There is also no significant deviation of the cross-scan position of the IRAS galaxy sample based on the galaxy positions. Table VII.C.1 does, however, show a small, but statistically

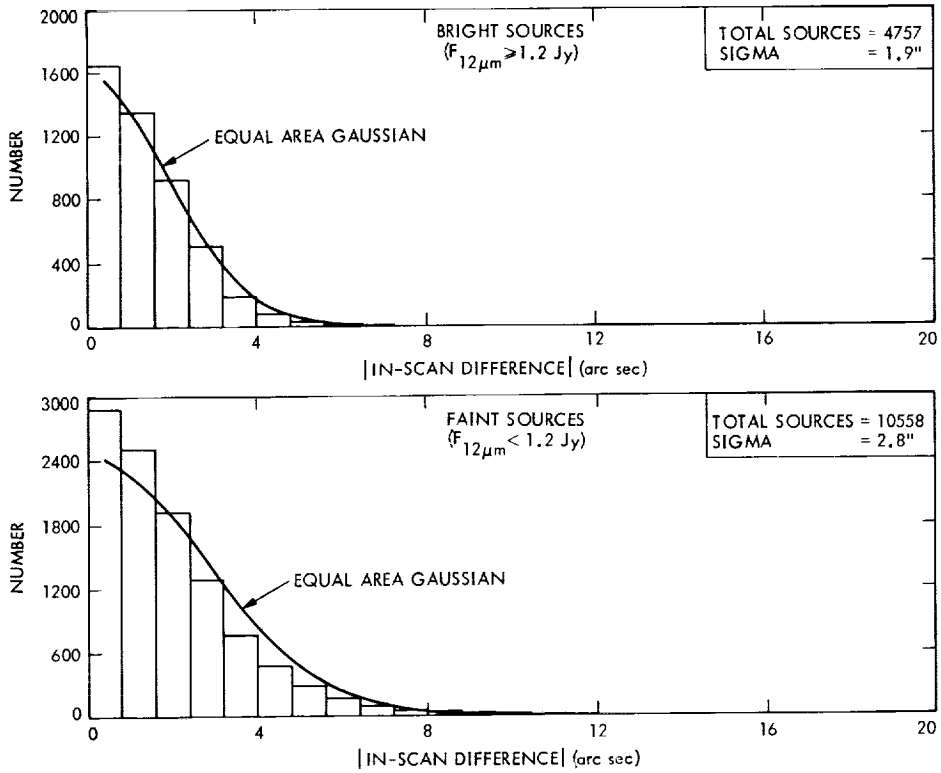

Figure VII.C.1 Position differences for the IRAS stellar sources associated with SAO stars in the in-scan direction. See text.

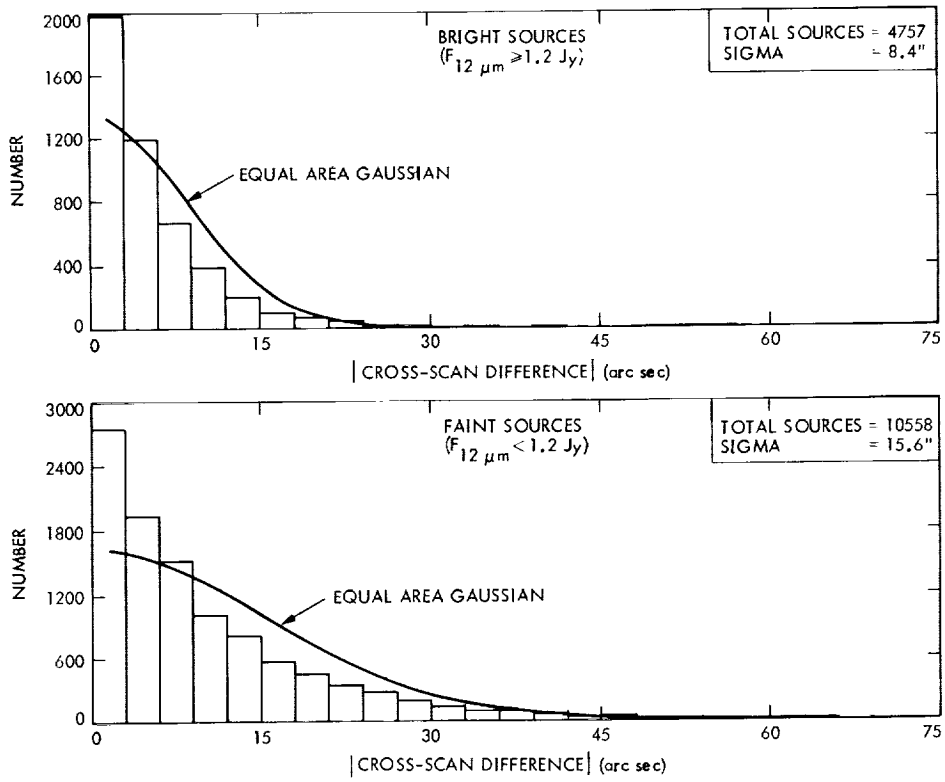

Figure VII.C.2 Position differences for the IRAS stellar sources in the cross-scan direction. See text.

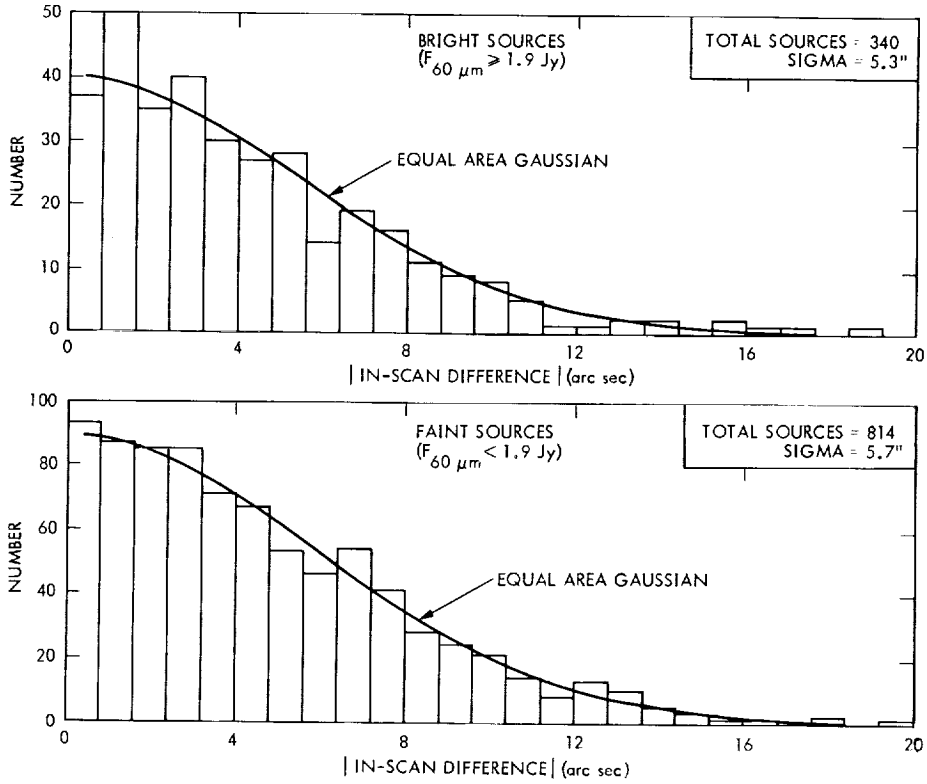

Figure VII.C.3 Position differences for the galaxies associated with Dressel and Condon galaxies in the in-scan direction. See text.

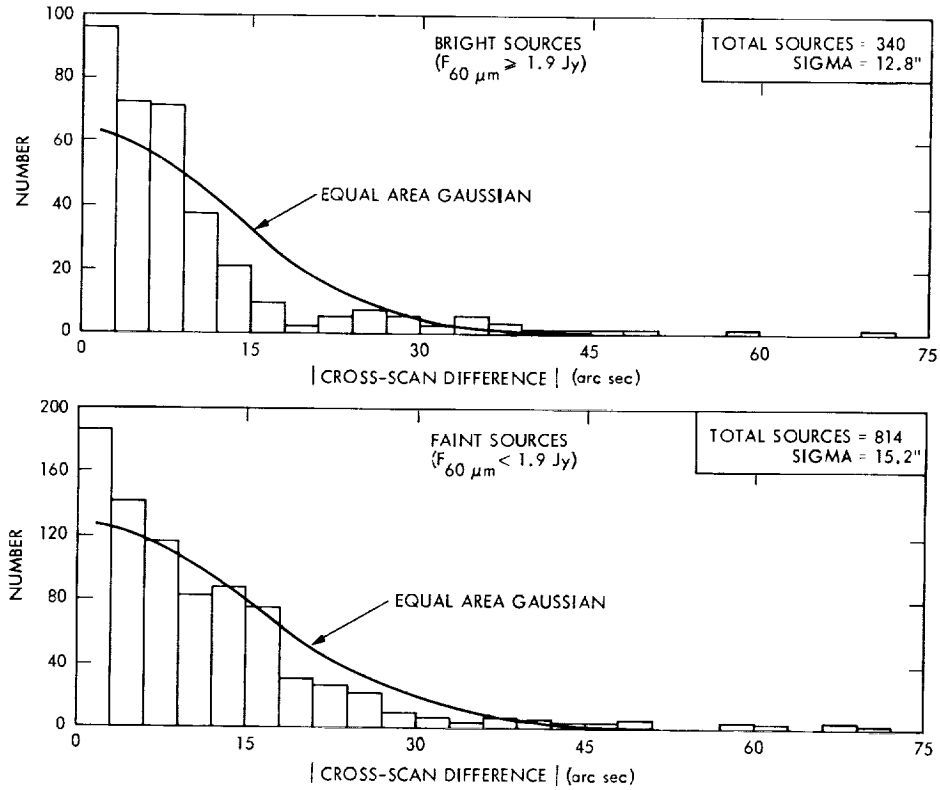

Figure VII.C.4 Position differences for the galaxies associated with Dressel and Condon galaxies in the cross-scan direction. See text.

significant discrepancy for the in-scan positions of the galaxies. This small error is consistent with the differences in the positions of the seconds-confirmed sightings in individual wavelength bands of sources seen at multiple wavelengths. While there is no significant discrepancy between the 12 μm and 25 μm positions, there is an 0.8″ discrepancy between the in-scan positions of sources as measured at 12 μm and 60 μm, and a 2.4″ discrepancy between the in-scan positions of sources as measured at 12 μm and 100 μm. A 0.2% error in the image scale of the telescope could account for this effect. Because the band-merging process used positional information from all detected bands for a source, multiband sources would suffer least from this error; sources detected only at 100 μm could suffer from the full 2.4″ error.

The standard deviations of the position errors, given in Table VII.C.1, show that the absolute position errors are quite small. The in-scan position errors depend, as expected, on source brightness and wavelength. The cross-scan positions of the brighter sources are significantly better than those of the faint sources, in large part because these sources were detected at multiple wavelengths. The difference between the errors in the bright stars and the errors in the galaxies is consistent with the expected diffraction effects and detector sampling rates.

C.1.b The Quoted Position Uncertainties

The quality of the IRAS position uncertainties is shown in Fig. VII.C.5 for the in-scan and cross-scan directions. Separately plotted for each of the bright and faint source samples are the mean absolute position differences of those sources as a function of the quoted standard deviation. For comparison, the value of this same quantity for a Gaussian distribution of position errors would be

$$\sqrt{\frac{2}{\pi}}\ \sigma_{IRAS} \quad \text{for stars} \qquad \text{and}$$

$$\sqrt{\frac{2}{\pi}}\ (\sigma_{IRAS}^2+\sigma_{DC}^2)^{1/2} \quad \text{for galaxies.} \tag{VII.C.1}$$

These relations are shown as a solid line in each figure. The difference in form for the galaxies is due to the 4″ uncertainty, σ_{DC}, in the Dressel and Condon catalog. From the figures it is evident that the IRAS position uncertainties are accurate estimates of the position errors only for small values and a considerable overestimate for large values.

The overall quality of the quoted error estimates is measured by the χ^2 parameter, defined as

$$\chi^2 = \sum_N \frac{(x_{IRAS}-x_{SAO})^2}{\sigma_{IRAS}^2} \quad \text{for stars}$$

$$\chi^2 = \sum_N \frac{(x_{IRAS}-x_{DC})^2}{(\sigma_{IRAS}^2+\sigma_{DC}^2)} \quad \text{for galaxies} \tag{VII.C.2}$$

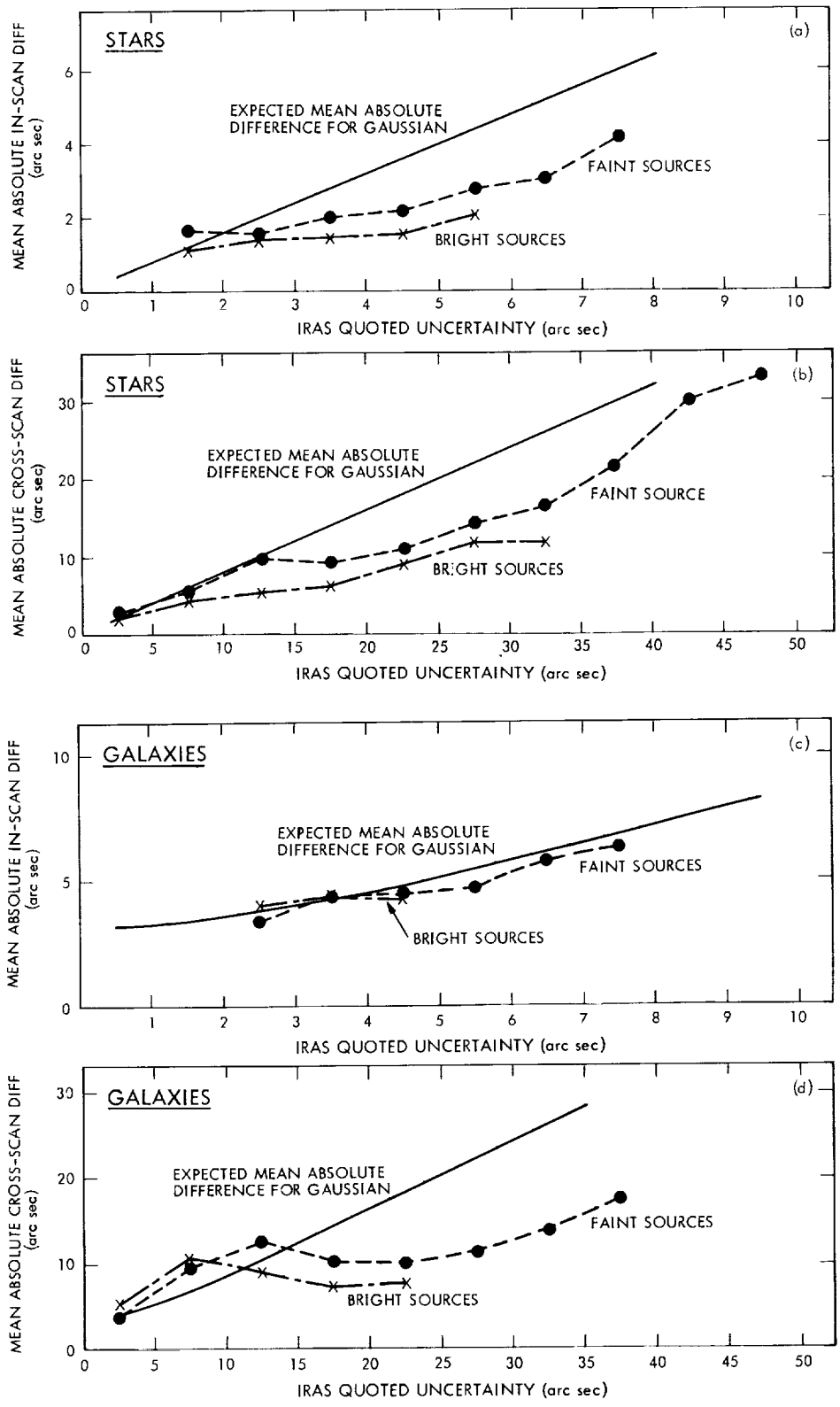

Figure VII.C.5 Observed position differences vs. the quoted uncertainties. The top panels are for stars and the bottom are for galaxies. See text.

Values of χ^2 per degree of freedom are given in Table VII.C.1 for the various samples. As can be seen from the table, the position uncertainties are overestimated for the stellar sources in both the in-scan and cross-scan directions, while the uncertainties are reasonably estimated for the galaxy population, as a whole.

It should be borne in mind that the observed position errors are not due entirely to pointing reconstruction errors. Detection timing errors form a significant component in the in-scan direction, so that the IRAS positions of the brighter stars are determined more precisely than those of the faint stars because of the greater accuracy of the timing of the detection of high signal-to-noise objects. In the cross-scan direction the uniform component of the position uncertainty due to the rectangular aspect of the detectors often dominated the errors of position reconstruction. To minimize this effect in assessing the performance of the pointing reconstruction processor only triple (edge) detections were used. In these cases the image of a source traversed the focal plane in the narrow region of overlap between three detectors in a single band.

C.2 Accuracy of Scan-by-Scan Pointing Reconstruction

As a check on the quality of the pointing reconstruction for each scan, the positions of seconds-confirmed band-merged sources were compared with the positions of a preselected set of standard stars (Sections V.B and V.D.4). This set was composed primarily of K stars selected from the SAO Catalog excluding stars within 2.5° of the Galactic plane or within 3′ of another detectable star.

It should be borne in mind that the observed position errors are not due entirely to reconstruction errors. Detection timing errors form a significant component in the in-scan direction, so that the IRAS positions of the brighter stars are determined more precisely than those of the faint stars because of the greater accuracy of the timing of the detection of high signal-to-noise objects. In the cross-scan direction the uniform component of the position uncertainty due to the rectangular aspect of the detectors often dominated the errors of position reconstruction. To minimize this effect in assessing the performance of the pointing reconstruction processor only triple (edge) detections were used. In these cases the image of a source traversed the focal plane in the narrow region of overlap between three detectors in a single band.

The differences between the IRAS and SAO positions after seconds-confirmation are summarized in Table VII.C.2. The data are reported for three different periods during the mission. The first and longest period had the best pointing reconstruction and lasted from the beginning of the survey (SOP 29) through the end of the second hours-confirming coverage (SOP 425). The second period began with the start of the third coverage (SOP 426) when the survey strategy required large cross-scan slews. These resulted in larger thermal misalignments and limit-cycle bursts (see Section V.B) and the quality of the pointing reconstruction suffered in both the in-scan and cross-scan directions. A third period started at SOP 466 when on-board attitude control was switched from the noisy z-axis gyro ZA to the quieter ZB gyro at SOP 466. The quality of the in-scan positions regained its earlier value, while the cross-scan accuracy, although improved, never returned to values seen earlier in the mission.

Table VII.C.2 IRAS-SAO Position Differences at Seconds-Confirmation

(In-Scan)

SOP Range	Bright Stars No. Matches	Bright Stars Mean (″)	Bright Stars Population Sigma (″)	Faint Stars No. Matches	Faint Stars Mean (″)	Faint Stars Population Sigma (″)
29-425	10332	-0.9	3.0	59805	-1.0	4.0
426-465	783	-0.7	5.9	5114	-0.6	7.0
466-600	2446	-0.2	3.0	15974	-0.1	4.0

(Cross-Scan)

SOP Range	Bright Stars No. Matches	Bright Stars Mean (″)	Bright Stars Population Sigma (″)	Faint Stars No. Matches	Faint Stars Mean (″)	Faint Stars Population Sigma (″)
29-425	1806	1.2	7.1 (4.1)*	3342	1.6	7.3 (4.5)*
426-465	138	-2.0	10.3 (8.5)*	306	-2.4	10.9 (9.2)*
466-600	457	1.3	8.7 (6.5)*	1010	0.9	9.3 (7.3)*

* Sigma after removal of the 10″ half-width uniform uncertainty associated with edge detections.

D. Photometric Accuracy

D.1 Absolute Calibration Uncertainty Checks

There are a number of checks which have been made to ensure that the absolute calibration, which was established with respect to the pointed observations, was carried consistently through the survey processing. Three specific checks include a comparison of the IRAS 12 and 25 μm observations of selected stars with the ground based observations of the same stars; a comparison of the quoted flux densities for the secondary standard NGC 6543 with those inserted into the processing; and a comparison of the flux density ratios between different wavelength bands with the relations assumed in Eq. (VI.C.2).

Table VII.D.1 lists the flux densities quoted in the catalog of a subset of bright stars observed by Rieke *et al.* (1984) and by Tokunaga (1984) at 10 and 20 μm. The selected stars showed no obvious

excess at the IRAS wavelengths, and thus the IRAS flux densities were color-corrected assuming their input energy distributions followed a 10,000 K blackbody. The flux densities are represented as magnitudes following the formulation of Eq. (VI.C.1). As in Section VI.D, for the purposes of easier comparison, the magnitudes of the ground-based observations were adjusted in their zero points to correspond to the IRAS magnitude and color conventions. It is seen that the agreement between the IRAS measurements and the ground-based measurements is excellent.

The second check of the photometry, that of comparing the quoted catalog values of the flux of NGC 6543 with those which were inserted in the processing is important in order to verify that no systematic errors were introduced in the complex processing procedure. In fact, the ratios of the quoted catalog flux densities to those entered in the processing are: 1.02 ± 0.02, 1.04 ± 0.01, 1.01 ± 0.01, and 0.97 ± 0.01 in the four wavelength bands. The quoted flux densities were the result of 18 hours-confirmed measurements of the source and the uncertainties quoted above are in the mean value derived from these observations. Thus the processing did, in fact, introduce some systematic bias into the calibration procedure, but this bias is less than 5%. The origin of this bias is not understood.

The final check on the photometric accuracy of the IRAS calibration is provided by Figs. VII.D.1, D.2 and D.3. In these figures, the 25, 60 and 100 μm flux densities are plotted versus the 12, 25 and 60 μm flux densities for all point sources in the IRAS survey at Galactic latitudes $|b| > 50°$. In each of the plots, the locus followed by hot stars is apparent as the top envelope of the plots. At the longer

Table VII.D.1 IRAS Survey versus Ground Based Magnitudes

	12 μm Band			25 μm Band		
Star	IRAS mag [1]	Δ_T [2]	Δ_R [3]	IRAS mag	Δ_T	Δ_R
β And	-2.11	-0.09	--	-2.14	-0.10	--
α Ari	-0.70	--	+0.08	-0.83	--	-0.03
α Tau	-3.08	-0.07	-0.07	-3.02	+0.02	+0.02
α Aur	-1.90	+0.02	+0.02	-1.95	-0.07	-0.02
α CMa	-1.36	+0.04	--	-1.38	-0.07	--
α CMi	-0.71	+0.03	+0.01	-0.72	-0.04	-0.01
β Gem	-1.21	+0.01	+0.00	-1.19	-0.03	+0.03
α Hya	-1.46	--	-0.04	-1.37	--	+0.07
μ UMa	-0.98	+0.03	--	-1.07	-0.04	--
α Boo	-3.22	-0.07	-0.07	-3.09	-0.01	+0.07
γ Dra	-1.44	--	+0.04	-1.50	--	+0.01
γ Aql	-0.68	+0.08	+0.07	-0.81	-0.04	-0.04
Avg =	--	-0.00	+0.00	--	-0.04	+0.01
Population Sigma =	--	0.06	0.06	--	0.04	0.04

[1] IRAS mag is the magnitude obtained from the survey using (Eq. VI.C.2).

[2] Δ_T is the difference between the survey magnitudes and those of Tokunaga (1984).

[3] Δ_R is the difference between the survey magnitudes and those of Rieke *et al.* (1984).

wavelengths the regions defining these stars becomes more spread out because of the presence of cooler envelopes around many of the stars. The color relations defined by Eq. (VI.C.2) and

$$[100\ \mu m] - [60\ \mu m] = 0.06\ mag \qquad \text{(VII.D.1)}$$

are included on the figures. Equation (VII.D.1) is based on the solar flux densities discussed in Section VI.C. The color relationships are seen to agree with the observed colors of the presumed hot stars, thus confirming the validity of the calibration and processing procedures at the 10% level.

D.2 Relative Photometric Accuracy

A global view of the quoted relative photometric errors of the catalog is shown in Table VII.D.2 including all sources of moderate or high quality flux densities (Section V.H.5). As with the analysis of the positional accuracy, the analysis of the photometric accuracy was done separately for bright sources, with flux densities greater than 1.2, 1.5, 1.9 and 4 Jy at 12, 25, 60 and 100 μm, and faint sources, with flux densities below these limits. In addition, the effects of excluding sources with a quoted probability of true variability greater than 50% at 12 and 25 μm (Section V.H.5) and sources in high source density regions (see Section V.H.6.a) are shown. In all cases, discrepant fluxes (i.e. sources with HCON-to-HCON flux ratios showing reduced χ^2 greater than 9; see Section V.H.5) were excluded from the samples.

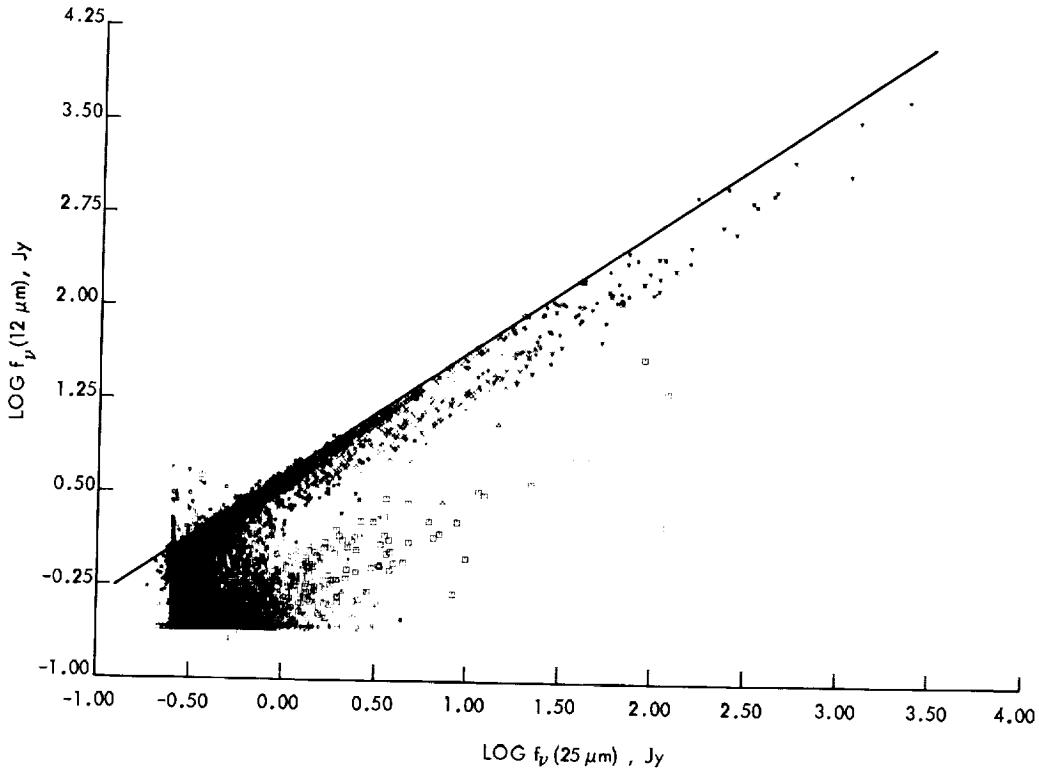

Figure VII.D.1 The 12 and 25 μm flux densities for cataloged sources are plotted. The line shows photospheric models (see Section VI.C).

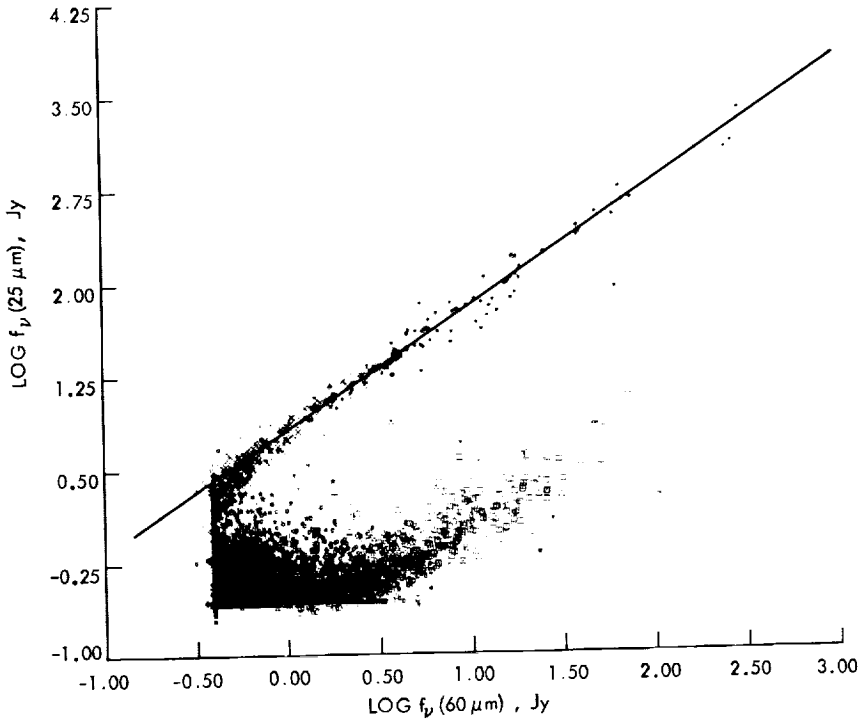

Figure VII.D.2 The 25 and 60 μm flux densities for cataloged sources are plotted. The line shows photospheric models (see Section VI.C).

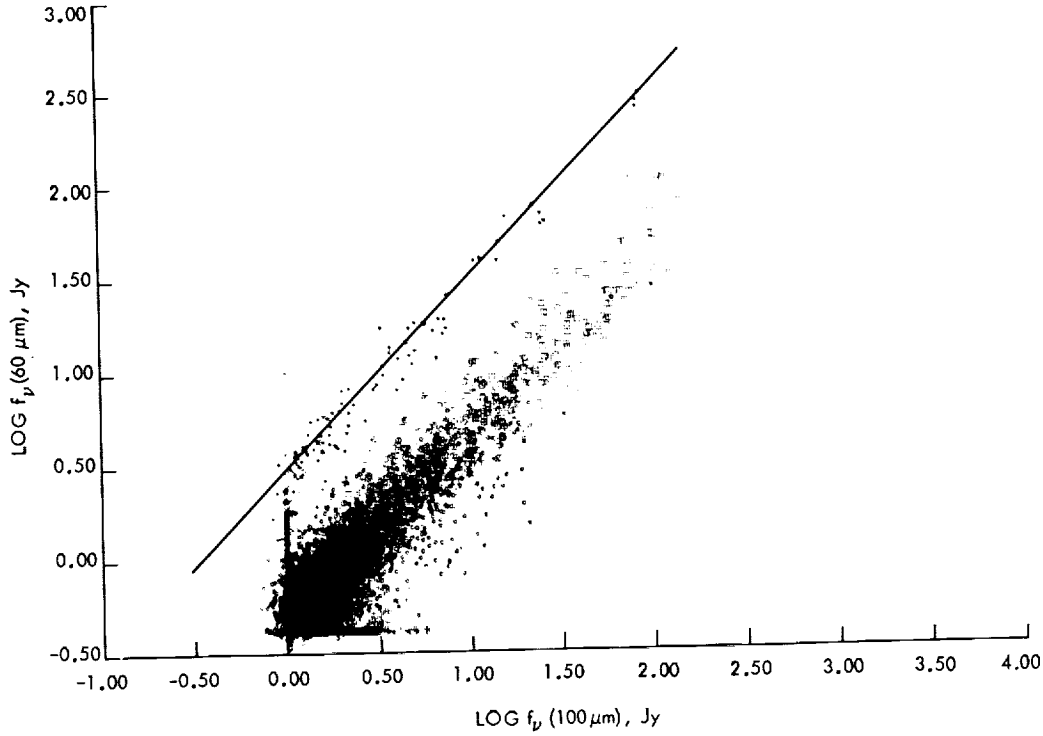

Figure VII.D.3 The 60 and 100 μm flux densities for cataloged sources are plotted. The line shows photospheric models (see Section VI.C).

Table VII.D.2 Point Source Catalog Relative Photometric Uncertainties						
	Bright Sources			Faint Sources		
wavelength (μm)	Number Sources	Mean[1] Unc.	Mean No. HCON	Number Sources	Mean Unc.	Mean No. HCON
(Moderate and High Quality Flux Densities)						
12	61,653	0.09	3.2	97,122	0.10	2.9
25	32,916	0.11	3.2	67,652	0.13	3.2
60	23,335	0.14	3.1	47,342	0.11	2.8
100	26,755	0.15	3.0	43,562	0.13	2.7
(High Source Density Regions Excluded)						
12	39,029	0.07	3.2	86,962	0.10	2.9
25	17,320	0.09	3.2	56,682	0.13	3.2
60	9,437	0.11	3.0	43,012	0.11	2.8
100	7,080	0.11	2.8	34,593	0.12	2.6
(High Source Density Regions and Probability of Variability >50% Excluded [2])						
12	30,228	0.06	3.1	82,869	0.10	2.9
25	11,586	0.07	3.1	48,609	0.125	3.2
60	8,055	0.11	3.0	41,056	0.11	2.8
100	6,809	0.11	2.7	34,358	0.12	2.6

[1] Mean unc. is the quoted fractional uncertainty

[2] Sources deemed variable at 12 and 25 μm were not used at 60 and 100 μm

Tests of the photometric accuracy were made by comparing the flux densities obtained for a given source on all possible pairs of HCONs. The ratio of two hours-confirmed flux densities belonging to a weeks-confirmed source is a random variable whose variance should be the sum of the variances in the two individual hours-confirmed flux densities.

D.2.a Relative Photometric Accuracy of HCONs

Figures VII.D.4 and VII.D.5 show histograms of the natural log of ratios of HCON flux densities for bright and faint weeks-confirmed sources. The samples were the bottom set described in Table VII.D.2. The flux density chosen to be in the numerator of the ratio is the one with the higher flux status (see Table V.D.5) or the later time of observation in cases of equal flux status.

The distributions in Fig. VII.D.4 and VII.D.5 were fitted to Gaussian distributions using only data above 25% of the peak value of the distribution. This choice fits the observations in the central region; the excess in the wings becomes quite visible. The significant non-Gaussian component is thought to come primarily from the effects of particle radiation, and is especially obvious for the brighter sources. In addition to particle radiation effects, there may also be some contribution due to intrinsic variability (which was significantly reduced in the samples discussed here), cross-scan variations in detector sensitivity particularly at 60 and 100 μm and the systematic selection of brighter fluxes at points in the processing where the measurements do not qualify for refinement (Section V.D). All of these effects are probably masked in fainter sources by their larger Gaussian noise.

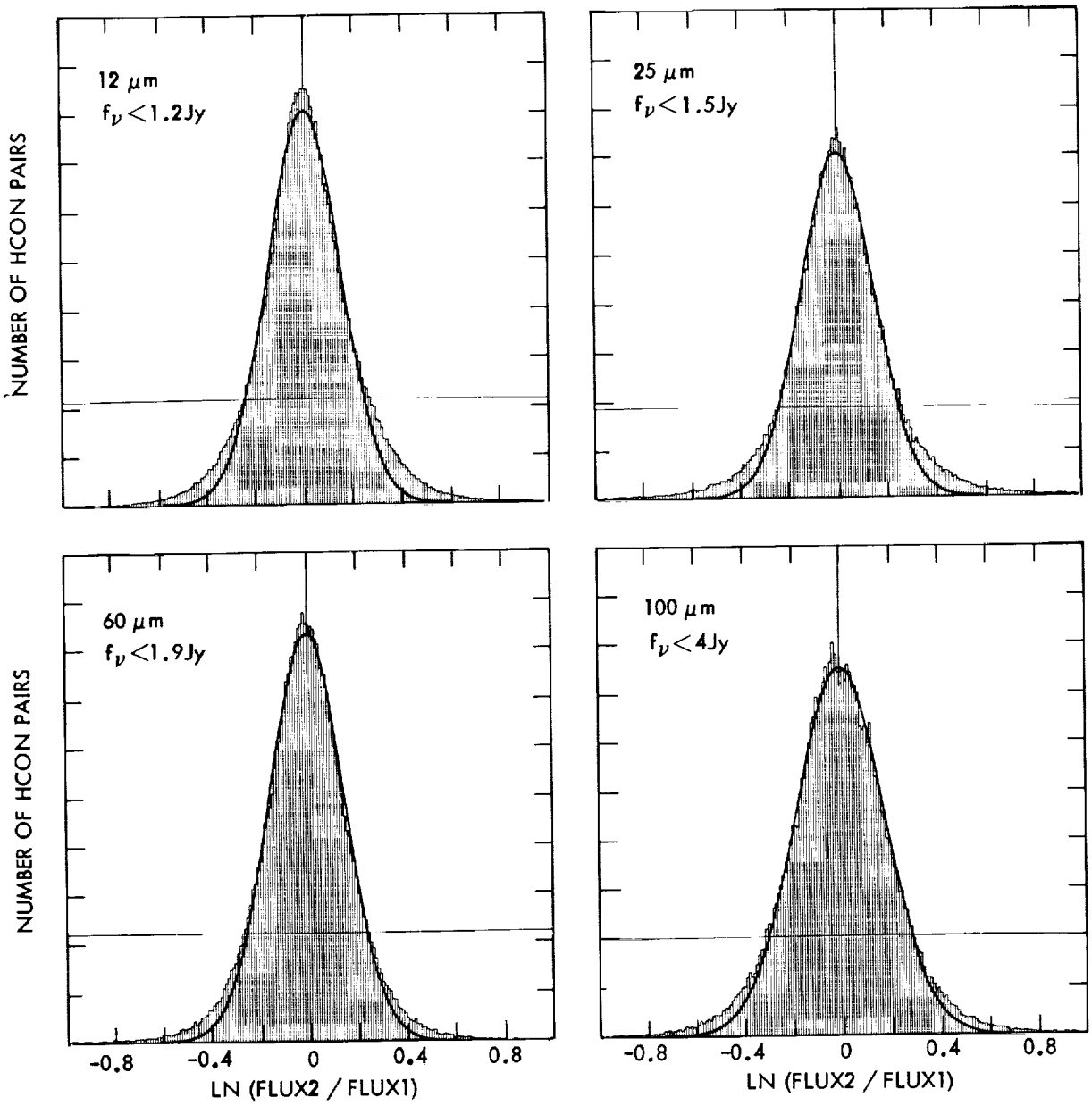

Figure VII.D.4 Histograms of ratios of pairs of HCON measurements for faint sources in the four wavelength bands.

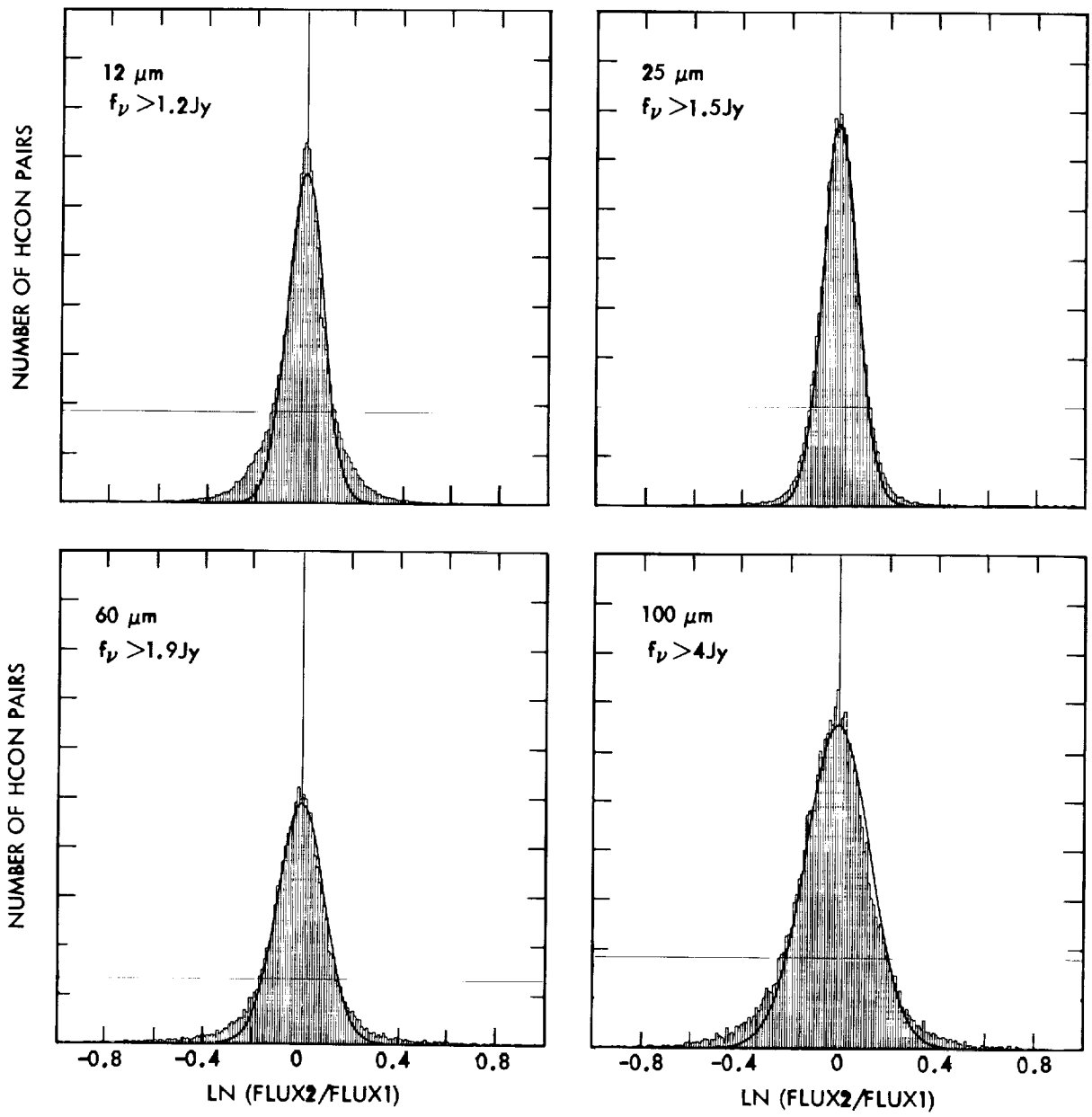

Figure VII.D.5 Histograms of ratios of pairs of HCON measurements for bright sources in the four wavelength bands.

The exact nature of the particle radiation effects on the photometry is not well understood, but it is clear that some subtle phenomena are involved. Large spikes were suppressed by the deglitcher circuits, and were most likely to inhibit the detection of a real point source, although a detection with a large photometric estimation error could result. Small spikes may easily have been lost in the other noise processes. Intermediate spikes tended to cause flux overestimation in cases which have been examined, but whether this led to setting the discrepant-flux flag depended on the actual brightness of the source relative to the spike as well as the uncertainties assigned to the fluxes.

Table VII.D.3 lists the widths (1σ) of the Gaussian fits to the ln $(f_\nu(2)/f_\nu(1))$ distributions shown in Fig. VII.D.4 and VII.D.5. If the variance of these distributions is twice the mean variance of a single HCON and if the catalog flux densities are generated from an average of three HCONs, the expected mean catalog relative photometric uncertainty would be 0.03, 0.03, 0.04 and 0.05 for bright sources in the 12, 25, 60 and 100 μm bands, respectively. This estimate of catalog flux density uncertainties is based on the intrinsic uncertainty of HCON pairs and is substantially smaller than the mean uncertainties listed in the catalog (Table VII.D.2). For the 12, 60 and 100 μm bands the differences can be attributed to effects of the non-Gaussian wings, although in the 25 μm band the non-Gaussian wings are quite small.

D.2.b The Quoted Flux Density Uncertainties

The uncertainties in the quoted flux densities are based on a statistical evaluation of the consistency of HCON ratios. As discussed below, the IRAS survey produced highly repeatable flux densities and therefore small quoted uncertainties. Systematic effects on the photometry, such as flux-dependent nonlinearities, are discussed in Chapters IV and VI and almost certainly dominate the true photometric uncertainties, especially for the brighter sources and longer wavelengths.

Table VII.D.3 Gaussian Fits to Distributions of Photometric Ratios

wavelength (μm)	Bright Sources Number	Bright Sources Gaussian[1] σ	Faint Sources Number	Faint Sources Gaussian σ
		$ln(f_\nu(2)/f_\nu(1))$		
12	107,932	0.074	245,465	0.15
25	44,551	0.072	145,069	0.15
60	25,867	0.096	101,274	0.15
100	17,234	0.13	72,003	0.18
		$ln(f_\nu(2)/f_\nu(1))/($ HCON uncertainty$)^2$		
12	107,932	0.65	245,465	0.92
25	44,551	0.51	145,069	0.71
60	25,867	0.44	101,274	0.77
100	17,234	0.60	72,003	0.87

[1]The Gaussian σ is derived from the fit to the upper 75% HCON pairs in Figs. VII.D.4, D.5, D.7, D.8

[2] The HCON uncertainty is the square root of the sum of the squares of the individual HCON uncertainties.

The repeatability of the quoted flux densities was assessed by a comparison of the flux ratio of two hours-confirmed flux densities belonging to a weeks-confirmed source with the HCON uncertainty, defined as the square root of the sum of variances of the hours-confirmed flux densities. The ratio of two such hours-confirmed flux densities divided by the square root of the sum of the variances should be a random variable with unit mean and unit variance.

Figure VII.D.6 shows such a histogram for the entire HCON sample in the 12 μm band including the Gaussian curve which best fits all the observations in the histogram. It can be seen that the fit is somewhat crude. The wings of the distribution do not fall off rapidly enough to be Gaussian, and so the fit acquires too large a variance. In this figure, the standard deviation of the Gaussian curve is 1.07. The difference from unity is the residual error in the assignment of photometric uncertainties at seconds-confirmation and the error associated with the Gaussian assumption used in flux refinement at seconds- and hours-confirmation.

Figures VII.D.7 and VII.D.8 show histograms of the HCON-to-HCON flux density ratios divided by the resultant HCON uncertainty defined above for the bright and faint sources in the selected sample. Included on each plot are the Gaussian fits using only data above 25% of the peak value, while Table VII.D.3 shows the widths (1σ) for the fits. The distributions typically show Gaussian variances significantly less than unity accompanied by substantial non-Gaussian wings. Together these two distributions produced the total photometric dispersion which led to the uncertainties quoted in the catalog.

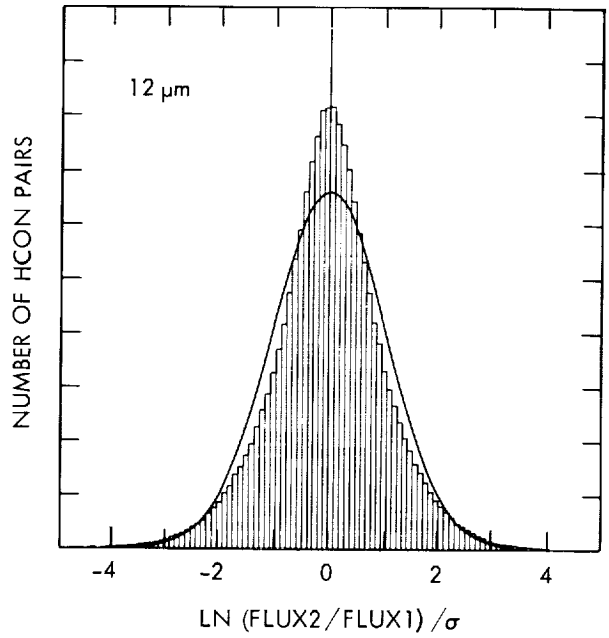

Figure VII.D.6 Histograms of ratios of pairs of HCON measurements normalized to the resultant HCON uncertainty for bright 12 μm sources. A Gaussian fit to all of the data is shown.

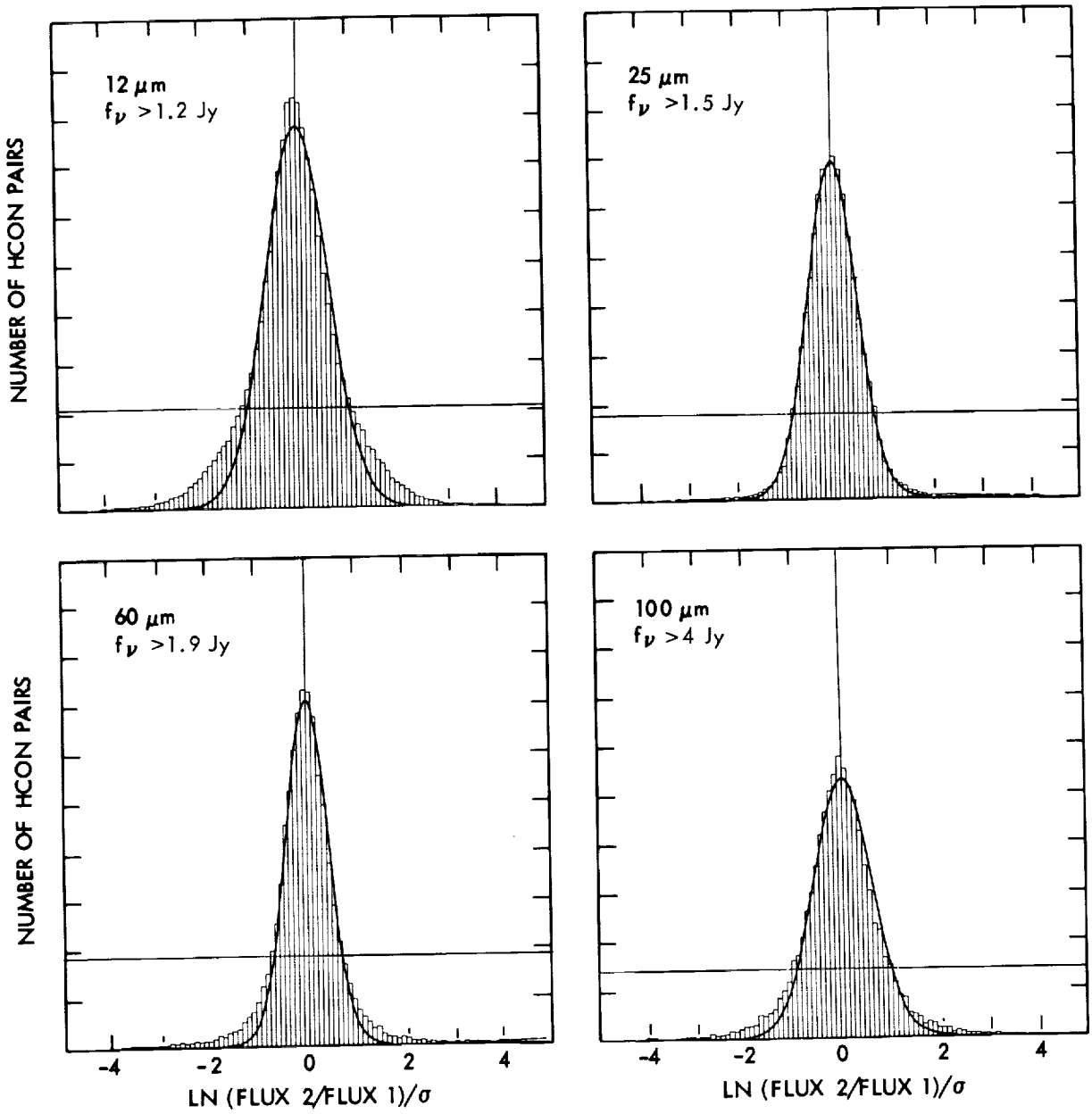

Figure VII.D.7 Histograms of ratios of pairs of HCON measurements normalized to the resultant HCON uncertainty for bright sources in the four wavelength bands. A Gaussian fit to the central portion of the data is shown.

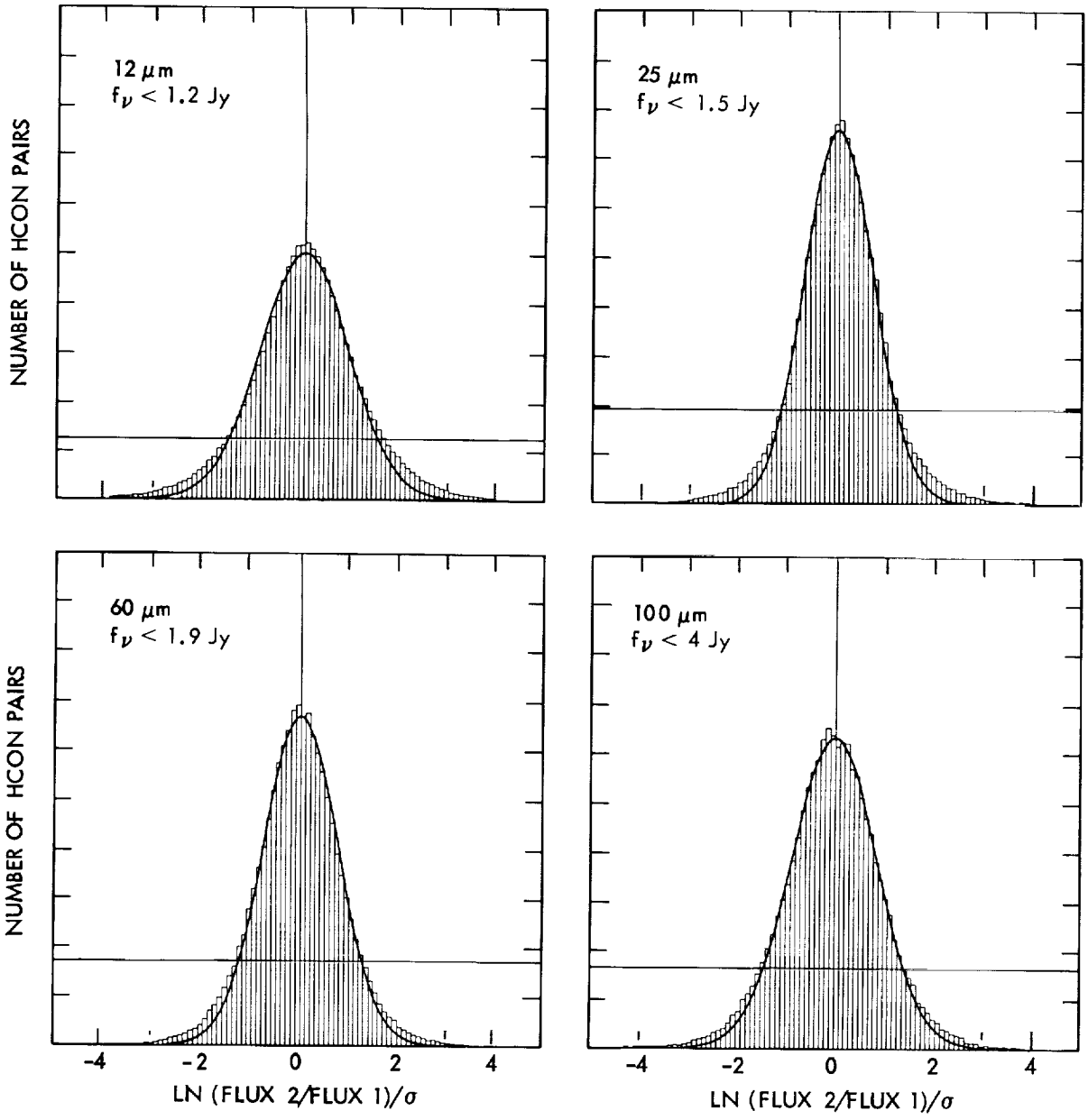

Figure VII.D.8 Histograms of ratios of pairs of HCON measurements normalized to the resultant HCON uncertainty for faint sources in the four wavelength bands. A Gaussian fit to the central portion of the data is shown.

The small variances of the fits imply that the quoted flux density uncertainties have been over-estimated, but this may well be an artifact of the selection criteria used to establish the sample. This suggestion is supported by the fact that during processing more reasonable χ^2 test results were obtained. In the 12, 60 and 100 μm bands the small variance may be due to fitting only the central portion of the distribution and excluding the broad wings. For the brightest objects, the small variance may be indicative of the true Gaussian dispersion which is superimposed on the broader distribution in the tails.

The brightest and faintest 10% of the sources in the samples show the same effects as discussed above in an enhanced manner. In addition, the faintest sources show a statistically significant deviation in the mean of about 2% although the fitting process assumed a mean of zero. This would slightly inflate the derived standard deviation of the Gaussian fit. The brightest sources show a small non-zero mean in the opposite direction from that of the faint sources. These effects are not understood.

D.3. Variable Sources

The method by which a probability of variability as quoted in the catalog is calculated for a source with 12 and 25 μm fluxes is given in Section V.H.5. Figure VII.D.9 shows the distribution of the flux density variations between HCONs in units of the standard deviation for 25 versus 12 μm flux densities. Only catalog sources in unconfused areas of the sky are plotted. Sources in the shaded region (a) have a "probability of variability" between 0.5 and 0.99. Those sources in the outer regions (b) are all flagged with a probability of variability greater than 0.99.

Table VII.D.4 gives the approximate relative change in the flux densities at 12 and 25 μm associated with a given probability of variability. Two values are given, one for bright sources and one for faint sources. The table shows that there is a strong increase in the observed relative flux change as the quoted probability of variability increase from 90 to 99%. It is seen that variable sources whose fluxes change by 20% or more at 12 and 25 μm can be identified reliably. A caution is necessary however. In regions of high source density, scan-to-scan variations in the baseline can affect the measurements enough to produce spurious indications of variability.

Table VII.D.4

Approximate Relative Flux Change at 12 and 25 μm

Probability of Variability	Bright Sources	Faint Sources
0.50	10%	15%
0.75	15%	20%
0.90	20%	30%
0.99	30%	40%

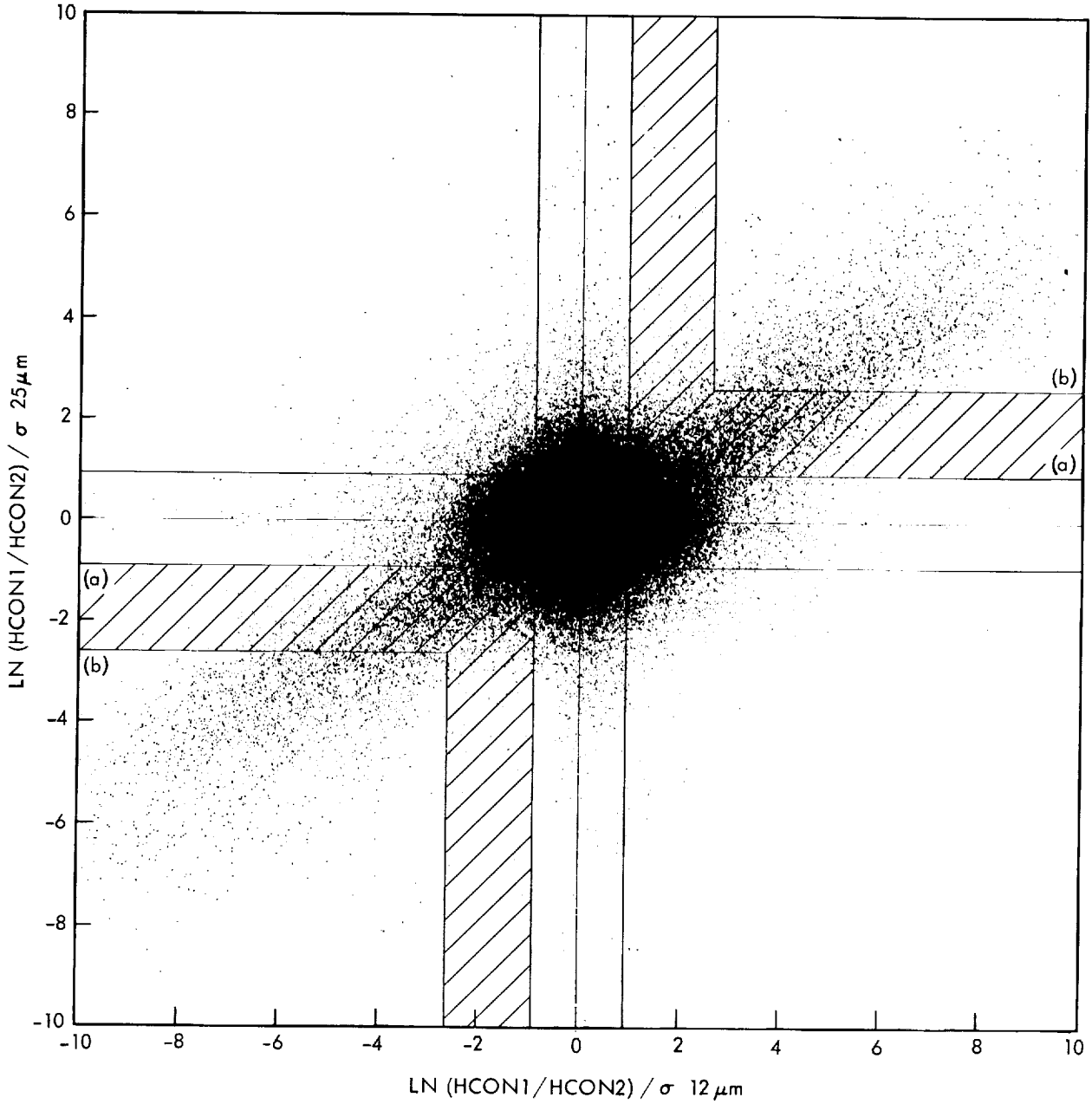

Figure VII.D.9 HCON-to-HCON flux variations at 12 and 25 μm, normalized with respect to the resultant HCON uncertainty.

Figure VII.D.10 shows the distribution in number of sources vs. probability of variability quoted in the catalog. Twenty-five percent of eligible sources have a probability of variability greater than 50%; 13% have a probability of variability above 90%. Sources with a high probability of variability preferentially vary on a long time scale with roughly ten times as many sources varying over a time scale of 6 months as on time scales of weeks.

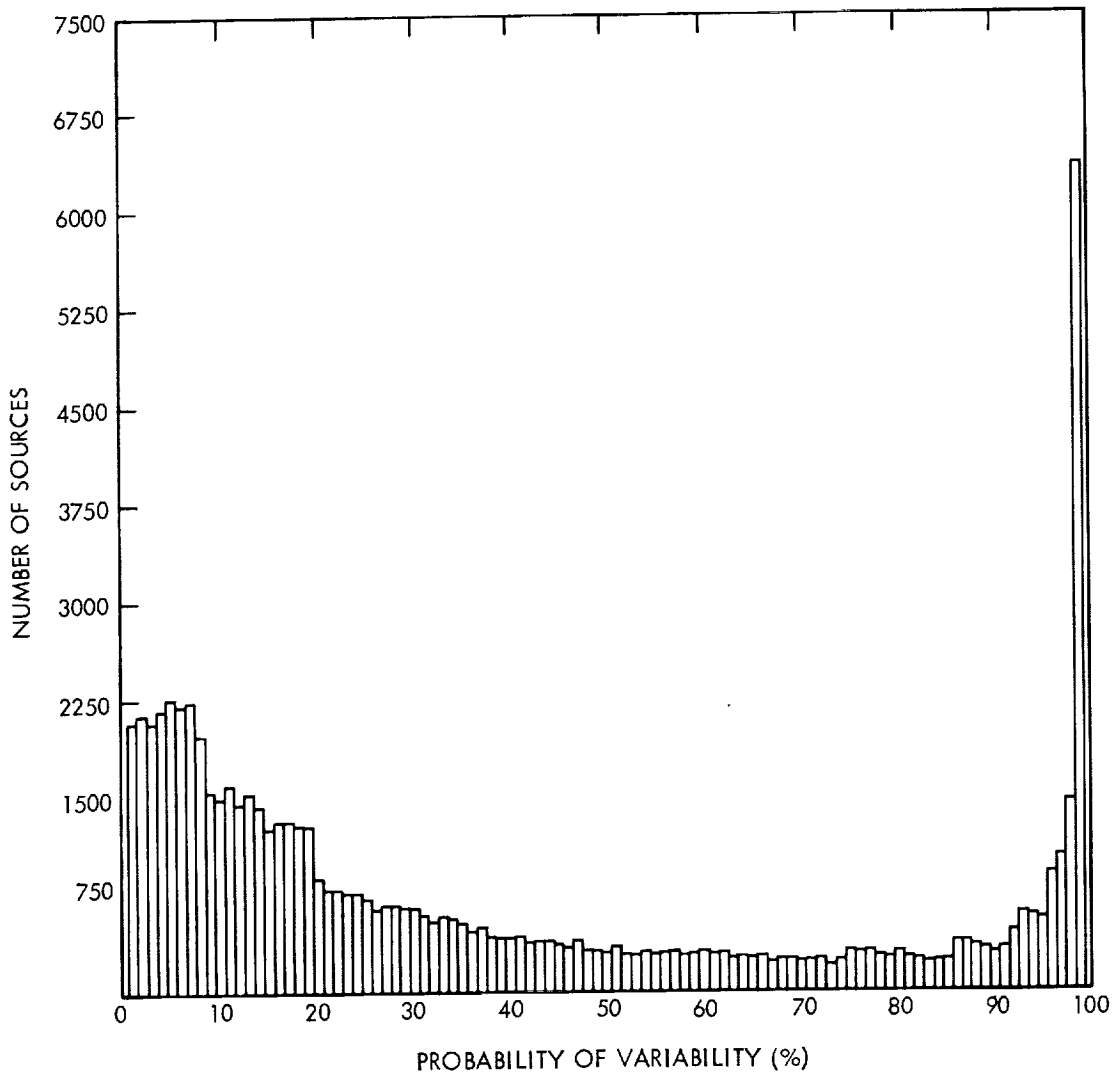

Figure VII.D.10 A histogram showing the number of sources with a given probability of variability.

Figure VII.Ap.16 shows the distribution on the sky of sources flagged with a probability of variability of 0.9 or greater. The plot clearly shows a population of sources occupying a region near the center of the Galaxy, probably due to a population of highly variable sources in the Galactic bulge. In the Galactic plane at Galactic longitude 320°, there is a diagonal edge showing a marked increase in the density of variable sources. This, as well as other more subtle structures, is probably a sampling effect since in this region the source density is high and the survey strategy produced extra HCONs at time intervals suitable for detecting variability. This same effect is also seen in the Large Magellanic Cloud, which because it was at the south ecliptic pole received many coverages.

D.4 Discrepant Fluxes

The distribution of sources with discrepant fluxes at 12 and 25 μm greatly resembles the distribution of variable stars, suggesting that time variability is the dominant cause of such discrepant fluxes. At

60 and 100 μm, the distribution is much different, since the sources cluster in two patches in the Galactic plane for reasons that are, at this time, unknown. Only about 1,000 sources have discrepant fluxes at 60 and 100 μm. It is worth noting that the sources with discrepant fluxes are not predominantly found close to the ecliptic plane so that asteroids are not a significant cause of this problem (Section VII.F).

Roughly 50,000 sources are tagged with discrepant upper limits. These sources are mainly near the Galactic plane where the erratic behavior of the noise estimator causes this variation.

E. Point Source Processing Considerations

E.1 The Nature of Rejected Sources

Detections had to survive a number of stringent confirmation tests to become an HCON. The nature of those sources that became HCONs but did not go on to become cataloged objects is of interest to those trying to understand the completeness and reliability of the IRAS survey (see Chapter VIII).

E.1.a Single HCONs

Away from highly confused regions there were three main causes of single HCONs. Single HCONs can be due to inertially fixed sources faint enough to be below the completeness threshold, to moving sources such as asteroids and comets, and to wholly spurious sources generated by noise, radiation hits, diffraction spikes, and debris near the spacecraft.

The number of true, fixed sources which appear only as single HCONs can be estimated from the completeness of the catalog in each flux range. A crude estimate based on the preliminary figures for completeness given in Section VIII.D suggests that half of all single HCON sources in the sky with two HCON coverages are real but incomplete; only one third of the single HCONs in the region covered with 3 HCONs are predicted to be real. An estimate of the number of asteroids and comets is given in Section VII.F.

Figures VII.Ap.17-20 show the distribution of single HCON sources detected in a given band in Galactic coordinates. These plots look much like the plots shown earlier for catalog sources, with the obvious addition of asteroids and comets in the ecliptic plane.

E.1.b Rejected Weeks-Confirmed Sources

Roughly 10,000 weeks-confirmed sources were rejected because they did not have consistent sightings of acceptable quality in at least one wavelength band. Most of these sources were caused by the ubiquitous infrared cirrus.

Regions with high source density were specially processed to generate sources that were relatively isolated, had repeatable fluxes and stood out prominently as point sources against the local background. High source density rules were applied to measurements in those wavelength bands for which the density of sources in a 1 sq. deg bin exceeded the confusion limit threshold. Sources were rejected from the catalog only if the high source density processor rejected *all* the bands that it processed *and* if the bands that it did not process failed to meet the normal rules for inclusion in the catalog (Section V.H.5).

The number of 1 sq. deg bins processed according to high source density rules was 690, 631, 1382 and 6192 at 12, 25, 60 and 100 μm, respectively, or roughly one-seventh of the sky at the longest

wavelength. In all, some 300,000 individual sources consisting of one or more hours-confirmed sightings were examined. Of these, approximately 170,000 were immediately rejected as having only one hours-confirmed sighting. Under no circumstances could any of these have reached the final catalog. About 40,000 were rejected for failing to have two hours-confirmed sightings with at least two "perfect" sightings (with FSTAT=7) in at least one band.

Another 17,000 weeks-confirmed sources subsequently failed one or more of the tests described in Section V.H.6. Because these objects lacked high quality fluxes in any band, they were thus excluded from the catalog.

Table VII.E.1 gives the fraction of sources for which a particular reason was the cause of the rejection of a measurement in a particular band. The tests were applied in the order listed in the table and represent an obstacle course that all bands being processed according to high source density rules had to survive. Since a band could be rejected at any point in the sequence, the reason that finally led to its rejection is counted in the table.

It can be seen from the table that the dominant reasons for rejection vary with wavelength. In all cases the first test which demanded at least two sightings with a correlation coefficient greater than 0.97 removed the bulk of the sources, particularly at 60 μm. The correlation coefficient test served to reject both low signal-to-noise sources and extended sources. The latter evidently dominate confused regions at 60 μm. The effects of neighboring sources accounted for most of the rest of the rejections.

Table VII.E.1 Reasons for Rejection of a Band
(Percent of Rejected Sources)

Reason	All Bands	12 μm	25 μm	60 μm	100 μm
Correlation Coefficient	87	47	57	96	75
Confusion Status	5	6	5	2	14
Inconsistent Fluxes	0	0	1	0	0
Weaker Neighbor	2	18	10	0	1
Confused Neighbor	6	29	26	2	10
Very Near Neighbors	0	0	1	0	0

Figures VII.E.1a-d show the effects of high source density processing on the number of sources within a 1 sq. deg bin in the four wavelength bands. In these histograms the open bars give the number of bins containing the specified number of sources, where in this case a source is counted in a band if it meets the criterion of having at least two hours-confirming sightings with FSTAT $\geqslant$ 3. The

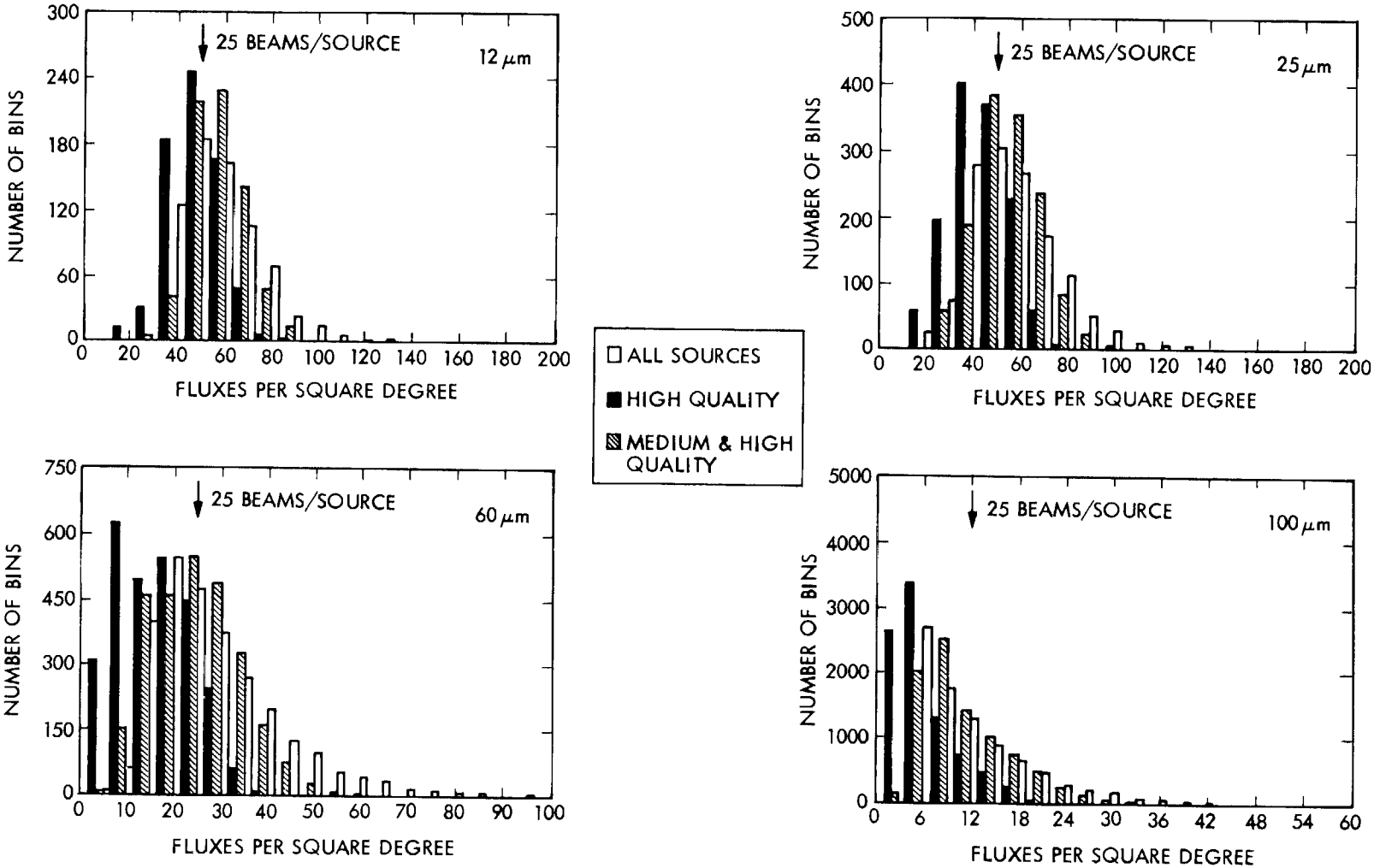

Figure VII.E.1a-d The effects of the high source density criteria are shown in the four wavelength bands. Plotted is the number of bins with a specified number of sources with a measured flux in a given band. The open bars show the number of bins with a given number of fluxes before high source density processing. The solid bars show the number of high quality fluxes that remain after processing. The striped bars show the number of high and medium quality fluxes than remain.

confusion limit corresponding to 25 beams per source is marked. The solid bars show the results after the high source density criteria are applied. In this case a source was counted only if it had a high quality flux in a given band according to the high source density criteria. The figure shows a drastic reduction in the average source density after the more stringent criteria were applied. There are relatively few 1 sq. deg bins with more than the confusion limited number of sources. The striped bars indicate that the number of sources per sq. deg increases when high *and* moderate quality fluxes are included suggesting that confusion effects may be important for moderate quality fluxes in highly populated areas.

E.2 Bright Source Problems

The point-spread function of the telescope caused bright point sources to illuminate many more detectors in the focal plane than just those over which their image centers passed. These extremely bright sources caused special problems and received special handling during the data processing. During final source selection the WSDB was searched for spurious sources due to optical cross-talk from bright sources. As discussed below, 22 of these were deleted.

Often, the extra detections of a bright source could not be combined into a single seconds-confirmed sighting and created a variety of problems: four detections from one source in one band were sometimes processed as two separate seconds-confirmations; sources with "too many" triple detections could fail to band-merge; leftover unconfirmed detections could take priority over the seconds-confirmed source to produce an incorrect measurement of the source in one or more bands; with enough extra detections both a primary and one or more false HCONs could be produced. The spurious sources could have either similar or much weaker fluxes than the primary source.

Many of these problems were solved in the normal course of the data processing. Optical cross-talk processing eliminated weaker neighbors of bright sources (Section V.D.2.c). Slot extensions for edge detections, priority for adjacent wavelength bands and priority for seconds-confirmed sources over non-seconds-confirmed objects produced more complete band-merging. Second-confirmed sources were given priority over non-seconds-confirmed sources in hours-confirmation. All of these changes had the effect of pulling more detections into a given confirmed source, leaving fewer odds and ends to confirm and to cause unreliable sources.

One product of bright source processing not corrected in the basic processing was the optical cross-talk detection of the diffraction image of the secondary support spider. The spider produced cross-talk emission in six arms in the focal plane, two in the in-scan direction and four oriented at angles of $\pm$ 60° and $\pm$ 120° with respect to the in-scan direction. Figure VII.E.2 shows an example of optical cross-talk. The source is IRC+10216 observed directly at 60 μm on only two detectors, 14 and 33. All the detectors show some evidence of its passage. Detections on 14 and 33 were well over the signal-to-noise threshold of 300, so that optical cross-talk processing suppressed the detections on 9 and 37. The double detections on detectors 10, 13, *et al.* are characteristic of the "spider-arm" diffraction and were not suppressed by cross-talk processing because they were outside the in-scan search window (Section V.D.2.c). Many potential detections did not survive because of poor correlation coefficients or poor in-scan alignment with potential partners. However, the detections marked on detectors 8 and 35 not only seconds-confirmed but went on to hours- and weeks-confirm as well.

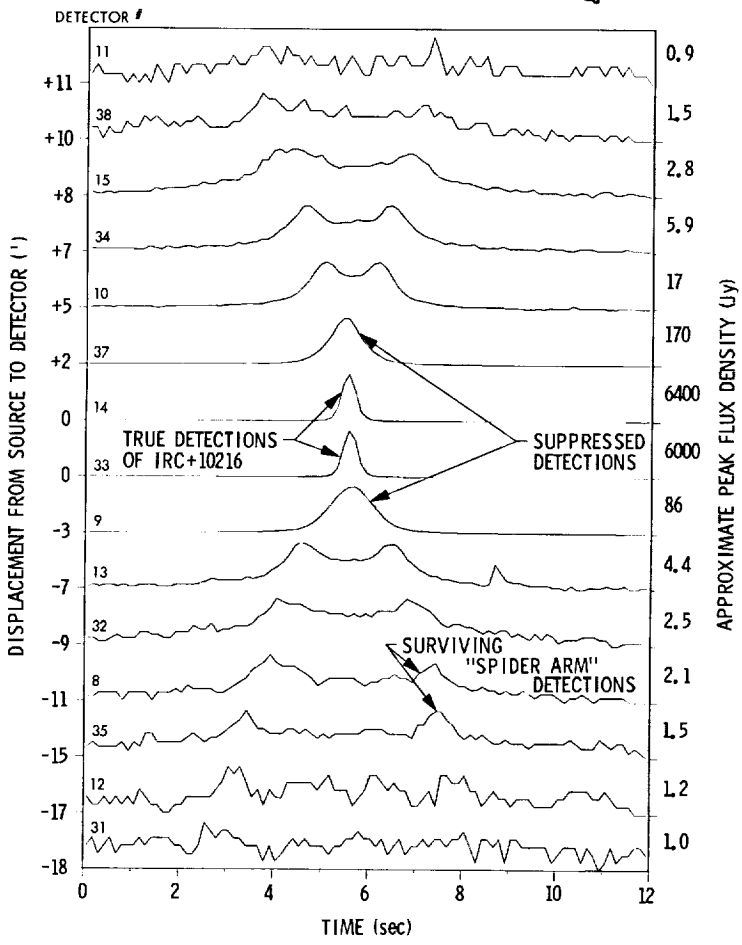

Figure VII.E.2 Strip-chart tracings of the detector outputs at 60 μm during a passage of IRC+10216 over the focal plane. The detector timing has been adjusted so that the detector samples correspond to the same in-scan positions.

Figure VII.E.3 shows the area around IRC+10216 in the WSDB. This figure shows the optical cross-talk problem at its worst. IRC+10216 generated spurious HCONs in three bands. Spurious sources line up in the typical spider arm pattern ±60 and ±120° from the in-scan direction. Because this source lies in the ecliptic plane, the scan angle was always along the local meridian so that there was no HCON-to-HCON variation in twist angle to prevent weeks-confirmation of the cross-talk sources. For sources at higher latitudes, however, the scan direction usually varied enough to prevent the weeks-confirmation of spurious HCONs. Eleven spurious weeks-confirmed sources surround IRC+10216, of which seven were good enough to pass initial catalog selection rules. These seven were deleted by hand from the final catalog, along with 15 other such sources.

The final catalog data base was searched for bright sources and their neighbors above Galactic latitude 5°. Catalog sources brighter than 450 Jy at 25 μm or brighter than 1000 Jy at 12, 60, or 100 μm were examined. These thresholds were selected after analysis of several hundred bright sources and are the levels at which cross-talk confirmations begin to survive final catalog screening. Any bright source neighbor, i.e., having a position within a 1000″ window and a high quality flux that was band-compatible

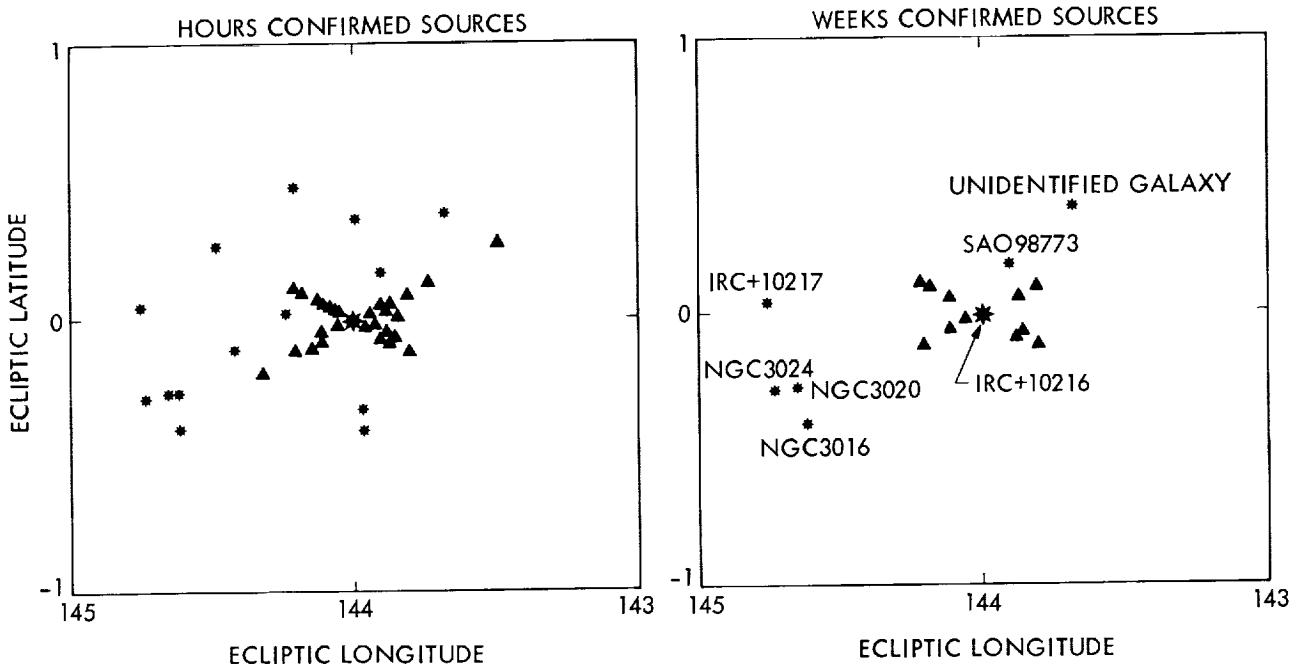

Figure VII.E.3 The vicinity of IRC+10216 is shown before and after the weeks- confirmation requirement was imposed on sources in the Working Survey Data Base. Spurious sources due to cross-talk are shown as triangles. Those that survived weeks-confirmation were subsequently deleted.

with the bright source, was identified and evaluated for evidence of optical cross-talk. Analysis of the raw data in strip chart form, e.g., Fig. VII.E.2, gave the surest evidence of cross-talk. Neighbors judged to be independent sources had detections that were free from influence of the nearby bright source: the detector plots showed local minima separating the two sources. Cross-talk neighbors, on the other hand, were not separated by a local minimum but were found on a plateau of emission that was a function of the intensity, direction, and distance from the central source.

In addition to being found next to an extremely bright source, cross-talk neighbors also tended to have the following characteristics: detection in only a single band; only 2 HCONs even if more were expected; a location in one of the preferred spider-arm directions; and a brightness proportional to its distance from the primary object.

Twenty-two neighbors survived final catalog screening but were found to be due to cross-talk. These are summarized in Table VII.E.2. Notice that only the cross-talk source near α Sco was confirmed in two wavelength bands. All others are single band sources. Galactic latitudes within 5° of the plane were not examined. In addition, the Orion region (especially around Mon R2, OMC 1, NGC 2024, and NGC 2071) had too many neighbors to examine. In such crowded regions the high source density processor suppressed most remaining cross-talk sources, but users should be aware that significant numbers of cross-talk sources may remain.

Table VII.E.2 Bright Source Neighbors Suppressed as Cross-talk

Name	Parent Source	Parent Flux Density (Jy)	Problem Band (μm)	Flux Ratio (X-talk/Parent)	Distance (″)	Total HCONs
04361-6208	R Dor	5549	12	3×10^{-4}	141	2
04399+3604	AFGL 618	1107	60	9×10^{-4}	345	2
04400+3559	"	"	60	9×10^{-4}	353	2
07204-2542	VY CMa	6651	25	5×10^{-5}	427	3
09501+6956	M 82	1145	100	2×10^{-3}	494	2
09509+7000	"	"	100	4×10^{-3}	411	2
09508+6955	"	1168	60	2×10^{-3}	283	2
09514+6958	"	"	60	3×10^{-3}	206	2
09443+1328	IRC+10216	5652	60	1×10^{-4}	780	2
09446+1340	"	23069	25	3×10^{-5}	750	2
09446+1329	"	"	25	5×10^{-5}	550	2
09446+1328	"	47525	12	3×10^{-5}	531	2
09448+1336	"	23069	25	6×10^{-5}	508	2
09455+1327	"	"	25	6×10^{-4}	303	2
09457+1332	"	"	25	1×10^{-4}	477	2
09461+1332	"	"	25	2×10^{-5}	812	2
09458+1320	"	"	25	3×10^{-5}	834	2
09431-2147	IRC-20197	495	25	2×10^{-3}	147	2
10494-2101	V Hya	459	25	4×10^{-3}	253	2
13271-2301	R Hya	585	25	2×10^{-3}	150	2
13271-2303	"	"	25	2×10^{-3}	158	2
16261-2617	α Sco	3198	12	2×10^{-4}	138	2
		690	25	3×10^{-3}		

E.3 Sources of Incompleteness

The causes of lost HCONs are various and include: (i) missing detections due to radiation hits or noise spikes (which cause correlation coefficients to fall below threshold); (ii) band-merge failure caused by noise detection in another band; and (iii) missing detections because the detections fell below the signal-to-noise ratio correlation coefficient thresholds. Causes (i) and (ii) usually are significant only because a failed detector also removed a detection as well. There exist two additional causes of incompleteness at 100 μm. First, the instability of the noise estimation caused by the presence of cirrus sometimes causes the noise to be erroneously estimated high by a factor of two. Second, cirrus itself often creates confusion and cross-scan position shifts, resulting in a failure to hours-confirm. Finally, as discussed in more detail in Section VII.F, asteroids can also cause lost HCONs. One bright source lost the HCON because of a coincidence with asteroid Valentine.

E.4 Effects of Failed Detectors

The data processing allowed for failed or degraded detectors by giving the status of *non-seconds-confirmed due to a failed detector* (NSCF) to any detection whose failure to seconds-confirm might have been caused by the potentially confirming detector being failed or excessively noisy. NSCFs enjoyed the same status as seconds-confirmed band-merged detections and had the effect of significantly increasing completeness at the cost of hurting reliability.

Because detectors 17 and 20 in the 25 μm band were dead, their seconds-confirming partners 40, 44, and 41 often produced NSCF detections as did detectors 9 and 13, opposite the dead detector 36 at 60 μm. Additional detectors declared dead due to their degraded performance were: 28, 25, and 26 at 12 μm and 42 at 25 μm. The designation of so many "dead" detectors produced a flood of NSCF detections with NSCFs outnumbering seconds-confirmations by about 5 to 1. The purpose of declaring active, but degraded, detectors as failed was to avoid penalizing the more sensitive, confirming detector. Bright sources could still confirm on both detectors, since seconds-confirmation was attempted for detections produced by the degraded detectors. Weaker sources had a chance of confirming in the nominal way on subsequent sightings with a more favorable combination of detectors.

An unfortunate side effect of allowing NSCFs was that weak radiation hits which passed the correlation coefficient test could masquerade as valid detections. When this occurred on the twelve detectors subject to NSCF status the radiation hit could band-merge and provide an erroneous flux or position for a true source. The requirement of weeks-confirmation in each wavelength band prevented this from becoming a serious source of error for the catalog.

Seconds-confirmation was still possible despite passage over a failed detector. Consider a bright source passing over detectors 20 (failed), and 44 and 40 (Fig. II.C.6). Although detections from 44 and 40 could seconds-confirm, they generally did not because any displacement from the overlap region resulted in a failure of the flux test. More than half the time the weaker detection band-merged into the main source while the stronger detection became a separate source. The weaker detection was more successful at band merging because it had a greater in-scan uncertainty than the stronger detection. Thus, at hours-confirmation one could often find two versions of the source, e.g., one with a good 25 μm flux and nothing else, the other with good fluxes at 12, 60, and 100 μm but a low flux at 25 μm. This problem was corrected in the reprocessing of SOPs 29-446 by suppressing the weaker detection in these nearly overlapping cases.An error in the computation of the cross-scan uncertainty prevented band merging of the stronger detection in about one-third of these special cases.

E.5 Setting the Seconds-Confirmation Threshold

When a confirmation threshold is set optimally, practically all true matches should be accepted, and practically all false matches should be rejected. One way to obtain a feeling for whether an acceptable threshold setting is possible and has been obtained is to process the same data with different thresholds. If one begins with a very high value, then lowering the threshold should result in a significant increase in the number of confirmations. Continuing to lower the threshold further should eventually yield little increase in the number of confirmations. This should happen as the completeness approaches unity. If the threshold is lowered still more, the number of confirmations will begin to rise again at some point as more spurious sources are accepted, unless there is no noise in the process at all.

If a reasonable range of threshold values is found in which the number of confirmations is essentially constant, then that range is assumed to contain the optimal value. Such a range should occur at thresholds which seem consistent with the properties of the measurement error. Assuming that gross blunders in estimating the measurement errors have not been made, then if no such range is found, even for threshold values which are clearly unreasonably large, then the noise contamination has probably blended significantly into the signal well before the onset of completeness for true matches.

The position test thresholds in the seconds-confirmation processing were varied as described above. The optimal range was found at 12, 60, and 100 μm. The search was not as successful in the 25 μm band. While the number of additional confirmations rolled off as the threshold was raised, the total number never reached a plateau such as those of the other bands. Time constraints prohibited a thorough study of this anomaly, and an attempt to identify the spatial distribution of the excess events was inconclusive. The flux distribution appeared to be more strongly concentrated to the fainter end than the overall distribution of objects detected.

A cursory analysis of the rate at which these sightings survived hours-confirmation indicated that only very few succeeded. It is likely that none at all passed through weeks-confirmation, so that no impact on the completeness or reliability of the catalog is expected.

F. Asteroids and Comets

F.1 Number Present in Catalog (Asteroid Source Density)

The WSDB contained 326 hours-confirmed sources associated with known asteroids and comets; among these, 108 sources have two or more hours-confirmations. Close examination of the sources with two or more HCONs reveals that they are all chance positional coincidences with inertially fixed objects. There is no case of any known asteroid or comet passing the weeks- or months-confirmation tests by self-confirmation.

To determine the impact of these chance encounters on the reliability of catalog sources and their stated fluxes, the selection criteria and flux averaging methods discussed in Section V.H.1 must be applied. Seventy-four sources associated with known asteroids meet all the selection criteria and appear in the IRAS catalog. In the case of 17 of these IRAS failed to detect the asteroid. Of those detected, 13 had no effect on the cataloged quantities. The remaining 44 sources all have contaminated fluxes. These sources are identified in Table VII.F.1 and have the following characteristics:

(1) Two-thirds of these sources had at least one high quality flux contaminated, although in no case did an asteroid association change the value of the flux quality flag.

(2) In the absence of the asteroid, 80% of these sources would have been detected at only a single wavelength, with equal probability for each of the four bands. Of the remainder, 10% had both 12 and 25 μm fluxes and 10% had both 60 and 100 μm fluxes.

(3) The flux discrepancy flag is only a weak indicator of the impact of the asteroid. All the correct flags are set in only 15% of the cases, but in 58% of the cases at least one flag was set correctly. In 37% of the cases no flag was set.

(4) Seventy-five percent of the affected flux densities are less than 1 Jy. The frequency of flux contamination is highest in the 25 μm band, however, and is a function of HCON as shown in Table VII.F.2.

(5) The ecliptic latitude distribution of the contaminated sources follows the density distribution of the numbered asteroids. All the contaminated sources lie within 25° of the ecliptic with 90% of them within 15°.

The true population of asteroids in the WSDB is underestimated by the numbered asteroids. A plot of log N vs. log f_ν, where N is the number of known asteroids detected with 25 μm flux density equal to or greater than f_ν, shows a steep rise ($N = kf_\nu^{-3/2}$) to N=100, a flatter region ($N = kf_\nu^{-1}$) from N=100 to 1000, and a gradual roll-off to N=3266. If the gradual roll-off is due to incompleteness of the numbered asteroids, extrapolation of the flat portion of the curve to the 25 μm flux limit estimates that the true population of single HCON asteroids in the WSDB is about 10,000. Since the frequency of chance encounters is proportional to the number of asteroids available, these numbers suggest that about 135 catalog sources could be affected. In general these may be expected to have characteristics similar to those discussed above for the numbered asteroids.

If the extrapolation of the asteroid population is valid, then there should be about 0.2×135 = 27 sources within 25° of the ecliptic plane observed only at 25 and 100 μm, resulting from the detection of infrared cirrus plus a faint asteroid. Of the 500 IRAS sources with measurements only at 25 and 100 μm, 34 of these clearly qualify as asteroid-cirrus combinations. The IRAS names of these objects are

Table VII.F.1 IRAS Names of Sources Contaminated by Numbered Asteroids

---NAME---	---NAME---	---NAME---	---NAME---	---NAME---
00260-1016	02449+0249	03341+1224	03301+1820	04369+0449*
05536+1944	06000+1644	07093+2522	07153+1128	07294+2521
08140+3940	07575+1756	08070+2503	08090+1239	08534+0850
09285+0847	10253+1101	15113-1310	15170-2739	15301-3259
15427-2604	16137-2047	16475-0930	16378-3133	16528-0808
16515-1634	17013-2451	17082-2903	17239-0259	17311-2013
17424-2331	17451-2102	17457-3623	17486-1701	17586-1724
18236-2320	18317-1646	18477-0940	18559-2045	18478+0215
19171-2047	19420-1304	19509-1925	21303-1858	23586-0116

*Source deleted by high source density processor.

Table VII.F.2 Frequency of Flux Contamination

# HCONs	Frequency (%) 12 μm	25 μm	60 μm	100 μm
2	8	97	81	16
3	60	53	27	7
4	25	50	25	0

given in Table VII.F.3. Considering the small size of the sample, the agreement between the observed and predicted numbers is satisfactory and gives confidence in the estimated influence of asteroids.

While non-inertial sources of infrared radiation have no place in a catalog of fixed point sources, they are of great interest to studies of the Solar system. As a part of the normal data processing all detections of sources with colors appropriate to solar system objects (30K < T < 400K) were written to off-line data files for further processing which attempts associations with a larger set of known asteroids.

Table VII.F.3 Cirrus Sources Possibly Contaminated by Asteroids

---NAME---	---NAME---	---NAME---	---NAME---	---NAME---
02428+0748	02313+2729	03105+0744	03100+1049	03408+0101
03085+3945	03484+1744	04070+1128	04063+1220	04012+2044
04055+1859	04438+1643	04376+2922	04362+3347	05063+2015
05341+3420	05369+2350	05533+3147	07113+1225	08230+2535
14200-1907	15049-2606	15246-2503	15455-2931	16447-1644
16478-3129	17052-2835	17343-0358	17397-1317	17538-0740
18285-2217	18371-3148	19160-1606	21531-1009	

G. Associations

As described in Section V.H.9, the associations of cataloged sources with IRAS sources were done purely on a positional basis, except that no association was allowed between a star and an IRAS source detected only at 100 μm. For the catalogs with small position errors, the search box was 45″ × 8″ (half-width), and the probability of a chance association with an IRAS source was less than 0.1%. For those catalogs where the search radius was significantly larger, e.g., galaxy catalogs and catalogs of diffuse objects, the probability of random associations was significantly greater. For the majority of the galaxy catalogs, where the search radius was 90″, the probability of chance associations with IRAS sources was about 0.3% at high galactic latitude ($|b| > 45°$) and increased with increasing IRAS source surface density. A particular concern is the association of galaxies with infrared cirrus. The far infrared properties of an external galaxy can be very similar to those of cirrus. The user is urged to examine the cirrus flags before attaching significance to such associations.

It must be emphasized that the associations are not identifications. To be certain of any specific identification of an IRAS source with a cataloged source, the user must investigate the IRAS source in some detail.

About 28% of IRAS sources were associated with cataloged objects. Approximately 46,000 IRAS sources were associated with cataloged stars and approximately 10,000 IRAS sources were associated with cataloged galaxies. Other classes of objects accounted for 15,000 associations. The vast majority of these were galactic nebulae and galaxies in the ESO (B) atlas. A measure of the fraction of spurious associations can be found in the number of IRAS sources associated with both stellar and galaxy-type objects. At high galactic latitudes ~ 0.6% of the IRAS sources had both galaxy and stellar associations.

H. Meaning of Point Source Flags

H.1 Confusion Flags

Confusion flags are essential in assessing the quality of a point source. Sources with all flags equal to zero can be accepted without question. Sources with non-zero flags may have some problems as discussed below.

The confusion flags include a count of neighbors around a given source that were found in either the point or small extended source WSDBs, as well as a flag which was set by the processors during seconds-confirmation, band-merging and hours-confirmations. This relatively large number of flags was required by the complexities of the processing and of the infrared sky.

H.1.a Point Source Neighbors

Point source neighbor flags warn of problems in the immediate vicinity of the source. The point source neighbors come from the cleaned-up WSDB. The number of neighbors is counted in a rectangle oriented along the largest position uncertainty direction. That rectangle usually reflects the original scan direction used to observe that source. The large dimension of the box is a half-width of $6'$ along the smallest position uncertainty axis, which corresponds to the maximum distance in which another source may have shadowed or stolen any detections of the source in question (Section V.C.7). The half-width is $4.5'$ along the orthogonal axis, corresponding to a full detector width. Neighboring sources within this distance produced at least one detection that was the sum of the two sources.

Weeks-confirmed and single hours-confirmed point source neighbors are counted separately in that box. Non-zero values for either count, but especially for PNEARW, the count of weeks-confirmed sources, should caution the user that one or more bands of the source may be reported incorrectly and to look in a small region around the source for confusing neighbors. Most sources with neighbors are found in regions of high source density.

H.1.b Small Extended Source Neighbors

Two types of small extended source counts are given. The SES1 flag counts separately in each band the total number of hours-confirmed small extended sources. Note that a weeks-confirmed small extended source containing three hours-confirmations would contribute three to this count, and a small extended source containing only one hours-confirmation would contribute one to this count. The SES2 flag counts separately in each band only the number of weeks-confirmed small extended sources. Both flags use the box described above for point source neighbor counting.

Both flags warn of the presence of structures larger than point sources, and hence cast doubt on whether the reported source is truly point-like or is only part of a larger complex. Two separate flags exist for the following reason. In confused regions containing only a single small extended source, SES1 would equal the number of hours-confirmations times SES2, and thus the flags would be redundant. However, in complex regions SES1 may be unrelated to SES2. That is, because of the effects of cluster analysis (Section V.E) there may have been no acceptable small extended source, even though many small extended source detections occurred. The distribution of sources with high values of SES1 and with non-zero values of SES2 is shown in Figs. VII.Ap.21 and Ap.22.

H.1.c Confuse Flag

A final flag related to near neighbor confusion is derived from the repeated occurrence of confusion during the processing of a source. In a given band, if more than one candidate per scan could confirm with the source at either seconds-confirmation (excluding edge detections), band-merging, or hours-confirmation, the processor set a flag. If any such flag was set in two separate hours-confirmations of a source, then the confuse flag was also set in that band. Thus if the confuse flag is set, something other than an isolated point source was present at or near the position of the source in question, and the user should again be cautious. The distribution of sources with the confuse flag set correlates well with high source density areas.

H.1.d Summary

The user examining an IRAS source can immediately rule out almost any problem if all of its neighbor flags are zero, and SES1 is 0 or 1. Sources that have all those flags set to zero are almost always completely clean point sources. There are about 63,000 such sources in the entire catalog, 25% of all sources. Above a Galactic latitude of 20°, the fraction is much higher, 30,000 out of 60,000 sources. Including sources with SES1 less than 2, which are still almost always clean sources, increases the percentage of clean sources to 38% in the entire sky, and to 70% in the sky above Galactic latitude 20°.

Sources with non-zero flags may be confused with point source neighbors or may only be part of an extended complex, and unfortunately must be examined in more detail.

H.2 Cirrus Flags

Cirrus flags are set to warn the user that a catalog source may be adversely affected by infrared cirrus or may even be no more than a bump in the infrared cirrus. These flags and the 2′ sky brightness images are the best possible substitutes for examining the raw detector data. If all cirrus flags are smaller than the limits discussed below, then one can infer that the source is unlikely to have been affected by cirrus.

CIRR1

CIRR1 gives an estimate of the existence of cirrus on the point source scale. CIRR1 is total number of sources detected only at 100 μm, including sources with single and multiple hours-confirmations, in a 1 sq. deg box centered on the source. The sky distribution of sources with CIRR1 greater than three is displayed in Fig. VII.Ap.23, and shows the areas where cirrus is a problem. This figure is similar to the map of sources detected only at 100 μm shown earlier (Fig. VII.Ap.10).

CIRR2

CIRR2 is a logarithmic function of the ratio of the 100 μm point source flux to an estimate of the 100 μm flux produced by cirrus, derived from the filtered 0.5° 100 μm data (Section V.H.4). Figure VII.Ap.24 shows that the distribution of sources with CIRR2 greater than 4 correlates well with other cirrus maps.

CIRR3

Another estimate of the importance of cirrus comes directly from the total 100 μm emission is a 0.5° beam data. CIRR3 is equal to the intensity of the 100 μm emission in MJy sr^{-1}.

SES1

The SES1 flag at 100 μm, discussed earlier, is also a good cirrus indicator. See the earlier discussion.

Summary

No clear-cut prescription can be given to a user to guarantee that cirrus has not adversely affected a given source. If the source has a strong 100 μm flux, no missing bands, and all cirrus flags are well below the cutoff values discussed above, then it is likely that few problems exist. If any of the above conditions are violated, a closer examination of nearby sources will usually indicate the importance of cirrus. However, in some cases, only an examination of images or, finally, the detector data will resolve all doubts.

I. The Small Extended Source Catalog

An analysis of the properties of this catalog will be presented in the final version of this Supplement after the catalog has been released in 1985.

J. Extended Source Products

J.1 Zodiacal Emission Effects

Since the detector signals were DC coupled, the extended source data products include emission from sources on all angular scales. In particular, emission from interplanetary dust, or zodiacal emission was a prominent large scale signal component in all survey bands. The contribution of the zodiacal emission to the observed intensity toward any direction on the celestial sphere depended upon the integrated emission from the interplanetary dust along the line of sight at the time of observation, which in turn depended upon the Earth's orbital position within the dust cloud (time of year) and the spatial structure of the cloud. Hence, repeated measurements in a given celestial direction at substantially different times of year gave different results. For example, for elongations near 90°, the 1° daily motion of the Sun produced about a 2% change in the sky brightness near the ecliptic plane in all survey bands, with the brightness decreasing with increasing elongation. Because the dust symmetry plane near 1 AU from the Sun was inclined with respect to the ecliptic plane, the brightness at high ecliptic latitudes varied sinusoidally annually with a peak-to-peak variation of about 20% in the bands.

For the purposes of preparing the extended source data products, the hours-confirming scans (typically separated by about two hours) were treated as if they had been obtained simultaneously and the results were averaged together. The difference in zodiacal brightness between one orbit and the next was less than 0.1% of the ecliptic plane brightness; within the maximum 36-hour spacing of an hours-confirming coverage, the brightness difference was less than 3%. The data from the three hours-confirming surveys were reduced separately and presented as three distinct sets of images. The data from the first two surveys, which each covered about 95% of the sky, were interleaved during the first 7 months of the survey, with the two weeks-confirming surveys typically separated by about 10 days at any given celestial position. The third survey, which covered 72% of the sky, was obtained during the last four months.

As an aid to modeling and extracting the zodiacal emission contribution in any of the extended source products, the time-ordered Zodiacal Observation History File (ZOHF) was created. This file contains, at 0.5° sample spacing, the time (UTC), celestial coordinates, Sun-referenced observing angles, and measured brightnesses in the survey bands for all observations included in the extended source image products.

J.2 Effective Resolution

As discussed above, the data for the sky plates and Galactic plane maps were smoothed in the time domain to a sample spacing corresponding to 2′. Additional smoothing was inherent in the process of projecting these data into image grids. It was estimated that the resulting effective resolution, or, ability to distinguish point sources in these images is about three pixels, or 6′.

J.3 Tests of Extended Source Calibration Consistency

The primary test of the extended source calibration consistency was an examination of the measured brightness in the survey data to show that the absolute baseline was being properly controlled through the daily observations of the baseline photometric reference area (the TFPR) as described in Section VI.B.3.

One check consisted of observing the time variation of the brightness of the TFPR in the Zodiacal Observation History File (ZOHF). The mean of the ZOHF data followed the model of the TFPR given in Table VI.B.1 to within 5% in all bands except for a short period of time about 20 days before the end of the mission where deviations approaching 10% brighter than the model occurred. The scatter of the measurements was non-Gaussian, most of the points scattered toward higher brightness, with 50% of the points lying within 7%, 5%, 12% and 12% of the model in the 12, 25, 60 and 100 μm, respectively.

As a second check the sum of the north and south ecliptic pole brightness, as measured from selected single scans of the telescope, was compared with parameter B_0 of the TFPR model in Table VI.B.1. The geometrical basis of the TFPR brightness model predicts that the sum of the north and south brightness will be constant and equal to twice B_0. This was found to be true to within 5% in all bands.

Authors:

C. Beichman, T. Chester, R. Benson, T.Conrow, J. Fowler, T.N. Gautier, F. Gillett,
G. Helou, J. Houck, H. McCallon, G. Neugebauer, B.T. Soifer, and R. Walker.

References:

Dressel, L.L. and Condon, J.J. 1976, *Ap.J.* [*Suppl.*], **31**, 187

Rieke, G., Lebofsky, M. and Low, F.J. 1984, preprint.

Smithsonian Astrophysical Observatory Star Catalog 1966, Smithsonian Institution, Washington, D.C.

Tokunaga, A., 1984, *A.J.*,**89**, 172.

Figure VII.Ap.1 The distribution of sources detected at 12 μm only (spectral combination "1000") shown in an Aitoff equal area projection in Galactic coordinates.

Figure VII.Ap.2 The distribution of sources detected at 12 and 25 μm (spectral combination "1100") shown in an Aitoff equal area projection in Galactic coordinates.

Figure VII.Ap.3 The distribution of sources detected at 12, 25 and 60 μm (spectral combination "1110") shown in an Aitoff equal area projection in Galactic coordinates.

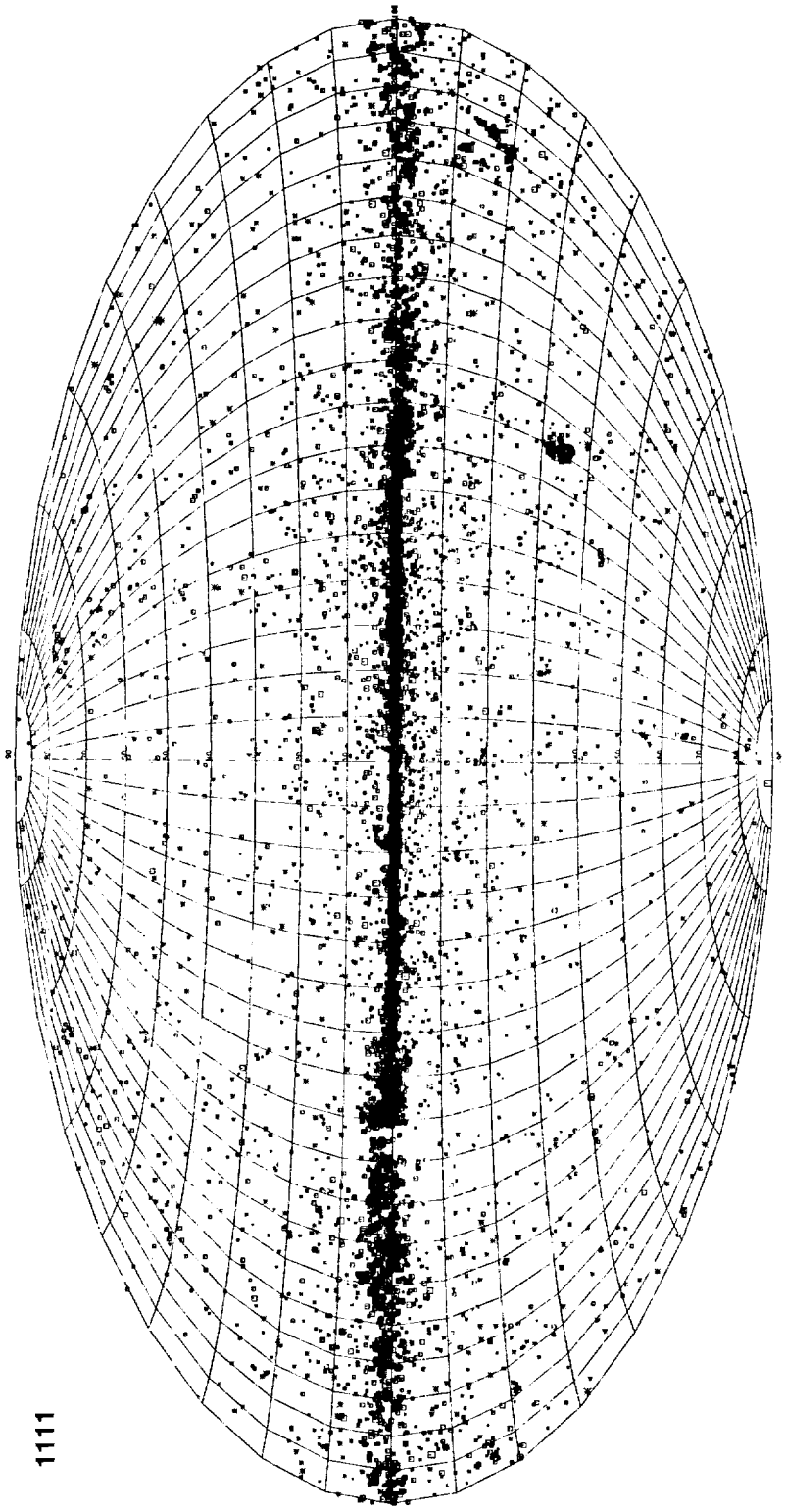

Figure VII.Ap.4 The distribution of sources detected at 12, 25, 60 and 100 μm (spectral combination "1111") shown in an Aitoff equal area projection in Galactic coordinates.

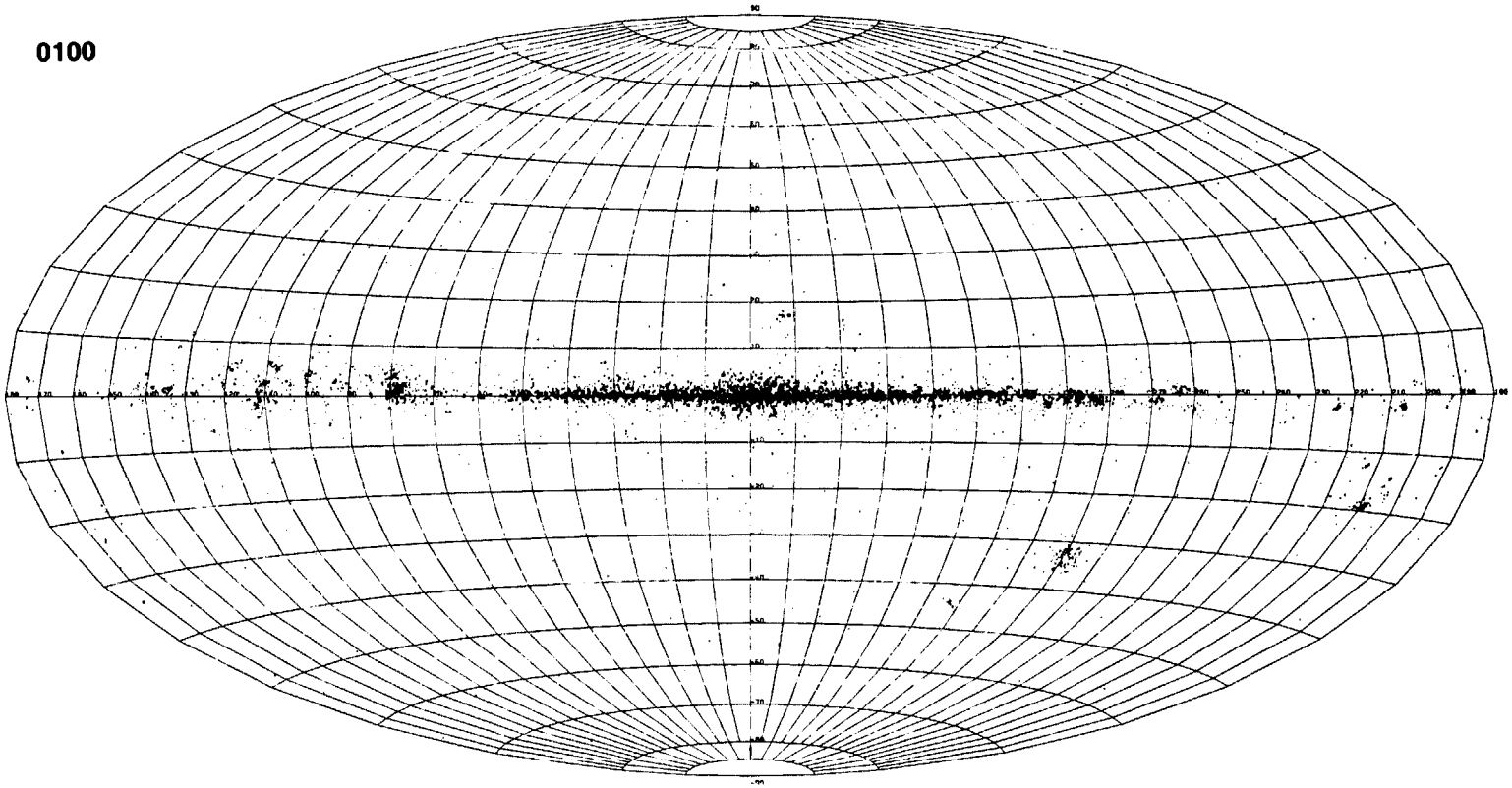

Figure VII.Ap.5 The distribution of sources detected at 25 μm only (spectral combination "0100") shown in an Aitoff equal area projection in Galactic coordinates.

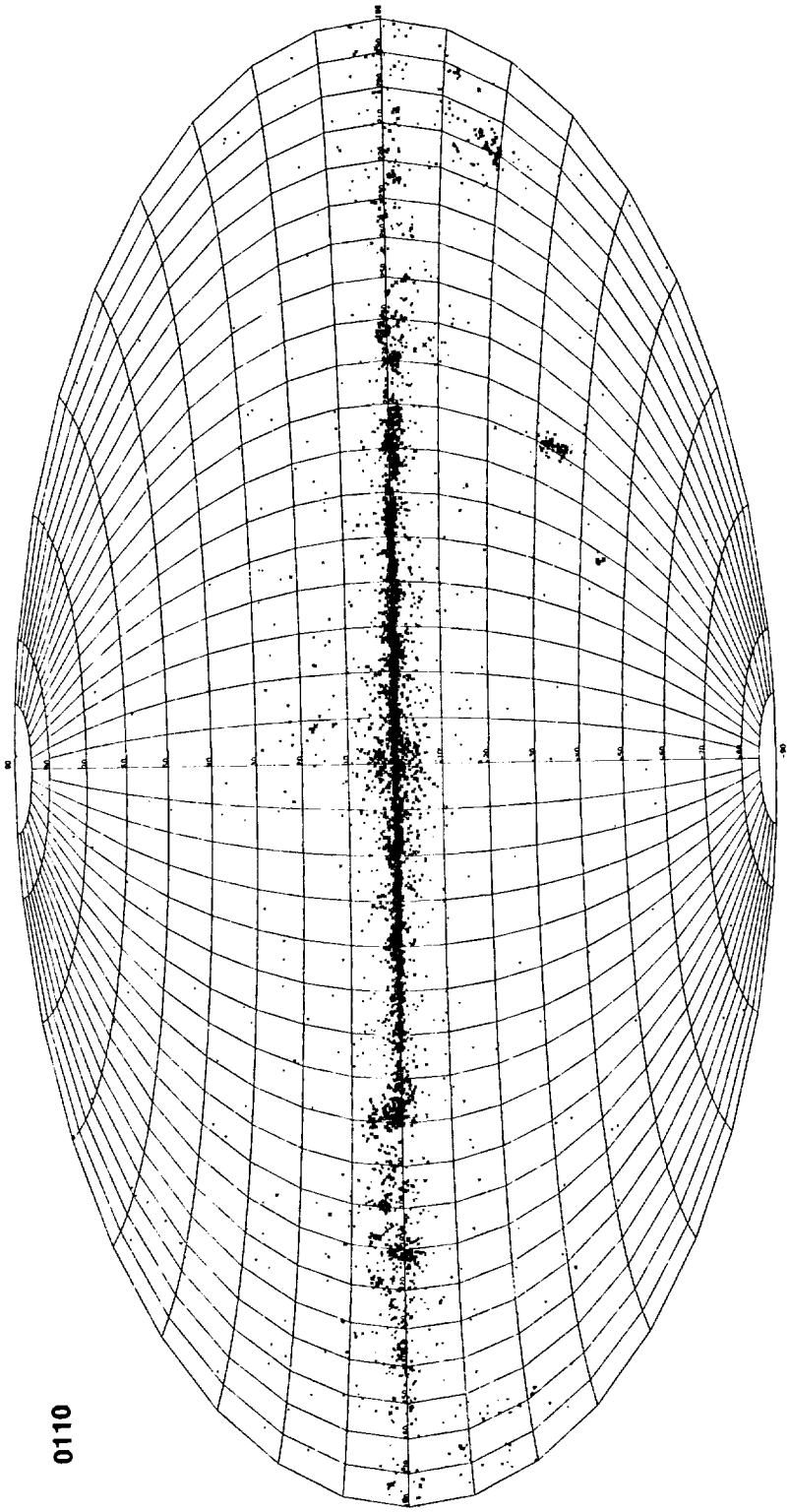

Figure VII.Ap.6 The distribution of sources detected at 25 and 60 μm (spectral combination "0110") shown in an Aitoff equal area projection in Galactic coordinates.

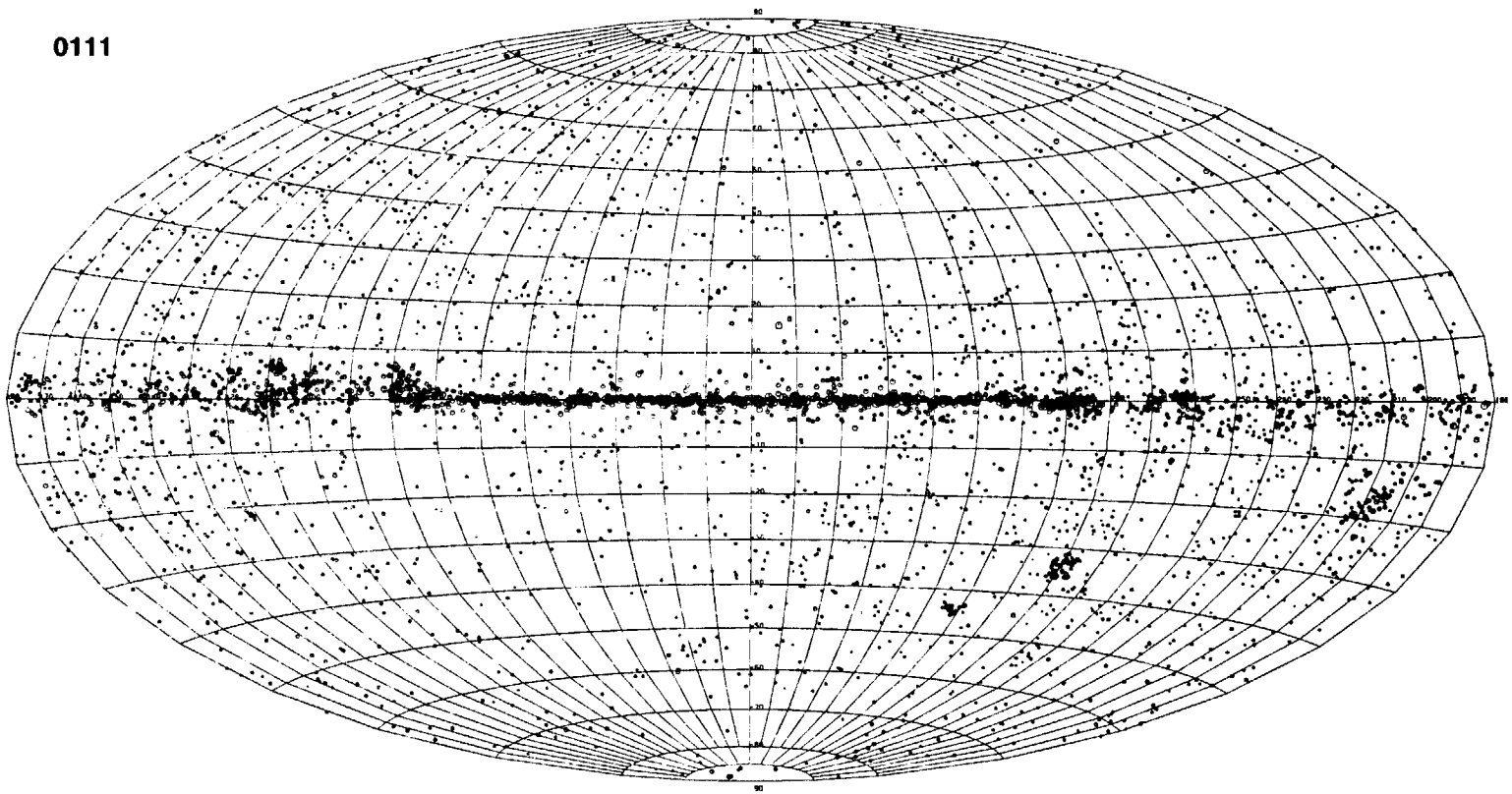

Figure VII.Ap.7 The distribution of sources detected at 25, 60 and 100 μm (spectral combination "0111") shown in an Aitoff equal area projection in Galactic coordinates.

Figure VII.Ap.8 The distribution of sources detected at 60 μm only (spectral combination "0010") shown in an Aitoff equal area projection in Galactic coordinates.

Figure VII.Ap.9 The distribution of sources detected at 60 and 100 μm (spectral combination "0011") shown in an Aitoff equal area projection in Galactic coordinates.

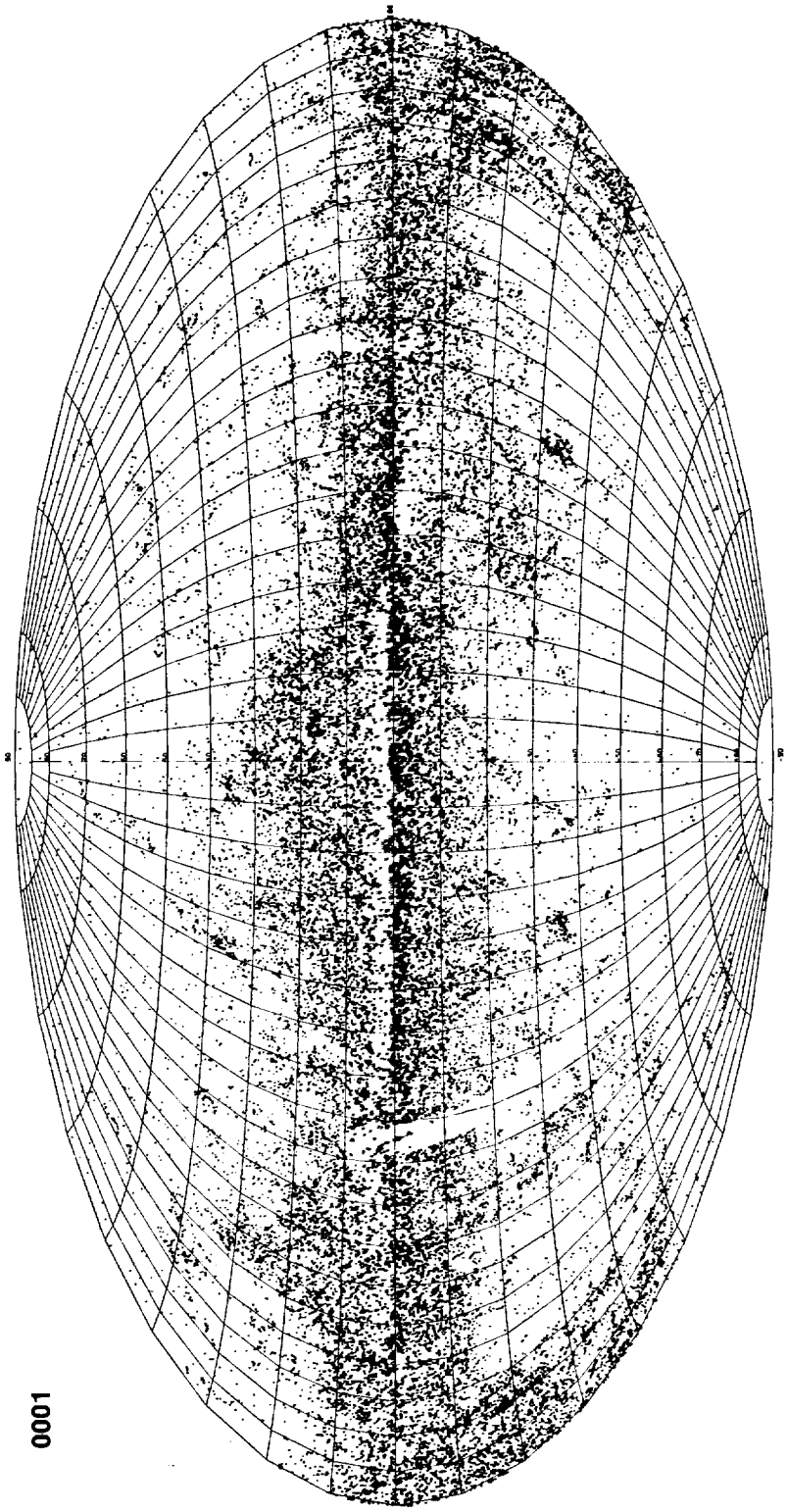

Figure VII.Ap.10 The distribution of sources detected at 100 μm only (spectral combination "0001") shown in an Aitoff equal area projection in Galactic coordinates.

Figure VII.Ap.11 The distribution of sources detected at 12 and 60 μm (spectral combination "1010") shown in an Aitoff equal area projection in Galactic coordinates.

Figure VII.Ap.12 The distribution of sources detected at 12 and 100 μm (spectral combination "1001") shown in an Aitoff equal area projection in Galactic coordinates.

Figure VII.Ap.13 The distribution of sources detected at 12, 25 and 100 μm (spectral combination "1101") shown in an Aitoff equal area projection in Galactic coordinates.

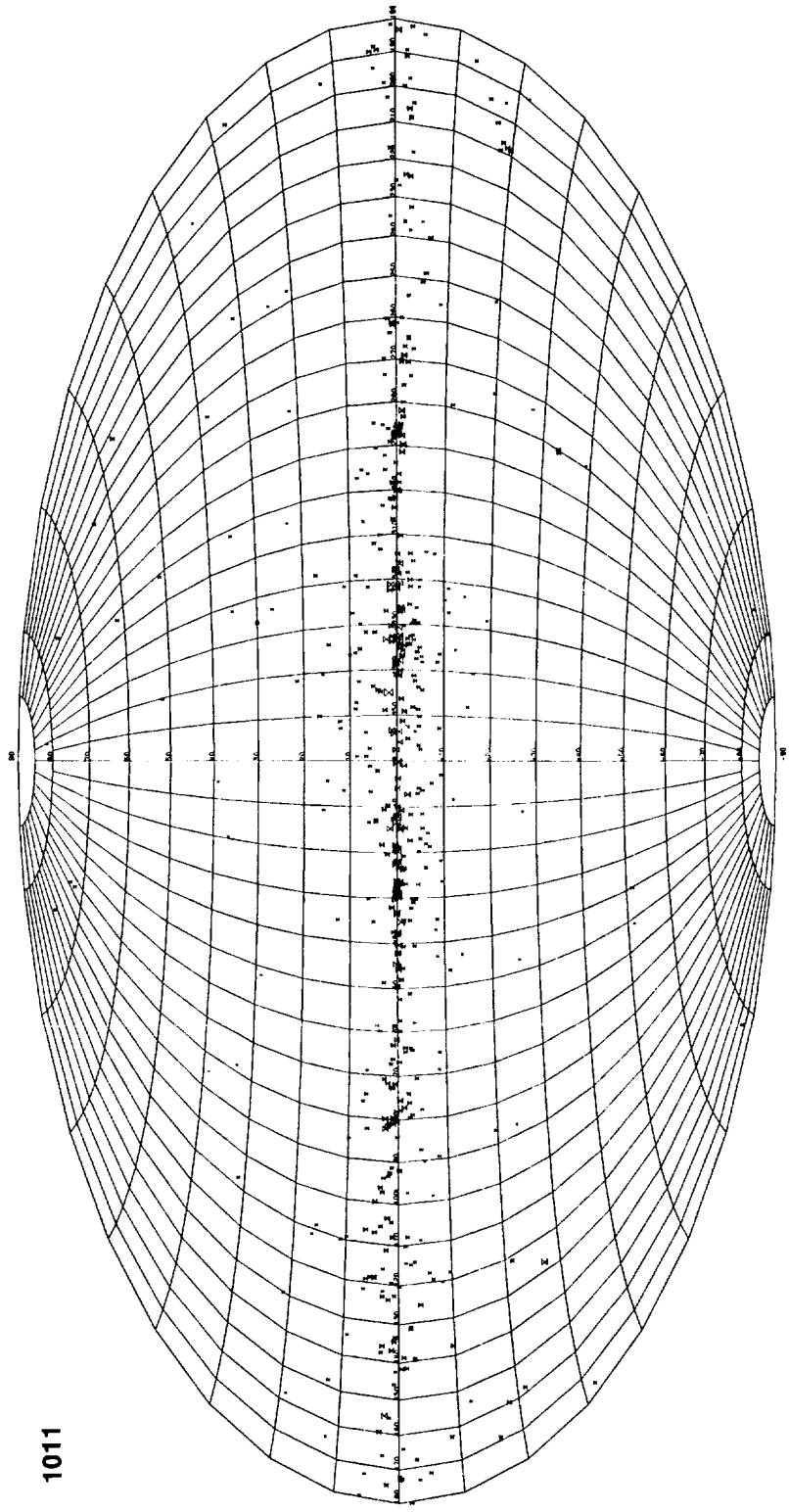

Figure VII.Ap.14 The distribution of sources detected at 12, 60 and 100 μm (spectral combination "1011") shown in an Aitoff equal area projection in Galactic coordinates.

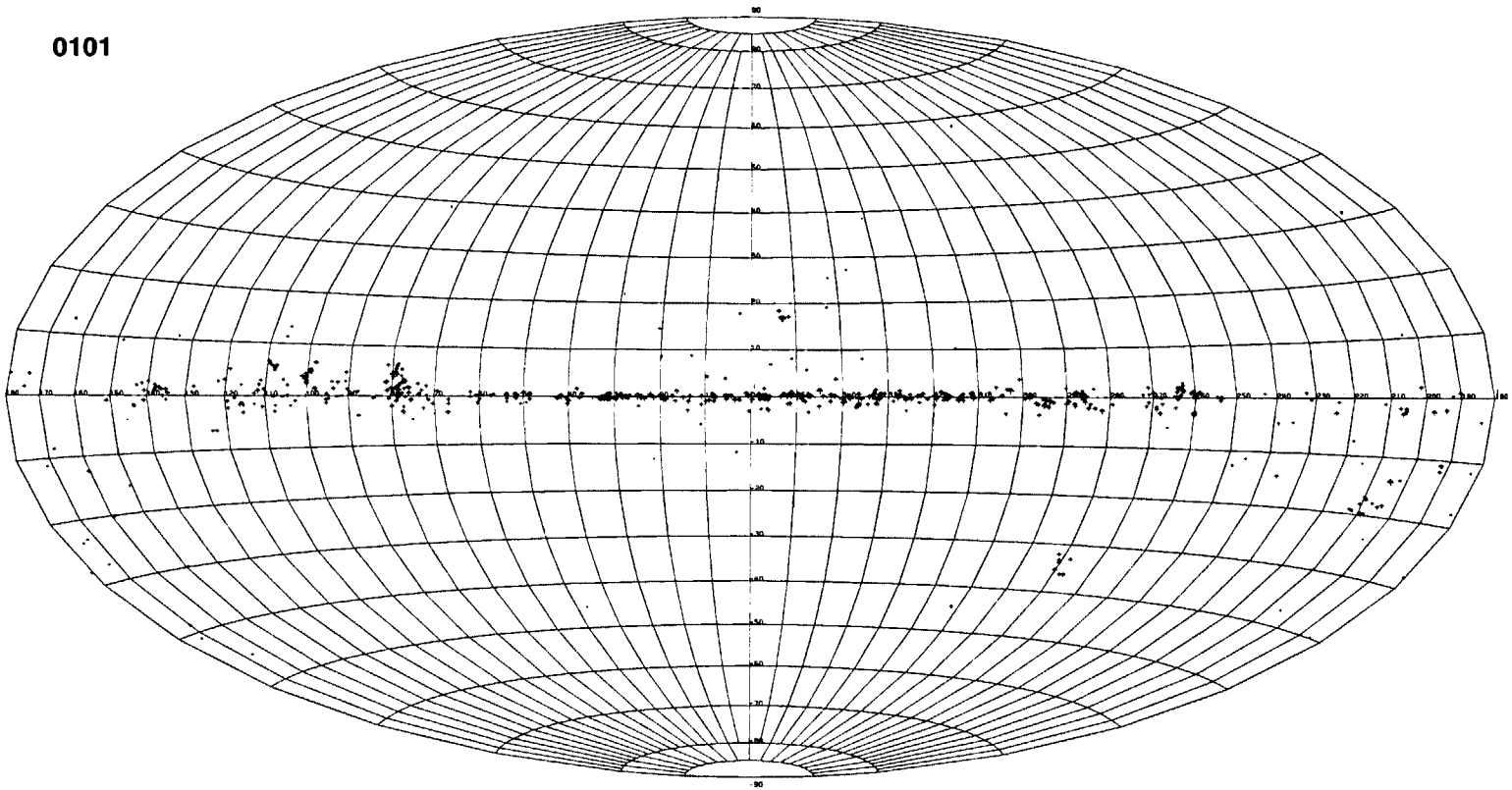

Figure VII.Ap.15 The distribution of sources detected at 25 and 100 μm (spectral combination "0101") shown in an Aitoff equal area projection in Galactic coordinates.

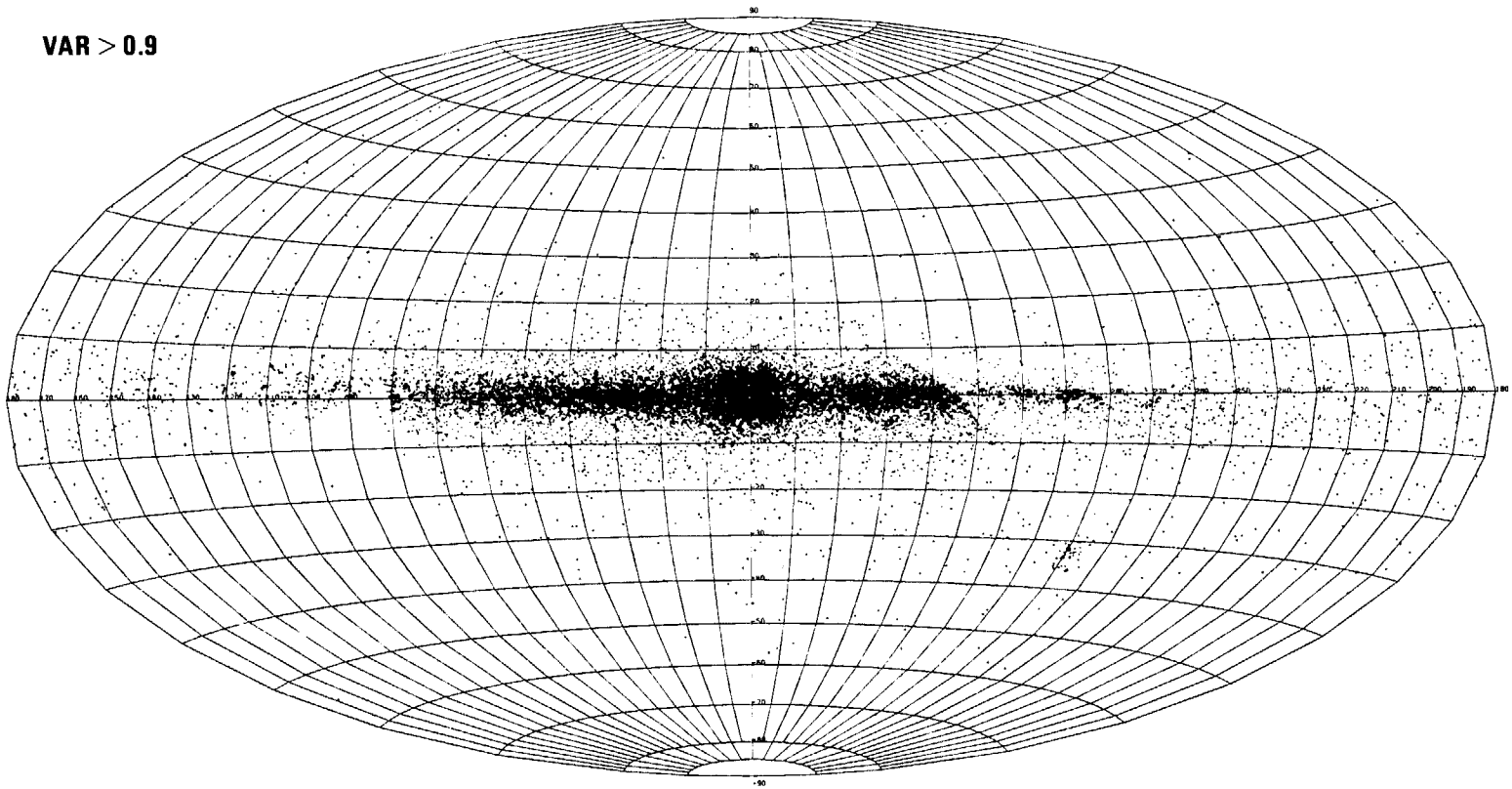

Figure VII.Ap.16 The distribution on the sky of sources with a probability of variability greater than 0.9 is shown in an Aitoff equal area projection in Galactic coordinates.

Figure VII.Ap.17 The distribution of 12 μm point sources that had only a single hours-confirmed sighting (an HCON) is shown in an equal area Aitoff projection in Galactic coordinates.

Figure VII.Ap.18 The distribution of 25 μm point sources that had only a single hours-confirmed sighting (an HCON) is shown in an equal area Aitoff projection in Galactic coordinates.

Figure VII.Ap.19 The distribution of 60 μm point sources that had only a single hours-confirmed sighting (an HCON) is shown in an equal area Aitoff projection in Galactic coordinates.

Figure VII.Ap.20 The distribution of 100 μm point sources that had only a single hours-confirmed sighting (an HCON) is shown in an equal area Aitoff projection in Galactic coordinates.

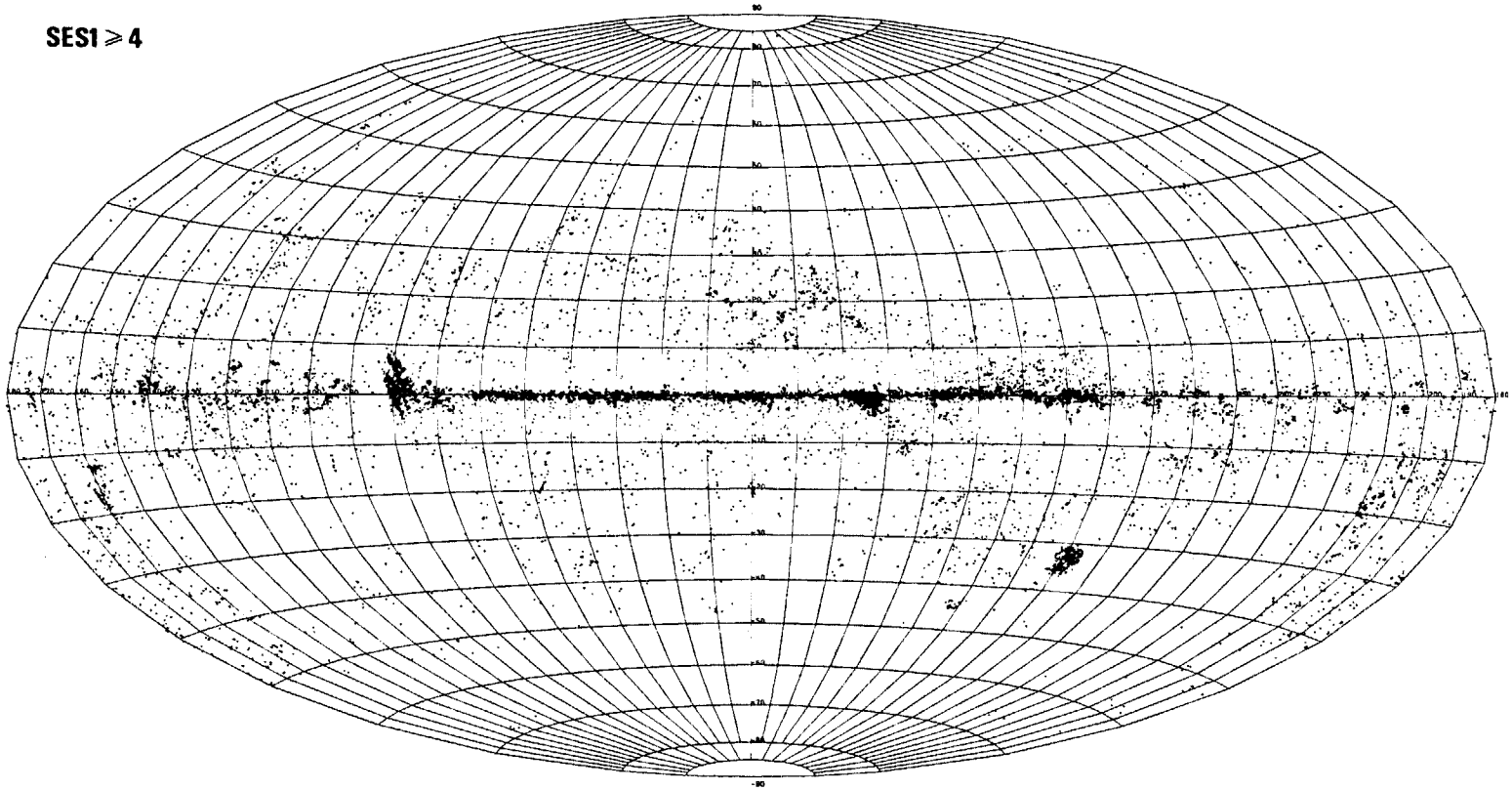

Figure VII.Ap.21 The distribution of point sources that were tagged as having four or more nearby, hours-confirmed small extended sources detected at 100 μm (SES1 ⩾ 4), and therefore likely to be corrupted by the infrared cirrus, is shown in an equal area Aitoff projection in Galactic coordinates.

Figure VII.Ap.22 The distribution of sources that were tagged as having one or more nearby, weeks-confirmed small extended sources (SES2 > 0) is shown in an equal area Aitoff projection in Galactic coordinates.

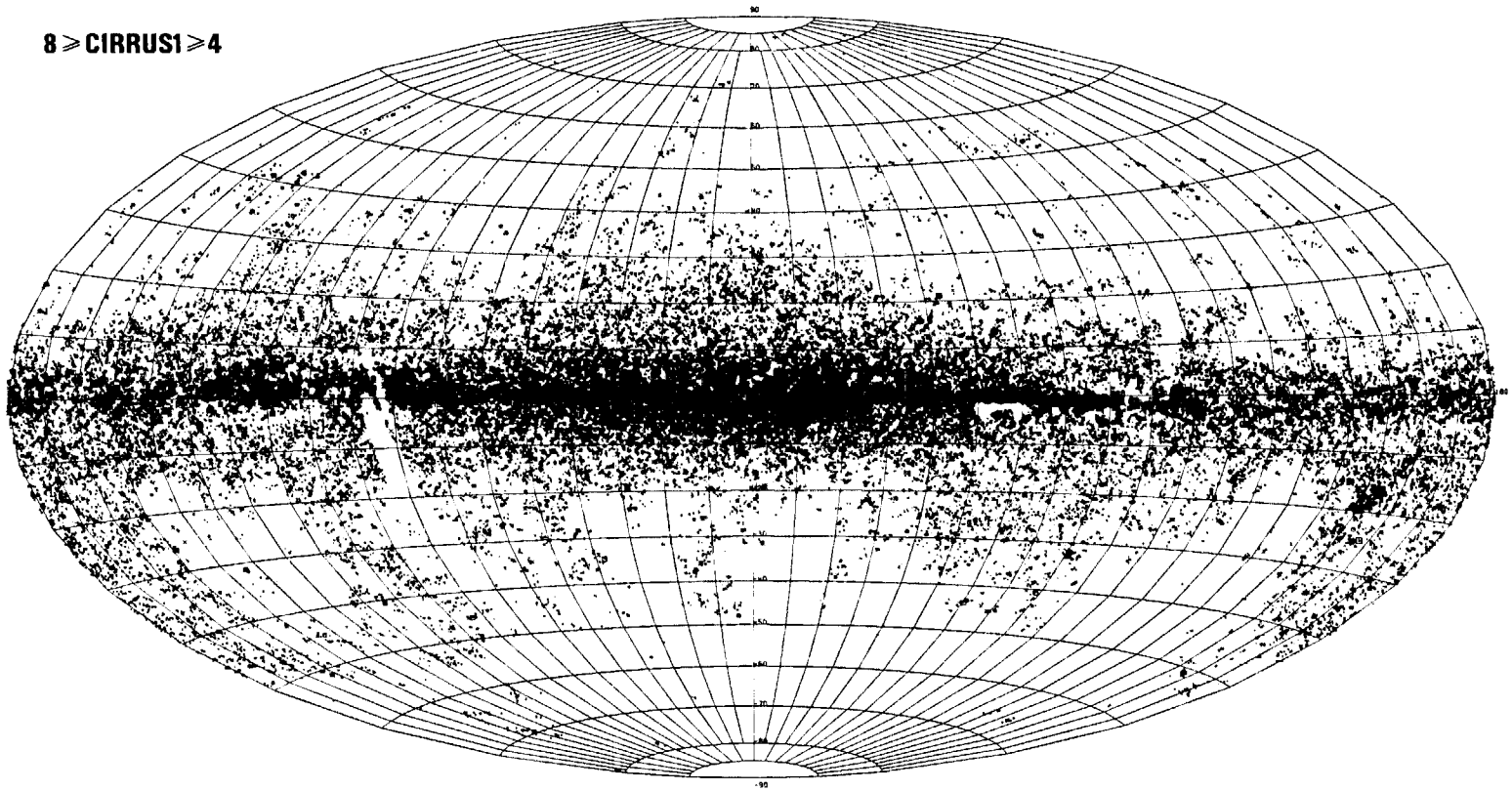

Figure VII.Ap.23 The distribution of sources that were tagged as having between four and eight nearby, hours-confirmed point sources detected only at 100 μm, (8>CIRR1>4), and therefore likely to be contaminated by the infrared cirrus, is shown in an equal area Aitoff projection in Galactic coordinates.

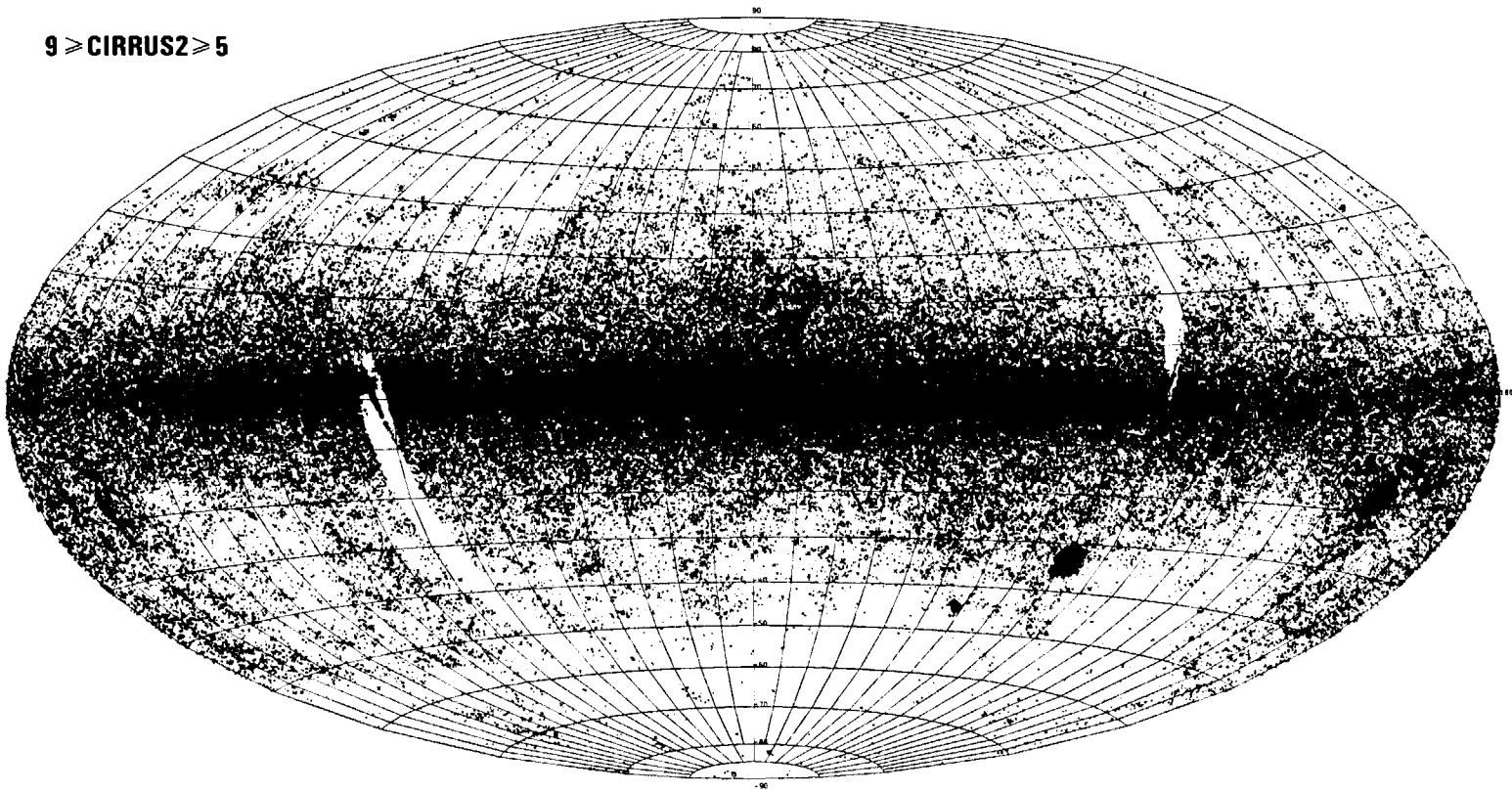

Figure VII.Ap.24 The distribution of sources that were tagged as having the cirrus flag CIRR2 in the range 5-9, and therefore likely to be contaminated by the infrared cirrus, is shown in an equal area Aitoff projection in Galactic coordinates.

VIII. SKY COVERAGE, CONFUSION, COMPLETENESS AND RELIABILITY

A. Introduction

The main results concerning the sky coverage, completeness and reliability of the IRAS survey can be summarized by noting that: 1) 96% of the celestial sphere was covered sufficiently to appear in the catalog; 2) at Galactic latitudes $|b|>20°$ and at wavelengths of 12, 25 and 60 μm the catalog is essentially complete for sources brighter than about 1.5 Jy; and 3) fewer than one source in 1000 having two hours-confirmed sightings is a spurious object.

At 100 μm the situation is more complicated due to the effects of "cirrus"-like emission (cf. Low *et al.* 1984) that often affects point source fluxes and completeness and reliability even at high Galactic latitudes. Whether a particular point source is an independent entity such as a galaxy or a dense condensation in a cirrus wisp has to be carefully considered. It is advisable to check the values of the cirrus and confusion flags for 100 μm flux densities because these may indicate extended emission at the point source position (see Sections V.H.4, VII.H.2 and X.B.1).

In regions of high point source density such as the inner parts of the Galactic plane and the Magellanic Clouds, the completeness of the catalog is likely to be poor. More stringent criteria for the selection of catalog sources were applied in these regions to ensure a high reliability of the sources. It is hard to arrive at good estimates of the completeness and reliability, particularly since these are also regions of strong extended emission. The completeness is very low in regions affected by the Galactic plane "shadow" caused by the lagging of the noise estimator.

The catalog of small extended sources is considerably less complete and reliable than the point source catalog due to the cruder algorithms used and to the effects of confusion from larger extended structures. These results are discussed in Section VIII.E.

B. Sky Coverage

The survey strategy was chosen to achieve a high degree of homogeneity of coverage of the sky. One hours-confirming (HCON) coverage is defined as the sky coverage obtained by two or more scans covering a given area of the sky with a separation in time ranging from one orbit of the satellite, 103 minutes, up to a maximum of 36 hours. Figures I.C.1 and III.D.3 show the distribution of the number of HCON coverages in equatorial and ecliptic coordinates. More detailed plots of the sky coverage are shown in Chapter XIII.

Ninety-six percent of the sky was covered with the two or more HCONs required for sources to be considered for inclusion in the catalog. A three HCON coverage was achieved over 72% of the sky. Roughly 15% of the sky received more than three HCON coverages. Areas receiving more than three HCON coverages arose mainly from the minisurvey (see below), from the overlap between lunes used in the survey strategy, from rescans scheduled to fill in coverage holes and from the tendency of scans to overlap at high ecliptic latitudes.

From the standpoint of the IRAS survey itself, the area of the "minisurvey" was the most important area receiving extra coverage (Section III.D.11). The particular area was selected because it was available immediately after the telescope cover was ejected. The region was surveyed intensively to check the

source detection and confirmation algorithms and to verify that the chosen survey strategy provided the desired completeness and reliability; see Rowan-Robinson *et al.* (1984). The minisurvey consisted of two strips of the sky centered approximately at ecliptic longitudes 60° and 250° and contained areas both of high source density near the Galactic plane and of reasonably low source density. Parts of the minisurvey received as many as four HCON coverages during the minisurvey proper. The whole minisurvey area received three more HCON coverages during the main survey. Thus some regions received as many as seven HCONs.

The part of the sky with no HCON coverage is entirely contained within two strips on opposite sides of the sky each roughly 5° wide and 60° long. This part of the sky was not observed because of the operational difficulties explained in Section III.D.5. At the borders of the gap there are strips 0.5° wide that received only one HCON coverage. In addition, there are various small areas of the sky which received only one HCON coverage. For the single HCON areas, comprising in total some 500 sq. deg, there are no entries in the catalog. The main cause of the small holes was the inability to take useful data when the spacecraft passed through the South Atlantic Anomaly (the SAA, see Section III.D.4). These areas are mainly concentrated in the south (see the detailed area coverage plots in Chapter XIII). Hours-confirmed detections made in the single HCON sky are contained in the catalog of rejected point sources.

C. Point Source Confusion

It is the aim of this section to show that confusion caused by background fluctuations due to the large numbers of sources below the detection threshold is insignificant in the IRAS point source catalog outside of the Galactic plane and other high source density areas.

Suppose that the mean density N (f_ν) of sources on the sky with flux density greater than f_ν obeys a power law:

$$N(f_\nu) = K f_\nu^{\,a} \qquad \text{(VIII.C.1)}$$

where a (<0) is a constant. In a small interval in flux density ($f_\nu, f_\nu + df_\nu$) and within a beam of solid angle Ω one expects on average $\Omega\, a\, N(f_\nu)\, f_\nu^{-1}\, df_\nu$ sources. The actual number will be a stochastic variable with a mean-squared deviation equal to the average value. The mean-squared deviation in the flux will be $f_\nu^{\,2}\times$ the deviation in the number. Thus the mean-squared flux deviation, $(\Delta f_\nu)^2$, from all sources below some threshold $f_{\nu 0}$ is given by

$$(\Delta f_\nu)^2 = \frac{-a}{2+a}\,\Omega\, N(f_{\nu 0}) f_{\nu 0}^2 \qquad \text{(VIII.C.2)}$$

Equation (VIII.C.2) can be used to estimate the effect of confusion on the IRAS survey in two ways. First, the confusion noise can be calculated directly from the equation using the observed density and distribution of sources. Differential sources counts, dN/d(log f_ν), are given in Fig. VIII.C.1a-d for sources in all wavelength bands with $|b| > 50°$. The plots demonstrate that at high Galactic latitudes, objects detected at 12 and 25 μm follow a power law distribution (Eq. (VIII.C.1)) with an index a equal to -1.0 and that sources brightest at 60 μm, mostly external galaxies, have a equal to -1.5. Sources brightest at 100 μm do not follow a simple power law due to the effects of cirrus and will be discussed separately in

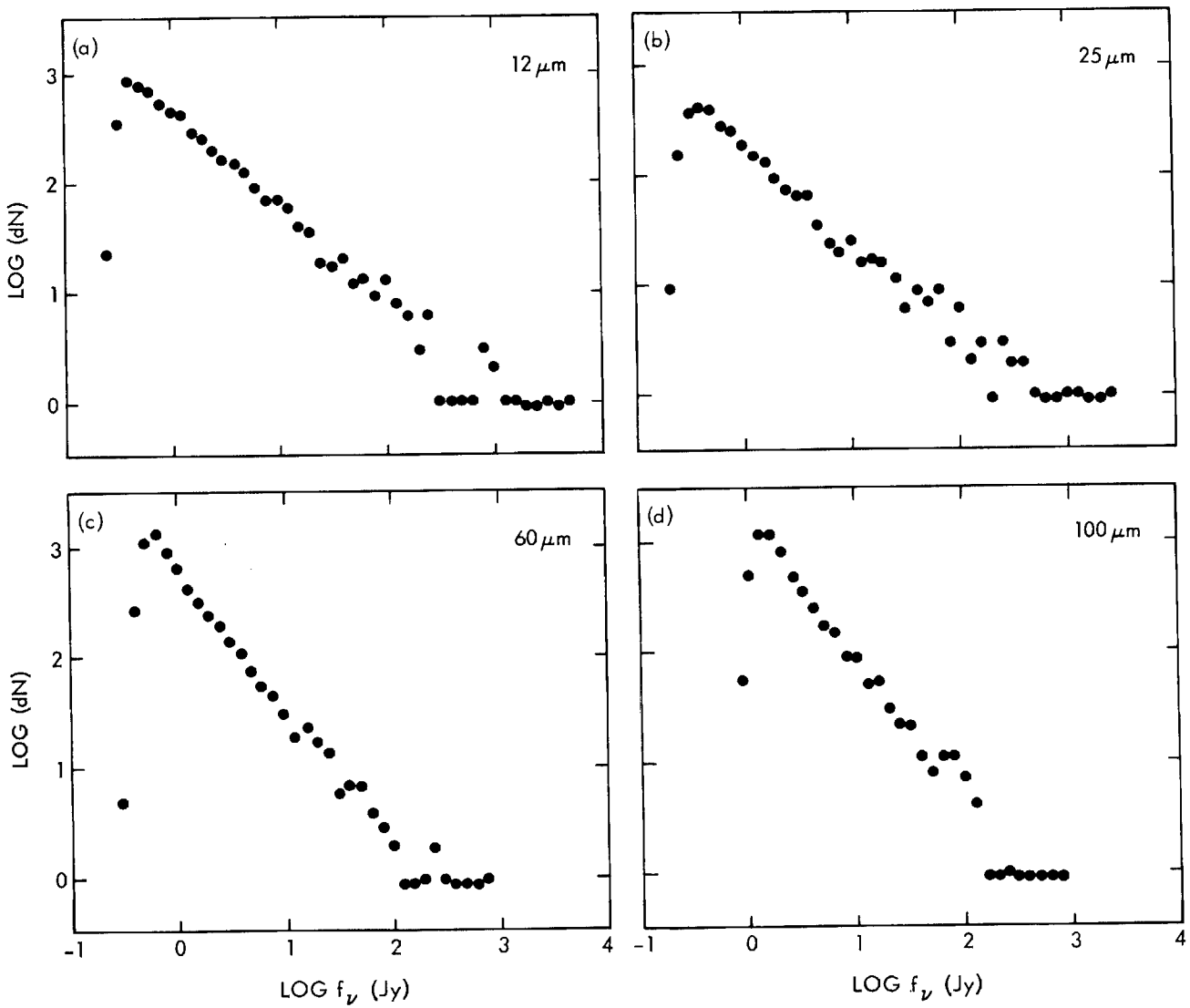

Figure VIII.C.1 Differential source counts as a function of flux density for the four wavelengths for sources with Galactic latitudes $|b|>50°$.

Section VIII.D.5. The typical source density for sources at 12, 25 and 60 μm with flux densities brighter than 0.5 Jy is 0.6 source per sq. deg at high Galactic latitudes. For typical detector areas the noise level due to confusion as calculated using Eq. (VIII.C.2) is ~15 mJy, far below the instrumental detection limits.

The second way to interpret Eq. (VIII.C.2) is to note that the critical term in determining the importance of confusion is the product ΩN which is the total number of sources per beam area. At high Galactic latitudes, the observed value of ΩN is less than 0.001 sources per beam for sources above the threshold of 0.5 Jy. The source densities over the whole sky for the four wavelength bands are shown in Figs. V.H.1.1-1.4. At the transition between the white and grey areas of these figures, the source density is less than 1 per 50 beams; this means that the confusion noise at the transition is less than 0.2 of the completeness limit at all wavelengths. Confusion noise can therefore be ignored in the white areas of Fig. V.H.1.1-.1.4. At 100 μm the shape of the unconfused regions is irregular and artificial due to the presence of infrared cirrus; the entire sky except at the highest Galactic latitudes can be confusion limited due to local infrared cirrus. In the darker areas of these figures confusion noise dominated the source recognition process, as will be discussed in Section VIII.D.5.

A signal-to-noise ratio of five which corresponds to the IRAS completeness limits at 12, 25 and 60 μm would, according to Eq. (VIII.C.2), be achieved at 75 beams per source for $a=-1.5$ and at 25 beams per source for $a=-1.0$. This latter value was used as the confusion limit for the high source density processor.

D. Point Source Catalog Reliability and Completeness

D.1 Definitions, Assumptions and Limitations

The completeness of the catalog above a given flux density at a specified wavelength is defined as the fraction of true sources above that flux density which are present in the catalog. The completeness can be quantified by statistical analysis of the detection history in an area with multiple HCON coverage under the assumption that two different detections of a real source are two statistically independent events, each with the same probability.

The reliability of the catalog is defined as the probability that a catalog entry corresponds to a true, celestially fixed source of radiation. An unreliable catalog entry would be created whenever a spurious HCON is confirmed by another spurious HCON on any subsequent survey scan. The survey strategy was developed so that observations of one area were repeated several times, thus lowering the probability that a chance detection would be confirmed.

Ideally, the completeness and reliability of sources with flux densities in a given range would be calculated separately for each wavelength. However, because band-merging occurred before hours-confirmation, completeness and reliability unavoidably depend on the spectrum of a source. In particular, two very different definitions of reliability must be understood. The reliability of a source, which is primarily discussed in this chapter, refers to the probability that a source in the IRAS catalog is a true celestial object measured in at least one wavelength band. The reliability of a flux measurement, on the other hand, refers to the probability that the flux density quoted for a source in a given band is a true measurement and not one due to spurious effects such as noise, radiation hits or asteroids. The concept

of high and medium quality flux densities is crucial in this discussion (Section V.H.5). A high quality flux density measurement is one which has met all the confirmation criteria on timescales of seconds, hours and weeks. The existence of a source is guaranteed and the quality of its flux density measurement in a band is assured according to the completeness and reliability values discussed in this chapter if, and only if, the source has a high quality flux density in that band. If a source has only a moderate quality flux density in a given band, then lower standards of reliability apply (Section VIII.D.4.c). This dual concept of reliability was necessitated by a desire to provide flux information in as many bands as possible for sources whose existence was guaranteed in at least one band.

The estimates of completeness and reliability given here are valid only for sources that are truly point-like. Sources which are slightly extended may still achieve an acceptable correlation with the point-source template in the in-scan direction, but extend across more than three detectors in the cross-scan direction. The point-source processing software resolved such sources into a string of two or more point sources with a spacing of a few arc minutes in the cross-scan direction. Successive passes may have resolved the source in different ways, causing the completeness of such sources to be poor. This problem is a common occurrence with "cirrus" at 100 μm and in all bands in the Galactic plane near the Galactic center. In regions of high source-density such strings of sources were discriminated against by the "confused-neighbor" and "weaker-neighbor" rejection criteria (see Section V.H.6).

In addition, the completeness estimates are valid only for point sources without close neighbors. Close neighbors can (i) cause the detections of both sources to be lost when the confused detections of both sources no longer match a point source template; (ii) cause detections from one source to be lost because of source shadowing (Section V.C); (iii) create cross-scan confusion and alter significantly the cross-scan position of the source.

D.2 Formalism for the Determination of Completeness and Reliability

D.2.a Completeness

It is necessary to estimate the fraction of real sources on the sky, above some limiting flux density value, which is actually present in the catalog. Let p be the probability that a genuine source in a given flux range fails to generate an HCON. The probability $P(N,M)$ that a source is detected on N HCONs out of a possible M HCONs is given by:

$$P(N,M) = {}_MC_N(1-p)^N p^{M-N} \qquad \text{(VIII.D.1)}$$

where ${}_MC_N$ is the binomial coefficient. The completeness $C(N_{\min},M)$ of a $N_{\min}/M$ survey, which requires a source to have at least $N_{\min}$ HCONs out of M possible in order to be included in the catalog, is then given by:

$$C(N_{\min},M) = \sum_{N=N_{\min}}^{M} P(N,M) \qquad \text{(VIII.D.2)}$$

For a survey where two HCONs are required out of a possible two HCONs, the completeness $C(2,2)$ is given by:

$$C(2,2) = (1-p)^2 \ . \qquad \text{(VIII.D.3)}$$

Seventy two percent of the sky was surveyed three times and a source was accepted if it was seen at least twice. For this "two-out-of-three" strategy, the completeness $C(2,3)$ is given by:

$$C(2,3) = 3(1-p)^2p + (1-p)^3$$

$$= (1+2p)(1-p)^2 \qquad \text{(VIII.D.4)}$$

where the first term on the right-hand side of the first equation corresponds to having seen the source twice out of the three possible times while the second corresponds to seeing it all three times. The completeness of the 2/3 survey is therefore a factor $(1+2p)$ greater than that of a 2/2 survey. This factor is appreciable since most sources are near the completeness limit where p approaches 1. In small areas of the sky the completeness will be better than suggested by Eq. (VIII.D.4) since there were as many as 23 HCON coverages, yet only two HCONs were required for inclusion in the catalog (see Table VII.B.1).

D.2.b Reliability

Let q be the probability, per unit area of the sky, that a false source is created on a single HCON coverage of the sky. Let A be the effective area for "weeks-confirmation" (see Sections V.D, V.H.2), i.e. the area within which a series of single HCONs must fall if they are to be considered as detections of the same source. Then qA is the probability that in a single HCON coverage a false source will be created at a given point on the sky with the possibility of being confirmed with another false source at the same position on a later HCON. The probability $Q(N,M)$ that a false source will be created in a given area N times out of M HCONs is therefore given by

$$Q(N,M) = {}_MC_N(qA)^N\,(1-qA)^{M-N} \quad . \qquad \text{(VIII.D.5)}$$

In fact, Eq. (VIII.D.5) is only true if $qA \ll 1$ since it does not allow for the possibility that more than one false source is created within A during a single HCON. This is a necessary assumption for the IRAS processing because, by its very nature, the processing can only produce one final source per HCON from an area A. The results obtained justify the approximation.

Let u be the density of true sources in a given region of the sky. The probability of detecting a true source on N out of M HCONs in a given area of the sky is $uA\ P(N,M)$ where $P(N,M)$ is given by Eq. (VIII.D.2); it is necessary that $uA \ll 1$. Hence the total probability $T(N,M)$ of finding a source, either false or true, on N out of M HCONs in a given area of the sky is given by

$$T(N,M) \sim Q(N,M) + uA\ P(N,M) \qquad \text{(VIII.D.6)}$$

where cross terms have been neglected. The reliability $R(N,M)$ of an N/M source is unity minus the probability that the source is false. The probability that a given source is false is the probability of finding a false source divided by the total probability of finding any source. Therefore,

$$R(N,M) \sim 1 - \frac{Q(N,M)}{[Q(N,M) + uA\ P(N,M)]} \qquad \text{(VIII.D.7)}$$

D.3 Estimation of Parameters

The only data available for estimating the parameters are the observed densities $n(N,M)$ of sources on the sky, observed N out of M possible times. There is no *a priori* information as to whether these sources are real or false. Let $E\langle x\rangle$ denote the expectation value of x. Then

$$E\langle\ n(N,M)\rangle = [Q(N,M) + uA\ P(N,M)] \times A^{-1} \tag{VIII.D.8}$$

where $Q(N,M)$ and $P(N,M)$ are given respectively by Eqs. (VIII.D.1) and (VIII.D.5) and contain the parameters p and q. It is clear that estimates $\hat{u}$, $\hat{p}$ and $\hat{q}$ of u, p and q can be obtained by replacing the expectation value of $n(N,M)$ in Eq. (VIII.D.8) by the observed values, bearing in mind that the value of $n(0,M)$ is unobservable. The following equations, from which $\hat{u}$, $\hat{p}$ and $\hat{q}$ can be estimated, are derived using Eqs. (VIII.1,5 and 8)

$$n(1,M) = M[\hat{q}(1 - \hat{q}A)^{M-1} + \hat{u}(1 - \hat{p})\hat{p}^{M-1}] \tag{VIII.D.9}$$

$$\sum_{N=1}^{M} n(N,M) = A^{-1}[1 - (1 - \hat{q}A)^{M}] + \hat{u}(1 - \hat{p}^{M}) \tag{VIII.D.10}$$

$$\sum_{N=1}^{M} n(N,M)N = M[\hat{q} + \hat{u}(1 - \hat{p})] \tag{VIII.D.11}$$

Since (qA) << 1 in the case of this survey, Eq. (VIII.D.9) and (VIII.D.10) can be approximated by:

$$n(1,M) \simeq M[\hat{q} + \hat{u}(1 - \hat{p})\hat{p}^{M-1}] \tag{VIII.D.12}$$

$$\sum_{N=1}^{M} n(N,M) \simeq M\hat{q} + \hat{u}(1 - \hat{p}^{M}) \tag{VIII.D.13}$$

The equations can be greatly simplified for sources of high signal-to-noise ratio when $p << 1$ if it is assumed that the true source density is not greatly in excess of the false density. Equation (VIII.D.12) becomes

$$\hat{q} \simeq \frac{n(1,M)}{M} \tag{VIII.D.14}$$

Equations (VIII.D.13) and (VIII.D.14) give

$$\hat{u} \simeq \sum_{N=2}^{M} n(N,M) \tag{VIII.D.15}$$

while Eqs. (VIII.D.11), (VIII.D.14) and (VIII.D.15) give

$$\hat{p} = 1 - \frac{\sum_{N=2}^{M} n(N,M)N}{\sum_{N=2}^{M} n(N,M)M}$$

$$= \frac{\sum_{N=2}^{M} n(N,M)(M-N)}{\sum_{N=2}^{M} n(N,M)M} \tag{VIII.D.16}$$

Each of these equations, which are valid *only* for bright sources, has a simple interpretation. Equation (VIII.D.14) says that the probability of generating false sources is given by the density of single HCONs divided by the number of chances of seeing them. The contribution of true sources which have lost all but one HCON is neglected. Equation (VIII.D.15) says that all sources with two or more HCONs are real. Finally, Eq. (VIII.D.16) says that the probability of missing an HCON is the sum of all the missed HCONs divided by the total possible number of HCONs; again the contribution of true sources which have lost $M-1$ HCONs is neglected.

The parameters u, p and q were estimated using Eqs. (VIII.D.11, 12 and 13). Only preliminary results are presented here because these parameters were directly affected by the last processing steps (clean-up, flux analysis, and high source density processing) used to generate the catalog.

D.4 Completeness and Reliability Outside of the Galactic Plane

D.4.a Estimates from Minisurvey Data

A preliminary analysis of the 12 μm completeness and reliability is given here for a 70 sq. deg area of the minisurvey covered by seven HCONs. It was bounded by ecliptic longitudes 60.5° and 64.0° and by ecliptic latitudes -40° and +10° and was thus out of the region of extremely high source densities near the Galactic plane. Table VIII.D.1 gives the number of sources in the seven HCON area, broken down by flux density range and number of observed HCONs, as well as the derived estimates of p, q, and u. The weeks-confirmation area, A, was taken to be $30'' \times 90''$.

The reliability of a two HCON source found in regions of the sky observed with two or three HCONs can be deduced from the values in the table and always exceeds 0.99997 in every range of flux density. The reliability of two HCON sources in regions with many more than two coverages, such as the minisurvey, is, however, considerably less than this value. A source seen only twice in a seven HCON area may have a reliability as low as 0.5. Sources with three or more HCONs are, however, almost completely reliable at any depth of HCON coverage, given the values of $\hat{p}$ and $\hat{q}$ deduced above.

Table VIII.D.1 Completeness and Reliability Data in 7 HCON Area

Range in 12 μm Flux Density (Jy)	Numbers of HCONs in 70 sq. deg 7 HCON Area							Parameters		
	N=1	2	3	4	5	6	7	$\hat{p}$[1]	$\hat{q}$[2]	$\hat{u}$[3]
0.25-0.32	26	5	1	0	0	0	0	0.911	0.018	0.699
0.32-0.40	31	4	4	1	4	0	0	0.555	0.060	0.208
0.40-0.50	22	0	3	2	2	5	7	0.201	0.045	0.270
0.50-0.63	9	0	0	1	2	5	13	0.082	0.018	0.300
0.63-0.79	6	0	0	0	0	3	8	0.039	0.012	0.157
0.79-1.58	10	0	0	0	0	2	18	0.014	0.020	0.286
>1.58	0	0	0	0	0	0	25	0.000	0.200	0.364

[1] $\hat{p}$ is the probability of failing to detect a genuine source in a single HCON.

[2] $\hat{q}$ is the probability, per sq. deg, that a false source is created on a single HCON coverage of the sky.

[3] $\hat{u}$ is the probability, per sq. deg, of there being a true source in a given region of the sky.

The completeness is plotted as a function of flux density in Fig. VIII.D.1a for a two HCON survey and in Fig. VIII.D.1b for a three HCON survey. Note that these figures give the differential completeness, not the cumulative completeness above a given flux density. The completeness is essentially unity above 1.5 Jy for a two HCON survey and above 0.6 Jy for a three HCON survey. It begins to fall sharply at 0.5 Jy for a two HCON survey and at 0.4 Jy for a three HCON survey. Some of the physical reasons for missing HCONs are discussed in section VII.E.3.

The completeness and reliability values quoted here for 12 μm also apply to 25 and 60 μm sources with the sharp fall-off in the completeness occurring at 0.5 and 0.6 Jy at 25 and 60 μm for a three HCON survey. The reliability is decidedly worse for sources seen only at 25 μm. The 100 μm values cannot be obtained from the minisurvey due to extensive cirrus contamination.

D.4.b Verification of the Completeness from Source Counts

The completeness of the catalog can be verified by the differential source-counts shown in Fig. VIII.C.1 for the four wavelength bands for $|b| > 50°$. The counts fall away sharply at 0.4, 0.5, 0.6, 1.0 Jy at 12, 25, 60, 100 μm. The completeness at 100 μm is severely degraded by cirrus below these Galactic latitudes.

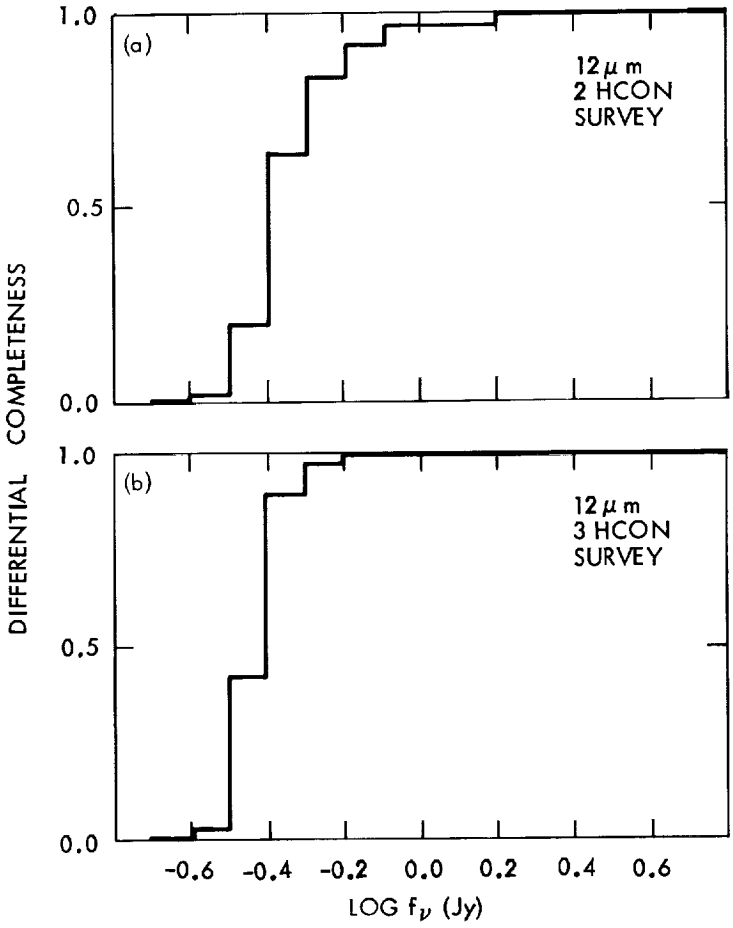

Figure VII.D.1 a) Completeness at 12 μm calculated for a two HCON survey (top); and b) for a three HCON survey (bottom). See XII.A.4 for a revised estimate of the completeness.

D.4.c Reliability of Point Sources with Flux densities of Moderate Quality

A moderate quality flux density is based on at least four detections (Section V.H.5), but the moderate status means that the source also failed to be detected on at least one occasion when it should have been seen. If there were no alibis from dead detectors, the source may have only been detected on four occasions out of a possible eight. If the source had a good quality flux density in another band, the reality of the source is established in that band. In this case there is a reasonable certainty that the source detection in the moderate quality band is real, but the quoted uncertainty in the quoted flux density is larger than that for good quality fluxes, typically by a factor of 1.41. Moderate quality flux densities should be used with caution. Sources with moderate quality flux densities in two adjacent bands are reliable.

D.5 Completeness and Reliability in the Galactic Plane

The completeness and reliability in regions of high source density, defined in Section V.H.6, can be estimated by methods similar to those discussed earlier in this section, but such estimates should be regarded with great caution. As an example, about 200 12 μm sources in a 4.5 sq. deg area from the minisurvey near the Galactic plane were analyzed. The region was covered with seven HCONs and has an average source density of 39 per sq. deg. Table VIII.D.2 gives counts of cataloged 12 μm sources as a function of flux density and the number of HCONs in this area.

If the parameters $\hat{p}$, $\hat{q}$ and $\hat{u}$ are evaluated for the high density regions using Eqs. (VIII.D.14-.D.16), i.e., assuming that all single HCON sources are false and all two or more HCON objects are real, then $\hat{p} < 0.2$ and $\hat{q} < 1.5$ (sq. deg)$^{-1}$ HCON^{-1} for $f_\nu \geq 1$ Jy. These values imply that for flux densities above 1 Jy the completeness of the survey in the two HCON high density sky exceeds 63% and in the three HCON high density sky exceeds 88%.

The reliability of a two or more HCON source can be estimated from the value of $\hat{q}$ and Eq. (VIII.D.7). For M equal to 2 or 3 and A equal to 25 beam areas, 0.02 sq. deg, the estimated reliability of a two HCON object brighter than 1 Jy at 12 μm exceeds 99.5%. The numbers in Table VIII.D.2 show that applying the formalism of Eqs. (VIII.D.14 - .D.16) to the high density region is not entirely valid. The fact that there is a minimum in the number of sources with a specified number of HCONs at a value of three HCONs suggests that sources with fewer than three HCONs are spurious. It should be noted, however, that including these false two and three HCON sources in the determination of q decreases the estimate of the net reliability of a source only slightly.

The existence of minisurvey sources (Table VIII.D.2) observed six or seven times in regions of high source density indicates that the completeness of bright sources is significant even in these regions. If the minisurvey region is representative of the entire Galactic plane region, then the completeness for sources with flux densities above 10 Jy will be about 86% for the part of the sky covered with two HCONs and about 98% for the sky covered with three HCONs. These results apply to sources observed at 12 and probably 25 μm where extended sources are few. At 60 and 100 μm the meaning of the reliability of a source is less clear because of the large population of extended objects seen against a very complex background. No attempt has been made to assess either the completeness or reliability of sources at these wavelengths.

Table VIII.D.2 Number of HCONs in a 7 HCON High Source Density Region

Range in 12 μm Flux Density (Jy)	Numbers of HCONs in High Source Density 7 HCON Area*						
	N=1	2	3	4	5	6	7
1-2	49	9	1	6	13	17	30
2-4	22	2	1	3	5	17	26
4-8	6	1	1	0	1	10	14
8-16	0	0	0	0	1	3	6
16-32	0	0	0	0	0	0	2
32-64	0	0	0	0	0	4	0
64-128	0	0	0	0	0	1	3

* the area consisted of two 1.5° × 1.5° regions with the following Galactic coordinates:

$334.5° < l < 336.0°$; $-2.0° < b < -0.5°$

$336.0° < l < 337.5°$; $-0.5° < b < +1.0°$

D.6 Galactic Plane Shadow

The strong lagging of the noise estimator at 100 and 60 μm after passage through the Galactic plane prevented the acceptance of a large number of sources because their *calculated* signal-to-noise ratio fell below the threshold. The effect is demonstrated in Fig. VIII.D.2 which shows counts of point sources in bins of 1° in latitude and 20° in longitude. The counts of sources seen only at 100 μm shows a decrease of about a factor of 10 just after the telescope scanned past the Galactic equator in the first two HCON coverages. This dearth of sources is called the Galactic plane shadow and takes roughly the form of two rectangular strips. The first extends from Galactic longitude $l = 10°$ to 30°, and from Galactic latitude $b = 0°$ to 5°, and the second extends from $l = 330°$ to 350°, and $b = 0°$ to -5°.

During the third HCON survey the telescope passed the Galactic equator in the opposite direction. Although many 60 and 100 μm sources were found in the shadow area, they were seen only on one HCON and were thus excluded from the catalog.

The noise shadow is far less important at the shorter wavelengths. The counts of the 12 μm sources shown in the figure are highly symmetric around $b = 0°$, but show a small 10% dip in the central two bins. The cause of this dip is probably the high source density clean up (see Section V.H.6) and not the noise lag.

E. Completeness and Reliability of the Catalog of Small Extended Sources

The completeness and reliability of this catalog will be discussed in the hard-bound version of the Supplement when it and the catalog of small extended sources are published in mid-1985.

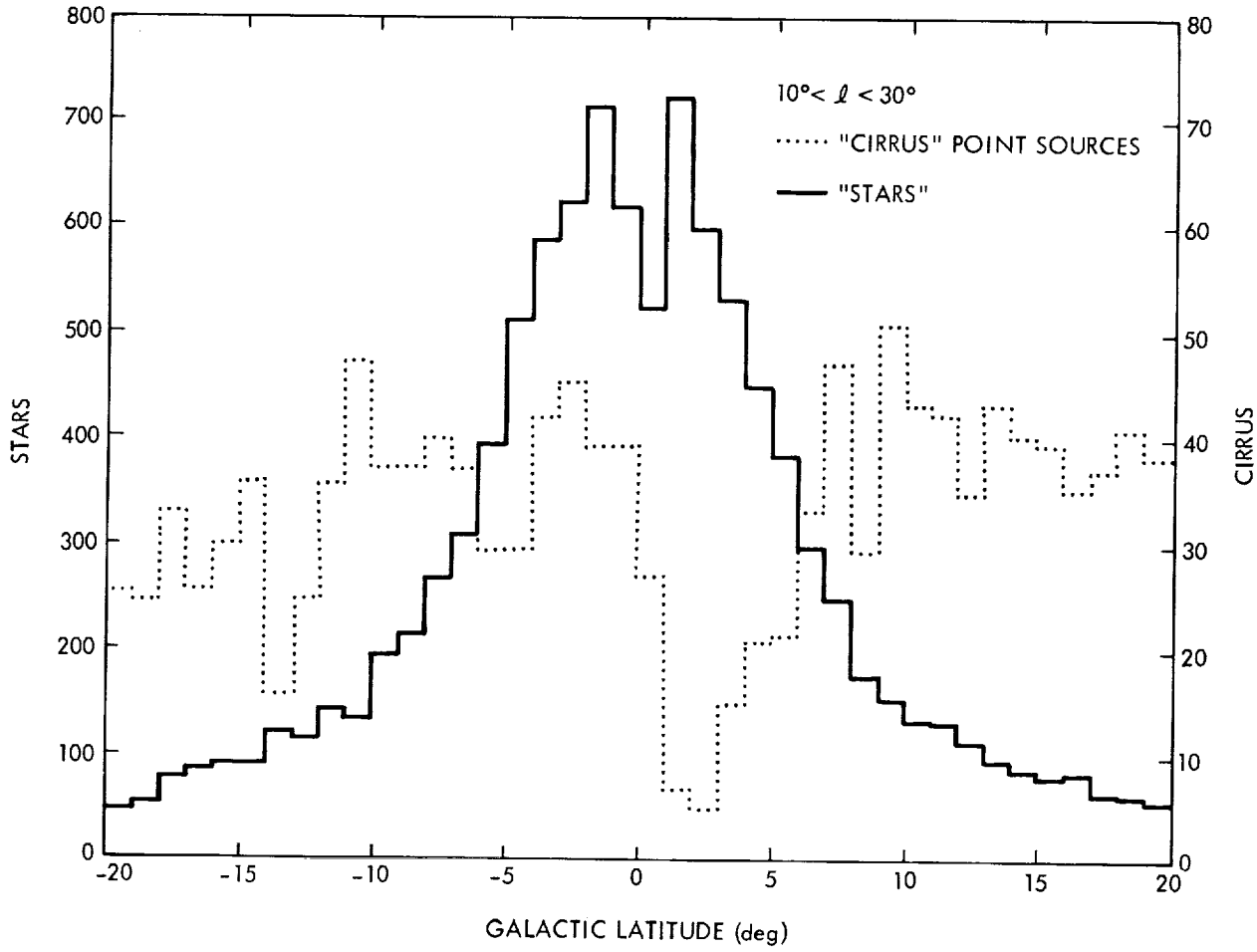

Figure VIII.D.2 The wavelength dependent effects of the Galactic plane shadow discussed in the text are shown. The solid lines are counts of 12 μm sources as a function of Galactic latitude; the dotted lines are counts of 100 μm sources.

Authors:

M. Rowan-Robinson, P. Clegg, C. Beichman, T. Chester, T. Conrow, H. Habing, G. Helou, G. Neugebauer, T. Soifer and D. Walker

References:

Low, F. J. *et al.*, 1984, *Ap.J.*, **278**, L19.

Rowan-Robinson, M. *et al.*, 1984, *Ap.J.*, **278**, L7.

IX. THE LOW-RESOLUTION SPECTRA

A. Instrumentation

A.1 Introduction

The IRAS survey instrumentation included a low-resolution spectrometer which covered the wavelengths between 8 and 22 μm. The spectrometer operated during the entire survey, providing spectra of the brighter point sources. This section briefly describes the instrument, dealing primarily with those aspects of its optics and its signal-handling electronics that have a direct bearing on the interpretation of the spectra. The spectra are presented in two forms -- a tape version, henceforth called "The Catalog of Low Resolution IRAS Spectra", or simply "The Catalog", and a hard-copy version, designated as "The Atlas of Low Resolution IRAS Spectra", containing graphical representations of the spectra.

Because the survey function required a passive instrument, a slitless design was selected. This design is equivalent to an objective prism spectrograph, oriented in such a way that the dispersion was aligned with the scan direction. Obvious penalties of this design are a degraded resolution for extended objects, sensitivity to spatial confusion, and short integration times.

The detectors were sampled continually during the mission, and the data were received on the ground together with the other survey data. The spectra were extracted during data processing on the basis of point source detections from the survey array.

A.2 Optical Properties

The spectrometer had a rectangular aperture mask in the focal plane that measured $6'$ in the dispersion direction and $15'$ across. Although the cross-scan width of the focal plane aperture was only half that of the survey array width, the overlap between adjacent scans in the survey strategy ensured full sky coverage.

Two overlapping wavelength ranges were scanned simultaneously, one extending from 7.7 to 13.4 μm and the other from 11.0 to 22.6 μm. The scan length was nominally $6'$ but an internal misalignment obscured the extreme low end of the short wavelength range. The resolution was primarily determined by the exit slit width of $15''$, although diffraction at the telescope aperture and electronic filtering caused significant smoothing. Figure IX.A.1 shows, respectively, the aperture location of a source, the effective monochromatic image size, and the resulting spectral resolution as functions of wavelength.

Several detectors were used in each of the two wavelength ranges to reduce confusion problems. Three short wavelength detectors each covered $5'$ of the aperture width. At the longer wavelengths two detectors each covered $7.5'$.

The optical layout of the spectrometer is shown in Fig. IX.A.2. A back-reflecting KBr prism with curved surfaces served the three functions of collimation, dispersion and refocusing in the long wavelength spectrometer. A field mirror imaged the telescope pupil onto the prism. The short wavelengths also passed through this system, but were given additional dispersion in a second spectrometer section with a curved NaCl prism, using a field mirror adjacent to the first exit slit. Field optics immediately behind the exit slits refocused the telescope pupil on each of the detectors.

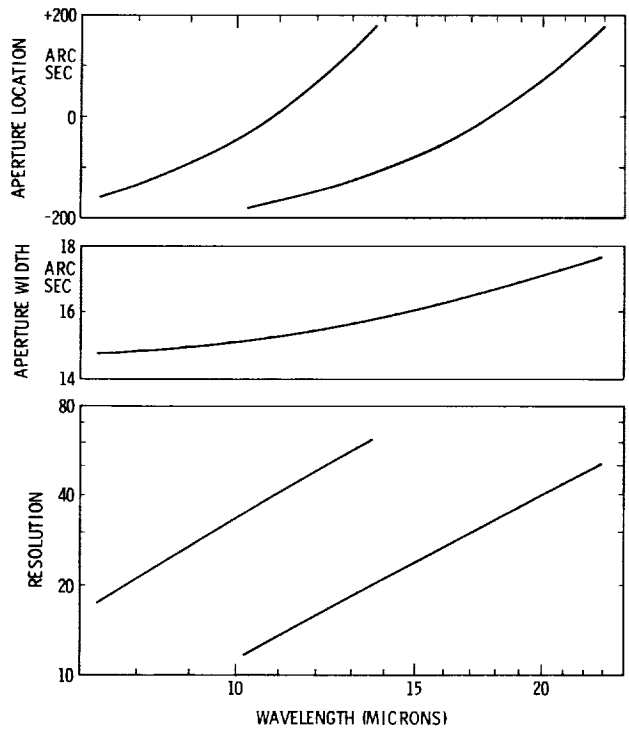

Figure IX.A.1. Relative location and width of the image of the exit slit in the field-of-view of the telescope, and the resulting spectral resolution are given as functions of wavelength. The width and resolution have been calculated taking into account the diffraction by the telescope and the electronic filtering.

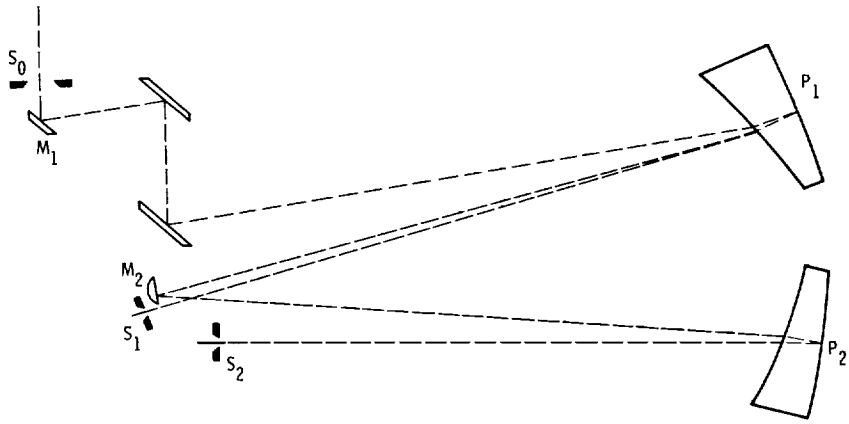

Figure IX.A.2. The optical layout of the spectrometer is shown schematically.S0 is the entrance aperture of the spectrometer in the focal plane of the telescope. The field mirror M1, the curved prism P1 and the exit slit S1 comprise the primary spectrometer. M2, P2 and S2 form a secondary system that provides most of the dispersion at the short wavelengths.

A.3 Electronics

Si:Ga photoconductive detectors for the short wavelengths and Si:As photoconductors for the long wavelengths were used in conjunction with trans-impedance pre-amplifiers. The electronics included spike suppression circuitry. The electronic bandwidth was 12 Hz and the sampling frequency was 32 Hz, corresponding to a sampling interval of 7.2".

An important aspect of the data handling was the encoding of signals with a large dynamic range into an 8-bit format. The output voltages were digitally encoded on a logarithmic scale with increments of 3.5% limiting the signal-to-noise ratio for single samples to less than 100. To avoid loss of precision, the baselines were kept at low positive levels by AC-coupling and "zero-clamping". Occasionally, the zero-clamping affected estimates of the baseline, as discussed in the next section. Fortunately, the occurrence of zero-clamping was rare among the spectra selected for the catalog, since the rejection of confused spectra tended to eliminate those with zero-clamps.

Further detail on the spectrometer electronics is contained in the instrument description by Wildeman, Beintema and Wesselius (1983).

A.4 Effects of the Zero-Clamp

Figure IX.A.3 shows a schematic representation of the circuit used for the AC-coupling and zero clamping. The voltage across the coupling capacitor equaled the difference between output and input signals and thus constituted an error signal. As long as the output signal remained positive, the circuit

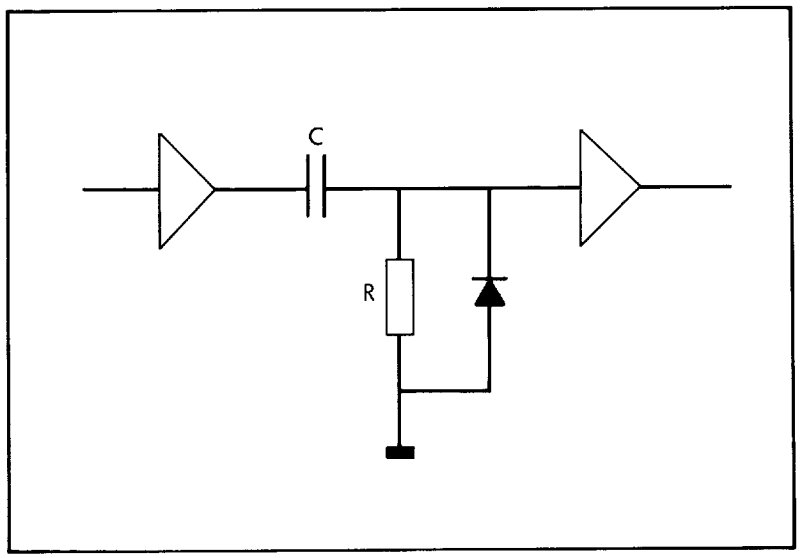

Figure IX.A.3. The AC-coupling and zero clamping circuit. Zero clamping occurred when the input signal was decreasing, resulting in an output signal of zero.

behaved like a high-pass R-C filter with a time constant of 10 seconds (a spectral scan lasts 1.5 seconds). The fact that the error signal changed at a rate proportional to the output signal was easy to correct. However, as soon as the output tried to drop below zero, the capacitor was instantaneously recharged to prevent any further drop; the output signal was clamped to the zero level. The error signal was now the inverse of the input and could rise rapidly, while the output indicated no rate of change. The clamp remained active as long as the input signal continued to decrease. As soon as the input signal rose again, the clamping ended and linear behavior was restored. The output signal again tracked the rate at which the error signal changed.

Normally, zero clamps occurred just after spectral scans or during negative noise excursions on "empty sky." However, a steeply decreasing background could continually clamp the output at zero, except during a spectral scan. In such a case, the presence of a sloping baseline would go unnoticed. Because of the direction in which the spectra were scanned, the result is then an underestimate of the signal at the shorter wavelengths of both spectral ranges. A rising background would only raise the baseline in the output signal with no worse effect than a reduced precision of digitization. Figure IX.A.4 illustrates the effects of background slopes.

A.5 Summary of Instrumental Characteristics

The design of the instrument and the planning of the IRAS mission resulted in the following global characteristics of the spectra:

- spectral coverage from 8 to 22 μm in two overlapping ranges;
- a spectral resolution for unresolved sources varying from 20 to 60;
- a sky coverage identical to the coverage of the IRAS survey;
- typically 2 or 3 observations per spectrum, together providing about 0.15 seconds of integration time per spectral element per source;
- slit widths corresponding to 15″ and instantaneous fields of view of 30′ square (short wavelengths) and 45′ square (long wavelengths);
- quantization steps of 3.5%, resulting in an rms digitization error of 1%;
- potential problems from negative backgrounds gradients.

B. Performance and Calibration

B.1 Detectors

The global properties of the detectors in the spectrometer are listed in Table IX.B.1. The weekly averages of the responses to flashes of the internal reference source (Section II.C) stayed within 1% of the values given, although systematic variations of up to 15% were found on shorter timescales. These were associated with passages through the South Atlantic Anomaly (SAA) and across the Galactic plane. The spectra were corrected for these effects by using a flash response interpolated between the most recent flash and the next one. As described below, other correction factors (especially the cross-scan gain) introduced larger uncertainties in the flux scale of the spectra.

The noise estimates given in Table IX.B.1 are based on baseline readings, and refer to a single spectral resolution element. Estimates for individual spectra deviate from the mean value by typically 20%.

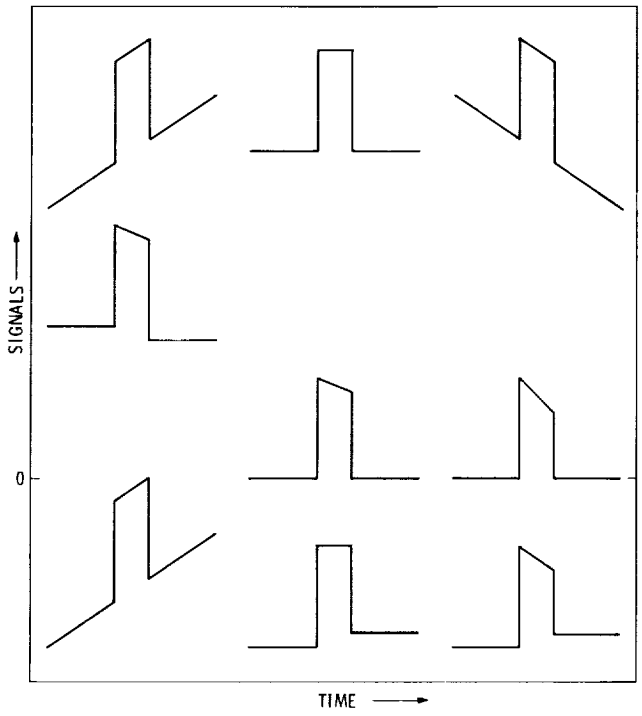

Figure IX.A.4. The effects of AC-coupling and zero clamping on flat spectral scans with sloping backgrounds. From top to bottom: input signals, output signals and reconstructed input signals. Absolute levels are relevant only for the output signals. During reconstruction, the possibility of zero-clamping is ignored. Within a spectral scan, wavelength decreased with time.

Table IX.B.1 Detector Characteristics

Detector Number	Response to Internal Reference (mV)	Noise level (mV)	NEFD (Jy)	Wavelengths (μm)
1	11.9	0.10	1.4	8 - 13
2	4.4	0.04	1.6	8 - 13
3	7.4	0.06	1.3	8 - 13
4	22.8	0.12	3.0	11 - 22
5	46.3	0.20	2.5	11 - 22

B.2 Wavelength Scale

The conversion from in-scan position to wavelength was adjusted and monitored using the lines in the spectrum of the planetary nebula NGC 6543. The wavelength scale is accurate within 0.1 μm.

The zero point of the wavelength scale could be determined by the in-scan position of the source as determined by the survey instrument during the same scan. The uncertainty in this position caused a jitter in the zero point of up to 1 sample (corresponding to 7″ or one-half of a spectral resolution element). This effect degraded the correction for wavelength-dependent gain and the averaging of individual spectra. A better estimate of the zero point was obtained using the four well-defined band edges of the spectrometer. A signal-to-noise ratio of 10 measured at one of the edges gave an accuracy of 0.3 sample (2″).

B.3 Cross-Scan Responsivity

The cross-scan responsivity of the detectors was determined by finely spaced raster scans across the star R UMi (as shown in Fig. IX.B.1.) where the curves are normalized over the central half of the detectors. The sharp dip in response of detector 4 was also found in the laboratory tests. Although the curves are accurate within a few percent, the derived value of the cross-scan correction is much less accurate. Because the cross-scan position determined by the survey instrument during a scan had a typical uncertainty of 1′. Except for sources passing over the very center of a detector this introduced an uncertainty in the cross-scan correction factor of 10-20%.

B.4 Wavelength-Dependent Responsivity

In order to determine the factor for conversion of sample values into flux densities, the observed spectra of α Tau were compared with a black body spectrum of 10,000 K. The resultant responsivity curves (Fig. IX.B.2) show the ratios of flux density to sample value as a function of wavelength. The curves have been normalized in the overlap region from 11 to 13 μm and are accurate to 2% at the shortest and to 4% at the longest wavelengths. No significant differences were found between detectors 1, 2 and 3, or between detectors 4 and 5. All detectors had somewhat better responsivity in the center of their wavelength range than at the edges. Except near the very edges of the band, the responsivity correction did not exceed 30%. The feature seen between 9 and 11 μm in the short-wavelength band is a characteristic of the instrument that is found in all raw spectra and was already known from laboratory tests.

B.5 Radiation Effects

Spikes caused by energetic particle radiation hits were removed by the electronic deglitcher without significantly increasing the noise. Only near the maximum of the SAA, where no regular observations were taken, were residual glitches and increased noise found. The polar horns appear to have had no effect on the detectors. Outside the SAA, baseline drifts on a time scale of 1.5 sec, roughly the dwell time of a point source on a detector had an amplitude of less than twice the noise level. Inside the SAA, the drifts increased by about a factor of ten.

B.6 Multiplexer Glitches

Occasionally, the data streams of the detectors were scrambled by the multiplexer. In most cases this was evident in the spectra as single-sample spikes. The larger ones were easily recognized and

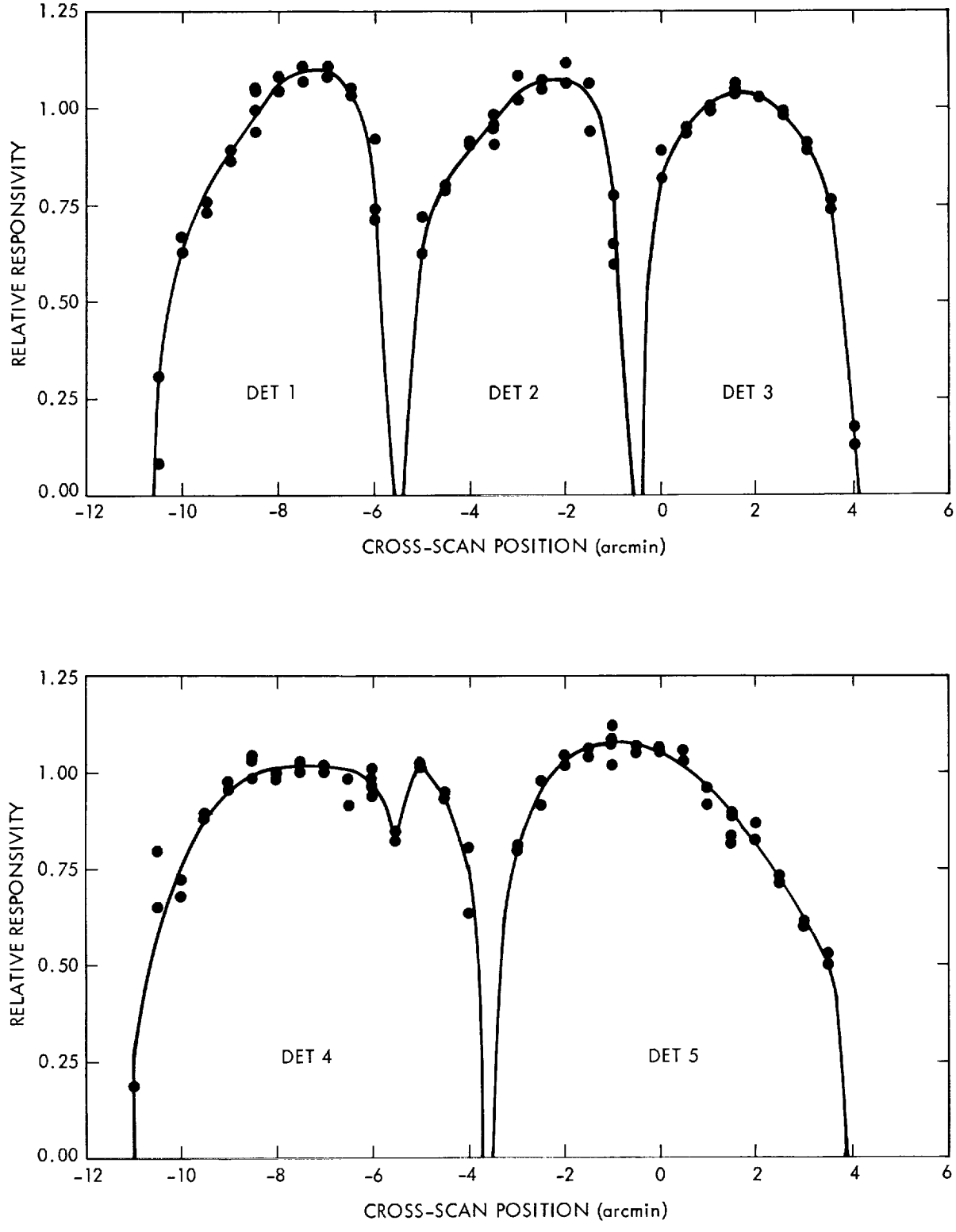

Figure IX.B.1. Cross-scan responsivity for each of the five spectrometer detectors. Detectors 1, 2 and 3 cover the 8-13 μm wavelength range, and detectors 4 and 5 cover the 11-22 μm wavelength range. Open circles indicate the R UMi results; the curves were used for the correction (Section IX.C.2.e).

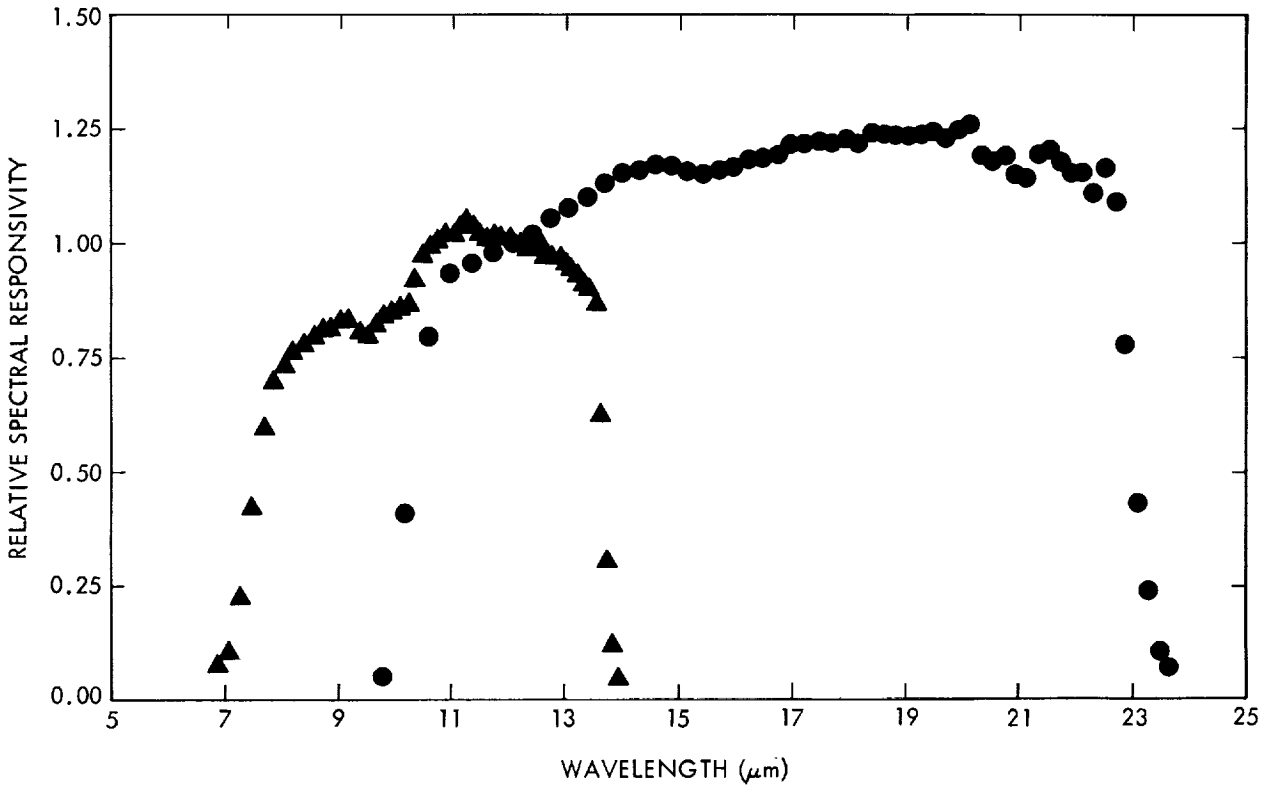

Figure IX.B.2. Wavelength dependent responsivity for the 8-13 and the 11-22 μm detectors, respectively, plotted on the standard samples (Section IX.C.2.c). The responsivities are normalized in the 11-13 μm region.

removed (see Section IX.C). In some cases a series of samples was scrambled and the spectrum could not be repaired without running the risk of erasing real features.

B.7 Confusion

Since the slitless spectrometer had a field-of-view of 5′ by 6′ (short wavelengths) or 7.5′ by 6′ (long wavelengths), regions that were confused in the short wavelength survey bands were also confused for the spectrometer. A spectrum could be confused by a nearby point source, or by extended structure associated with the source itself or in the background. In most cases such confusion was recognizable as a difference in the baseline level between the two sides of each spectrum-half. However, as discussed below, if the test of baseline asymmetry was made too restrictive, otherwise good spectra were lost.

B.8 Photon Induced Responsivity Enhancement

No evidence was found for photon induced responsivity enhancement (Section IV.A.8 and VI.B.4c), although it would have been hard to discover. In the first place, most spectrometer sources were stars or star-like sources with flux densities gradually decreasing towards longer wavelengths. Since the spectra were scanned starting at the long wavelengths, and thus at the lowest flux density, the deformation of the spectra was minimized. Secondly, close to the Galactic plane, where the effects were greatest, there were very few clean, isolated point sources. Confusion probably masked any effects of photon induced enhancement present.

B.9 Memory Effects

Changes in the detector responsivity on a time scale of minutes due to exposure to a bright source or to a prolonged exposure to a medium bright source like the Galactic plane were found to occur. The latter effect was compensated for to within 5% by using interpolated internal reference flash responses to correct the flux densities.

Memory effects did not cause differences in response of the system between spectral lines and continuous spectra. The planetary nebula NGC 6543 was scanned at the nominal survey rate and at 1/2, 1/4, and 1/8 of that speed. The line intensities did not change noticeably as a function of the different scan speeds.

B.10 Linearity Checks

It is expected that any non-linearity effects were small, although no comprehensive linearity tests were made. This statement is based on the agreement between two different determinations of the wavelength dependent responsivity curves. One set of curves was determined using α Tau, a star with a spectrum that rises steeply towards shorter wavelengths. The second set of curves was determined using asteroids -- cool objects which are brightest at the longer wavelengths. The differences between the two sets were small, and the comparison was limited by the accuracy with which the asteroid curves could be determined.

B.11 Overall Flux-Density Scale

After processing a large sample of spectra with the correction techniques described in Section IX.C, the integrated fluxes in the spectra (after convolution with the survey pass-band) were compared with the fluxes measured by the survey array at 12 μm. Comparison with the 25 μm survey fluxes was not attempted because the spectrometer hardly overlaps the survey 25 μm pass-band. Systematic factors of 0.75 and 1.00, respectively, were applied to the data to make the 8-13 and 11-22 μm spectrometer fluxes agree with the survey fluxes. On the average the spectrometer flux densities in the catalog are consistent with the survey flux densities to within 10-15%.

C. Data Processing

C.1 The Database

The spectrometer data consist of three types of data: (i) uncorrected spectra with header information, (ii) calibration tables, and (iii) administrative files. The spectra were extracted out of the data stream whenever an hours-confirmed source with a signal-to-noise ratio greater than 25 or a source specified as "known source" (Section V.D.4), crossed the spectrometer aperture. Extractions were also made for designated calibration sources. The spectra were linked to survey sources using index-association records produced by the hours- and weeks-confirmation processors (Section V.D.7).

There were three types of calibration tables: (a) the responses of the five detectors to the internal reference source flashes and the intensities of the flashes as derived by the survey calibration processor; (b) correction tables for the relative responsivity as a function of position across the five detectors; (c) correction tables for the relative responsivity as a function of wavelength. The cross-scan and wavelength dependent responsivity tables were derived from special observations (see Section IX.B).

C.2 Processing the Individual Spectra

Processing of the data always started with the raw data. This allowed the correction procedures to be improved continuously up to the time of production of the catalog. The major processing steps are discussed below.

C.2.a Despiking

Single sample spikes with an amplitude greater than 8% caused by multiplexer errors (Section IX.B) were removed and replaced by an interpolated value using a simple algorithm operating on the raw data. Multiple-sample spikes were not removed, but their presence was noted so that the spectrum-half would be rejected later (see Section IX.C.3).

C.2.b Conversion to a Linear Scale

A lookup table of 256 entries was used to convert the raw data to voltages on a linear scale.A standard reconstruction of the input-voltage to the high-pass filter from the measured output voltage was carried out. An offset correction was reset to zero whenever the sample voltage dropped below a specified threshold because of the effects of the zero clamping (Section IX.A.4).

C.2.c Interpolation to a Standard Wavelength Grid

For ease of processing, an interpolation was carried out to a standard regular grid of angular positions in the dispersion direction. Because the dispersion of the spectrograph changed rapidly as a function of the angular position (Fig. IX.A.1), the wavelength values corresponding to the standard sample values were not equidistant. Before the interpolation, allowance was made for variations in the scan speed of the telescope. For the spectra of the brighter sources (signal-to-noise ratio greater than 10) the well-defined in-scan detector edges were used to center the spectrum. The centering correction reduced the in-scan errors to approximately 2″, corresponding to approximately 0.03 μm in wavelength.

C.2.d Correction for Wavelength-Dependent Responsivity

The interpolated samples were multiplied by a responsivity table sampled at the same standard grid. There was a table for each of the five detectors derived from observations of α Tau (Fig. IX.B.2). Although the software allowed selecting a different table for each of 16 regularly spaced cross-scan positions on the detector, the evidence for a cross-scan variation of the wavelength-dependent gain was too weak to justify using this option.

C.2.e Correction for Cross-Scan-Dependent Responsivity

Depending on the nominal cross-scan position of the source, a correction (Fig. IX.B.1) was applied for the decrease of responsivity towards the edges of the detectors. This correction was the weakest link in the calibration process because of the relatively large uncertainty in the cross-scan position. The correction applied is uncertain by up to 20%, although this uncertainty was decreased by the process of joining the two spectrum-halves together (see Section IX.C.2.g).

C.2.f Overall Responsivity

The overall responsivity depended on the individual detector, on the time and/or on the sky position. To account for these variations a correction was derived from the voltage responses to the two internal reference source flashes bracketing the time of observation. After applying the responsivity

correction to a large sample of spectra, the integrated fluxes in the spectra were compared to the fluxes measured by the survey array. Systematic factors of 0.75 and 1.00 were applied to the integrated spectrometer fluxes to bring them in line with the survey observations.

C.2.g Joining of the Two Spectrum Halves

The two spectrum-halves (8-13 μm and 11-22 μm) were treated independently until this point. Because of uncertainties in the cross-scan position of the scan path over the detectors and therefore in the nominal cross-scan responsivity correction, the two spectrum-halves often differed by up to 15 or 20% after subtraction of a linear baseline. The overlapping portion of the spectrum-halves was used to determine another correction factor. In doing so, the nominal relative cross-scan positions were used to determine which half of the spectrum to change by the largest amount. If either half had been observed by the central part of a detector, it was considered reliably calibrated, and that portion was not changed by the joining process, and the half of the spectrum observed near the edge of a detector was shifted up or down towards the other half. If both halves were considered equally reliable, then each was scaled by the square root of the ratio between the overlapping sections. This joining process reduced the overall error in the responsivity correction to less than 10%.

C.3 Averaging Spectra, Quality Checks

Before spectra were averaged, a number of quality checks were performed on the individual measurements of the two halves of a source's spectrum. First, all measurements made within 18" of the edge of any detector were flagged. Measurements were rejected:

(a) if they contained multiple-sample spikes (Section IX.C.2);

(b) if the join-factor obtained before (Section IX.C.2) was outside the range 0.30 to 3.3;

(c) if the measurement was confused by neighboring sources; this was considered to occur when the measurement met one of two criteria: (i) the central portion was below the baseline determined from signal-free parts of the spectrum-half; (ii) the baseline at the low wavelength end of the spectrum-half differed from that at the high wavelength end by more than 20% of the signal in the 8-13 μm band or by 10% in the 11-22 μm band. The lower limit of these thresholds was 2.5 times the sample noise.

(d) if the measurement did not correlate with the "reference measurement", defined as the measurement with the smallest number of check-flags. This choice gave preference to measurements passing over the central part of the detector.Any 8-13 μm measurement for which the correlation coefficient with the reference was below 60% or any 11-22 μm measurement for which it was below 50% was rejected. For line spectra without a continuum in the 8-13 μm region the first criterion was waived.

At least 80% of the spectra in the catalog had correlation coefficients above 70 and 60% in the short and long wavelength halves, respectively. Some 40% correlated internally with coefficients better than 80% in both spectrum-halves (see Section IX.C.4).

The spectrum-halves passing through all of the above tests were averaged using the inverse of the square of the noise as a weighting factor. At least two measurements in each of the two spectrum-halves

(8-13 and 11-22 μm) had to be accepted before the spectrum could be averaged and included in the spectral catalog.

After averaging, the two spectrum-halves were rejoined, giving both halves equal weight (see Section IX.C.1). Generally the join factors differed from 1.00 by only a few percent.

The averaged spectrum was convolved with the 12 μm survey passband. The integrated flux thus obtained, was compared to the average 12 μm survey flux of the source. The ratio between the two fluxes is given in the low resolution spectrometer catalog record and has a 1 σ dispersion around unity of about 15%. Exceptions to this rule will be spectra with sharp lines (classes 8 and 9; see Section IX.D.2) or small 12 μm fluxes.

C.4 Final Selection of Spectra

Three selection criteria were applied for inclusion in the Catalog of Low Resolution Spectra.

(i) The source is contained in the IRAS point source catalog.

(ii) The entire spectrum must have been observed at least twice and the individual measurements should be mutually consistent. Individual spectra must pass all the checks mentioned in Section IX.C.3 and must have a minimum correlation coefficient of 50% between any two measurements of the source. The large majority of spectra had, however, much higher correlation coefficients (see below).

(iii) The source must pass a subjective visual inspection. About 2.5% of all sources were rejected by this process, mostly because they showed non-point source characteristics or confusion with other sources.

Four samples of sources were selected for inclusion in the catalog.

a. Sources whose 12 μm survey flux density was larger than 25 Jy or whose 25 μm survey flux density was larger than 50 Jy. Individual spectrum-halves were required to correlate with each other with a correlation coefficient of 80% in either spectrum-half.This sample contains about 2150 sources.

b. Sources with 12 μm flux densities larger than 1 Jy or 25 μm flux densities larger than 2 Jy but not contained in Sample a. The vast majority of these sources proved to be brighter than approximately 5 Jy at 12 μm or 10 Jy at 25 μm. The correlation coefficients were required to exceed 70% in the 8-13 μm band and 60% in the 11-22 μm band. This sample contains about 2450 sources.

c. Sources in the same flux density range as sample b but with lower correlation coefficients: between 60 and 70% in the 11-22 μm spectrum-half or between 50 and 60% in the 11-22 μm half, respectively. There are roughly 850 sources in this sample.

d. Sources with minimum survey flux densities of 1 Jy at 12 μm or 2 Jy at 25 μm. Of these sources only the 11-22 μm spectrum-half was required to have been measured consistently with a minimum correlation coefficient of 50% between individual measurements. Out of this sample only sources with specified spectral lines and not contained in sample a, b, c were selected for the catalog. The selection was carried out by the classification program: only classes 8 and 9 (see Section IX.D.2 and Table IX.D.1) were kept. There are approximately 40 spectra with lines in this sample.

Samples a, b, and c contain continuum sources and approximately 75% of the line sources of the catalog; sample d contains the remainder of the line sources.

D. Classification

D.1 Introduction

Visual inspection of spectra shows that they fall naturally into a number of classes. A characterization program was used to return a two-digit code for each spectrum. The first digit characterizes the overall shape of the spectrum (main class) and the second digit gives quantitative information on the dominant feature in the spectrum (subclass).

This classification code appears to be an adequate description of the spectra of more than 95% of the sources in the catalog. Although the classification is based on spectrometer data only, and therefore independent of other astrophysical classification schemes, most classes are dominated by a well-known, well-defined type of sources.

D.2 Classification Scheme

D.2.a Overview

There are five general types of spectra distributed in nine main classes. The five types are: *Blue* continuous energy distributions, *Red* continuous energy distributions, spectra with spectral lines including the 11.3 μm line, spectra with lines but not the 11.3 μm line and "others" which fit into none of the preceding classes.

As a first step *blue* and *red* spectra were separated using the long-wavelength part of the spectrum. For *red* sources the flux density per octave (λf_λ) rises from 14 to 22 μm, and for *blue* spectra it decreases.

The second step was the determination of the relative excesses or deficiencies in narrow bands (0.5 μm wide) centered on the two broad features often seen in the spectra: the 10 μm silicate band and the 11 μm SiC band. The local "continuum" level was estimated by a logarithmic interpolation between narrow bands just outside the features. Also determined were the excess fluxes in 7 narrow bands (0.5 to 1 μm wide) centered on the emission lines at 9.0 μm [Ar III], 10.5 μm [S IV], 11.3 μm (unidentified), 12.8 μm [Ne II], 14.5 μm [Ne V], 15.5 μm [Ne III], and 18.8 μm [S III]. Those were the only lines that were seen in the spectra with the possible exception of the [Ne VI] line at 7.5 μm, just on the edge of the pass-band. The local continuum was estimated by a linear interpolation between two similar bands on both sides of the line.

Table IX.D.1 summarizes the classification scheme described below and lists the number of sources of each type. Figures IX.D.2.1-3 give examples of some of the different kinds of spectra.

D.2.b Sources with *Blue* Energy Distributions: Classes 1*n*,2*n*,3*n*,4*n*

Sources with *blue* energy distributions without the 11.3 μm or other narrow spectral lines were classified according to the relative strengths of the 10 and 11 μm emission or absorption features. Spectra with no emission or absorption features at all were assigned to class 1*n*, where the subclass *n* is equal to *twice* the absolute value of the spectral index between 8.0 and 13.0 μm. The spectral index, β, is defined according to

$$f_\lambda \propto \lambda^\beta \qquad \text{(IX.D.1)}$$

Normal K stars have no emission or absorption and show a Rayleigh-Jeans tail at these wavelengths with β=-4. Such stars are thus assigned code 18.

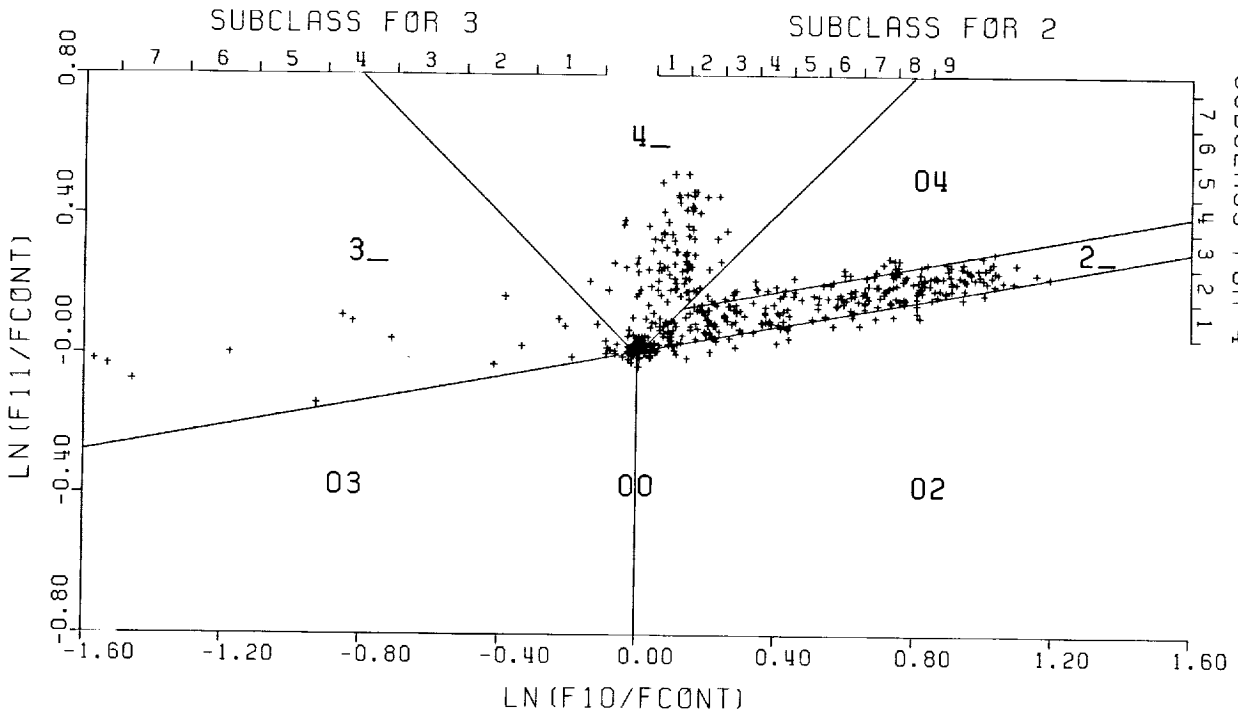

Figure IX.D.1. The classification scheme for *blue* spectra. (See text.)

Sources with *blue* energy distributions showing 10 μm silicate band *emission* were assigned to class $2n$, sources with silicate *absorption* to class $3n$. For class $2n$ the subclass n was defined according to the strength of the emission band with respect to the adjacent continuum following the equation:

$$n = 10 \times [\ln f_\lambda(9.8\mu m) - (0.589 \ln f_\lambda(7.9\mu m) + 0.411 \ln f_\lambda(13.3\mu m)] \quad \text{(IX.D.2)}$$

For class $3n$, the subclass n was derived on the basis of the strength of the absorption band:

$$n = -5 \times [\ln f_\lambda(9.8\mu m) - (0.589 \ln f_\lambda(7.9\mu m) + 0.411 \ln f_\lambda(13.3\mu m)] \quad \text{(IX.D.3)}$$

Sources with *blue* spectra showing 11 μm SiC band emission were assigned to class $4n$ with the subclass n derived from the strength of the band according to

$$n = 10 \times [\ln f_\lambda(11.4\mu m) - (0.506 \ln f_\lambda(9.8\mu m) + 0.494 \ln f_\lambda(13.3\mu m)] \quad \text{(IX.D.4)}$$

Figure IX.D.1 shows how the classification depends on the ratios of the total flux to the narrow band fluxes at 10.0 and 11.0 μm. In the figure the uncertainties in the positions in the points is less than 0.01, approximately the size of the plotting symbols. The cluster of sources at the center of the figure shows objects with no significant excesses or deficits at either wavelength (Class $1n$). The loci of the other *blue* main classes and subclasses are indicated on the figure.

D.2.c Sources with *Red* Energy Distributions: Classes $5n$,$6n$,$7n$

Sources with *red* energy distributions (as defined above), but without the 11.3 μm line or other narrow spectral features, were classified according to the presence or absence of 10 μm silicate emission or absorption. No 11 μm emission or absorption features due to SiC were seen in these *red* sources.

Table IX.D.1 Spectral Classification Scheme

Class	Characteristic	Number	Typical objects
0*n*	other class -subclasses *n*=0,2,3,4: see text -subclass *n*=1: *blue*, low S/N -subclass *n*=5: *red*, low S/N	363	unknown
1*n*	*blue*, featureless -subclass: *n*=2 times spectral index	2246	stars with spectral type earlier than M5
2*n*	*blue*, 10 μm emission -subclass: *n*= band strength	1738	stars with not too thick oxygen-rich envelopes
3*n*	*blue*, 10 μm absorption -subclass: *n*= band strength	230	stars with thick oxygen-rich envelopes
4*n*	*blue*, 11 μm emission -subclass: *n*= band strength	542	stars with carbon-rich envelopes
5*n*	*red*, no line, no 10 μm band -subclass: *n* = 2 times spectral index	64	unknown
6*n*	*red*, 10 μm emission -subclass: *n*= band strength	78	stars with very thick oxygen-rich envelopes
7*n*	*red*, 10 μm absorption -subclass: *n*= band strength	67	stars with extremely thick oxygen-rich envelopes and hot spots in molecular clouds
8*n*	11.3 μm emission line -subclass *n*=0: no atomic line -other subclasses: strongest line [Ne II],12.8 μm:*n*=1 [S III],18.8 μm:*n*=2 [Ar III],9.0 μm:*n*=3 [S IV],10.5 μm:*n*=4 [Ne III],15.5 μm:*n*=5 [Ne V], 14.5 μm:*n*=6	71	compact HII regions and planetary nebulae
9*n*	same as class 8, but without 11.3 μm line	50	unknown

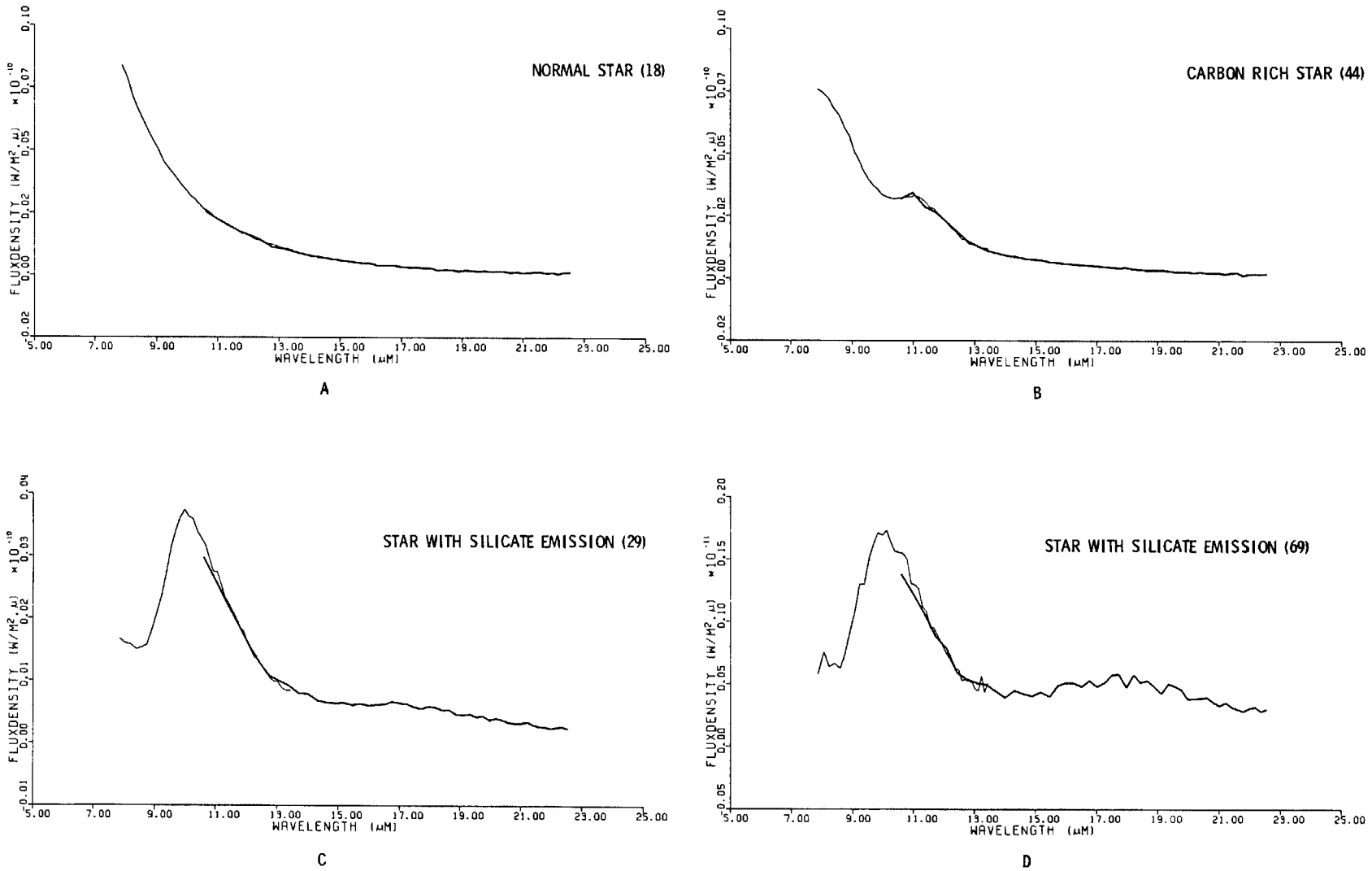

Figure IX.D.2.1 Representative low resolution spectra. Numbers refer to the spectral classes defined in the text.

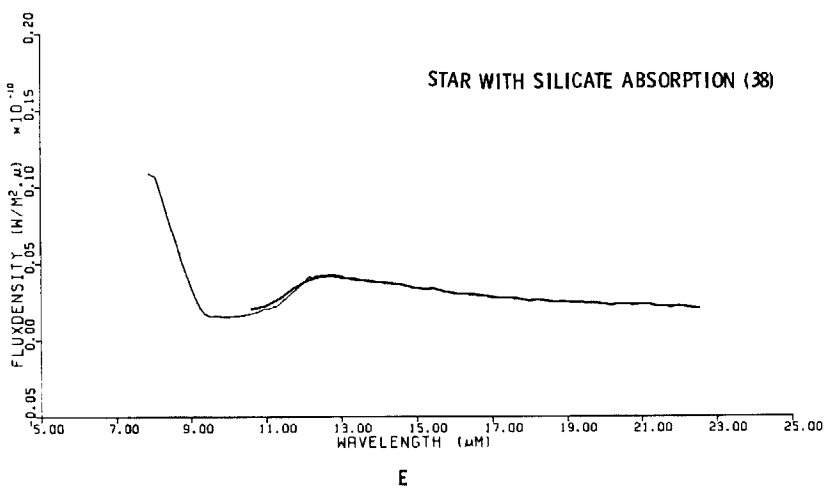

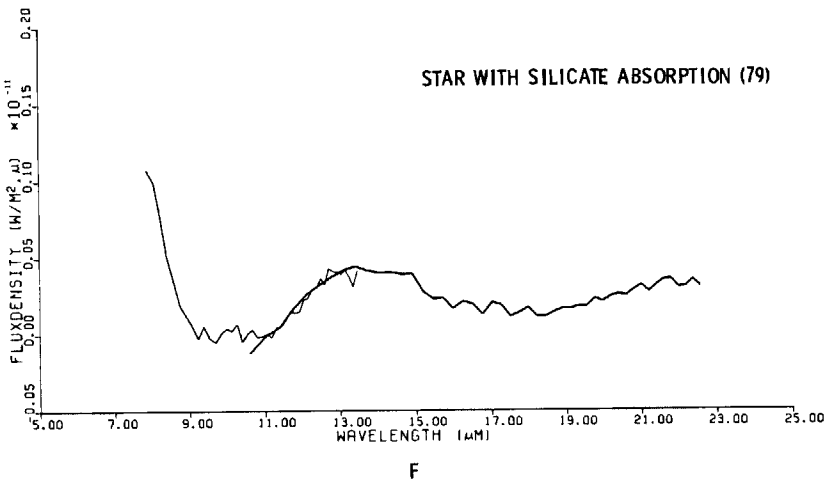

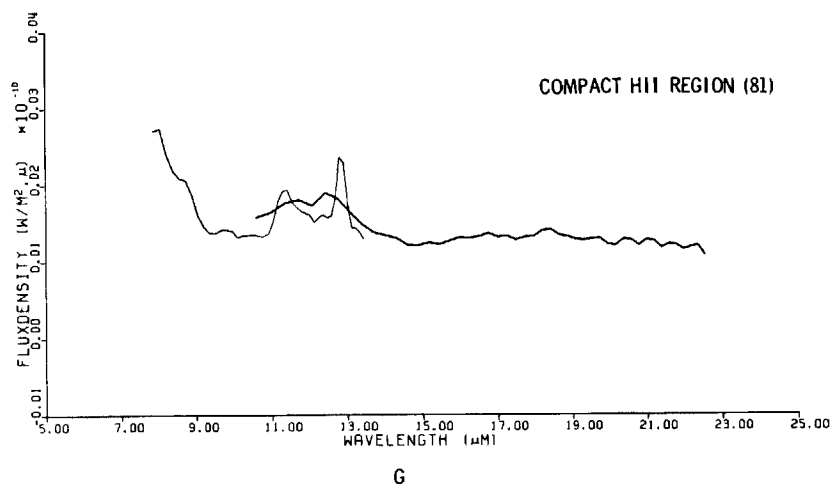

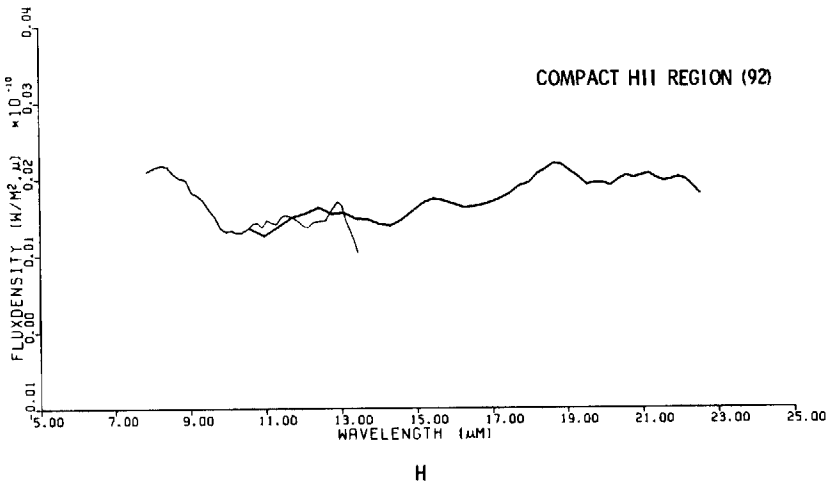

Figure IX.D.2.2 Representative low resolution spectra. Numbers refer to the spectral classes defined in the text.

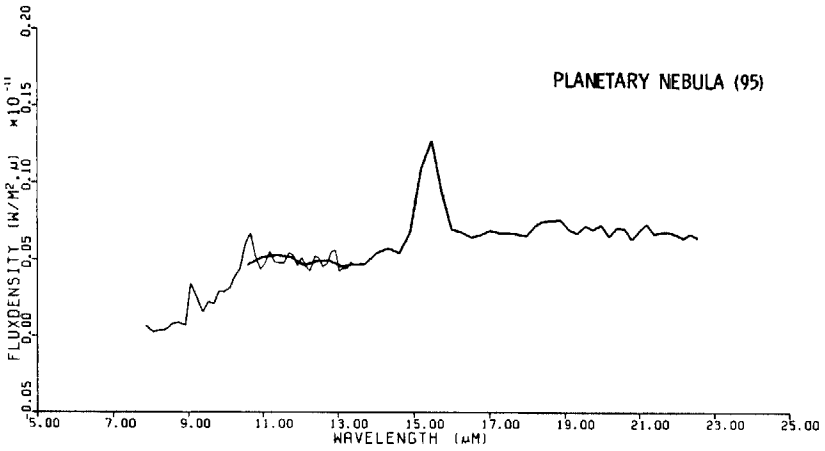

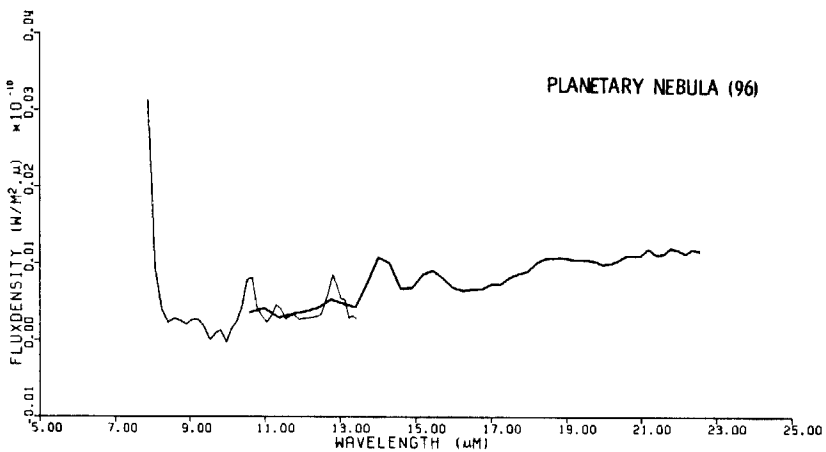

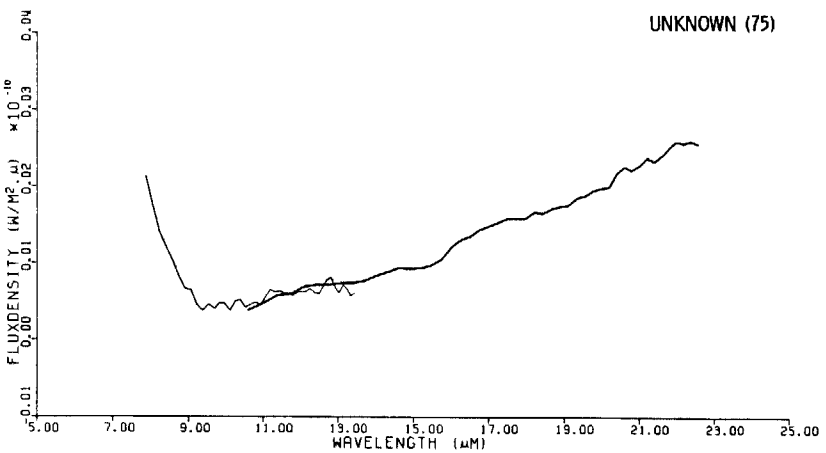

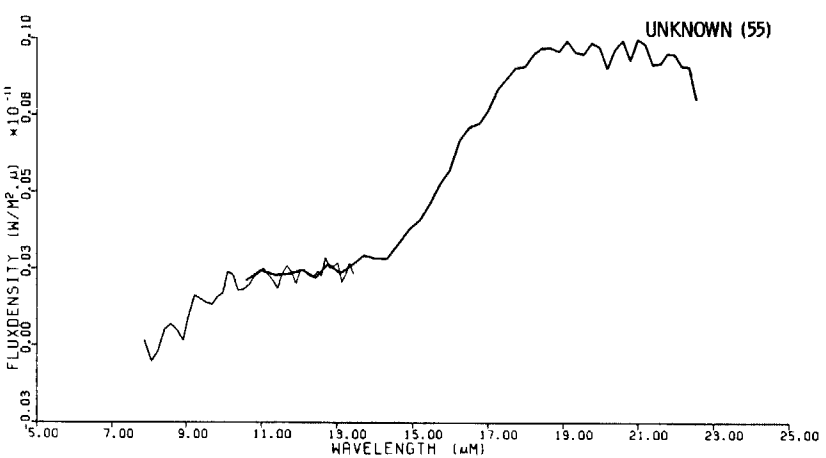

Figure IX.D.2.3 Representative low resolution spectra. Numbers refer to the spectral classes defined in the text.

Class 5*n* objects showed no significant 10 μm excess or deficit. The subclass *n* is again equal to *twice* the spectral index between 14 and 22 μm.

Sources with *red* spectra showing 10 μm silicate band *emission* were assigned to class 6*n*; sources with silicate *absorption* were assigned to class 7*n*. In both cases the subclass *n* was derived from the strength of the emission or absorption with respect to the adjacent continuum according to (Eq. IX.D.2,3).

D.2.d Spectra with Spectral Lines: Classes 8*n*,9*n*

For sources with spectral lines the classification proceeded independently of the *red* or *blue* shape of the overall energy distribution. The classification processor searched down to the 4 σ level for the seven spectral lines listed in Section IX.D.2.a. If the 11.3 μm line was among those found, then the source was assigned to class 8*n*. If the 11.3 μm line was not present, then the source was assigned to class 9*n*. The subclass *n* was based on which of the six remaining lines, in order of increasing excitation, was strongest (see Table IX.D.1).

D.2.e Miscellaneous Spectra: Class 0*n*

Spectra that did not fit into one of the above categories, or which were of lower quality, were assigned to class 0*n*. Class 01 spectra had such low signal-to-noise ratios that excesses or deficits greater than 0.5 (Eq. IX.D.2-4) were not significant; spectra more than 5 sigma away from the boundaries of the 1*n*,2*n*,3*n*,4*n* spectra were given codes 00, 02, 03, and 04. These subclasses had only a few sources. Code 05 was given to those objects with low signal-to-noise *red* spectra without significant lines or bands.

D.3 Performance of the Classification Scheme

About 90% of the sources in the catalog fall in the *blue* classes 1*n* to 4*n*. Figure IX.D.1 shows the adequacy of the classification scheme, with most of the strong sources located in three well-defined areas.

The featureless stars (K and early M spectral types) cluster in the center, and their spectral indices in both the short- and long-wavelength parts of the spectrum are close to -4, as expected.

The class 2*n* objects (oxygen-rich stars with 10 μm emission bands) lie in a narrow strip indicating that the shape of the 10 μm band is fairly constant. Moreover, the spectral indices increase systematically as the 10 μm band becomes stronger. The class 4*n* objects (carbon-rich stars with 11 μm emission bands) are well separated from the class 2*n* objects except in the lowest subclasses, where confusion between the two types occurs.

The class 4*n* objects occupy a less clearly defined area in Fig. IX.D.1 because of variable structure shortward of the 11 μm band. A few objects with code 04 and in the class 4*n* seem to be oxygen-rich stars where the 10 μm band is self-absorbed. For these sources, simple classification schemes break down.

The class 3*n* sources (oxygen-rich stars with 10 μm absorption) suffers from the problem that the 10 μm band becomes so broad that it covers most of the short-wavelength half of the spectrum, leaving no part of the spectrum for an estimate of the continuum. The class 3*n* crosses show a large scatter in Fig. IX.D.1.

The *red* classification was tuned to detect as many emission-line sources as possible, and very liberal criteria were applied for significance. Consequently, the automatic classification program contaminates

classes 8*n* and 9*n* with objects that belong to other categories. Deep 10 μm absorption bands combined with the instrumental short-wavelength band edge near 13.5 μm often produced spurious 12.8 μm lines; 10 and 11 μm emission bands gave rise to features that resembled 11.3 μm lines. All line spectra were inspected by eye and the classification was changed where needed.

For the strongest 300 sources, the individual spectra contributing to the coverage were classified independently by visual inspection. Apart from the expected problems around the boundaries between the various classes, the classifications were consistent within one subclass.

Another test of the classification scheme was done on the line sources. Spectra were extracted for more than a hundred planetary nebulae. Roughly twenty had acceptable line spectra according to the criteria given in Section IX.C.4. The classification processor correctly described those sources.

E. Some Characteristics of the Catalog

E.1 Completeness

No sharp flux density limit can be specified above which completeness is strongly guaranteed, because of the stringent rejection criteria (see Section IX.C.3). In general, completeness is much better at high than at low Galactic latitudes since most of its selection criteria were meant to discriminate against confused sources. Figure IX.E.1 shows plots of log (number) versus log (f_ν) where f_ν is the flux density at 12 μm. The three most populated main classes have been plotted as well as the total sample. The total number follows a power law with a slope of ~-1.3, while for sources with flux densities between 15 and 100 Jy the slope of the power law is closer to -1.0. These slopes are consistent with a population of Galactic sources. The catalog is obviously incomplete below ~15 Jy. The variation of slope with f_ν is rather large for classes 4 and 2, while the slope of the class 1 curve is steeper than any of the others and much more constant. These differences can be understood if the spectral features characterizing classes 2 to 4 become unrecognizable to the classification program for fainter sources. Consequently, the fainter class 2-4 sources tend to migrate into class 1 at lower flux densities, thus causing an over-population of class 1 and an under-population of classes 2-4.

E.2 Checks on the Shape of the Spectra

The general shape of the spectra is largely determined by the wavelength- dependent responsivity correction, the deviation of which has been discussed in Section IX.B.2. If a considerable error were made in assuming that the infrared spectrum of α Tau was consistent with that of a 10000 K black body, this would show up as a systematic variation of the ratio of integrated spectral flux over 12 μm survey flux with spectral index. Some individual spectra observed from the ground have been compared with the IRAS spectra. The comparison showed satisfactory results.

A word of caution is due with respect to line spectra. Relative line strength observed in different spectrum-halves (8-13 and 11-22 μm) of spectra with little or no continuum, may not be reliably calibrated. This uncertainty is because of the uncertainty in the cross-scan dependent responsivity correction (see Sections IX.B.3 and C.2.e). Without the presence of a continuum in the overlap region of the two spectrum-halves, joining the spectrum-halves is uncertain and has generally not been done. Each spectrum-half may therefore have an uncertainty of up to 20%.

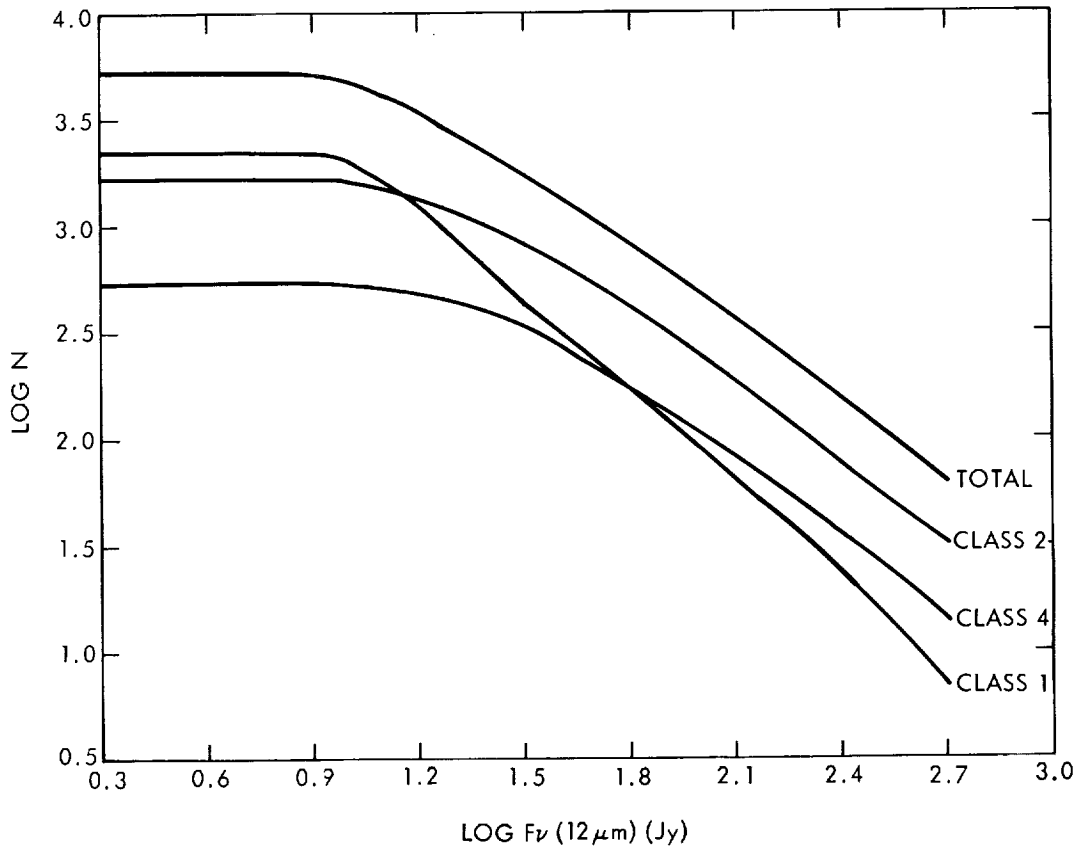

Figure IX.E.1. Plot of log (number) versus log f_ν for sources seen with the spectrometer. The number plotted in the ordinate is the integrated number of sources with flux densities less than the designated flux density. The flux densities plotted in the absissca have been obtained from the main point source catalog. The bottom three curves correspond to individual spectral classes defined in Section IX.D.

Authors:

E.Raimond, D. A. Beintema, and F. M. Olnon.

References

Wildeman, K.J., Beintema, D.A. and Wesselius, P.R. 1983, *Journal British Interplanetary Soc.*, **36**, 21.

X. THE FORMATS OF THE IRAS CATALOGS AND ATLASES

A. Introduction

This chapter describes the formats of the point source and small extended source catalogs, the total intensity images and the low-resolution spectra in their printed and machine-readable forms. A brief description is given of each entry in the catalogs; tables describe each column of the catalog in more detail and give, for the machine readable versions, the logical type of each variable and its length in bytes. Each tape containing IRAS catalog information has at least one header file containing the date and version number of the data on the tape (Table X.A.1).

Table X.A.1 Format of Header Files

Start Byte	Name	Description	Length
00	NAME	Name of IRAS data product	30A1
30	DATE	Date of production	12A1
42	VERS	Version Number	5A1
47	COMMENT	32 bytes of comment	32A1

IRAS images are presented in the FITS format (Wells, Greisen and Harten 1981). Sample headers are given for the sky plates, the Galactic plane map and the all-sky map. The format of the 1/2° beam zodiacal history file is described in this chapter. The format of the extragalactic specialty catalog is described at the beginning of that catalog.

IRAS data products discussed in this chapter include:

Point Sources:

Machine-readable version of the Catalog (Section X.B.1)

Printed version of the Catalog (Section X.B.2)

Machine-readable version of the Working Survey Data Base (Section X.B.3)

Small Extended Sources:

Machine-readable version of the Catalog (Section X.C.1)

Printed version of Catalog (Section X.C.2)

Extended Emission Images:

16.5° Images (photographic representation - Section X.D.3a)

16.5° Images (machine readable format - Section X.D.3b)

Galactic Plane Images (all formats - Section X.D.4)

Low-Resolution Maps (all formats - Section X.D.5)

Zodiacal History File (machine readable - Section X.D.6)

Low-Resolution IRAS Spectra:

Catalog of spectra (machine readable - Section X.E)

B. Point Sources

The information about infrared point sources is presented in increasing detail, progressing from the printed volumes to the tape version of the catalog to the detailed description of the observational and processing history of each source in a file known as the Working Survey Data Base (WSDB) augmented by its ancillary file. The printed version (Section X.B.2) is intended for users at the telescope or at institutions without computerized information retrieval systems. The catalog tape (Section X.B.1) is intended for astronomers desiring to make statistical studies and to search the catalog for large numbers of sources. The WSDB and ancillary file (Section X.B.3) are meant to give the sophisticated researcher all the available data on any given source such as its brightness on each hours-confirmed sighting, the detectors involved and the details of the data reduction such as confusion with neighboring sources.

Another catalog available only in machine readable form lists the WSDB entries for all sources that failed one or more of the confirmation and confusion criteria and were not, thus, included in the main catalog. This file of REJECTED sources includes spurious objects, including: processing failures, space debris, asteroids and comets, and celestial sources that, due to incompleteness at faint levels or to variability, failed to achieve the minimum criterion of two hours-confirmed sightings. In regions of high source density the file includes sources rejected by the more severe criteria for reliability applied there (Section V.H.6). *Caveat emptor.*

B.1 The Machine Readable Version of the Point Source Catalog

The point source catalog tape is divided into six individual files, covering the range 0 to 24 hr in right ascension in blocks of four hours each. Each file contains from 20,000 to 90,000 sources arranged in order of increasing right ascension. Each of the six catalog files is *preceded* by a file containing a single 80-character ASCII record which lists the date and version number of the catalog. Thus to read the entire catalog one must read sequentially through 12 files, six containing the data and six containing dates and version numbers.

Table X.B.1 describes each entry in the catalog tape. Those columns that are also included in the printed version are marked. Each catalog entry requires $160 + NID \times 40$ bytes of ASCII data where NID is the number of positional associations for each source. In the table the column "Format" refers to the length and type of the (FORTRAN) character field used to read or write each entry. Figure X.B.1 describes the format of the printed version of the catalog.

The tape is written with 80-character (ASCII) logical records and blocked with 256 logical records per physical record so that one can regard the tape as a sequence of card images. The entries are arranged so that the source data fits into two records. Association information requires an additional 40 characters per association and appears in subsequent records, two associations per record. If one assumes an average

Table X.B.1 Format of Point Source Catalog Tape

Start Byte	Name	Description	Units	Format
00	NAME[1]	Source Name	----	11A1
11	HOURS	Right Ascension 1950.	Hours	I2
13	MINUTE	Right Ascension 1950.	Minutes	I2
15	SECOND[1]	Right Ascension 1950.	deci-Seconds	I3
18	DSIGN[1]	Declination Sign	±	A1
19	DECDEG	Declination 1950.	Arc Deg	I2
21	DECMIN	Declination 1950.	Arc Min	I2
23	DECSEC[1]	Declination 1950.	Arc Sec	I2
25	MAJOR[1]	Uncertainty ellipse major axis	Arc Sec	I3
28	MINOR[1]	Uncertainty ellipse minor axis	Arc Sec	I3
31	POSANG[1]	Uncertainty ellipse position angle	Degree (East of North)	I3
34	NHCON[1] (<25)	Number of times observed	---	I2
36	FLUX[1]	Averaged non-color corrected flux densities (1 value per band)	Jansky (10^{-26}W m^{-2} Hz^{-1})	4E9.3
72	FQUAL[1]	flux density quality. (1 value per band)	---	4I1
76	NLRS	Number of significant LRS spectra	---	I2
78	LRSCHAR[1]	Characterization of averaged LRS spectrum.	---	2A1
		(----------new record----------)		
80	RELUNC[1]	percent relative flux density uncertainties (1 value per band).	---	4I3
92	TSNR	ten times the minimum signal-to-noise ratio in each band	---	4I5
112	CC[1]	point source correlation coefficient (1 value per band).	---	4A1
116	VAR[1]	percent Likelihood of Variability		I2
118	DISC	Discrepant Fluxes flag (one per band, hex-encoded)	---	A1
119	CONFUSE[1]	Confusion flag (1 flag per band, hex-encoded)	---	A1
120	PNEARH[1]	Number of nearby hours-confirmed point sources	---	I1
121	PNEARW[1]	Number of nearby weeks-confirmed point sources	---	I1

Table X.B.1 Format of Point Source Catalog Tape (Continued)

Start Byte	Name	Description	Units	Format
122	SES1[1]	Number of seconds-confirmed nearby small extended sources (1 value per band)	---	4I1
126	SES2[1]	Number of nearby weeks-confirmed small extended sources (1 value per band)	---	4I1
130	HSDFLAG[1]	Source is located in high source density bin (1 value per band, hex-encoded)	---	A1
131	CIRR1[1]	Number of nearby 100 μm only WSDB sources	---	I1
132	CIRR2[1]	Spatially filtered 100 μm sky brightness ratio to flux density of point source (see text)	---	I1
133	CIRR3	Total 100 μm sky surface brightness	MJy sr^{-1}	I3
136	NID[1] (<25)	Number of positional associations	---	I2
138	IDTYPE	Type of Object	---	I1
139	SPARE*	21 spare bytes*	---	21A1*
		(----------new record----------)		
160	CATNO[1]	Catalog number	---	I2
162	SOURCE[1]	Source ID	---	15A1
177	TYPE[1]	Source Type/Spectral Class	---	5A1
182	RADIUS[1]	Radius Vector from IRAS Source to Association	Arc Sec	I3
185	POS	Position Angle from IRAS Source to Association	Degree E of N	I3
188	FIELD1[2]	object field #1 (magnitude/other)	catalog dependent	I4
192	FIELD2[2]	object field #2 (magnitude/other)	catalog dependent	I4
196	FIELD3	object field #3 (size/other)	catalog dependent	I4
200 -240 etc.		continuation of associations[3] in blocks of 40 bytes		

[1]Quantities listed in printed version of catalog.

[2]FIELD1 is listed in printed version of catalog, except for catalogs 2 and 19, where FIELD2 is listed.

[3]CATNO, SOURCE, TYPE, RADIUS, POS, FIELD1-3 are repeated in blocks of 40 bytes, 2 per logical record, as necessary. The definition and formats of FIELD1-3 depend on the individual catalog in which the association is found. See Table X.B.4.

*For Version 2.0 of the Catalog, see Table XII.A.3.

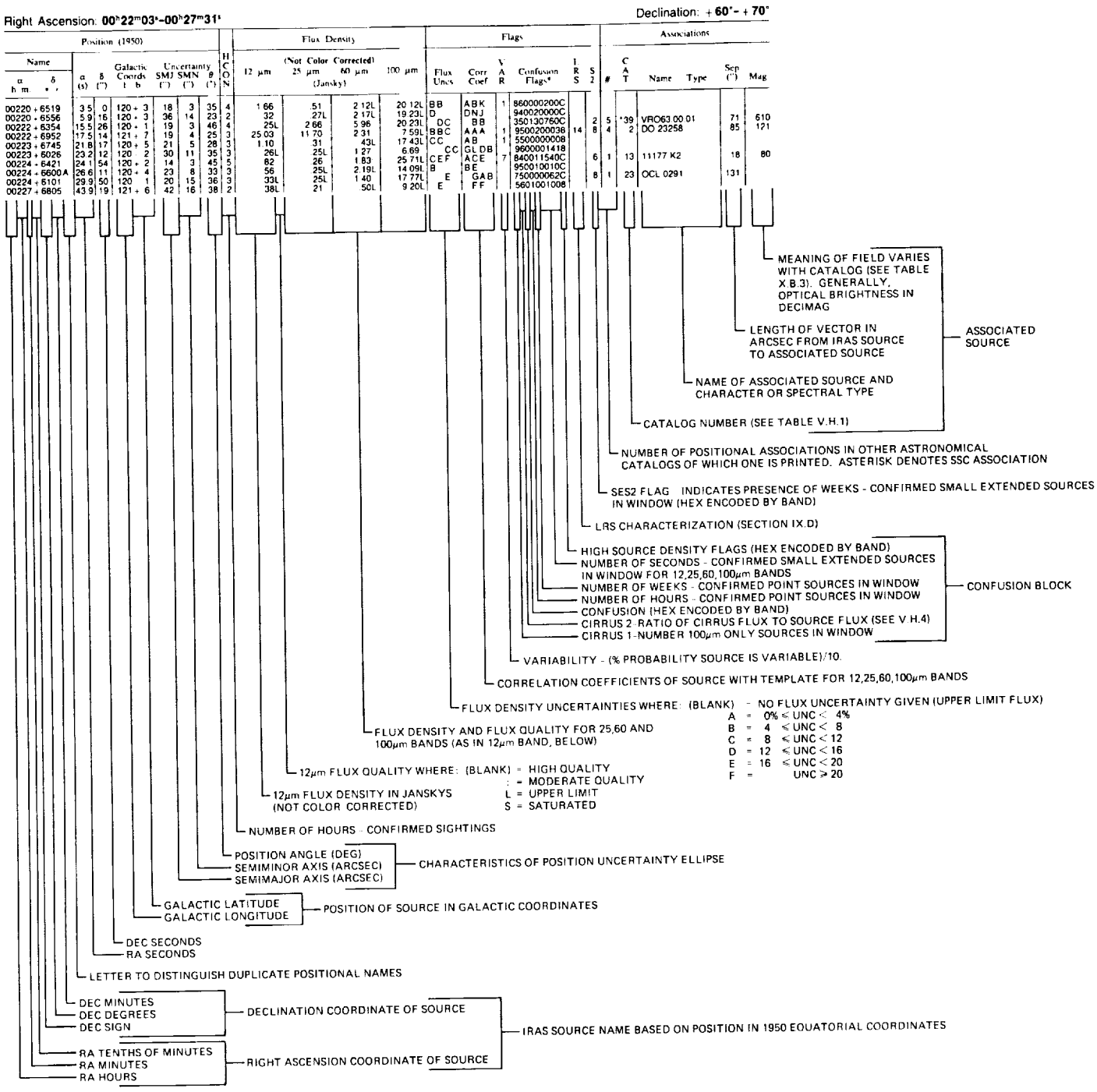

Figure X.B.1 Explanation of format of printed version of point source catalog.

of two associations per source, then a file for one of the right ascension blocks will require about 10 Mbytes.

In general, for quantities that have a value in each wavelength band, subscripts or array indices range from 1 to 4 and refer, respectively, to 12, 25, 60 and 100 μm. A number of the flags discussed below have values in each of the four wavelength bands. For compactness these are encoded into a single base-16 (Hex) digit (values 0-F) in the following manner (Table X.B.2). The four bits of that hex digit correspond to the four wavelength bands with bit 0 (Least Significant Bit) for 12 μm, bit 1 for 25 μm, bit 2 for 60 μm and bit 3 for 100 μm. The presence of a flag in a band is denoted by setting its bit to 1. Thus a source with a particular flag, e.g. CONFUSE, set at 12 and 25 μm would have CONFUSE=0011=3(Hex) while one confused in 25,60 and 100 μm would have CONFUSE=1110=E(Hex). A flag encoded in this manner will be referred to as "hex-encoded by band".

The remainder of this section discusses individual entries in the catalog.

Table X.B.2 Meaning of Hex Encoded Flags

Flag Set in A Particular Band				Resultant Value
100 μm (Bit 3)	60 μm (Bit 2)	25 μm (Bit 1)	12 μm (Bit 0)	of Encoded Flag xxxx = HEX=Decimal
0	0	0	0	0000 = 0 = 0
0	0	0	1	0001 = 1 = 1
0	0	1	0	0010 = 2 = 2
0	0	1	1	0011 = 3 = 3
0	1	0	0	0100 = 4 = 4
0	1	0	1	0101 = 5 = 5
0	1	1	0	0110 = 6 = 6
0	1	1	1	0111 = 7 = 7
1	0	0	0	1000 = 8 = 8
1	0	0	1	1001 = 9 = 9
1	0	1	0	1010 = A =10
1	0	1	1	1011 = B =11
1	1	0	0	1100 = C =12
1	1	0	1	1101 = D =13
1	1	1	0	1110 = E =14
1	1	1	1	1111 = F =15

Source Name: NAME

The IRAS source name is derived from its position by combining the hours, minutes and tenths of minutes of right ascension and the sign, degrees and minutes of the declination. In obtaining the minutes of right ascension and declination for the name, the positions were truncated. The letters 'A', 'B', 'C', etc. are appended to names of sources so close together that they would otherwise have had identical names. Names were uniquely assigned to both catalog and reject file sources, with catalog sources receiving letters first.

Position: (HOURS,MINUTE,SECOND,DSIGN,DECDEG,DECMIN,DECSEC)

Positions are given for the equinox 1950.0, and epoch 1983.5. Hours (HOURS) and minutes (MINUTE) of right ascension are given as integers while seconds (SECOND) are rounded to integer deciseconds. The declination is given as a character sign (DSIGN) followed by integer values of degrees (DECDEG), minutes (DECMIN) and seconds (DECSEC).

Position Uncertainty: MAJOR, MINOR, POSANG

As discussed in Section VII.B.2, the uncertainty in the position for a source depends on its brightness in the various wavelength bands, its path across the focal plane and the number of sightings. The final uncertainty after position refinement is expressed as a 95% confidence uncertainty ellipse (see Section V.D.9) whose semi-major (MAJOR) and semi-minor (MINOR) axes are given in seconds of arc. The orientation (POSANG) of the ellipse on the sky is expressed in terms of the angle between the major axis of the ellipse and the local equatorial meridian. It is expressed in degrees east of north.

Number of Sightings: NHCON

The number of hours-confirmed sightings is given. This number of flux entries will be found in the WSDB.

Flux Density: FLUX (4)

Each of the four wavelengths has a **non-color-corrected** flux density in units of Janskys, (1Jy = 10^{-26} W m^{-2} Hz^{-1}). The quoted value is an average of all the hours-confirmed sightings as obtained by the prescription described in Section V.H.5. The quality of each flux density is designated by FQUAL (see below).

The flux densities have been calculated assuming an intrinsic source energy distribution such that the flux density f_ν is proportional to ν^{-1}. Corrections to other spectral shapes can be made by consulting Section VI.C.

The flux densities for sources so bright that they saturated the analog-to-digital converter on every sighting are lower limits based on the brightest value recorded. The uncertainties are given as ten times the quoted flux density and a flag is set indicating saturation has occurred (Table X.B.7a).

Signal-to-Noise Ratio: TSNR(4)

The signal-to-noise ratio given for an individual hours-confirmed sighting is the highest value of the detections comprising that sighting (Section V.C.2). The values quoted in the catalog are *ten (10) times the minimum* of the signal-to-noise ratios for the various sightings (HCONs) of the source. A value is given for each wavelength band with a high or moderate quality measurement and for those upper limits coming from a non-seconds-confirmed detection. Values of TSNR greater than 30,000 are given as 30,000.

Source Variability: VAR

VAR is the percent probability (0-99) that a source is variable based on an analysis of the 12 and 25 μm flux densities and their uncertainties (see Section V.H.5). The value "-1" indicates that the source was not examined for variability.

Discrepant Fluxes: DISC(4)

The DISC flag indicates whether any one of the fluxes in a given band disagrees with others in that band, hex-encoded by band (Section V.H.5).

Flux Density Quality: FQUAL(4)

As described in Section V.H.5, a flux density measurement can be either high quality (FQUAL=3), moderate quality (FQUAL=2) or an upper limit (FQUAL=1).

Low-Resolution Spectra: NLRS,LRSCHAR

The Low-Resolution Spectrometer obtained 8-22 μm spectra of bright 12 and 25 μm sources (Chapter IX). NLRS gives the number of statistically meaningful spectra available for the source. LRSCHAR gives a short characterization of the nature of the spectrum (Table IX.D.1). All of the LRS spectra are available in tape and printed forms (*Astronomy and Astrophysics Supplement*, 1985) as described below (Section X.E) and in Chapter IX.

Flux Density Uncertainties: RELUNC (4)

Each flux density measurement other than an upper limit has an associated uncertainty expressed as a 1 σ value in units of $100 \times \delta f_\nu / f_\nu$. Uncertainties are discussed in Sections V.H.5 and VII.D.2.

Point Source Correlation: CC (4)

As described in Section V.C.4, the point source correlation coefficient can have values between 87-100%. These are encoded as alphabetic characters with A=100, B=99...N=87, one value per band. The value quoted is for the highest correlation coefficient seen for that source on any sighting.

Confusion: CONFUSE,PNEARH,PNEARW,HSDFLAG

As described in Section V.D.2, a great deal of care went into trying to untangle instances of confusion between neighboring sources. In parts of the sky where the source density is low, confusion processing was sometimes able to separate sources that are quite close together. The CONFUSE flag is set if two or more sightings of the source in a given band had confusion status bits set indicating confusion in the seconds-confirmation or band-merging processes. This flag is hex-encoded by band.

Other indicators of possible confusion are given by PNEARH and PNEARW which are, respectively, the numbers of hours-confirmed and weeks-confirmed point sources located within a 4.5′ cross-scan and 6′ in-scan (half-widths) window centered on the source. Values larger than 9 are given as 9.

Regions of high source density received special processing to improve the reliability of the quoted sources (see Section V.H.6). The regions are band-dependent. If a particular band of a given source went through high source density processing, then the appropriate bit in HSDFLAG (Table X.B.7) is set. HSDFLAG is hex encoded by band.

Small Extended Sources: SES1(4), SES2(4)

SES1 is the number of seconds-confirmed, small extended source detections in a given band found within a window centered on the source. The size of the window is 6′ in-scan × 4.5′ cross-scan (half-widths). As described in Sections V.H.3-4 and VII.H.1, values of SES1 greater than 1 should caution the

reader that significant extended structure may exist in the region and that the source in question may be a point-source like piece of a complex field.

SES2 is the number of weeks-confirmed small extended sources in a given band,located within a $6'$ in-scan $\times$ $4.5'$ cross-scan window (half-width) centered on the source. SES2 greater than 0 means that the point source flux measurement should be treated with caution as the source in question may, in fact, be extended. The flux quoted in the catalog of small extended sources may provide a better value for the source.

Cirrus Indicators: CIRR1, CIRR2, CIRR3

Over a large range of Galactic latitudes the infrared sky at 100 μm is characterized by emission from interstellar dust on a wide range of angular scales. The so-called "infrared cirrus" can seriously hamper efforts to extract point source detections from the data. To aid the user in interpreting the quoted 100 μm measurements three quantities have been established (Section V.H.4 and VII.H).

CIRR1 gives the number of 100 μm-only WSDB sources located within a $\pm 1/2°$ box in ecliptic coordinates centered on the source. The sources included in this count are the weeks-confirmed sources prior to high source density region processing (if applicable) plus those sources hours-confirmed but not weeks-confirmed. Values of CIRR1 greater than 3 may indicate contamination by cirrus with structure on the point source size scale.

CIRR2 gives a cirrus indication on a larger scale than CIRR1 and compares a "cirrus flux" with the source flux at 100 μm (see (Eq. V.H.2)). Values larger than 4~5 indicate the presence of considerable structure in the 100 μm emission on a $1/2°$ scale. A value of 0 indicates that no $1/2°$ data were available for the source in question.

CIRR3 is the total surface brightness of the sky surrounding the source in a $1/2°$ beam at 100 μm, clipped to exclude values greater than 254 MJy sr^{-1}. Values of CIRR3 greater than 30 MJy sr^{-1} indicate emission from dust with an appreciable column density. A value of CIRR3 = -1 means that no data were available.

Positional Associations: NID,IDTYPE,CATNO,SOURCE,TYPE,RADIUS,POS,FIELD1-3

Much of the utility of the IRAS catalog comes from the association of infrared objects with sources known to exist from other astronomical catalogs. As described in Section V.H.9, a large number of catalogs have been searched for positional matches. The total number of matches found is given by NID. Each match results in a forty-character description (2 per record).

IDTYPE ranges from 1 to 4 and states whether an association was found in an extragalactic catalog (1), a stellar catalog (2), other catalogs (3), or matches in multiple types of catalogs (4). CATNO is the number of the catalog in which the match was found (Tables V.H.1, X.B.4).

SOURCE is the name of the object in that catalog and TYPE its character or spectral type, if available. A vector is drawn from the IRAS position to the associated object. RADIUS is the length of that vector in arc seconds. POS is the angle between the vector and the local equatorial meridian expressed in degrees east of north. Three fields (FIELD1-3) have values depending on the catalog in question (Table X.B.4). Typically FIELD1,2 are magnitudes (in decimag) and FIELD3 a size.

B.2 The Printed Version of the Point Source Catalog

The printed version of the catalog is a strict subset of the information described in the preceding section. A number of fields have been abbreviated or deleted to make possible a single line entry for each source. The entries in the book are discussed below and shown as a figure in Fig. X.B.1

Name: (NAME)

The full IRAS name is derived from the hours(HH), minutes(MM) and tenths of minutes (T) of right ascension and from the sign, degrees (DD) and minutes (MM) of declination. The right ascension and declination have been truncated.

Position:(RA(s), DEC(″))

To conserve space, only the seconds of time for the right ascension and the arcseconds of declination are given. To reconstruct the source position one must also take the hours and minutes of the right ascension and the degrees and minutes of declination from the source name. Because the source name was obtained by truncating rather than rounding the positions, values of RA(s) and DEC(″) as large as 60 are possible.

Galactic Coordinates

Galactic coordinates ($l^{(II)}$, $b^{(II)}$) are given to a precision of 1°.

Positional Uncertainties (SMAJ,SMIN,PA)

Semi-major, semi-minor axes (″) and the position angle (°) of the uncertainty ellipse are given as described in the previous section.

Number of Sightings (NH)

The number of hours-confirmed sightings.

Flux Densities

Non-color-corrected flux densities are given in Janskys in the four bands. A single character following the measurement denotes the flux quality of the observation (Section V.H.5). A blank denotes a high quality measurement, a ':' denotes a moderate quality measurement and an 'L' denotes an upper limit. An 'S' indicates that *all* measurements in that band were saturated and that the value listed is the largest of all the saturated values.

Flux Density Uncertainties (FLUX/UNCS)

The relative uncertainties are given in each band for each high or moderate quality measurement according to the following convention (where the uncertainty was first rounded to two significant figures):

Symbol	Uncertainty Range
A	$0.00 \leqslant \delta f_\nu / f_\nu < 0.04$
B	$0.04 \leqslant \delta f_\nu / f_\nu < 0.08$
C	$0.08 \leqslant \delta f_\nu / f_\nu < 0.12$
D	$0.12 \leqslant \delta f_\nu / f_\nu < 0.16$
E	$0.16 \leqslant \delta f_\nu / f_\nu < 0.20$
F	$\delta f_\nu / f_\nu \geqslant 0.20$

Correlation Coefficient (CORR/COEF)

As described in the previous section, the correlation coefficient of the source with the point source template is given in each band according to the convention A=100%, B=99%,...N=87%.

Variability (VAR)

The probability (0-99%) that a source detected at 12 and 25 μm is variable is truncated to a single digit 0-9. A blank indicates that the source did not qualify for variability testing.

The Confusion Block

Ten flags or values each consisting of a single digit are combined into a block to denote the presence of nearby sources of possible confusion. The flags are discussed in detail in the preceding section and in Section V.H and include:

C1 = CIRR1 - the number of 100 μm only point sources.

C2 = CIRR2 - the ratio of 1/2° extended emission to the source flux.

CF = CONFUSE - hex-encoded flag indicating bands in which confirmation processor found confusion.

PH = PNEARH - number of nearby hours-confirmed sources.

PW = PNEARW - number of nearby weeks-confirmed sources.

S1-S4 = SES1 - number of nearby hours-confirmed small extended sources per band.

HD = hex-encoded flag indicating which bands, if any, were processed according to high source density rules (Section V.H.6).

Low-Resolution Spectra (LRS)

The presence of a low-resolution spectrum is indicated by this two-digit classification of the spectrum (Section IX.D).

Small Extended Source (S2)

The presence of one or more weeks-confirmed small extended sources is denoted by a hex-encoded flag denoting the bands in which a small extended source was found.

The Associations Block (NID,CAT,NAME,TYPE,RAD,MAG)

When an IRAS source is found to have at least one positional association with objects in other astronomical catalogs, one such association is printed. Six pieces of information are given as described in the previous section and in Section V.H.9. NID gives the total number of associations found in searching all catalogs. CAT is the number of the catalog (Tables V.H.1, X.B.4). The NAME and the TYPE (usually spectral or Hubble type) of the object are given. RAD is the distance from the IRAS source to the position of the associated object in arcsec. FIELD1, which is usually a magnitude, is given in the MAG field, when available, for all catalogs except 2 and 19, for which FIELD2 is given.

The association printed is chosen first by catalog within a catalog type (IDTYPE) as follows:

Catalogs in Order of Printing Priority																
		Printing Sequence														
IDTYPE	Type	1	2	3	4	5	6	7	8	9	10	11	12	13	14	15-31
1	extragalactic	9	6	12	10	29	25	26	27	28	30	31	-	-	-	-
2	stellar	13	4	15	2	1	7	16	17	18	19	24	-	-	-	-
3	other	14	22	21	20	23	3	5	8	11	-	-	-	-	-	-
4	multiple	13	9	14	1	2	3	4	5	6	7	8	10	11	12	15-31

If more than one association was found in the catalog chosen by the priority scheme, the closest associated source (smallest RAD) is printed.

B.3 The Working Survey Data Base

The most complete observational and data reduction history for point sources is contained within the Working Survey Data Base (WSDB). The WSDB is broken up into 20 files, one for each range of ecliptic longitudes called a Lune (see below). Each file is preceded by a header file containing a single 80-character ASCII record giving the date and version of the WSDB (Table X.A.1). Except as noted below, the entries are similar to those listed above for the catalog tape. Table X.B.3a lists the entries, their variable type and length. A second file, called the Ancillary File (Table X.B.3b) contains additional flags and derived quantities obtained during final product generation. Most of the information in the Ancillary file is the same as that in the catalog tape described in Section X.B.1. Character variables are in ASCII format. All arithmetic quantities are in integer format with the high order byte first.

It is important to note that the WSDB and Ancillary files are in binary format with variable length, blocked records (due to the variable number of hours-confirmed sightings or associations). Extra information has been added to the WSDB and Ancillary file tapes to make it possible to read in these variable length records. Each physical block on the tape begins with a *Block Control Word* of length I*4. Its high order two bytes give the length of the physical block in bytes; this length includes the 4-byte length of the Block Control Word itself. In addition, each logical record within the physical block is preceded by a *Segment Control Word* of length I*4. Its high order two bytes give the length of the logical record in bytes; again, this length includes the 4-byte length of the Segment Control Word itself. The inclusion of this information should make it possible for computers than can work with Variable Block formats to read the tape easily. In no case does the information for a single source span two physical blocks.

The remainder of this section describes WSDB and ancillary file entries not discussed above.

SDAS Lune Number: LUNE

In the data reduction the sky was divided into twenty "lunes" based on ecliptic coordinates. Lune 1 comprises that part of the sky with $\beta > 60°$; Lune 2 comprises that sky with $\beta < -60°$. Lunes 3-20 comprise that part of the sky with $|\beta| \leqslant 60°$ and ecliptic longitudes, λ, in 20° wide blocks. Lune 3 extends from $0° < \lambda < 20°$, lune 4 from $20° < \lambda < 40°$. etc.

Ecliptic Bin Number: BIN

To aid the data reduction the entire sky was divided into some 40,000 1 sq. deg bins. The bin structure is quite simple in ecliptic coordinates (Fig. X.Ap1.1) and an algorithm for generating bin numbers is given in Appendix X.1.

Ecliptic Coordinates: ELAT, ELONG

Ecliptic coordinates are given in units of 10^{-8} radians in the equinox 1950.

Scan Angle: SCAN

After weeks-confirmation SCAN gives the average scan angle of the focal plane with respect to the south-going local ecliptic meridian.

Positional Uncertainty: SIGY, LZ, SIGZ

As discussed in detail in Section V.D, the position refinement describes the source positional uncertainty in terms of 1 σ in-scan and cross-scan gaussian uncertainties (SIGY and SIGZ) and a uniform uncertainty (of half-width LZ) whose size depends on the exact paths of the source across the focal plane.

Number of LRS Extractions: LRSX

Each time a source with a signal-to-noise ratio greater than 25 at either 12 or 25 μm transversed the focal plane, the data reduction software automatically triggered a request to extract a spectrum from the low-resolution spectrometer data (Chapter IX). The threshold was purposefully set quite low so that sources with weak continuua but strong lines could be detected. Many sources with LRSX>0 will fail to have meaningful spectra and will thus have NLRS=0.

Known Source ID: KSID

The positions and predicted brightnesses of some 32,000 point sources including SAO stars, IRC objects and asteroids were incorporated into the data reduction software to provide a check on the positional and photometric accuracy of the IRAS sources. Table X.B.5 lists the range of KSID values assigned to sources of various types.

The following values are given for each hours-confirmed sighting:

Flux and Flux Uncertainty: FLUX(4), SIGF(4)

Flux and flux uncertainty measurements are given in units of 10^{-16}W m^{-2} for each hours-confirmed sighting. Note that an instrumental flux, *not* the flux density, is given. In order to convert the instrumental flux to flux density, one must divide the instrumental flux by 13.48, 5.16, 2.58, 1.00×10^{12} Hz at 12, 25, 60 and 100 μm respectively. The derivation of flux uncertainties and the averaging of the individual hours-confirmed fluxes to give the average value (see AVGFLUX, below) quoted in the catalog is discussed in Section V.H.5.

Signal-to-Noise Ratio: TSNR(4)

If a source is detected (but not necessarily even seconds-confirmed) in a given band, then a value equal to ten times the maximum signal-to-noise ratio (SNR) observed on any detector in that band in the hours-confirmed sighting is retained. In relatively simple parts of the sky the noise estimator used to derive SNR gives reasonable values. In more complex regions near the Galactic plane (see Section V.C.2) the utility of SNR is very limited.

Correlation Coefficient: CORR

The maximum point source correlation coefficient (see Section V.C.4.) obtained during a hours-confirmed sighting is retained for each band. The values for each band, expressed as percentages up to a maximum of 100, are encoded into a single integer according to the following algorithm:

$$CORR = CC(1) \times 2^{24} + CC(2) \times 2^{16} + CC(3) \times 2^{8} + CC(4) \qquad \text{(X.B.1)}$$

Flux Status: FSTAT

In each band there is a hierarchy of measurement quality depending on how many times a given source is observed within a given hours-confirmed sighting. FSTAT plays a crucial role in determining whether a source is included in the catalog at all, whether a flux is of high, medium or low quality and how the flux averaging was performed (Section V.H.5). For the meaning of each FSTAT value refer to Section V.D.8.

The values of FSTAT for the four bands are compressed into a single integer according to the following algorithm:

$$FSTAT = FSTAT(1) \times 2^{12} + FSTAT(2) \times 2^{8} + \qquad \text{(X.B.2)}$$

$$FSTAT(3) \times 2^{4} + FSTAT(4)$$

Detector ID's: DETID

The identities of all detectors observing a given source on the sightings (up to a maximum of 3 sightings) comprising a given hours-confirmed observation are recorded in the array DETID(I,J). The four bands run from I=1 to 4 while the three sightings run from J=1 to 3.

Each value of DETID contains an integer that must be decoded according to the following algorithm to obtain the detectors observing the source:

$$DETID(I,J) = D1 \times 2^{10} + D2 \times 2^{5} + D3 \qquad \text{(X.B.3)}$$

where detector numbers, D1, D2 and D3, range from 1 to 16 within each band. Table X.B.6 lists the correspondence between detector number within a band to the true detector number. The order of detector number is significant as described in V.D.5. It should be emphasized that when three detectors are named in a sighting, indicating the presence of an edge detection, the weakest of the edge detections may not have played any part in the assignment of flux or position.

Detector Name: DNAM, TNAM

Throughout the course of the data processing each hours-confirmed sighting is known by a combination of the first detector measuring the object (DNAM) and the time (in deci-UTCS since 1981, January 1, 0h UT) of that sighting (TNAM).

Confusion Status: CSTAT, PNEARH, PNEARW

At various stages in the reconstruction of a point source attempts are made to recognize (and remedy) the effects of confusion between nearby sources. The confusion status word CSTAT plays an important role in selecting sources to be treated by the "clean-up" processor (Section V.H.2) and in determining which sources to keep in regions of high source density (see Section V.H.6). For a detailed discussion of confusion processing see Section V.D.2. Values of CSTAT and brief descriptions of their meaning are given in Section V.D.8.

The values of CSTAT for each band are encoded into a single integer according to the following algorithm:

$$CSTAT = CSTAT(1) \times 2^{24} + CSTAT(2) \times 2^{16} + STAT(3) \times 2^{8} + CSTAT(4) \quad \text{(X.B.4)}$$

The number of hours- and weeks-confirmed point sources within $6' \times 4.5'$ (half-widths) of the quoted source, PNEARH and PNEARW, are encoded into a single byte:

$$PNEAR = PNEARW \times 2^{4} + PNEARH \quad \text{(X.B.5)}$$

Cirrus Flags: CIRRUS, CIRR1, CIRR2, CIRR3

The three flags denoting the presence of extended 100 μm emission ("cirrus") as discussed in Section V.H.4, are encoded in two bytes according to the algorithm:

$$CIRRUS = CIRR3 \times 2^{8} + CIRR1 \times 2^{4} + CIRR2 \quad \text{(X.B.6)}$$

Values of CIRR2 = 0 and CIRR3 = -1 mean no data were available.

Small Extended Source Flags: SES1, SES2

The two small extended source flags for each band discussed in Section V.E.1 are encoded into two integers according to the following algorithm:

$$SES1 = SES1(1) \times 2^{12} + SES1(2) \times 2^{8} + SES1(3) \times 2^{4} + SES1(4) \quad \text{(X.B.7)}$$

and

$$SES2 = SES2(1) \times 2^{12} + SES2(2) \times 2^{8} + SES2(3) \times 2^{4} + SES2(4) \quad \text{(X.B.8)}$$

Clean up Processors: CLEAN, BRIGHT, ACCEPT, HSDPROC, MISC

In creating the WSDB from the weeks-confirmed data, several processors were applied in order to fix various known problems (see Section V.H). These processors set various flags that allow the user to understand what processing occurred. The clean-up processor allowed the weeks-confirmation of various WSDB sources that did not previously have an opportunity to weeks-confirm for purely technical reasons or which were incorrectly split asunder during band merging. The flags set by that processor are described in Table X.B.7a., and include flags indicating saturated fluxes. Optical crosstalk from certain bright objects such as Saturn and IRC+10216 produced a few spurious sources. These were marked for deletion. The byte BRIGHT (Table X.B.7b) notes these cases and also contains flags denoting final acceptance (ACCEPT) or rejection of the source in each band. The flags from the High Source Density processor (HSDPROC, see Section V.H.6) are given in 2 bytes per band (Table X.B.7c). Miscellaneous flags are set in MISC (Table X.B.7d) and include the presence of flux discrepancies in each band, whether the in-scan positional uncertainties needed to be increased (Section VII.C) and whether the source was accepted in the catalog.

Table X.B.3a. The Catalog Working Survey Data Base (WSDB)

Start Byte	Name	Description	Units	Type
0*	LUNE	SDAS Lune number	---	I*4
4	BIN	Ecliptic Bin Number	---	I*4
8	ELONG	Ecliptic longitude 1950.	10^{-8} rad	I*4
12	ELAT	Ecliptic latitude 1950.	10^{-8} rad	I*4
16	SCAN	average scan angle with respect to ecliptic meridian	milli-rad	I*2
18	SIGY	In-scan Gaussian position uncertainty	μ-rad	I*2
20	LZ	Cross-scan Uniform position uncertainty	μ-rad	I*2
22	SIGZ	Cross-scan Gaussian position uncertainty	μ-rad	I*2
24	LRSX	Total number of LRS extraction requests	---	I*2
26	KSID	Known Source ID	---	I*2
28	NHCON (<25)	Number of Hours-confirmed sightings	---	I*4
The following values repeat for each hours-confirmed sighting:				
32	FLUX	FLUX(I)=In-band power	10^{-16}W m^{-2}	4I*4
48	SIGF	SIGF(I)=Uncertainty in FLUX(I)	10^{-16}W m^{-2}	4I*4
64	TSNR	TSNR(I)=10x(max SNR)	---	4I*2
72	CORR	Maximum correlation coefficient (1 value per band, Eq. X.B.1)	---	I*4
76	FSTAT	Flux status word (1 value per band, Eq.X.B.2)	---	I*2
78	DETID	Detector ID Array (4,3) for 4 bands (Eq.X.B.3)	---	12I*2
102	LRSXNO	Number of LRS extraction requests	---	I*1
103	DNAM	detector part of source name	---	I*1
104	TNAM	deci-UTCS part of source name	deci-sec	I*4
108	CSTAT	Confusion status flags (Eq.X.B.4)	---	I*4
112---191 192---271 etc...		repeats bytes 32-111 for subsequent hours confirmed sightings.		

* See X.B.3 for discussion of block and segment control words

Table X.B.3b. Ancillary WSDB File

Start Byte	Name	Description	Units	Type
0[1]	PNEAR	Nearby hours- and weeks-confirmed neighbors	---	I*1
1	CLEAN	Clean up Processor flags	---	I*1
2	SES1	Number of nearby unconfirmed SES (4 bands encoded)	---	I*2
4	SES2	Number of nearby weeks-confirmed SES (4 bands encoded)	---	I*2
6	CIRR1, CIRR2	Number of 100 μm only WSDB sources, spatially filtered 100 μm emission.	---	I*2
	CIRR3	value of 100 μm half-degree beam total intensity	MJy sr^{-1}	
8	AVGFLUX	AVGFLUX(I) Averaged flux (in-band power) in band I.	10^{-16}W m^{-2}	4I*4
24	AVGUNC	AVGUNC(I) Uncertainty in averaged (in-band) flux in band I.	10^{-16}W m^{-2}	4I*4
40	HSDPROC	HSDPROC(I). Flags set by the high source density processor in band I	---	4I*2
48	RA	Right ascension 1950	10^{-5}°	I*4
52	DEC	Declination	10^{-5}°	I*4
56	NAME	source name	---	A*12
68	NLRS	Number of meaningful LRS spectra	---	I*2
70	LRSCHAR	characterization of LRS spectra	---	A*2
72	BRIGHT ACCEPT	Bright Source Clean up Flag for catalog sources accepted in the catalog		I*1
73	VAR	Percent likelihood of Variability	---	I*1
74	FQUAL	FLUX Quality flags (one per band) BIT 0-1, 12 μm BIT 2-3, 25 μm, etc.	---	I*1

Table X.B.3b. Ancillary WSDB File (Continued)

Start Byte	Name	Description	Units	Type
75	MISC	Miscellaneous Status bits, incl. DISC ACCEPT,SIGY See Table X.B.7d	---	I*1
76	LUNE	SDAS Lune number	---	I*4
80	BIN	Ecliptic Bin Number	---	I*4
84	ELONG	Ecliptic longitude	10^{-8}rad	I*4
88	ELAT	Ecliptic Latitude	10^{-8}rad	I*4
92	NID[2] (<25)	Number of Associations to follow		I*2
94	IDTYPE	Type of association	---	I*2
96	CATNO	Catalog Number	---	I*2
98	SOURCE	Source ID	---	A*15
113	TYPE	Source Type/Spectral Class	---	A*5
118	RADIUS	Position difference	(")	I*2
120	POS	Position Angle	° E of N	I*2
122	FIELD1	object field #1	---	I*2
124	FIELD2	object field #2	---	I*2
126	FIELD3	object field #3	---	I*2
128 -160 etc.		continuation of association[3] in blocks of 32 bytes		

[1] See X.B.3 for discussion of block and segment control words

[2]If NID=0, one blank association field of 32 bytes is written.

[3]CATNO,SOURCE,TYPE,RADIUS,POS,FIELD1-3 are repeated in blocks of 32 bytes, 2 per logical record, as necessary. The definition and formats of FIELD1-3 depend on the individual catalog in which the association is found. See Table X.B.4.

Table X.B.4 Meaning of the Source Association Fields

Catalog	Field and Meaning*	
1 GCVS	Type	Blank
	Field1 =	Code gives meaning for Fields 2-3
	if Field1 = 1	Field2 and Field3 are B mag [decimag] at max,min
	= 2	Field2 and Field3 are V mag [decimag] at max,min
	= 3	Field2 and Field3 are photographic mag [decimag] at max,min
	= 4	Field2 and Field3 are estimated V mag [decimag] at max,min
	= 5	Field2 is 999 and Field3 is 0
2 Dearborn Obs.	Type	Blank
	Field1	Code for Field2 (1,2)
	Field2	if Field1 is 1, Field2 is red magnitude [decimag] *
		if Field1 is 2, Field2 is 999
	Field3	0
3 Revised AFGL	Type	Blank
	Field1	Magnitude at 4.2 μm [decimag]
	Field2	Magnitude at 11 μm [decimag]
	Field3	Magnitude at 27 μm [decimag]
4 2-μm Sky Survey	Type	Blank
	Field1	K magnitude [decimag]
	Field2	I magnitude [decimag]
	Field3	0
5 Globules (Wesselius)	Type	Blank
	Field1	999
	Field2	Minimum diameter [arcsec]
	Field3	Maximum diameter [arcsec]
6 R C 2	Type	Blank
	Field1	Harvard V magnitude [decimag]
	Field2	B_T [decimag]
	Field3	D_o [arcsec]
7 Stars with em. lines	Type	Blank
	Field1	V magnitude [decimag]
	Field2	999
	Field3	0

Table X.B.4 Meaning of the Source Association Fields (Continued)

Catalog	Field and Meaning *	
8 Equatorial IR Cat.	Type	Blank
	Field1	Flux density [10^{-16} W cm^{-2} μm^{-1}] at 2.7 μm
	Field2	999
	Field3	0
9 UGC	Type	Blank
	Field1	Zwicky magnitude [decimag]
	Field2	Minimum diameter [arcsec] in B
	Field3	Maximum diameter [arcsec] in B
10 MCG	Type	Blank
	Field1	999
	Field2	Minimum diameter [arcsec] in B
	Field3	Maximum diameter [arcsec] in B
11 Strasbourg Planetary Nebulae	Type	Blank
	Field1	V magnitude of Nebula [decimag]
	Field2	B magnitude of Central Star [decimag]
	Field3	Minimum diameter of Nebula [arcsec]
12 Zwicky	Type	Blank
	Field1	Zwicky magnitude [decimag]
	Field2	999
	Field3	0
13 SAO	Type	Spectral Type
	Field1	V magnitude [decimag]
	Field2	p_g magnitude [decimag]
	Field3	0
14 ESO/ UPPSALA	Type	First 3 characters of object type
	Field1	B magnitude [decimag]
	Field2	Maximum diameter [arcsec]
	Field3	Minimum diameter [arcsec]
15 Bright Stars	Type	Spectral Type
	Field1	V magnitude [decimag]
	Field2	B-V [centimag]
	Field3	U-B [centimag]

Table X.B.4 Meaning of the Source Association Fields (Continued)

Catalog	Field and Meaning *	
16 Suspected Var.	Type	Spectral Information
	Field1	V magnitude at maximum [decimag]
	Field2	999
	Field3	0
17 Carbon Stars	Type	Spectral Type (May be truncated)
	Field1	p_g magnitude [decimag]
	Field2	V magnitude [decimag]
	Field3	I magnitude [decimag]
18 Gliese	Type	Spectral Type (May be truncated)
	Field1	V magnitude [decimag]
	Field2	B-V magnitude [millimag]
	Field3	U-B magnitude [millimag]
19 S Stars	Type	Blank
	Field1	p_g magnitude [decimag]
	Field2	V magnitude [decimag]
	Field3	I magnitude [decimag]
20 Parkes HII Survey	Type	Blank
	Field1	999
	Field2	Minimum diameter [arcsec]
	Field3	Maximum diameter [arcsec]
21 Bonn HII Survey	Type	Blank
	Field1	Flux density at 4.875 GHz (Jy)
	Field2	Diameter [arcsec]
	Field3	0
22 Blitz	Type	Blank
	Field1	Diameter [arcsec]
	Field2	V_{CO} [Km/s]
	Field3	Peak T_A [°K]
23 OSU	Type	Blank
	Field1	999
	Field2	999
	Field3	Diameter [arcsec]

Table X.B.4 Meaning of the Source Association Fields (Continued)

Catalog	Field and Meaning *	
24 IRC w/good pos.	Type	C if 2.2 μm sources are possibly confused, blank otherwise
	Field1	Right ascension difference (IRC-IRAS) [deciseconds of time]
	Field2	Declination difference (IRC-IRAS) [seconds of arc]
	Field3	0
25 DDO	Type	Blank
	Field1	999
	Field2	999
	Field3	0
26 Arp	Type	Blank
	Field1	999
	Field2	999
	Field3	0
27 Markarian	Type	Blank
	Field1	999
	Field2	999
	Field3	0
28 Strong 5 GHz	Type	Object type (GAL or QSO)
	Field1	V magnitude [decimag]
	Field2	5 GHz flux density [deciJy]
	Field3	0
29 Veron-Veron	Type	Object classification
	Field1	V magnitude [decimag]
	Field2	Redshift × 1000
	Field3	0

Table X.B.4 Meaning of the Source Association Fields (Continued)		
Catalog	Field and Meaning*	
30 Zwicky 8 Lists	Type	Blank
	Field1	999
	Field2	999
	Field3	0
31 VV	Type	Blank
	Field1	Special flag, (see below) 999 otherwise
	Field2	999
	Field3	0
32 IRAS Small Scale Structure	Type	Blank
	Field1	Hex coded bands
	Field2	Blank
	Field3	Blank
39† OSU Radio	Type	Blank
	Field1	Frequency
	Field2	Flux (deci Jy)
	Field3	0
40 Michigan Spectral	Type	Class**
	Field1	Mag (decimag)
	Field2	HD number (low byte)
	Field3	HD number (high byte)
41 Serendipitous Survey	Type	Blank
	Field1	Hex coded SSC bands
	Field2	First SSC flux (m Jy)
	Field3	Second SSC flux

* In the printed version FIELD1 is listed if present except for catalogs 2 and 19, where FIELD2 is given.

**Source name and type fields were combined to hold spectral type and class.

† Catalog numbers 33-38 reserved for internal use.

VV Catalog Flags (Catalog 31)

FIELD1	Explanation
10	VV 10 has the same coordinates as VV 29 in the VV Atlas. The UGC was used to confirm that the coordinate is correct for VV 29 and erroneous for VV 10. The UGC position for VV 10 = UGC 10814 was adopted.
11	The VV position is substantially different (>400″) from positions for the object in other catalogs. The VV position has been assumed to be in error because two or more other catalogs agree on a different position. The UGC position has been adopted.
12	Same as for 11, but the OSU position has been adopted.
13	The position in the VV Atlas, and the position listed for the VV object in the OSU are in disagreement. The true position has been established to be close to that of the OSU by the use of overlay transparencies on the POSS. The OSU position has been adopted.
14	Same as for 13, but the OSU position is not very good either, so a new position has been measured (accurate to about 1′).

Table X.B.5 Known Source ID's

Range	Source Type
1-465	Selected AFGL catalog sources
466-3157	Two Micron Sky Survey sources without SAO counterparts
3158-26979	Selected SAO stars (mostly M and K stars).
26980-27497	Selected objects for Low-Resolution Spectrometer
$\geqslant$30000	Solar System Objects (asteroids, comets and outer planets)

Table X.B.6 Detector Number

In Band Detector Number	True Detector Number 12 μm	25 μm	60 μm	100 μm	In Band Detector Number	True Detector Number 12 μm	25 μm	60 μm	100 μm
1	23	16	08	01	9	47	40	31	56
2	24	17	09	02	10	48	41	32	57
3	25	18	10	03	11	49	42	33	58
4	26	19	11	04	12	50	43	34	59
5	27	20	12	05	13	51	44	35	60
6	28	21	13	06	14	52	45	36	61
7	29	22	14	07	15	53	46	37	62
8	30	39	15	55	16	54	00	38	00

Table X.B.7a. CLEAN Bit Assignment

Bit #	Meaning
0-3	Bits 0-3 denote a flux limit derived solely from saturated detections. Bit 0=12 μm, Bit 1=25 μm.
4	Source failed to weeks-confirm with another WSDB source in the mini-survey region.
5	Source resulted from weeks-confirming at least two WSDB sources in the mini-survey region.
6	Source failed to weeks-confirm with another WSDB entry observed within 36 hours.
7	Source resulted from weeks-confirmation of two separate WSDB sources observed within 36 hours of each other.

Table X.B.7b. BRIGHT/ACCEPT Bit Assignment

Bit #	Meaning
0	False source generated by nearby bright source
1-4	Source satisfies single band acceptance criteria BIT 1 = 12 μm, Bit 2=25 μm,etc.
5-7	Source satisfies adjacent band acceptance criteria BIT 5 = 12 and 25 μm BIT 6 = 25 and 60 μm BIT 7 = 60 and 100 μm

Table X.B.7c. HSDPROC High Source Density Processor Flags

Bit #	Meaning
	Byte 1
0 and 1	00=0---not processed
	01=1---low quality flux
	10=2---medium quality
	11=3---high quality flux
2	Band rejected
3	Band accepted
4-7	final reason for rejection
	0000=0= not rejected
	0001=1= not weeks-confirmed
	0010=2= bad flux status
	0011=3= bad correlation coefficients
	0100=4= bad confusion status
	0101=5= inconsistent fluxes
	0110=6= weaker neighbor
	0111=7= confused neighbor
	1000=8= merging problems
	9-15= spare
	Byte 2 (Faults with Source)
0	not weeks-confirmed
1	bad flux status
2	bad correlation coefficient
3	bad confusion status
4	inconsistent fluxes
5	weaker neighbor
6	confused neighbor
7	merging problems

Table X.B.7d. MISC Bit Assignment

Bit #	Meaning
0-3	Discrepant Flux found in band. BIT 0, 12 μm, BIT 1, 25 μm, etc.
4,5	SPARE
6	σ_y fix (Section VII.C)
7	Source accepted in catalog

C. The Small Extended Source Catalog

The formats of the Small Extended Source Catalog (also known as the Small Scale Structure Catalog) and a description of the final generation of that catalog are given in Volume 7 of this series.

D. Extended Emission

D.1 Introductory Comments

The extended emission data are presented as maps of the infrared sky at two different scales in all four wavelength bands. The entire sky surveyed is mapped with 2' pixels at an effective resolution of 4'-6' in 212 16.5° × 16.5° fields and also with an effective resolution of 1° in a single field. A special map of the region within ±10° of the Galactic plane was also made at 4'-6' resolution. All of these maps are available in both digital and photographic formats. In addition, data from the survey averaged in a 1/2 ° × 1/2 ° beam is available in time ordered form. The details of the presentation of each of these products are described below. The methods used to produce the products were described in Section V.G. All the map projections used are described below.

The survey covered most parts of the sky several times and the extended emission data have been separated for the reasons outlined in Section V.G.1. The data released in Nov. 1984 includes the 188 fields in the 75% of the sky covered in the third sky coverage, along with the associated Galactic plane and low-resolution all-sky maps. Subsequent releases include a small part of the sky covered by the "minisurvey" done at the beginning of the mission (Section III.C.11) and the first and second coverages, each of about 95% of the sky.

D.2 Map Projections and Transformation Equations

Three separate map projections were used. The descriptions below provide enough information for the user of the IRAS data. More information can be found Richardus and Adler (1972).

D.2.a Gnomonic Projection - 16.5° Images

The gnonomic projection used for 16.5° images produces a geometric projection of the celestial sphere onto a tangent plane from a center of projection at the center of the sphere. Each individual field has its own tangent projection plane with the tangent point at the center of the field. This projection is neither conformal (angle preserving) nor equivalent (equal area) but does have the property that all straight lines in the projection are great circles on the sphere. All projections were done so that the sky coordinate associated with a pixel refers to the position at the center of the pixel. For the 16.5° fields the maximum distortion of angles is 0.6° and the maximum distortion of area is 6%. The area distortion is approximately proportional to the inverse cube of the cosine of the angular displacement from the center of the field. The distortion is in the sense to make extended areas cover more sq. arcminute pixels than their true solid angles would require. This results in over estimating fluxes when integrating sources within fixed intensity contours.

The transformation equations for conversion between line and sample number in the map and right ascension and declination on the sky are shown below.

Forward:

define

$scale$ = 30 pixels/degree

$$A = \cos(\delta) \times \cos(\alpha - \alpha_0)$$

$$F = scale \times (180/\pi)/[\sin(\delta_0) \times \sin(\delta) + A \times \cos(\delta_0)] \qquad \text{(X.D.1)}$$

then

$$LINE = -F \times [\cos(\delta_0) \times \sin(\delta) - A \times \sin(\delta_0)]$$

$$SAMPLE = -F \times \cos(\delta) \times \sin(\alpha - \alpha_0) \qquad \text{(X.D.2)}$$

Reverse:

define

$$X = SAMPLE/(scale \times 180/\pi)$$

$$Y = LINE/(scale \times 180/\pi)$$

$$\Delta = arctan[(X^2 + Y^2)^{1/2}]$$

$$\beta = arctan(-X/Y)$$

$$XX = \sin(\delta_0) \times \sin(\Delta) \times \cos(\beta) + \cos(\delta_0) \times \cos(\Delta)$$

$$YY = \sin(\Delta) \times \sin(\beta)$$

then

$$\delta = arcsin[\sin(\delta_0) \times \cos(\Delta) - \cos(\delta_0) \times \sin(\Delta) \times \cos(\beta)]$$

$$\alpha = \alpha_0 + arctan(YY/XX) \qquad \text{(X.D.3)}$$

where δ_0 and α_0 are the declination and right ascension of the field center. The arctangent functions for β and α must be four quadrant arctangents.

D.2.b Equivalent Cylindrical Projection - Galactic Plane Fields

The Lambert normal equivalent cylindrical projection was used to provide an equal area projection of the sky within 10° of the Galactic plane. The projection cylinder is tangent to the celestial sphere at the Galactic equator and the projection proceeds by projecting radially outward from each point on the polar axis of the Galactic coordinate system in a plane parallel to the equatorial plane. The maximum angular distortion (deviation of bearing) is 0.9°. The equal area property of the transformation preserves photometric accuracy when integrating fluxes for an extended source.

The transformation equations are:

Forward:

define

$scale$ = 30 pixels/degree

then

$$LINE = -scale \times 180/\pi \times \sin(b^{II})$$

$$SAMPLE = -scale \times (l^{II} - l_0^{II}) \qquad \text{(X.D.4)}$$

Reverse:

$$l^{II} = l_0^{II} - SAMPLE/scale$$

$$b^{II} = -arcsin\,[LINE/(scale \times 180/\pi)] \qquad \text{(X.D.5)}$$

where b^{II} and l^{II} are Galactic latitude and longitude and subscript zero denotes the field center.

D.2.c Aitoff Projection - Low-Resolution All-Sky Maps

The Aitoff equal area projection was used to provide a photometrically correct map of the entire celestial sphere. Galactic coordinates were chosen as a convenient and natural coordinate system. The transformation equations are:

Forward:

define

$scale$ = 2 pixels/degree

$$\rho = arccos\,[\cos(b^{II}) \times \cos(\{l^{II} - l_0^{II}\}/2)]$$

$$\theta = arcsin\,[\cos(b^{II}) \times \sin(\{l^{II} - l_0^{II}\}/2)/\sin(\rho)] \qquad \text{(X.D.6)}$$

then

$$SAMPLE = -4 \times scale \times 180/\pi \times \sin(\rho/2) \times \sin(\theta)$$

$$LINE = \pm 2 \times scale \times 180/\pi \times \sin(\rho/2) \times \cos(\theta) \qquad \text{(X.D.7)}$$

where the '+' applies to $b^{II} < 0$ and the '-' to $b^{II} >= 0$.

Reverse:

define

$$Y = -LINE/(2 \times scale \times 180/\pi)$$

$$X = -SAMPLE/(2 \times scale \times 180/\pi)$$

$$A = (4 - X^2 - 4 \times Y^2)^{1/2}$$

then

$$b^{II} = 180/\pi \times arcsin(A \times Y)$$

$$l^{II} = l_0^{II} + 2 \times 180/\pi \times arcsin\,[A \times X/(2 \times \cos\{b^{II}\})] \qquad \text{(X.D.8)}$$

where l^{II} and b^{II} are Galactic longitude and latitude and subscript zero denotes the field center.

D.3 16.5° Images

The 16.5° images the high-resolution presentation of the IRAS sky survey in image form. Two hundred twelve (212) 16.5° × 16.5° fields cover the whole sky with field centers spaced by approximately 15°. The three sky coverages of the full mission are presented as three separate sets of 212 maps, with

some maps not included in the third coverage (Table X.D.1). A list of plate numbers vs. plate centers comprises Appendix X.2 and a map of plate locations is given in Fig. X.D.1. An individual map consists of 499×499 array of 2′×2′ pixels into which the IRAS survey data were mapped using a gnomonic projection (described in Section X.D.2.a). The 16.5° images are available as photographic prints and as digital magnetic tape. The formats of these two forms are described below. Detailed descriptions of the procedures used to produce the maps are given in Section V.G.

Table X.D.1 Plates Missing From the Third Sky Coverage

47	95	130
60	96	131
70	97	132
71	107	143
72	108	144
83	118	154
84	119	155
94	120	168

D.3.a Prints of 16.5° Images

Photographic black and white negative transparencies were produced from the digital map data with a film recorder. All four bands of each field were reproduced side by side in a rectangular format approximately 5 inches sq. intended for enlargement to 16 inches by 20 inches. Two hundred fifty-six (256) brightness levels were available with the film recorder and the brightness range in each band of each field was individually compressed, clipped and scaled to fit within these 256 levels.

The compression, clipping and scaling were accomplished by first extracting the fifth root of the surface brightness to compress the dynamic range of the data. A histogram of the fifth root map was made and the pixel values were shifted and scaled into the 0-255 range so as to saturate the lower and upper one percent of the histogram. The approximate surface brightness value of any pixel can be recovered by first comparing the density of the pixel of interest to the grey scales which show every 17th pixel value from zero to 255. The shift and scale are removed using the 0 DN = X Jy sr^{-1} and 255 DN = Y Jy sr^{-1} information in the label (see the sample label below).

The complete formula is:

$$\text{surface brightness (Jy sr}^{-1}) = \left[\frac{D}{255}(Y^{1/5} - X^{1/5}) + X^{1/5}\right]^5 \qquad \text{(X.D.9)}$$

where D is the pixel value determined by comparison with the grey scale and Y and X are obtained from the label.

Final calibration factors were not applied to the third sky coverage data before production of the photo products. Therefore, the intensities obtained using the procedure above on the third coverage may not agree with intensities found on the magnetic tape versions of the maps. The magnetic tape version uses the final IRAS catalog calibration and should be used in case of discrepancy. Intensities obtained

ORIGINAL PAGE IS
OF POOR QUALITY

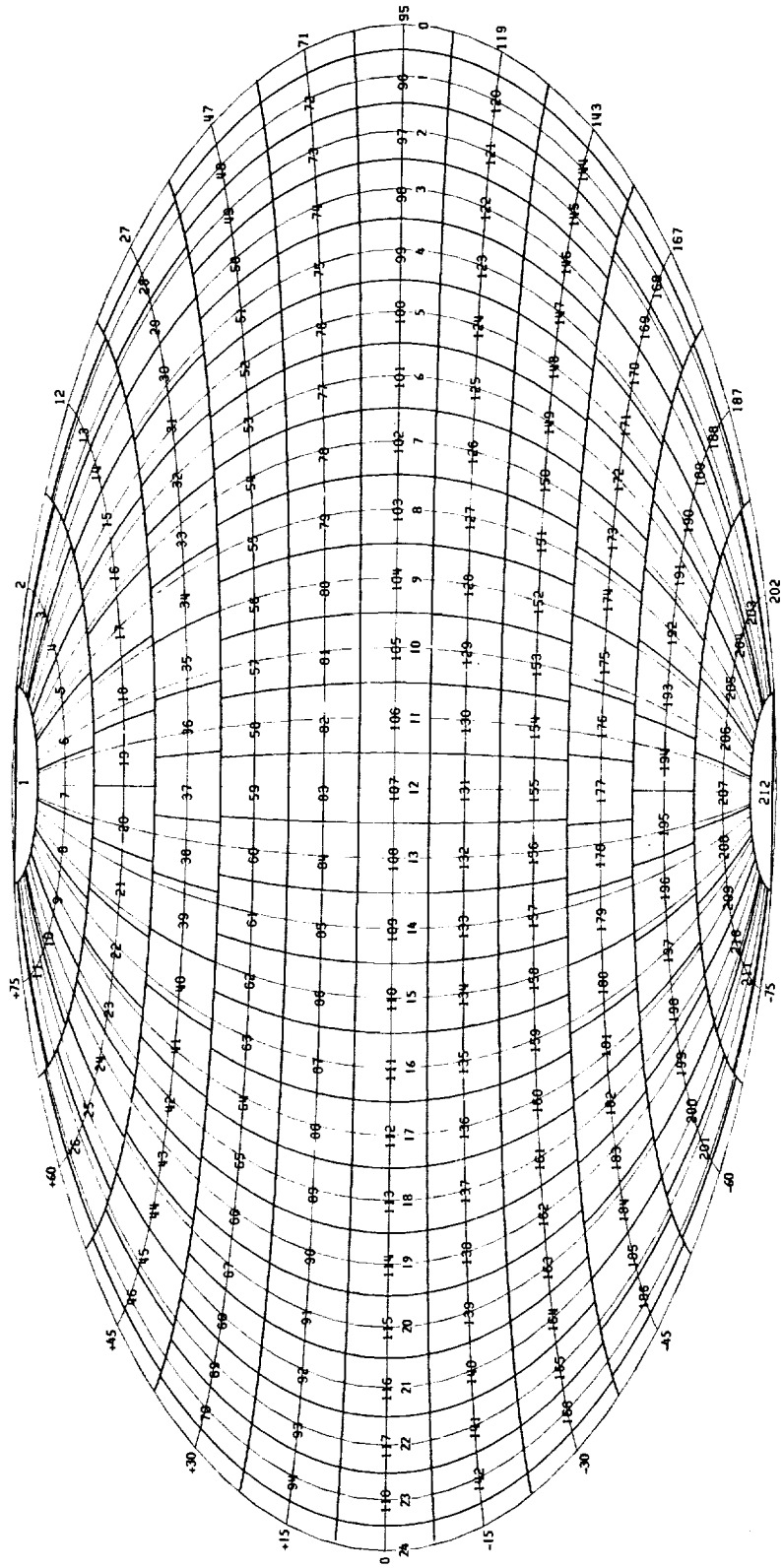

Figure X.D.1 Map of 16.5° image boundaries in equatorial coordinates.

from the third coverage photo products can be approximately corrected to the final calibration by multiplying the intensity derived from a photograph by the following factors:

12 μm	0.84
25 μm	0.80
60 μm	0.80
100 μm	0.69

The first, second and mini-survey coverage photos were corrected to the final calibration.

The coordinate system of each map is arranged so that when viewed with the printing in the label right side up north is up and east is to the left at the field center, which is adopted as pixel (0,0). In this orientation the horizontal rows of pixels are by convention called lines and the pixels within each line are called samples. Line numbers increase from top to bottom and sample numbers increase from left to right. The line numbers of the top and bottom lines are given in the label as TOP and BOTTOM, respectively. Similarly the left and right extreme sample numbers are given as LEFT and RIGHT. With this information and the tic marks along the sides of the image area the line and sample coordinates of any pixel can be determined for application of the inverse map projection formulae given above in Section X.D.2. The tic marks also allow alignment of the co-ordinate overlay grids as described in Section X.D.7.

Color composite negative transparencies in 4×5 inch format of each sky plate field have been produced by recording the 100 μm map in red (positive), the 60 μm map in green and the 12 μm map in blue. These color versions of the data are not intended for quantitative analysis. The shift and scale information in the label is difficult to read and no attempt has been made to produce a consistent color balance among the plates. In one plate a particular hue will indicate one ratio to 100 μm to 60 μm to 12 μm brightness and in another plate the ratio for that hue will be somewhat different.

Sample Label from 16.5° Image Photograph

IRAS SKYFLUX HCON: 3 FIELD: 153 DEC:-30 RA: 10:00 25 MICRON
R.A. & DEC GNOMONIC PIXEL: 2.00 ARCMIN JD:2445654.25-2445660.25
TOP:-249 BOTTOM: 249 LEFT:-249 RIGHT: 249 1 TIC = 5 PIXELS
0DN= 4.28E+ 2 JY/SR 255DN= 5.38E+ 2 MJY/SR 5TH ROOT DATE:84/08/10

First line:

SKYFLUX: refers to the 212 maps which cover the whole sky with 2′ pixels. Can also be ALL SKY for the 1/2° pixel all-sky maps.

HCON: serial number of the sky coverage

FIELD: IRAS field number. See maps in Fig. X.D.1. Can also be Galactic Plane field.

DEC,RA: coordinates of field center. DEC in degrees, RA in hours and minutes. Can also be LON and LAT for Galactic coordinate (l^{II},b^{II}) projections.

MICRON: wavelength band of the map.

Second line:

RA & DEC GNOMONIC: Projection type.
Can also be EQUIVALENT CYLINDRICAL or LON & LAT AITOFF

PIXEL: Pixel size.

JD: Julian dates of the earliest and latest data in the map, accurate to 1/2 day.

Third line:

TOP,BOTTOM,LEFT,RIGHT: Line and sample numbers at the edges of the map.

1 TIC: Spacing between the tic marks around the edge in pixels

Fourth line:

0DN, 255DN: Surface brightness values of the minimum and maximum pixels in the map.

5TH ROOT: Indicates that the fifth root of the actual surface brightness is shown. Can also be LINEAR in which case the true, uncompressed, surface brightness is shown.

DATE: Year/Month/Day on which the map was assembled.

D.3.b Tapes of 16.5° Images

The magnetic tape form of the 16.5° images contains the calibrated surface brightness data in 499×499 arrays of 2′×2′ pixels recorded in the FITS format. The article by Wells *et al.* (1981) in conjunction with the label records of each tape file gives a detailed description of the format of each map image. A brief description of the format follows and a listing of a sample FITS label can be found in Appendix X.3.

One sky coverage consists of 27 tapes of 6250 bpi (bits per inch) density. The third coverage has only 24 tapes with a total of 188 plates. Each plate consists of four surface brightness maps and four statistical weight maps, one of each for each wavelength band. The plates are ordered on the tapes by plate number and within a plate the image files are ordered: 12 μm brightness, 12 μm weight, 25 μm brightness, 25 μm weight, 60 μm brightness, 60 μm weight, 100 μm brightness and 100 μm weight. The first two records of each file contain the label, then the image appears as a stream of pixel values divided into 2880 byte records without regard for line length. The stream begins with the smallest line and smallest sample number and the sample number increases fastest. The last record is padded to 2880 bytes with zeros. Four-byte integers are used for brightness image data numbers and 2-byte integers for weight images, high order byte first. All this and other information necessary to successfully regenerate a map is contained in the FITS label records described in Appendix X.3.

D.4 Galactic Plane Maps

For convenience in dealing with the Galactic plane the survey data within 10° of the Galactic plane were remapped from the into a set of images in Galactic coordinates to cover the full circle of the Galaxy. This remapping from the 16.5° images resulted in a slight degradation in resolution even though the pixel size was the same in both sets of maps. Twenty-four 16.7° × 20° fields cover the Galactic plane with field centers at integral multiples of 15° Galactic longitude. The three sky coverages of the survey were separated into three sets of maps. The image format is 499 lines of 599 samples each, projected from Galactic coordinates with an equal area cylindrical projection (see Section X.D.2.b). Galactic plane maps are available in both photographic and FITS tape formats. Two 6250 bpi tapes of 12 maps each hold the 24 Galactic plane maps. The differences in the FITS label between the 16.5° images and the

Galactic plane maps are noted in the description and listing of the FITS label in Appendix X.3. No statistical weight images are included for the Galactic plane maps. Statistical weight information may be obtained from the 16.5° maps. Coordinate overlays described in Section X.D.7 are available for the Galactic plane maps.

D.5 Low-Resolution All-Sky Maps

The 1/2° × 1/2° beam data contained in the Zodiacal History file described below was split into the three separate sky coverages and assembled into three all-sky maps with an Aitoff equal area projection in Galactic coordinates. Two fields of each sky coverage were produced; one centered on the Galactic center and one centered on the Galactic anti-center. The pixel arrays consist of 325 lines of 649 samples each. Galactic north is in the direction of decreasing line number (up) and Galactic east in the direction of decreasing sample number (left). The all-sky maps are available in both photographic and FITS tape forms. The formats of the photographic and tape forms of all-sky maps are very similar to those of the 16.5° images (see Section X.D.3) with the differences described in the labels of the photographs and tape files. Coordinate overlays described in Section X.D.7 are available for the all-sky maps.

D.6 Zodiacal Observation History File

For convenience in the analysis and treatment of background emission from interplanetary dust (zodiacal emission) and other extremely large scale emission features, the survey data were averaged to 1/2° × 1/2° beam size and along with pointing information was preserved as a time ordered data set containing all three sky coverages of the survey. This file is available on magnetic tape written with the format described in Appendix X.4.

D.7 Coordinate Overlays

A set of coordinate overlays for the photographs is available as photographic negative transparencies in the 5 inch sq. format. The scale is identical to the corresponding map product so the overlays will be the correct size if enlarged by the same factor as the map. One overlay is provided for each declination zone from -30° to +30° where the overlays for zones of opposite sign are obtained by rotating the grids through 180°. Five overlays are provided for each declination zone between 45° and 75° to accommodate the fact that integer hour meridians cross the plates in these zones in five different configurations. Again the overlay for the zone of opposite sign is obtained by rotating the grid 180°. All integer hour meridians are labeled 00M. The hour of right ascension should be determined from the position of the plate center given in the label on the photograph. The plate numbers to which a particular overlay pertains are printed in the lower right corner of the overlay. The overlays are aligned by matching the two triangular fiducials along each edge of the overlay with the two large map border tics which straddle the center of each side of the map. The two overlays for the polar regions are similarly aligned with the fiducials and tics. The correct orientation makes the lettering on the overlay read the same way as the lettering in the plate label.

One overlay is used for all Galactic plane maps. It is aligned with the same method as the sky plates. One orientation of the overlay is used for even numbered fields and has 0° as the center longitude; the other orientation, used for all fields, has 5° as the center longitude. The tens digit of the true longitude should be obtained from label of the picture.

The overlays for the low-resolution all-sky maps come in only two varieties, $l^{II} = 0.0°$ in the center and $l^{II} = 180.0°$ in the center. Alignment of the overlays is similar to that for the other maps.

E. Low-Resolution Spectra

Two files give the data for the low-resolution spectra (LRS) which, as described in Chapter IX, consist of two bands (8-13 μm and 11-22 μm). The first file on the tape consists of a single 80-character ASCII record giving the date and version of the LRS data. The next file lists only the wavelengths corresponding to each sample of the spectra (Table X.E.1a). The last file contains the spectra and associated header information (Table X.E.1b). The spectra are in order of increasing right ascension. Both files have 80-character ASCII logical records and 256 logical records per physical record. An atlas of the spectra will be published as an *Astronomy and Astrophysics Supplement.*

E.1 Catalog Header File

Distance from Slit. ANGLE (100)

As described in detail in Chapter IX, each sample in the spectrum corresponds to a certain in-scan distance of the source from the centerline of the spectrometer entrance aperture. ANGLE lists these angular distances.

Wavelength Calibration: LAMBDA1, LAMBDA2

There is a non-linear relation between the displacement of the source from the centerline of the spectrometer and the sampled wavelength. The wavelengths corresponding to each sample (or ANGLE) are given in LAMBDA1 and LAMBDA2 for the two wavelength bands. The beginning and end of each spectrum contain measurements that lie outside of the wavelength coverage of the instrument but which can be used for electronic baseline determination. The wavelength values corresponding to these values of sample number (or ANGLE) are set to 0.

E.2 Spectra Records

The items starting at bytes 0 through 25 are identical to the items with the same names in the point source catalog (see Section X.B.1). This is also the case for the items starting at bytes 71, 73, 75 and 960.

Number of Spectra: NSPECTRA, NACCEPT

NSPECTRA is the number of spectra of this source observed; NACCEPT are the numbers of 8-13 μm and the 11-22 μm spectrum halves ultimately averaged to make the entry in the catalog.

Characterization of the Spectrum: LRSCHAR

A description of the method of characterization is given in Section IX.D. Table X.E.2 lists the spectral classes used to characterize the spectrum.

Quality of the Spectrum Halves: SPQUAL

Depending on the signal-to-noise ratio of the 8-13 μm and 11-22 μm halves of the spectra, the number of accepted spectra halves and the difference in level of the baselines on either side of the spectrum halves, a quality digit is assigned to each half of the spectrum; 1 indicates good quality, 2 moderate quality, and 3 barely acceptable.

Scale Factor for All Spectrum Flux Densities: SCALE

Multiplying the integers BASELINE, NOISE, and SPECTRUM by the factor SCALE converts the values into units of W m^{-2} μm^{-1}.

Baseline of Spectrum Halves: BASELINE

These four values give the average value of samples 1 through 20 (short wavelength end) and 81 through 100 (long wavelength end) of both the 8-13 μm and the 11-22 μm halves of the spectrum.

RMS Noise: NOISE

Using the twenty samples on the long wavelength end used for BASELINE, the rms noise per spectrum half is determined.

Signal-to-Noise Ratio: SNR

The average value of the samples in the wavelength ranges 8-13 μm and 11-22 μm, respectively, are divided by the NOISE values determined.

Baseline Asymmetry: ASYMM

This value indicates by what fraction of the average signal the baselines on the short and long wavelength sides of the spectrum halves differ. A large baseline asymmetry indicates that a confusing source may have contaminated the spectrum. The baseline asymmetry is usually large near the Galactic plane.

LRS/Survey Flux Ratio: SRATIO

The ratio of the integrated flux (after convolution of the spectrum flux densities with the 12 μm band pass of the survey instrument) in the spectrum and the 12 μm survey flux is given in this item. Normally this value should be close to unity (Section IX.C). As the 11-22 μm part of the LRS spectrum hardly overlaps with the 25 μm survey band, a ratio of LRS/survey for this band is not significant.

The Spectrum: SPECTRUM

The integer values of the spectrum must be multiplied by SCALE for conversion to W m^{-2} μm^{-1}.The wavelengths corresponding to the 100 samples given for the 8-13 μm and the 11-22 μm halves of the spectrum are given in the catalog header file. Values for non-significant wavelengths are set to zero. For baseline interpolation, either the sample numbers or the ANGLE (distance in arcmin from the spectrometer center line) can be used.

Table X.E.1a Header Information for Catalog of Spectra

Start Byte	Name	Description	Units	Format
0	ANGLE	Angle from center of slit (one number per sample)	arc min	100F8.4
800	LAMBDA1	Wavelength in 8-13 μm corresponding to each sample	μm	100F8.4
1600	LAMBDA2	Wavelength in 11-22 μm corresponding to each sample	μm	100F8.4

Table X.E.1b. Format of Spectra in Catalog

Start Byte	Name	Description	Units	Format
0	NAME	Source name	---	11A1
11	HOURS	RA 1950	hrs	I2
13	MINUTE	RA 1950	min	I2
15	SECOND	RA 1950	deci-sec	I3
18	DSIGN	Declination sign	±	A1
19	DECDEG	DEC 1950	arc deg	I2
21	DECMIN	DEC 1950	arc min	I2
23	DECSEC	DEC 1950	arc sec	I2
25	FLUX	Averaged non-color corrected flux densities (1 value per band)	Jy	4E9.3
61	NSPECTRA	No. of observed spectra	---	I2
63	NACCEPT	No. of accepted spectrum halves	---	2I2
67	LRSCHAR	Characterization of spectrum	---	2I1
69	SPQUAL	Quality of 8-13 μm and 11-22 μm parts of spectra	---	2I1
71	VAR	Percent of variability likelihood (from catalog)	---	I2
73	NID (<25)	No. of associations	---	I2
75	IDTYPE	Type of association	---	I1
76	SPARE	4 spare bytes	---	4A1
		(----------new record----------)		
80	BASELINE	Average of outer 20 samples of spectra. Short and long wavelength end for each spectrum half	scaled by SCALE	4I4
96	NOISE	RMS noise per sample (one value per spectrum half)	scaled by SCALE	2I4
104	SNR	Signal-to-noise ratio (average signal in spectrum part divided by noise, one value per spectrum half)	---	2E10.3

Table X.E.1b Format of Spectra in Catalog (Continued)

Start Byte	Name	Description	Units	Format
124	ASYMM	Relative baseline asymmetry (difference of left and right baselines divided by average signal. one value per band)	--- ---	2E10.3
144	SRATIO	Ratio of integrated LRS flux to 12 μm survey flux	---	F5.2
149	SCALE	Scale factor for all flux densities	$W\ m^{-2}\ \mu m^{-1}$	E11.5
		(----------new record----------)		
160	SPECTRUM	100 samples for each of the two bands (8-13 μm, 11-22 μm), scaled by SCALE	scaled by SCALE	200I4
		(----------new record----------)		
960	ID#1	Association field from main catalog (see Section X.B.1)	---	40A1
1000	ID#2	additional records as required.		

Authors:

C. Beichman, T. Chester, T.N. Gautier, G. Helou, C. Oken, E. Raimond, B.T. Soifer and D. Walker.

References:

Richardus, Peter and Ron K. Adler, 1972, *Map Projections for Geodesists, Cartographers and Geographers*, North-Holland Publishing Company, Amsterdam-London and American Elsevier Publishing Company, New York.

Wells, D., Greisen, E.R. and Harten, R. 1981, *Astron. and Astrophys.* [*Suppl.*], **44**, 363.

Appendix X.1 Regions of High Source Density

As discussed in section V.H.6, regions with more sources per sq. deg than the confusion limit in a given band were processed according to more stringent rules to insure the reliability of the data presented in the catalog. The regions so processed were selected on a band by band basis depending on the number of sources with high or moderate quality fluxes located within a 1 sq. deg bin in ecliptic coordinates.

Users of the catalog who want to know the identity of those regions may use a machine readable file that lists the bin number (see below), a flag called HSD which indicates which bands in that bin were processed according to high source density rules, the ecliptic coordinates of the center of the bin, and its length in ecliptic longitude. All bins have a height of 1° in ecliptic latitude. The file consists of 80-character ASCII records with 256 records per physical block. The information for two bins fits within a single 80-character logical record. This file is preceded on the tape by a short file which contains a single 80-character ASCII record which lists the date and version number of the information.

The flag HSD is hex-encoded by band, as described in Table X.B.2. In this notation each band corresponds to one of the four bits of a hex digit. 12 μm corresponds to bit 0 (Least Significant Bit) and 100 μm to bit 3, etc. If a band went through high source density processing in that band, then the appropriate bit in the hex digit was set. Thus, if high source density rules were invoked at 25, 60 and 100 um, HSD would have the value 1110 (binary) = E (hex).

Ecliptic bins start at the ecliptic north pole and step around the sky in bands of constant ecliptic latitude, stepping 1° southward after completing each band. The length of the bin, in ecliptic longitude, was adjusted for the cosine of the ecliptic latitude to maintain an approximately constant area. FORTRAN programs are given below to convert from bin number to ecliptic coordinates and vice versa. There is a known bug in the computation of bins at ecliptic latitude 60°, causing bin 2842 to be skipped. The following program, while incorrect in this way, will give results consistent with the bin numbers used in the data processing. To avoid problems with roundoff errors within a few arcseconds of bin boundaries, all arithmetic should be calculated in double precision.

FORTRAN Program to Convert between Ecliptic Position and Bin Number

```
C
C CONVERT AN ECLIPTIC POSITION TO BIN NUMBER.
      SUBROUTINE P2BIN(LAM,BET,BIN)
      IMPLICIT REAL*8 A-H, P-Z
      REAL*8 LAM,BET,LSIZE,R2D/57.2957795/
      INTEGER*4 BIN,I,J,N,MAXBIN(182)
      COMMON /LATBND/MAXBIN
C
      I = 90. - BET*R2D + 2.5
      N = MAXBIN(I) - MAXBIN(I-1)
      LSIZE = 360./FLOAT(N)
      J = LAM*R2D/LSIZE + 1
      BIN = MAXBIN(I-1) + J
      RETURN
      END


C
C CONVERT A BIN NUMBER TO A CENTER POSITION AND LONGITUDE LENGTH.
      SUBROUTINE BIN2P(BIN,CLON,CLAT,LWIDTH)
      IMPLICIT REAL*8 A-H, P-Z
      INTEGER*4 BIN,I,J,MAXBIN(182),FIRST
      REAL*8 CLON,CLAT,LWIDTH,R2D/57.2957795/,NBINS
      COMMON /LATBND/MAXBIN
C
      DO 100 I=1,182
        IF(MAXBIN(I) .GE. BIN) GOTO 150
  100 CONTINUE
  150 I = I - 1
      FIRST = MAXBIN(I) + 1
      NBINS = MAXBIN(I+1) - FIRST + 1
      LWIDTH = 360./NBINS
      J = BIN - FIRST
      CLON = DFLOAT(J)*LWIDTH + LWIDTH/2.
      CLAT = 90. -DFLOAT(I-1)
      LWIDTH = LWIDTH/R2D
      CLON = CLON/R2D
      CLAT = CLAT/R2D
      RETURN
      END
C
C DATA SUBPROGRAM.
        BLOCK DATA
        INTEGER*4 MAXBIN(182)
        DATA MAXBIN
     *    /0,1,7,19,37,62,93,130,173,223,279,341,409,483,563,
     *    650,743,842,947,1058,1175,1298,1427,1561,1701,1847,1999,
     *    2156,2319,2488,2662,2841,3026,3216,3412,3613,3819,4030,
```

```
*     4246,4467,4693,4924,5160,5400,5645,5895,6149,6407,6670,
*     6937,7208,7483,7762,8045,8332,8623,8917,9215,9516,9821,
*     10129,10440,10754,11071,11391,11714,12040,12368,12699,
*     13032,13368,13706,14046,14388,14732,15078,15425,15774,
*     16124,16476,16829,17183,17538,17894,18251,18609,18967,
*     19326,19685,20044,20403,20763,21122,21481,21840,22199,
*     22557,22915,23272,23628,23983,24337,24690,25042,25392,
*     25741,26088,26434,26778,27120,27460,27798,28134,28467,
*     28798,29126,29452,29775,30095,30412,30726,31037,31345,
*     31650,31951,32249,32543,32834,33121,33404,33683,33958,
*     34229,34496,34759,35017,35271,35521,35766,36006,36242,
*     36473,36699,36920,37136,37347,37553,37754,37950,38140,
*     38325,38505,38679,38848,39011,39168,39320,39466,39606,
*     39740,39869,39992,40109,40220,40325,40424,40517,40604,
*     40684,40758,40826,40888,40944,40994,41037,41074,41105,
*     41130,41148,41160,41166,41167/
COMMON /LATBND/MAXBIN
END
```

Table X.Ap1.1 Format of File of High Source Density Bins

Start Byte	Name	Description	Units	Format
00	BINNUM	SDAS Bin Number	---	I6
06	HSD	Bands processed for high source density, hex encoded by band.	---	A2
08	LAMBDA	Ecliptic longitude of bin center	deg	10.5
18	BETA	Ecliptic latitude of bin center	deg	10.5
28	LENGTH	Length of bin in ecliptic longitude	deg	10.5
38	SPARE	2 spare bytes	---	2A1
40-79		bytes 00-39 are repeated for next bin		

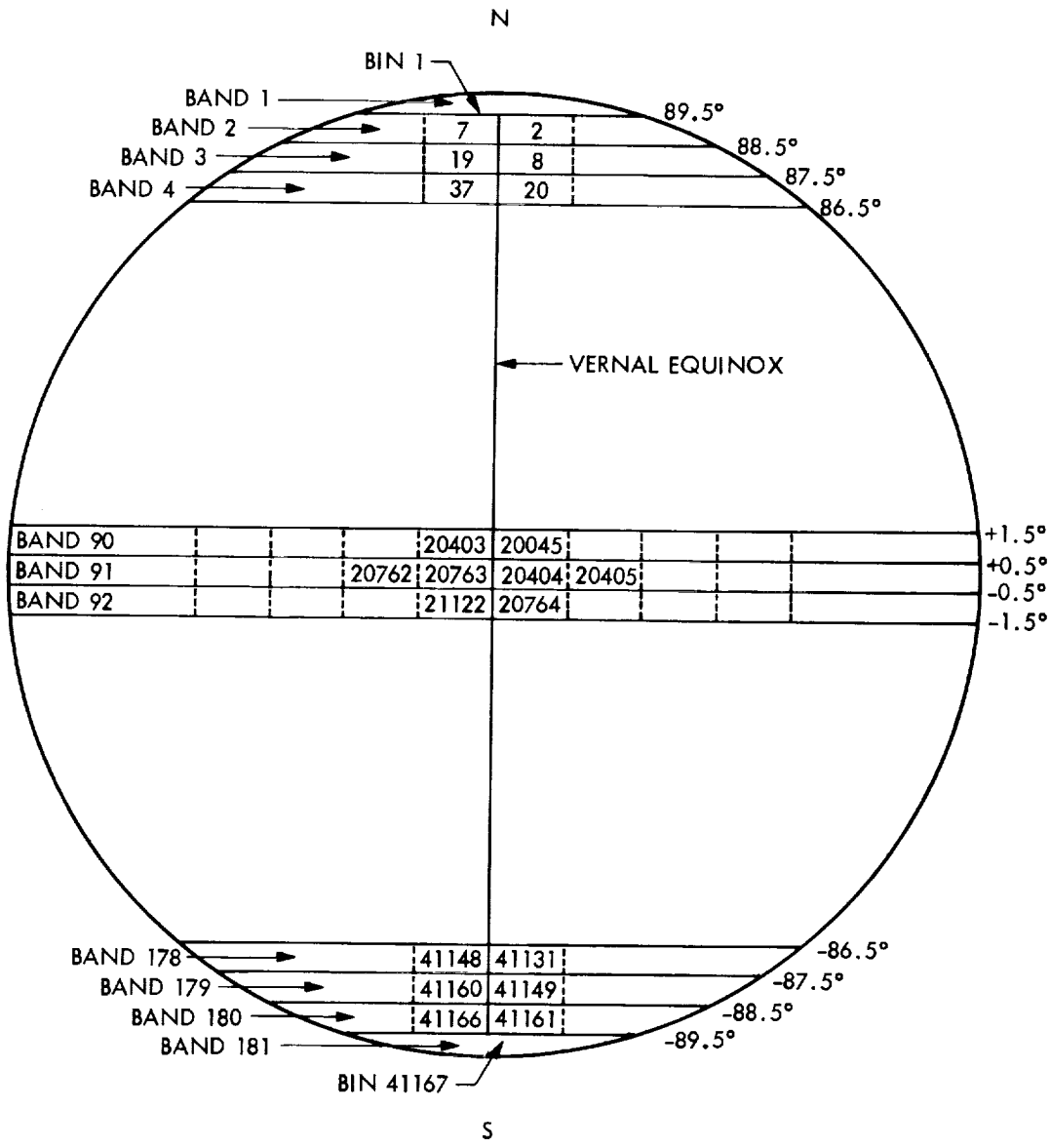

Figure X.Ap.1 Scheme for obtaining 1 sq. deg bins in ecliptic coordinates.

Appendix X.2 Location of 16.5° Image Fields

Table X.Ap2.1 16.5° Field Centers (Equinox 1950)

PLATE	DEC	RA	PLATE	DEC	RA	PLATE	DEC	RA
1	+90	0H 00M*	43	+45	19H 12M	87	+15	16H 00M
			44		20H 24M	88		17H 00M
2	+75	0H 00M	45		21H 36M	89		18H 00M
3		2H 24M	46		22H 48M	90		19H 00M
4		4H 48M	47	+30	0H 00M	91		20H 00M
5		7H 12M	48		1H 00M	92		21H 00M
6		9H 36M	49		2H 00M	93		22H 00M
7		12H 00M	50		3H 00M	94		23H 00M
8		14H 24M	51		4H 00M	95	+0	0H 00M
9		16H 48M	52		5H 00M	96		1H 00M
10		19H 12M	53		6H 00M	97		2H 00M
11		21H 36M	54		7H 00M	98		3H 00M
			55		8H 00M	99		4H 00M
12	+60	0H 00M	56		9H 00M	100		5H 00M
13		1H 36M	57		10H 00M	101		6H 00M
14		3H 12M	58		11H 00M	102		7H 00M
15		4H 48M	59		12H 00M	103		8H 00M
16		6H 24M	60		13H 00M	104		9H 00M
17		8H 00M	61		14H 00M	105		10H 00M
18		9H 36M	62		15H 00M	106		11H 00M
19		11H 12M	63		16H 00M	107		12H 00M
20		12H 48M	64		17H 00M	108		13H 00M
21		14H 24M	65		18H 00M	109		14H 00M
22		16H 00M	66		19H 00M	110		15H 00M
23		17H 36M	67		20H 00M	111		16H 00M
24		19H 12M	68		21H 00M	112		17H 00M
25		20H 48M	69		22H 00M	113		18H 00M
26		22H 24M	70		23H 00M	114		19H 00M
						115		20H 00M
27	+45	0H 00M	71	+15	0H 00N	116		21H 00M
28		1H 12M	72		1H 00M	117		22H 00M
29		2H 24M	73		2H 00M	118		23H 00M
30		3H 36M	74		3H 00M	119	-15	0H 00M
31		4H 48M	75		4H 00M	120		1H 00M
32		6H 00M	76		5H 00M	121		2H 00M
33		7H 12M	77		6H 00M	122		3H 00M
34		8H 24M	78		7H 00M	123		4H 00M
35		9H 36M	79		8H 00M	124		5H 00M
36		10H 48M	80		9H 00M	125		6H 00M
37		12H 00M	81		10H 00M	126		7H 00M
38		13H 12M	82		11H 00M	127		8H 00M
39		14H 24M	83		12H 00M	128		9H 00M
40		15H 36M	84		13H 00M	129		10H 00M
41		16H 48M	85		14H 00M	130		11H 00M
42		18H 00M	86		15H 00M	131		12H 00M

Table X.Ap2.1 16.5° Field Centers (Continued)

PLATE	DEC	RA	PLATE	DEC	RA	PLATE	DEC	RA
132	-15	13H 00M	171	-45	4H 48M	211	-75	21H 36M
133		14H 00M	172		6H 00M	212	-90	0H 00M*
134		15H 00M	173		7H 12M			
135		16H 00M	174		8H 24M			
136		17H 00M	175		9H 36M			
137		18H 00M	176		10H 48M			
138		19H 00M	177		12H 00M			
139		20H 00M	178		13H 12M			
140		21H 00M	179		14H 24M			
141		22H 00M	180		15H 36M			
142		23H 00M	181		16H 48M			
			182		18H 00M			
143	-30	0H 00M	183		19H 12M			
144		1H 00M	184		20H 24M			
145		2H 00M	185		21H 36M			
146		3H 00M	186		22H 48M			
147		4H 00M						
148		5H 00M	187	-60	0H 00M			
148		5H 00M	188		1H 36M			
149		6H 00M	189		3H 12M			
150		7H 00M	190		4H 48M			
151		8H 00M	191		6H 24M			
152		9H 00M	192		8H 00M			
153		10H 00M	193		9H 36M			
154		11H 00M	194		11H 12M			
155		12H 00M	195		12H 48M			
156		13H 00M	196		14H 24M			
157		14H 00M	197		16H 00M			
158		15H 00M	198		17H 36M			
159		16H 00M	199		19H 12M			
160		17H 00M	200		20H 48M			
161		18H 00M	201		22H 24M			
162		19H 00M						
163		20H 00M	202	-75	0H 00M			
164		21H 00M	203		2H 24M			
165		22H 00M	204		4H 48M			
166		23H 00M	205		7H 12M			
			206		9H 36M			
167	-45	0H 00M	207		12H 00M			
168		1H 12M	208		14H 24M			
169		2H 24M	209		16H 48M			
170		3H 36M	210		19H 12M			

* These RA's produce the correct orientations when used in the transformation formulae.

Appendix X.3 Sample FITS Headers

Header for Sky Plate Intensity

```
SIMPLE =                          T  / STANDARD FITS FORMAT
BITPIX =                         32  / 4 BYTE TWOS COMPL INTEGERS
NAXIS =                           3  / NUMBER OF AXES
NAXIS1 =                         nn  / # SAMPLES PER LINE (FASTEST VARY INDEX)
NAXIS2 =                         mm  / # LINES OF DATA IN IMAGE FILE
NAXIS3 =                          1  / # WAVELENGTHS
BSCALE =                S.ssssssE-ee  / TRUE=TAPE*SCALE+BZERO
BZERO =                        0.0   /
BUNIT =      'JY/SR'                 / INTENSITY
BLANK =                  -2000000000  / TAPE VALUE FOR EMPTY PIXEL
CRVAL1 =                       DD.dd  / RA AT ORIGIN (DEGREES)
CRPIX1 =                        xxx.  / SAMPLE AXIS ORIGIN (PIXEL)
CTYPE1 =     'RA---TAN'              / DECREASES IN VALUE AS SAMPLE INDEX
COMMENT                                INCREASES   (GNOMONIC PROJECTION)
CDELT1 =            -3.333333E-02    / COORD VALUE INCREMENT DEG/PIXEL
COMMENT                                AT ORIGIN ON SAMPLE AXIS
CRVAL2 =                       DD.dd  / DEC AT ORIGIN (DEGREES)
CRPIX2 =                        yyy.  / LINE AXIS ORIGIN (PIXEL)
CTYPE2 =     'DEC--TAN'              / DECREASES IN VALUE AS LINE INDEX
COMMENT                                INCREASES   (GNOMONIC PROJECTION)
CDELT2 =            -3.333333E-02    / COORD VALUE INCREMENT DEG/PIXEL
COMMENT                                AT ORIGIN ON LINE AXIS
CRVAL3 =                     zzzE-6  / WAVELENGTH IN METERS
CRPIX3 =                         1.
CTYPE3 =     'LAMBDA  '
CDELT3 =                         0.
DATAMAX =            D.ddddddE ee    / JY/SR   (TRUE VALUE)
DATAMIN =            D.ddddddE ee    / JY/SR   (TRUE VALUE)
EPOCH =                       1950.  / EME50
DATE-MAP =   '01/11/84'              / MAP RELEASE DATE
DATE =       'DD/MM/YY'              / DATE THIS TAPE WRITTEN
ORIGIN =     'JPL-IRAS'              / INSTITUTION
TELESCOP =   'IRAS    '
INSTRUME =   'SKYPLATE'              / IRAS SKY PLATE
OBJECT =     'PLnnn Hn'              / PLATE NUMBER / HCON
PROJTYPE =   'GNOMONIC'              / PROJECTION TYPE
COMMENT                                MINSOP = MMM;   MAXSOP = NNN
COMMENT                                LOGTAG = VSFLOG( 7.6)
COMMENT                                GEOMTAG = GEOM( 7.5)
COMMENT
COMMENT      PROJECTION FORMULAE:
COMMENT          FORWARD FORMULA; RA0 AND DEC0 ARE THE PLATE CENTER
COMMENT      R2D = 45. / ATAN(1.)
COMMENT      PIX = 30.
COMMENT      A = COS(DEC) * COS(RA0 - RA)
COMMENT      F = PIX * R2D / (SIN(DEC0) * SIN(DEC) + A * COS(DEC0))
COMMENT      SAMPLE = -F * COS(DEC) * SIN(RA-RA0)
COMMENT      XLINE = -F * (COS(DEC0) * SIN(DEC) - A * SIN(DEC0))
COMMENT
COMMENT          INVERSE FORMULA; REQUIRES ARCSINE
```

```
COMMENT     X = SAMPLE / (PIX * R2D)
COMMENT     Y = LINE / (PIX * R2D)
COMMENT     DELTA = ATAN(SQRT(X*X + Y*Y))
COMMENT     BETA = ATAN2(-X,Y)
COMMENT     DEC = ASIN(SIN(DEC0)*COS(DELTA)-COS(DEC0)*SIN(DELTA)*COS(BETA))
COMMENT     XX = SIN(DEC0)*SIN(DELTA)*COS(BETA)+COS(DEC0)*COS(DELTA)
COMMENT     YY = SIN(DELTA)*SIN(BETA)
COMMENT     RA = RA0 + ATAN2(YY,XX)
COMMENT     REFERENCES:
COMMENT     IRAS SDAS SOFTWARE INTERFACE SPECIFICATION(SIS)  #623-94/NO. SF05
COMMENT     ASTRON. ASTROPHYS. SUPPL. SER. 44,(1981) 363-370 (RE:FITS)
COMMENT     RECONCILIATION OF FITS PARMS W/ SIS SFO5 PARMS:
COMMENT     NAXIS1 = (ES - SS + 1); NAXIS2 = (EL - SL + 1);
COMMENT     CRPIX1 = (1 - SS);      CRPIX2 = (1 - SL)
END
```

Header for 16.5 deg Image Weight

```
SIMPLE =                                T  / STANDARD FITS FORMAT
BITPIX =                               16  / 2 BYTE TWOS COMPL INTEGERS
NAXIS =                                 3  / NUMBER OF AXES
NAXIS1 =                               nn  / # SAMPLES PER LINE (FASTEST VARY NDEX
NAXIS2 =                               mm  / # LINES OF DATA IN IMAGE FILE
NAXIS3 =                                1  / # WAVELENGTHS
BSCALE =                               1.  / TRUE=TAPE*SCALE+BZERO
BZERO =                               0.0  /
BUNIT =                    '        '      / STATISTICAL WEIGHT
BLANK =                                 0  / TAPE VALUE FOR EMPTY PIXEL
CRVAL1 =                            DD.dd  / RA AT ORIGIN (DEGREES)
CRPIX1 =                             xxx.  / SAMPLE AXIS ORIGIN (PIXEL)
CTYPE1 =           'RA---TAN'              / DECREASES IN VALUE AS SAMPLE INDEX
COMMENT                                      INCREASES   (GNOMONIC PROJECTION)
CDELT1 0=                    -3.333333E-02  / COORD VALUE INCREMENT DEG/PIXEL
COMMENT                                      AT ORIGIN ON SAMPLE AXIS
CRVAL2 =                            DD.dd  / DEC AT ORIGIN (DEGREES)
CRPIX2 =                             yyy.  / LINE AXIS ORIGIN (PIXEL)
CTYPE2 =           'DEC--TAN'              / DECREASES IN VALUE AS LINE INDEX
COMMENT                                      INCREASES   (GNOMONIC PROJECTION)
CDELT2 =                     -3.333333E-02  / COORD VALUE INCREMENT DEG/PIXEL
COMMENT                                      AT ORIGIN ON LINE AXIS
CRVAL3 =                           z.zzE-6  / WAVELENGTH IN METERS
CRPIX3 =                                1.
CTYPE3 =           'LAMBDA  '
CDELT3 =                                0.
DATAMAX =                    D.ddddddE ee   / DIMENSIONLESS
DATAMIN =                    D.ddddddE ee   / DIMENSIONLESS
EPOCH =                              1950.  / EME50
DATE-MAP =         '01/11/84'               / MAP RELEASE DATE
DATE =             'DD/MM/YY'               / DATE THIS TAPE WRITTEN
ORIGIN =           'JPL-IRAS'               / INSTITUTION
TELESCOP =         'IRAS    '
INSTRUME =         'SKYPLATE'               / IRAS SKY PLATE
OBJECT =           'PLnnn Hn'               / PLATE NUMBER / HCON
PROJTYPE =         'GNOMONIC'               / PROJECTION TYPE
COMMENT                                      MINSOP = MMM;   MAXSOP = NNN
COMMENT                                      LOGTAG = VSFLOG (7.8)
COMMENT                                      GEOMTAG = GEOM (7.5)
COMMENT
COMMENT    PROJECTION FORMULAE:
COMMENT        FORWARD FORMULA; RA0 AND DEC0 ARE THE PLATE CENTER
COMMENT    R2D = 45. / ATAN(1.)
COMMENT    PIX = 30.
COMMENT    A = COS(DEC) * COS(RA0 - RA)
COMMENT    F = PIX * R2D / (SIN(DEC0) * SIN(DEC) + A * COS(DEC0))
COMMENT    SAMPLE = -F * COS(DEC) * SIN(RA-RA0)
COMMENT    XLINE = -F * (COS(DEC0) * SIN(DEC) - A * SIN(DEC0))
COMMENT
COMMENT        INVERSE FORMULA; REQUIRES ARCSINE
COMMENT    X = SAMPLE / (PIX * R2D)
COMMENT    Y = LINE / (PIX * R2D)
COMMENT    DELTA = ATAN(SQRT(X*X + Y*Y))
```

```
COMMENT     BETA = ATAN2(-X,Y)
COMMENT     DEC = ASIN(SIN(DEC0)*COS(DELTA)-COS(DEC0)*SIN(DELTA)*COS(BETA))
COMMENT     XX = SIN(DEC0)*SIN(DELTA)*COS(BETA)+COS(DEC0)*COS(DELTA)
COMMENT     YY = SIN(DELTA)*SIN(BETA)
COMMENT     RA = RA0 + ATAN2(YY,XX)
COMMENT     REFERENCES:
COMMENT     IRAS SDAS SOFTWARE INTERFACE SPECIFICATION(SIS)  #623-94/NO. SF05
COMMENT     ASTRON. ASTROPHYS. SUPPL. SER. 44,(1981) 363-370 (RE:FITS)
COMMENT     RECONCILIATION OF FITS PARMS W/ SIS SFO5 PARMS:
COMMENT     NAXIS1 = (ES - SS + 1); NAXIS2 = (EL - SL + 1);
COMMENT     CRPIX1 = (1 - SS);      CRPIX2 = (1 - SL)
END
```

Header for Galactic Plane Fields

```
SIMPLE =                          T  / STANDARD FITS FORMAT
BITPIX =                         32  / 4 BYTE TWOS COMPL INTEGERS
NAXIS =                           3  / NUMBER OF AXES
NAXIS1 =                         nn  / # SAMPLES PER LINE (FASTEST VARY NDEX)
NAXIS2 =                         mm  / # LINES OF DATA IN IMAGE FILE
NAXIS3 =                          1  / # WAVELENGTHS
BSCALE =              S.SSSSSSE-ee   / TRUE=TAPE*SCALE+BZERO
BZERO =                        0.0   /
BUNIT =  'JY/SR'                     / INTENSITY
BLANK =                -2000000000   / TAPE VALUE FOR EMPTY PIXEL
CRVAL1 =                     DD.dd   / GALACTIC LONGITUDE AT ORIGIN (DEGREES)
CRPIX1 =                      xxx.   / SAMPLE AXIS ORIGIN (PIXEL)
CTYPE1 =  'LON       '               / DECREASES IN VALUE AS SAMPLE INDEX
COMMENT                               INCREASES   (LAMBERT EQUIVALENT
COMMENT                               CYLINDRICAL PROJECTION)
CDELT1 =           -3.333333E-02      / COORD VALUE INCREMENT DEG/PIXEL
COMMENT                               AT ORIGIN ON SAMPLE AXIS
CRVAL2 =                       0.0   / GALACTIC LATITUDE AT ORIGIN (DEGREES)
CRPIX2 =                      yyy.   / LINE AXIS ORIGIN (PIXEL)
CTYPE2 =  'LAT-SIN   '               / DECREASES IN VALUE AS LINE INDEX
COMMENT                               INCREASES   (LAMBERT EQUIVALENT
COMMENT                               CYLINDRICAL PROJECTION)
CDELT2 =           -3.333333E-02      / COORD VALUE INCREMENT DEG/PIXEL
COMMENT                               AT ORIGIN ON LINE AXIS
CRVAL3 =                   zzzE-6    / WAVELENGTH IN METERS
CRPIX3 =                       1.
CTYPE3 =  'LAMBDA    '
CDELT3 =                       0.
DATAMAX =            D.ddddddE ee    / JY/SR   (TRUE VALUE)
DATAMIN =            D.ddddddE ee    / JY/SR   (TRUE VALUE)
EPOCH =                     1950.    / EME50
DATE-MAP =  '01/11/84'               / MAP RELEASE DATE
DATE =  'DD/MM/YY'                   / DATE THIS TAPE WRITTEN
ORIGIN =  'JPL-IRAS'                 / INSTITUTION
TELESCOP =  'IRAS    '
INSTRUME =  'GALPLANE'               / IRAS GALACTIC PLANE
OBJECT =  'GPLnn Hn'                 / GALACTIC PLANE PLATE NUMBER / HCON
PROJTYPE =  'LAMBECYL'               / PROJECTION TYPE
COMMENT
COMMENT   PROJECTION FORMULAE:
COMMENT       FORWARD FORMULA; XLON0 IS THE LONGITUDE OF PLATE CENTER
COMMENT   R2D = 45. / ATAN(1.)
COMMENT   PIX = 30.
COMMENT   XLINE = -SIN(XLAT) * PIX * R2D
COMMENT   SAMPLE = -(XLON - XLON0) * PIX
COMMENT
COMMENT       INVERSE FORMULA; ARCSINE IS REQUIRED
COMMENT   XLON = XLON0 - SAMPLE / PIX
COMMENT   XLAT = -ASIN(XLINE / (PIX * R2D))
COMMENT   REFERENCES:
COMMENT   IRAS SDAS SOFTWARE INTERFACE SPECIFICATION(SIS)  #623-94/NO. SF05
COMMENT   ASTRON. ASTROPHYS. SUPPL. SER. 44,(1981) 363-370 (RE:FITS)
```

COMMENT RECONCILIATION OF FITS PARMS W/ SIS SFO5 PARMS:
COMMENT NAXIS1 = (ES - SS + 1); NAXIS2 = (EL - SL + 1);
COMMENT CRPIX1 = (1 - SS) CRPIX2 = (1 - SL)

Header for Low-Resolution All-Sky Image (Galactic Center)

```
SIMPLE =                          T   / STANDARD FITS FORMAT
BITPIX =                         32   / 4 BYTE TWOS COMPL INTEGERS
NAXIS =                           3   / NUMBER OF AXES
NAXIS1 =                         nn   / # SAMPLES PER LINE (FASTEST VARY NDEX)
NAXIS2 =                         mm   / # LINES OF DATA IN IMAGE FILE
NAXIS3 =                          1   / # WAVELENGTHS
BSCALE =                S.ssssssE-ee   / TRUE=TAPE*SCALE+BZERO
BZERO =                        0.0    /
BUNIT =      'JY/SR'                  / INTENSITY
BLANK =                  -2000000000  / TAPE VALUE FOR EMPTY PIXEL
CRVAL1 =                       DD.dd  / GALACTIC LONGITUDE AT ORIGIN (DEGREES)
CRPIX1 =                        xxx.  / SAMPLE AXIS ORIGIN (PIXEL)
CTYPE1 =     'LON-ATF '               / DECREASES IN VALUE AS SAMPLE INDEX
COMMENT                                 INCREASES   (AITOFF PROJECTION)
CDELT1 =                        -0.5  / COORD VALUE INCREMENT DEG/PIXEL
COMMENT                                 AT ORIGIN ON SAMPLE AXIS
CRVAL2 =                        0.0   / GALACTIC LATITUDE AT ORIGIN (DEGREES)
CRPIX2 =                        yyy.  / LINE AXIS ORIGIN (PIXEL)
CTYPE2 =     'LAT-ATF '               / DECREASES IN VALUE AS LINE INDEX
COMMENT                                 INCREASES   (AITOFF PROJECTION)
CDELT2 =                        -0.5  / COORD VALUE INCREMENT DEG/PIXEL
COMMENT                                 AT ORIGIN ON LINE AXIS
CRVAL3 =                     z.zzE-6  / WAVELENGTH IN METERS
CRPIX3 =                          1.
CTYPE3 =     'LAMBDA  '
CDELT3 =                          0.
DATAMAX =              D.ddddddE ee   / JY/SR   (TRUE VALUE)
DATAMIN =              D.ddddddE ee   / JY/SR   (TRUE VALUE)
EPOCH =                        1950.  / EME50
DATE-MAP =   '01/11/84'               / MAP RELEASE DATE
DATE =       'DD/MM/YY'               / DATE THIS TAPE WRITTEN
ORIGIN =     'JPL-IRAS'               / INSTITUTION
INSTRUME =   'ALL SKY '               / IRAS LOW RES ALL-SKY
OBJECT =     'CENTER n'               / ALL-SKY GALACTIC CENTER / HCON
PROJTYPE =   'AITOFF  '               / PROJECTION TYPE
COMMENT                                 MINSOP = MMM;   MAXSOP = NNN
COMMENT
COMMENT     PROJECTION FORMULAE:
COMMENT     FORWARD FORMULA; XLON0 IS THE CENTER LONGITUDE OF THE
COMMENT         MAP.   ARC-SINE AND ARC-COSINE FUNCTIONS ARE REQUIRED.
COMMENT     R2D = 45. / ATAN(1.)
COMMENT     PIX = 2.
COMMENT     RHO = ACOS( COS(XLAT) * COS((XLON-XLON0)/2.) )
COMMENT     THETA = ASIN( COS(XLAT) * SIN((XLON-XLON0)/2.) / SIN(RHO) )
COMMENT     F = 2. * PIX * R2D * SIN(RHO/2.)
COMMENT     SAMPLE = -2. * F * SIN(THETA)
COMMENT     XLINE = -F * COS(THETA)
COMMENT     IF(XLAT .LT. 0.)   XLINE = -XLINE
COMMENT
COMMENT     REVERSE FORMULA; XLON0 IS THE CENTER LONGITUDE OF THE MAP.
COMMENT         ARC-SINE AND ARC-COSINE FUNCTIONS NEEDED.
COMMENT     R2D = 45. / ATAN(1.)
```

```
COMMENT     PIX = 2.
COMMENT     Y = -XLINE / (PIX * 2. * R2D)
COMMENT     X = -SAMPLE / (PIX * 2. * R2D)
COMMENT     A = SQRT(4.-X*X-4.*Y*Y)
COMMENT     XLAT = R2D * ASIN(A*Y)
COMMENT     XLON = XLON0 + 2. * R2D * ASIN(A*X/(2.*COS(XLAT)))
COMMENT
COMMENT     REFERENCES:
COMMENT     IRAS SDAS SOFTWARE INTERFACE SPECIFICATION(SIS)  #623-94/NO. SF05
COMMENT     ASTRON. ASTROPHYS. SUPPL. SER. 44,(1981) 363-370 (RE:FITS)
COMMENT     RECONCILIATION OF FITS PARMS W/ SIS SFO5 PARMS:
COMMENT     NAXIS1 = (ES - SS + 1); NAXIS2 = (EL - SL + 1);
COMMENT     CRPIX1 = (1 - SS);        CRPIX2 = (1 - SL)
END
```

Header for Low-Resolution All-Sky Intensity Galactic Anti-Center

```
SIMPLE =                          T   / STANDARD FITS FORMAT
BITPIX =                         32   / 4 BYTE TWOS COMPL INTEGERS
NAXIS =                           3   / NUMBER OF AXES
NAXIS1 =                         nn   / # SAMPLES PER LINE (FASTEST VARY NDEX
NAXIS2 =                         mm   / # LINES OF DATA IN IMAGE FILE
NAXIS3 =                          1   / # WAVELENGTHS
BSCALE =                S.ssssssE-ee   / TRUE=TAPE*SCALE+BZERO
BZERO =                        0.0    /
BUNIT =          'JY/SR'              / INTENSITY
BLANK =                  -2000000000  / TAPE VALUE FOR EMPTY PIXEL
CRVAL1 =                      180.0   / GALACTIC LONGITUDE AT ORIGIN (DEGREES)
CRPIX1 =                      xxx.    / SAMPLE AXIS ORIGIN (PIXEL)
CTYPE1 =         'LON-ATF '           / DECREASES IN VALUE AS SAMPLE INDEX
COMMENT                                 INCREASES   (AITOFF PROJECTION)
CDELT1 =                      -0.5    / COORD VALUE INCREMENT DEG/PIXEL
COMMENT                                 AT ORIGIN ON SAMPLE AXIS
CRVAL2 =                       0.0    / GALACTIC LATITUDE AT ORIGIN (DEGREES)
CRPIX2 =                      yyy.    / LINE AXIS ORIGIN (PIXEL)
CTYPE2 =         'LAT-ATF '           / DECREASES IN VALUE AS LINE INDEX
COMMENT                                 INCREASES   (AITOFF PROJECTION)
CDELT2 =                      -0.5    / COORD VALUE INCREMENT DEG/PIXEL
COMMENT                                 AT ORIGIN ON LINE AXIS
CRVAL3 =                   z.zzE-6    / WAVELENGTH IN METERS
CRPIX3 =                       1.
CTYPE3 =         'LAMBDA  '
CDELT3 =                       0.
DATAMAX =          D.ddddddE ee       / JY/SR   (TRUE VALUE)
DATAMIN =          D.ddddddE ee       / JY/SR   (TRUE VALUE)
EPOCH =                     1950.     / EME50
DATE-MAP =       '01/11/84'           / MAP RELEASE DATE
DATE =           'DD/MM/YY'           / DATE THIS TAPE WRITTEN
ORIGIN =         'JPL-IRAS'           / INSTITUTION
TELESCOP =       'IRAS    '
INSTRUME =       'ALL SKY '           / IRAS LOW RES ALL-SKY
OBJECT =         'ACENTERn'           / ALL-SKY GALACTIC ANTI-CENTER / HCON
PROJTYPE =       'AITOFF  '           / PROJECTION TYPE
COMMENT                                 MINSOP = MMM;   MAXSOP = NNN
COMMENT
COMMENT   PROJECTION FORMULAE:
COMMENT   FORWARD FORMULA; XLON0 IS THE CENTER LONGITUDE OF THE
COMMENT       MAP.   ARC-SINE AND ARC-COSINE FUNCTIONS ARE REQUIRED.
COMMENT   R2D = 45. / ATAN(1.)
COMMENT   PIX = 2.
COMMENT   RHO = ACOS( COS(XLAT) * COS((XLON-XLON0)/2.) )
COMMENT   THETA = ASIN( COS(XLAT) * SIN((XLON-XLON0)/2.) / SIN(RHO) )
COMMENT   F = 2. * PIX * R2D * SIN(RHO/2.)
COMMENT   SAMPLE = -2. * F * SIN(THETA)
COMMENT   XLINE = -F * COS(THETA)
COMMENT   IF(XLAT .LT. 0.)   XLINE = -XLINE
COMMENT
COMMENT   REVERSE FORMULA; XLON0 IS THE CENTER LONGITUDE OF THE MAP.
COMMENT       ARC-SINE AND ARC-COSINE FUNCTIONS NEEDED.
```

```
COMMENT     R2D = 45. / ATAN(1.)
COMMENT     PIX = 2.
COMMENT     Y = -XLINE / (PIX * 2. * R2D)
COMMENT     X = -SAMPLE / (PIX * 2. * R2D)
COMMENT     A = SQRT(4.-X*X-4.*Y*Y)
COMMENT     XLAT = R2D * ASIN(A*Y)
COMMENT     XLON = XLON0 + 2. * R2D * ASIN(A*X/(2.*COS(XLAT)))
COMMENT
COMMENT     REFERENCES:
COMMENT     IRAS SDAS SOFTWARE INTERFACE SPECIFICATION(SIS)  #623-94/NO. SF05
COMMENT     ASTRON. ASTROPHYS. SUPPL. SER. 44,(1981) 363-370 (RE:FITS)
COMMENT     RECONCILIATION OF FITS PARMS W/ SIS SFO5 PARMS:
COMMENT     NAXIS1 = (ES - SS + 1); NAXIS2 = (EL - SL + 1);
COMMENT     CRPIX1 = (1 - SS);        CRPIX2 = (1 - SL)
END
```

Appendix X.Ap.4 Zodiacal Observation History File (ZOHF) Format

The ZOHF is a low-resolution version of the entire IRAS sky survey. The average of all detectors within a band produced a 1/2° wide fan beam which was then boxcar averaged for eight seconds to produce a 30″ × 32″ beam. Pointing information was similarly averaged over eight seconds to accompany the infrared data. The data base is time ordered and retains the subdivision of the original survey into semi-daily Satellite Operation Programs (SOP) and individual continuous survey scan observations (OBS).

Data Base Organization:

The ZOHF is organized into 572 files, with two consecutive file marks after the last file on each tape. There is one SOP per file starting with SOP 29, i.e. File 1 corresponds to SOP 29, and File 572 to SOP 600. Within a file, each 80-byte logical record contains the timing, pointing and infrared data for a single eight-second average. Each logical record is identified with an OBS, but OBSs are not otherwise separated from one another within a SOP file. SOPs for which no survey data exist contain one dummy record which has a valid SOP number but zeros in all other fields.

The ZOHF is available only as an unlabelled, ASCII formatted magnetic tape. The logical record length is 80 bytes with a physical block size of 200 logical records or 16000 bytes. The approximate size of the data base is 96 Mbytes. All of the fields contain data. There are no header or trailer records.

Table X.Ap4.1 Format of ZOHF

start byte	name	description	units	type
1	NSOP	SOP number	--	I3
4	NOBS	OBS number	--	I3
7	NUTCS[1]	Time UTCS	sec	I10
17	INCL	Inclination	degrees	F6.2
23	ELONG[2]	solar Elongation	degrees	F6.2
29	BETA	Ecliptic Latitude	degrees	F6.2
35	LAMBDA	Ecliptic Longitude	degrees	F6.2
41	I_{ν_1}	12 μm Brightness Density[3]	Jy sr^{-1}	E10.4
51	I_{ν_2}	25 μm Brightness Density	Jy sr^{-1}	E10.4
61	I_{ν_3}	60 μm Brightness Density	Jy sr^{-1}	E10.4
71	I_{ν_4}	100 μm Brightness Density	Jy sr^{-1}	E10.4

[1]UTCS is elapsed time in seconds since 0 hours UT, 1 Jan 1981

[2]Elongation is the angle between the line of sight and the Sun. Inclination is the angle between the ecliptic plane and the plane containing the Earth, Sun, and observation direction (i.e., the azimuth angle about the Earth-Sun axis). Elongation was fixed in each OBS, and inclination increased at a constant rate. These angles are related to geocentric ecliptic coordinates by the following expressions:

$$\cos(ELONG) = \cos(\beta)\cos(\lambda - \lambda_\odot)$$

$$\sin(INCL) = \sin(\beta)/\sin(ELONG)$$

where $\lambda_\odot$ is the ecliptic longitude of the Sun.

[3]Conversion from in-band brightness to brightness density assumes a source with an energy distribution which is flat in flux per unit octave as explained in Section VI.C.

Table X.Ap4.2 Table of Missing SOPs[1]

053	258	264	598
054	259	442	
055	260	594	
056	261	595	
058	262	596	
200	263	597	

[1]A dummy data record consists of a valid SOP number and zeros in all other data fields.

XI. KNOWN PROCESSING ANOMALIES

In any undertaking of the magnitude of the IRAS data reduction, there are bound to be errors or software design deficiencies, which were either generic in the processing, discovered too late in the processing schedule to be fixed for all the observations or considered minor enough not to warrant fixing. In this chapter, all those errors which were recognized at the time of publication of the catalog (November 1984) are listed. It is realized that this list does not encompass all the actual errors in the catalog.

A. Processing of Extended ("Cirrus") Sources as Point Sources

As discussed in Section V.C, the point source recognizer can be triggered by sources that are of unlimited extent in the cross-scan direction as long as they are less than about $1'$ in the in-scan direction. While this characteristic was recognized early in the design of the software, it was felt that this situation would arise much less frequently than the case where several true point sources triggered many cross-scan detectors simultaneously. The presence of "infrared cirrus" and the extended sources in the Galactic plane means that at 100 μm in particular the sky is dominated by extended structures rather than by clusters of point sources. The detection and confirmation software thus created strings of pseudo-point sources spread along the cross-scan direction.

In retrospect, it would have been better to adopt a different approach. For example, whenever four or more cross-scan detectors were triggered, all such detections should have been discarded from the point source catalog or placed in a special data base to compare different scans to verify that these detections were in fact due to several true point sources. The consequences of the present approach are clear. At 100 μm the point source catalog is unavoidably contaminated by the presence of point-like condensations within the extended emission and by the effects of cirrus on discrete point sources that include missing fluxes at shorter wavelengths caused by band-merging difficulties.

B. Instability and Lag of the Noise Estimator

The noise estimator (Section V.C.2) was picked for its computational speed and its performance in quiet areas of the sky. It performed poorly in regions of rapidly changing noise amplitude. As a result, the noise estimator near regions of high source density was a major reason for incompleteness for sources that would properly have had a signal-to-noise ratio of three or more because the estimator erroneously increased the noise level so that the computed signal-to-noise ratio fell below the threshold. Furthermore, the noise estimator exhibited a lag which resulted in the almost complete excision of sources within a degree or two on one side of the Galactic plane.

C. Frequency Dependence of Responsivity with Amplitude

The observations described in Section IV.A.4 established that flux densities greater than 10 Jy at 60 and 100 μm are in error of at least 30% at 60 μm and up to 70% at 100 μm because the responsivity of the detectors varied with the total flux on the detectors. This effect depends on the background as well as

on the brightness of the source itself. The photometry of any source in a background greater than 10 MJy sr^{-1} at 60 and 100 μm is therefore suspect.

D. Errors in Cross-Scan Uncertainties Related to Failed Detectors

Several changes were made in the course of the processing to ameliorate the effects of failed detectors. While all of the changes resulted in overall improvements, the last change introduced an error as well. The last change handled the situation when an edge detection occurred opposite a failed detector and when the fluxes of the detections differed by more than a factor of two, so that the detections failed to seconds-confirm. Since only one detection could band-merge with the rest of the source, an improvement was made to select always the brighter detection and to delete the fainter one. An error in the software assigned a wildly incorrect cross-scan uniform uncertainty to the remaining detection one-third of the time.

This change still resulted in a net improvement in the quality of the sources. The erroneous cross-scan uncertainties were immediately eliminated if band-merging was successful. A problem was created when the faulty detection was merged with another real source that had transited the focal plane at precisely the same time. No restriction on cross-scan position existed because of the impossibly large cross-scan uniform uncertainty associated with the detection. The resulting, incorrectly band-merged source failed to have upper limits from being assigned to unobserved (or unmerged bands). Thus, the Working Survey Data Base (WSDB) contains some hours-confirmations with some bands with FSTAT=0, and detectors all 0 (see Section V.D.8). A detailed comparison of the processing of the data with and without this error showed that no sources with signal-to-noise ratio greater than 9 were lost due to to this error.

E. Photon-Induced Responsivity Enhancement

The observations described in Sections IV.A.8 show that a correction of as much as 20% should be applied to the photometry in the 100 μm band because of the photon-induced responsivity enhancement caused by passage over the Galactic plane.This correction depends on the detailed history of the individual scans which go into making up a source. The correction scheme described in Section VI.B.4 is only valid in a statistical sense and is based on guess-work for those areas which were not covered by ascending and descending scans. It should be emphasized that these corrections were not incorporated into the instrumental fluxes recorded in the WSDB.

No correction has been attempted for the extended emission maps.

F. Artifacts in the Digital Image Data Base

The final calibration corrections for baseline and scale factor in the 16.5° image digital data base delivered in November 1984 (third HCON coverage only) were based on the Zodiacal History File. There was insufficient time before the delivery date to perform the corrections properly on the time ordered data and reassemble the high resolution maps. As a result, the 2′ digital data show a patchwork structure of 30′ squares which varies in intensity from one part of the sky to another. The maximum discontinuity across the edge of one of the squares amounts to about 5 digitization levels of the satellite's

electronics in all bands (Section II.C) regardless of the instantaneous sky brightness. This translates to maximum jumps of about 0.9, 2.0, 0.5 and 1.0 MJy sr^{-1} at 12, 25, 60 and 100 μm, respectively. The problem should be of little concern in high brightness regions such as the Galactic plane but may compromise the data for some purposes in low brightness regions near the Ecliptic and Galactic poles. In most cases the patchwork amplitude is smaller than the residual striping left by the flat fielding procedure.

No attempt was made to smooth out the discontinuities. A number of fields where the problem was most severe were deleted and are listed in Table XI.F.1. The calibration of the third coverage will be corrected properly and a complete data set reissued. The photographic data products released in November, 1984 do not suffer from the problem because no corrections were applied to these data as discussed in Section X.D.3. The first and second HCON coverages as well as the reprocessed third HCON will be properly corrected.

Table XI.F.1 Fields Deleted from 3rd HCON

7	18	19	20	21	22
23	24	36	43	44	56
58	82	92	116	127	140
141	170	173	185	186	187
188	190	191	192	201	203
205	209	210	-	-	-

G. Photometric Processing

As stated in Section VII.D, the flux densities quoted for the secondary standard NGC 6543 differed from those assumed as inputs to the processing by up to 4%. The cause of these discrepancies is unknown at this time and the effect, although statistically significant, was considered too small, compared to the relative photometric uncertainties, to be remedied.

H. Insufficient Specification of HCON Coverage

In order to understand the reliability of a given source, a knowledge of the number of total HCONs possible is necessary. This information is not available in either the catalogs or the WSDB and can be obtained only by recourse to the raw data.

I. Position Uncertainties

As described in Section VII.C.1.b, the IRAS position uncertainties are significantly overestimated for brighter objects. An additional source of overestimation of the uncertainties for some objects was a processing error that added 3″ in quadrature to the in-scan uncertainty for all sources with a cross-scan

uniform uncertainty of 1″. It had been intended to do this only for faint sources, about 40% of the catalog, but was inadvertently applied to sources of all flux levels meeting the uncertainty criterion, about 60% of the catalog.

J. Overestimated Weak Fluxes

There is a systematic error associated with the measured flux densities, particularly those of moderate quality, near the noise limit of the detectors, which can increase the quoted value by as much as a factor of two compared with the true value. Weak sources were often detected when positive noise excursions pushed the source signal above the 3σ signal-to-noise (SNR) cutoff imposed by the processing. Negative excursions dropped the signal below the SNR cutoff and so were not included in the flux averaging. While the problem is complicated by the uneven sensitivities of the detectors, a simple analysis demonstrates the problem and leads to a simple correction factor.

Assume that all of the noise sources are Gaussian and neglect spikes and cosmic ray hits as second order effects (see Sec. VII.D of the Supplement). Define

The noise level = σ.
The true source flux density, f_{true} = nσ.
The flux threshold = mσ.
The measured flux density, $f_{obs} = n'\sigma$.

A source will be detected whenever the measured flux density exceeds the threshold, i.e. $n' > m$. For a perfectly uniform focal plane with no failed detectors the fraction of times, p, that a source was seen is given by:

$$p = (2\pi)^{-1/2} \int_{m-n}^{\infty} e^{-y^2/2} dy \qquad \text{(XI.J.1)}$$

The expectation value of the observed flux density is given by the average of all detected values,

$$<n'> = \frac{\int_{m}^{\infty} y e^{-(y-n)^2/2} dy}{\int_{m}^{\infty} e^{-(y-n)^2/2} dy} \qquad \text{(XI.J.2)}$$

Then the expectation value of the ratio of the observed flux density to the true flux density is given by

$$<n'/n> = <observed/true> = 1 + \frac{1}{m} \frac{e^{-1/2(m-n)^2}}{\int_{m}^{\infty} e^{-y^2/2} dy} \qquad \text{(XI.J.3)}$$

The fraction of possible times the source was detected, p, (Eqn. XI.J.1) can be used to estimate the fractional amount, $<n'/n>$ (Eqn. XI.J.3) by which the source's flux density was overestimated.

Table 1 gives the relationship between p and $<n'/n>$ for two SNR thresholds, 2σ and 3σ, to bracket the range of sensitivities of the focal plane detectors. To use the table, one must determine from the Working Survey Data Base the number of times the source should have been seen and the number of times it actually was seen. The ratio of those two numbers is approximately equal to p which can then be used to estimate a correction factor to the quoted flux density using Table XI.J.1.

The correction factor has been verified by using the moderate quality detections at 25 μm of hot stars with accurate 12 μm detections. At low flux levels the 12μm-25μm flux density ratio deviates from the Rayleigh Jeans limit. Application of this correction algorithm reduces this error considerably.

It should be emphasized that this correction procedure ignores the effects of radiation hits and of extra sensitive detectors. For cases where very accurate photometry is required, one should co-add the survey data.

Table XI.J.1 Relation between Fraction of Possible Sightings (p) and Flux Overestimate ($<n'/n>$)

Frac. of Sightings	Flux Overestimate SNR THRESHOLD (= 2σ)	(= 3σ)
p	<n'/n>	<n'/n>
0.16	2.51	1.76
0.31	1.76	1.60
0.50	1.40	1.27
0.69	1.20	1.15
0.84	1.10	1.07
0.94	1.04	1.02

K. Minor Problems

1) An unmodelled source of position errors was present in the data, as evidenced by the need to increase in-scan σs for sources that had a cross-scan position error without a significant uniform component.
2) Radiation hits and noise spikes caused some sources to have significantly larger cross-scan errors than quoted.

3) In order to improve completeness, it was necessary to allow detections without a confirming partner due to a failed detector to bypass seconds-confirmation. This resulted in a large number of spurious detections being accorded a status equal to that of a truly seconds-confirmed source. These false detections could at times replace valid detections in band-merging.

4) A second effect of failed detections was that an edge detection pair opposite a failed detector was often not seconds-confirmed, allowing two separate detections to be present at band-merging. The weaker detection, with its larger error basis, was usually chosen in band-merging resulting in a depressed flux in that band.

5) A third effect of failed detectors resulted from detectors that were impaired but not dead. They would produce detections that were too weak to seconds-confirm with detections on the partner detectors. Again, the weaker detection would often be chosen in band-merging resulting in a depressed flux.

6) Strong radiation hits could also result in a seconds-confirmation failure which, in a small fraction of cases caused incorrect fluxes or flux status.

7) Responsivity changes due to particle or photon radiation caused baseline changes of order 10% in some observations.

8) The optimum thresholds for accepting the seconds-confirmed sources were set by varying the threshold level and evaluating the numbers of sources passed as a function of threshold value (Section VII.E.6). The method worked satisfactorily in all the wavelength bands but the 25 μm band where the total number never reached the predicted plateau.

9) The CIRR2 flag is incorrectly set to 0, implying no all sky data, for about 40 sources at the 0°-360° ecliptic longitude boundary.

10) For many catalogs, the truncation instead of rounding of optical magnitudes leads to a 0.1 *mag* error in the reported magnitudes.

11) For the ESO/Uppsala Survey of the ESO (B) Atlas, only the first two characters of the catalog description were used for the type field.

Authors:

T. Chester, G. Neugebauer, C. Beichman and T.N. Gautier.

XII. ERRATA AND REVISIONS AS OF 1987

The second release of some portions of the IRAS data reflects a number of changes, corrections and improvements to the data. This chapter, written in late 1986-early 1987, describes changes to each of the major datasets and records a number of changes to the formats of the data which will be of importance to people using the various products. The history of the releases of the IRAS data is described in Table XII.A.1.

A. Version 2.0 of the Point Source Catalog

The most important difference between the first and second versions of the IRAS Point Source Catalog (hereafter denoted PSC-1 and PSC-2) is the application of a statistical correction to reduce the overestimation of the flux densities of sources near the detection threshold (see XI.J for a discussion of the effect); changes of as much as a factor of two were made for some weak sources.

A number of other, less significant changes were also made. Flux densities for almost all sources changed by a few percent due to refined calculations of certain calibration factors; a few sources changed by as much as 10%. Corrections to errors in some calibration and confused source processing algorithms resulted in the loss of 6 sources from and the addition of 56 new objects for a revised total of 245,889 individual sources in PSC-2. Table XII.A.5 lists 12 sources which were omitted from *both* PSC-1 and PSC-2 due to a software error, but which are of sufficient quality to be noted for completeness. A number of new catalogs were added to the list used for associations. Finally, a number of minor errors in calculations of some of the quantities associated with point sources, e.g. the number of neighboring sources, were corrected.

A.1 The Flux Overestimation Correction

As described in detail in Chapter V, sources were extracted from individual detector streams by means of a zero-sum filter followed by a template fit to the data. Only if the detection exceeded thresholds in its signal to noise ratio (SNR) and in its correlation with the template of a "perfect" point source was the detection accepted for subsequent processing. A source was accepted into the catalog only if it had enough valid detections to confirm its existence on time scales of seconds, hours and weeks. However, a failing of this strategy (as described in more detail in Section XI.J) is that the flux density of weak sources is overestimated, since the combination of a weak source and positive-going noise (Gaussian excursions or spikes due to radiation hits) resulted in a "valid" detection, while the combination of a weak source and negative-going noise (Gaussian excursions) forced the detection below the acceptable thresholds. Thus, for weak sources, the detections used to form the average flux density

Table XII.A.1 IRAS Data Products
Status as of March 1987

PRODUCT	DESCRIPTION	MEDIUM	VERSION	DATE
Explanatory Supplement	Detailed description of hardware, data processing, and products	Book	1.0	Nov. 1984
	Revisions, New Chap XII, Index	Book	2.0	Jun. 1987
Point Source Catalog	245,839 point sources (PSC-1)	Tape, Microfiche,	1.0	Nov. 1984
		Tape	1.1	Jan. 1986
	245,889 point sources (PSC-2). Updates described in this Chapter	Tape	2.0	Nov. 1986
		Book	2.0	Jun. 1987
Ancillary File	More detailed information on point sources	Tape	2.0	Nov. 1984
			2.1	Jan. 1986
			3.0	Nov. 1986
Working Survey Data Base	More detailed information on point sources	Tape	2.0	Nov. 1984
			3.0	Feb. 1986
			4.0 (PSC-2)	Nov. 1986
High Source Density Bins	Bins processed by high source density processor for Catalog	Tape	1.0	Nov. 1984
Point Source Reject File	372,774 rejected point sources	Tape	available at IRAS data centers only	
Reject File Ancillary File	More detailed information on rejected point sources	Tape	available at IRAS data centers only	
Reject File Working Survey Data Base	More detailed information on rejected point sources	Tape	available at IRAS data centers only	
LRS Spectra Catalog	Spectra of 5,425 catalog point sources (8-22 μm). See XII.C	Tape, Hard Copy	1.0	Nov. 1984
Zodiacal History File	Time-ordered data at 0.5° resolution	Tape	1.0	Nov. 1984
			2.0	May 1986
All Sky Maps	All sky images at 0.5° resolution	Tape Negatives	1.0	Nov. 1984

Table XII.A.1 IRAS Data Products (Continued)

PRODUCT	DESCRIPTION	MEDIUM	VERSION	DATE
Sky Brightness Images (HCON 3)	16 × 16° field 2′ Resolution	B/W, Color Negatives	1.0	Nov. 1984 (Sept-Nov)[a]
		Tapes	1.0	Nov. 1984
		B/W Negatives	2.0	May 1986 (Dec. 1985)[a]
		Tapes	2.0	May 1986 (Mar. 1986)[a]
Sky Brightness Images (HCON 1)	16 × 16° field 2′ Resolution	B/W Negatives	1.0	Aug. 1985 (Feb-Apr)[a]
		Tapes	1.0	Aug 1985 (May 1985)[a]
Sky Brightness Images (HCON 2)	16 × 16° field 2′ Resolution	B/W Negatives	1.0	June 1986 (Apr 1986)[a]
		Tapes	1.0	June 1986
Sky Brightness Images (Overlays)	16 × 16° field	B/W Negatives	1.0	Nov. 1984
Galactic Plane Images (HCON 3)	2° × 15° field 2′ resolution	B/W Negatives, Tapes	1.0 2.0	Jan. 1985 July 1986
Galactic Plane Images(HCON 1)	2° × 15° field 2′ resolution	B/W Negatives, Tapes	1.0	Oct. 1985
Galactic Plane Images (HCON 2)	2° × 15° field 2′ resolution	B/W Negatives, Tapes	1.0	Jul. 1986
Cataloged Galaxies and Quasars	11,444 point sources associated with cataloged galaxies and quasars	Book	1.0	Feb. 1985
Pointed Observations	13,853 images with 0.25′-1.0′ resolution, each covering ~1 square degree	Tapes	1.0	Oct. 1985
Pointed Observations User's Guide[b]	Description of AO's, data reduction, and released grids	Book	1.0	Nov. 1985
Serendipitous Survey Explanatory Supplement[c]	Description of Catalog	Book	1.0	Dec. 1986
Serendipitous Survey Catalog[c]	43,866 point sources derived from the Additional Observations	Tape, micro-fiche	1.0	Dec. 1986

Table XII.A.1 IRAS Data Products (Continued)

PRODUCT	DESCRIPTION	MEDIUM	VERSION	DATE
Small Scale Structure Catalog Explanatory Supplement	Description of Catalog	Book	1.0	Dec. 1985 Mar. 1987
Small Scale Structure Catalog	16,740 sources with sizes $< 8'$	Tape, Microfiche, Book	1.0	Dec. 1985 Mar. 1987
CPC Explanatory Supplement	Detailed description of CPC hardware, data, processing, and products	Book	1.0	Aug. 1985
CPC data	Chopped photometric channel image data	3 tapes	1.0	Jan. 1986
IRAS Asteroid and Comet Survey	IRAS and derived data on known asteroids	Tape	1.0	Oct. 1986
IRAS Asteroid and Comet Survey Explanatory Supplement	Description of Catalog and Summary Information	Book	1.0	Oct. 1986

[a]Internal product dates on tape versions show months in this range
[b]Young *et al.* 1985
[c]Kleinmann *et al.* 1987

reported in PSC-1 were systematically high. This problem predominantly affected moderate quality fluxes of weak sources; brighter sources detected with high quality fluxes generally had enough detections that flux overestimation was not a large problem.

The most direct way of measuring the overestimation is to compare the brightness of sources in PSC-1 with the values obtained from the more sensitive pointed mode of the satellite (Young *et al.* 1985). Observations made in the pointed mode were three to five times more sensitive than the scans making up the survey so that the sources detected in the pointed mode would not suffer from threshold effects at the same flux level. The Serendipitous Source Catalog (Kleinmann *et al.* 1987, hereafter denoted as the SSC) is the catalog of sources extracted from selected pointed mode observations and was used as a "truth table" to determine the magnitude of the flux overestimation effect and to help develop a correction for it. Figures XII.A.1a-4a show the ratio of SSC to PSC-1 flux densities for the four bands as a function of SSC flux density; the presence of an overestimate in the PSC-1 values below about 2 Jy is obvious.

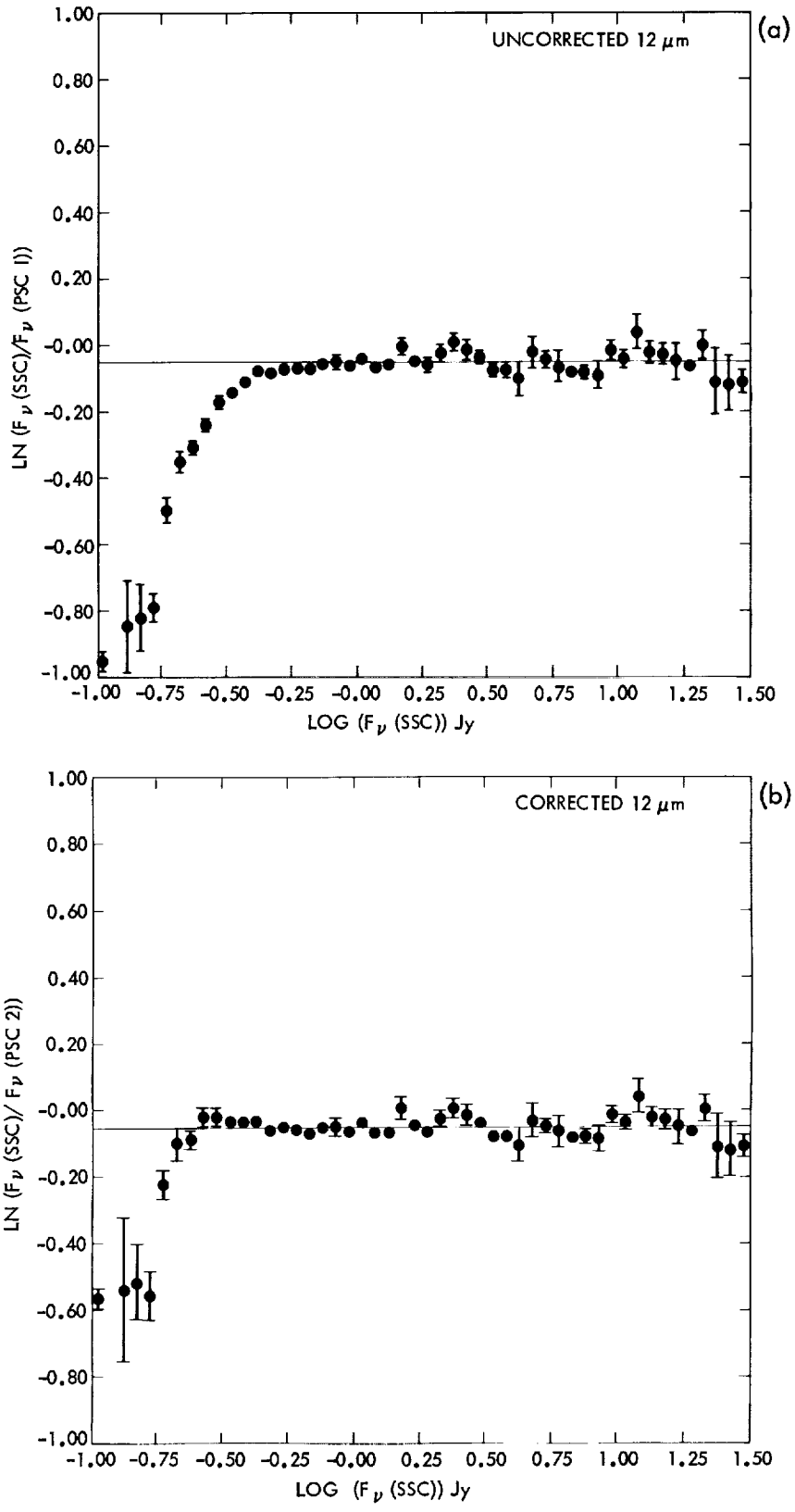

Figure XII.A.1 Ratio of SSC to PSC-1 (a) or PSC-2 (b) 12 μm flux densities vs. SSC flux density before (a) and after (b) the correction of the overestimation effect.

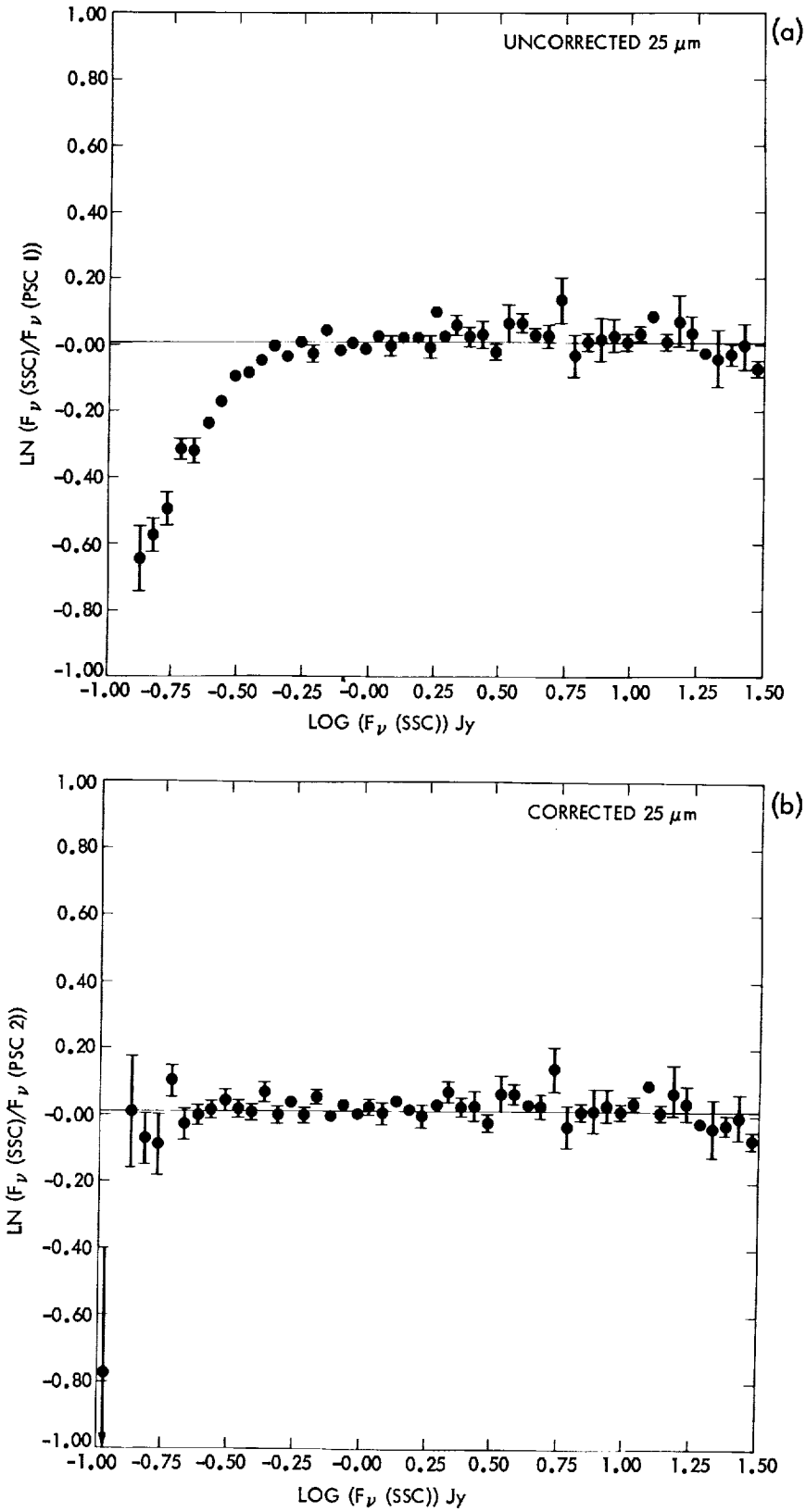

Figure XII.A.2 Ratio of SSC to PSC-1 (a) or PSC-2 (b) 25 μm flux densities vs. SSC flux density before (a) and after (b) the correction of the overestimation effect.

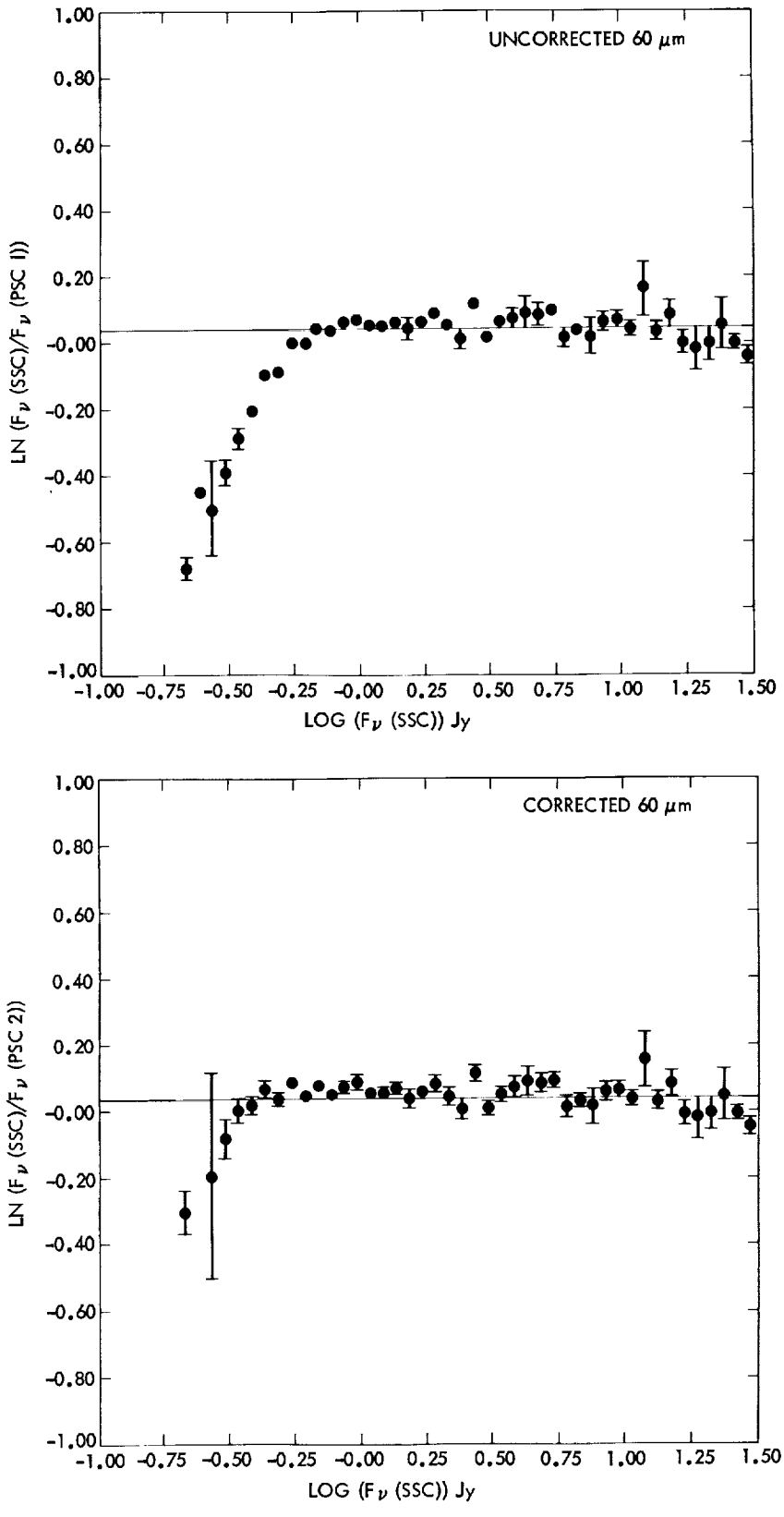

Figure XII.A.3 Ratio of SSC to PSC-1 (a) or PSC-2 (b) 60 μm flux densities vs. SSC flux density before (a) and after (b) the correction of the overestimation effect.

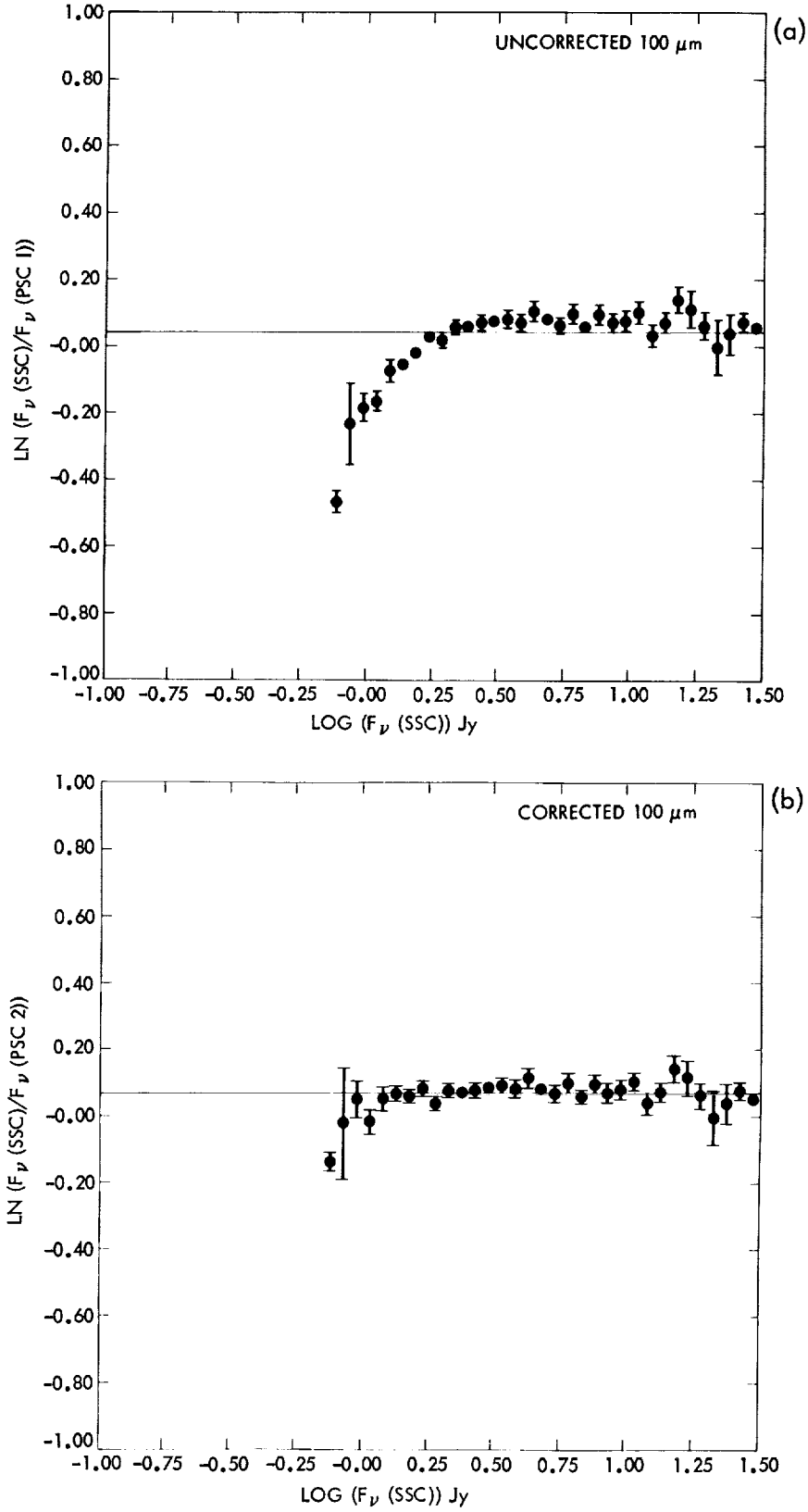

Figure XII.A.4 Ratio of SSC to PSC-1 (a) or PSC-2 (b) 100 μm flux densities vs. SSC flux density before (a) and after (b) the correction of the overestimation effect.

A simple model for the overestimation described in Section XI.J leads to an algorithm for the correction of the effect. Consider a detector stream with an intrinsic Gaussian noise level σ and a source with an intrinsic brightness of $n\sigma$. The zeroth moment of the Gaussian distribution above the threshold of $m\sigma$ for a source with true flux $n\sigma$ gives the probability of detection (Eqn. XI.J.1) and the first moment above $m\sigma$ gives the observed flux (Eqn. XI.J.2). These moments were used to relate the flux correction factor to the observed fraction of possible sightings for a given source.

The algorithm was implemented in the following manner. The Working Survey Data Base (WSDB) contains the number, N, of all accepted detections. If the total number of possible detections is denoted by M, then the ratio N/M is an estimate of the probability of detection, denoted by p, which can be used in Equation XI.J.1 to estimate the quantity $n-m$. This value can be used with Equation XI.J.3 to derive the ratio n'/n which is an estimate of the amount by which the true brightness of the source was overestimated in PSC-1.

For each source fainter than a certain, band-dependent level (2 Jy at 12, 25 and 60 μm and 3 Jy at 100 μm), the number of accepted detections, N, was determined from the WSDB. At the same time the total number of possible detections, M, was determined from a detailed calculation of the satellite's pointing history over the entire mission. If the source passed within the central portion of a working detector then a possible sighting was recorded. The central portion of the detector was defined by a distance in from the edge of the detector and was considered a free parameter, denoted by δZ, in each band; the value of this parameter affected the number of possible detections for a given source.The resultant value of N/M was used along with an estimate of the cutoff threshold, m, in that band to derive the correction factor as described above.

The SSC data represented in Figure XII.A.1a-4a were assumed to give the true brightness for faint sources and were used to adjust the parameters δZ and m on a band by band basis to make the curves as flat as possible. The algorithm was applied only to those sources which were neither confused nor located in regions of high source density in a given band. Approximately 100,000 sources were adjusted in at least one wavelength. Values of δZ and m and the maximum derived correction factors are given in Table XII.A.2.

Table XII.A.2 Flux Overestimation Parameters

Wavelength (μm)	m (SNR Threshold)	δZ (′)	Max. Correction
12	4	0.2	1.72
25	2	0.4	3.00
60	3	0.7	2.01
100	3	1.0	2.38

The photometric uncertainty associated with each flux was also adjusted slightly by examining how uncertainties in the pointing of the telescope could affect the number of possible sightings. Variations in the N/M ratio were propagated through Eqs. XI.J.1 and XI.J.3 and the resulting uncertainty added in quadrature to the uncertainty already given in the catalog.

The above formalism obviously ignores many complications such as differing sensitivities among the detectors within a band and non-Gaussian noise sources like radiation hits and cirrus which could increase a source's flux on some occasions, but not others. Detections could have fallen below thresholds for any number of reasons including sightings by a detector of poor sensitivity or passage over the edge of a detector rather than over its center. A sighting could have been rejected for failing to exceed either the SNR or template thresholds. All of these effects were ignored in the above algorithm. As a result, although the corrections are quite good in a statistical sense, they may be considerably in error in any individual case.

Despite these simplifications, the algorithm worked remarkably well. Figure XII.A.1b-4b shows the comparison of the PSC-2 and SSC fluxes. While some structure including a slight offset in some bands is still evident in the data, the curves are much flatter than those in figure XII.A.1a-4a; the offset may be due to residual uncertainties in the calibration of the photometry in PSC-2 and the SSC.

Figure XII.A.5 shows the effect of the flux overestimation on the photometry for weak sources in PSC-1 and the effectiveness of the correction applied in the generation of PSC-2. The figure plots the 12/25 μm color of stars as a function of their 12 μm brightness. In Fig. XII.A.5a the flux density ratio comes from PSC-1 and the 12 μm brightness from the SSC. Above about 2 Jy a distinct population of stars with colors characteristic of hot (>3000 K) photospheres is apparent, but below 2 Jy the population of stars with photospheric colors disappears and all stars appear to have a 25 μm excess. This astrophysically puzzling result can be understood in terms of the 25 μm flux being systematically overestimated for faint stars. The corrected colors from PSC-2 (Fig. XII.A.5.b) reveals a distinct population of stars with normal photospheres at faint levels.

As a result of this correction algorithm, the machine readable version of PSC-2 includes five new fields: MHCON, the number of possible hours confirmed sightings a source could have had and the four band dependent correction factors that were applied to the PSC-1 flux densities to produce the PSC-2 fluxes. These quantities are given only for those sources for which a flux overestimation correction was made. It should be noted that the value of MHCON for any given source could be uncertain by one or two sightings.

The format of the Catalog tape has been revised to incorporate these new quantities. Table XII.A.3 lists the changes to the original format (Table X.B.1, page X-4).

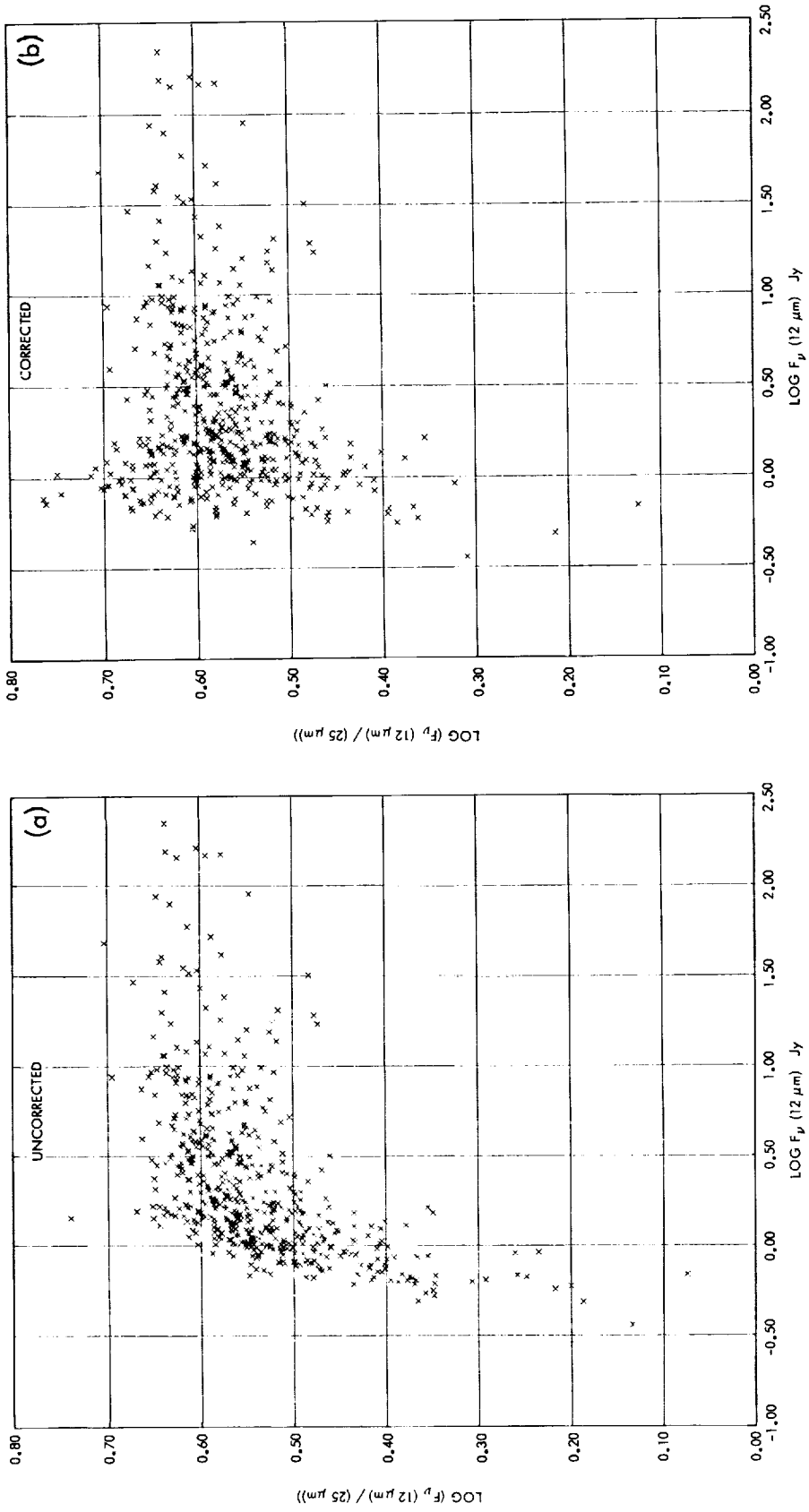

Figure XII.A.5 Ratio of 12 μm to 25 μm flux densities from the PSC-1 (a) or PSC-2 (b) vs. 12 μm flux density from the SSC before (a) and after (b) the correction of the overestimation effect.

Table XII.A.3 Revised Portion of Catalog Tape Format

(see Table X.B.1)

Start Byte	Name	Description	Units	Format
139	MHCON	Possible number of HCONs	---	I2
141	FCOR	Flux Correction Factors Applied (×1000) (1 value per band)	---	4I4
149	SPARE	3 Spare bytes	---	3A1

A.2 Additional Flux Density Changes

Flux densities for all sources in the PSC-2 were adjusted by a few percent to make them consistent with the final calibration described in Chapter VI. The differences arose because PSC-1 used a preliminary version of the all-sky intensity maps to correct for the non-linearities of the feedback resistor (Section VI.A.5). Also, as a result of this change, minimum upper limit fluxes are now exactly 0.25, 0.25, 0.40, and 1.0 Jy, instead of varying by a few percent from these values.

In two areas of the sky, from 0° to 29° ecliptic longitude at -90° to -67° latitude and at 60° to 65° latitude, flux densities reported in PSC-1 were factors of 1.076, 1.099, 1.013, and 0.967 too high at 12, 25, 60 and 100 μm, respectively. Approximately 1% of all sources were affected by this error which has been corrected in PSC-2.

A.3 New and Deleted Sources

A number of effects changed the total number of point sources present in PSC-2. First, six sources present in PSC-1 were deleted from PSC-2 because the small flux changes mentioned above pushed the fluxes for these sources below a threshold used by the high source density processor. Second, fifty six sources were added to PSC-2 because the very near neighbor window was set incorrectly in parts of the production of PSC-1. Thus, the total number of sources in PSC-2 is 245,889. The names of the changed sources are given in Table XII.A.4.

Finally, a software error, discovered after the release of PSC-2, led to the exclusion of a small number of sources from *both* PSC-1 and PSC-2. Examination of the Working Survey Data Base (WSDB) led to the discovery of sources with similar fluxes located within ±30″ in-scan and ±90″ cross-scan of one another. In each case only a single hours confirmed sighting was reported for each object. Evidently, the weeks confirmation software failed to confirm and merge these objects into a single source which would then have appeared in the catalog.

Table XII.A.4 New or Deleted Point Sources

New Sources

01241-7332	05265-6840	08220-4404	18373-0918
04531-6708	05299-6830	08573-4718	19514+4306
04532-6710	05303-6951	09040-7402	21097+4953
04534-6657	05305-6952	09101-5100	21099+4954
05044-7012	05341-6632	09179-7034	21314+5805
05046-7014	05371-6944	09215-7028	21329+5126
05122-6829	05374-6946	09437-6034	21345+5706
05150-6629	05375-6650	10075-5747	21445+5653
05150-6631	05392-6847	10075-5824	21446+5655
05207-6636	05393-6930	10182-5742	21478+5649
05236-6702	05448-6720	12376-6122	22126+6905
05239-6939	05486-7001	13191-6245	22299+6440
05242-6940	08003-5012	18092+4419	22510+7138
05264-6730	08005-5013	18285-0830	22512+7140

Deleted Sources

04526-6951	13046-6222	20250+4316	21503+5105
04538-6952	15574-0052		

A procedure was developed for finding these objects systematically in the WSDB. First, the WSDB was searched for all sources with only one hours confirmed sighting, located above an absolute galactic latitude of 10° and above an ecliptic latitude of -80° (to avoid the Large Magellanic Cloud). Second, sources detected only at 25 μm or only at 100 μm were eliminated to avoid contamination by asteroids or cirrus. This sample was examined for objects having companions within ±30″ in-scan and ±90″ cross-scan. Those objects with nearby companions and meeting the final catalog selection criteria (Sections V.H.2 and V.H.7.) were taking as real objects. A final position was derived by simply averaging the position from each sighting; final flux densities were computed by averaging the logarithms of the flux densities without using any weights.

Forty-three objects were selected by this procedure. Examination of the raw data led to the elimination of seven of these 43 as being due to either cirrus or confused objects. Finally, to avoid any problems of source reliability or flux overestimation only sources with a flux density greater than 1 Jy in at least one band were selected for inclusion in Table XII.A.5. The format of the table is similar to that of the printed version of the catalog, as described in Section X.B.2. It should be emphasized that these sources appear *only* in the table and *are not included* in the printed or machine readable versions of either PSC-1 or PSC-2.

Table XII.A.5

Bright Sources Missing from the Point Source Catalog with $|b| > 10°$

--- Name --- α (1950) δ HHMMT DDMM	α (s)	δ (″)	Gal Coord l b	NH	----- Flux Density in Janskys ----- (Not Color-Corrected) 12μm	25μm	60μm	100μm	C 1	P W	S 2	N I D	C A T	---- Association ---- --Name & Type--	MAG
00125-0723	33.5	10	98-68	2	.25L	.44L	1.46	4.62	0			1	10	M-01-01-060	999
11434+2042	26.3	50	234+74	2	.25L	.46:	3.19:	6.45	1			2	10	M+04-28-050	999
12337+2616	47.4	51	230+86	2	.52:	.53	4.50	23.31	0	1	7	6	9	U07772	103
21492+3716	13.4	1	88-12	2	.36:	.25L	.48	2.95	15		4	1	2	DO 20951	1
22261+8025	9.1	59	117+20	2	1.01	.28L	.40L	1.63L	7			1	13	3746 K0	67
22308+4105	50.3	26	97-14	2	2.05	.54	.40L	6.60L	3			2	13	52130 K0	77
22324+4024	28.4	35	97-15	2	4.43	18.49	29.10	64.39	12			2	27	MKN 914	999
22325+4054	32.0	25	97-15	2	.25L	.26L	1.08	7.01	8	1	4	1	32	X2232+408	4
22326+4031	37.8	9	97-15	2	.41L	.25L	1.10	7.33L	9			1	23	DG 187	999
22376+2426	36.8	3	89-29	2	.29L	.25L	1.05	2.68	0						
23019+3405	57.7	32	99-23	2	.25L	.25L	1.45	2.50	0						
23132+2449	14.4	12	97-33	2	.25L	.25L	.48	1.35	4			3	9	U12460	155

A.4 Revised Completeness Estimates for PSC-2

The completeness of PSC-2 was investigated in two different ways. First, PSC-2 was internally checked through analysis of the differential source counts. Second, PSC-2 was externally checked against the SSC which is complete to significantly fainter flux densities than PSC-2. Results from both methods corroborate the general statements made in Chapter VIII that the survey (PSC-1 or PSC-2) is complete, in unconfused regions of the sky, to 0.4, 0.5, 0.6 and 1.0 Jy at 12, 25, 60, and 100 μm.

PSC-1 and PSC-2 differ in the flux density level associated with a given completeness level. Figures XII.A.6a,b show the differential $\log N/\log S$ curves for 12 and 60 μm for PSC-1 and PSC-2 at high Galactic latitudes covered with two sets of hours confirming scans. Because of the correction for flux overestimation, the peak of the curves is broader in PSC-2 than in PSC-1. The shapes of the curves implies that PSC-2 has more weak sources than PSC-1, but that those sources are very incompletely represented, e.g., ~10% completeness at 0.3 Jy at 12μm. At the same time, PSC-2 does not achieve a 90% completeness level until a slightly higher flux density than PSC-1.

Tables XII.6a,b summarize the flux densities at which a given completeness is reached derived from the source counts in PSC-1 and PSC-2. Values are given for regions with both two or three sets of hours confirming scans (2 or 3 HCONs). To the extent that the flux overestimation algorithm was successful, the table for PSC-2 reflects the true completeness of the IRAS survey as a function of flux density. Note that while it is quite accurate to derive the completeness from the $\log N/\log S$ curves below completeness levels of about 50%, it is difficult to derive accurate estimates above that level. Thus the flux density values at completeness levels of 90% and 95% are indicated in the tables as uncertain.

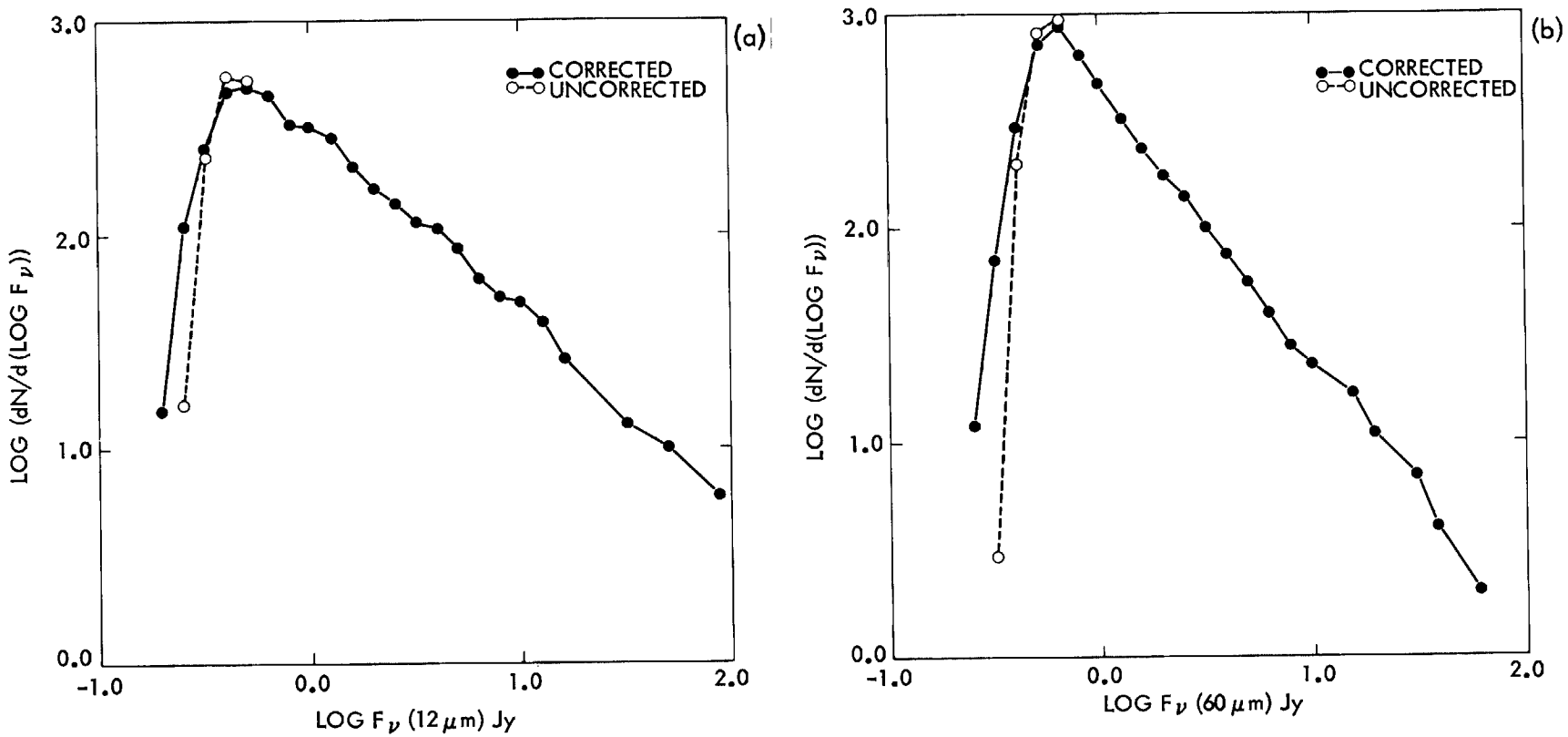

Figure XII.A.6 a) The differential source counts versus 12 μm flux density for PSC-1 (dashed line) and PSC-2 (solid line).

b) The differential source counts versus 60 μm flux density for PSC-1 (dashed line) and PSC-2 (solid line).

Table XII.A.6a

Flux Densities for a Given Completeness Level (PSC-1)

Completeness (%)	Flux Density (Jy) 2 HCON sky 12μm	2 HCON sky 60μm	3 HCON sky 12μm	3 HCON sky 60μm
95	[.42]*	[.59]	[.38]	[.52]
90	[.40]	[.56]	[.36]	[.50]
50	.33	.47	.32	.44
10	.29	.40	.29	.39
5	.28	.37	.28	.38

* Numbers in brackets are uncertain

Table XII.A.6b

Flux Densities for a Given Completeness Level (PSC-2)

Completeness (%)	Flux Density (Jy) 2 HCON sky 12μm	2 HCON sky 60μm	3 HCON sky 12μm	3 HCON sky 60μm
95	[.47]*	[.60]	[.46]	[.60]
90	[.44]	[.59]	[.44]	[.57]
50	.35	.48	.30	.45
10	.24	.38	.23	.33
5	.22	.34	.22	.30

* Numbers in brackets are uncertain

The second way to evaluate the completeness of the survey is to use the SSC, which, as discussed above, reaches three to five times fainter than the survey. A comparison was made of all SSC sources at Galactic latitudes $b > 30°$ and $b \leqslant 50°$ (to avoid the Magellanic Clouds). The SSC sources were divided into stars [$f_\nu(12\mu m) > f_\nu(25\mu m)$ and $f_\nu(12\mu m) > f_\nu(60\mu m)$] and galaxies [$f_\nu(12\mu m) < f_\nu(60\mu m)$], in order to isolate the 12 and 60 μm bands as much as possible. A search radius of 120″ was used to find counterparts in PSC-2. Tables XII.A.7a,b summarize the completeness derived from the percentage of SSC sources that were found in PSC-2 for both the 2 and 3 HCON sky at 12 and 60 μm. Given in the table are the number of actual objects in PSC-2 (denoted N') compared with the possible number of objects (denoted M') found in the more complete SSC.

As a check on the consistency of these two approaches and on the agreement of the results in the 2 and 3 HCON sky areas, all the above numbers can be converted to an estimate of the completeness of a single HCON and plotted on the same graph. To do so, recall from Chapter VIII that in terms of the single HCON completeness C (= 1 − p), the completeness of the PSC in the 2 HCON sky is C^2 and in the 3 HCON sky is $C^2(3 - 2C)$.

Figures XII.A.7a,b show the single HCON completeness at 12 and 60 μm. There is good agreement between the $\log N/\log S$ and the SSC vs PSC-2 results. In addition, the numbers from the 2 HCON sky and the 3 HCON sky are also consistent. However, the 12 μm results are significantly different from the results shown in Figure VIII.D.1 derived from sources in the minisurvey. Because those sources were in the 7 HCON sky, they suffered tremendously from the effects of flux overestimation. This results in a shift of the minisurvey completeness curves to erroneously higher flux densities. Table XII.A.8 summarizes the Catalog completeness at 12 and 60 μm as derived from the curves shown in Figure XII.A.6a,b.

Table XII.A.7a

12 μm Completeness from SSC

Flux density (Jy)	2 HCON sky N'	M'	Completeness	3 HCON sky N'	M'	Completeness
0.50-0.55	6	6	1.00	16	16	1.00
0.45-0.50	4	5	.80	18	18	1.00
0.40-0.45	13	15	.87	17	17	1.00
0.35-0.40	7	11	.64	15	15	1.00
0.30-0.35	8	17	.47	15	23	.65
0.25-0.30	6	24	.25	24	39	.62
0.20-0.25	3	26	.12	4	50	.08

Table XII.A.7b

60 μm Completeness from SSC

Flux density (Jy)	2 HCON sky N'	M'	Completeness	3 HCON sky N'	M'	Completeness
0.60-0.65	14	17	.82	11	11	1.00
0.55-0.60	10	13	.77	17	20	.85
0.50-0.55	14	25	.56	20	24	.83
0.45-0.50	8	22	.36	18	29	.62
0.40-0.45	5	29	.17	14	35	.40
0.35-0.40	4	36	.11	13	66	.20
0.30-0.35	5	49	.10	10	70	.14

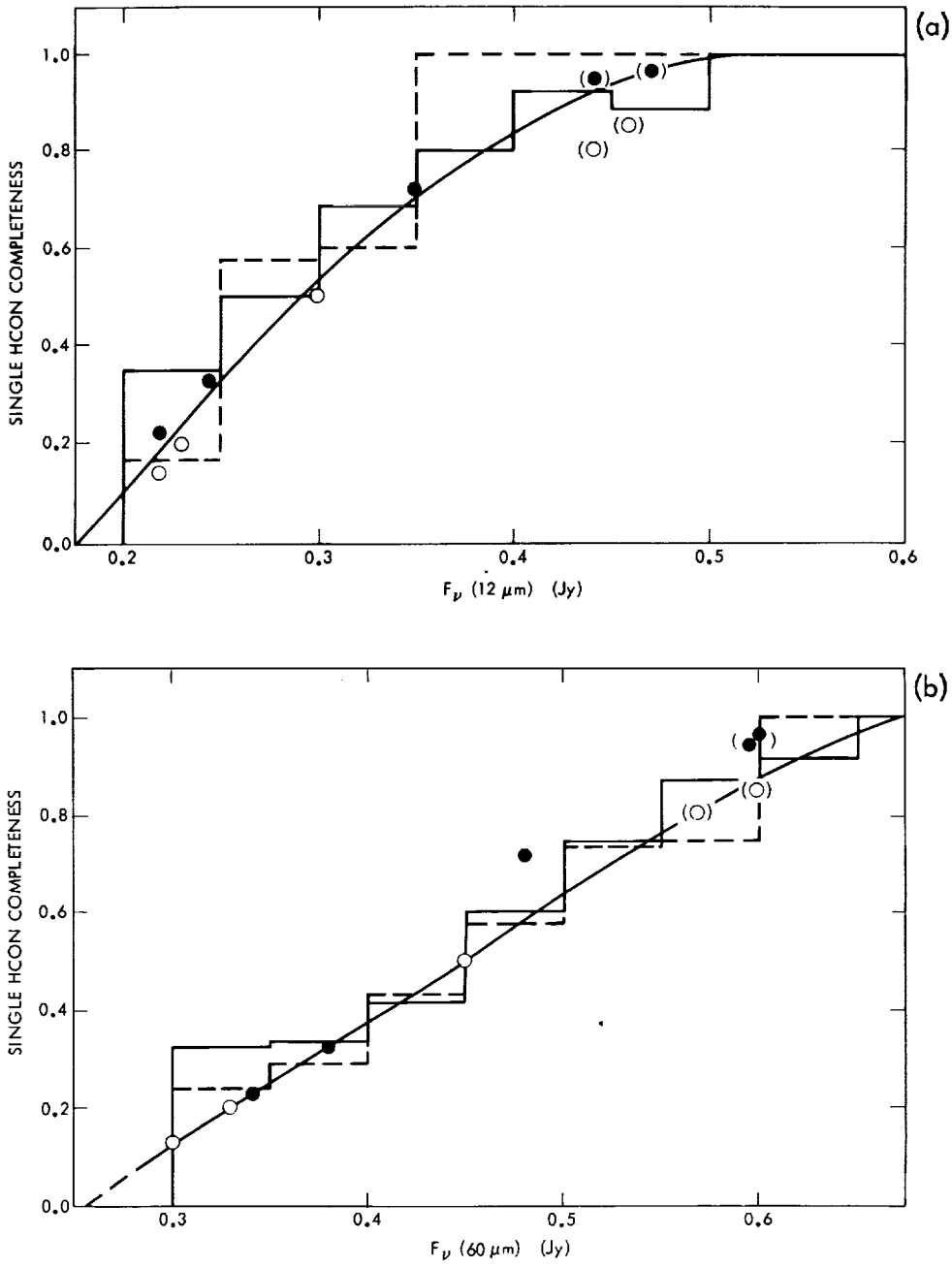

Figure XII.A.7 a) The single HCON completeness versus 12 μm flux density. A smooth solid line has been drawn through the data. The other solid line is from the 2 HCON SSC results, the dashed line from the 3 HCON SSC results, the solid points from the 2 HCON $\log N/\log S$ results, and the open points from the 3 HCON $\log N/\log S$ results. Uncertain points are in parentheses.

b) The single HCON completeness versus 60 μm flux density. The smooth solid line has been drawn through the data. The other solid line is from the 2 HCON SSC results, the dashed line from the 3 HCON SSC results, the solid points from the 2 HCON $\log N/\log S$ results, and the open points from the 3 HCON $\log N/\log S$ results. Uncertain points are in parentheses.

Table XII.A.8

Best Estimate of Completeness Level

(PSC-2)

Completeness (%)	Flux Density (Jy) 2 HCON sky 12μm	2 HCON sky 60μm	3 HCON sky 12μm	3 HCON sky 60μm
95	.46	.65	.41	.58
90	.45	.64	.38	.56
75	.41	.59	.34	.51
50	.35	.52	.29	.45
25	.29	.45	.25	.38
10	.25	.38	.23	.32
5	.23	.34	.22	.30

A.5 Associations

The PSC-2 contains associations with sources in four additional catalogs not used in the preparation of PSC-1: the IRAS Small Scale Structure Catalog, the IRAS Serendipitous Survey Catalog, the OSU catalog of radio sources and the Michigan Spectral Catalog. Parameters for these new catalogs are given in revised versions of Tables V.H.1 and X.B.4. These catalogs were added at the end of the queue for the printing priority in the printed version of the PSC. However, in the printed version of PSC-2, an asterisk in the column giving the number of associations (NID) denotes an association of a PSC-2 source with an object in the Serendipitous Survey Catalog.

There was an error in associating PSC-1 sources with stars in the Gliese catalog since the proper motion in right ascension was erroneously taken as seconds of arc per year instead of seconds of time per year. Remedying this error resulted in the addition of 37 associations in PSC-2 and the deletion of five associations originally presented in PSC-1. The changed associations are given in Table XII.A.9.

The ESO/Uppsala Catalog, catalog 14, was previously given a "multiple" classification instead of "other". This has been corrected in PSC-2.

Table XII.A.9 Changed Gliese Associations

Newly Associated Sources

00027-3737	01365-1812	06562-4413	16451-4737
00156+4344	01416-1611	08053+6952	16564+4726
00176-6509	01504-2240	11027+4347	17023-0459
00235-7731	02085-5103	13275+1038	20017+2312
00295+6657	02334+0639	13432+1508	20542-4419
00348-2502	03168-6245	13469-2151	21141-3904
00461+5732	03172-6241	14006-4634	21598-5700
00589+7124	03180-4315	14260-6227	22070-0452
01051+5439	05100-4502	14359-6031	23029-3607
			23110+5653

Sources No Longer Associated

07483+8023	08355-3958	16267+1831	19145+0505
21362-2732			

The following minor changes exist in the associations with all catalogs for sources in the area bounded by ecliptic longitude 260°-280° and ecliptic latitude -60° to 60°. The truncation error mentioned in Supplement XI.K.10 has been fixed. One new association with the catalog of Suspected Variables, catalog 16, was made exactly at the maximum 90″ radius allowed (source 18237-2417). The latest version (1984) of the SAO catalog was used in the generation of PSC-2; six new associations were made and eight old associations were lost. These sources are given in Table XII.A.10. All 14 of these associations were at the maximum radius allowed.

Table XII.A.10 Changed SAO Associations

Newly Associated Sources

17167-3229	17370-3843	18311-1734	18402-7755
17326-3324	17510-3726		

Sources No Longer Associated

16516-6705	17337-0220	17458-0937	17555+3324
17236-2125	17394+2611	17519-3035	17557+3351

A.6 Source Names

Source names were derived from the equatorial position by taking the hours, minutes and tenths of minutes (truncated, not rounded) of right ascension as well as the sign, degrees and minutes of declination. For example a source at $\alpha = 12^h22^m15.5^s$ and $\delta = -15°20'15''$ has the name 12222-1520. Separate sources which would have been given the same name based on the above scheme were distinguished from one another by appending letters of the alphabet to their

name. It should be noted that since sources were named before the decision to retain them in the catalog was made, it is possible that not all of the sources with names distinguished only by a letter will be present in the Catalog, e.g. 12222-1520B might be in the catalog, but not 1222-1520A.

A.7 Revised Positional Uncertainties for Bright Sources

As described in the Section VII.C.1.b, an additional 3″ was supposed to be added in quadrature to the in-scan uncertainty of sources that were both faint and had the minimum possible (1″) in-scan uncertainty. That correction was inadvertently applied in PSC-1 to all sources, faint and bright, with the minimum uncertainty. PSC-2 corrects this problem and has 84,287 sources with this increased uncertainty, as opposed to 144,403 sources in PSC-1. The minimum uncertainty ellipse is now 3″ × 5″, as opposed to 3″ × 7″.

A.8 Correction of Point Source Neighbor Counts

In PSC-1 the counts of hours and weeks confirmed neighbors, denoted PNEARH and PNEARW, of a given source are in error for objects near which a forced weeks confirmation took place (Section V.H.3). This problem has been fixed for PSC-2.

A.9 Spurious 25 μm Only Sources

The following three sources have been found to be spurious on the basis of examination of co-added detector data, but were left in the catalog since no general rule could be used to delete them. They are: 05570-6722, 08291-6146, and 18021+6556. The first and third sources were produced by noise and radiation hits; the second resulted just from noise.

A.10 Working Survey Data Base, Ancillary File and Reject Files

The version of the WSDB corresponding to PSC-2 is 4.0 (Nov. 1986) and differs from 3.0 only in the revised number of sources in the catalog described above (56 additions, 6 deletions). Version 3.0 (Feb. 1986) corrected a calibration error in the flux densities of individual HCON sightings. Version 2.0 was the first publicly released version of the WSDB.

Two errors were remedied in Version 3.0 of the Ancillary file. First, the "fault" byte in HSDDROC (see Table X.B.7c) was incorrect for a small number of sources due to the incorrect very near neighbor window. This is now corrected. Second, the first publicly released version of the Ancillary File (version 2.0) contained associations with the weeks-confirmed file for the Small Scale Structure Catalog: only about half of these weeks-confirmed sources survived to the final SSS catalog. The hex coding of the bands in which an extended source was detected

was calculated incorrectly. These problems have been fixed in version 3.0 of the Ancillary File.

Listings of point sources that failed the catalog selection criteria, e.g., confusion or insufficient number of HCONs, were not publicly released, but are available from the IRAS data center in Pasadena.

B. Total Intensity Data

B.1 Total Intensity Maps

A number of fields were omitted from the first release of the third HCON sky images due to the misapplication of a calibration factor (Section XI.F.1). This error has been corrected and the second release of the third HCON includes all the possible fields.

B.2 Version 2.0 of the Zodiacal Observation History File

The Zodiacal Observation History File (ZOHF) was recreated to correct a 0.5° in-scan position error found in Version 1.0. Several additional improvements were incorporated at the same time. A calibration correction that partially adjusts for errors in the electronic baseline was added. The sampling interval was decreased to 4 seconds of time (~1/4°) from 8 seconds of time (~1/2°). The 8 second (~1/2°) boxcar filter size remains the same. All records in Version 2.0 represent 8 seconds of contiguous data, whereas in Version 1.0, non-contiguous data were incorporated in the file when possible. Data from the edge detectors were not used in the new file. This means the averaged values represent, in cross-scan, 27.3′ for the 12 μm wavelength band and 28.5′ for the 60 μm wavelength band. Though data from edge detectors in the 25 and 100 μm bands were also removed, the remaining full-sized detectors in these bands cover the full 30′ width of the focal plane.

C. Low Resolution Spectrometer

No significant errors in the processing of the data from the Low Resolution Spectrometer (LRS) have been reported. A complete atlas of LRS spectra appears in *Astronomy and Astrophysics (Supplement)*, 1986, **65**, 1.

D. Other Anomalies Fixed In this Release

The preceding chapter (XI) lists a variety of anomalies in the data processing that either were discovered too late in the processing to be fixed in PSC-1 or for which no fix was deemed possible. The status of each is detailed in Table XII.D.1.

Table XII.D.1 Status of Anomalies From First Release

A.	Processing of Cirrus	No change
B.	Noise Estimator	No change
C.	Frequency Dependent Responsivity	No change
D.	Cross-scan Uncertainties	No change
E.	Photon-induced Responsivity Enhancement	Analysis in Progress
F.	Artifacts in Maps	Fixed
G.	Photometric Processing of NGC 6543	No change
H.	Unknown Number of Possible HCONs	Partially fixed
I.	Position Uncertainties	Fixed
J.	Flux Overestimation	Fixed
K.	Minor Problems 9,10	Fixed
K.	Minor Problem 7	Analysis in Progress
K.	Other Minor Problems	No change

Authors:

T. Chester, C. Beichman and T. Conrow

References:

Kleinmann,S.G., Cutri, R.M., Young, E.T., Low, F.J. and Gillett, F.C., 1986, *Explanatory Supplement to the IRAS Serendipitous Survey Catalog.*

Young, E.T., Neugebauer, G., Kopan, E.L., Benson, R.D., Conrow, T.P., Rice, W.L., and Gregorich, D.T., 1985, JPL/IPAC Preprint 008.

XIII. CONTRIBUTORS TO IRAS

Many people, agencies, and companies have contributed to the success of IRAS. Those listed below were among the many who have worked on the project since its inception in 1975.

The US National Aeronautics and Space Administration (NASA) was responsible for the design and development of the telescope. NASA also provided the launch of the satellite by Goddard Space Flight Center (GSFC) with a Delta 3910 Rocket at the Western Test Range and ground tracking and communication during the early weeks after launch. NASA was also responsible for the final data processing of the survey data.

The Netherlands Agency for Aerospace Programs (NIVR) was responsible for the design and development of the spacecraft and the intergration of the satellite. NIVR also was responsible for the ground facility and services for the operation of the satellite while in orbit.

The UK Science and Engineering Research Council (SERC) carried out the design, development and operation of the real time tracking and data acquisition facility which controlled the satellite, and supported the design, development and implementation of the non real time control software and the preliminary analysis facility at the Rutherford Appleton Laboratory (RAL).

The overall IRAS project management was co-chaired by Peter Linssen and Gene Giberson. A series of managers have played important roles during the lifetime of IRAS. These include: W. Bloemendal, E. K. Casani, D. Compton, R. Dalziel, J. de Koomen, W. de Leeuw, E. Dunford, T. Harmount, B. Martin, G. M. Smith, and G. Squibb.

Participating at the headquarters of the three agencies were: M. Bensimon, N. Boggess, J. Clapp, L. Dondey, B. Edelson, R. Halpern, C. Hartman, N. Hinners, J. Holtz, L. Jones, L. Kline, W. Logan, F. Martin, B. Norris, C. Pellerin, A. Stofan, D. Stoughton, and D. Wrublick (NASA); N. de Boer, E.F.F.M. Braun, D. de Hoop, A.P. Hoeke, and M. van der Matten (NIVR); and H.H. Atkinson (SERC).

A joint science team defined the overall mission and saw that the scientific requirements were fullfilled. Initially the joint team consisted of H.H. Aumann, D.A. Beintema, N. Boggess, J. Borgman, P.E. Clegg, T. de Jong, F.C. Gillett, H. J. Habing, M.G. Hauser, J. R. Houck, R.E. Jennings, F.J. Low, P.L. Marsden, G. Neugebauer, S.R. Pottasch, B.T. Soifer, R. van Duinen, and R.G. Walker. G. Neugebauer and R. van Duinen served as American and European co-chairmen of the joint team. During the course of the project, B. Baud, C.A. Beichman, J.P. Emerson, T.N. Gautier, S. Harris, G. Miley, F.M. Olnon, E. Raimond, M. Rowan-Robinson, P.R. Wesselius and E. Young joined the science team; in 1982 H. J. Habing became the European co-chairman of the joint science team.

Telescope Development

The Jet Propulsion Laboratory (JPL), operated by Caltech, and the NASA Ames Research Center managed the telescope development.

The participants in the project management activities at JPL were: M.J. Alazard, D. Bane, A.P. Bowman, F.E. Bristow, J.W. Clough, A.G. Conrad, S.L. Conrad, K.R. Cooke, M.Y. Cook, G.G. Coyle, W. Crosson, R.R. Dagelen, D.A. Elliott, R. Hernandez, G.J. Hodges, R.F. Klotz, K.G. Korkus, L.L. Lievense, D. Low, S.L. Molina, M.B. Murrill, H. Otake, G.K. Robinson, C.J. Silvio, C.W. Snyder, J.W.

Stockemer, R.F. Stott, J.J. Van der Woude, and R.H. White.

The participants in the telescope system management at Ames Research Center were: D.L. Ciffone, D. Compton, P. Dyal, R.R. Nunamaker, G.W. Thorley, and L.S. Young.

JPL personnel who participated in the telescope development and testing were: K. Ahlberg, B. Anderson, D.M. Anderson, B. Beidebach, T.J. Borden, L. Broms, B.D. Brown, G.G. Coyle, D.M. Engler, E.L. Floyd, J.A. Garba, J.R. Gatewood, A. Giandomenico, W. Gin, C.S. Guernsey, E.J. Heising, K.G. Holmes, L.E. Hovland, H.B. Hotz, W.P. Hubbard, H.W. Jackson, J.C. Koenig, J.J. Landeros, D.E. Langford, H. Lin, H.R. Long, R.A. Mallgren, D.P. Martin, P.V. Mason, S.D. Mayall, L.F. McGlinchey, F.A. Morelli, K.I. Moyd, F.L. Murphy, W.C. Neiderheiser, C.D. Newby, W.G. Orchard, H. Otake, T. Ozawa, J.D. Patzold, D. Petrac, S.W. Petrick, W.I. Purdy, B. Rax, J. Real, R. Richter, D.K. Rubin, W.M. Ruff, D.R. Rupnik, R.P. Salazar, C.N. Sasaki, K.B. Sigurdson, J. Slonski, J.F. Smith, Jr., J.B. Stephens, G.E. Tennant, E.F. Tubbs, E. Tward, H.D. Von Delden, L. Wen, J. Winther, J.L. Wolfe, C. Wong, E.C. Wong, W. Wood, and F.H. Wright.

In addition, JPL personnel were added that specifically worked during the period of the focal plane redesign. These personnel were: R.H. White, A. Bailey, M.N. Carney, C.D. Carter, S. Chavez, C.T. Cruzan, B.C. Debusk, C.G. Derkson, S. Dodge, D. Eastwood, H.L. Fitzhugh, R. Frazer, D.E. George, J.K. Hofman, R. Irigoyen, C.C. LaBaw, J.O. Lonborg, C.G. Lowell, M. Marquess, M.J. McKelvey, W. Powell, J.J. Simmonds, S. Thompson, A. Toppits, L.S. Varnell, and J. Vasbinder.

At Cornell University, D. Briotta, P. Graf, and G. Gull helped develop the retrofit 100 μm detectors.

At the University of Arizona, K. Armstrong, and R. Kurtz helped develop the 60 and 100 μm filters and the JFET modules. The spectral response of the Ge detectors and the long-term radiation effects on the Si and Ge detectors were also measured. E. Young devised the "bias boost" strategy. The internal reference sources, components of the spectral filters and the JFET moules were manufactured at Infrared Laboratories, Inc., Tucson, Arizona with the assistance of L. Richardson.

Ames Research Center personnel who participated in the telescope system development were: G. Anderson, S. Baker, C. Ball, W. Barrows, T. Bridges, W. Brooks, D. Cusano, G. De Young, M. Dix, L. Edsinger, A. Fernquist, W. Gilbreath, J. Goebel, T. Harmount, R. Hedlund, G. Hillen, E. Iufer, P. Kittel, M. Kiya, R. Lavond, C. Leidich, K. Lorell, H. Lum, Jr., C. McCreight, E. Melugin, G. Nothwang, C. Neel, R. Pittman, L. Polaski, F. Prevost, J. Prucha, S. Rathjen, C. Ritchie, C. Robbins, E. Somer, W. Vanark, J. Vorreiter, R. Walker, T. Weber, C. Yetka, and E. Zimmerman.

The definition study management team at GSFC consisted of E. Hymowitz, S. Mosier, and M. Mumma.

The major companies participating in the design and development of the telescope were:

Ball Aerospace Systems Division - Telescope System

Rockwell International - Focal Plane

Perkin-Elmer Corporation - Optics

Personnel participating in the design and development of the telescope system at Ball Aerospace Systems Division were: T. Abbott, D. Adam, T. Alarez, L. Anderson, R. Anderson, L. Andreozzi, R.

C-5

Arentz, H. Argue, J. Austin, J. Bamberg, C. Barkley, A. Barner, R. Barnes, W. Beck, R. Bemis, W. Bengston, M. Berger, V. Berry, R. Bingham, K. Booth, R. Bradford, J. Briggs, J. Brown, J. Byrnes, W. Cash, H. Chameroy, C. Chambellam, J. Conlan, L. Cotsamire, J. Cowder, J. Cowley, J. Cox, F. Cutter, N. Daly, R. Darnell, D. Davis, T. Davis, D. Dehogg, L. Derouin, W. Deshler, W. Devereux, C. Downey, J. Droge, J. Duncan, G. Emerson, J. Emming, P. Encinias, D. Erickson, M. Erickson, B. Etheridge, D. Evans, B. Evans, L. Ferner-Sinn, L. Fisher, R. Fisher, T. Fleener, B. Fox, H. Freeman, L. Frobom, A. Gabriel, J. Gallegos, J. Godden, D. Grabosky, E. Gray, R. Greenwall, R. Grunz, T. Hadsell, R. Haight, W. Hammel, R.D. Hamlin, R.J. Hamlin, S. Hanley, M. Harrell, K. Hegy, R. Herring, R. Hershey, G. Hicks, D. Hillis, L. Hovda, R. Hopkins, L. Housewright, and L. Hughes. Others include P. Iverson, R. Jackman, G. James, S. Johnson, J. Johnson, J. Jones, M. Kerr, J. Kinsey, W. Lamb, K. Laughlin, T. Le Blanc, D. Lennon, J. Lester, D. Livingston, D. Lloyd, E. Long, R. Loomis, P. Lostroh, M. Maine, R. Manning, J. Marcantonio, J. Mateyka, D. Mathews, K. McDaniel, M. McKeever, V. McNeil, R. Mellon, R. Misch, A. Mord, W. Morley, G. Morris, D. Mount, H. Mynleiff, L. Nall, P. Nelson, M. Noble, P. Olbert, A. Olsen, C. Olson, R. Ortega, A. Pankaskie, D. Payne, J. Penner, K. Peterson, C. Pherson, H. Poehlmann, S. Porrine, M. Poyer, R. Price, P. Puzo, C. Rafferty, D. Regenbrecht, J. Reidy, R. Reinker, D. Roalstad, J. Rodgers, J. Rodriquez, K. Roller, L. Rouse, C. Rowe, H. Royer, S. Scott, G. Seigal, L. Smeins, G. Smiley, R. Snook, J. Sparks, N. Stoffer, D. Strecker, A. Stroeve, R. Sullivan, M. Swoboda, J. Tarpley, J. Taylor, D. Tennant, J. Thorngren, B. Tolhurst, J. Tracy, A. Urbach, D. Van Gundy, L. Vandello, S. Varlese, R. Viano, H. Vogt, J. Wanger, D. Warlick, R. Weary, H. Wells, R. Wendler, R. Werholz, W. Whitehead, W. Wickstrom, K. Willis, B. Wise, R. Wolfkiel, D. Wood, R. Woolley, R. Venne and N. Zaun.

Participants at Rockwell International were: G. Audick, B.R. Bailey, E.C. Banks, D.J. Chiaverini, C.M. Cornelius, M.E. Dews, R.F. Flanagan, W.H. Flaugh, A.L. Gable, C.L. Hall, D.O. Hopwood, E.R. Hutchinson, C. Ju Wu, M.S. Keith, L.W. Kelsey, R.M. Lack, E. Lax, W.C. Milo J.C. Monson, D.G. Moss, A.J. Nicoli, M.D. Petroff, V.S. Pottas, C.A. Randolph, D. Randolph, D.L. Rawlins, J.C. Roth, J. Savela, N. Sclar, L. Silverstein, W.E. Southworth, A.S Squillance, P.G. Tally, J.C. Torres, P.S. Vigneault, J.M. Walz, and J.V. Westling.

Participants at Perkin-Elmer were: B. Alte, R. Altenhof, W. Arndt, J. Ashinasi, J. Bacich, T. Barletto, B. Boyce, W. Craighead, J. Dunn, G. Erdtmann, G. Fabich, G. Ferrera, D. Gabriel, L. Gardella, M. Gillen, F. Gillespie, S. Gowrinathan, R. Grosso, W. Gunther, H. Hall, N. Harned, R. Harned, G. Hawkins, A. Hellerung, G. Huse, R. Jones, R. Jung, D. Kittel, T. Konoski, G. Lester, E. Lotocki, C. McGlynn, M. McGuirk, J. Malloy, J. Mandle, D. Marshall, M. Matrullo, P. Mehta, H. Moeller, P. Naiden, B. Nardella, V. Nichols, R. Noll, J. Oberheuser, T. O'Neil, A. Osanitch, W. Papas, R. Paquin, W. Petrie, D. Phillips, C. Radcliff, R. Rowley, J. Russo, M. Schreibman, D. Shafer, F. Sileo, J. Stites, R. Stoll, D. Stramiello, J. Tolan, D. Trost, N. Vancho, B. Voytek, A. Westfall, N. Woodbury, P. Young, and P.S. Young.

The additional focal plane instrument (DAX) was designed, developed, manufactured, and tested by the Laboratory for Space Research, University of Groningen, with assistance from the Technical Physics Department of the Netherlands Organisation for Applied Research (TPD-TNO). Participants were J. Evers, A. de Jonge, W. Luinge, K. Wildeman, W. Werner, and J. Achthoven.

Spacecraft

The spacecraft was designed and built by ICIRAS, an industrial consortium of Fokker and Signaal, the Dutch National Aerospace Laboratory (NLR) as a subcontractor. Participating at Fokker, Signaal and NLR were: W. van Es, R. Grijseels, P. Kant, H. Koot, J. Keijzer, W. Ligtenberg, C. de Leng, T. Olivierse, P. de Pijper, W. Pasteuning, G. Rietdijk, R. Schuren, J. Seeboldt, M. Vreeman, H. Vreeling, R. Waayer, D. Weber.

Participants in the design and development at Fokker, Signaal, and NLR were: H. Bakker, W. Berkepeis, R. van Bezooyen, H. Buiter, J. Bisschop, P. Buurs, J. Field, A. Fok, R. Gibson, W. de Graaf, J. van de Heuvel, D. Jongeling, J. Kanis, A. Koekenberg, F. Koorevaar, G. van der Kruys, W. van der Laan, P. Lindhout, S. Maltaric, A. Mooij, J. Nolte, D. Noordhorn, N. Pennings, J. Piebinga, F. Rekers, H. Rouws, W. Schenck, D. Schermer, B. Scholte van Marst, H. Sprengers, N. Smilde, M. Thijssen, P. Verveen, J. Wantsing, M. Wattel, J. van der Weerdt, C. van Wesel, H. Witte, J. Wijker, J. Wijnen.

Apart from involvement in design and development, the following persons also prepared and carried out the spacecraft check-out and monitoring during operations: E. Boom, J. van Casteren, R. van Doorn, M. van Dijk, G. Hameetman, L. Karsten, K. de Kluiver, M. Lamers, W. van Leeuwen, J. Prins, A. Pouw, C. P. R. C. Slippens, A. van Swieten, F. Teule, and C. van der Voort Maarschalk.

Integration and Test

The ICIRAS industrial consortium (Fokker and Signaal), assisted by NLR, had the prime responsibility for the satellite integration and test effort. Their Integration and Test team cooperated with that of JPL and with specialists from Ball Aerospace. The success in making this a unified effort was a major accomplishment of the IRAS project.

Personnel supporting the integration and test of the satellite from JPL were: M.J. Alazard, G. Alba, D.M. Anderson, M.J. Argoud, J.C. Beckert, C. Beichman, D.J. Boatman, K. Breski, L. Broderick, B.D. Brown, R. Brown, R.W. Burt, L.V. Butler, N. Carte, W.J. Castellana, A.G. Conrad, G.G. Coyle, R. Daniel, F. Geno, D.C. Hammond, J. Harrel, E.J. Heising, J. Holbrook, W.R. Irace, J. Johnstone, J. Juric, F.L. Lane, T. Laney, P.V. Mason, J. MacConnell, J. Meehan, F.L. Murphy, E. Nave, J.D. Patzold, K. Port, D.L. Potts, D. Rosing, D.S. Ross, C.N. Sasaki, W. Schaefle, T. Shain, R.L. Sicol, A.G. Silliman, J.J. Simmonds, J.P. Slonski, S.T. Smith, L. Steimle, M. Temple, P. Van Velzer, J. Vasbinder, W. Walker, R. Weaks, C. Weidmann, R.H. White, V.A. Wirth, Jr., and W.R. Woods.

Those individuals who supported the satellite test and integration from BASD were: L.C. Andreozzi, D.K. Chaffey, L.D. Davis, D.A. Durbin, R.O. Einertson, N. Erickson, E.C. Long, N.E. Magette, V.B. McNeill, R.M. Paris, W.E. Pinon, D.P. Runyon, C.A. Springer, J.L. Tucker, J.L. Tracy, Jr., A.R. Urbach, R.G. Voorhees, and J.A. Wells.

Support provided by individuals at Fokker, Signaal, and NLR were: A. Bleekrode, C. Blom, R. van de Brink, J. Buesink, H. Carrington, H. Van Daalen, A. Van Dorsten, H. Hanekamp, D. van 't Hof, L. Huesken, J. Klaaskate, H. Keppel, J. Kollen, W. Kollen, J. Lageman, T. Lamberts, M. Van Leeuwen, P. Moes, R. Nicolai, W. van Nifterick, R. Overgauw, T. Pasteuning, C. Schmeitink, A. Van Soolingen, B. Stenneke, J. van der Straaten, C. Taylor, S. Tensen, H. Vaassen, D. Van de Vegt, J. Verhey, A. Vialle, J.

Webbers, P. Wielsma, J. Zuidam, and J. Zwarts.

Launch

The NASA Delta Project Office at the Goddard Space Flight Center and the Delta Launch Operations of the Kennedy Space Center were responsible for the launch of the satellite.

Ground Operations Software

The software for the IRAS Ground Operations (IGO) was developed by a joint team from NLR and RAL under the management of R. van Holtz, R. Holdaway and A. Buck, and consisted of L. Baldwin, L. Barendse, I. Beharrel, A. Chipperfield, T. Dimbylow, D. Drummond, R. Ely, J. McDougall, B. Miller, K. Mount, E. Oord, P. de Pagter, W. Pol, M. Reid and H. Young. The onboard software was the responsibility of the NLR.

The Preliminary Analysis Software, managed by G. Thomas, was written by J. Abolins, P. Barber, J. Fairclough, S. Green, S. Martin, M. Oliver, J. Renes, P. Richards, A. Stevens and B. Stewart.

Operations

The overall running of the mission was coordinated by the Mission Operations Manager, R. van Holtz, and his deputy A.J. Rogers. Operations at the Rutherford Appleton Laboratories, Chilton, Oxfordshire, were managed by H. Bevan, A. Buck, R. Holdaway, A. Lowe, J. McDougall, P. McPherson, M. Reid and G. Thomas.

The generation of the IRAS Satellite Observation Plans was the responsibility of the IRAS Ground Operations Team consisting of J. MacDougall, L. Baldwin, J. Gourlay, S. Martin, E. Oord, W. Pol, G. Spalding and H. Young.

Commanding of the satellite and receipt of the data were performed by the Chilton Operations Team led by D. Ewart, L. Harris, B. Rathbone, J. Stenning and J. Wright.

Monitoring of the housekeeping data and a preliminary analysis of the scientific data were the responsibility of the Post Pass Analysis and Science Support Team consisting of J. Abolins, T. Dimbylow, J. Fairclough, K. Mount, M. Oliver and P. Richards. H. Walker monitored the short-term progress of the survey and modified the Observations Plans accordingly.

J. MacDougall and B. Stewart had overall responsibility for maintaining the uplink and downlink software respectively.

The Chilton Operations Support Team of H. Bevan, J. Cathrew, B. Champion, A. Chipperfield, A. Smith and G. Walkers maintained the ground hardware and provided support facilities.

W. McLaughlin, S. Lundy, and D. Wolff designed and implemented the details of the survey strategy with the assistance of C. Lau, H. Ling, R. Schlaifer and V. Wang.

JPL personnel supporting operations at RAL were: A.I. Beers, B.D. Brown, J.B. Carraway, P.E. Doms, D.M. Engler, W.R. Irace, D.E. Langford, P.V. Mason, J.J. Rakiewicz, R.P. Salazar, C.W. Snyder and T. Sweetser.

Personnel supporting operations at JPL were: D. Bender, D.C. Bluhm, D.F. Finnerty, J.A. Holladay, E.D. Jahelka, and R.J. Springer.

Data Reduction

The survey observations were reduced to their final form at the Science Data Analysis System (SDAS) facility at JPL. The final data processing system was developed under the management of J. Duxbury, T. Chester, P. Poulson, W. Scholey and W. Underwood. System design was by P. Poulson, D. Wittman and D. McCreary. Raw data input and conversion was by B. Sorensen and S. Pang. Calibration was by D. Elliot and S. Wheelock. Data detection was by T. Hibbard. Pointing reconstruction was by H. McCallon. Confirmation was by J. Fowler, E. Rolfe and H. Pham. Small extended sources was by E. Rolfe and R. Pomphrey. Sky flux was by R. Stagner and R. Narron. Deep sky was by E. Kopan. Final product processing for the point source catalog was by T. Chester, C. Beichman, R. Beck, J. Bennett, J. Chillemi, N. Chin, T. Conrow, C. Oken, T. Sesplaukis and D. Wittman. Data base design was by T. Sesplaukis, C. Biller, J. Chillemi and F. Akers. Asteroid extraction was by S. Peters, T. Kia and J. Fowler. Simulation was by S. Kitzis and K. Moyd. User support software was by J. Bennett. Science and operations analysis by T. Chester and R. Benson. Image processing was by B. Hartley.

Post processing and product analysis was by T. Conrow, J. Good, D. Gregorich, P. Hacking, G. Helou, S. Pohjala, C. Oken, W. Rice, D. Walker, P. Ramsey and K. Sedwick.

Operations and technical support at JPL was accomplished by a team managed by J. Duxbury, T. Chester, R. Von Allmen, G. Smith and G. Lairmore. The data management team consisted of G. Smith, G. Lairmore, R. Beck, M. Alexander, H. Ashby, R. Bailey, S. Banks, S. Bedrossian, G. Benn, A. Bollin, M.R. Boykins, B.R. Brewer, I. Chan, J. Cisneros, T.J. Crawford, W. Currie, D.M. Engler, I.M. Esquivel, L. Fischer, D.E. Fritsche, L. Fullmer, G.W. Garneau, M. Garza, D. Hermsen, D. Hines, O. Hodges, L.M. Hughes, C.N. Hull, D. Hurwitz, D. Jackson, T. Jay, G. Johnson, B. Kaneshiro, B. Kahr, L. Lampley, L.A. Lloyd, C. Lonsdale, P.J. Lynn, Jr., T.G. MacDuff, F. Macias, I. Miller, N. Parson, G.S. Pate, L.E. Perrine, W.H. Peters, B. Pondo, J. Radbill, P. Ramsey, L. Ray, D. Richardson, E. Robles, A.L. Sacks, M.S. Saul, K. Sedwick, B. Smith, A.E. Stansel, W. Starr, S. Taylor, N.W. Thomas, W.J. Trimble, R. Urban, B.M. Vance, J.E. Walsh, L.L. White, C. Wiley, J.L. Wilson, Jr., and C.A. Wolfe.

The compilation of astronomical catalogs for the final processing was the responsibility of a group at GSFC consisting of J. Mead, T. Nagy and R. Hill.

Pre-Publication Catalogs

The following people and organizations outside the IRAS project provided catalogs on short notice and before publication: S. Kleinman and R. Joyce--catalog of accurate positions of sources from the Two Micron Sky Survey; M.P. Veron-Cetty and P. Veron--the Catalog of Quasars and Active Nuclei; the European Southern Observatory--the ESO/Uppsala Survey of the ESO(B) Atlas; J. Huchra--catalog of Seyfert galaxies; D. Gezari--the Catalog of Infrared Observations; and R. Hill--the most up-to-date version of the CLAS catalog. We also acknowledge the efforts of W. Warren and the Astronomical Data Center at the NASA Goddard Space Flight Center in providing many of the astronomical catalogs used during the IRAS mission and data processing.

The Explanatory Supplement

The Explanatory Supplement was assembled with the enthusiastic assistance of J. Boyd, S. Conrad, R. Dumas (Hernandez), S. Foster, R. Hernandez, S. Livingston, P. Neill, C. Race, J. Serpa. J. Boyd and R. Dumas (Hernandez) helped prepare the second edition of the Supplement.

The Printed Version of the IRAS Catalogs

The computer typeset versions of the IRAS catalogs were prepared by C. Oken, R. Beck and D. Turney. K. Simon oversaw the publication of the IRAS catalogs and the Supplement.

XIV. SURVEY SKY COVERAGE

Plots of the sky surveyed by IRAS are given in the following pages so that the user of the catalog who fails to find a source at some position can verify that the position was, in fact, scanned enough times to result in a confirmable object. At least two hours-confirmed sightings were required for a source to be included in the catalog. A region of the sky was considered as a hole in one of the hours-confirming coverages if: 1) the telescope simply did not observe that region; 2) only failed detectors covered the region; or 3) the particle radiation level was sufficient to increase the detector noise by more than a factor of two.

The broad overview of the sky coverage was given as Fig. I.C.1 The more detailed maps presented here in equatorial coordinates show the *departures* from a "perfect coverage" which is considered to consist of three or more sets of hours-confirming scans. A region receiving three or more coverages shows no deviation from the baseline level, while a region that received only two coverages, i.e., a "level 1 hole", is marked by a single-height box spanning the appropriate range of coordinates; a region that received only one coverage, a "level 2 hole", is marked by a double-height box; and a region that was not scanned at all is shown as a triple-height box. Regions with double or triple height boxes, i.e., having only single or no HCON coverage, do not or cannot contribute sources to the catalog.

Coverage holes due to radiation effects are shown indistinguishably from geometrical holes in these plots. However, data for these regions were processed normally, so that sources may be found in some nominally forbidden regions (Section III.D.2). This applies particularly in the regions of the polar horns where radiation effects were occasionally severe enough to increase the noise level to qualify as a hole, yet not so bad as to prevent the detection of sources.

IRAS SURVEY THROUGH 22 NOV 83

HOLES IN COVERAGE OF EQ. R.A. 0 TO 60 DEG

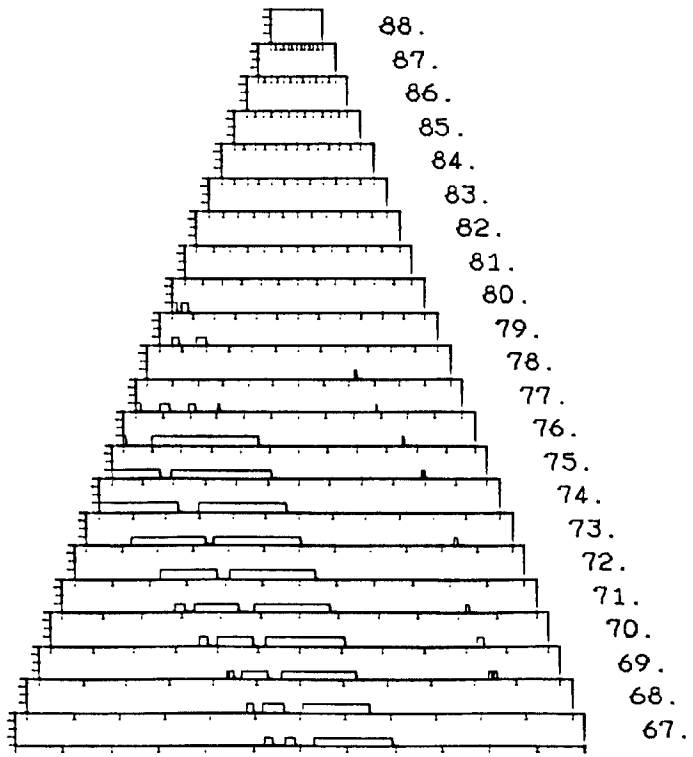

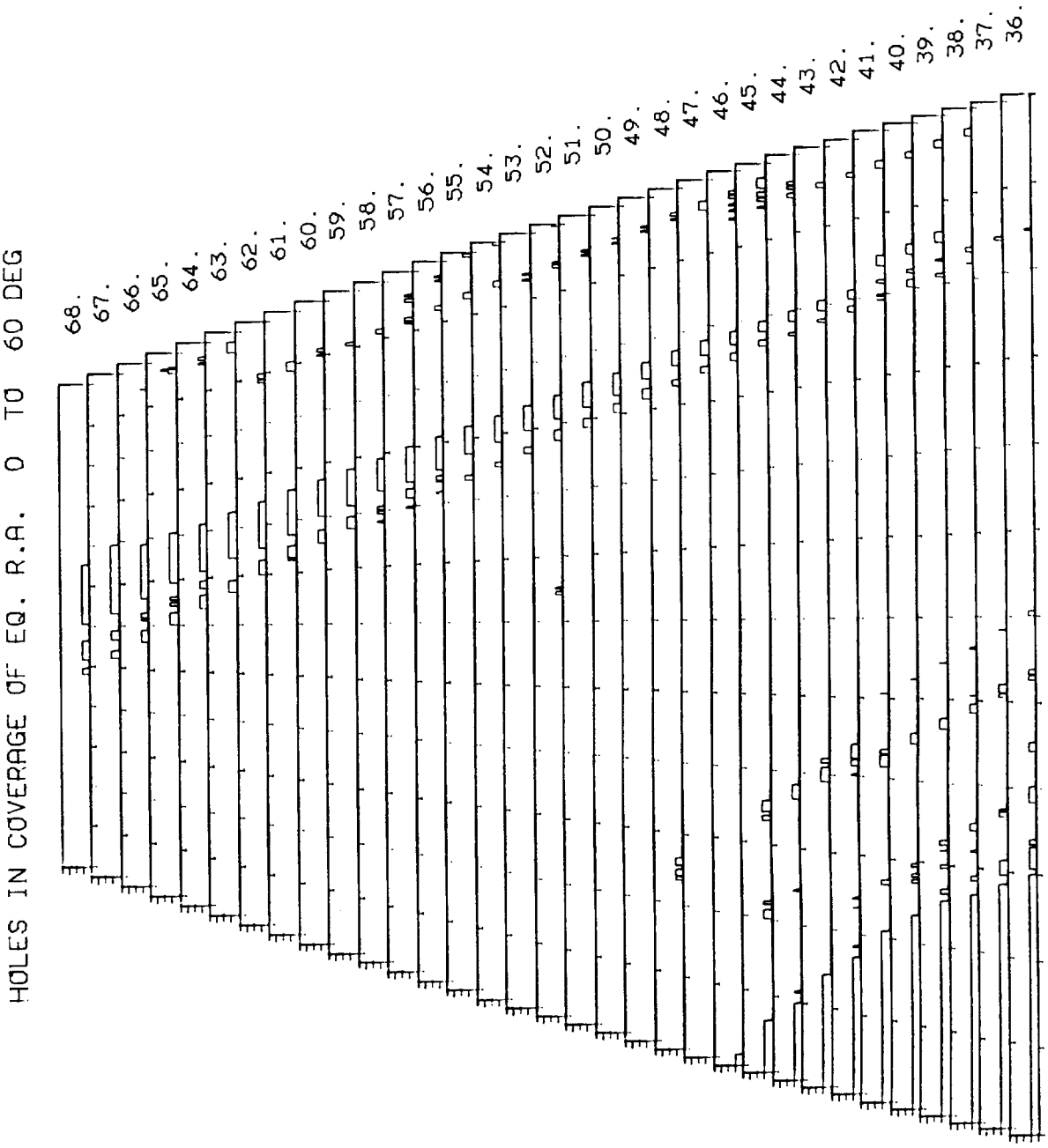

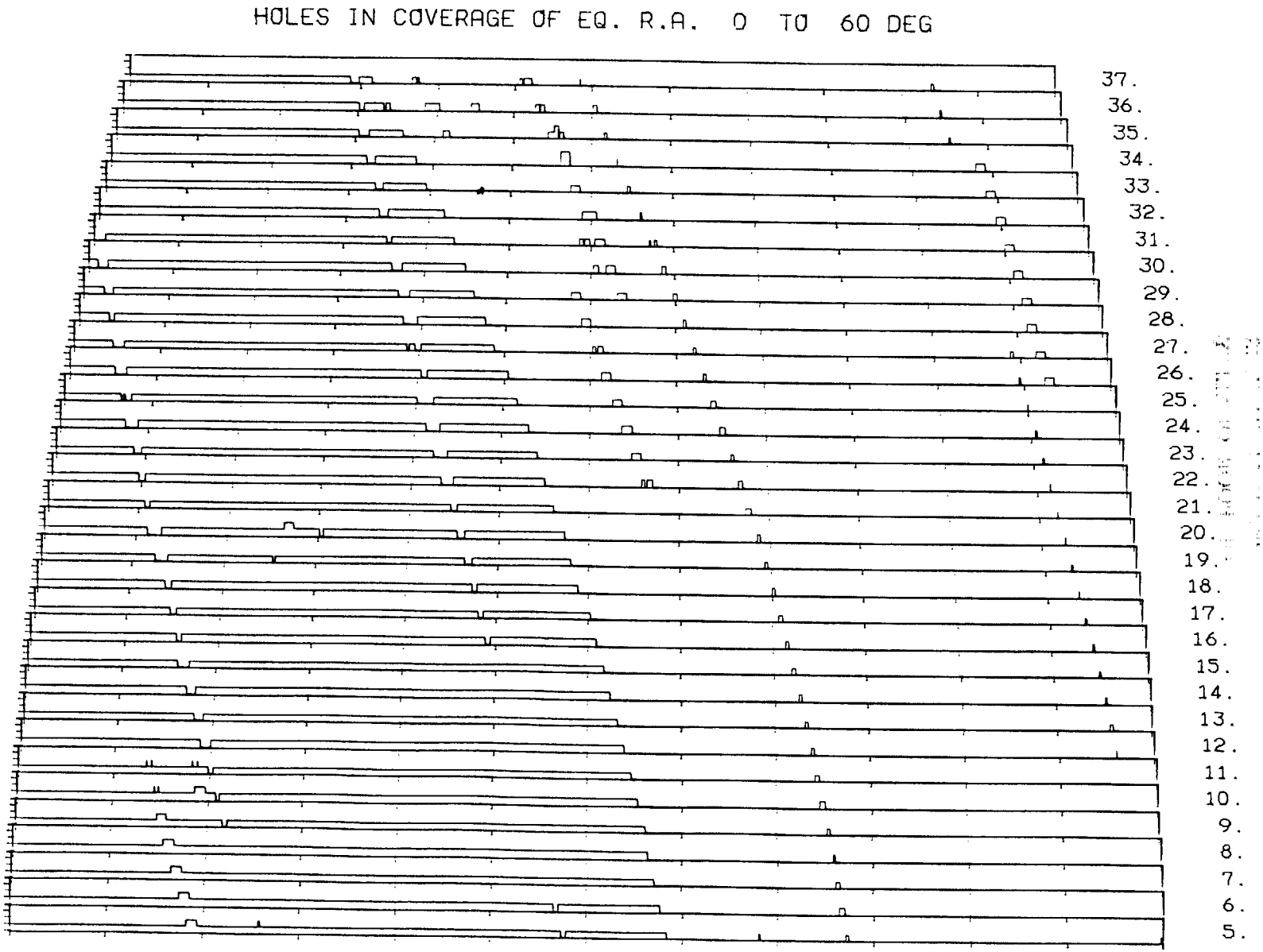

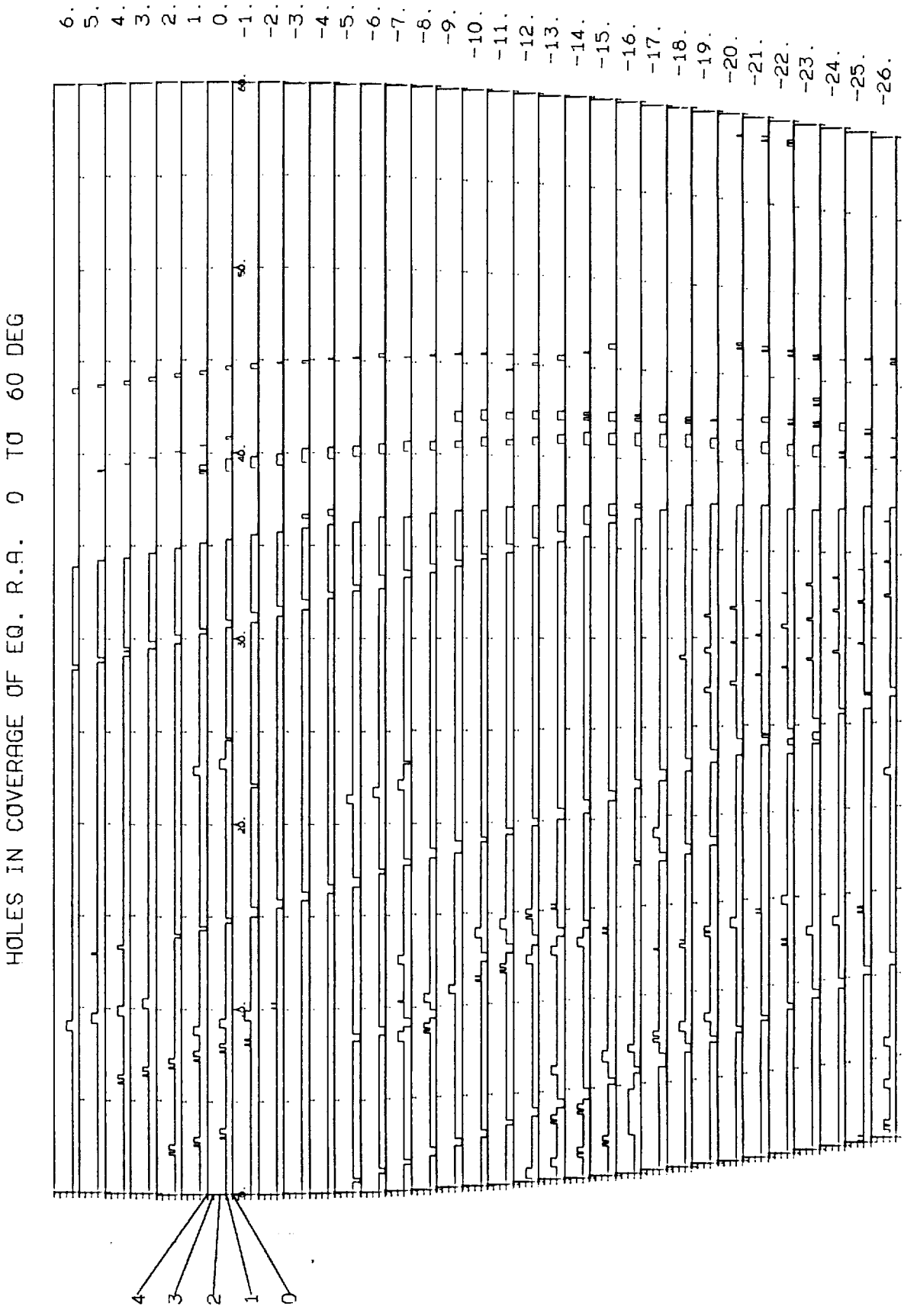

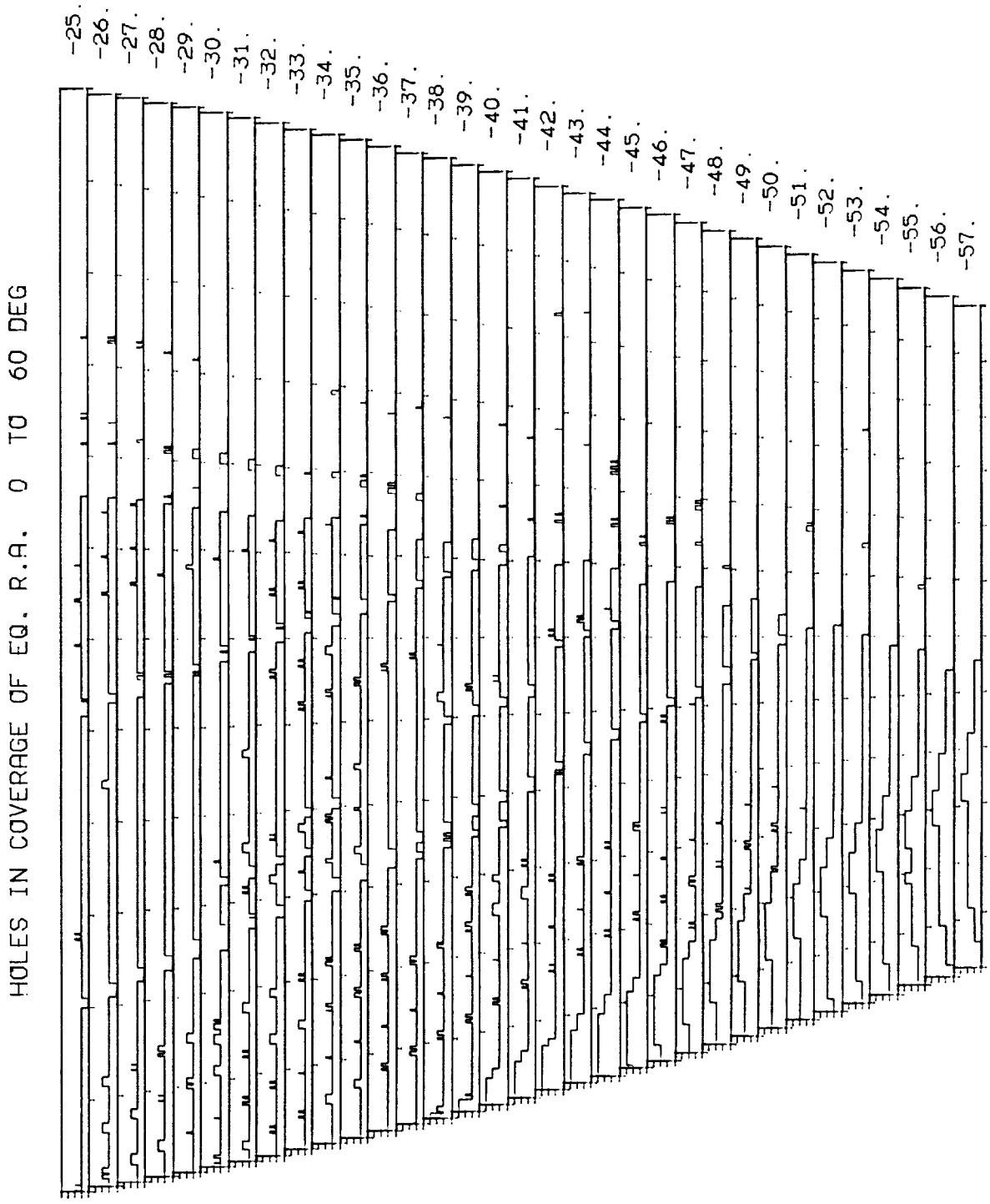

ORIGINAL PAGE IS
OF POOR QUALITY

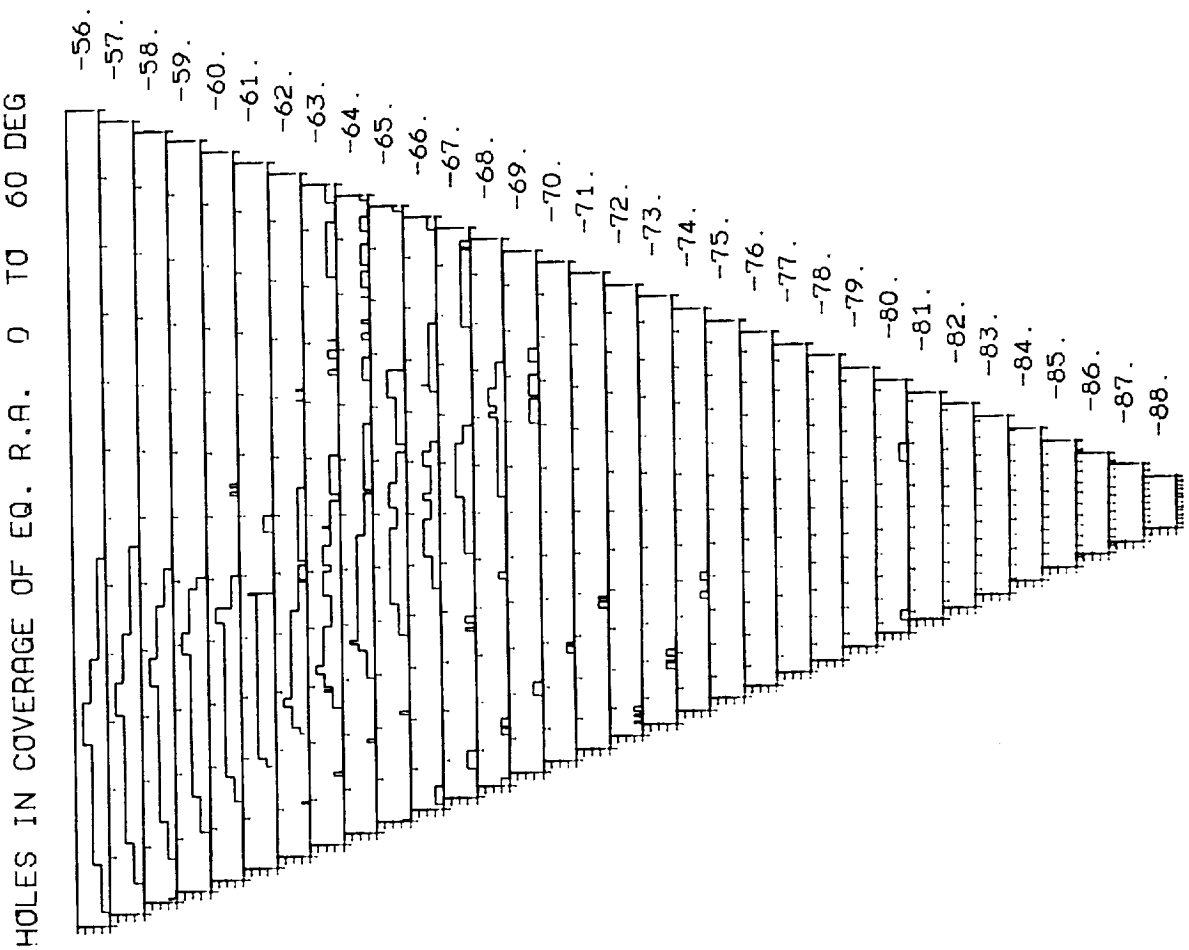

IRAS SURVEY THROUGH 22 NOV 83
HOLES IN COVERAGE OF EQ. R.A. 60 TO 120 DEG

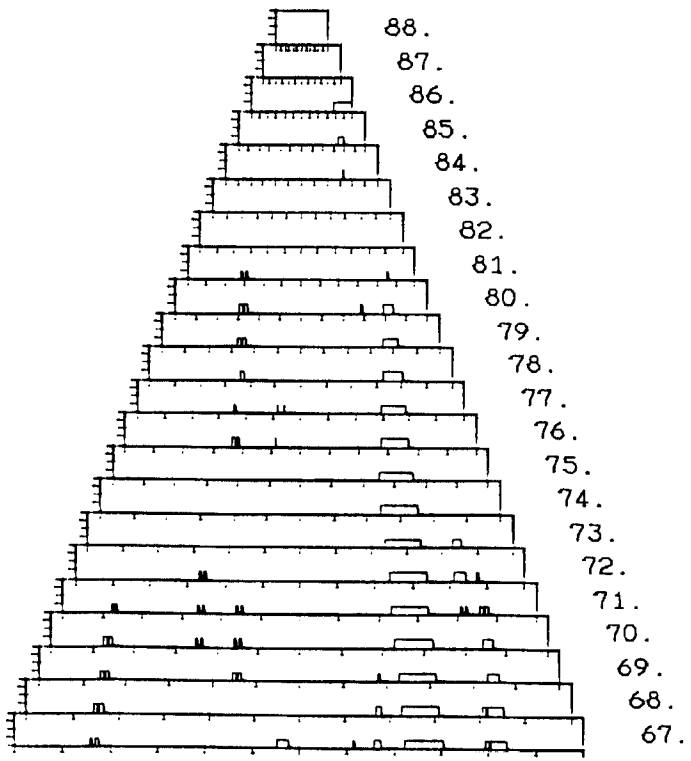

ORIGINAL PAGE IS
OF POOR QUALITY

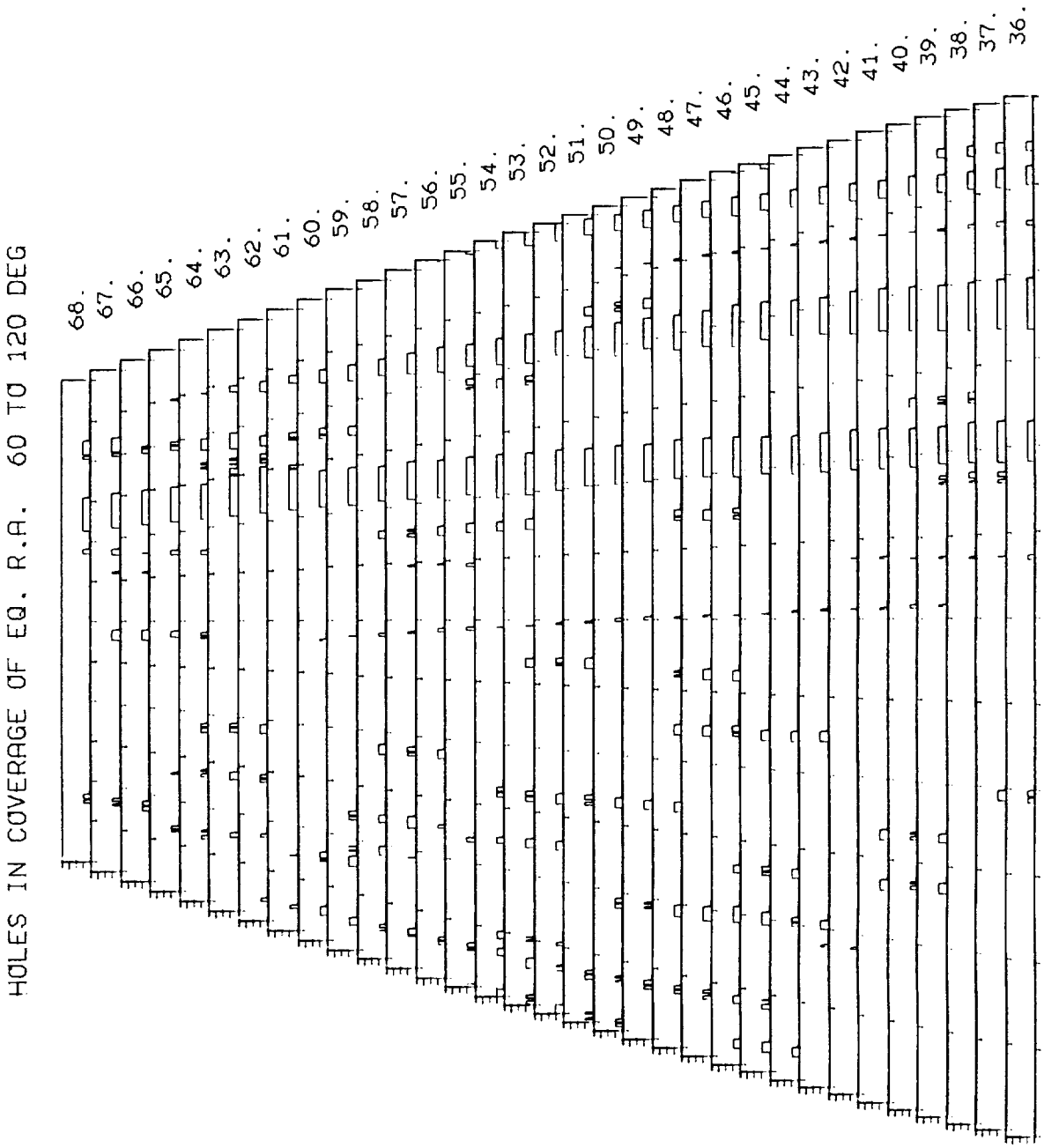

ORIGINAL PAGE IS
OF POOR QUALITY

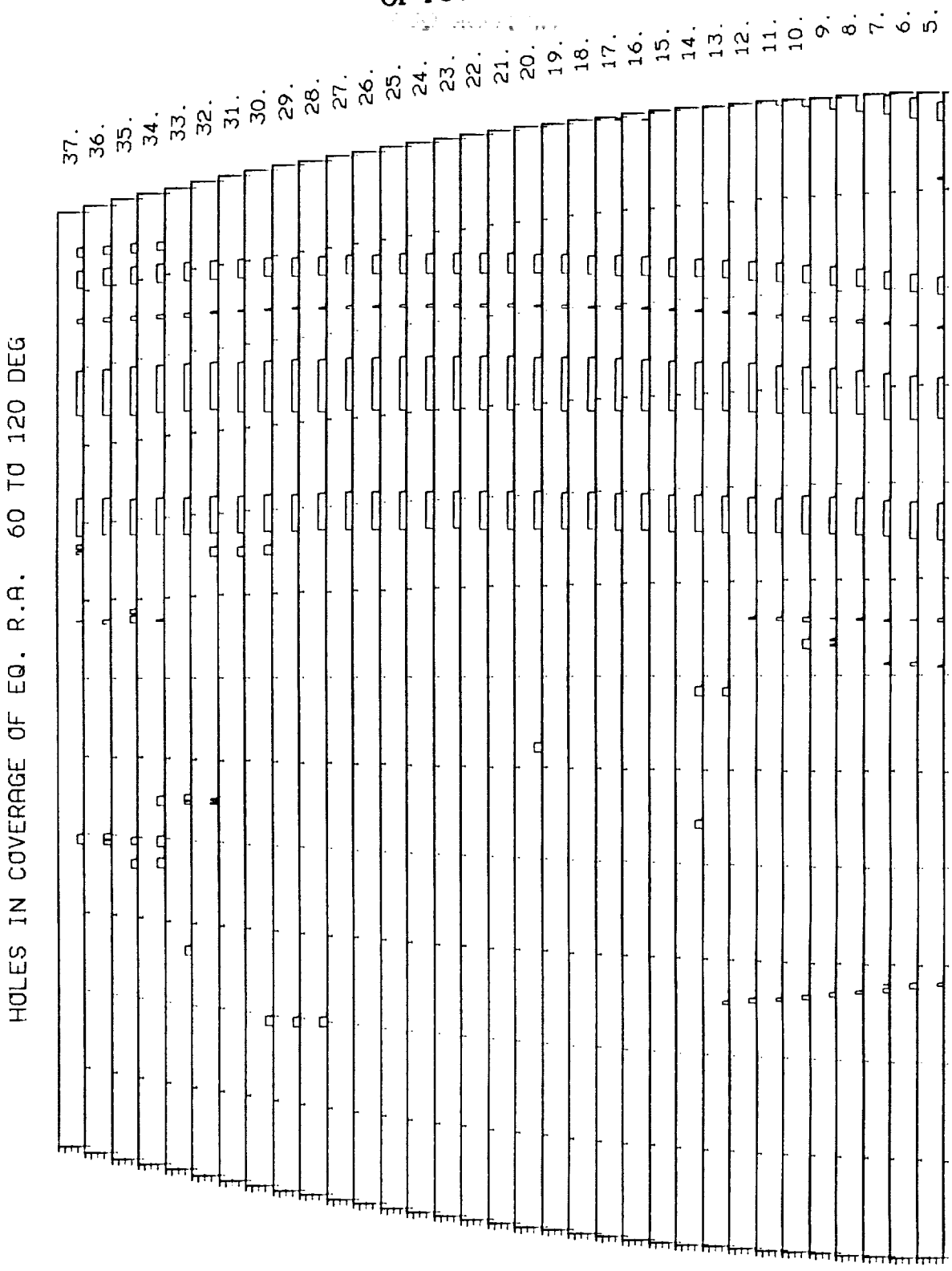

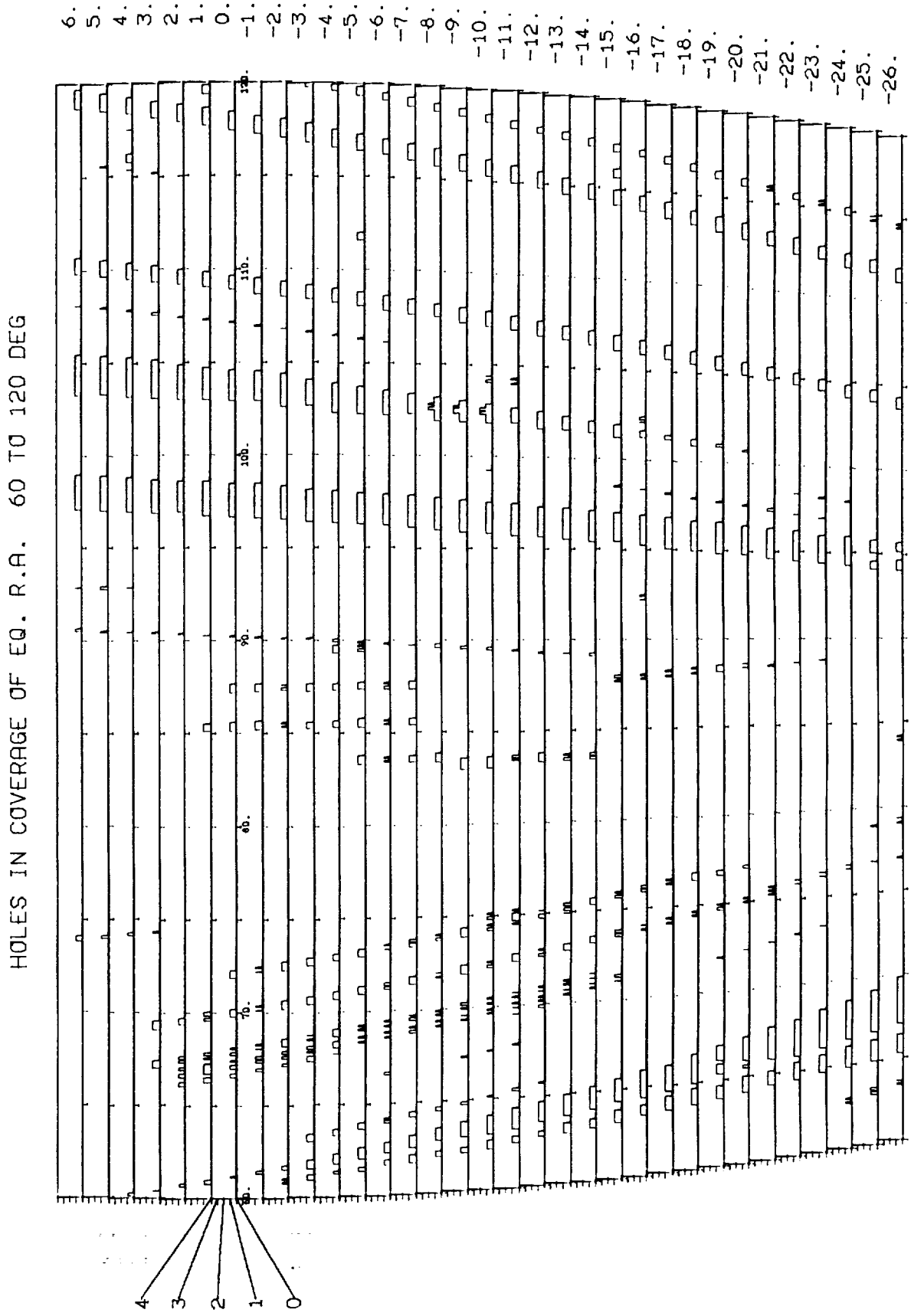
HOLES IN COVERAGE OF EQ. R.A. 60 TO 120 DEG
6.
5.
4.
3.
2.
1.
0.
-1.
-2.
-3.
-4.
-5.
-6.
-7.
-8.
-9.
-10.
-11.
-12.
-13.
-14.
-15.
-16.
-17.
-18.
-19.
-20.
-21.
-22.
-23.
-24.
-25.
-26.
120.
110.
100.
90.
80.
70.
60.
4
3
2
1
0

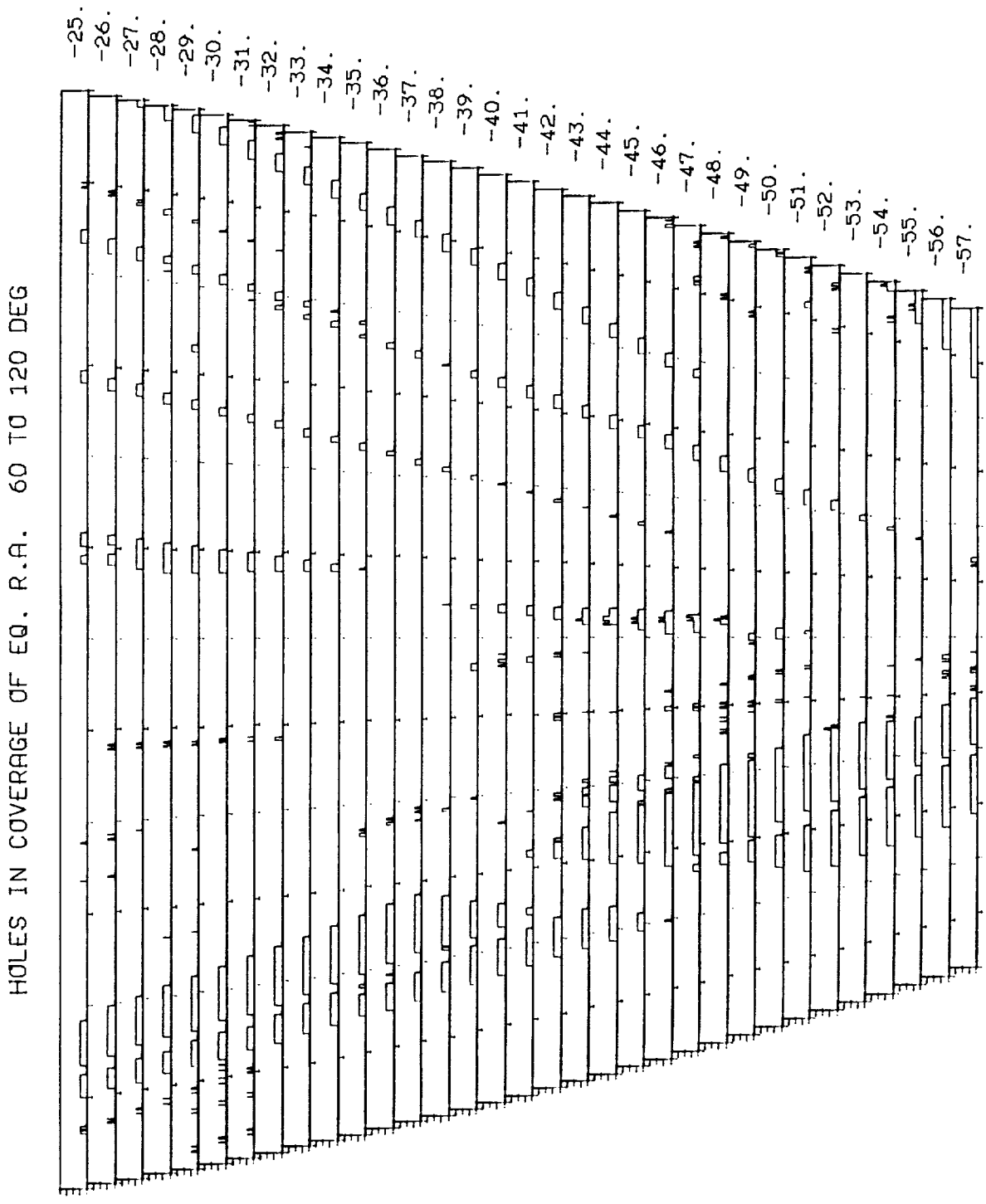

HOLES IN COVERAGE OF EQ. R.A. 60 TO 120 DEG

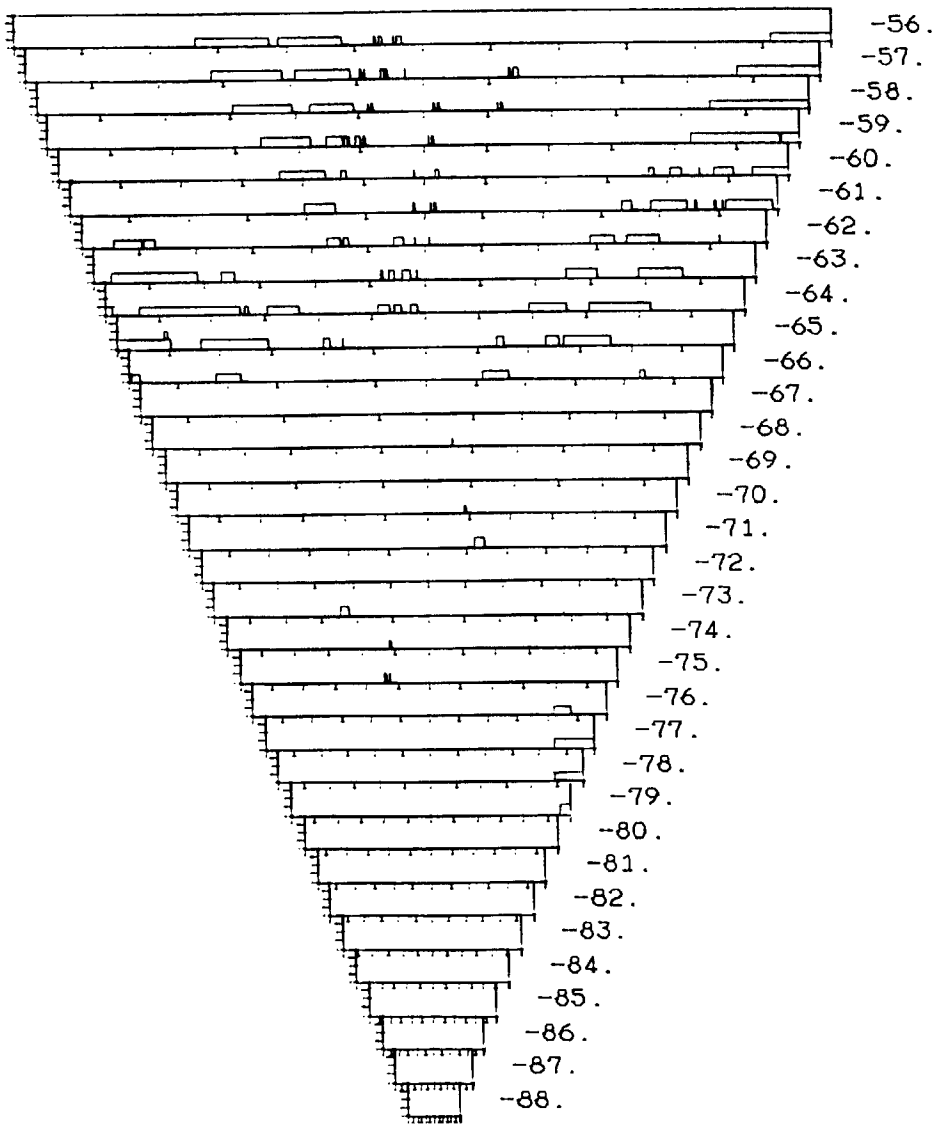

IRAS SURVEY THROUGH 22 NOV 83
HOLES IN COVERAGE OF EQ. R.A. 120 TO 180 DEG

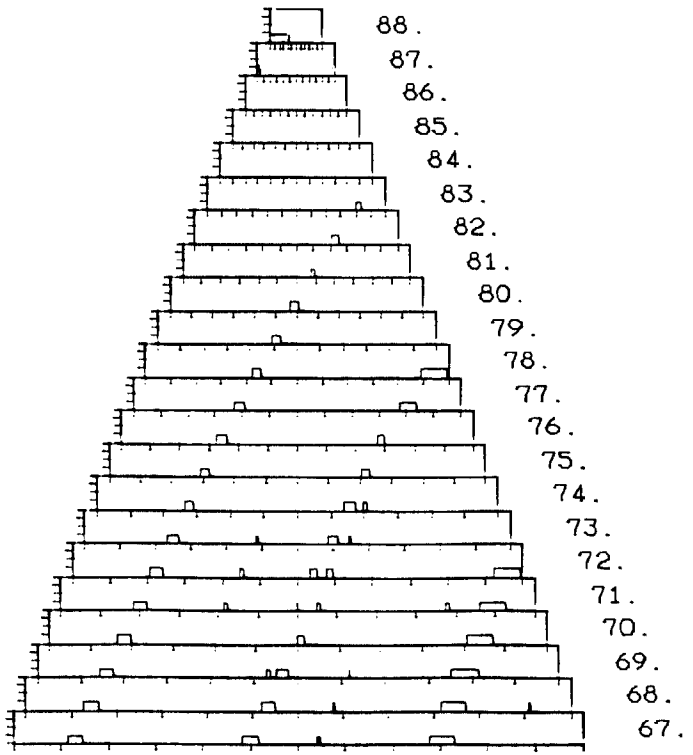

ORIGINAL PAGE IS
OF POOR QUALITY

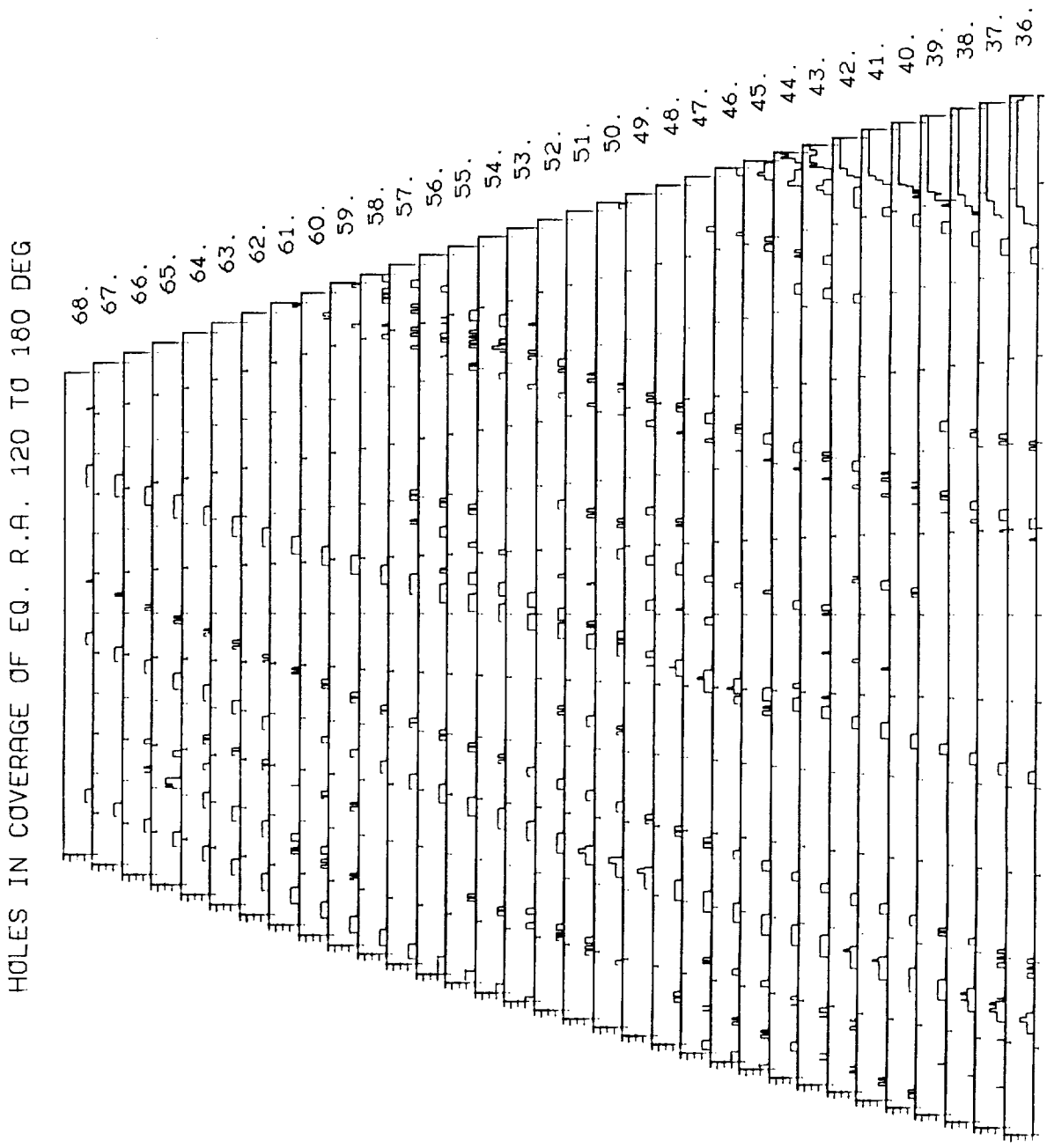

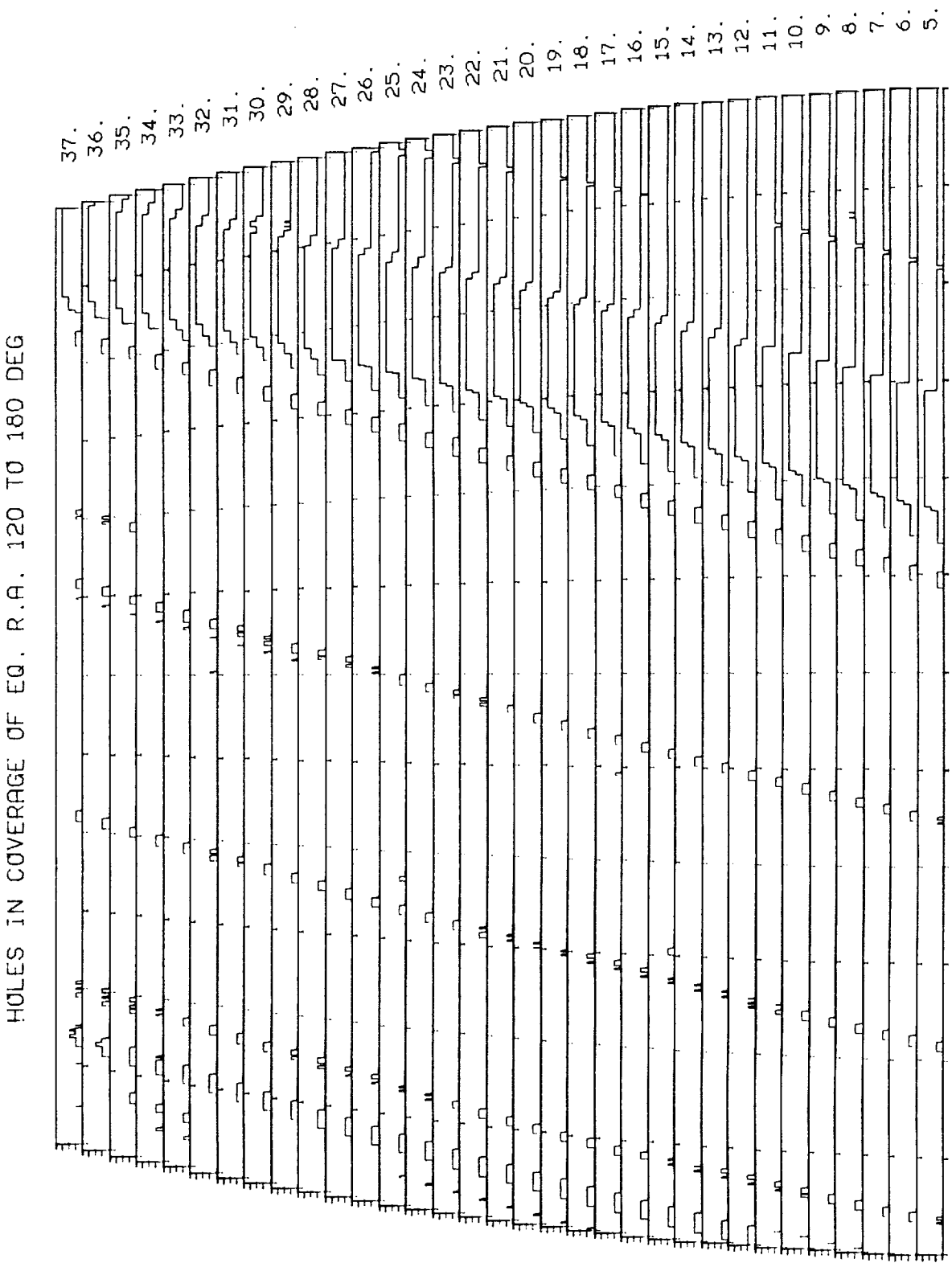

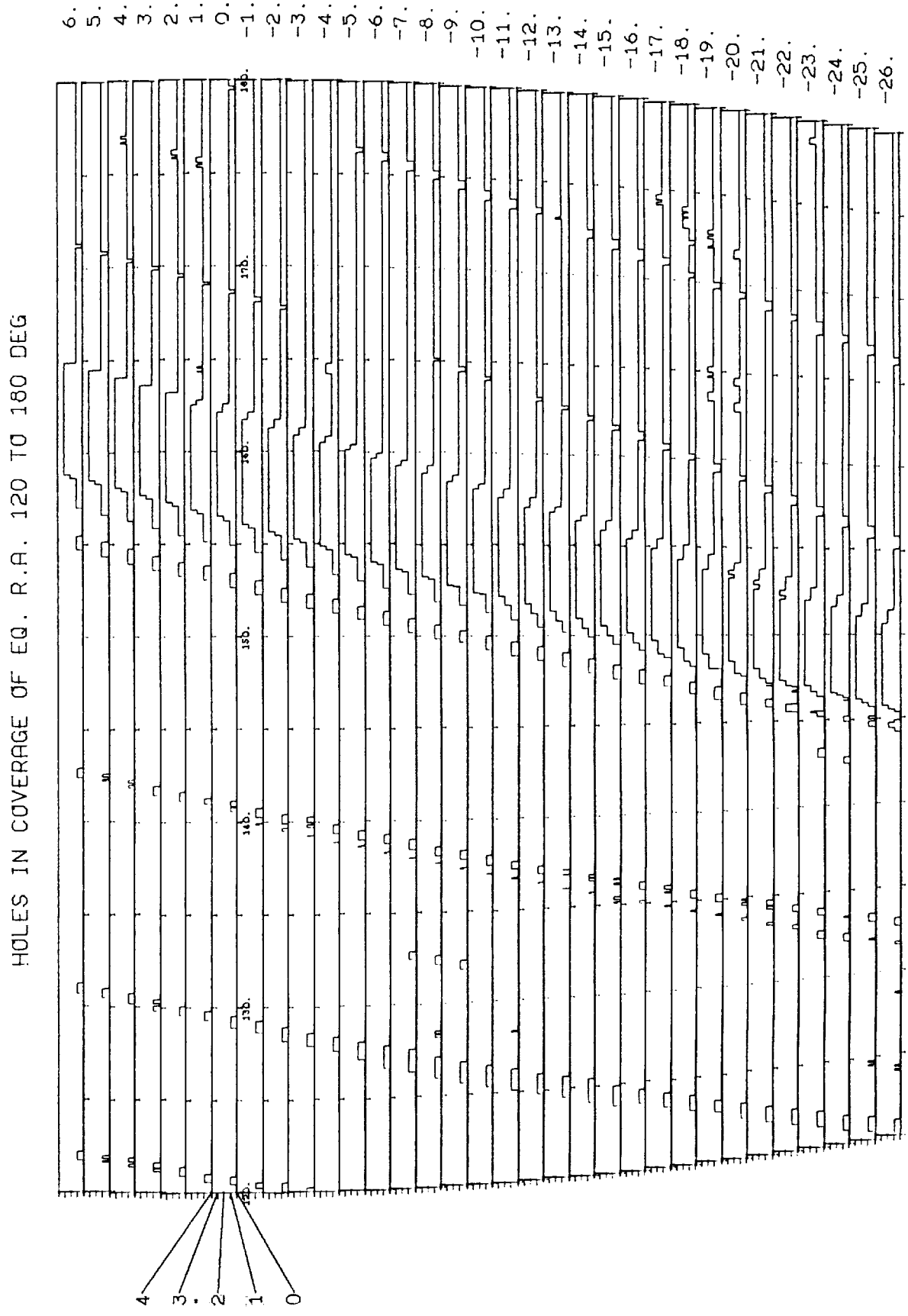

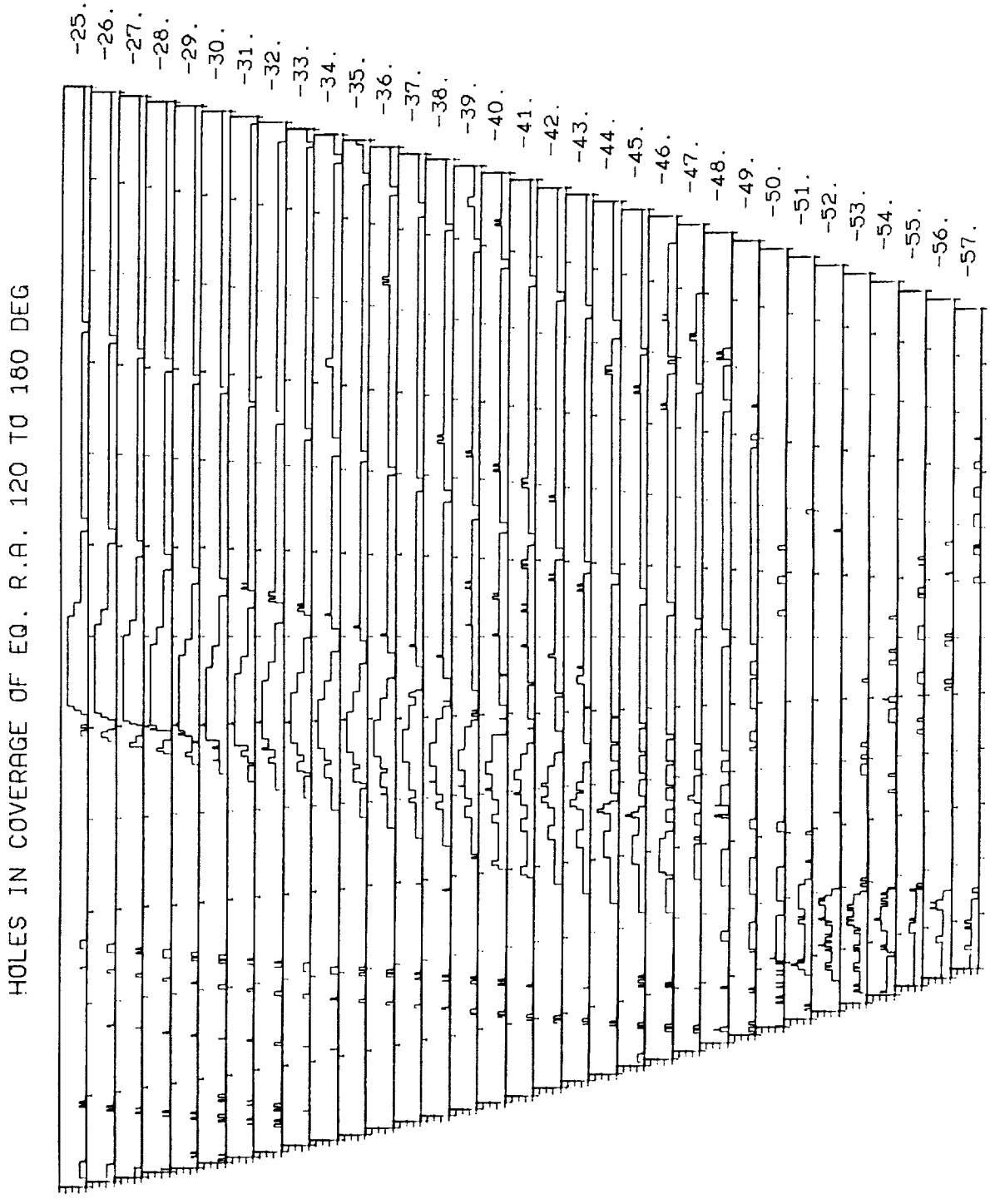

HOLES IN COVERAGE OF EQ. R.A. 120 TO 180 DEG

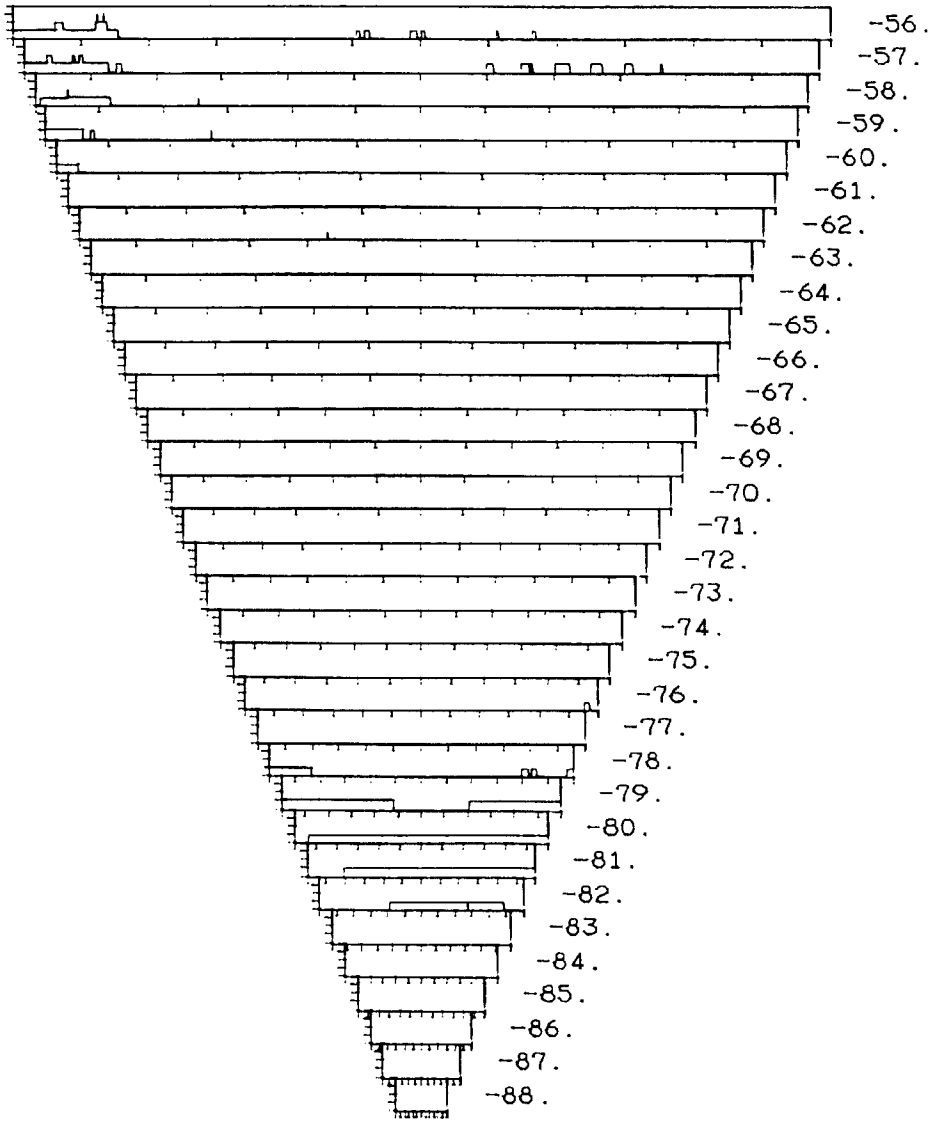

IRAS SURVEY THROUGH 22 NOV 83
HOLES IN COVERAGE OF EQ. R.A. 180 TO 240 DEG

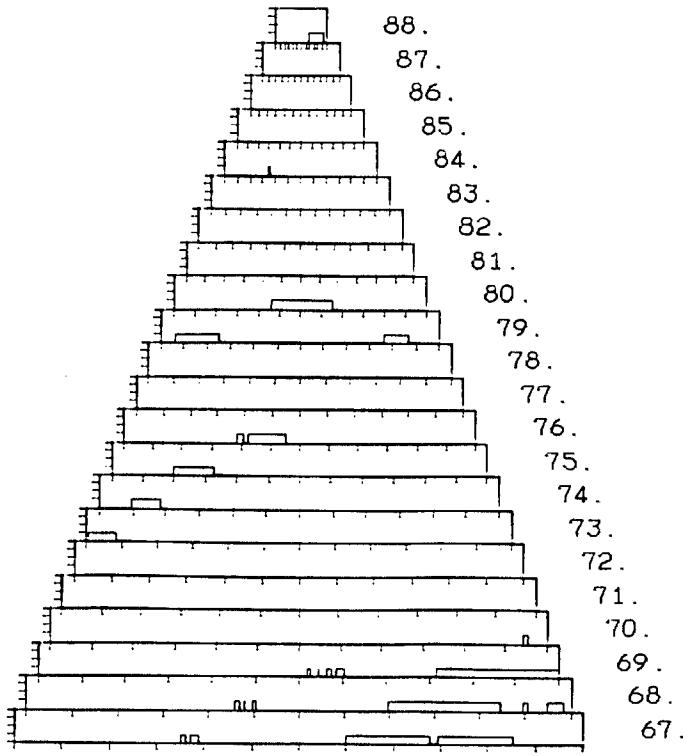

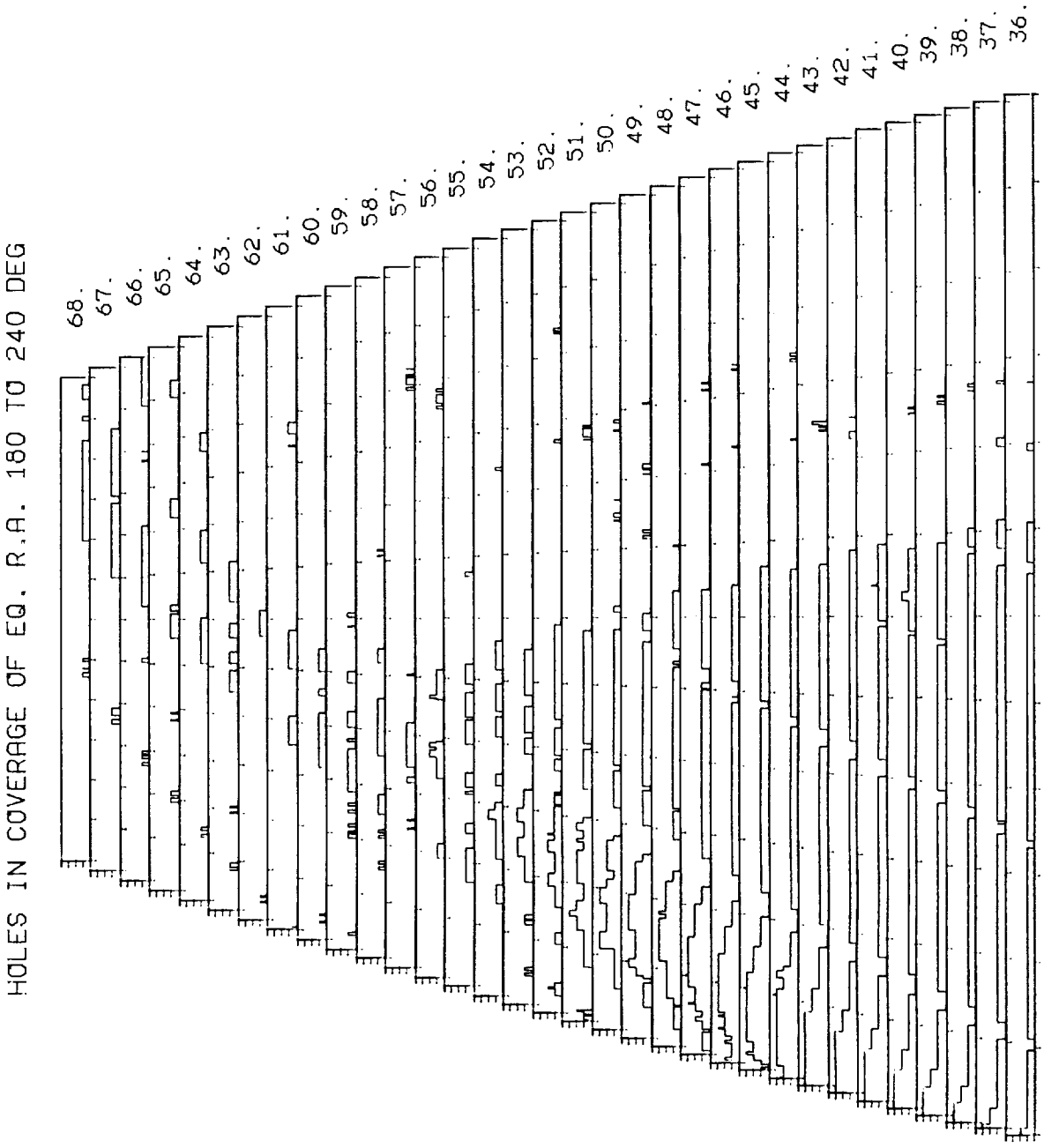

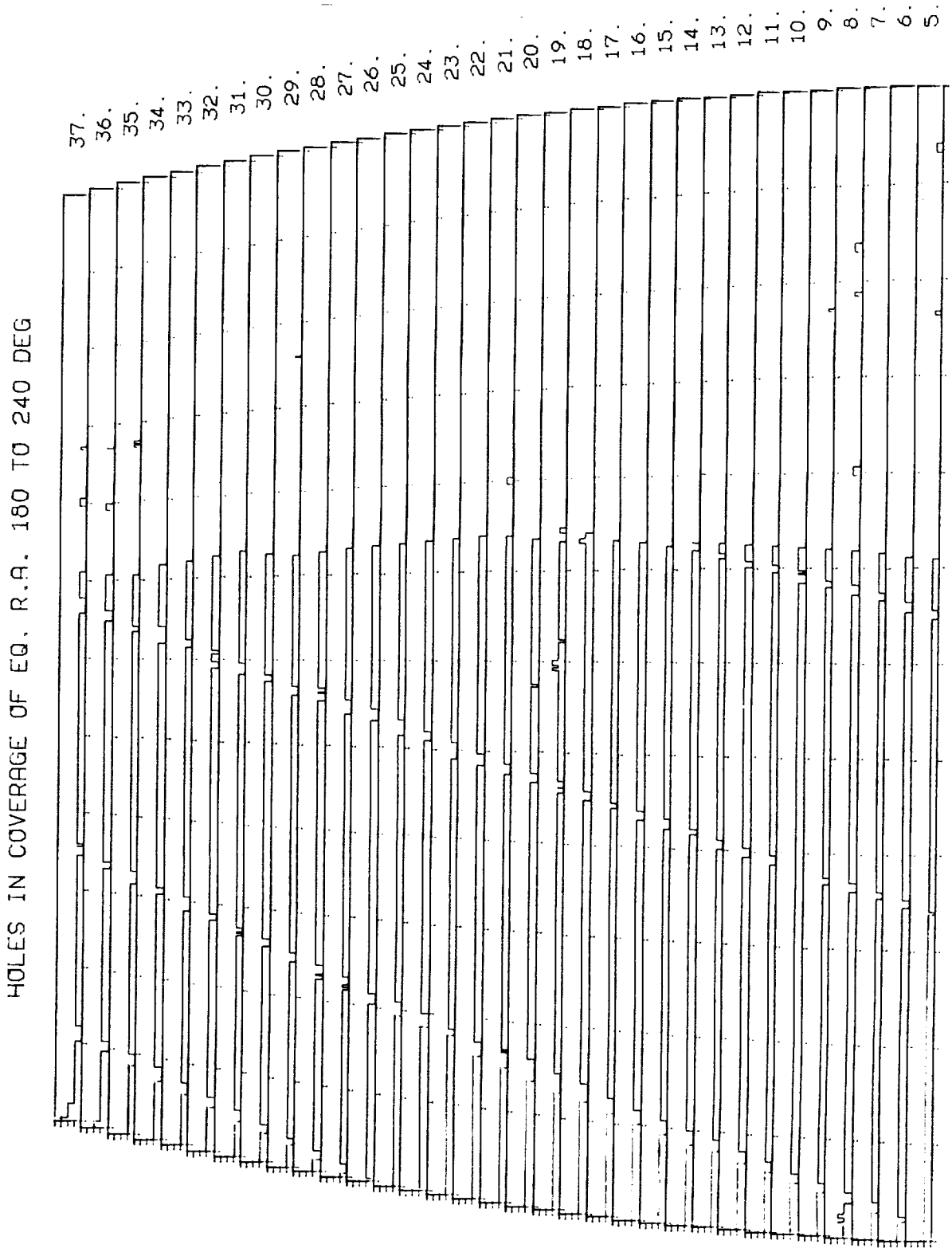

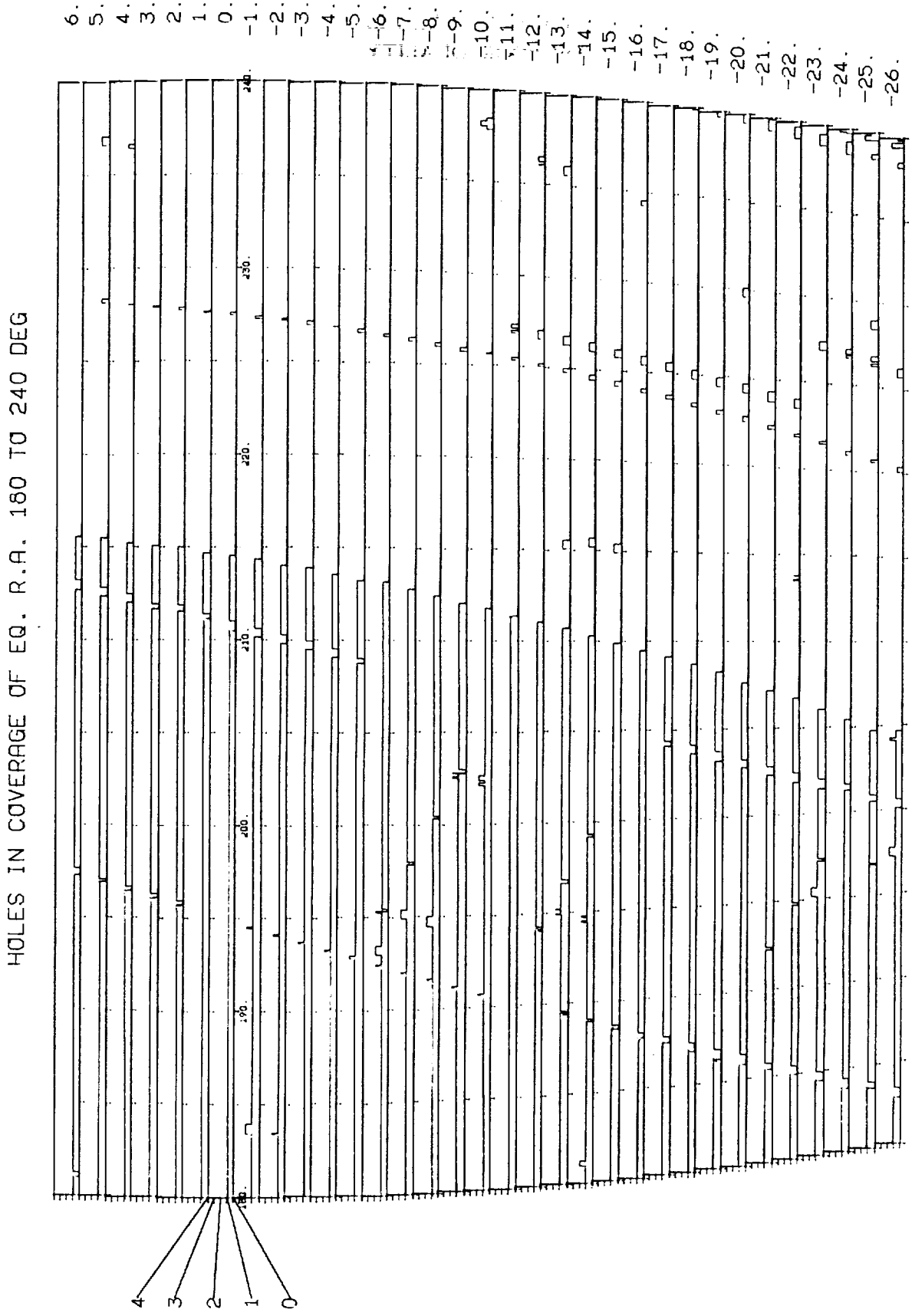

ORIGINAL PAGE IS
OF POOR QUALITY

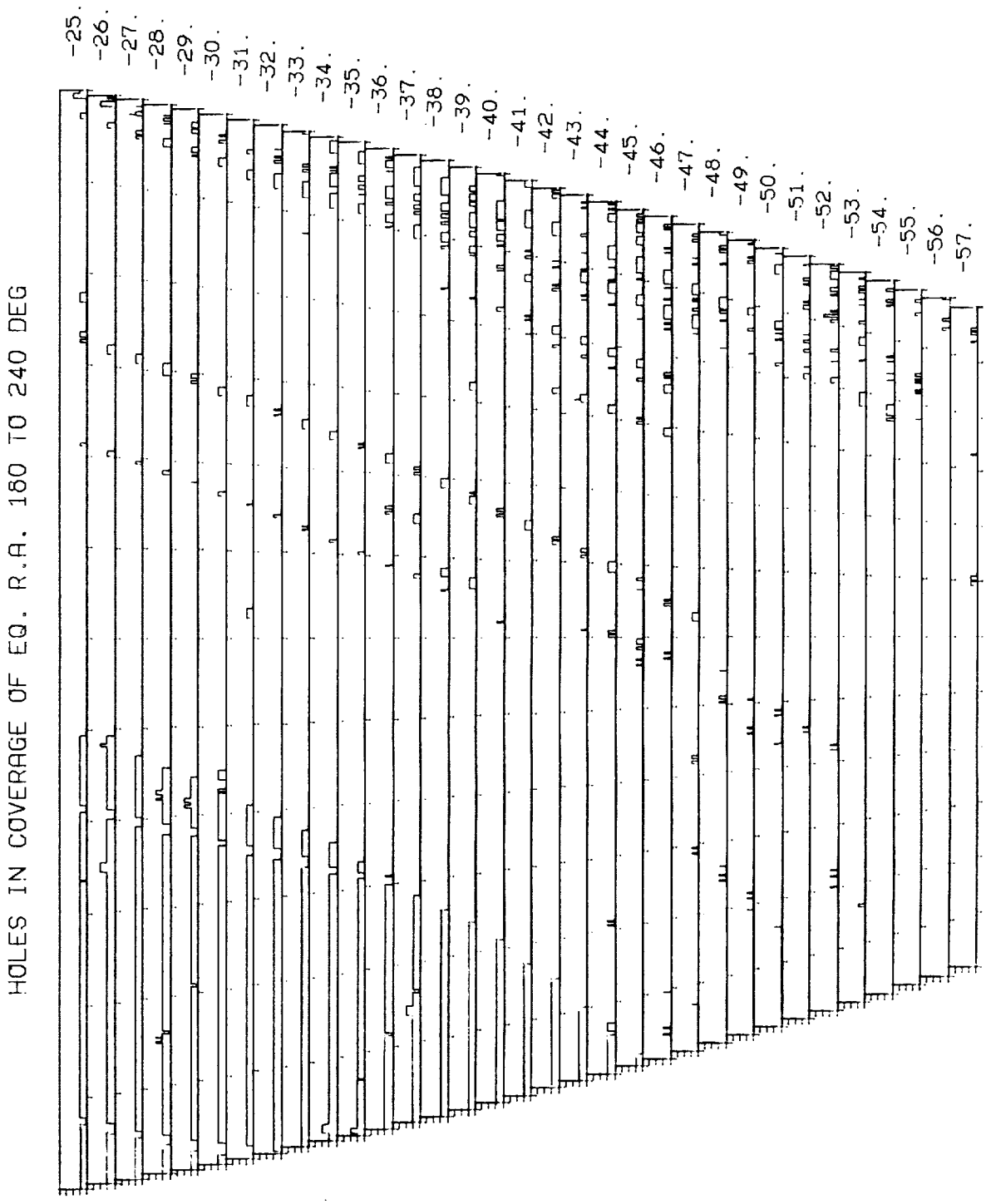

ORIGINAL PAGE IS
OF POOR QUALITY

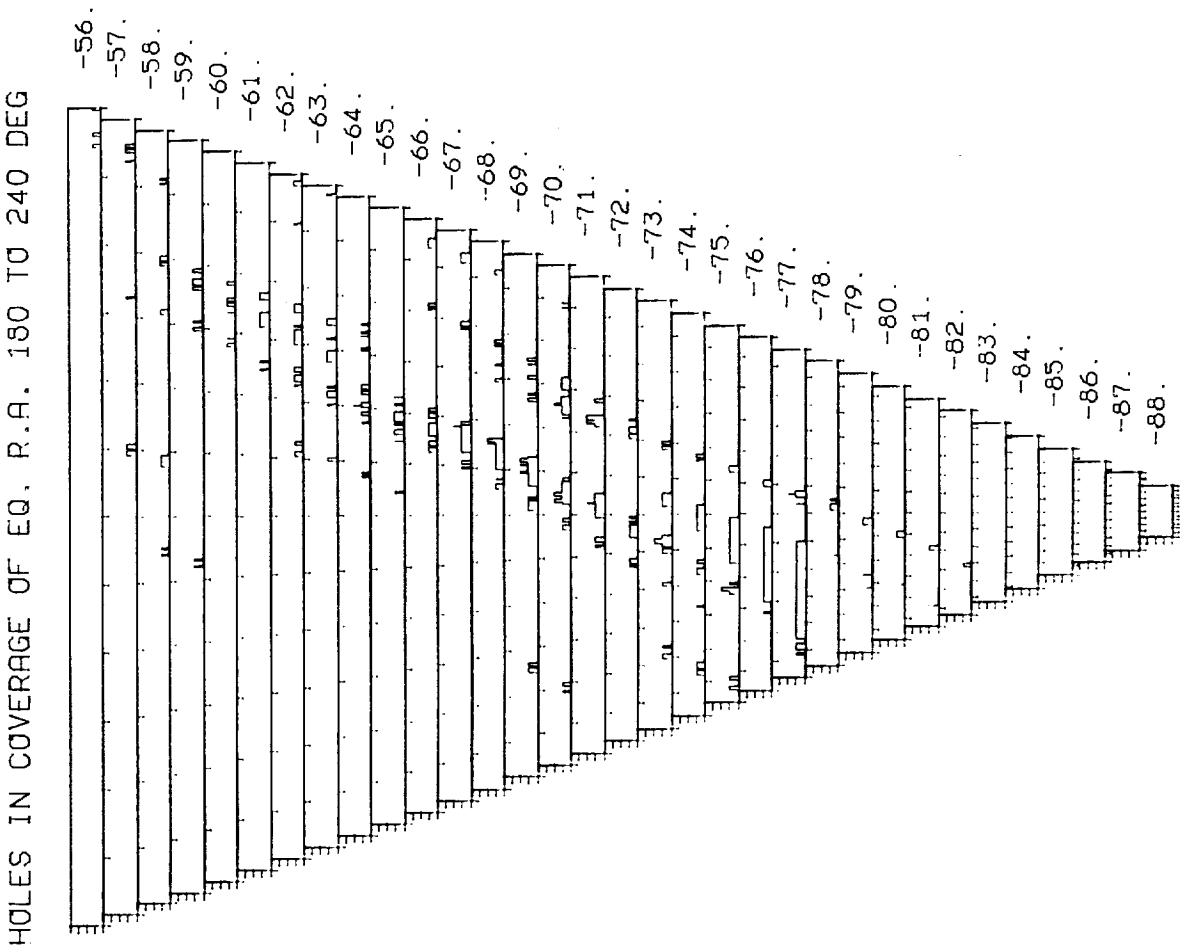

IRAS SURVEY THROUGH 22 NOV 83
HOLES IN COVERAGE OF EQ. R.A. 240 TO 300 DEG

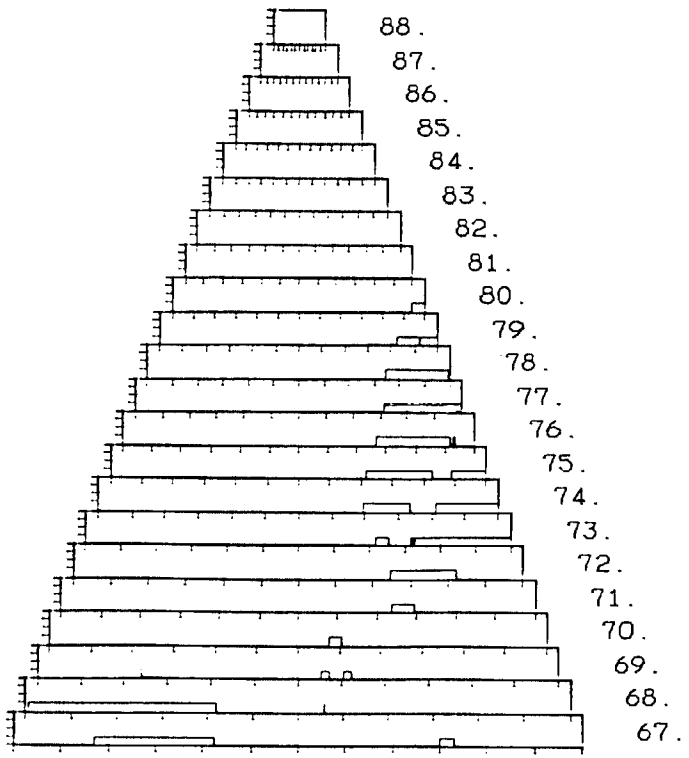

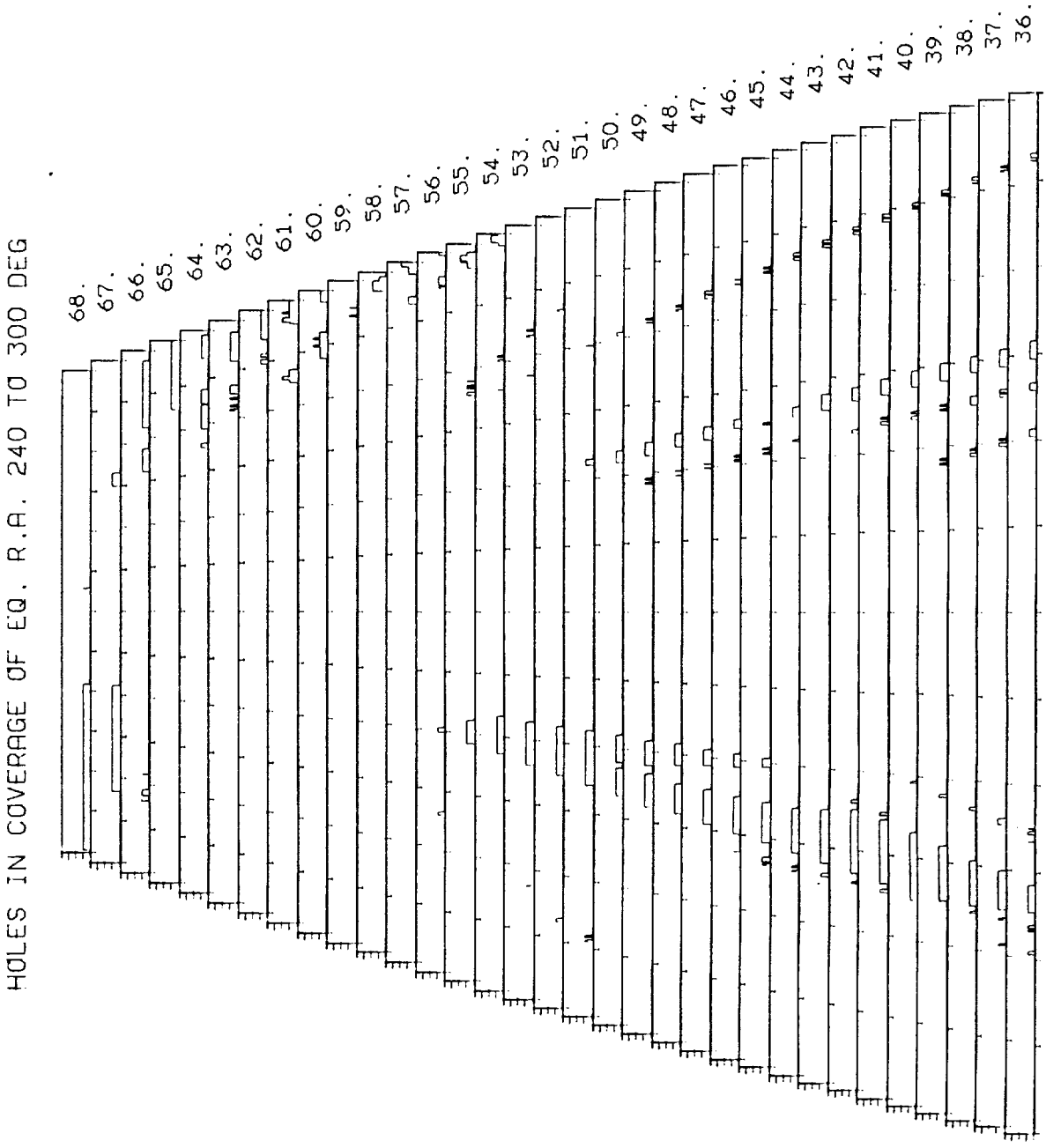

ORIGINAL PAGE IS
OF POOR QUALITY

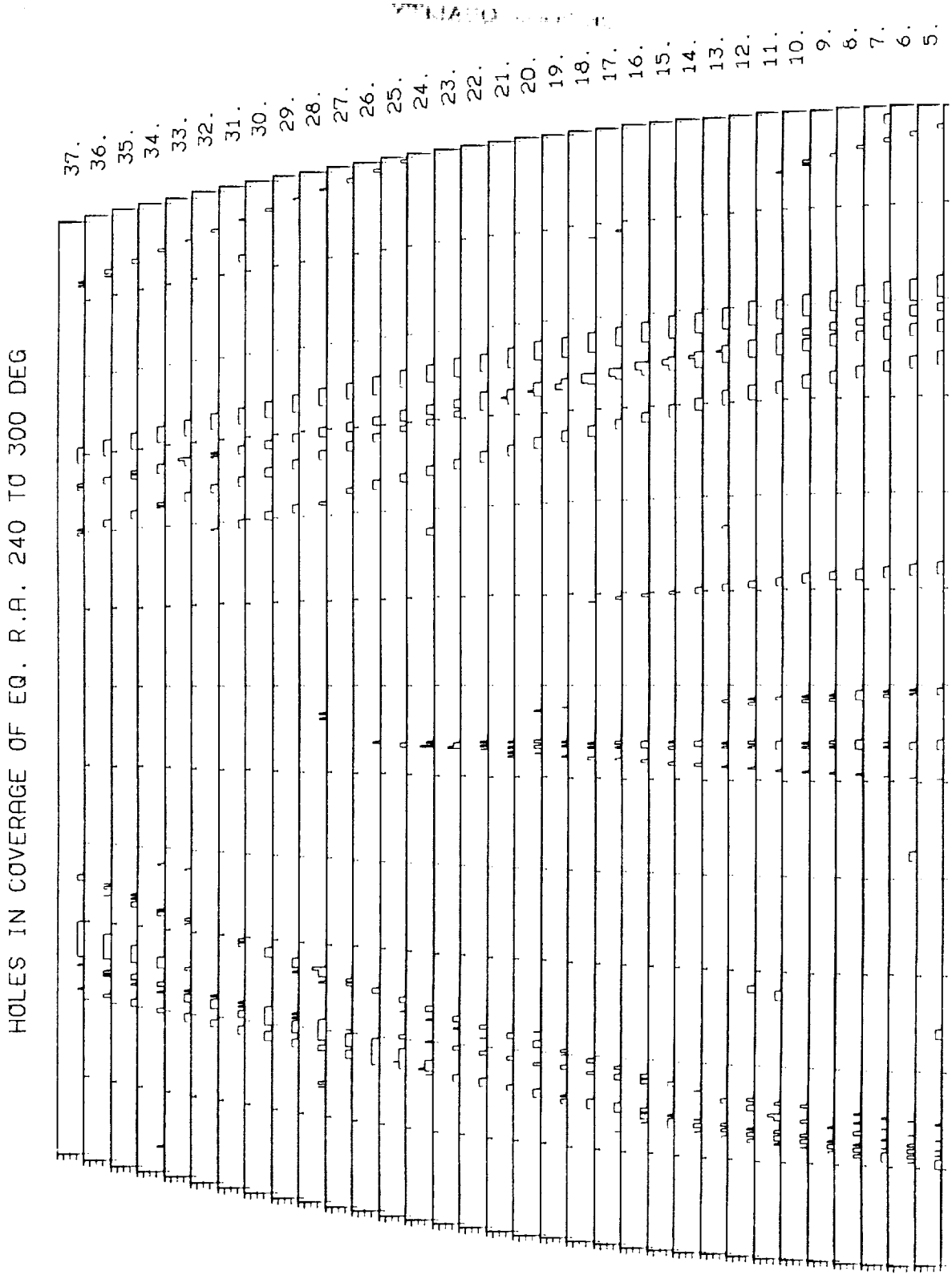

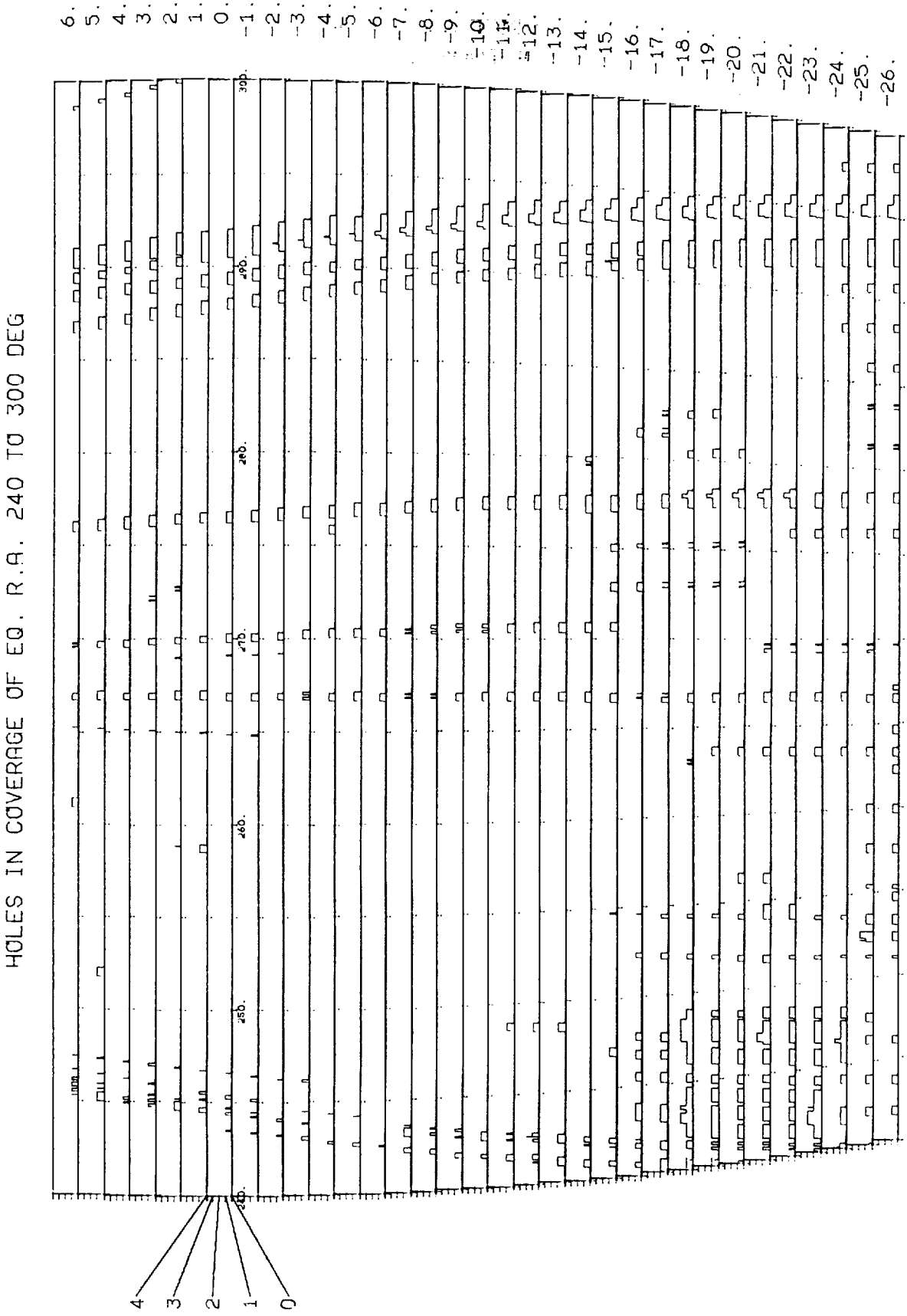
HOLES IN COVERAGE OF EQ. R.A. 240 TO 300 DEG
6.
5.
4.
3.
2.
1.
0.
-1.
-2.
-3.
-4.
-5.
-6.
-7.
-8.
-9.
-10.
-11.
-12.
-13.
-14.
-15.
-16.
-17.
-18.
-19.
-20.
-21.
-22.
-23.
-24.
-25.
-26.
4
3
2
1
0

ORIGINAL PAGE IS
OF POOR QUALITY

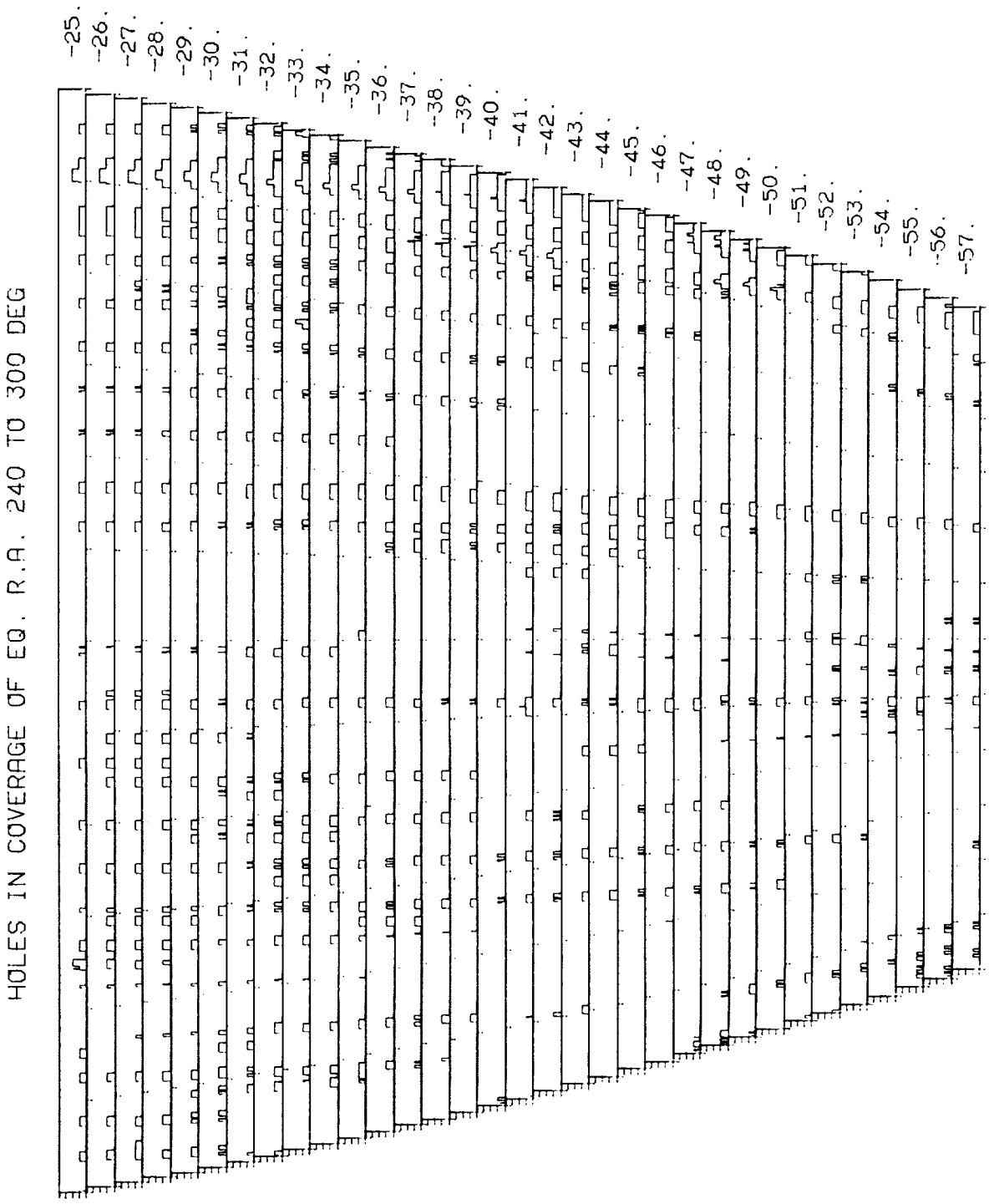

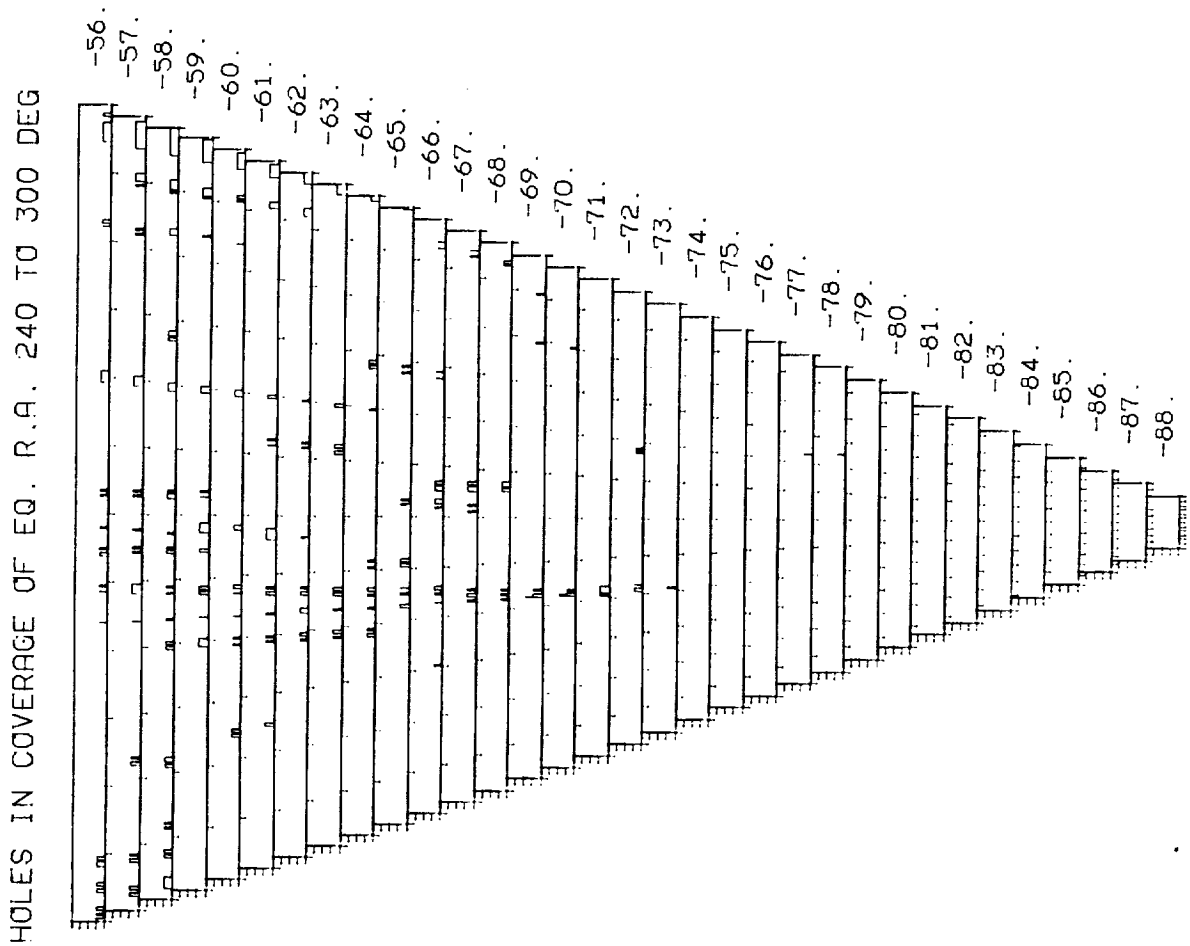

IRAS SURVEY THROUGH 22 NOV 83
HOLES IN COVERAGE OF EQ. R.A. 300 TO 360 DEG

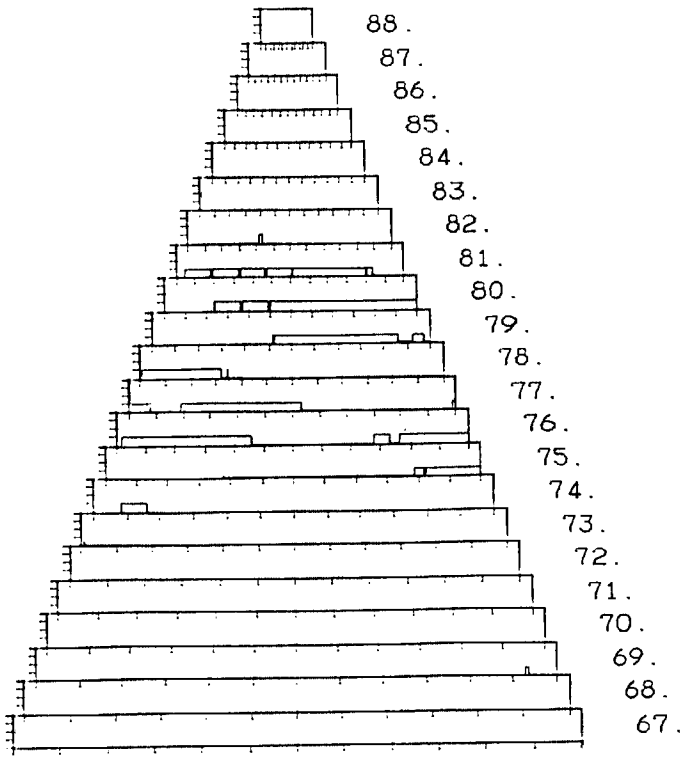

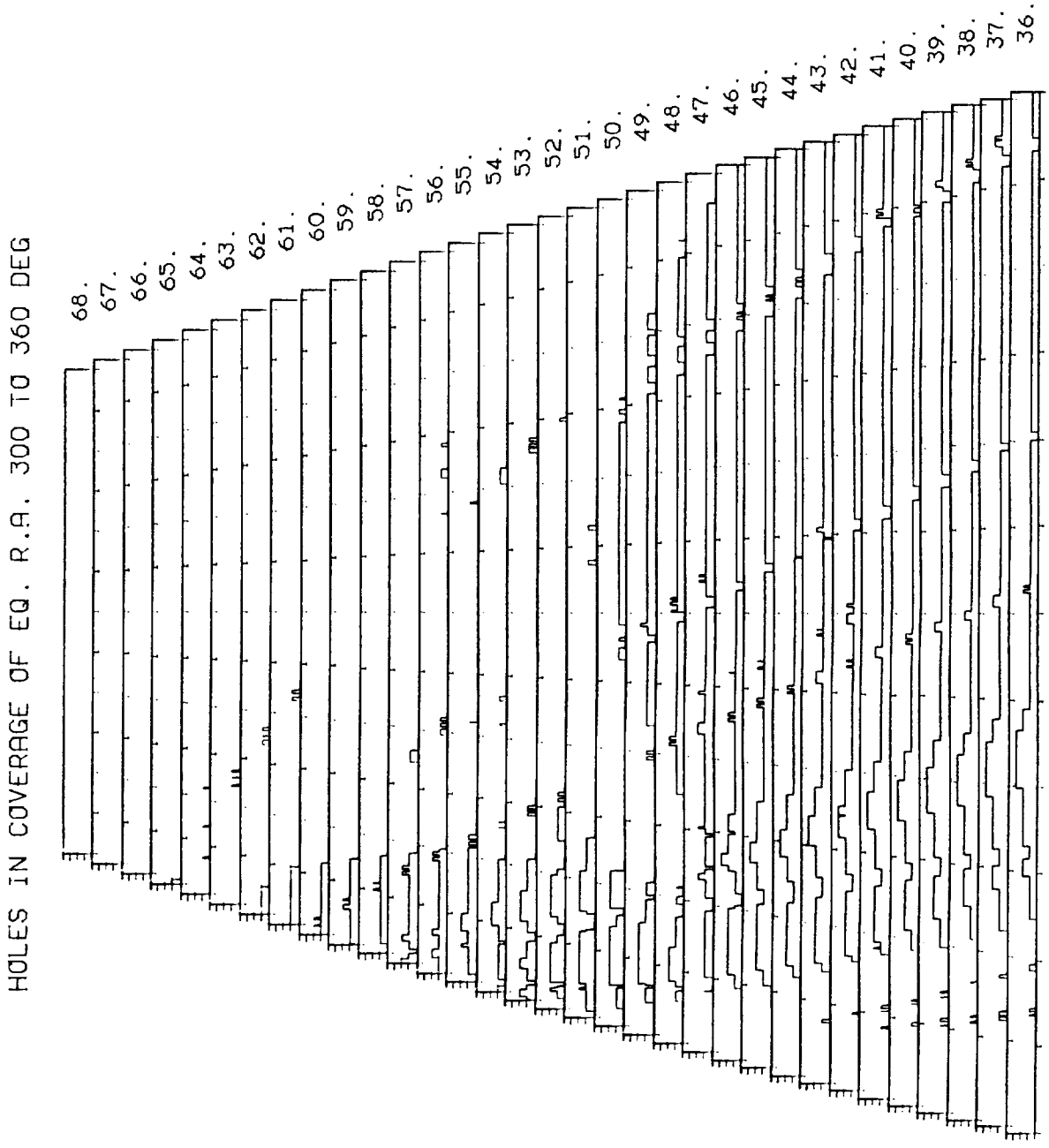

ORIGINAL PAGE IS
OE POOR QUALITY

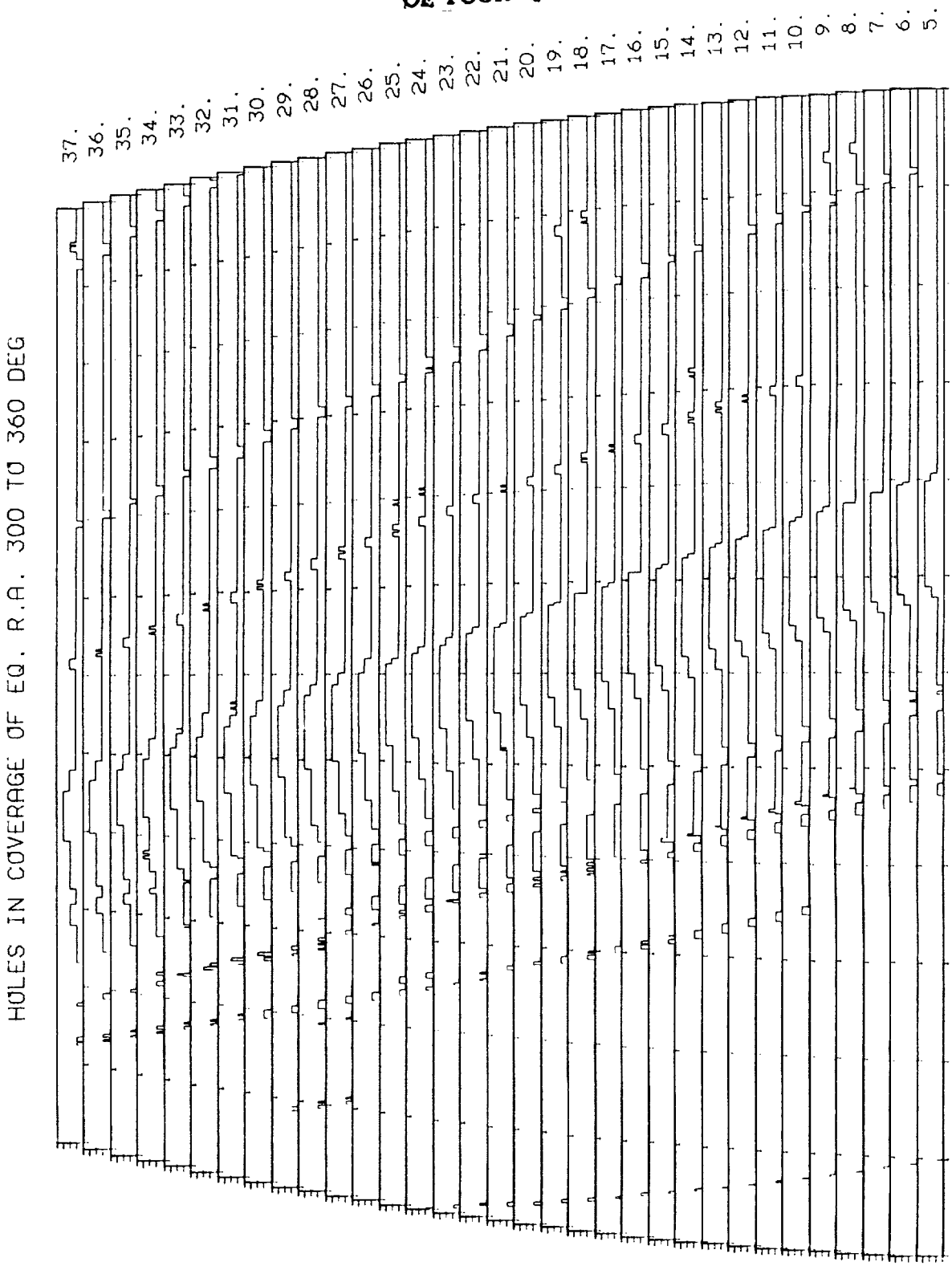

ORIGINAL PAGE IS
OF POOR QUALITY

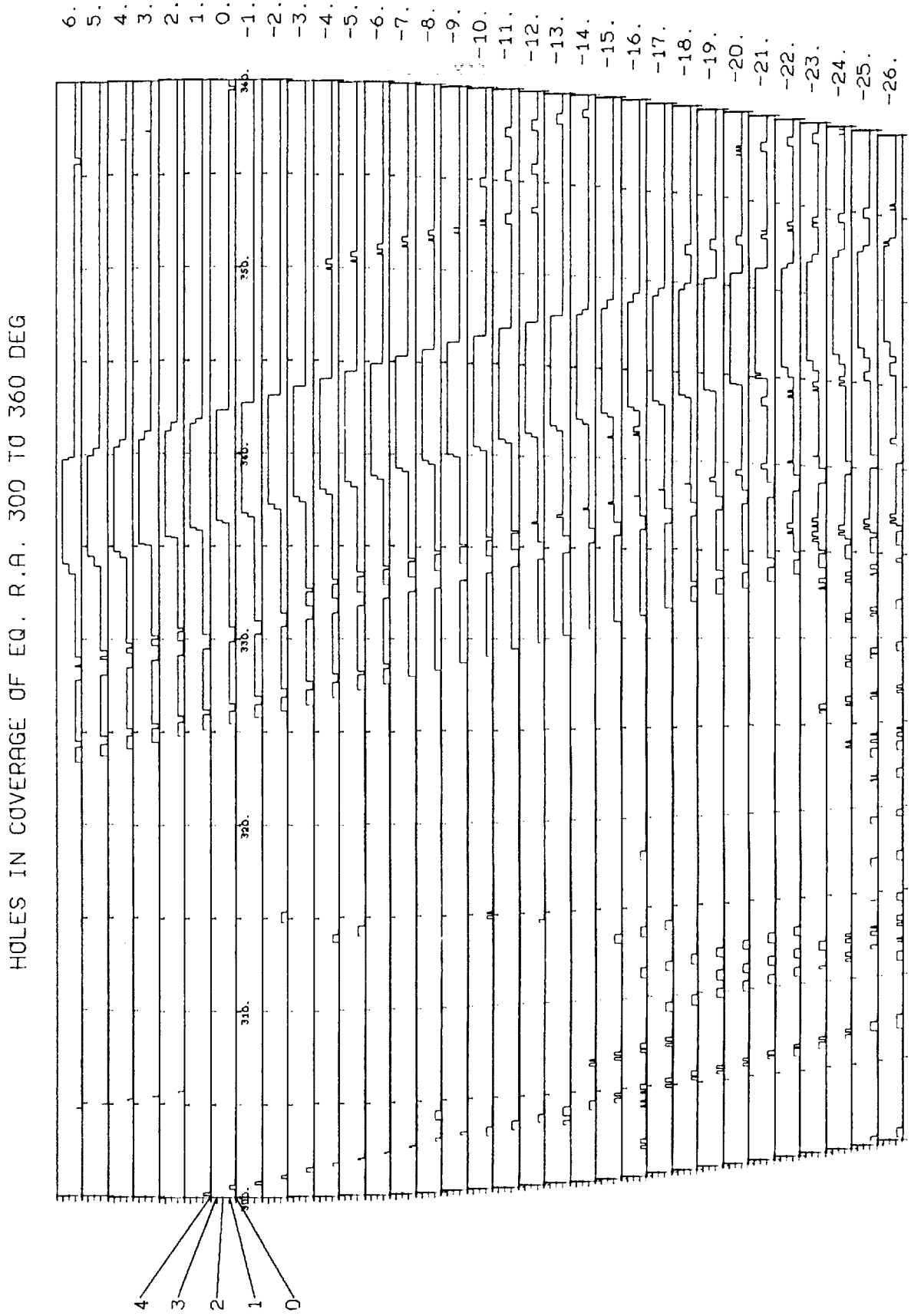

ORIGINAL PAGE IS
OF POOR QUALITY

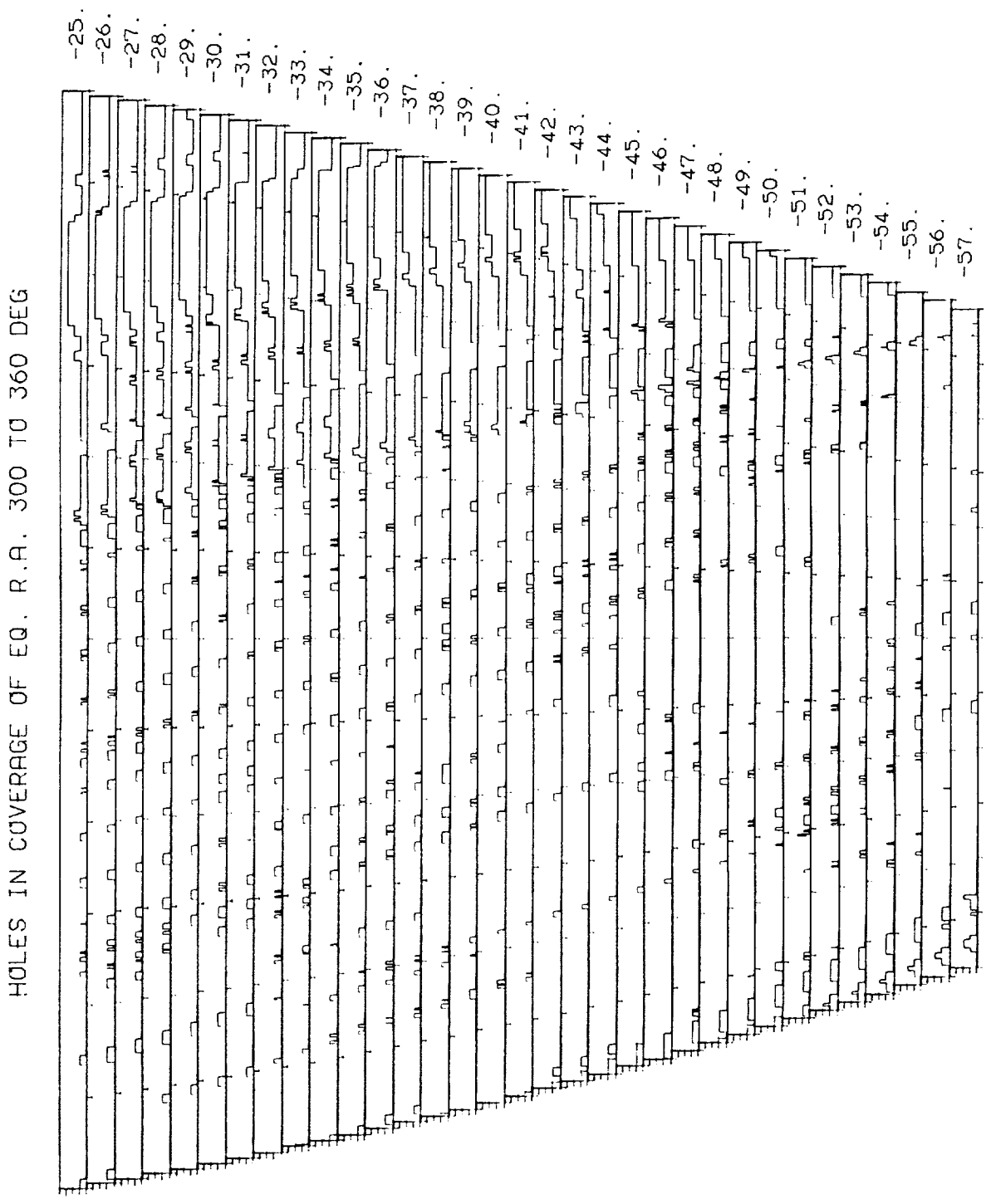

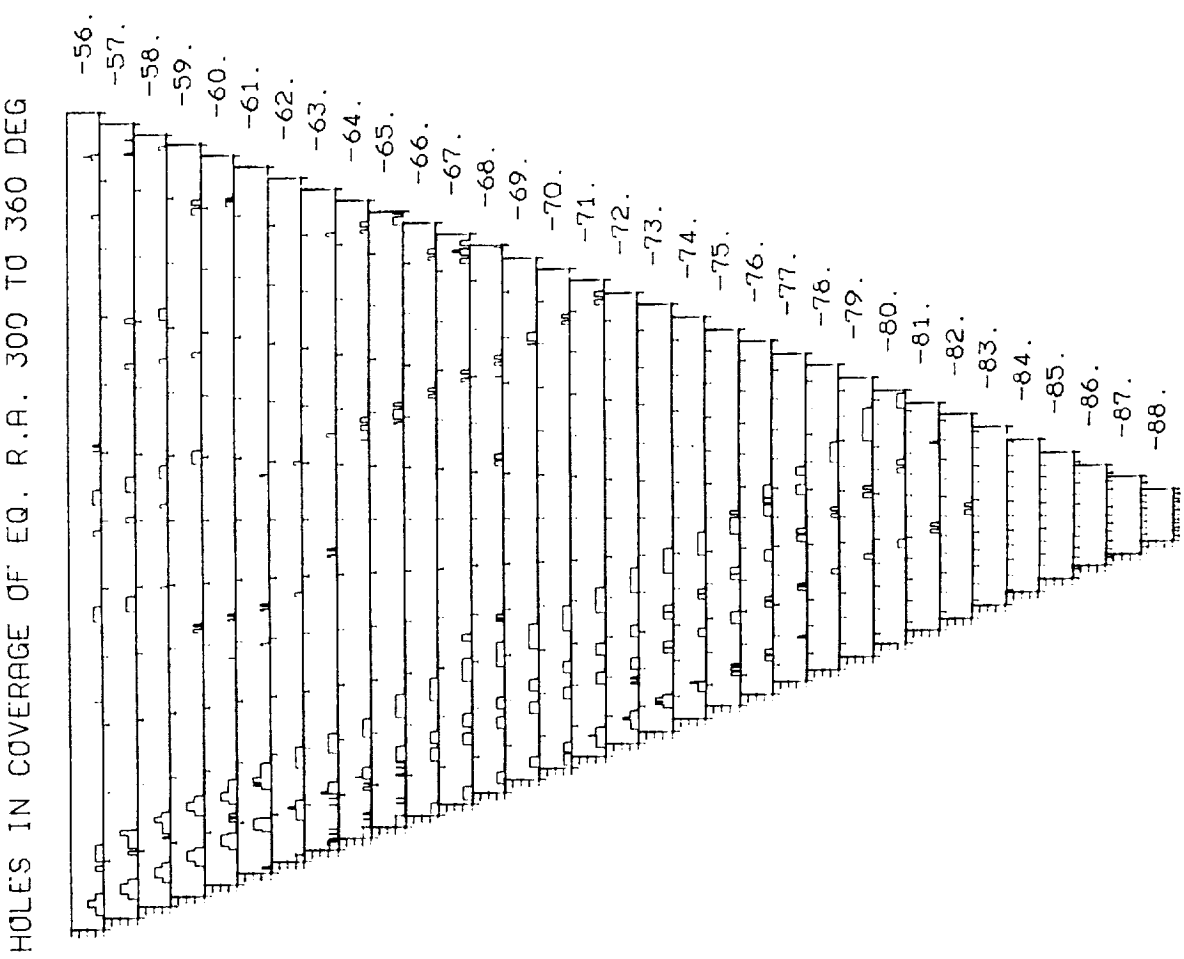

XV. INDEX

Note: Some topics discussed in Chapter XII (Errata) may not appear in this Index.

A

E

F

L

M

N

O

P

R

S

T

Z

NASA National Aeronautics and Space Administration

Report Documentation Page

1. Report No.	2. Government Accession No.	3. Recipient's Catalog No.
NASA RP-1190 volume 1		

4. Title and Subtitle
Infrared Astronomical Satellite (IRAS) Catalogs and Atlases

Volume 1 Explanatory Supplement

5. Report Date
1988

6. Performing Organization Code

7. Author(s)
C.A. Beichman, G. Neugebauer,* H.J. Habing,**
P.E. Clegg,*** and T.J. Chester, editors

8. Performing Organization Report No.

10. Work Unit No.

9. Performing Organization Name and Address
Jet Propulsion Laboratory
Pasadena, CA 91109

11. Contract or Grant No.

13. Type of Report and Period Covered
Reference Publication

12. Sponsoring Agency Name and Address
Office of Space Science and Applications, Astrophysics Division
National Aeronautics and Space Administration
Washington, DC 20546

14. Sponsoring Agency Code

15. Supplementary Notes
*California Institute of Technology, Pasadena, Calif.
**Sterrewacht, Leiden, The Netherlands
***Queen Mary College, London, United Kingdom

16. Abstract

The Infrared Astronomical Satellite (IRAS) was launched on January 26, 1983. During its 300-day mission, IRAS surveyed over 96% of the celestial sphere at four infrared wavelengths, centered approximately at 12, 25, 60, and 100 microns.

Volume 1 describes the instrument, the mission, and data reduction. Volumes 2-6 present the observations of the approximately 245,000 individual point sources detected by IRAS; each volume gives sources within a specified range of declination. Volume 7 gives the observations of the approximately 16,000 sources spatially resolved by IRAS and smaller than 8'.

17. Key Words (Suggested by Author(s))		18. Distribution Statement
astronomy	interstellar matter	Unclassified - Unlimited
infrared	IRAS	
all-sky survey	cosmology	Subject Category 90
galaxies	catalogs	
star formation	stars	

19. Security Classif. (of this report)	20. Security Classif. (of this page)	21. No. of pages	22. Price
Unclassified	Unclassified	462	A01 A18

NASA FORM 1626 OCT 86

For sale by the National Technical Information Service, Springfield, VA 22161

TABLE Suppl.VI.C.6 Color Correction Factors, K[1]

INTRINSIC POWER LAW[2]	RATIO OF FLUX DENSITIES BEFORE COLOR-CORRECTION			CORRECTION FACTOR			
α	$\frac{f_\nu(12\ \mu m)}{f_\nu(25\ \mu m)}$	$\frac{f_\nu(25\ \mu m)}{f_\nu(60\ \mu m)}$	$\frac{f_\nu(60\ \mu m)}{f_\nu(100\mu m)}$	K(12 μm)	K(25 μm)	K(60 μm)	K(100 μm)
-3.0	0.113	0.063	0.21	0.91	0.89	1.02	1.02
-2.5	0.162	0.102	0.275	0.92	0.91	1.00	1.01
-2.0	0.232	0.164	0.355	0.94	0.93	0.99	1.00
-1.5	0.333	0.262	0.460	0.97	0.96	0.99	1.00
-1.0	0.480	0.417	0.600	1.00	1.00	1.00	1.00
-0.5	0.694	0.662	0.786	1.04	1.04	1.02	1.00
0.0	1.005	1.045	1.037	1.10	1.10	1.05	1.01
0.5	1.459	1.642	1.378	1.17	1.16	1.09	1.02
1.0	2.123	2.567	1.843	1.25	1.23	1.15	1.04
1.5	3.094	3.992	2.484	1.35	1.32	1.23	1.06
2.0	4.519	6.170	3.373	1.47	1.41	1.32	1.09
2.5	6.610	9.480	4.617	1.61	1.53	1.44	1.12
3.0	9.681	14.475	6.370	1.78	1.67	1.59	1.16

INTRINSIC	RATIO OF FLUX DENSITIES BEFORE COLOR-CORRECTION			CORRECTION FACTOR			
TEMP (K)	$\frac{f_\nu(12\ \mu m)}{f_\nu(25\ \mu m)}$	$\frac{f_\nu(25\ \mu m)}{f_\nu(60\ \mu m)}$	$\frac{f_\nu(60\ \mu m)}{f_\nu(100\ \mu m)}$	K(12 μm)	K(25 μm)	K(60 μm)	K(100 μm)
10000	4.345	6.050	3.350	1.45	1.41	1.32	1.09
5000	4.172	5.931	3.327	1.43	1.40	1.32	1.09
4000	4.086	5.872	3.316	1.42	1.40	1.31	1.09
3000	3.944	5.773	3.297	1.41	1.39	1.31	1.09
2000	3.666	5.578	3.259	1.38	1.38	1.31	1.09
1000	2.891	5.005	3.145	1.27	1.34	1.29	1.08
800	2.545	4.730	3.088	1.22	1.32	1.28	1.08
600	2.036	4.287	2.995	1.15	1.29	1.27	1.08
500	1.692	3.950	2.920	1.09	1.26	1.26	1.08
400	1.272	3.478	2.810	1.01	1.22	1.24	1.08
300	0.785	2.780	2.630	0.92	1.15	1.21	1.07
290	0.734	2.693	2.606	0.91	1.15	1.21	1.07
280	0.684	2.602	2.580	0.90	1.14	1.20	1.07
270	0.633	2.506	2.553	0.89	1.13	1.20	1.07
260	0.583	2.407	2.523	0.88	1.12	1.19	1.07
250	0.534	2.304	2.491	0.87	1.11	1.19	1.07
240	0.486	2.196	2.457	0.86	1.09	1.18	1.07
230	0.438	2.084	2.420	0.85	1.08	1.18	1.07
220	0.392	1.967	2.381	0.85	1.07	1.17	1.07
210	0.347	1.845	2.338	0.84	1.06	1.16	1.06
200	0.304	1.719	2.291	0.83	1.04	1.16	1.06
190	0.263	1.589	2.240	0.83	1.02	1.15	1.06
180	0.224	1.455	2.184	0.83	1.01	1.14	1.06
170	0.188	1.317	2.124	0.83	0.99	1.13	1.06
160	0.154	1.176	2.057	0.84	0.97	1.12	1.06
150	0.124	1.034	1.983	0.85	0.95	1.11	1.05
140	0.097	0.892	1.901	0.87	0.93	1.09	1.05
130	0.073	0.751	1.810	0.90	0.91	1.08	1.05
120	0.053	0.614	1.709	0.94	0.89	1.06	1.04
110	0.036	0.484	1.595	1.01	0.86	1.04	1.04
100	0.023	0.363	1.468	1.12	0.84	1.02	1.04
95	0.018	0.307	1.400	1.19	0.83	1.01	1.03
90	0.014	0.256	1.326	1.28	0.83	1.00	1.03
85	0.010	0.208	1.249	1.39	0.82	0.99	1.03
80	0.007	0.165	1.168	1.54	0.81	0.97	1.02
75	0.005	0.127	1.082	1.74	0.81	0.96	1.02
70	0.003	0.095	0.993	2.01	0.81	0.95	1.01
65	0.002	0.067	0.898	2.40	0.82	0.94	1.01
60	0.001	0.045	0.801	2.97	0.83	0.93	1.00
55	---	0.028	0.700	3.86	0.86	0.92	1.00
50	---	0.016	0.597	5.35	0.90	0.91	0.99
45	---	0.008	0.493	8.09	0.97	0.92	0.98
40	---	0.003	0.391	13.79	1.08	0.93	0.98

[1] f_{ν_o}[actual] = f_{ν_o}[quoted]/K (See Suppl.VI.C.3); spectral response given in Table Suppl.II.C.5.

[2] $f_\nu = \nu^\alpha$